Investigating the interactions between fluvial processes and floodplain forest ecology in the Amazon basin

Submitted by Simon Buckley, to the University of Exeter as a thesis for the degree of Doctor of Philosophy in Geography, September 2014.

Abstract

Amazonian tropical forests account for 20-50% of global primary productivity and up to 40% of carbon stored in terrestrial biomass (Phillips et al., 1998). The Amazon is also home to the Earth's largest river system, accounting for approximately 20% of the world's total river discharge (Richey et al., 1989). Despite the clear global significance of the Amazon basin, substantial uncertainties remain in terms of both aboveground wood biomass and carbon storage within its extensive forests (Houghton et al., 2001), and the functioning of its river systems, particularly in terms of floodplain inundation (Wilson et al., 2007).

This thesis addresses the aforementioned uncertainties through providing new insight into the interaction between fluvial processes and Amazonian floodplain varzea forests, for the Beni floodplain in north east Bolivia. Flood inundation dynamics for the Beni floodplain are quantified through application of a 1D-2D hydraulic model code, with topographical forcing provided through bare earth DEMs derived from the SRTM global elevation dataset (Farr and Kobrick, 2000). Subsequently, in the final part of the thesis, aboveground wood biomass estimates are generated for the Beni floodplain, through extrapolation of plot scale inventory measurements with respect to spatially distributed remote sensing datasets. These estimates are subsequently integrated with modelled flood inundation and maps depicting Beni river channel migration, in order to explore the influence which fluvial processes exert upon aboveground wood biomass storage in varzea forest stands.

Overall, results presented within this thesis quantitatively demonstrate that fluvial processes, specifically flood inundation and lateral channel migration, exert significant impacts upon aboveground biomass storage within Beni floodplain forests. Furthermore, as a result of these influences, aboveground wood biomass storage within Beni floodplain forests is substantially lower than would be expected based upon published estimates for varzea forests across the Amazon (Baker et al., 2004; Saatchi et al., 2007). This implies that systematic overestimation of aboveground wood biomass storage for Amazonian varzea forests may constitute a significant source of uncertainty in basin scale biomass estimates.

Acknowledgements

I would like to thank my supervisory team Professor Andrew Nicholas, Dr Luiz Aragao and Professor Rolf Aalto for their scientific input and advice throughout the course of this PhD research, and also to the NERC grant awarded to the supervisory team for helping to funding the PhD project. I would also like to thank Dr Arved Schwendel, particularly for his contribution to the field work campaign and scientific input into numerous aspects of the work presented here.

I would like to recognise the University of Exeter Geography department laboratory staff, particularly Dr Stephen Haley, Dr Shirley Wynne, Angela Elliot, Natascha Steinberg and Joana Zaragoza-Castells who provided much needed support in the laboratory work undertaken within this project. Special thanks go to the staff of Bala Tours in Rurrenabaque, Bolivia. Without their expertise and knowledge of the Beni floodplain this research would not have been possible.

Further thanks go to Dr Sassan Saatchi of NASA JPL and Professor Stephen Hamilton of Michigan State University, who kindly provided a processed remote sensing datasets which was utilised within this research. In addition I would like to show recognition of the contribution of the Alaska Data Facility, who supplied ALOS PALSAR images which formed an important part of the validation of the flood inundation model. I would also like to thank the Canadian Space Agency, NASA and USGS for useful advice relating to the remote sensing datasets utilised within this research.

Finally I would like to thank my family and friends, particularly my parents Julie and Steve Buckley, for their help and support over the course of this PhD research project.

Contents

List of Figures

Chapter Four

Chapter Five

Chapter Six

List of Tables

Chapter Seven

Chapter One

Introduction

1. Introduction

1.1 The Amazon basin

The Amazon basin covers a total area of 6.7 million km^2 of South America, constituting approximately 40% of the total land area of the continent. The western limit of the vast basin is denoted by the Andean Cordhilheira and sub-Andean region, whilst the northern and southern limits are defined by the Guyana and Brazilian Shields respectively (Martinelli et al., 2003). The Amazon river system is contained within the vast basin, with headwaters being located across the Peruvian, Colombian and Brazilian Andes (Hall et al., 2011). The Amazon comprises an extensive network of tributaries, the largest of which include the Madeira, Japura, Purus, Tocantins and the Negro. Indeed in terms of discharge the Negro and Madeira individually constitute the world's fifth and sixth largest rivers respectively (Meade et al., 1991). The Amazon and its first order tributaries are commonly 1 km in width, whilst the maximum width of the main stem is in excess of 6 km (Filizola et al., 2009). Furthermore, as a result of its large drainage network the Amazon is characterised by an average annual flux of water into the Atlantic Ocean of 200,000 m^3/s, constituting approximately 20% of the world's total river discharge (Richey et al., 1989).

Estimates made in 2001 indicate that tropical forests cover an area of approximately 5.4 million km^2 within the Amazon basin, constituting roughly 87% of their original extent prior to widespread anthropogenic influence (Soares-Filho et al., 2006). The Amazon is the largest single tropical forest on earth, comprising greater than 50% of the world's total tropical forested area (Metcalfe et al., 2010). Tropical forests are highly significant in terms of the global carbon cycle (Luyssaert et al., 2007), having been shown to account for 20-50% of global primary productivity and up to 40% of carbon stored in terrestrial biomass (Phillips et al., 1998). Accordingly, quantifying the storage and assimilation of above ground wood biomass and carbon within Amazonia is of a high level of global significance.

Despite the clear importance of the Amazon basin in terms of the global hydrological cycle, significant uncertainties remain with regards to the functioning of Amazonian river systems, particularly the annual inundation of its extensive floodplains (Wilson et al., 2007; Hall et al., 2011). Substantial

uncertainties also remain concerning the storage of biomass and carbon within Amazonian tropical forests (Houghton et al., 2001; Saatchi et al., 2007), despite their recognised importance within the global carbon cycle. Particularly uncertain is the functioning of the ecosystems in which the two aforementioned areas of research intersect; Amazonian floodplain forests, known widely as varzea (Junk et al., 1989). Therefore the inundation dynamics of Amazonian floodplains, along with the storage of biomass and carbon within varzea forests represent the primary focus of this PhD research project. The following review documents the previous work which has been undertaken within the aforementioned areas of research and identifies the key uncertainties which will be addressed within this thesis.

1.2 Interaction of rivers and floodplains within the Amazon basin

Amazonian floodplains primarily consist of alluvial deposits from the late Pleistocene and Holocene (Hamilton et al., 2004), whilst land cover is dominated by evergreen forest and open savannas. Unlike other floodplains worldwide, which are commonly highly populated and heavily modified through human activity, Amazon floodplains are relatively pristine and tend to retain their natural hydrological characteristics (Junk et al., 1989). As a result of a number of factors, primarily precipitation patterns, discharge characteristics and low longitudinal slopes (Richey et al., 1989), inundation of Amazonian floodplains generally occurs through an annual flood pulse (Junk, 1989). This flood pulse is characterised by an annual period of prolonged inundation of considerable depth over a vast area of the floodplain. Indeed, within central Amazonia the average amplitude of water levels is approximately 10 m (Junk et al., 1997), with flood inundation persisting for up to 230 days per year. Consequently, floodplains within the Amazon basin are characterised by the occurrence of distinct aquatic and terrestrial phases during the course of a single year (Junk, 1983). Through utilisation of GRACE data, Alsdorf et al., (2010) estimated that approximately 5% of the overall discharge of the Amazon river has been routed through floodplains.

It is widely acknowledged that floodplains represent significant components of fluvial systems (Vannote et al., 1980). This is particularly true for the Amazon basin, which is characterised by a high level of dynamic interaction between its

rivers and their adjacent floodplains (Mertes et al., 1996). Indeed given the high magnitude of river discharges and prolonged residence time of flood waters within Amazonian floodplains during seasonal inundation, interactions between the channel and floodplain attain an increasing significance. It has been shown that numerous active processes, including sedimentation, nutrient uptake through biota and changes in redox conditions (Richey et al., 1989, Mertes et al., 1996, Hamilton et al., 1997) lead to marked biogeochemical changes in Amazon floodwaters whilst they reside upon adjacent floodplains.

Seasonal flood waters also impart a profound effect upon the floodplain through a multitude of processes (Schongart et al., 2007). The high order impact of flooding upon geomorphology means that the maximum inundation extent delineates the floodplain ecosystem (Mertes et al., 1996). Annual inundation also exerts an influence over fauna and flora (Junk, 1989), specifically plant productivity (Wittmann et al., 2004), nutrient dynamics (Melack and Forsberg, 2001), sedimentation (Dunne et al., 1998; Aalto et al., 2003) and the carbon cycle (Richey et al., 2002, Melack et al., 2004), whilst also being central to human occupation and land use (Junk et al., 2000) . In terms of ecological functioning, the seasonal timing, predictability and interannual variability of the flood pulse is particularly important, as these characteristics are responsible for the magnitude of disturbance experienced within the floodplain ecosystem (Lewis et al., 2000).

In summation it is clear that rivers and floodplains are closely linked within the context of Amazonia, where the high magnitude, wide extent and extended duration of inundation enhances the interdependence of these systems. However despite the significance of inundation within Amazonian floodplains, at present the spatial and temporal dynamics of flooding are not well quantified (Wilson et al., 2007).

1.3 Amazon floodplain inundation dynamics

Alsdorf et al., (2007) utilised a unique interferometric JERS-1 SAR dataset in order to observe the dynamics of flood inundation for a portion of the central Amazonian floodplain upstream of the confluence with the Negro river near Manaus. Observations at a previously unprecedented spatial resolution revealed important new insights into the dynamics of flood inundation upon

Amazon floodplains, which were shown to be more complex than previously assumed. Specifically, the significance of localised flows at spatial scales of ~100 m and over time scales of less than 24 hours were shown during the passage of the flood wave through the central Amazon floodplain. Prior to the work of Alsdorf et al., (2007), flow of water within Amazonian floodplains was quantified based upon the assumption that floodplain water levels were equivalent to those within the main channel (Richey et al, 1989). Hence the findings of the aforementioned authors demonstrate the need to quantify the dynamics of flood inundation within the Amazon basin at appropriate spatial and temporal scales.

Due to the large size of the Amazon basin and remote location of many of its rivers and floodplains, the provision of in situ data is limited. The most rudimentary hydrological datasets such as gauged discharge records are sparse for the Amazon main stem, whilst many of its tributaries remain ungauged (Wilson et al., 2007). Furthermore, there is no provision of systematic in situ quantitative hydrological data for Amazonian floodplains (Alsdorf et al., 2005). Hence it is clear that the provision of in situ data is not sufficient to enable quantification of the complex spatial and temporal dynamics of Amazonian flood inundation.

Remote sensing datasets offer an alternative means of quantifying the dynamics of flood inundation upon Amazon floodplains (Hall et al., 2011). Accordingly, a variety of remote sensing platforms have been utilised in order to provide measurements of inundation extent, water levels and floodplain water storage volumes (Hess et al., 2003; Birkett et al., 2002; Alsdorf et al., 2010). Whilst remote sensing has provided valuable insights into the dynamics of inundation upon Amazonian floodplains (Alsdorf et al., 2007) it is commonly limited in terms of spatial and temporal resolution and/or coverage. Optical sensors such as Landsat TM are obscured by dense and continuous cloud cover during the wet season, and are thus ineffective within studies of Amazonian inundation dynamics (Hall et al., 2011). Synthetic Aperture Radar (SAR) images, such as those from JERS-1, enable the derivation of inundation extent at high resolution (<100 m), but are limited in terms of spatial coverage and temporal resolution (Hess et al., 2003). Satellite altimeters such as TOPEX-POSEIDON are able to measure the water surface elevation of the main

channel and overbank inundation, however measurements are recorded along tracks that are spaced at intervals of greater than 300 km (Zakharova et al., 2006). Passive microwave instruments are able to provide information relating to inundation area with repeat frequency of days, however the coarse resolution of 0.25 degrees precludes the investigation of complex inundation dynamics (Hamilton et al., 2002). Similarly GRACE is able to provide floodplain water volumes with good temporal resolution, although the spatial resolution of 1 degree renders it suitable exclusively for application at regional scales (Alsdorf et al., 2010).

In light of the deficiencies associated with in situ and remote sensing observations, numerical modelling offers perhaps the best opportunity to quantify flood inundation upon Amazonian floodplains at the relevant spatial and temporal scales. The earliest approaches to modelling of Amazonian river systems were constituted by the representation of channel flow through a simple Muskingum routing scheme, whilst overbank flows were calculated based upon the assumption of a flat floodplain and water levels equivalent to those within the main channel (Richey et al., 1989). Water balance and transport models have also been applied to the Amazon river network (Vorosmarty et al., 1989; Costa and Foley, 1997; Coe et al., 2002). However these models have focused primarily upon the quantification of discharge of the channel network and have not included an appropriate representation of floodplain flows. Of these water balance and transport approaches, the model of Coe et al., (2002) contained the best representation of two dimensional floodplain flow dynamics, although this was based upon a spatial grid resolution of the order 9 km. Hence early attempts to model Amazon river processes did not include an adequate representation of the complex flow dynamics elucidated by Alsdorf et al., (2007).

In recent years a handful of studies have addressed the limitations associated with early attempts to model Amazonian river systems through application of coupled 1D-2D hydrodynamic modelling approaches to study areas along the Amazon main stem (Wilson et al., 2007; Trigg et al., 2009; Baugh et al., 2013). The implementation of these studies was facilitated by the provision of topographical data from the Shuttle Radar Topography Mission (SRTM) which flew in 2000, enabling the derivation of a distributed representation of

topography for Amazonian floodplains. Prior to the SRTM a dearth of topographical data precluded the application of two dimensional models within Amazonia, as these codes require a distributed representation of floodplain topography in order to facilitate accurate representation of floodplain flow dynamics (Bates and De Roo, 2000). Increasing availability of remote sensing datasets also facilitated the application of 1D-2D codes within the Amazon, enabling rigorous validation of both modelled inundation extent and depth (Wilson et al., 2007).

Wilson et al., (2007) demonstrated the feasibility of implementing coupled 1D-2D flood inundation models within Amazonia through application of the LISFLOOD-FP model (Bates and De Roo, 2000) to a 13,000 km^2 study area within the central Amazon floodplain for a 22 month simulation period. The model performed well at high water with respect to observed inundation extent and water level, but substantially over predicted inundation during low water periods. Poor performance during low water was attributed to the poor representation of floodplain dewatering, as hydrological processes were not considered within the model, whilst the 270 m spatial resolution DEM did not resolve floodplain channels that are postulated to facilitate drainage of the floodplain. Another factor that limited the accuracy of modelled inundation within Wilson et al., (2007) was constituted by the quality of the bare earth floodplain DEM derived from SRTM.

Within forested regions the SRTM dataset is characterised by a systematic positive bias (Berry et al., 2007). The elevation reported in the SRTM dataset corresponds to the vertical location of the C-band phase centre (Rabus et al., 2003). In areas characterised by surface vegetation C-band microwaves penetrate into the canopy where they are scattered by physical vegetation elements, hence the C-band phase centre is located at a height between ground elevation and the top of the canopy (Carabajal and Harding, 2006). Therefore the magnitude of vertical bias within the SRTM varies as a function of forest height and other structural variables such as tree density and degree of canopy closure (Hofton et al., 2006). Amazonian floodplains are characterised by dense varzea forest cover and as a consequence the SRTM is subject to positive biases that must be removed in order to produce a bare earth DEM (Yamazaki et al., 2011), which is required in order to accurately represent

floodplain flows (Lane et al., 2006). Wilson et al., (2007) corrected positive biases in the SRTM through application of a spatially uniform estimate of canopy height derived from field measurements. In order to account for penetration of the SRTM C-band phase centre into the forest canopy, the correction was reduced to 50% of the original canopy height estimate. However, Amazonian floodplain forests are characterised by a high level of structural heterogeneity (Wittman et al., 2002) and thus correction through utilisation of a constant canopy height resulted in local under and over prediction of floodplain elevation, ultimately manifesting as errors in resulting predictions of inundation.

The difficulties associated with accurate correction of the SRTM, and lack of alternative topographical data sources, remain perhaps the most significant barrier to the widespread application of flood inundation models within the Amazon basin. Accordingly, Baugh et al., (2013) demonstrated the potential for use of global canopy height datasets (Simard et al., 2011) in order to facilitate systematic removal of the positive bias contained within SRTM and generation of bare earth DEMs. In order to account for penetration of SRTM into the canopy, the global canopy height map was adjusted by a range of correction factors. The resulting bare earth DEMs were utilised within hydrodynamic modelling in order to test the viability of the use of the global canopy height map for removal of vegetation biases. Results illustrated that correction of the SRTM with respect to the global canopy height map substantially improved the accuracy of simulations in comparison to application of the uncorrected SRTM dataset. Indeed comparison with inundation extent derived from JERS-1 imagery illustrated that RMSE improved from 0.52 to 0.07 for high water and from 0.22 to 0.12 at low water. RMSE of simulated water levels also improved with respect to satellite altimetry measurements.

Recent studies of Wilson et al., (2007) and Baugh et al., (2013) have demonstrated the feasibility of the application of 1D-2D model codes within the central Amazon floodplain using bare earth DEMs derived from SRTM. Whilst these studies have achieved promising results, on a basic level additional applications of hydrodynamic models are required in order to provide a greater level of insight into the complex spatial and temporal dynamics of flood inundation upon floodplains within other parts of the Amazon basin. In addition, the role of floodplain hydrological processes and small sub grid scale channels

were not addressed in the aforementioned studies, despite their hypothesised importance (Aalto et al., 2003; Pouilly et al., 2004). Moreover, given the first order influence which topography exerts upon inundation, there is a need to further test the efficacy of methods utilised by Wilson et al., (2007) and Baugh et al., (2013) in order to generate bare earth DEMs for floodplains based upon SRTM data. The generation of an accurate bare earth DEM for another floodplain study area located within the Amazon basin and subsequent application of this DEM within a hydrodynamic model presents an opportunity to address the deficiencies in past inundation modelling studies, and thus forms a primary focus of this research.

1.4 Amazon forest biomass and carbon storage

Despite being the subject of much research, the spatial distribution and total volume of aboveground wood biomass storage within Amazonia remains uncertain (Houghton, 2003). For example, estimates of total biomass storage within the Brazilian Amazon have varied between 39 PgC (Olson et al.,1983) to 93 PgC (Fearnside, 1997), a factor of greater than two. Furthermore, in a rigorous analysis of Amazonian biomass estimates Houghton et al., (2001) found that the basin wide biomass estimates were associated with little spatial agreement. Uncertainty in relation to biomass stocks currently forms the largest source of error when calculating carbon fluxes relating to changes in land use and land cover in the Amazon (Houghton et al., 2005). Therefore further research is required in order to reduce levels of uncertainty associated with biomass storage and fluxes within Amazonia.

Saatchi et al., (2007) presented one of the most recent attempts to quantify Amazonian biomass, estimating a total storage of 86 PgC for the Amazon basin. The basic approach utilised by the authors was similar to that applied within previous studies and centred around the spatial extrapolation of plot level biomass estimates across the basin with respect to coarse scale environmental gradients (Fearnside 1996; Brown, 1997). Within Saatchi et al., (2007) environmental gradients were represented through remote sensing datasets such as NDVI, LAI and percentage tree cover derived from MODIS, radar backscatter from QuikSCAT and JERS-1 along with elevation from SRTM. Past attempts to derive Amazonian biomass have represented environmental

gradients through interpolation (Malhi et al., 2006) or modelling approaches (Potter et al., 2001). Although the approach adopted by Saatchi et al., (2007) produced an improved estimate of Amazonian biomass storage, this figure remained associated with a relatively large degree of uncertainty, estimated by the authors at 20%.

A portion of the uncertainty within estimates of Amazonian biomass are accounted for by methodological errors associated with plot scale measurements (Chave et al., 2005) and spatial resolution of remote sensing datasets (Houghton et al., 2005) that are unique to the study of Saatchi et al., (2007). Approaches utilised within other studies are associated with similar methodological errors (Houghton et al., 2001). However, a more important and fundamental source of error within estimates of Amazonian biomass is constituted by uncertainty with respect to the environmental variables that are fundamentally responsible for controlling the spatial distribution of biomass across the Amazon basin (Saatchi et al., 2007). Whilst numerous studies have found a relationship between biomass distribution and climate (Eva et al., 2003), it is clear that climate is not preponderant in determining biomass everywhere and that other variables such as soil, geomorphology and hydrology exert a significant impact upon forest characteristics (Saatchi et al., 2007).

1.5 Amazonian varzea forests

As detailed within section 1.2, Amazonian rivers are characterised by a substantial level of interaction with their adjacent floodplains (Junk et al., 1989; Mertes et al., 1996; Dunne et al., 2002). Indeed given the presence of large areas of tropical forest upon Amazonian floodplains, fluvial disturbance constitutes an environmental variable which is likely to be important in determining the spatial distribution of biomass within parts of the Amazon basin. As a direct result of the influence that fluvial disturbances exert upon the ecological functioning of Amazonian floodplains, seasonally inundated varzea forests are considered to be largely distinct from Terra Firme forests, which lie outside the maximum limit of annual inundation (Melack et al., 2001). Varzea forests flank the Amazon River and many of its tributaries, constituting one of the largest riverine wetlands in the world (Junk, 1997). The precise spatial extent of the Amazonian varzea is difficult to determine due to the interannual

variation in flooded area and the difficulties associated with monitoring flood inundation over such large scales. Consequently, estimates vary considerably from 140,000 km^2 to 500,000 km^2 (Seyler et al., 2009). Hence varzea forests constitute approximately 4-5% of the overall spatial extent of the Amazon basin (Hess et al., 2003).

Whilst varzea forests are less abundant than Terra Firme forests within Amazonia, these ecosystems are important in their own right (Junk et al., 2000) and seasonally inundated forests nevertheless represent a substantial contribution to the overall storage of biomass and assimilation of carbon within the basin. It is widely acknowledged that varzea forests are associated with lower biomass densities and higher rates of carbon assimilation in comparison to Terra Firme forests (Phillips et al., 1998; Baker et al., 2004), although this is based upon a relatively small number of plot level estimates from across the basin. Beyond these plot level estimates little is known about the spatial distribution of biomass/carbon storage and assimilation within varzea forests, or how these forest characteristics are modulated by fluvial processes.

A substantial volume of research has documented the effects that fluvial systems exert upon varzea forest stands (Kalliola et al., 1992; Wittmann et al., 2002; Witmann et al., 2004), although thus far the scope of this research has been limited to the analysis of species distributions and basic structural characteristics and has not been extended to consider biomass. These studies have demonstrated that fluvial disturbance is of preponderant importance in determining the distribution of floodplain forest stands and their structural characteristics. Intuitively this further suggests that fluvial disturbance is likely to exert a significant influence upon biomass distributions within varzea forests. The overall impacts that Amazonian rivers exert upon forest dynamics can be attributed to three key processes; channel migration, seasonal inundation and overbank sediment supply.

1.6 The effects of channel migration upon varzea forests

The high levels of dynamism exhibited by Amazonian rivers can be attributed to high sediment loads (Meade, 1985) and low slopes which occur over much of the Amazon foreland basin (Irion et al., 1997). As a result, channel patterns are commonly meandering or anastomosing and are characterised by continuous

destruction and recreation of fluvial forms (Gautier et al., 2007). Erosional processes that manifest at the outer cut bank can result in the destruction of large areas of floodplain, and subsequently mature forest, during a single flood pulse (Kalliola et al., 1992). Simultaneously, deposition of sediment on point bars on the inner, convex channel bank leads to the creation of new land which is colonised by pioneer plant species (Puhakka and Kalliola, 1995). Therefore rapid rates of channel shifting have been shown to exert a significant impact upon varzea forest distribution, being responsible for loss of large areas of old growth forest stands and the inception of large areas of primary successions (Salo et al., 1986).

The findings of the aforementioned studies were significant, illustrating that the primary mode of forest regeneration within Amazonian floodplains varies substantially from that observed within Terra Firme forests. In Terra Firme forests regeneration usually occurs through the growth of established vegetation within relatively small gaps following tree falls (Kalliola et al., 1991). The process of regeneration is inherently different for varzea forests, both due to the fact that succession must begin from the earliest phases of colonisation by pioneer species, whilst at any given time there are relatively larger areas of vegetation within early stages of development than would be observed in Terra Firme forests (Salo et al., 1986). Worbes et al., (1992) detailed the successional sequence observed for varzea forest stands, from initial colonisation of freshly deposited alluvial sediment on point bars to late successional forests that develop after 100-300 years. The authors found that species richness increased through successional development; from initial monospecific stands to stands characterised by diversity of 100 species ha^{-1}. This pattern was marked by an associated decrease in stem density from 1000 stems ha^{-1} to 500 stems ha^{-1} and a significant increase in canopy height from early successional stages (10-15m) to late successional stages (25-35m). Overall, site turnover rate, in addition to natural successional development on point bars after initial colonisation results in the formation of a patchwork of forest stands characterised by varying ages and successional stage (Salo and Kalliola, 1991).

The aforementioned studies demonstrated the fundamental impact that fluvial processes exert upon varzea forest dynamics through loss of mature forests and generation of new primary successions. However these early accounts of

the interactions between river channel migration and floodplain forest dynamics were largely descriptive, and did not quantitatively assess the effect of erosional and depositional processes upon the distribution of varzea stands over varying spatial and temporal scales (Richards et al., 2002). Furthermore, within these early studies the implications of channel shifting were not assessed in terms of associated effects upon aboveground wood biomass/carbon storage and assimilation within varzea forests.

The limitations of early work have begun to be addressed by Peixoto et al., (2009), who monitored channel migration and distributions of pioneer and old growth floodplain forest as a function of channel shifting within Solimoes and Japura rivers in western Brazil. The authors found that during the 21 year study period the area of pioneer vegetation increased by 5.8% with respect to the total areal extent of the study area. As deposition and erosion were well balanced within the studied reach, the abundance of late successional forests decreased by a roughly equivalent area. Local estimates of aboveground biomass (Schongart, 2003) were applied in order to calculate the overall carbon balance of the study area over the 21 year period. Carbon sequestration through new pioneer vegetation was estimated at ~3,185- 46,068 Mg year^{-1}, whilst C releases due to erosional processes were ~22,734-64,623 Mg year^{-1}. Thus overall, the results presented suggest that migration of the Japura and Solimoes rivers within the studied reach is associated with an overall net loss of aboveground biomass and carbon storage within adjacent varzea forests (Peixoto et al., 2009).

The study of Peixoto et al (2009) represents the first attempt to assess the impacts of channel shifting upon the distribution of floodplain forests and the associated implications for aboveground biomass and carbon dynamics. However, calculations of net aboveground wood biomass and carbon balance made by Peixoto et al., (2009) are based solely upon the loss of late successional forest and generation of new pioneer vegetation and the application of a uniform value for carbon storage to each vegetation type. Clearly this represents a highly simplified view of the distribution of floodplain forests, as varzea are known to comprise a mosaic of forest stands characterised by a range of ages and successional stages (Wittmann et al., 2002). The effects of channel shifting upon forest dynamics are clearly more

complex than a simple balance between removal of late successional forest and colonisation by new pioneer species. Although to date, no attempts have been made to quantify how the relatively large areas of vegetation within early stages of successional development contribute to overall storage and assimilation of aboveground wood biomass and carbon within Amazonian varzea forests.

1.7 The effects of flood inundation upon varzea forests

Amazonian rivers are characterised by an annual flood pulse, resulting in a high magnitude and duration of inundation within adjacent floodplains (Junk et al., 1989). It is widely acknowledged that an excess of water inhibits growth of vegetation (Schueler and Holland, 2000), with total submergence resulting in mortality for many species. Excess water manifests in terms of oxygen deprivation, dramatic changes in the availability of carbon dioxide and mineral nutrients, low redox potentials, light deprivation, in addition to changes in concentrations of phytotoxins and decomposition of organic matter (Crawford, 1992, Schluter and Crawford, 2001). Importantly, these conditions ultimately preclude respiration and impose a strict limitation upon vegetation growth during inundation.

Intuitively, the magnitude and extended duration of inundation experienced within Amazonian floodplains leads to the presence of excess water for a large portion of the year (Wittmann et al., 2006b). The effects of inundation upon varzea forests are particularly significant, as inundation occurs within the period when temperature and light levels mean that growth conditions are optimal (Parolin and Junk, 2002). Accordingly, annual flooding influences ecophysiology of varzea tree species, that have developed a variety of adaptations in order to cope with the excess water associated with the annual flood pulse (Parolin, 2001). Species found within varzea forests are able to survive extended anoxic conditions through a broad range of adaptations including the development of adventitious roots, hypertrophic lenticels, buttressed or stilt roots and leaf shedding (Worbes, 1985, Piedade et al., 2006, Scarano et al., 1994). Importantly, although a variety of physiological, anatomical and phenological adaptations allow varzea species to tolerate flood conditions without mortality, growth is strongly linked to flood periodicity and is restricted almost completely to the dry season (Parolin, 2009).

Research has begun to address how annual flooding influences the growth of Amazon floodplain forests. For example, Wittmann et al., (2006a) illustrated the effect of inundation upon the wood specific gravity of varzea trees. Wood specific gravity reflects the amount of biomass accumulated per unit volume of living material (Yao, 1970) and is negatively correlated with mean tree diameter increment (Worbes et al., 1992). Results showed that wood specific gravity was positively associated with magnitude and duration of inundation and was thus higher within low varzea stands. These results reflect the shorter growing seasons of forest stands located within areas characterised by a higher magnitude of inundation and demonstrate, on a basic level, the impact that flooding exerts upon growth of the varzea (Wittmann et al., 2006a). Further, Schongart et al., (2004) used a dendrochronological approach in order to demonstrate the strong relationship between tree growth within varzea forests and flood characteristics governed by the El Nino Southern Oscillation. This work of Schongart et al., (2004) demonstrated that El Nino events induce an increase in productivity and growth within floodplain forests, attributed to lower flood magnitude and longer growing seasons. The opposite effect was observed during La Nina years, where increased discharges and flood inundation magnitude/duration were associated with lower productivity (Schongart and Junk, 2007). These results provide further evidence of the strong influence which annual flood inundation imparts upon forest growth and aboveground wood biomass within Amazonian floodplains.

The effects of periodic inundation upon vegetation have been well documented in terms of species diversity and floristic composition within the varzea (Wittmann et al., 2002). Overall, it has been shown that Amazonian floodplain forests contain fewer species than Terra Firme forests within the same region (Balslev et al., 1987), whilst the distribution of species is known to exhibit a strong zonation according to the flood level gradient (Ayres, 1993). The observed zonation of species led Wittmann et al., (2002) to divide Amazon floodplain forests into high and low varzea, based upon the mean annual height and duration of inundation. Low varzea are located in areas where the annual average water column height exceeds 3m and inundation occurs for over 50 days per year. In contrast, the high varzea constitute areas where the water column averages <3m and the annual inundation period is less than 50 days

per year. As a result of varying flood inundation characteristics, high and low varzea forests are clearly distinct in terms of floristic distributions and structural characteristics (Wittmann et al., 2002).

Within low varzea, successional stage determines forest structure and species composition, with a strict limitation in species diversity imposed by the high magnitude of inundation. Therefore, low varzea are characterised by the establishment of early successional stages, commonly resulting in a prevalence of monospecific stands (Wittmann et al., 2002). These stands are dominated by flood tolerant and light demanding pioneer species, characterised by fast growth rates and short life cycles (Wittmann et al., 2004). In contrast, high varzea forests exhibit greater species diversities of up to 150 species ha^{-1}, which is of the order of non-flooded Terra Firme forests (Ribeiro et al., 1999). In addition tree species located within the high varzea are typical of late successional stages and are characterised by a lower flood tolerance and slower growth rates than those within low varzea. Consequently, high varzea stands resemble Terra Firme forests much more closely. Wittmann et al., (2002) demonstrated the difference in species composition between the high and low varzea, finding that 94 species were located exclusively within low varzea sites and 103 species restricted solely to the high varzea, indeed only a few species were present across the whole flood level gradient. Most significantly, the findings of Wittmann et al., (2002) suggest that areas subject to substantial annual flood inundation are maintained within early successional stages. Given the spatial extent and magnitude of flooding upon Amazonian floodplains, this suggests that flood inundation may be responsible for maintaining relatively large areas of varzea forests in stages of successional growth.

Through a synthesis of existing research it can be concluded that annual inundation exerts a significant influence upon varzea forests. Annual inundation is preponderant in controlling the spatial distribution of tree species and biophysical characteristics of varzea forests (Wittmann et al., 2002). Given the wide spatial extent and extended duration of inundation upon Amazonian floodplains this suggests that large areas of varzea may be maintained within successional stages of development. This is likely to be important in terms of aboveground wood biomass and carbon storage/assimilation due to the markedly different growth characteristics observed between successional

forests and old growth forests (Baker et al., 2004). To date, accounts of the influence that flood inundation exerts upon varzea forests have predominantly focussed upon floristic composition and basic biophysical parameters such as diameter distributions, basal area and stem density. Therefore there is a clear need for the scope of analyses to be extended in order to examine the effects of inundation upon aboveground wood biomass stocks and carbon assimilation within varzea forests.

1.8 The effects of sedimentation upon varzea forests

Despite the large volumes of sediment deposited upon the floodplains of Amazonian rivers, to date, Wittmann et al., (2004) constitutes the only example of a study that has considered the implications of overbank sedimentation for the dynamics of varzea forests within Amazonia. Results presented by Wittmann et al., (2004) demonstrated that floodplain sedimentation plays an integral role within the successional development of Amazon varzea forest stands. The authors elucidated that colonisation of newly created areas of floodplain by pioneer species was associated with greater flow resistance during periods of overbank inundation. Intuitively, an increase in frictional resistance causes lower flow velocities and increased deposition of suspended sediment within these areas. Subsequently, enhanced rates of sediment deposition and the associated increase in stand elevation leads to a decline in flood inundation magnitude and diminishing sediment supply. Importantly, reduction in the depth and duration of inundation facilitates the establishment of tree species associated with later successional stages. The aforementioned development of forest stands can be described as ‘allogenic’ succession (Tansley, 1929), as changes in vegetation are attributable to changes in site conditions. Through continued succession and associated increases in elevation and decreases in the influence of flood inundation, low varzea stands transition to high varzea stands. Therefore, it is clear that modification of physical site conditions through overbank sedimentation is implicit within the process of floodplain succession (Wittmann et al., 2004).

Whilst sedimentation is likely to exert other impacts upon varzea forest stands, these currently remain unexplored. Field observations and measurements have illustrated that deposition of sediment can decrease aeration of floodplain soils,

leading to shortage of oxygen in the rhizosphere and potential mortality of trees (Wittmann and Parolin, 2005). However the spatial extent of such effects remains unquantified at present. This can be partially attributed to the spatial and temporal heterogeneity in sediment deposition upon Amazon floodplains (Aalto et al., 2003), rendering accurate quantification of sediment deposition through field measurements and remote sensing techniques problematic. Whilst this has not been quantified, observations suggest that the deposition of large volumes of sediment in crevasse splay formations following levee breaches by rapid rise floodwaters can lead to the mortality of vast swathes of varzea forest (Aalto, personal communication). Therefore, like meander migration and flood inundation, floodplain sedimentation possesses the potential to exert considerable influence upon varzea forest dynamics and above ground wood biomass and carbon storage.

1.9 Implications for varzea biomass

Based upon the preceding review of literature, it is clear that fluvial processes exert a significant influence upon varzea forest dynamics. Although previous research has focussed upon species distributions and basic structural characteristics of varzea forest stands, it is likely that the same factors are significant in controlling biomass distributions. It remains unclear why research has not been extended in order to consider biomass, although this could be attributed to the fact that full forest inventories including measurements of tree height and wood specific gravity are required in order to calculate biomass accurately using allometric equations (Chave et al., 2005). The difficulty associated with quantifying fluvial disturbances such as flood inundation, detailed further in 1.3 is also likely to be a factor here. Clearly, shortcomings in the quantitative knowledge of fluvial disturbances themselves preclude elucidation of their subsequent effects upon varzea forest biomass.

Nevertheless the dearth of knowledge relating to varzea forest biomass is subsequently reflected in the current approaches adopted in order to estimate biomass at the basin scale (Houghton et al., 2001; Saatchi et al., 2007). At present, biomass measurements from plots located within varzea forests are utilised as inputs into classification algorithms (Houghton et al., 2001). However the same broad scale environmental gradients utilised in order to extrapolate

biomass for Terra Firme forests are also applied for varzea forests. Thus current extrapolation procedures do not reflect the local scale fluvial disturbances that have been shown to be preponderant in the determination of varzea forests characteristics, and are likely to control biomass distributions. Therefore further research is required in order to improve understanding of the functioning of Amazonian varzea with respect to biomass storage. An improved understanding of the interaction of fluvial processes and varzea forests could subsequently contribute towards a more adequate representation of the contribution of varzea forests to basin scale estimates of biomass, and a reduction of uncertainties associated with these estimates. Thus quantification of the biomass of varzea forests and investigation of the interactions with fluvial processes forms the second primary focus of this research.

1.10 Summary

The Amazon basin covers approximately seven million square kilometres of South America, encompassing over half of the worlds' total tropical forested area (Metcalfe et al., 2010). Given the importance of Amazonian forests within the global carbon cycle, much research has been undertaken in order to quantify the storage and overall fluxes of above ground wood biomass and carbon within the basin (Houghton et al., 2001). However, despite a wealth of research the spatial distribution of forest biomass (Saatchi et al., 2007), which constitutes one of the most important elements of overall carbon flux within Amazonia, remains uncertain.

To date, much research into aboveground wood biomass and carbon dynamics within Amazonia has focused upon Terra Firme forests (Phillips et al., 1998; Baker et al., 2004), this is well justified given that these forests comprise the vast majority of the total forested area of the Amazon basin. However, the Amazon basin also encompasses the largest fluvial system on Earth, accounting for 20% of the world's total river discharge (Richey et al., 1989). Seasonally inundated floodplain forests cover an area of up to 300,000 km^2 (Parolin, 2009), constituting around 5% of the total forested area of the Amazon basin. Therefore, the floodplain forests of Amazonia constitute a highly significant ecosystem in their own right, particularly given that varzea forests are

largely distinct from Terra Firme forests in terms of biophysical characteristics and ecological processes (Wittmann et al., 2004).

Intuitively, the differences in ecological processes observed within floodplain forests and Terra Firme forests can largely be attributed to the influence of fluvial systems. Rapid rates of channel shifting lead to the loss of relatively large areas of mature forest stands and the generation of new primary successional forests (Salo et al., 1986). The large extent and extended duration of annual flood inundation has been shown to preclude vegetation growth (Parolin, 2009) and maintain large areas of forest within early successional stages (Wittmann et al., 2002). Further, it has been demonstrated that overbank sedimentation plays a key role within allogenic forest succession within varzea (Wittmann et al., 2004).

Therefore, it is clear that fluvial disturbances impart a significant impact upon the ecological functioning and biophysical characteristics of Amazonian varzea forests. Specifically, the maintenance of large areas of floodplain forests within successional stages through channel migration (Kalliola et al., 1992) and overbank inundation (Wittmann et al., 2004) suggests that volumes of aboveground wood biomass and carbon stored within these forests is likely to vary substantially from Terra Firme forests which are subject to lower levels of natural disturbance. Whilst it is broadly acknowledged that floodplain forests are associated with lower aboveground wood biomass and carbon density than Terra Firme forests (Baker et al., 2004), current knowledge is largely based upon plot level estimates with limited scope. Significantly, to date there have been no coherent accounts or quantitative assessment of the impacts that fluvial systems exert upon floodplain forests with respect to aboveground wood biomass and carbon storage.

The dearth of knowledge relating to the functioning of floodplain forests with respect to fluvial processes can be partially attributed to a lack of understanding of the functioning of Amazonian river systems themselves. Despite being characterised by km of water courses and constituting 20% of the worlds river discharge (Richey et al., 1989), the Amazon fluvial system remains understudied and is not well understood at present. As a result of the large extent of the basin, in situ observations of discharge and water level are sparse

(Alsdorf et al., 2007). Remote sensing observations have been useful and have enhanced understanding of flooding within Amazonia (Hall et al., 2011). However, remotely sensed data is often limited in terms of spatial and temporal resolution/extent and thus is not able to adequately quantify inundation dynamics of Amazonian rivers/floodplains (Wilson et al., 2007).

Numerical modelling constitutes perhaps the best approach to elucidation of the complex inundation dynamics observed upon Amazonian floodplains (Alsdorf et al., 2007b). As a result of a dearth of accurate topographical data early attempts to model flood inundation within Amazonia were not able to adequately represent floodplain inundation dynamics (Richey et al., 1989; Coe et al., 2002). In recent years a handful of studies have utilised the SRTM global 90 m topographical dataset in order to facilitate modelling of complex inundation dynamics of Amazonian floodplains (Wilson et al., 2007; Baugh et al., 2013). However more widespread application of flood models remains limited by the difficulties in deriving a bare earth representation of topography from the SRTM dataset for densely forested Amazonian floodplains (Yamazaki et al., 2012). Therefore in order to build upon recent advances it is clear that further modelling applications are required in order to increase understanding of floodplain inundation dynamics within Amazonia.

1.11 Research aim

The overall aim of this PhD research is to use a combination of remote sensing, field datasets and numerical modelling in order to investigate the interactions between fluvial processes and above ground wood biomass storage within Amazonian varzea forests.

This overall research aim will be addressed through the completion of five specific objectives, one of which will form the basis of each of the methods and analysis chapters which make up this thesis. The organisation of chapters and their associated objectives are elaborated in section 1.12. More detailed aims are introduced later, within each individual chapter.

1.12 Thesis structure and specific objectives

Methods and analysis chapters (chapters 3-7) represent a progression towards addressing the overall research aim, and are preceded by a description of the

study site, and followed by final discussions and conclusions. The content of each of the subsequent chapters is elaborated in greater detail below, whilst figure 1.1 provides a visual illustration of the thesis structure.

1.12.1 Chapter 3: Beni floodplain land cover classification

Objective 1

- To generate an accurate classification of land cover within the Beni floodplain study area using multispectral satellite imagery.

Chapter outline

Within chapter 3, a land cover map is produced for the Beni floodplain study area from multispectral satellite imagery, using a number of supervised classification techniques. A knowledge of floodplain land cover represents an important precursor to further analysis undertaken within this thesis. Specifically, the land cover map is utilised in order to produce a forest mask which used to generate bare earth DEMs in chapter 5, whilst it is also used to produce a map of floodplain roughness which is required to facilitate flood inundation modelling in chapter 6.

Key outcomes

- Map depicting the dominant land cover classes on the Beni floodplain
- A basic understanding of the hydrological functioning of the Beni floodplain

1.12.2 Chapter 4: Accuracy of the SRTM dataset for the Beni floodplain

Objective 2

- To quantitatively assess both the vertical accuracy of the SRTM dataset, and magnitude of SRTM C-band phase centre penetration into Beni floodplain forest canopies.

Chapter outline

In the first part of Chapter 4, the SRTM global elevation dataset is validated for the Beni floodplain study area using highly accurate DGPS points collected during field survey. Validation is necessary in order to identify and correct

absolute vertical errors which are known to characterise the dataset, prior to bare earth DEM generation. In the second part of Chapter 4, penetration of the SRTM C-band phase centre into Beni floodplain forest canopies is quantified through direct comparison of field measured canopy height and canopy height extracted from the SRTM dataset at 35 sites across the Beni floodplain. This comparison enables the positive vertical SRTM bias relating to vegetation cover to be quantified, which represents an important prerequisite to the successful production of bare earth DEMs in Chapter 5.

Key outcomes

- A quantification of the vertical accuracy of the SRTM dataset for the Beni floodplain
- Estimates of Beni floodplain forest canopy height
- An estimate of SRTM C-band phase centre penetration into Beni floodplain forest canopies

1.12.3 Chapter 5: Beni floodplain bare earth DEM generation

Objective 3

- To generate and validate a collection of bare earth DEMs for the Beni floodplain through correction of positive biases which characterise the SRTM dataset within forested areas.

Chapter outline

Quantitative validation of the SRTM within Chapter 4 demonstrates that the dataset contains positive vertical elevation biases within forested areas of the Beni floodplain. This is problematic within the context of this thesis, as a representation of bare earth elevation of the Beni floodplain is required in order to facilitate accurate simulation of overbank flows within hydraulic modelling undertaken in Chapter 6. Hence, in Chapter 5 the vertical bias which characterises forested areas within the SRTM is removed, producing a bare earth DEM for the Beni floodplain. In order to remove the positive vertical bias canopy height maps are generated for the Beni floodplain through combination of canopy height measurements, obtained through field survey and from remote sensing, with the land cover classification produced within Chapter 3.

Subsequently, bare earth DEMs are utilised in order provide topographical forcing for the hydraulic model within Chapter 6, whilst canopy height maps are utilised in order to extrapolate plot scale biomass estimates in Chapter 7.

Key outcomes

- A set of quantitatively and qualitatively validated bare earth DEMs for the Beni floodplain study area

1.12.4 Chapter 6: Beni floodplain inundation modelling

Objective 4

- To simulate flood inundation upon the Beni floodplain using a coupled 1D-2D flood inundation model, and to quantitatively validate the model with respect to observed datasets derived from remote sensing.

Chapter outline

Within Chapter 6 flood inundation is simulated for the Beni floodplain using a coupled 1D-2D hydraulic flood inundation model. The bare earth floodplain DEMs generated in Chapter 5 provide topographical forcing within the model, whilst the land cover classification produced in Chapter 3 is utilised in order to create a spatially distributed map of floodplain roughness coefficients. Floodplain inundation is simulated for a number of flood events of different magnitudes, and model predictions validated at both high and low water using remotely sensed datasets. Predictions of inundation extent and depth are subsequently utilised within Chapter 7 in order to assess the influence which flooding exerts upon floodplain forest biomass storage.

Key outcomes

- A validated hydraulic model for the Beni river
- Spatially distributed predictions of flood inundation extent/depth/velocity for the Beni floodplain

1.12.5 Chapter 7: Successional forest development and aboveground wood biomass storage on the Beni floodplain

Objective 5

- To quantify the characteristics of successional forest stands upon the Beni floodplain with emphasis upon above ground wood biomass and carbon storage, and to investigate the influence which fluvial processes exert upon the characteristics of these forest stands.

Chapter outline

In the first part of Chapter 7 plot level forest inventory data for successional stands upon the Beni floodplain are analysed, and an initial relationship with flood inundation is established. Subsequently, an analysis of historical satellite imagery is utilised in order to quantify channel migration since 1960, this is combined with plot scale forest inventory data in order to estimate the net change in aboveground wood biomass storage attributable to channel shifting within this period. Within the final part of the Chapter maps of aboveground wood biomass are generated for the Beni floodplain through integration of plot level forest inventory data and canopy height maps, generated in Chapter 5. Aboveground wood biomass storage is correlated with flood inundation depth, predicted by the hydraulic model in Chapter 6, across the Beni floodplain, providing unique insight into the influence which flooding exerts upon forest ecology.

Key outcomes

- Plot level aboveground wood biomass estimates for successional forests of different ages upon the Beni floodplain
- Spatial maps of aboveground wood biomass stocks for the Beni floodplain
- Estimates of the net change in aboveground wood biomass on the Beni floodplain attributable to lateral channel migration
- A quantitative relationship between flood inundation characteristics and aboveground wood biomass density for the Beni floodplain

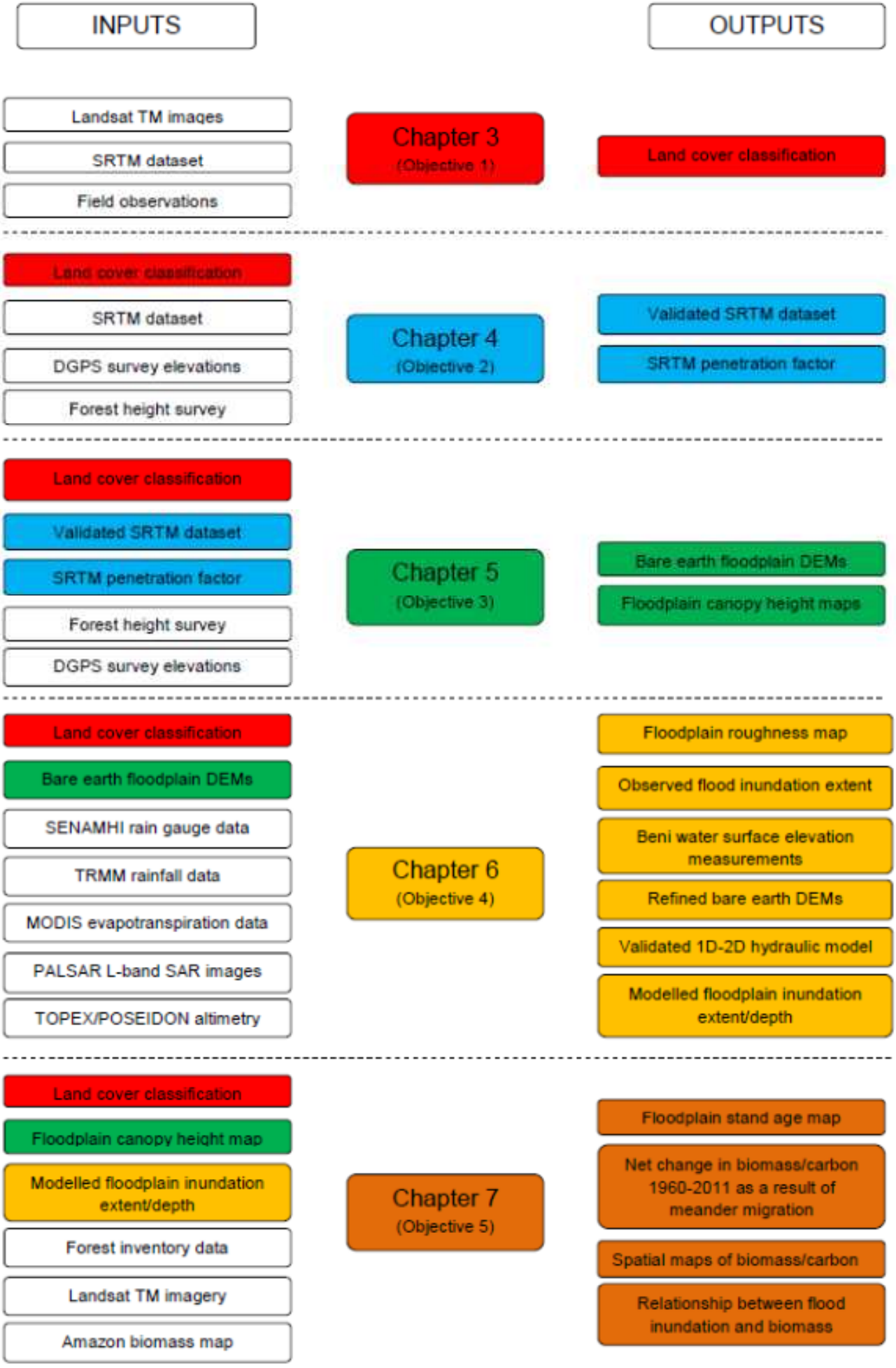

Figure 1.1. Conceptual diagram illustrating the main inputs and outputs to each chapter

Chapter Two

Study area- The Beni floodplain, Bolivia

2. Study area- The Beni floodplain, Bolivia

Given the aims and objectives of this research project, the field site selected within the Amazon basin was characterised by strong interaction between fluvial processes and tropical varzea forests. The Beni river, a second order tributary of the Amazon, is a large white water river located in north eastern Bolivia. Within its lowland basin the floodplain of the Beni forms part of the *Llanos de Mojos*, a large wetland which covers 126,000 km^2 of northern Bolivia and is subject to extensive annual flood inundation (Hamilton et al., 2004). In addition, in its lowland reaches the Beni river is characterised by highly dynamic geomorphology, attributable to rapid rates of channel migration and overbank sedimentation. This dynamic behaviour is attributable to the rivers high sediment load and unique tectonic setting (Aalto et al., 2003). The Beni floodplain is characterised by the presence of extensive tropical broadleaf forest cover in close proximity to the main channel, whilst within the distal floodplain forests give way to savanna land cover. Given these characteristics the lowland reaches of the Beni river and its adjacent floodplain, delineated in figure 2.1, represent an ideal location for this research.

Figure 2.1. Location of the Beni river floodplain study area within the Amazon basin.

2.1 The Beni river catchment

The Bolivian Amazon basin constitutes a large part of the upper catchment of the Madeira river, occupying approximately two thirds of the total area of Bolivia (Gautier et al., 2007). The Madeira represents the most important southern tributary of the Amazon, constituting 23% of the total area of the Amazonian watershed and 15% of the overall discharge (Guyot et al., 1999). The Beni river is one of the major tributaries of the Madeira and drains a catchment of approximately 282,000 km^2. The Beni catchment is characterised by large variations in climate and morphodynamic features, which can be attributed to its large topographical variability. Elevation ranges from 6400 m within the upper catchment in the Andes, to less than 200 m in the foreland basin (Gautier et al., 2010).

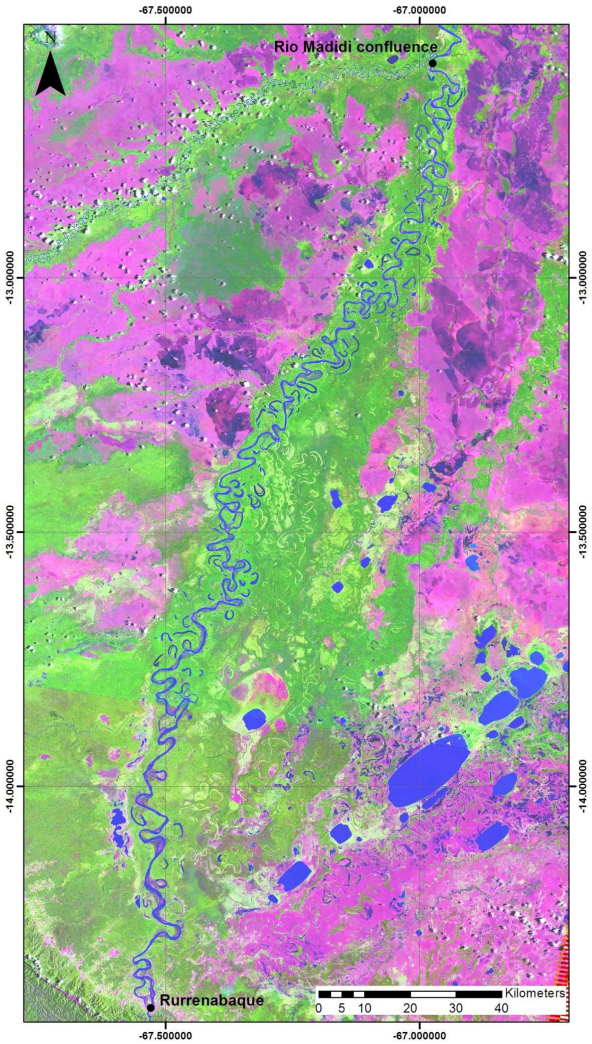

Figure 2.2. Extent of the Beni floodplain study area, imagery is Landsat TM. The upstream limit of the studied reach is constituted by Rurrenabaque and the downstream limit by the confluence with the Madidi.

The upper sub catchments of the Beni river drain the Andean and sub Andean ranges. Within the Cordillera Real and semi-arid Altiplano, tributary channels are highly incised and are characteristic of an upland river (Ronchail et al., 2005). From the Altiplano, the Beni flows downstream through the densely forested piedmont until it emerges onto the floodplain of its foreland basin at the town of Rurrenabaque, which represents the southern limit of the study area (figure 2.2). At Rurrenabaque elevation is 190 m, whilst the Beni drains an area of approximately 70,000 km^2 and discharge averages 2200 m^3s^{-1} (Gautier et al., 2010). From Rurrenabaque the Beni flows through its foreland basin and 800 km of channel to Riberalta. At this location the total drainage area is 119,000 km^2 and elevation is approximately 120 m. The northern limit of the study reach is marked by the confluence of the Beni with the Madidi river around 200 km north of Rurrenabaque (figure 2.2).

2.2 Geomorphology of the lowland reach

Within the foreland basin the active channel of the Beni is approximately 500 m wide, whilst the adjacent floodplain exhibits a very low longitudinal gradient of the order 10^{-4}m m^{-1}. As a result of high suspended sediment loads and weak banks, the Beni is highly dynamic within the study reach. Channel pattern is characterised by highly mobile meanders, with an overall sinuosity index of 1.6 to 2.5 (Gautier et al., 2007). Rapid channel migration, and the incidence of cut-offs forms a complex arrangement of abandoned channels and relic fluvial features (figure 2.3).

Over annual to decadal time scales, migration of the Beni channel is characterised by a high level of spatial variability in both space and time. Intuitively, migration rates are highest at meander bends whilst straight sections of the channel are generally more stable and are characterised by lower rates of lateral shifting. Average annual migration for meander bends is approximately 30 m per year, whilst this can reach 120-140 m per year at specific locations (Gautier et al., 2007). Migration rates also vary between different reaches of the Beni. Between Rurrenabaque and the Madidi confluence the river meanders freely, whilst the presence of consolidated tertiary deposits further downstream constrains meander migration (Gautier et al., 2010). Rates of channel shifting also show significant spatial variability within the studied reach. Gautier et al., (2007) found that the upstream portion of the reach to approximately 90 km

north of Rurrenabaque was characterised by the highest levels of erosion and deposition. Erosion and deposition were less pronounced within the middle section of the reach whilst lateral migration rates declined strongly in the lower reach, just upstream of the Madidi confluence, due to the presence of consolidated tertiary deposits similar to those located further downstream. Gautier et al., (2007) also observed a high level of interannual variability of Beni river migration, which was shown to be positively associated with discharge characteristics. Since 1960 the Beni channel has occupied a total area of 420 km^2, representing approximately 25 % of the total area of the contemporary channel belt. Over this period an average of 8.25 km^2 of floodplain per year has been lost to erosional processes, whilst an average of 7.5 km^2 per year of new floodplain has been formed by deposition of fresh alluvial sediment. An example of the creation/loss of floodplain sites through lateral migration of the Beni river is illustrated in figure 2.4. During the period from 1967-2001 27 new cutoffs were formed along the reach between Rurrenabaque and the Madidi confluence (Gautier et al., 2010).

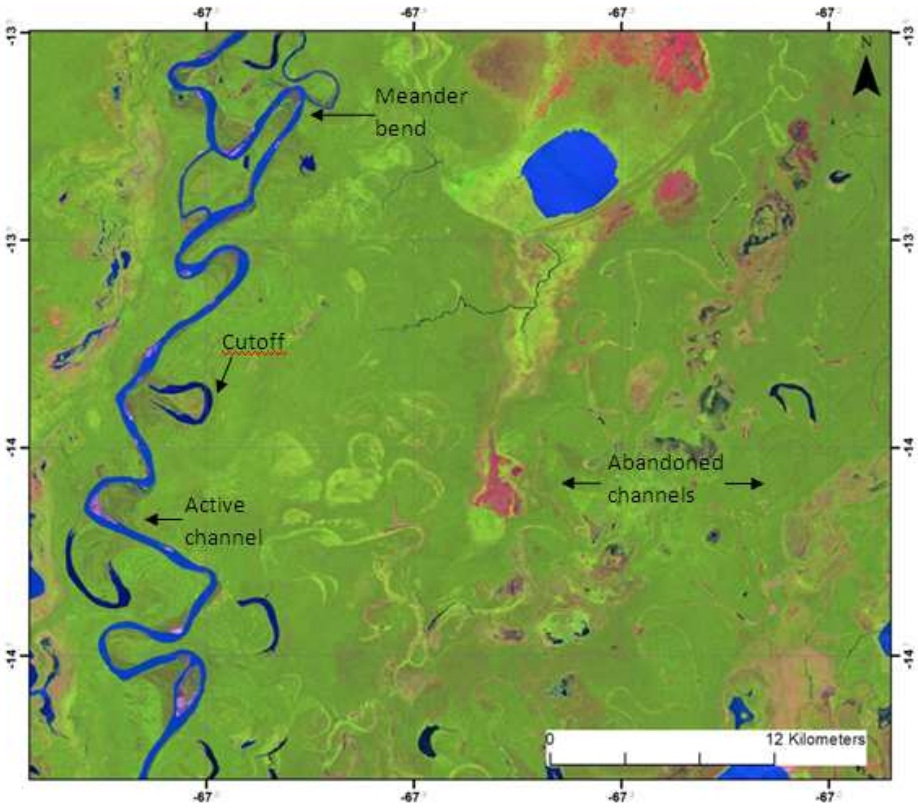

Figure 2.3. Beni floodplain map, illustrating typical channel plan form features in addition to active and abandoned channels

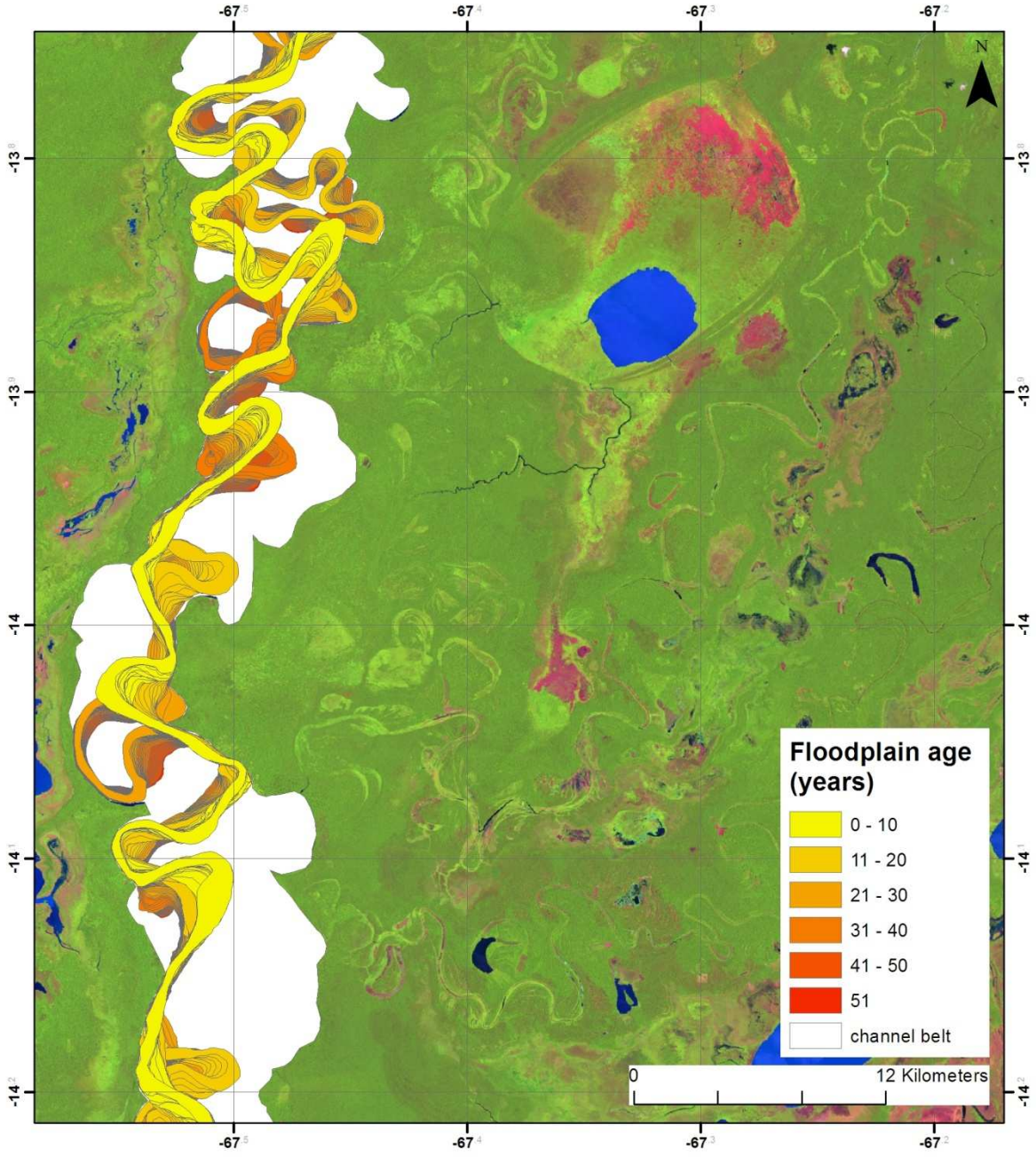

Figure 2.4. Stand age map for the Beni floodplain generated through interpolation of manually digitised channel locations based upon historical Landsat TM imagery. The extent of the contemporary channel belt is also included.

Over millennial timescales the position of the Beni channel is controlled by tectonic processes (Dumont, 1996). Currently the Beni river occupies the western part of the Llanos de Mojos, as a result of counter-clockwise migration across the foreland basin (Plafker, 1964). It is hypothesised that this counter clockwise migration was caused by the neotectonic uplift of the central part of the Beni basin, stretching north east from the town of Reyes. Based upon extensive field study Hanagarth and Dumont (1996) identified five previous locations of the Beni channel, these are illustrated in figure 2.5. The most recent

abandoned channels are currently occupied by the rivers Yata, Biata and Negro which constitute tributaries of the Beni in the present day. Relic features within these former channel belts are characterised by widths and meander wavelengths which are equivalent to the contemporary Beni, whilst data suggests that the Beni occupied the Yata as recently as 2500 years B.P.

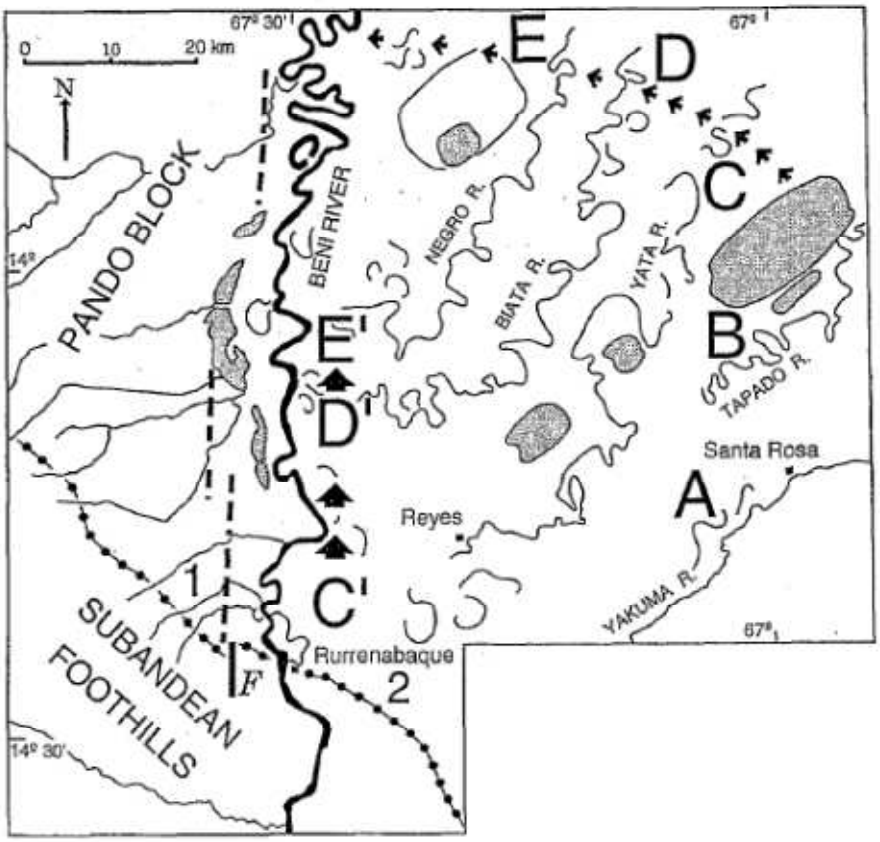

Figure 2.5. Illustration of former courses of the Beni channel, with successive migration occurring from A-E. Taken from Dumont (1996).

2.3 Climatic characteristics of the Beni floodplain

Within the Beni river floodplain study area mean annual temperatures of 25.9 degrees and mean annual rainfall of 1800 mm have been recorded (Hanagarth, 1993). In contrast, further north at Riberalta the average temperature is 26.8 degrees with mean annual precipitation of 1566 mm (Haase and Beck, 1989). The lowland Beni floodplain possesses a strongly seasonal tropical climate, characterised by a dry season which stretches from June to September and a longer wet season from October through April. The months of December, January, February and March contribute approximately 50% of the annual precipitation total within the study area (figure 2.6)

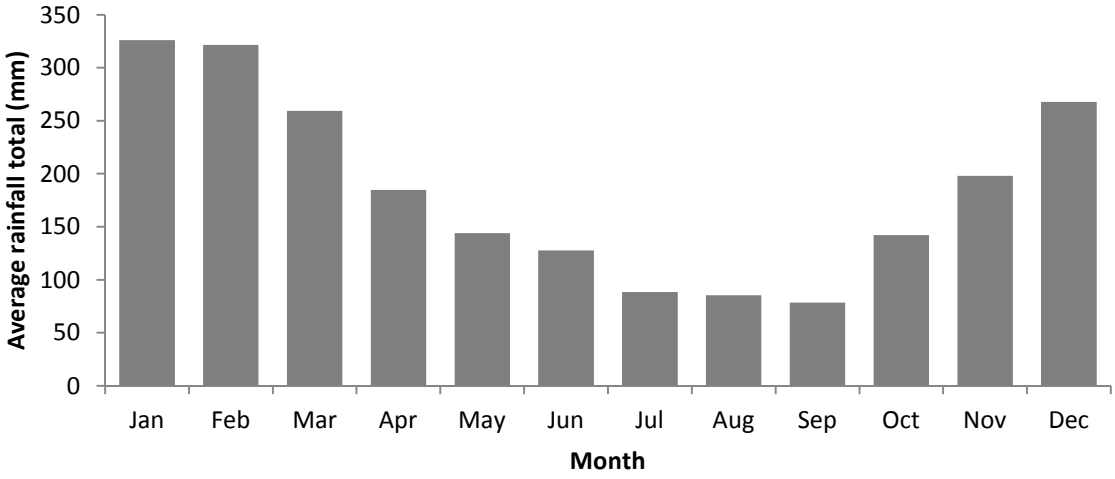

Figure 2.6. Average monthly rainfall recorded at Rurrenabaque for the period 1970-2010, calculated based upon data provided by the Bolivian Metereological Service (SENAMHI)

2.4 Beni floodplain inundation

The Beni river floodplain makes up the western portion of the Llanos de Mojos, a spatially extensive, flat plane constructed of late Miocene and Quaternary deposits (figure 2.7). The Bolivian Llanos encompass the area between the Beni, Mamore and Guapore rivers, making up the largest wetland in Amazonia which is flooded for up to five months per year. Inundated area for the Llanos de Mojos from 1979-1987 is illustrated in figure 2.8. In average years an area of approximately 100,000 km^2 of the Llanos de Mojos is subject to flooding, whilst this increases to a maximum of 150,000 km^2 in years of peak inundation (Denevan, 1980). Figure 2.8 illustrates that inundated area of the Llanos de Mojos shows a defined seasonal cycle, with elevated levels of inundation observed from January to May. In most years inundated area rises and falls unimodally, although multi modal flood peaks occur within some years. In addition a substantial area of the Llanos remains inundated throughout the dry season. Hamilton et al., (2004) found that inundated area within the Llanos showed a stronger correspondence with river discharge than rainfall totals.

The discharge regime of the Beni river can be defined as the Austral tropical pluvial type (Hanagarth, 1993; Guyot, 1993), and high water levels are experienced through the wet season from December to April (figure 2.9). Accordingly the Beni is characterised by high water levels through the warm rainy season, with flood inundation occurring when flow exceeds the estimated bankfull discharge of 7000 m^3s^{-1} (Gautier et al., 2007). Although bankfull

discharge is exceeded during the course of most years (Gautier et al., 2010), peak water levels vary markedly from year to year. The interannual variability in discharge is demonstrated within figure 2.9, for the period from September 1998 to August 2011. This period encompasses two of the largest flood events to occur within the Beni floodplain during the last century, in 1999 and 2011, with events characterised by peak discharges in excess of 20,000 m^3s^{-1}. In typical years annual peak discharge falls within the range 10,000-13,000 m^3s^{-1}, whilst the lowest annual discharge peak was observed within March 2004 at approximately 9,000 m^3s^{-1}. Through the period from 1967 to 2003 eleven major floods, defined as events characterised by a peak discharge greater than12,500 m^3s^{-1}, occurred within the Beni floodplain.

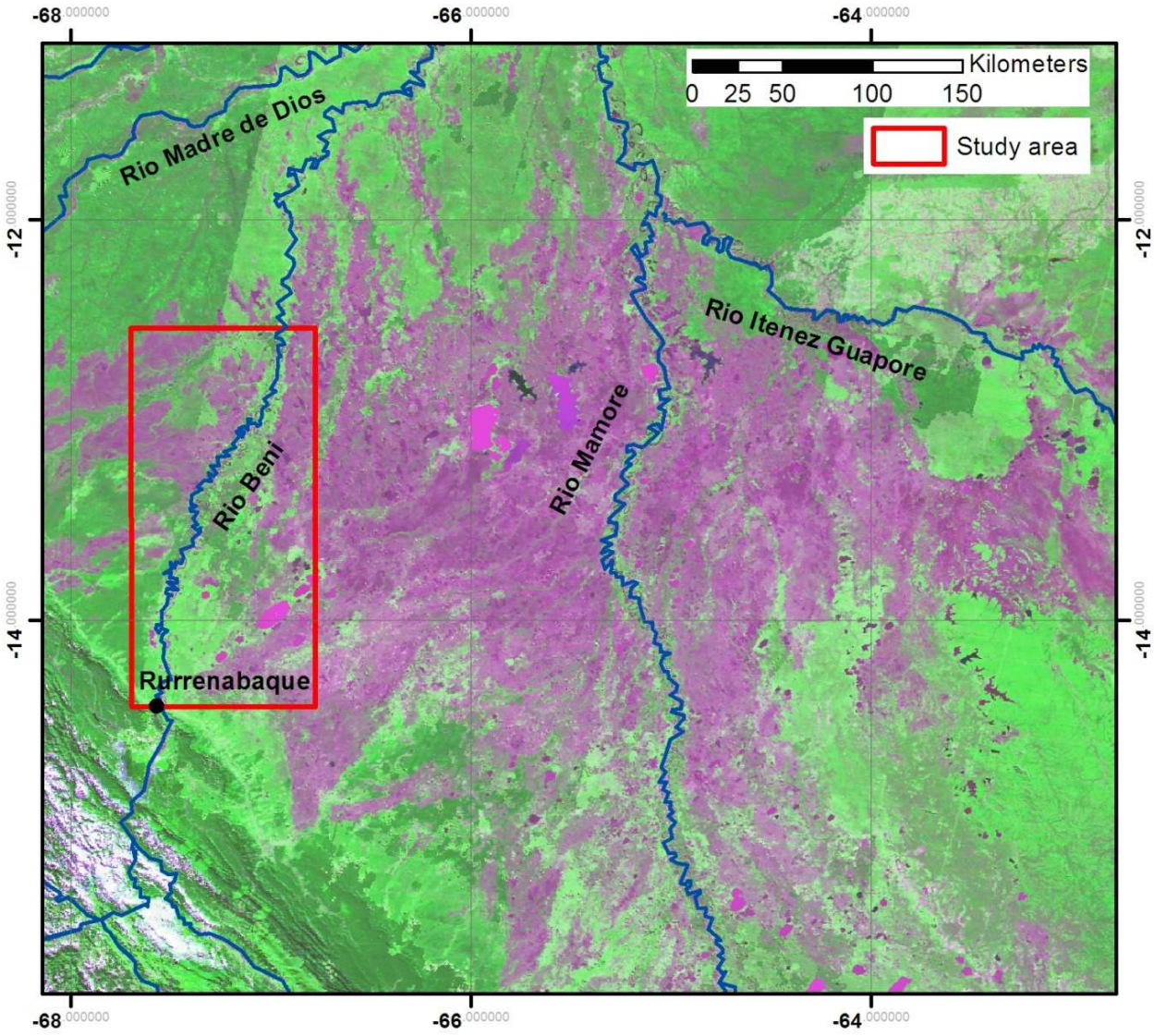

Figure 2.7. Location of the Beni river and study area within the Llanos de Mojos. Multispectral imagery is the MODIS MOD09 surface reflectance product.

Inundated area upon the Beni floodplain shows a similar seasonal cycle and interannual variability to the Llanos de Mojos (figure 2.8). Increases in inundation extent coincide well with the wet season and elevated river discharge observed from December to April. Accordingly inundation of the Beni floodplain has been attributed to the influence of both exogenous and endogenous processes (Pouilly et al., 2004). The arrival of the flood wave from the upper Beni catchment constitutes the exogenous driver of flooding in the study area. Exogenous flooding is characterised by overbank flow of white water which spreads over the floodplain, facilitated by the extensive network of abandoned channels (Bourrel et al., 1999).

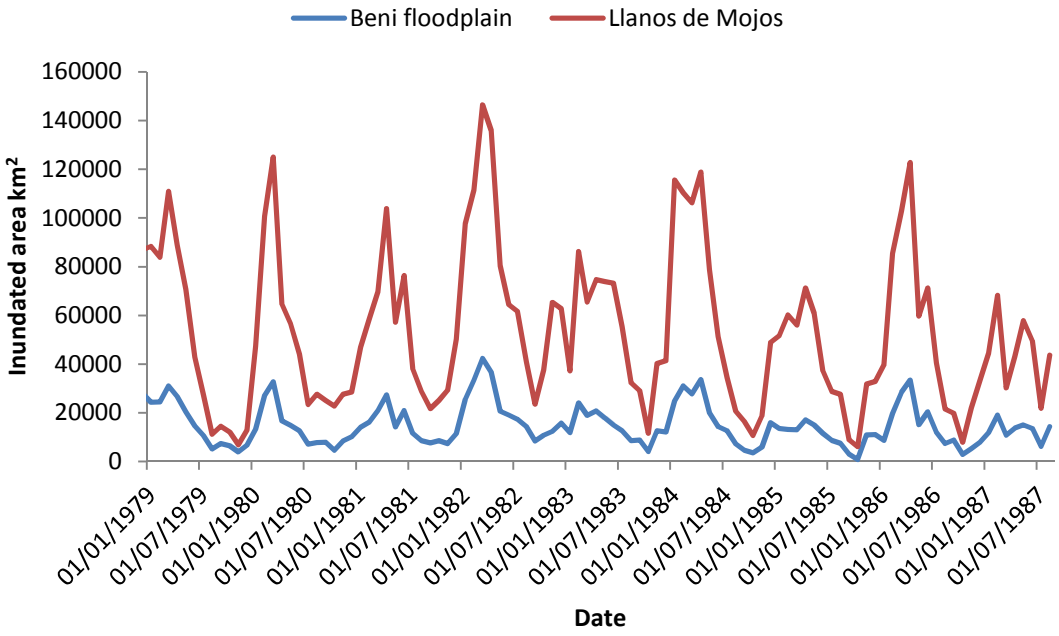

Figure 2.8. Inundated area for the Llanos de Mojos and the Beni floodplain. Reproduced from Scanning Multichannel Microwave Radiometer (SMMR) data utilised within Hamilton et al., (2004).

In contrast, endogenous flood inundation is generated within the study area as a result of local precipitation. The occurrence of high intensity rainfall leads to runoff and overflow of groundwater, which is exacerbated by the poor infiltration capacity of fine textured soils which make up the Beni floodplain (Haase and Beck, 1989). Endogenous flooding produces clear water inundation containing very little suspended sediment, which subsequently drains from the floodplain through small black water tributaries (Hamilton et al., 2002). Intuitively, the coincidence of both exogenous and endogenous drivers is responsible for the occurrence of the highest magnitude of flooding upon the Beni floodplain, such

as those events experienced in 1999 and 2011 (Bourges et al., 1992; Ronchail et al., 1995).

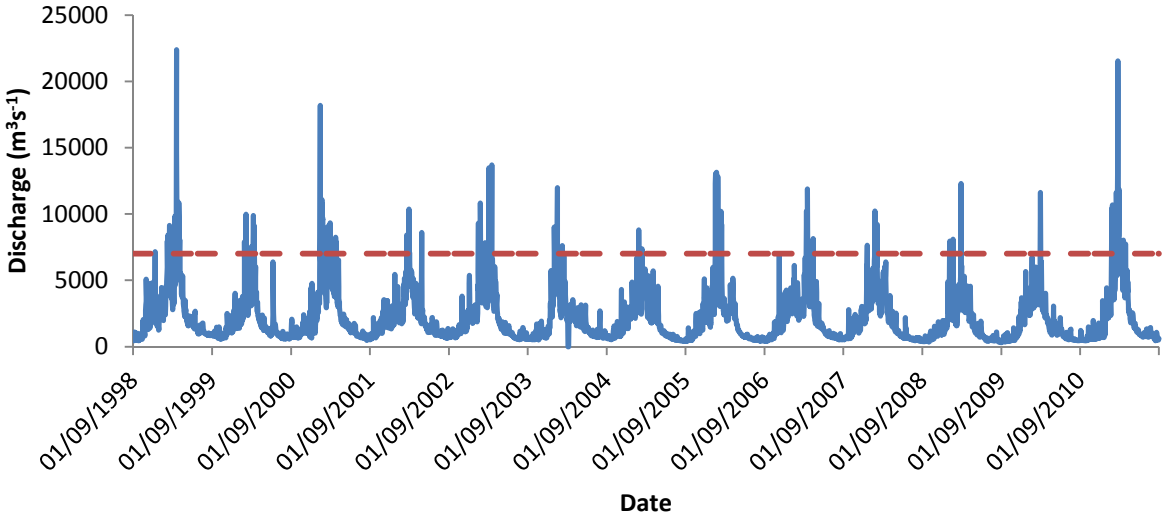

Figure 2.9 Discharge hydrograph for the Beni at Rurrenabaque provided by ORE Hybam. Red dashed line indicates bankfull discharge.

2.5 Beni floodplain sedimentation

The Beni can be classified as a white water river due to its large suspended sediment load (Prance, 1979), which totals approximately 192 million tonnes per annum at Rurrenabaque (Gautier et al., 2010). Large volumes of sediment are supplied to the Beni river through processes of denudation and mass wasting which occur within the rivers Andean headwaters (Guyot, 1993). Sediment fluxes within the Beni exhibit strong seasonal and interannual variability, with peak loads corresponding to the high water period which occurs from January to March. It is estimated that 82% of annual sediment exportation occurs during this three month window (figure 2.10). Overall, the Beni supplies an estimated 70% of the total suspended sediment load of the Madeira river (Gautier et al., 2007).

Within the foreland basin of the Beni the adjacent floodplain is subject to high levels of sedimentation as a result of annual flood inundation and high sediment loads. Indeed, it is estimated that approximately 100 Mt y^{-1} sediment is deposited annually upon the Beni floodplain (Aalto et al., 2003). It has been demonstrated by Aalto et al., (2003) that sediment accumulation on the Beni floodplain is episodic. Dating of sediment within floodplain cores through analysis of ^{210}Pb activity profiles demonstrated that most floodplain locations

were characterised by the arrival of discrete sediment packages. The deposition of these sediment packages is discontinuous in both time and space. Accordingly periods of decades are observed between depositional events at a given floodplain location, whilst the same depositional events are not recorded uniformly across the floodplain (Aalto et al., 2003).

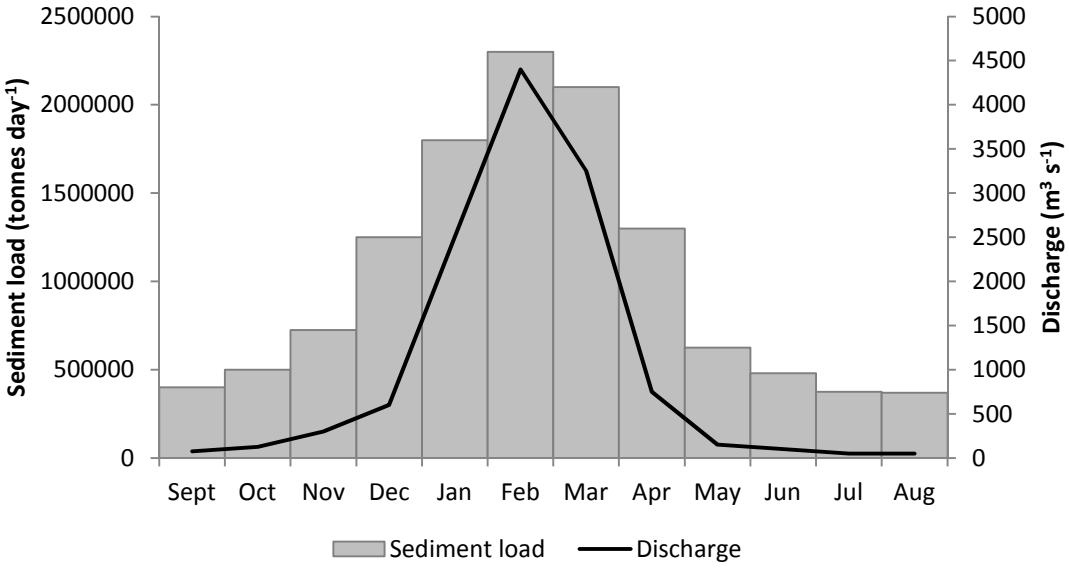

Figure 2.10. Mean discharge and mean sediment load for the Beni, reproduced from Gautier et al., (2010)

When averaged spatially, sediment accumulation rates are approximately 5 cm yr^{-1} in close proximity to the channel, falling to around 1 cm yr^{-1} in the distal floodplain (figure 2.11). Contrary to the episodic nature of deposition which characterises the floodplain at large, consistently high rates of sedimentation were observed in areas close to the Beni channel (Aalto et al., 2003). The consistent nature of accumulation in proximal areas reflects frequent deposition of sediment on raised levees which flank the channel during annual overbank flood events. In contrast, the episodic nature of sediment accumulation observed outside proximal areas has been attributed to a rather different mechanism. Aalto et al., (2003) hypothesise that large rapid rise floods linked to ENSO lead to the occurrence of levee failures, which facilitate the flow of sediment rich white water onto the floodplain. Large volumes of sediment are subsequently deposited in the form of crevasse splays as flood waters diverge and are subject to frictional resistance from dense floodplain vegetation.

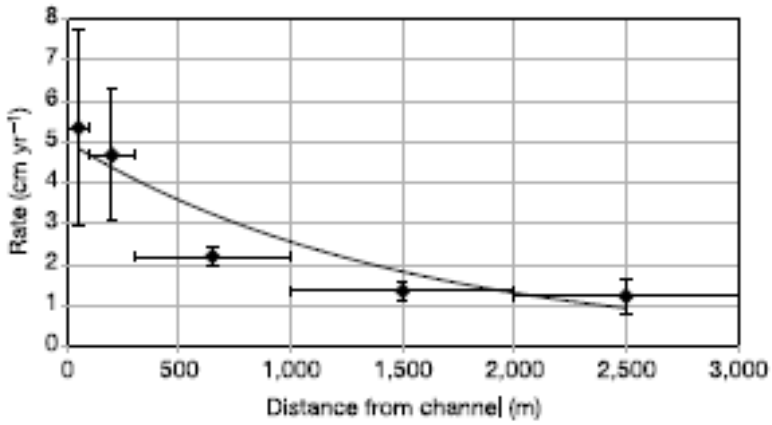

Figure 2.11. Sediment accumulation rates for the Beni floodplain averaged according to distance from the main channel. Taken from Aalto et al., (2003).

2.6 Beni floodplain land cover

The hydrodynamic functioning of the Beni river can be attributed as the primary cause of the high levels of biodiversity which exist within the ecosystem of the adjacent floodplain (Junk, 1997; Pouilly et al., 2004). Land cover of the Beni floodplain comprises a complex mosaic of savanna and tropical forest stands, which is interspersed with areas of open water such as meander cutoffs and shallow flat bottomed lakes. Overall the total extent of the study area comprises 48 % tropical varzea forest, 49 % savannas and grasslands, whilst areas of open water make up the remaining 3 %. This distribution of land cover can be observed within figure 2.2. The Beni is flanked by tropical forest stands along the length of the study reach, with these forest stands extending to a distance of greater than 50 km from the channel on the eastern floodplain. With increasing distance from the channel tropical broadleaf forests transition to savanna land cover, locally known as Pampas.

It is commonly acknowledged that the spatial distribution of land cover within the Llanos de Mojos is predominantly controlled by flood inundation, which is dependent upon local topography (Hanagarth, 1996). Within flat low lying regions of the distal floodplain open savannas are maintained by annual flood inundation which causes prolonged anoxic conditions and physiological heat stress, precluding the growth of woody tree species (Mayle et al.,2007). It is postulated that the location and characteristics of forest stands are heavily influenced by flood inundation. Accordingly it is thought that forest stands are preferentially located upon topographical features such as levees and terraces

of abandoned river channels (Hanagarth and Sarmiento, 1990), which are characterised by lower magnitude and duration of flood inundation. However, it is significant to note that extensive areas of savanna land cover are also present within the north east of the study area (figure 2.2), these areas are characterised by relatively high elevation as a result of neotectonic uplift described in 2.2. Given that these raised areas are likely to be associated with low flood inundation magnitude, the fact that they are maintained as savanna suggests that other hydrological factors in addition to flood inundation are significant in controlling the spatial distribution of land cover upon the Beni floodplain.

Other fluvial processes, specifically sedimentation and meander migration, exert significant controls upon forest cover within the Beni floodplain. The deposition of thick lenses of sediment associated with the formation of crevasse splays (Aalto et al., 2003) can cause the mortality of large areas of forest in close proximity to the channel. Lateral migration of the Beni channel is responsible for the erosion of relatively large areas of floodplain, whilst associated sediment deposition is responsible for the creation of an approximately equal area of new sites when averaged over the long term (Gautier et al., 2007). This is significant for forest dynamics as erosional processes are responsible for the loss of mature forest stands on the outside of meander bends, whilst new areas of alluvial sediment deposited on point bars are colonised by pioneer species which form the incipient stages of primary succession (Kalliola et al., 1991).

2.7 Summary

In summation, the lowland floodplain of the Beni river represents an area in which a highly dynamic fluvial system exhibiting rapid rates of channel shifting, annual flood inundation and large volumes of overbank sedimentation interacts with a large area of tropical varzea forest. In addition, the foreland basin of the Beni is devoid of artificial levees and dams, whilst the area has not experienced significant deforestation or cultivation. Having been subjected to minimal anthropogenic disturbance, the Beni river and its lowland floodplain can be considered relatively pristine (Aalto et al., 2003). Consequently the reach of the Beni river which stretches north from Rurrenabaque to the confluence with the Madidi represents an ideal location to address the overall research aims of this research project which were outlined in the previous chapter.

Chapter Three

Beni floodplain land cover classification

3. Beni floodplain land cover classification

3.1 Introduction

Land cover is a globally important variable which constitutes an important link between human and physical environments (Foody, 2002). Land cover change as a direct result of human settlement, agriculture and other influences constitute some of the most evident and significant impacts upon the environment. Vitousek (1994) stated that land cover change can be regarded as the single most important contributor to ecosystem change on a global scale, with an overall impact equivalent to, or exceeding that of climate change (Skole, 1994). Land cover is projected to play a major role in global biodiversity change over the next century (Friedl et al., 2002), primarily through its strong association with biogeochemical fluxes (Penner, 1994), climate, ecosystem functioning and sustainable land use (Uhl et al., 1990). Consequently, a quantitative understanding of the spatial distribution of land cover and the dynamics of land cover change is of fundamental importance for a multitude of applications, including natural resource management (Townshend, 1992) and modelling of climate and carbon exchange on a global scale (Sellers et al., 1997).

Historically, the dearth of knowledge relating to land cover dynamics can be attributed to poor provision of quantitative land cover data (DeFries and Townshend, 1994). Traditional maps compiled from logistically challenging and time consuming ground surveys were limited in terms of spatial extent, whilst being associated with low levels of accuracy and consistency (Belward et al., 1999). In the latter half of the 20th century, classification of remotely sensed images has emerged as an alternative method for the derivation of land cover maps (Foody, 2000). Remote sensing platforms are able to provide a consistent and continuous representation of earth surface characteristics over a range of spatial and temporal scales (Townshend, 1992). Hence, manual or automated classification of remotely sensed data is able to produce thematic maps which represent a vast improvement over those generated from ground based data collection in terms of accuracy, consistency and spatial extent/resolution (Hansen et al., 2000). Automated classification algorithms can be broadly separated into two types. Unsupervised classifiers operate through grouping of

spectrally similar pixels, with minimal input from the expert user. Supervised classification algorithms separate pixels into a number of classes, which are predefined by the expert user based upon the analysis of the spectra of different land cover types (Foody, 2002). The choice of classification algorithm commonly depends upon a number of factors; primarily accuracy requirements, ground truth data provision, knowledge of the study area and experience of the expert. Unsupervised classification tends to be employed where relatively little is known about the study area and field observations are limited. If the expert user possesses a priori knowledge of the study area and field observations are sufficient to enable delineation of training areas, supervised classifiers are often utilised in order to produce more accurate maps of land cover (Lillesand et al., 2008).

Whilst clearly being an issue of global importance, the spatial distribution and dynamics of land cover are equally significant at regional and local scales. Hence a broad range of classification exercises have been undertaken using remote sensing imagery; ranging from coarse 1 km resolution global land cover classification (Townshend, 1992; Loveland et al., 1999), to classification of small study areas at fine (<10 m) resolutions (Puissant et al., 2005). The Amazon basin covers a total area of approximately 6,000,000 km^2 of South America (Saatchi et al., 2000). The region is characterised by a wide range of different forest and non forest land cover types. Terra Firme forests are never flooded and are comprised of dense forests, open forests, dry forests and montane forests (Prance, 1979). The spatial distribution of these forest types is controlled by environmental variables such as annual rainfall totals, elevation and soil characteristics (Saatchi et al., 2000). Inundated varzea forests are located upon the floodplains of Amazonian rivers, and are ecologically distinct from Terra Firme forests due to the influence of the annual flood pulse (Junk, 1997). Savannas constitute the primary non forest land cover type and can be subdivided according to vegetation and soil characteristics (Veloso et al., 1991).

Since 1970, Amazonia has experienced increasing levels of human colonisation, agricultural expansion and widespread construction of infrastructure. As a direct result, an accelerated rate of deforestation and land cover change has been observed within the region. It has been estimated that up to the year 2000, a total area of 590,000 km^2 of tropical forest has been

cleared within the Brazilian Amazon (INPE, 2002), in the process producing anthropogenic vegetation land cover types. It is estimated that 30-50 % of this deforested area is now characterised by secondary successional growth (Lu et al., 2004a), whilst the remainder has been converted to agriculture, pasture or tree plantation. Thus, anthropogenic influences have accentuated the natural heterogeneity of land cover within the Amazon basin.

Amazonia constitutes a region of high scientific importance, in terms of both its unique ecology and role within the global carbon budget (Houghton et al., 2001), both of which are influenced by large scale land cover change (Skole, 1994). Therefore an accurate quantitative representation of land cover within Amazonia is required for a multitude of scientific applications, for example in studies of ecosystem functioning, and to derive accurate estimates of carbon storage and fluxes across the basin (Loveland et al., 2000). Given the large extent and remote nature of many study areas within the Amazon basin, classification of remotely sensed imagery represents the most efficient methodology by which to provide the required quantitative land cover information (Brondizio et al., 1996). Consequently, much research has focused upon the development of classification techniques to maximise the accuracy of land cover classification within the Amazon basin, with particular emphasis placed upon the separation of different forest types and successional stages (Lu et al., 2004b).

Despite a plethora of scientific studies, classification of Amazonian land cover, particularly accurate discrimination of different forest types, remains problematic (Lu et al., 2007). This can be attributed to two primary factors which are closely linked; heterogeneity in vegetation and spatial resolution of satellite imagery. Different forest types and stages of succession possess marked variation in physical characteristics such as stand age, species diversity, diameter distributions, stem density and height. Despite variation in some biophysical parameters, it is not uncommon for different forest types to possess similar canopy structures (Budreski et al., 2007). As remote sensing platforms primarily image the canopy surface, distinct forest types may be characterised by similar spectral signatures within optical imagery, making them very difficult to separate during classification (McCleary et al., 2008). The converse problem may also arise, whereby significant variations in forest physical characteristics are

observed within a single class. For example, Lu et al., (2004a) found separation of degraded pasture and initial successional stages difficult, whilst more advanced successional stages are often spectrally similar to anthropogenic vegetation types. This issue of heterogeneity is most prevalent when attempting to classify successional forests, as the transition between stages is often very smooth (Lu et al., 2004b).

Problems associated with heterogeneity of forest cover are often exacerbated by the limited spatial resolution of remotely sensed imagery. The remote location and large extent of many Amazonian study areas, along with the influence of cloud cover means that Landsat TM/ETM often constitutes the best source of multispectral imagery available for use within land cover classification (Lu et al., 2002). Whilst Landsat TM/ETM is highly versatile, in heterogeneous areas its medium (30 m) spatial resolution makes the imagery prone to the mixed pixel problem, whereby a single pixel contains multiple different land cover types. The presence of mixed pixels makes the classification of multispectral images difficult, particularly using traditional per pixel approaches, for example Maximum Likelihood Classification (MLC) or Minimum Distance algorithms (Mausel et al., 1993). Per pixel classifiers generally develop an aggregate spectral signature based upon all pixels within a training set and hence do not account for mixed pixels. As a result many studies have circumvented the difficulties associated with the separation of forest types, adopting a simplified approach to classification featuring fewer forest classes (Lucas et al., 1993; Adams et al., 1995; Rignot et al., 1997).

However, separation of different forest types and successional stages is important for a number of scientific reasons, particularly for utilisation within estimation of basin wide carbon stocks and assimilation rates. Therefore a number of studies have sought to maximise the potential of land cover classification within the Amazon basin through application of a variety of image processing techniques and classification algorithms. Spectral mixing analysis, referred to here as Linear Spectral Unmixing (LSU), is an image analysis technique which has been successfully utilised within numerous Amazonian land cover classification exercises (Lu et al., 2004a ; Lu et al., 2004b; Kawakubo et al., 2009). LSU is based upon the assumption that the spectra of a given pixel is comprised by a linear mixture of its constituent land cover classes,

and therefore offers a quantitative solution to the mixed pixel problem (Adams et al., 1995). LSU analysis separates a multi spectral image into a series of fraction images, which represent the areal proportions of a set of pre defined pure end members for each pixel. Fraction images derived from LSU are subsequently used as an input into classification algorithms in order to provide a source of sub pixel information (Small, 2004).

For a study area located within Rondonia, Brazil, Lu et al., (2004a) employed a number of different classification methodologies, with the aim of identifying which approach generated the most accurate representation of land cover. The study found that classification of LSU derived fraction images using a decision tree algorithm produced an overall accuracy of 86%, compared to traditional per pixel classifiers whose accuracy varied between 77% - 80 %. Benefits of the LSU decision tree approach were accrued primarily through classification of different successional stages with a greater level of accuracy. The authors concluded that choice of the most appropriate classifier depends largely upon context specific factors, although more complex classification schemes perform better within areas characterised by heterogeneous land cover.

In another study undertaken within the same area of the Brazilian Amazon, Lu et al., (2004b) investigated the potential for improvement of land cover classification accuracy both through further processing of input multispectral imagery and implementation of different classification algorithms. Results illustrated that adoption of an LSU DTC approach yielded a 5% increase in overall accuracy when compared to an MLC classifier and thus were consistent with the findings of Lu et al., (2003a; 2004a). The authors found that implementation of Minimum Noise Fraction (MNF) or Principal Components Analysis (PCA) transformations were associated with an increase in overall accuracy, whilst spectral subsetting of Landsat TM/ETM also yielded a modest increase inthe accuracy of resulting land cover maps. The authors concluded that correlation between Landsat TM bands limited classification accuracy, whilst appropriate image processing techniques were able to reduce this correlation and associated data redundancy.

In summation it is clear that classification of Amazonian study areas is time consuming and problematic. High heterogeneity of land cover (Batistella et al.,

2009) combined with limited spatial resolution of remotely sensed imagery constitute unavoidable issues which limit the accuracy of classification (Kawakubo et al., 2013), particularly the separation of different forest types and successional stages. The study of Lu et al., (2004a) illustrated that no single optimum approach to land cover classification exists, indeed all classifiers including traditional per pixel algorithms are able to provide useful land cover information for Amazonian study areas. However, selection of the most appropriate classification scheme, based upon the characteristics of a given study area can maximise the quality of resulting land cover maps. In particular, the aforementioned studies have demonstrated the benefits which can be accrued through implementation of more complex classification algorithms/image processing routines when undertaking classification in a region characterised by highly heterogeneous land cover. A common conclusion amongst all of the aforementioned studies was that classification accuracy depended largely upon the quality of training datasets, with extensive and high quality field observations required in order to produce an accurate classification of land cover in heterogeneous Amazonian study areas.

Within this study, an accurate quantification of the spatial distribution of land cover is important for understanding the hydrological and ecological functioning of the Beni floodplain. Furthermore, a high quality land cover classification constitutes an important input dataset for analyses which will be undertaken in subsequent chapters, particularly floodplain DEM generation and production of inundation maps. The Beni floodplain study area is characterised by a complex mosaic of varzea forest and savanna land covers, and is comparable to the wider Amazon basin. This suggests that the classification approaches investigated by Lu et al., (2003; 2004) are appropriate for application within this study.

3.2 Research aims

The primary aim of this chapter is to generate an accurate classification of land cover within the Beni floodplain study area, using Landsat TM multispectral imagery. The primary aim will be realised through the completion of four specific objectives.

1. To identify and characterise distinct land cover classes which comprise the Beni study area through field observations and analysis of spectral characteristics.
2. To produce five floodplain land cover maps through application of maximum likelihood and decision tree classification algorithms to a number of different input datasets
3. To interpret floodplain land cover maps in light of ancillary datasets and field observations in order to gain insights into the spatial distribution and dynamics of land cover upon the Beni floodplain
4. To assess the accuracy of floodplain land cover maps with respect to field observations in order to identify the optimum classification methodology.

3.3 Data sources

3.3.1 Landsat TM images

Initially two Landsat 5 TM scenes (Path 1, Row 69/70), acquired on the 16th November 2011, were obtained from USGS Earthexplorer (http://earthexplorer.usgs.gov/). These represented the highest quality scenes available in the closest temporal proximity to the ground truth data collection, which occurred in September 2011. Images which were temporally synchronous with the collection of ground truth data were selected in order to mitigate the potential influence of human induced and seasonal changes in land cover on the Beni floodplain.

Although multispectral imagery is available from numerous different satellite platforms, Landsat TM was adjudged to be most suited to this particular classification exercise. Landsat TM/ETM sensors have a resolution of approximately 30 m, individual tiles cover an area ~31,450 km^2, and each tile has a maximum repeat frequency of ~16 days. Within the context of this study the characteristics of Landsat TM facilitate a classification with an appropriate level of detail, whilst allowing complete coverage of the ~ 26,000 km^2 study area with two tiles. In addition, the repeat frequency of Landsat TM is sufficient to provide high quality cloud free scenes in close temporal proximity to the collection of ground truthing data. Despite offering both excellent spatial and temporal coverage, the application of MODIS was limited by its 500 m spatial

resolution, which precludes the production of a classification with a sufficient level of detail for this study. ASTER images are characterised by a superior spatial resolution of 15 m, however individual tiles cover a much smaller area and are associated with a lower repeat frequency. Therefore it proved impossible to obtain a consistent cloud free ASTER coverage of the study area in close temporal proximity to the field campaign.

3.3.2 SRTM dataset

The Shuttle Radar Topography Mission was a joint project between NASA and the USGS which flew in February 2000 (Farr and Kobrick, 2000). The SRTM collected global elevation data using C-band SAR, which was subsequently processed and released as a digital elevation model at a resolution of 1 arc second (30 m) for the United States and 3 arc seconds (90 m) for the rest of the world (USGS, 2003). Extensive validation efforts have confirmed that the SRTM comfortably exceeded its pre mission vertical accuracy requirements of 16 m linear error at the 90 % confidence interval (Berry et al., 2007). However, a systematic positive bias has been observed for the SRTM within areas of vegetation cover (Carabajal and Harding, 2005). This positive bias occurs as C-band SAR interacts strongly with physical vegetation elements, hence within forested areas the reported DEM elevation lies somewhere between the height of the ground surface and the top of the vegetation canopy (Bhang et al., 2007). Here the SRTM DEM is utilised solely to aid interpretation of the land cover classification and thus underwent no further processing. A more detailed description of this dataset will be provided later in Chapter 4.

3.3.3 Field observations

Observations of land cover characteristics were acquired for the purpose of ground truthing, during a field campaign which took place during September 2011. Land cover was surveyed at 249 locations, both in close proximity to the main river channel and in the distal floodplain (figure 3.1). The surveyed locations were stratified across an array of different land cover types which were deemed to be representative of the floodplain at large.

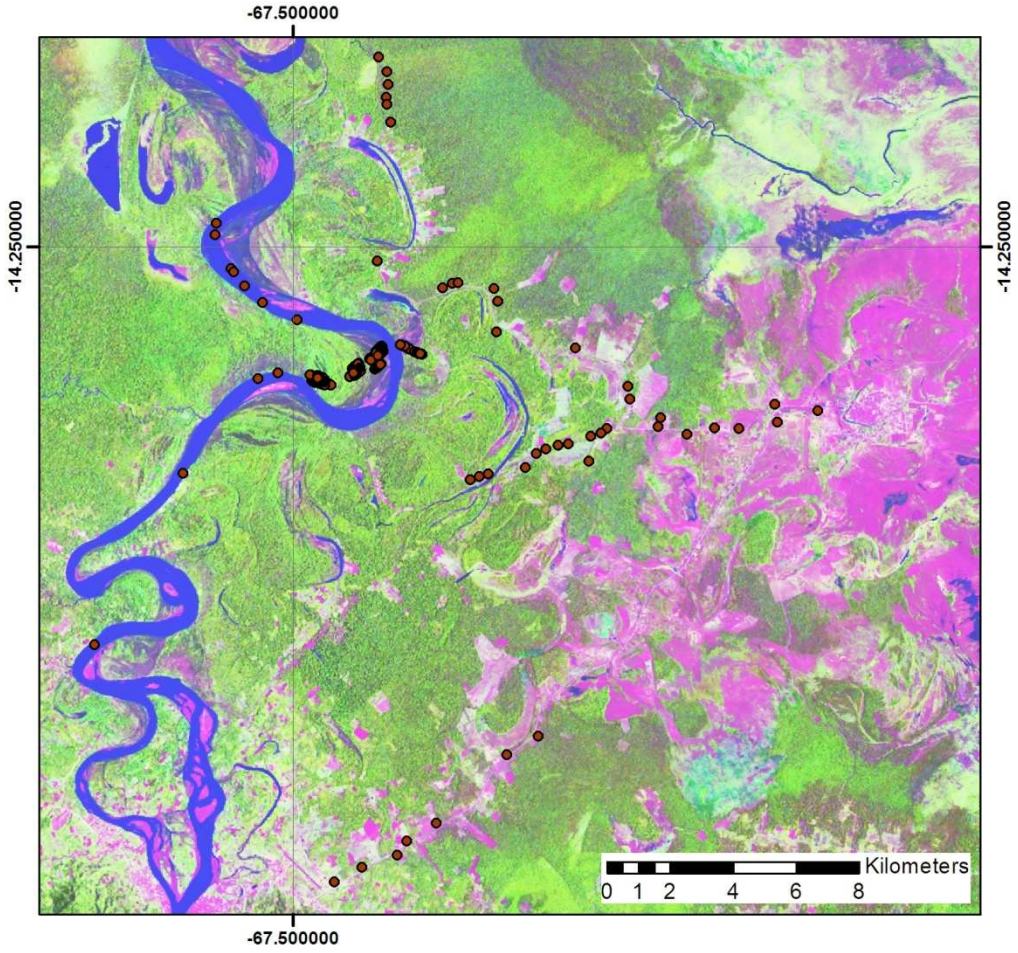

Figure 3.1. Landsat TM false colour composite image showing the location of land cover observations for the Beni floodplain.

In forested locations, 25 m^2 inventory plots were established, in which the diameter at breast height (DBH), height and species was measured for each individual > 10 cm DBH, stems > 5 cm DBH were subsampled in 9 m^2 plots. Forest inventories were analysed in order to separate forests into early successional forests, late successional forests and mature forests. Within non forested locations, land cover type was determined in situ and descriptions of the salient land cover characteristics were recorded. All surveyed locations were marked with a handheld GPS unit in order to facilitate integration with GIS/Image analysis software. After the completion of field work, GPS points were converted into a shape file within ArcGIS and overlain upon a colour composite of the Landsat TM image in order to ensure the consistency between field and remotely sensed datasets.

3.4 Methodology

3.4.1 Landsat TM preprocessing

In order to prepare Landsat 5 TM tiles for land cover classification it was necessary to undertake a series of pre processing procedures, implemented within the ENVI image analysis software package. Initially, scenes were geometrically rectified using control points obtained from the NASA Geocover image. Georectification was accomplished using nearest neighbour resampling, producing a root mean square error of less than 1 pixel. Geometrically rectified Landsat TM scenes were then subject to radiometric and atmospheric corrections. During radiometric calibration, pixel values were converted from digital number into radiance (equation 3.1) and subsequently to top of the atmosphere reflectance (equation 3.2) using gain and offset values for each band and the sun elevation angle extracted from the Landsat 5 TM header files. Conversion to reflectance was necessary in order to facilitate direct comparison between the spectral response of image pixels and different land cover types in published spectral libraries.

$$L_\lambda = \left(\frac{LMAX_\lambda - LMIN_\lambda}{QCALMAX - QCALMIN}\right) * (QCAL - QCALMIN) + LMIN_\lambda \qquad (3.1)$$

$$\rho_\lambda = \pi * L_\lambda * \frac{d^2}{ESUN_\lambda} * cos\theta_s \qquad (3.2)$$

Remaining atmospheric influences were removed from the calibrated Landsat TM scenes through the dark object subtraction technique, using a pixel obtained from a deep water floodplain lake (Lu et al., 2002). The dark object subtraction technique is predicated upon the assumption that the dark object, in this case deep clear water, absorbs all incoming radiation (Chavez, 1996). Any reflectance observed within the selected pixels is assumed to be attributable to atmospheric effects and is subtracted from the spectra of the remaining pixels in the image. The effects of radiometric calibration and atmospheric correction are shown in Figure 3.1.

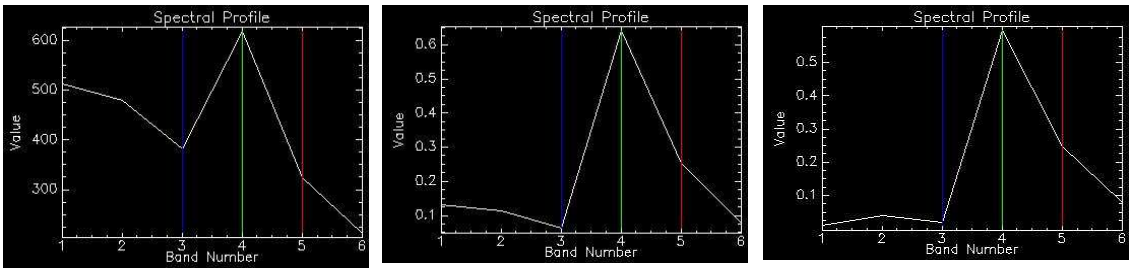

Figure 3.2. Spectral profiles of a vegetated Landsat TM pixel through calibration and atmospheric correction. Left- digital number. Centre- reflectance. Right- atmospherically corrected reflectance.

3.4.2 Linear spectral unmixing

The first and most important stage in Linear Spectral Unmixing (LSU) is the selection of appropriate pure end members for the image to be classified (Van der Meer and De Jong, 2000). Ustin et al., (1996) stated that the variance in any given multispectral image can usually be characterised by between 2-6 end members. In past applications of LSU within Amazonian land cover classification green vegetation (GV), soil and shade have constituted the 3 primary end members, whilst in some instances non photosynthetic vegetation (NPV) has been included as a fourth end member (Smith et al., 1990; Aguiar et al., 1999; Small, 2001).

$$R_i = \sum_{k=1}^{n} f_k \, R_{ik} + \epsilon_i \qquad (3.3)$$

Within this study, end members were obtained from the Landsat TM scene, in order to ensure that spectra were commensurate with the scale of the image space. This is often not the case with end members taken from spectral libraries or derived from field measurements (Roberts et al., 1998a). A sufficiently pure NPV end member could not be identified within the Beni floodplain study area, therefore three end members; GV, soil and shade were selected iteratively from the Landsat TM image. The shade end member was obtained from a deep water lake, whilst GV and soil end members were located in the extremes of the image space using scatter plots of Landsat bands TM 3,4 and 5 (Roberts et al., 1998b). The end members were checked for consistency against spectral profiles for GV and soil obtained from the ASTER Spectral Library in figure (http://speclib.jpl.nasa.gov/).

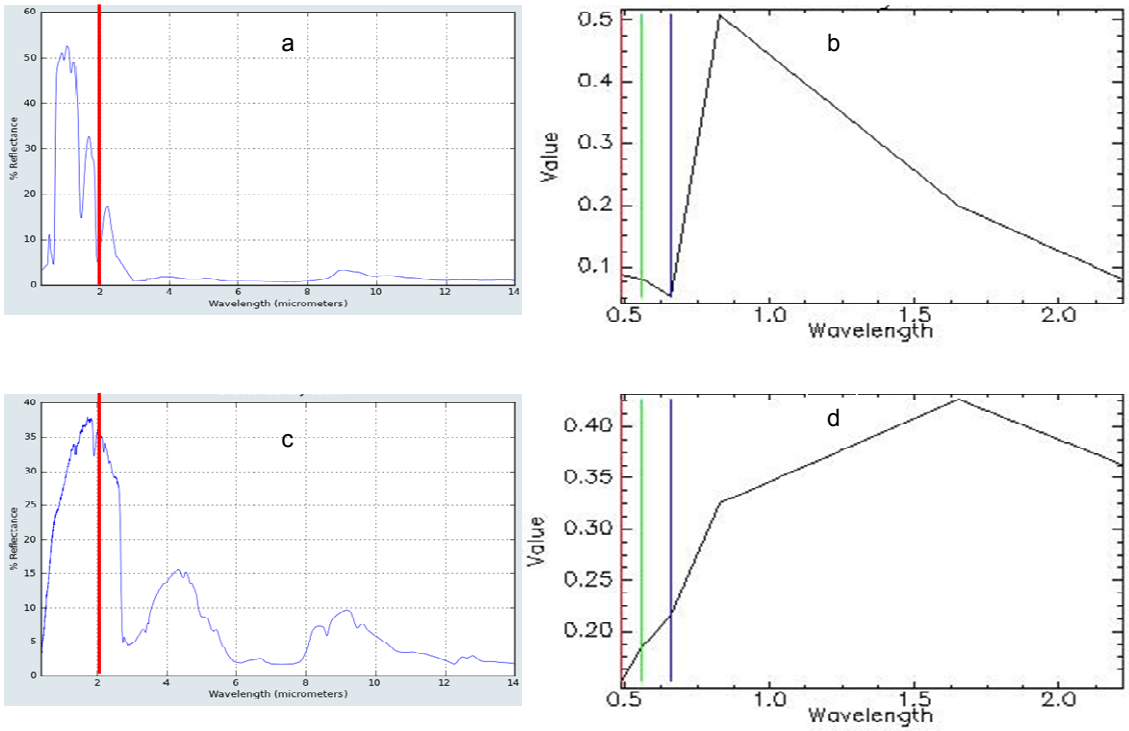

Figure 3.3. Spectral profiles for a) green vegetation spectra, taken from ASTER spectral library b) green vegetation spectra, taken from Landsat TM image soil c) soil spectra, taken from ASTER spectral library d) soil spectra, taken from Landsat TM image. Vertical red line in a) and c) delineates the portion of the spectrum shown within b) and d).

End members were subsequently used as input into a least squares linear spectral unmixing model (equation 3.3), which unmixed the Landsat TM scenes into three fraction images using a constrained solution. A constrained solution differs from an unconstrained solution as it is subject to the conditions of equation 2.4, which mean that the different fractions must sum to one and cannot assume negative values (Garcia-Haro et al., 1996). A further step involved the combination of both the green vegetation and shade fractions in order to generate a shade ratio image. This was achieved by simply dividing the green vegetation image by the shade fraction image (Lu et al., 2003a). The shade ratio image contains information relating to canopy structure and can be used to discriminate between different types of forest (Shimabukuro et al., 1998).

$$\sum_{k=1}^{n} f_k = 1 \text{ and } 0 \leq f_k \leq 1 \qquad (3.4)$$

3.4.3 Land cover classification

In order to attain the highest levels of accuracy possible given the datasets available, and to explore the potential benefits offered by adoption of different classification algorithms/image processing techniques five different classification schemes were implemented. Four land cover maps were produced using Maximum Likelihood Classification (MLC) with different input datasets, whilst the final map was the output from combined Linear Spectral Unmixing-Decision Tree Classification (LSU-DTC). Processing of input datasets and land cover classification was implemented within ENVI Image Analysis software.

The Beni floodplain was separated into a total of eight classes, which were determined based upon field observations and satellite imagery. Forests were divided into three constituent classes; primary successional stage, late successional stage and mature forests. Other non forest classes were pasture, grasslands, water, savanna and 'burnt' savanna. Non forest classes were associated with a degree of similarity and the differences are further elucidated within 3.5.1. Suitable training plots for the different land cover types were established across the study area. Quality of the training plots was checked using the Jeffries-Matusita distance measure, which quantifies the statistical separability between the spectral curves of different land cover classes on a scale from 0-2, with values exceeding 1.9 indicating good separability (Richards, 1999).

The Maximum Likelihood Classification (MLC) algorithm represents one of the most widely used per pixel classifiers, and separates land cover types through the development of a series of average spectral signatures based upon all pixels within a training set. MLC calculates the probability that a pixel belongs to a certain class, relying upon assumption of a near normal spectral distribution for a given feature and an equal a priori probability between classes (Lillesand et al., 2008). Variability within classes is incorporated through application of a covariance matrix (Richards and Jia, 1999). Here, training areas were established for each land cover class based upon the field land cover survey and interpretation of Landsat TM imagery. MLC was implemented using four different sets of input images, derived from Landsat TM, with the aim to

illustrate how different processing techniques could affect classification accuracy. The different sets of input images comprised the original Landsat TM image (Digital Number values); calibrated Landsat TM image (Reflectance values); spectral subset of the calibrated Landsat image (Bands 3, 4, 5, 7) and Landsat TM subject to a Minimum Noise Fraction (MNF) transform. Intuitively the use of different sets of input images produced distinct land cover maps which were named as follows; Landsat TM digital number- Map 1; calibrated Landsat TM- Map 2; Landsat TM MNF transform - Map 3; spectral subset of calibrated Landsat TM - Map 4.

The final land cover map was produced through application of a Decision Tree Classification (DTC) algorithm, using physically based fraction and shade ratio images output from LSU (Lu et al., 2004a). A DTC is a hierarchical classification tool which is characterised by no a priori statistical assumptions. Input images are separated into classes based upon a set of rules or thresholds which are defined by the expert user for the specific requirements of the classification (Rogan et al., 2002). Here, each rule provides only two possible outcomes and only one class is separated at each level, therefore it can be considered a binary DTC. In order to derive thresholds which are applied as rules within the DTC, regions of interest were defined for each land cover class based upon field observations and statistics extracted from the fraction images. Statistics were analysed and a set of thresholds developed which facilitated most accurate discrimination between land cover classes. Thresholds were applied within the DTC and the resulting classification assessed using ground truth data. This process was repeated iteratively, refining thresholds in order to increase the classification accuracy. The final land cover map produced using LSU-DTC was named as Map 5.

In the post classification stages a majority filter was applied to the land cover classification in order to remove spurious pixels. In addition the two savanna classes were merged, hence the final land cover maps contained seven classes.

3.4.4 Accuracy assessment

Accuracy of the Beni floodplain land cover classifications was assessed with respect to a set of field observations, the collection of which is detailed within

3.3.1. Importantly these observations were independent of the training dataset used as input into the classifiers. Observations of land cover across the Beni floodplain formed the basis for construction of an error matrix and implementation of kappa analysis. The error matrix is a widely used tool for the validation of land cover maps and displays measures of producers accuracy (PA), users accuracy (UA) and overall accuracy (OA).

User accuracy quantifies errors of commission and is calculated by dividing the number of correctly classified pixels within each category by the total number of pixels classified within that category. Overall this represents the probability that a pixel classified into a given category actually represents that category on the ground (Smits et al., 1999). Producers accuracy considers errors of omission, indicating how well reference pixels of a particular ground cover type are classified. Producers accuracy is calculated through division of the number of correctly classified pixels in each category by the number of reference pixels which are known to be of that category (Foody, 2002). Overall accuracy is a simple measure which is calculated through the division of the number of correctly classified pixels by the total number of pixels. Overall accuracy may provide a misrepresentation of the performance of a classifier if a large number of validation points are located within easily distinguishable classes such as water (Congalton, 1991).

$$\mathrm{K}=\frac{\mathrm{N}\sum_{\mathrm{k}} x_{\mathrm{kk}}-\sum_{\mathrm{k}} \mathrm{x}_{\mathrm{k}\sum}\mathrm{x}_{\sum\mathrm{k}}}{\mathrm{N}^{2}-\sum_{k} \mathrm{x}_{\mathrm{k}\sum}\,\mathrm{x}_{\sum\mathrm{k}}} \qquad (3.5)$$

In order to provide a more robust assessment of the accuracy of the different classification procedures, the error matrix was supplemented by the implementation of kappa analysis. The kappa coefficient is a measure of interobserver variation and considers the difference between observed agreement and the agreement which would be expected to arise as a result of chance (Congalton and Green,). Kappa analysis can be implemented in order to analyse both a single error matrix and the difference between error matrices. Although kappa analysis possesses the scope to perform inter matrix comparison (Hudson and Ramm, 1987), in this study the technique will be applied solely to assess classification performance within single matrices.

3.5 Results

3.5.1 Characterisation of floodplain land cover classes within Landsat TM and end member fraction images

Figure 3.4 shows the spectral profiles extracted from the Landsat TM image for each of the eight land cover classes. The shape of the spectral profiles of different forest classes is broadly similar within Landsat TM bands 1-5. Forests are characterised by a steep spectral profile, with low reflectance (< 0.1) in bands 1 (0.45-0.52 micrometers),2 (0.52-0.60 micrometers) and 3 (1.55-1.75 micrometers) 7 (2.08-2.35 micrometers), and a pronounced peak in reflectance within the near infrared red part of the spectrum (band 4- 0.76-0.9 micrometers) and to a lesser extent for band 5 (1.55-1.75 micrometers). Although different forest types are characterised by spectral profiles with broadly the same shape, reflectance values for near IR and band 5 are lowest for SS1. SS2 and mature forest classes possess very similar reflectance intensities, with the spectral profiles overlapping for these two classes. A quantification of this visual analysis is provided by Jeffries-Matusita values shown in table 3.1. Jeffries-Matusita coefficients for pairs of classes including forest classes generally exceed 1.8, indicating that these classes are generally characterised by a high level of separability. However, the visual similarity of the spectra for SS2 and mature forest is reflected in the Jeffries-Matusita value of 1.28, which suggests that separation of these forest types during classification is likely to be problematic.

The spectral profile of grasslands is similar in shape to that of the forest classes, although reflectance values in near IR and band 5 are the highest of any land cover class. The pasture land cover class is characterised by a spectral response which is similar to that of mature forests for bands 1-4, however higher reflectance values are retained for bands 5 and 7, leading to lower gradient in the tail of the spectral profile. The spectral response of savanna classes is distinct from other terrestrial land cover classes, most notably due to low reflectance observed within Landsat TM band 4. The spectral profile is relatively flat, indicating an even spectral response across the different wavelengths captured by Landsat TM. Table 3.1 suggests that the non forest classes have a high level of separability from both forest classes and other non forest classes, with Jeffries-Matusita values exceeding 1.9 in all cases. Water is

characterised by the lowest spectral response overall, with reflectance peaking in band 2 and falling to close to zero for bands 5 and 7.

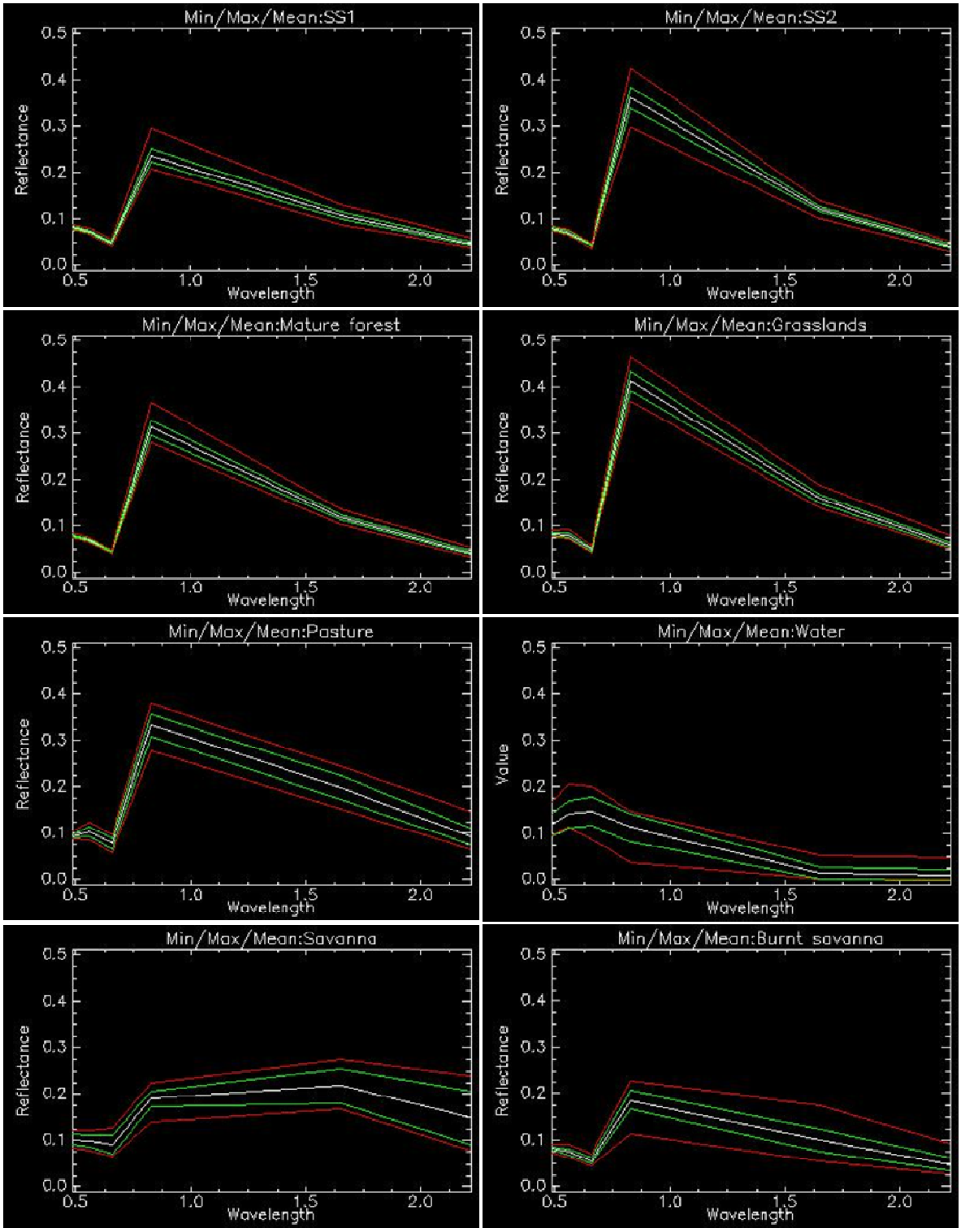

Figure 3.4. Landsat TM spectral profiles of Beni floodplain land cover classes. White line-mean reflectance, green lines- upper and lower quartiles, red lines-minimum and maximum reflectance. Landsat band wavelengths (micrometers); Band 1- 0.45-0.52; Band 2- 0.52-0.60; Band 3- 0.63-0.69; Band 4- 0.76-0.90; Band 5- 1.55-1.75; Band 7- 2.08-2.35. Band 6 is a thermal band and is therefore excluded here.

Table 3.1. Jeffries-Matusita index of separability for Beni floodplain land cover classes.

Class 1	Class 2	Jeffries-Matusita distance
SS1	SS2	1.99
SS1	Mature forest	1.96
SS2	Mature forest	1.28
Mature forest	Pasture	1.98
SS2	Grasslands	1.95
Pasture	Savanna	1.99
Water	Mature forest	2.00
Water	Savanna	2.00

Figure 3.5 shows end member fraction images and a shade ratio image for the Beni floodplain, annotated with polygons which delineate areas of different land cover types. This is supplemented by figures 3.6 and 3.7, which graphically illustrate typical end member fraction values observed for the floodplain land cover classes. It is possible to elucidate the basic characteristics of the floodplain land cover classes through simple visual analysis of these figures. Water is perhaps the most clearly defined and easily differentiated land cover type within the study area, possessing high values for the shade end member fraction, whilst exhibiting minimal response in GV and soil. Forest classes (SS1, SS2 and Mature forest) generally possess high values in the GV and shade classes and very low values in the soil fraction. SS1 is characterised by the highest shade and soil fractions whilst exhibiting the lowest value for GV. End member fraction values for SS2 and mature forests are very similar, although SS2 exhibited a slightly higher value for GV and a lower value for shade. These attributes are reflected and accentuated in the shade ratio image, where SS2 exhibited the highest value, followed by mature forest and SS1. Fraction values for grasslands are comparable to those of forest classes, this is intuitive given the similarity in spectral responses. However grasslands are distinct from forests as they exhibit the highest shade ratio value of any class, this is attributable to the combination of high values for GV and low values for shade.

The soil fraction image is generally very dark in comparison to both the GV and shade fractions, which is unsurprising given that forest dominates land cover within the region of the Beni floodplain shown in figure 3.5. The spatially limited

regions which appear bright within the soil fraction image generally correspond to savanna land cover located to the south east corner of the image. Figure 3.7

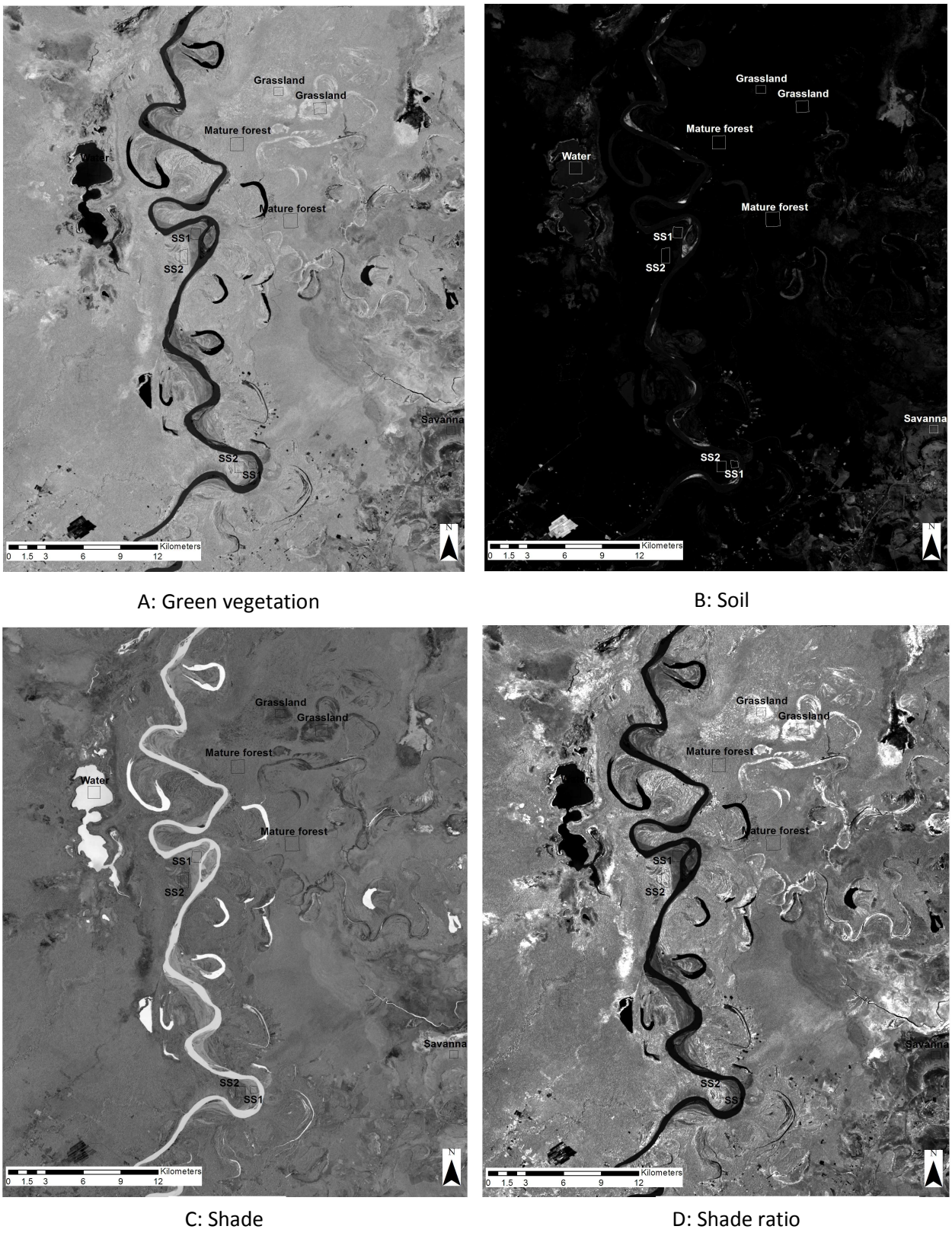

Figure 3.5. Fraction images derived through linear spectral unmixing of Landsat TM scene. Lighter areas denote high fraction values.

illustrates that savanna possesses the highest soil fraction values of any class, accompanied by relatively high values for shade, whilst possessing the lowest GV fraction value of any terrestrial land cover class. It is difficult to visually distinguish areas of pasture from the fraction images displayed in figure 3.5. However, figure 3.7 illustrates that pasture land cover possess a unique response in terms of end member fractions. This response is typified by relatively high values for GV, whilst the value of for soil is lower than for savanna but greater than for all other classes.

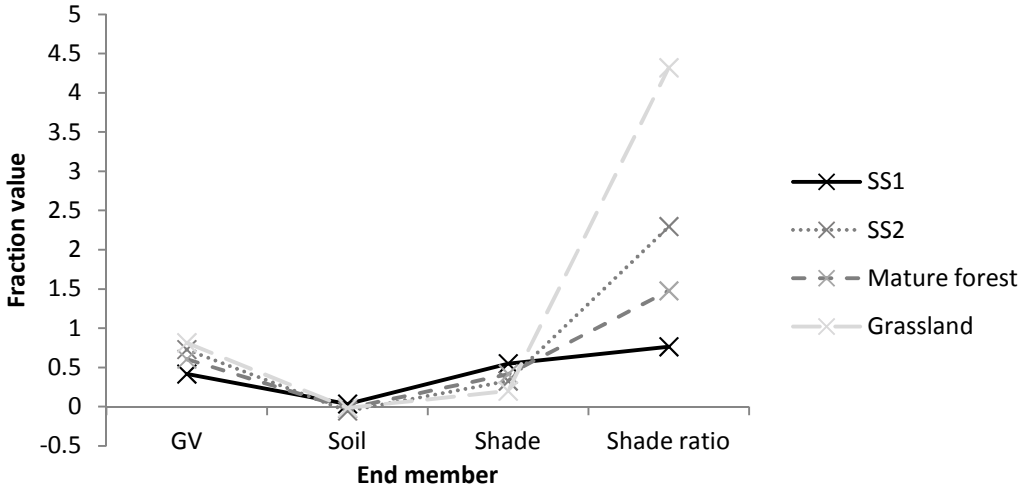

Figure 3.6. Average end member fraction values for forest/grassland classes.

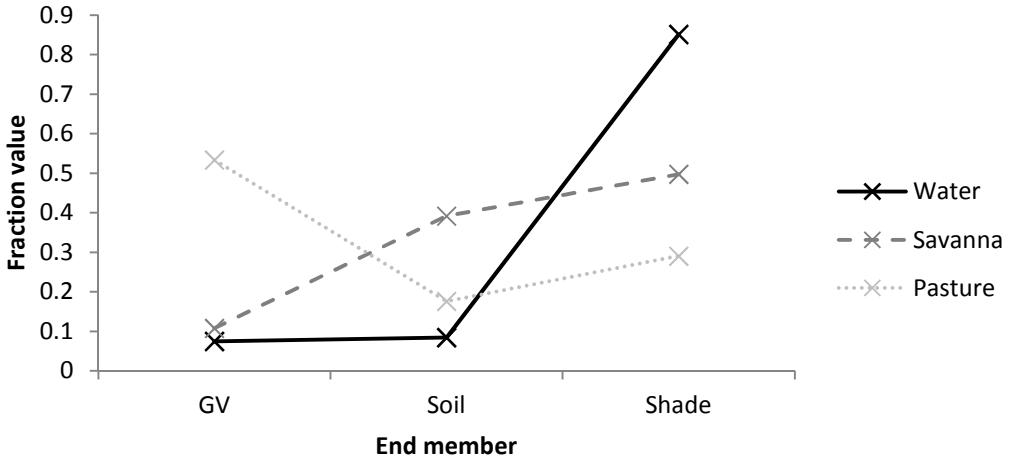

Figure 3.7. Average end member fraction values for unforested land cover classes.

These results illustrate that floodplain land cover classes can be differentiated using end member fraction images derived from Linear Spectral Unmixing. Analysis of these results is a precursor to the elucidation of thresholds which

can subsequently be applied within a decision tree classification framework. Forested land cover classes generally exhibit very low values in the soil fraction, enabling them to be distinguished relatively easily from non forested land cover types, with the exception of grasslands. Despite possessing relatively similar characteristics in terms of end member fractions, forests/grasslands vary systematically in the balance between GV and shade end member fractions, which is enhanced within the shade ratio image. Water is predominated by the shade fraction and is therefore distinct from all terrestrial classes. Savannas and pastures are the most spatially extensive non forest classes and are relatively easily differentiated, with savannas characterised by a higher soil and lower green vegetation response when compared to pasture.

3.5.2 Spatial distribution of Beni floodplain land cover

Figures 3.8 and 3.9 illustrate that the Beni floodplain is dominated by broadleaf forest and savanna/pasture land covers, which account for 45 % and 46 % of the areal extent of the study area respectively. The third largest land cover class is water, comprising the Beni main stem, plus numerous smaller floodplain river channels and the large lakes located to the east of the study area. Areas of grassland are relatively localised and occupy only 2 % of the study area. These are the primary constituent classes which make up the complex mosaic of Beni floodplain land cover.

A large continuous area of broadleaf forest flanks the main stem of the Beni to the east and west for the length of the study area. For the upstream portion of the reach (stretching from the southern limit of the study area, to around 75 km north of Rurrenabaque) forest cover is extensive on both sides of the river channel. To the west of the Beni continuous forest extends to the foot of the sub-Andes, with the exception of an unforested basin, approximately 40 km in length, which contains of a series of lakes and areas of grassland/pasture. The SRTM DEM (figure 3.10) illustrates that this unforested basin possesses an elevation which is comparable to the floodplain on the east side of the channel, whilst surrounding forest stands upon the west side of the channel are located upon ground which is characterised by higher elevations. On the eastern side of

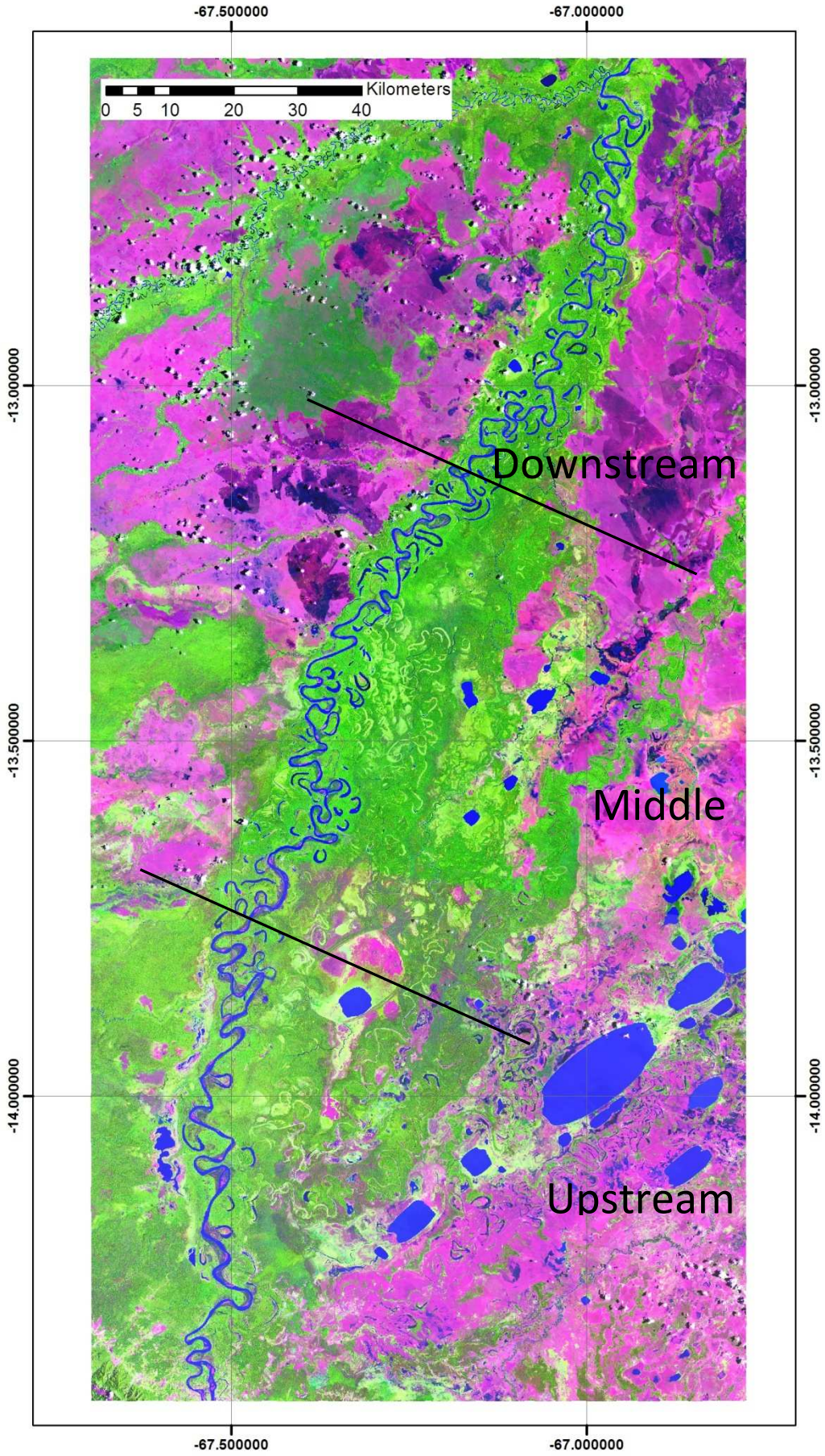

Figure 3.8. Landsat TM false colour composite image for the Beni floodplain study area.

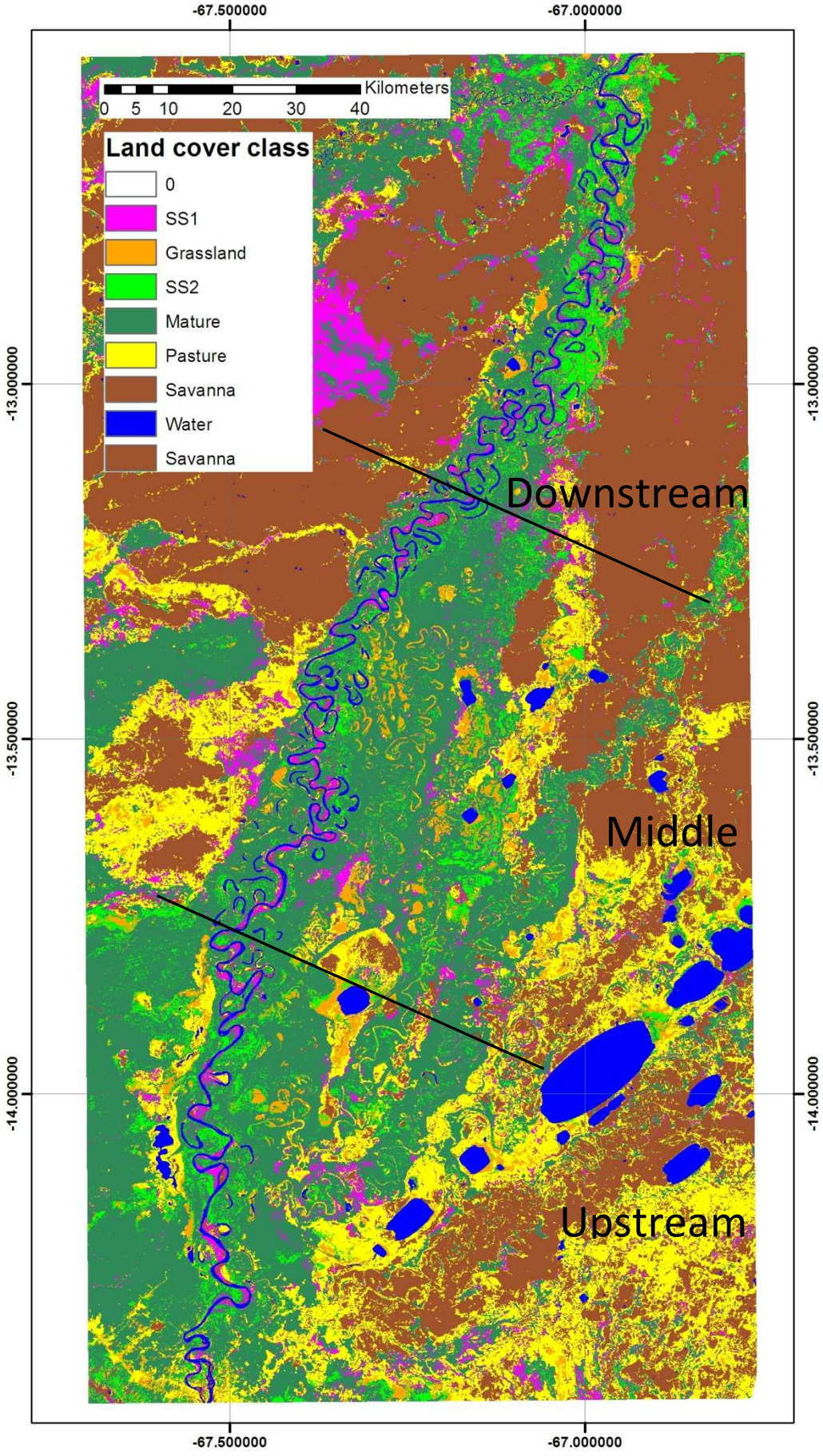

Figure 3.9. Map 5, Beni floodplain land cover produced by LSU-DT classification.

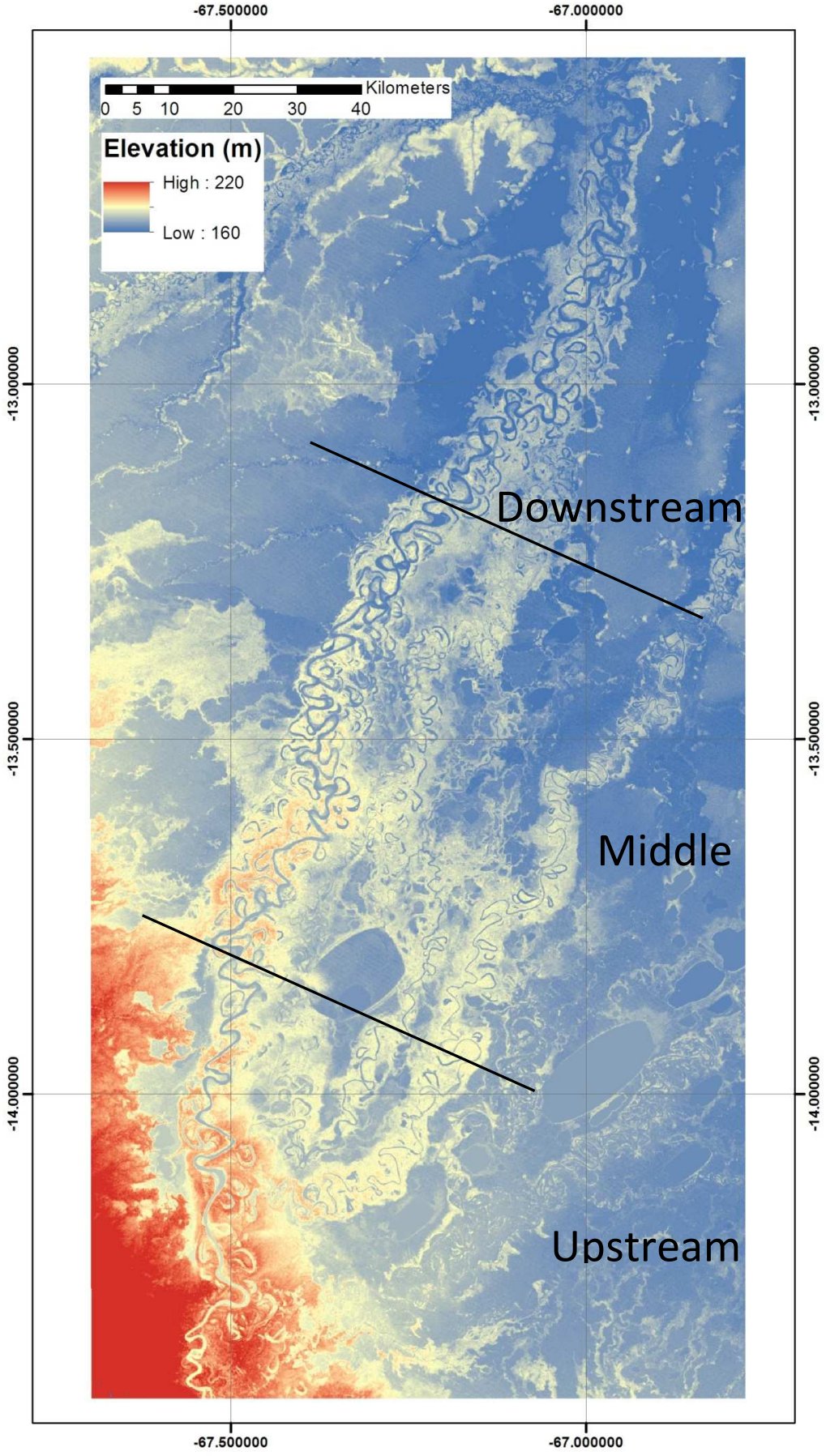

Figure 3.10. SRTM DEM for the Beni floodplain study area.

the river channel in the upper reaches the corridor of floodplain forest increases in width with distance down the floodplain, at its maximum extent the forested area extends to a distance of approximately 50 km from the channel.

Overall forest cover within this part of the floodplain is dominated by 'Mature' stands which account for ~85 % of forested areas. Successional forests constitute a smaller proportion of forest cover, with 'SS1' and 'SS2' accounting for 7 % and 8 % of total forest cover respectively. Although stands of successional forest can be found across the floodplain, they are most commonly located in close proximity to the river channel. SS1 stands proliferate most commonly upon point bars, whilst late successional (SS2) stands can be found adjacent to SS1 stands on older point bar deposits or on the cut bank side of the channel. The distal floodplain within the upper reaches of the study area, located to the east of the large group of lakes, is characterised by savanna/ pasture land cover classes and is known locally as 'pampas'. No clear boundary exists between forest and savanna in this part of the floodplain, rather a transitional zone exists which is characterised by a complex mosaic of different forest/ non forest land cover types. The SRTM DEM indicates that this region of the floodplain is characterised by a low level of topographical variation, with elevation decreasing gradually away from the main Beni channel.

In the middle section of the study reach the floodplain forest on the west side of the Beni extends away from the channel for only 5 - 10 km, where it borders a large expanse of savanna. This area of savanna extends as far as the confluence of the Beni and the Madidi river at the downstream end of the reach, and is intersected by several thin stands of gallery forest which are located along the course of small tributaries of the Beni. A similar narrowing of the corridor of floodplain forest is observed on the east side of the floodplain within the middle section of the reach. The presence of a large region of savanna, which dominates the north east of the study area, limits the extent of the floodplain forest. Consequently, within the downstream section of the reach forest stands extend only 5-10 km away from the Beni channel. In contrast to the upstream/middle reach where a complex mosaic of forest/savanna land cover exists, the downstream section of the reach exhibits a much clearer transition between forest and savanna. The SRTM DEM illustrates that topography within the downstream part of the reach is more complex, with

savanna areas on the east and west side of the channel being characterised by a significant increase in elevation in comparison to the adjacent forested areas.

3.5.3 Land cover classification accuracy assessment

Table 3.2 is an error matrix which illustrates results of the accuracy assessment of the five land cover maps generated within this study. The least accurate land cover classification was produced through application of MLC to uncalibrated Landsat TM imagery (Map 1), exhibiting an overall accuracy level of 79.91%. An improvement in overall accuracy and kappa coefficient was observed in all cases where MLC was applied to Landsat TM images subject to further processing. A relatively small increase in accuracy (~1.2%) was achieved through use of calibrated Landsat TM images (Map 2). Larger, but modest increases were observed from MNF transformed Landsat TM images (Map 3) ~3.4 %, and a subset of Landsat TM bands (Map 4) ~4.8 %. The highest levels of overall accuracy (90.47%) were attained for the land cover map produced through using end member fraction and shade ratio images as input into DTC. Kappa coefficient values increase in a similar manner with additional processing, providing further support to the overall accuracy results. The assessment of overall classification accuracy illustrates that significant increases in classification performance can be accrued through expanding the scope of land cover classification in terms of classification algorithms and input datasets. Implementation of simple MLC classification techniques on uncalibrated multispectral imagery produced the least accurate land cover classification, whilst application of DTC using LSU derived fraction images resulted in an increase in classification accuracy of > 10%.

A more detailed analysis of classification accuracy undertaken at the level of individual classes illustrates that the highest levels of accuracy are achieved for the non forest classes of pasture and water. The minimum users and producers accuracy for these classes across the different classifications approaches is 80%, although 100% accuracy is commonly achieved. Similar levels of accuracy (commonly exceeding 90%) are observed for the early successional forest class (SS1). However, a significant decline in performance is evident for late successional and mature forest classes, which are less well separated than

Table 3.2. Error matrix illustrating the accuracy and kappa coefficient of Beni land cover maps derived using different classification schemes. Map 1 is produced through MLC of raw Landsat TM images with digital number values. Map 2 is produced through MLC of calibrated Landsat TM images with reflectance values. Map 3 is generated based upon MLC of MNF transformed Landsat TM image. Map 4 is generated through classification of a subset of Landsat TM bands (bands 3,4,5,7). Map 5 is derived based upon a combined LSU-DTC approach. The variation in land cover distribution displayed within the different land cover maps illustrated within this table is relatively small and difficult to determine visually at the scale of the whole floodplain. Therefore only one floodplain land cover map is presented here (Map 5) in figure 3.9, in order to visually illustrate the broad distribution of land cover across the floodplain.

	Map 1		Map 2		Map 3		Map 4		Map 5	
	Landsat TM		Calibrated		MNF		Subset		LSU-DTC	
Land cover	UA	PA	UA	PA	UA	PA	UA	PA	UA	PA
SS1	93.33	92.11	91.89	89.47	91.67	86.84	92.11	92.11	94.74	96.00
SS2	100	46.15	97.62	52.56	97.87	58.87	100	60.26	75.00	100
Mature	59.09	97.01	61.32	97.01	65.66	97.01	68.75	98.51	98.51	78.57
Pasture	94.12	100	100	100	80	100	84.21	100	100	100
Water	100	100	100	100	100	100	100	100	100	90.91
OA	79.91		81.12		82.32		84.73		90.47	
Kappa	0.7168		0.7325		0.7498		0.782		0.8695	

other floodplain land cover classes. This decline in performance is marked by the larger disparity which exists between the UA and PA for SS2 and mature forest classes. Typically SS2 has a users accuracy which is very high and a producers accuracy which is considerably lower, whilst the reverse is true for the mature forest class which features a high value for PA and a lower value for UA. The disparity between UA and PA varies for the different classification procedures. For MLC using uncalibrated Landsat TM imagery (Map 1) the disparity between UA and PA for SS2 and mature forests is in excess of 50 % and 35% respectively. This disparity is ameliorated through application of more complex classification methodologies, with increases in accuracy for SS2 and mature forests corresponding in line with increases in overall accuracy. The best performance for SS2 and mature forest classes are observed for the LSU-DTC approach (Map 5), where PA and UA exceed 75% for both SS2 and mature forests, constituting a considerable increase in accuracy in comparison to simple MLC.

3.6 Discussion

The spectral profiles of forest classes (figure 3.4) are characterised by a sharp decline in reflectance to Landsat TM band 3 and peak reflectance in band 4, which correspond to the red and near infra red parts of the electromagnetic spectrum. This is intuitive, given that chlorophyll in green vegetation is known to absorb strongly in the red part of the spectrum, whilst forest canopies reflect strongly in Landsat TM band 4 (Jones and Vaughn, 2010). Although the spectral profiles of grasslands and SS1 forests are distinct from other classes, mature forests and SS2 forests exhibit partially overlapping profiles, indicating that separation of these classes based solely upon their spectra is likely to be problematic. The similarity in spectral response of forests is also reflected in the typical end member fraction values for each class. However, figures 3.6 and 3.7 suggest that the fraction images and shade ratio image accentuate the difference between the forest types, enhancing the ability to separate these classes (Shimabukuro et al., 1998). This strongly suggests that unmixing of the Landsat TM image into end member fractions enhances the ability to differentiate between forest types (Kawakubo et al., 2013).

Figure 3.12. A typical SS1 forest stand located upon a point bar deposit, illustrating high density of *Tessaria integrifolia* and the giant grass *Gynerium sagittatum.*

Figure 3.13. A typical SS1 forest stand characterised by *Cecropia spp*, and *Gynerium Sagittatum* which form an open canopy.

Figure 3.14. A typical SS2 forest stand located upon a point bar deposit, of older ages form a closed canopy.

Figure 3.15. A typical mature forest stand located upon the cut bank side of the Beni, characterised by a closed canopy with greater vertical structure.

Figure 3.16. A typical mature forest stand on the cut bank side of the Beni.

End member fraction images have a physical basis (Roberts et al., 1995), and thus the values for each land cover class can be interpreted based upon field observations. SS2 and Mature forest are relatively similar in terms of fraction values, with both classes possessing a very low proportion of the soil end member (Lu et al., 2004b). Green vegetation and shade fraction values are relatively similar, with SS2 characterised by marginally greater proportions of GV and lower proportion of shade. The difference between SS2 and mature forests is enhanced within the shade ratio image, which provides the most effective means to discriminate between the two classes. This similarity is largely unsurprising given that late successional forests and mature forests are often comparable in terms of their biophysical, and hence spectral characteristics (Batistella, 2001). Within the Beni floodplain study area SS2 and mature forests are characterised by a closed canopy, shown in figures 3.14-3.15, precluding a high proportion of soil within the fraction images. Field observations suggest that the canopy of mature forests feature a greater level of heterogeneity in their vertical structure. Consequently the degree of shading is higher in mature forests, leading to a lower shade ratio value than that observed for SS2, which exhibits a more uniform canopy structure. A similar effect was observed by Lu et al., (2003a), who found that the proportion of the

shade end member increased from successional to mature forests as a result of the increase in vertical structure/geometric heterogeneity of the forest canopy due to the presence of emergent trees and gaps.

Figure 3.17. A typical area of grassland upon the Beni floodplain featuring high vegetation vigour and minimal shading effects.

Figure 3.18. A typical area of grassland upon the Beni floodplain.

SS1 is the only forest class which possesses a shade fraction value exceeding that of green vegetation, whilst also exhibiting a higher soil fraction than both

SS2/Mature forest. Reconciliation of fraction values with field observations for SS1 is slightly more complex than for the aforementioned forest classes. SS1 forests upon the Beni floodplain are commonly dominated by *Gynerium sagittatum,* a large fast growing species of grass, interspersed with light demanding trees such as *Tessaria integrifolia* and *Cecropia spp*. These stands form homogeneous open canopies, illustrated in figure 3.13, characterised by a relatively low Leaf Area Index (LAI) which can be attributed as the primary reason for the relatively small GV and elevated soil fraction values associated with this class. The high proportion of shade fraction exhibited by SS1 forests is somewhat counter intuitive, as field observations suggest that the relatively simple open canopy structure and low LAI results in a relatively low degree of shading. However it is hypothesised that the high proportion of shade can be attributed to the presence of significant volumes of Non Photosynthetic Vegetation (NPV) in the understory of SS1 forests, pictured in figure 3.12. In the absence of a dedicated end member, the NPV which characterises SS1 stands is primarily constituted by live and dead stems of *Gynerium sagittatum*, is allocated to the shade fraction during the unmixing process.

Of the four classes illustrated in figure 3.6, grasslands are characterised by the highest value for green vegetation and the lowest value for shade, resulting in the highest shade ratio values. The high proportion of the green vegetation fraction which characterises grasslands can be attributed to the intense vigour of the continuous grass/herbaceous vegetation cover which occupies these areas, illustrated in figures 3.17 and 3.18. In addition, the absence of vertical structure within the vegetation results in negligible amounts of shading. In terms of their vegetation structure, these grasslands can be classified as ‘bajios’, seasonally inundated lands characterised by high water availability and vigorous growth of herbaceous vegetation (Haase and Beck, 1989).

Of the remaining non forest classes, water is characterised by a flat spectral profile indicating a low response in all Landsat TM bands. This characteristic is reflected in the end member fractions, with water marked by a strong response in the shade image. Clear water, shown in figure 3.25, absorbs at all wavelengths within the portion of the electromagnetic spectrum covered by Landsat TM (Jones and Vaughan, 2010), and thus appears similar to shaded areas in terms of Landsat TM reflectance. Water exhibits a slightly elevated

response in the vegetation fraction, which can be attributed to the high levels of turbidity observed within many water bodies within the Beni study area as a result of high suspended sediment concentrations (Guyot, 1993), illustrated in figure 3.23 and 3.24.

Figure 3.19. A typical area of pasture upon the Beni floodplain, characterised by short grass and sporadic trees/palms.

Figure 3.20. A typical area of pasture upon the Beni floodplain.

Figure 3.21. A typical area of savanna upon the Beni floodplain, exhibiting exposed bare soil interspersed with grass tussocks and small shrubs/trees.

Figure 3.22. A close up view of the bare ground tussock structure which typifies savanna land cover upon the Beni floodplain.

For the pasture class, fraction values broadly reflect field observations, with a high response for the GV end member attributable to grass coverage which is illustrated in figures 3.19 and 3.20. Smaller contributions from shade/soil can be

linked to the presence of sporadic tree/palm cover which were observed in the field, and areas of exposed soil which arise due to grazing of these lands by large numbers of cattle. The spectral response of savanna regions is distinct from other land cover classes found upon the Beni floodplain, with high proportions of soil and shade fractions and a low response for green vegetation. Savannas observed within the Beni study area were typically characterised by bare ground covered with dry bunchgrass, interspersed by shrubs and small trees. Typical savanna land cover observed upon the Beni floodplain is shown in figure 3.21 and 3.22. Field observations suggest that these savannas can be characterised as the 'Altura' dry bunchgrass savannas documented by Haase and Beck (1989), which form within areas of well drained soils. Field work was undertaken in October at the end of the dry season, whilst Landsat TM scenes were captured in November before the onset of the rainy season. At this stage of the hydrological year, soils were very dry and vegetation within savanna regions showed visual signs of water stress. Hence, it is hypothesised that the high proportion of shade which characterises the savanna class can be explained by the allocation of dry vegetation to NPV rather than green vegetation during the unmixing process, in a similar manner to SS1 forests.

Figure 3.23. The Beni channel, illustrating a high level of turbidity as a result of high suspended sediment concentrations.

Figure 3.24. Lake Rocagua, the largest of the Beni floodplain lakes, characterised by a high level of turbidity.

Figure 3.25. The Negro, a black water tributary which confluences with the Beni in the downstream section of the study reach.

Through interpretation of the land cover map with respect to Landsat TM imagery, the SRTM DEM and field observations it is possible to gain some initial insights into the functioning of the Beni floodplain. Despite a scarcity of quantitative work, numerous past studies have described land cover dynamics

within the Llanos de Mojos. Haase and Beck (1989) stated that the spatial arrangement of land cover within the Llanos is primarily dependent upon elevation. Relatively small differences in elevation are pre eminent in controlling both flood duration during the wet season in addition to water availability during the dry season, and thus the length of the overall growing season for floodplain vegetation.

Through visual analysis of the land cover map and the SRTM DEM it is clear that for large areas of the Beni floodplain, non forest land cover is prevalent within areas characterised by lower elevations. A clear example of this is illustrated by the basin located within the upstream part of the study reach to the west of the river channel, which contains a large lake and is characterised by a relatively low elevation with respect to surrounding areas. SAR images, detailed further in chapter 6, indicate that this basin is commonly inundated to a substantial depth during the wet season as the lake expands, precluding forest growth over a significant area. In contrast, surrounding areas which are characterised by higher elevation, and hence are not subject to flood inundation, are characterised by continuous dense forest cover. This effect is also observed over vast areas of the distal floodplain to the east of the Beni channel in the upper and middle reaches of the study area, which is dominated by savanna land cover known locally as ‘pampas’. The distal floodplain is associated with a lower elevation than raised levees located in close proximity to the channel, hence flood waters accumulate in distal areas, which experience extended periods of inundation and are maintained as pampas.

The results and observations made within this chapter support previous hypotheses relating to the functioning of the Beni floodplain (Haase and Beck, 1989). The findings demonstrate that flood inundation precludes growth of forest stands, and in turn demonstrates that excess surface water present during the wet season exerts a first order control upon land cover. It is well established that the extended duration of inundation upon Amazonian floodplains exerts a significant impact upon the growth of woody tree species, through the creation of anoxic conditions (Junk et al., 1997). Amazonian tree species are characterised by a wide variety of adaptations which allow individuals to tolerate flooding (Parolin et al., 2008). However Wittmann et al., (2004) demonstrated that depth and duration of inundation are preponderant in

determining the successional stage of floodplain forest stands, with a higher magnitude of flooding maintaining forests within early stages of succession. Accordingly, it is clear that large areas of the Beni floodplain are characterised by low elevations and are subject to annual inundation of a duration which precludes the establishment of successional forest stands, supporting the growth of only herbaceous vegetation.

Further investigation of floodplain land cover maps and the SRTM dataset also reveals the presence of large areas of savanna land cover that are characterised by higher ground elevations than adjacent forest stands. Perhaps the clearest example of a 'raised' savanna is constituted by the area of relatively high elevation located to the east side of the Beni channel in the middle to downstream section of the reach. This area of raised elevation can be attributed to the processes of tectonic uplift (Dumont, 1996), further elaborated within chapter 2. The SRTM DEM suggests that this surface is 3-4 m higher than the ground elevation of surrounding forest stands. Indeed field observations corroborated this, confirming that a step in elevation exists around the edge of the raised surface, with the forest- savanna boundary roughly corresponding with the top of this elevation step. This step in elevation, which resembled a terrace formation, is likely the product of fluvial erosion of the tectonically raised surface by the Beni during its occupation of former channel belts to the east of its current position (Dumont and Hanagarth, 1993). Raised savannas are also observed extensively to the west of the Beni main stem.

The 'raised' savannas, which constitute a substantial portion of the study area, pose interesting questions relating to the hydrological functioning of the Beni floodplain. As these areas are typically 3-4 m higher than surrounding areas of forested floodplain, they are not subject to overbank inundation, even during the largest floods. Rather, field observations and anecdotal evidence suggest that the raised savannas are inundated to a shallow depth (up to ~20-30 cm) during the wet season, as a result of surface run off in response to heavy rainfall. It is postulated that water drains quickly from these areas via small channel networks to lower parts of the floodplain, hence the raised savannas are not thought to be inundated for extended durations. As broadleaf forest stands are able to develop upon adjacent regions of the floodplain characterised by lower elevation, which are subject to greater depths and duration of inundation, the

maintenance of raised areas as savanna cannot be attributed to water excess induced by flooding. Rather, it is hypothesised that forests are unable to establish due to a water deficit which manifests within areas of high elevation during the dry season. Herbaceous vegetation located within these areas exhibited clear signs of water stress at the end of the dry season, whilst soils across the savannas were also extremely dry. As the savannas are typically raised by an elevation of 3-4 m, it is thought that the water table in these areas is further below the ground surface relative to other surrounding areas of the floodplain, meaning that ground water is less readily available for utilisation by vegetation, thus limiting growth.

These results and observations are significant, with the presence of savannas in areas of higher elevation than neighbouring forest stands indicating that flood inundation does not exert the dominant influence upon land cover in all parts of the Beni floodplain (Haase and Beck, 1989). Overall, findings suggest that the spatial distribution of forest and savanna land covers is dependent primarily upon elevation, which in turn controls the balance between water excess associated with flood inundation dynamics in some areas, and dry season water availability in other parts of the floodplain (Haase and Beck, 1989).

Within the study area SS1 forest stands are primarily located within close proximity to the Beni main channel upon new point bar deposits. Point bars are formed through the process of channel migration and are associated with the youngest stand ages, making them the most common location for the inception of primary successional vegetation growth (Peixoto et al., 2009). SS1 stands are also located within isolated locations away from the main river channel. In these areas stands are much older and it is likely that SS1 forests represent the incipient stages of secondary succession following natural or anthropogenic disturbances.

SS2 stands are also most commonly located upon older point bar deposits which are located adjacent to SS1 stands, this is intuitive as they form the next stage of the primary successional sequence (Wittmann et al., 2002). SS2 stands are more widely distributed throughout the channel belt, whilst a visual analysis suggests an increase in their extent within the downstream section of the reach. However, the increased extent of SS2 forests within the downstream

portion of the study reach, along with potential reasons for this change, are difficult to quantify as logistical constraints prevented access to these areas during the field campaign. Mature forests are widespread and account for the majority of the area of forest which make up to 50% of the areal extent of the Beni study area. Within the channel belt, mature forests are generally located within stable locations which have not been disturbed through lateral movement of the river channel (Peixoto et al., 2009). Outside the channel belt, direct influence from the Beni diminishes and mature forests account for a greater proportion of overall forest cover.

The distribution of non forest classes shows a distinct spatial pattern which differs between the upstream and downstream parts of the Beni floodplain study area. In the upstream part of the study reach, non forested areas are characterised by both savanna and pasture land covers which form a highly heterogeneous spatial mosaic. Areas of grasslands are also prevalent within the upstream part of the study reach, being preferentially located within abandoned channel features which are associated with greater water availability, promoting vigourous vegetation growth. However the spatial distribution of non forest land cover changes significantly within the downstream reach of the study area, with non forested regions of the floodplain dominated almost exclusively by savanna land cover. This disparity in pasture may be attributable in part to anthropogenic influence as the majority of the population of the study area is concentrated in the upstream part of the study reach around the towns of Rurrenabaque, Reyes and Santa Rosa. However, field observations suggest that the primary difference between the upstream/downstream portions of the study area is water availability, which is strongly linked to floodplain elevation. The vast expanses of ‘altura’ savanna which dominate non forest land cover in the downstream part of the study reach are located upon areas of raised elevation which are not subject to overbank inundation from the Beni. Field observations, particularly microtopography of mounds and depressions, indicate that these ‘altura’ areas are subject to shallow inundation as a result of local precipitation during the wet season (Pouilly et al., 2004). However the soils within these areas are well drained, suggesting that these ‘alturas’ quickly lose their water at the onset of the dry season, hence limiting the length of the growing season and restricting vegetation types to primarily perennial bunchgrasses (Sarmiento,

1984). In contrast, the non forested region within the upstream part of the reach is characterised by lower elevations and subject to inundation sourced from both overbank flooding and local precipitation and can be broadly classed as 'bajio' (Haase and Beck, 1989). Bajios are characterised by less well drained soils and exhibit higher water availability which persists through the dry season. This facilitates the growth of a greater diversity of herbaceous vegetation species, resulting in a more heterogeneous mosaic of land cover types. These results and interpretations provide further evidence that floodplain elevation and hydrology are pre eminently important in determining the spatial distribution of land cover upon the Beni floodplain.

The overall levels of accuracy associated with the land cover maps generated here are very good and are equivalent to studies which have been undertaken in other parts of Amazonia. The accuracy of Beni floodplain land cover maps varies between 79.9 % for a simple MLC approach and 90.47% for a combined LSU-DT classification. The accuracy of land cover classification achieved within studies undertaken within the Brazilian Amazon, varied from 77% to 86% (Shimabukuro, et al., 1998; Lu et al., 2003a; Kawakubo et al., 2013). Kappa coefficient values are also equivalent to those observed within other studies. In a broader sense the results of this classification exercise are also comparable with the findings of Lu et al., (2004a; 2004b), in terms of the increasing levels of performance offered by the implementation of more sophisticated classifiers such as a combined LSU-DTC approach in comparison to simple supervised classification. These results suggest that the implementation of sophisticated algorithms is maximising the potential of land cover classification for Amazonian study areas, and that overall accuracy levels of 80-90% can be realistically achieved when utilising medium resolution multispectral imagery such as Landsat TM.

Although overall classification accuracy is very good, it is clear that this bulk measure of performance masks some of the poorer results obtained at the level of individual classes (Foody, 2002). SS1, water and pasture are characterised by a producers and users accuracy which exceed 90 % for all classification approaches. This high level of accuracy indicates that these classes are easily differentiated, even by the simpler classification algorithms. In contrast, the poor producers accuracy observed for SS2 and users accuracy for mature forests

can be considered unsatisfactory. For the simple MLC classification approach PA and UA for SS2 and mature forests respectively were lower than 60%. These results can be considered symptomatic of a systematic over classification of mature forest and under classification of SS2. A low users accuracy for Mature forest is attributable to the large number of total pixels classified within this class, generating errors of commission (Richards, 1999). Low producers accuracy for SS2 is indicative of errors of omission resulting from a low number of correctly classified pixels within this class.

Low levels of accuracy observed for SS2 and mature forests can be attributed to the combined effects of vegetation heterogeneity, smooth transitions between forest types and limited resolution of Landsat TM (Shimabukuro et al., 1998). As a direct consequence of these factors SS2 and Mature forests possess very similar spectral signatures, this is reflected in the poor separability indicated by the Jeffries-Matusita index value for the two classes. Importantly, the utilisation of the LSU-DT algorithm significantly increased the performance of the classification with respect to SS2 and Mature forests, with accuracies exceeding 75% for both classes. This suggests that utilisation of a more complex classification algorithm which possesses the ability to quantitatively address the problem of mixed pixels ameliorates the problems faced by simple per pixel classifiers when classifying heterogeneous regions of forest (Kawakubo et al., 2009). Therefore, within this particular classification exercise, the improvements in overall accuracy offered by the more complex LSU-DT classifier are accrued primarily through improvements in the discrimination of different forest types. Lu et al., (2003a) obtained comparable results, finding that differentiation of forest classes often proved difficult due to the allied issues of forest heterogeneity, smooth transitions between forest types and inadequate resolution of multispectral imagery. The authors of the aforementioned studies also concluded that forests could be separated more easily using LSU derived fraction images than Landsat TM spectral signatures.

The Beni floodplain study area covers a vast, largely inaccessible area and is characterised by high levels of heterogeneity in terms of both forest and non forest land cover. Logistical factors limited the scope of field observation, hence field data covered only a relatively small proportion of the overall floodplain area. Therefore, although the land cover classification performed very well in

quantitative validation, the spatial limitations of the field dataset introduces the potential for proliferation of ‘unknown’ errors, which constitute the primary limitation of this classification exercise. Perhaps the most significant of these uncertainties is the potential presence of further forest/non forest land cover types upon the Beni floodplain which were not observed during the field survey and hence could not be differentiated during classification. This is somewhat inevitable given the extent of the Beni floodplain study area and the considerable variability which exists in the characteristics of these land cover types across environmental gradients and due to anthropogenic factors (Beck, 1983). However visual inspection and interpretation of the multispectral Landsat TM imagery did not reveal the presence of any obvious further classes for inclusion within the classification scheme.

Whilst it is not possible to quantify such unknown errors, an awareness of the implications of both quantified and unquantified uncertainties is important within the context of this study. Particularly significant here are the implications of uncertainties when the map is utilised within data processing and analysis in subsequent chapters. Within chapter five the land cover map will form a key input dataset for the generation of a bare earth DEM, facilitating the removal of positive vegetation biases from the SRTM DEM (Yamazaki et al., 2012). The land cover classification will be utilised in order to generate zonal average canopy height maps, in which each forest class is assigned an average canopy height value. Intuitively, within misclassified areas an incorrect value for canopy height will be applied within the correction of vegetation bias, leading to underestimation or overestimation of the bare earth elevation (Baugh et al., 2013). In addition, within chapter 6 the land cover map is utilised in the processing of L-band PALSAR SAR and SMMR imagery in order to derive flood inundation information for the Beni floodplain study area. In these analyses the land cover map was applied as a forest mask, owing to the fact that the backscatter response is distinct for forest/non forest areas within these imageries. Results presented here suggest that the classification algorithms perform well when separating forest/non forest classes, thus uncertainties in the land cover map are unlikely to constitute a significant source of error in derived flood inundation extent. In addition, the confusion amongst non forest classes is

unlikely to propagate significant errors within any of the subsequent analyses in this thesis,

3.7 Conclusions

Overall, acceptable levels of accuracy were obtained for all classification approaches adopted within this study, illustrating that useful land cover information can be extracted for Amazonian study areas using Landsat TM imagery and simple supervised classification approaches (Shimabukuro et al., 1998). However, a more in depth analysis revealed that accurate separation of the different forest types is problematic using traditional per pixel approaches to classification (Lu et al., 2003a). These challenges can be attributed to the problems posed by the presence of mixed pixels, which occur due to the limited spatial resolution of Landsat TM imagery combined with the spectral similarity and smooth transition between different forest classes (Budreski et al., 2007).

Despite the problems faced when attempting to accurately classify Amazonian land cover, the results of this study suggest that the utilisation of more advanced image processing techniques and classification algorithms yield significant benefits in terms of overall accuracy (Kawakubo et al., 2013). Indeed the implementation of a combined Linear Spectral Unmixing-Decision Tree classification approach resulted in an increase in overall accuracy of > 10 % when compared to simple Maximum Likelihood Classification. Improvements were accrued primarily through more successful discrimination of different forest types, facilitated by the ability of the LSU-DT classification scheme to quantitatively address the mixed pixel problem (Van der Meer and De Jong, 2000).

The overall accuracy of the land cover map produced through LSU-DT classification was 90 %, slightly greater than accuracy levels obtained by Lu et al., (2003a; 2004a). Such levels of overall accuracy can be considered excellent given the issues of data availability combined with the complex nature of the study area, and indicate that the land cover map is appropriate for use as input to further analysis in subsequent chapters. Nevertheless it is important to consider the uncertainties associated with the land cover map, particularly the difficulty in differentiation of SS2 and mature forest, and the potential

implications of this misclassification of forest types within the generation of bare earth DEMs (Yamazaki et al., 2012; Baugh et al., 2013).

Through interpretation of the land cover classification in light of field observations and ancillary datasets, primarily the SRTM, it has been possible to elucidate basic information with respect to the ecological functioning of the Rio Beni. Results suggest that hydrological characteristics, namely flood inundation and dry season water availability, are preeminent in determining land cover distribution upon the Rio Beni. More specifically it is clear that substantial areas of savanna are maintained upon the tectonically raised surfaces within the north eastern part of the floodplain (Dumont, 1996) where water availability is low, thus precluding forest growth. Extensive savannas are also present at relatively low elevations in the distal floodplain within the upstream and middle sections of the reach (Hanagarth, 1996). These areas are characterised by relatively low elevation and experience high magnitudes of inundation, which preclude the establishment of continuous tropical forest stands (Haase and Beck, 1989).

Chapter Four

Accuracy assessment of the SRTM dataset for the Beni floodplain

4. Accuracy assessment of the SRTM dataset for the Beni floodplain

4.1 Introduction

The Shuttle Radar Topography Mission (SRTM) was flown aboard the Space Shuttle Endeavour between the 11th February and 22nd February 2000 and constituted the world's first spaceborne fixed-baseline interferometric synthetic aperture radar (Rabus et al., 2003). SRTM orbited at an altitude of 233 km with an inclination angle of 57^{o}, thus facilitating collection of topographic data for approximately 80% of the Earths' land surface between latitudes of 60^{o} north and 57^{o} south. Two InSAR systems operated aboard the mission; the C-band (5.6 cm, 5.3 GHz) sensor which was commissioned by the United States and the German X-band (3.1 cm, 9.6 GHz) sensor. The swath width of the C-band was 225 km, resulting from the 60 m fixed baseline configuration and operation in ScanSAR mapping mode (Rodriguez et al., 2006). During the 11 day mission which featured 159 orbits, the C-band and X-band sensors mapped a total area of 177 million km^2, collecting over 12 terabytes of data.

Following the mission, interferometric processing of the C-band SRTM dataset was undertaken by NASA Jet Propulsion Laboratory (JPL). Multiple data takes were averaged and noise present in the interferogram was reduced through utilisation of a boxcar low pass filter and power spectral filtering (Hensley et al., 2000). In the final processing step SRTM data were smoothed using a variable width boxcar filter (Smith and Sandwell, 2003). SRTM datasets were released at a spatial resolution of 1 arc-second (30 m) for the United States, and 3 arc-seconds (90 m) for the rest of the world, vertical elevation was referenced to the WGS84 geoid.

Pre mission accuracy specifications stated that the SRTM was expected to possess an absolute horizontal circular accuracy of less than 20 m, whilst absolute and relative vertical accuracy were expected to be better than 16 m and 10 m respectively at the 90% confidence level (Bamler 1999). Since release, SRTM data have been validated extensively with respect to Ground Control Points (GCPs) obtained from numerous sources including field surveys and other remote sensing observations (Curkendall et al., 2003; Sun et al.,

2003). Results of the initial accuracy assessment indicated that the SRTM dataset can be considered both the highest resolution and most accurate global representation of topography generated to date (USGS, 2005). Rodriguez (2005) found that horizontal accuracy of SRTM was better than 12 m whilst absolute and relative vertical accuracy were 9 m and 10 m respectively, indicating that the dataset comfortably exceeded its initial expectations in terms of accuracy. However it is important to consider that many practical applications of SRTM demand a higher level of accuracy than the stated pre mission requirements (Bamler, 1999). Therefore a more detailed understanding of the quality and error characteristics of the SRTM dataset is required prior to its application as a source of topographical data for quantitative land process and modelling studies (Blumberg, 2006; Huggel et al., 2008).

The vertical error present within the SRTM dataset can be separated into two primary components; relative vertical errors and absolute vertical errors (Farr and Kobrick, 2000). Absolute errors arise within SRTM data as a result of errors in both the roll of the interferometric baseline and measurement of the length of the interferometric baseline (Walker et al., 2007). Absolute errors generally manifest in terms of a significant deviation of SRTM elevation from the true surface elevation (Reuter et al., 2007), which typically varies over scales on the order of thousands of kilometres (Bamler, 1999). Hence absolute errors are associated with the presence of a vertical offset in SRTM which is constant for all but the largest study areas.

As a result of their consistency over the scales of typical study areas, absolute errors can commonly be quantified and corrected through utilisation of ground control points (Bhang et al., 2007). For a bare earth agricultural area located within Iowa in the United States Kellndorfer et al., (2004) observed a vertical offset in the SRTM of order 4 m when compared to a high resolution and independently validated NED DEM. Whilst Weydahl et al., (2007) found a consistent error of order 3.3 m within a Norwegian study area, through comparison of SRTM with ground control points extracted from a high resolution validated DEM. In both studies the offset of the SRTM was taken as the mean deviation from the GCPs, and after correction of this offset the

remaining residual errors were Gaussian in distribution and were characteristic of relative errors.

Relative errors occur independently of absolute errors and can be attributed to three primary sources; soil roughness and moisture uncertainty; polarisation and incidence angle uncertainty and phase noise uncertainty (Walker et al., 2007). The height of the SRTM scattering phase centre is determined by the characteristics of both the SRTM sensor and the target surface. Intuitively perturbations in these characteristics can be attributed as the cause for the proliferation of relative errors (Brown et al., 2005). For the specific configuration of the SRTM C-band sensor both the wavelength and baseline length/attitude remain constant, whilst polarisation and incidence angle are variable for each swath.

Although the influence of variations in polarisation and incidence angle are dependent upon the characteristics of the imaged surface, Sarabandi and Lin (2000) postulate that variations in these sensor characteristics are typically associated with variations in the SRTM elevation of 1-2 m based upon simulated results. Integration of multiple data takes during post processing sought to minimise the influence of polarisation and incidence angle (USGS, 2003). However this integration makes direct quantification of the contribution of incidence angle variations to scattering phase centre elevation impossible, as the incidence angle information relating to individual swaths is not included within the released versions of the SRTM. Hence incidence angle errors are regarded as a residual uncertainty inherent within the SRTM (Franceschetti et al., 2000).

Soil roughness and moisture uncertainty is the smallest contributor to overall relative error, indeed for the wavelength and incidence angle range of the SRTM soil uncertainty is expected to contribute less than 0.5 m to the variability of the overall height response (Walker et al., 2007). As a result of both the difficulty associated with accurately measuring soil roughness/moisture over large areas and small contribution to overall relative error, further quantification of soil uncertainty has not been undertaken. Hence, like polarisation and

incidence angle error, soil error is treated as an additional residual uncertainty (Koch and Heipke, 2001).

Phase noise can be considered the greatest contributor to SRTM relative error. The presence of phase noise in the SRTM dataset can be attributed to the thermal/quantisation noise associated with the radar receiver (Bamler, 1999). SRTM vertical error related to phase noise was expected to be less than 10 m (Hensley et al., 2000), hence in order to meet these requirements a number of approaches to phase noise mitigation were implemented during post processing of the dataset. Initial phase noise reduction was achieved through the application of filtering techniques to the C-band interferograms, whilst multiple data takes were combined within the process of signal averaging as errors attributable to phase noise decrease with the square root of the number of looks used within averaging (Rosen et al., 2001).

Although data quality was improved through mitigation approaches implemented during post processing, a substantial phase noise component remained within the SRTM dataset proliferating as normally distributed random elevation errors. Kellndorfer et al., (2004) found that this residual phase noise could be reduced substantially through implementation of simple block averaging of the SRTM dataset. For a flat, unvegetated agricultural area located in Iowa in the United States averaging within a 7 x 7 pixel window (1 arc second pixels) was associated with a reduction in the noise range from 13 m to 4 m. The noise range gradually decreased with increasing numbers of pixels averaged, and was reduced to less than 1 m when a 25 x 25 pixel window was utilised (Kellndorfer et al., 2004). This demonstrated that a simple block averaging approach was sufficient to substantially decrease the magnitude of residual phase noise present within the SRTM dataset.

Numerous studies have found that the vertical accuracy of the SRTM declines significantly within vegetated areas (Sarabandi and Lin, 2000; Treuhaft and Siquiera, 2000). This decline occurs as a result of a systematic positive bias within the dataset, which can be attributed to the interaction of SRTM C-band microwaves and vegetation. Due to their relatively short wavelength C-band microwaves are strongly scattered by physical vegetation elements of forest

canopies such as leaves and branches. Consequently within vegetated areas the C-band phase centre, which determines SRTM elevation, does not represent either the ground surface or the top of the canopy but rather some intermediate height between the two (Hofton et al., 2006).

Carabajal and Harding (2006) utilised ICESat Geoscience Laser Altimeter System (GLAS) elevation data in order to assess the quality of the SRTM within vegetated study areas across the globe. The study found that as tree cover increased the SRTM phase centre was displaced further upwards into the canopy, with greater resulting positive bias indicating that the SRTM became a less reliable measure of ground elevation in densely forested areas. In a global validation of SRTM, Berry et al., (2007) observed a substantial positive bias for South America which was not observed for any other continent. This bias was attributed to the presence of the Amazon rainforest and illustrates the influence of vegetation effects upon SRTM accuracy at large scales. Due to the presence of positive biases the SRTM dataset must be classified as a Digital Surface Model (DSM), which is defined as a topographical representation of the ground including surface features, rather than a Digital Elevation Model (DEM) which provides a representation of bare earth topography (Smith and Sandwell, 2003).

Sensitivity to the vertical structure of vegetation is both a useful and problematic attribute of SRTM depending upon the specific application of the dataset (Walker et al., 2007). In instances where a representation of bare earth topography is required, vegetation effects are necessarily treated as an unwanted feature to be removed (Kocak et al., 2004). However sensitivity to vegetation structure also presents the potential for the derivation of forest properties such as canopy height and biomass from SRTM data (Hofton et al., 2006). Numerous past studies have successfully utilised Interferometric Synthetic Aperture Radar (InSAR) data in order to retrieve canopy height information with an acceptable level of accuracy (Treuhaft et al., 1995; Kobayashi et al., 2000; Brown, 2003). In light of the limitations associated with both LiDAR and optical sensors, SRTM has emerged as an alternative source of remotely sensed data for application within forest studies. As a result of its C-band operating wavelength, relatively high resolution and spatial coverage, the SRTM dataset has been utilised in order to derive spatially

continuous information relating to vertical forest structure for large study areas (Carabajal and Harding, 2006; Hofton et al., 2006).

Regardless of whether vegetation effects in the SRTM are considered as a useful signal to be exploited or an unwanted bias to be removed, quantification of the magnitude of C-band penetration into forest canopies is necessary to utilise the dataset within vegetated study areas. An estimate of this parameter is required in order to scale canopy height derived from the SRTM with actual canopy height, and to facilitate integration of the SRTM with other remotely sensed/field datasets. Quantification of the magnitude of SRTM C-band penetration requires canopy height and ground elevation measurements from other ancillary sources, as this information is not provided in the SRTM dataset. In most studies this information has been provided through LiDAR surveys, whose waveforms facilitate the derivation of both ground and canopy top elevations (Carabajal and Harding, 2006; Hofton et al., 2006). A quantification of C-band phase centre canopy penetration allows forest height estimates obtained from other sources to be scaled appropriately and applied in order to correct vegetation effects within the SRTM dataset.

A number of studies which have utilised the SRTM dataset within vegetated study areas have investigated penetration of the C-band phase centre into forest canopies. Carabajal and Harding (2006) used spaceborne LiDAR data acquired by the ICESat Geoscience Laser Altimeter System (GLAS) in order to investigate the quality of the SRTM dataset for vegetated study areas across the globe. The authors found that SRTM phase centre elevation was located between the first and last returns of the GLAS waveform and corresponded closely to the GLAS centroid. Penetration of the SRTM C-band phase centre into forest canopies was consistent across all study sites and on average represented an elevation which was 40% of the distance from the canopy top to the ground (Carabajal and Harding, 2006).

For study areas located within the United States and Costa Rica, Hofton et al., (2006) investigated SRTM-forest interactions through comparison with Laser Vegetation Imaging Sensor (LVIS) data. The authors found that the SRTM-LVIS top of canopy elevation difference, a proxy for the magnitude of SRTM canopy

penetration, was adequately described by a linear model. The linear models were similar for all study areas within the United States, which were characterised by mixed evergreen/deciduous forest. However for the Costa Rica site, which comprised dense closed tropical rainforest, the coefficient of the linear model was significantly higher. These results illustrate that interaction of the C-band phase centre with vegetation depends upon physical characteristics of forest canopies such as density and degree of canopy closure, and that the magnitude of penetration varies between different forest types. The authors calculated that the average magnitude of SRTM penetration was 14 m within the mixed forests of the United States and 8 m for the tropical forests of Costa Rica.

Bourgine and Baghdadi (2005) provided an assessment of the SRTM dataset for a study area located within French Guiana, which was characterised by dense tropical forest cover. Availability of a heliborne bare earth DEM and airborne laser survey of the forest canopy provided measurements of canopy height whilst also facilitating derivation of SRTM canopy height for the study area. The authors found that the average height of forest stands was 35 m, whilst the average canopy height derived from SRTM was 26.5 m. Hence on average the SRTM penetrated 8.5 m into the forest canopy, equating approximately 25% of the distance from the top of the canopy to the ground. Therefore the findings of Bourgine and Baghdadi (2005) are roughly in agreement to those of Hofton et al., (2006) in terms of SRTM penetration.

Overall, a plethora of past studies have shown that the accuracy of the SRTM DEM comfortably exceeded initial mission expectations (Rodriguez, 2005; Berry et al., 2007). Nevertheless results have indicated that the dataset is characterised by both relative and absolute errors of a significant magnitude, which vary spatially in an unpredictable manner (Kellndorfer et al., 2004). Therefore a thorough accuracy assessment of the SRTM dataset for the Beni floodplain study area must be conducted in order to facilitate the use of this dataset for generation of bare earth DEMs and extraction of a floodplain canopy height map within chapter 5. Here the vertical accuracy of the SRTM DEM for the Beni floodplain will be assessed with respect to a series of high quality post processed DGPS points.

4.2 Research aims

The overall aim of this chapter is to quantitatively assess both the accuracy of the SRTM DEM for the study area and the interaction of the SRTM C-band phase centre with Beni floodplain forests. This aim will be accomplished through completion of four specific objectives.

1. To identify and correct any vertical offset observed in the SRTM dataset for the Beni floodplain study area
2. To assess the absolute vertical accuracy of the SRTM dataset for the Beni floodplain through comparison with GCPs derived from a differential GPS survey
3. To quantify the relationship between field measured canopy height and SRTM derived canopy height using a linear model
4. To calculate the average magnitude of SRTM penetration into Beni floodplain forest canopies

4.3 Data sources

4.3.1 SRTM dataset

For this study the 'version 2' SRTM dataset at 3 arc second resolution was obtained through the USGS seamless service (http://seamless.usgs.gov). The justification for the use of the 'version 2' SRTM dataset is provided within 5.3.1. The data were acquired as 1^{o} x 1^{o} tiles which were mosaiced using ArcGIS in order to construct a continuous representation of topography for the Beni floodplain study area. The SRTM dataset was subject to minimal processing, in order to retain original elevation values, however a relatively small number of voids which were located in areas of water were filled using simple interpolation techniques.

4.3.2 Beni floodplain canopy height survey

Canopy height was surveyed at 35 locations across the Beni floodplain, with the spatial distribution of these plots illustrated in figure 4.1. Due to the large extent of the study area and poor accessibility offered by Beni floodplain road network, a modified random sampling strategy was devised and implemented within ArcGIS. The floodplain road network was digitised using high resolution Google

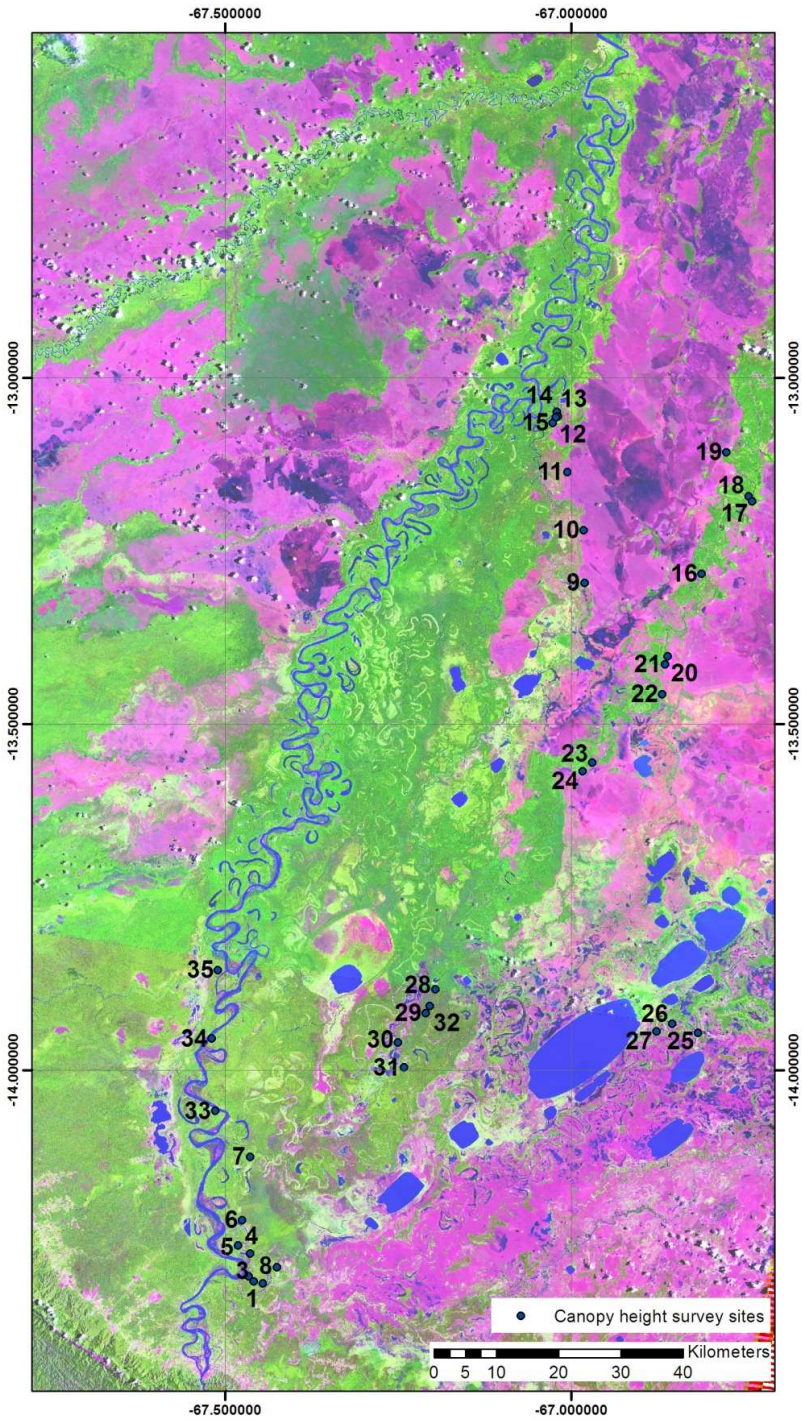

Figure 4.1. Canopy height survey plot locations overlain upon Landsat TM false colour composite

Earth imagery, whilst the floodplain land cover classification generated in chapter 3 was converted into a forest mask. ArcGIS tools were subsequently utilised in order to generate a buffer zone which ran adjacent to floodplain roads at a distance of between 100 m and 200 m. This layer delineated a zone which was accessible via the floodplain road network, whilst being at a sufficient distance to preclude the influence of edge effects. In the final step ArcGIS was

used to generate random points in the area where the buffer zone intersected the forest mask. These points were loaded onto a handheld GPS to enable plots to be located whilst in the field.

Canopy height surveys were undertaken using an adapted multiple-nearest-tree technique (Newton, 2007). After navigating to the predefined starting point using a handheld GPS unit, a 100 m transect was established at a predefined bearing using a compass, and poles were inserted at 25 m intervals. At each pole the four tallest trees within a radius of 12.5 m were identified along with the four trees located in closest proximity to the pole. Identified trees were measured for diameter at breast height (DBH) using a diameter tape, total height and crown height using a laser rangefinder, whilst species name and distance from the pole were also recorded. Measurement of the tallest trees enabled characterisation of the height of the canopy top, whilst measurement of the four closest trees facilitated estimation of stand density. The multiple-nearest-tree approach was adapted in order to reliably and efficiently characterise the canopy height of forest stands without undertaking a time consuming full forest inventory. This facilitated survey of a greater number of stands across a wider area of the Beni floodplain.

4.3.3 Beni floodplain elevation survey

Ground elevation points were collected across the Beni floodplain using two Trimble differential GPS (DGPS) units, which were associated with a maximum vertical accuracy of 50 cm. The first unit was vehicle mounted and is pictured in figure 4.2, facilitating both kinematic and stationary observations, whilst the second unit was used for static surveys only. Initial post processing and analysis of DGPS elevation data revealed the presence of inconsistencies in the kinematic surveys, indicated by the presence of significant elevation differences for repeat observations of the same area. Therefore the kinematic surveys were excluded from the analysis of the SRTM DEM, which was conducted using the more accurate and consistent stationary survey points. Static points were measured with a minimum occupation time of 10 minutes, with extended occupation allowing the DGPS to acquire a greater number of satellites and determine ground elevation with a higher level of accuracy. To further maximise the quality of the validation dataset, static points were filtered in order to remove those observations which were associated with a vertical error exceeding ± 1 m.

Finally, in order to ensure maximum vertical accuracy the filtered static points underwent precise point positioning using a web application provided by Natural Resources Canada http://webapp.geod.nrcan.gc.ca/geod/tools-outils/index.php#ppp . Precise point positioning (PPP) uses GNSS orbit and clock information in order to compute higher accuracy positions from raw observations obtained by a differential GPS. Therefore after filtering and PPP, the final accuracy of the DGPS survey points utilised in validation was expected to be a minimum of ± 1 m with many of the GCPs being associated with an accuracy of better than ± 0.5 m.

Figure 4.2. Vehicle mounted with differential GPS at front left, used for kinematic and static floodplain elevation surveys.

The distribution of the DGPS points used for assessment of SRTM accuracy is shown within figure 4.3. Of the total 105 points, 48 were located in forested areas, 34 represented savanna/pasture land cover, whilst the remaining 23 points were located within other land covers or at the forest savanna transition. Remote sensing observations suggest that land cover of the Beni floodplain comprises approximately 48% forest, 49% savanna or other open areas and 3% water. Therefore in proportional terms forests are over represented within the GCP dataset, whilst savannas are underrepresented.

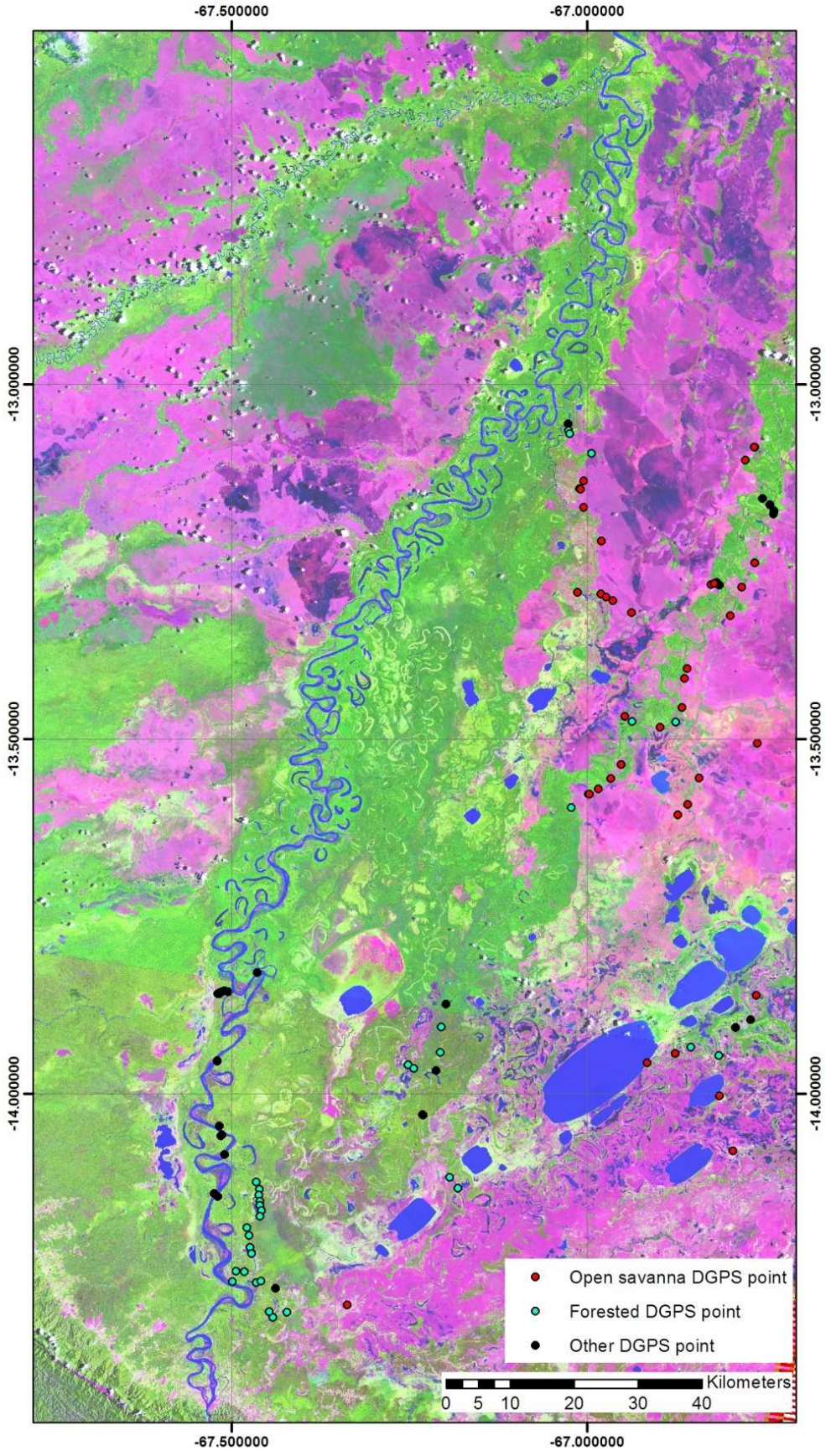

Figure 4.3. Beni floodplain study area showing the location of static DGPS points overlain upon a Landsat TM false colour composite image.

4.4 Methodology

4.4.1 SRTM accuracy assessment for the Beni floodplain study area

In this study SRTM vertical offset was quantified through comparison of SRTM and DGPS survey elevations. In order to eliminate the positive bias associated with vegetation effects, DGPS survey points were separated according to land cover type, only elevations surveyed within open savanna regions (n = 33) were included in the analysis. Vertical offset was characterised through plotting of scatter graphs and a histogram illustrating the deviation between the SRTM and DGPS elevations, before being corrected using the mean average deviation between the two datasets (Kellndorfer et al., 2004). After correction for vertical offset the absolute vertical accuracy of the SRTM DEM was assessed through calculation of standard accuracy statistics including mean error, standard deviation and RMSE. These statistics were supplemented by calculation of linear error at the 90% confidence level (LE90) and the number of samples within +- 16 m, statistics adopted in order to standardise the results of SRTM validation exercises (Bamler, 1999). Statistics were computed for the complete DGPS dataset (n=105) in addition to for open savannas (n=33) and forested areas (n=48), enabling a comparison between different land cover types.

Figure 4.4. Photograph illustrating typical open savanna areas upon the Beni floodplain, points from which were used for assessment of SRTM vertical offset.

4.4.2 SRTM- Beni floodplain forest interactions

Quantification of SRTM- Beni floodplain forest interaction centred around the comparison of SRTM derived canopy height and field measured canopy height. On a basic level, calculation of the difference between actual canopy height measured within the field and the vertical bias contained within the SRTM, referred to here as SRTM derived canopy height, at the same location allows the magnitude of SRTM C-band phase centre penetration to be inferred (Kellndorfer et al., 2004).

In order to calculate field measured canopy height forest inventory data were entered into a spreadsheet and relevant statistics were calculated. Initially, basal area was calculated for each individual through application of the formula for the area of a circle to the radius of the stem, calculated based upon the DBH. Mean basal area, mean canopy height and standard deviation of canopy height were subsequently calculated for each plot based upon the four tallest individuals at each point along the forest transect. As points were located at intervals of 25 m along the 100 m transect, statistics for each plot were calculated from a total sample of twenty trees. In addition, plot density was calculated based upon the four closest trees to each point using equation 4.1 (Bullock, 1996).

$$plot\ density = \frac{1}{(2D_2)^2} \tag{4.1}$$

In equation 4.1, D_2 represents the mean distance from the four measured individuals to the point marked on the transect. Mean canopy height simply presents an aggregate estimate of the height of the top of the canopy for the plot, whilst standard deviation provides an estimate of the vertical structure of the canopy within the plot. Mean basal area and plot density provide additional ancillary information about the structure of the forest stand.

SRTM canopy height was subsequently calculated for each forest canopy height plot measured in the field survey. The SRTM canopy height was computed through subtraction of ground elevation, measured in the field using the DGPS at a point along the transect, from the average SRTM elevation extracted from a 3 x 3 pixel window centred around the location of the field plot. The average SRTM elevation was extracted from a 3 x 3 pixel window in order

to minimise the influence of phase noise (Walker et al., 2007). In order to estimate the magnitude of SRTM C-band phase centre penetration into Beni floodplain forest stands it was necessary to compare field measured canopy height and SRTM derived canopy height. Hofton et al, (2006) found that SRTM penetration increased linearly with canopy height, therefore SRTM derived canopy height was modelled here using linear regression with field measured canopy height as the independent variable. Initially the relationship was modelled using each of the 35 canopy height sites as an individual observation (figure 4.8).

However in a previous study Kellndorfer et al., (2004) found that the relationship between SRTM derived and field measured canopy height was characterised by a substantial level of noise at the level of individual plots, which was attributed to the influence of phase noise. The authors found that adoption of a linear binning approach, in which individual plots were aggregated in order to simulate stand level forest characteristics, resulted in a significant reduction of phase noise and increase in the fit between SRTM derived and field measured canopy height. Accordingly, here the 35 individual canopy height survey plots were binned into 9 stands according to forest type and geographical location (table 4.3), in order to simulate stand level forest characteristics in a similar manner to Kellndorfer et al., (2004). The relationship between SRTM derived canopy height and field measured canopy height was subsequently remodelled based upon the binned dataset in order to reduce the influence of phase noise (figure 4.11).

4.5 Results

4.5.1 SRTM accuracy assessment

Figure 4.5 illustrates the comparison between SRTM and DGPS measured ground elevation in the form of a scatter plot. Simple qualitative visual analysis indicates that SRTM elevation increases approximately linearly with GPS elevation, however, points are distributed between 5-10 m above the 1:1 line which is symptomatic of a positive vertical offset. In order to ensure the consistency of this potential offset, a linear relationship was fitted to the dataset, whilst the residuals were plotted in a histogram in figure 4.6. The coefficient of the linear relationship was close to 1, demonstrating direct proportionality

between SRTM and DGPS elevations, whilst the r^2 value of 0.8162 (n=33) indicated a good level of fit between the two datasets. Figure 4.6 illustrates that the SRTM-DGPS residuals are normally distributed and centred around a mean of 6.74 m, which equates to the mean vertical offset of the SRTM. Figure 4.7 shows the relationship between GCPs and the SRTM dataset after correction for vertical offset. As expected, the data points are distributed around the 1:1 line, with normally distributed residual errors.

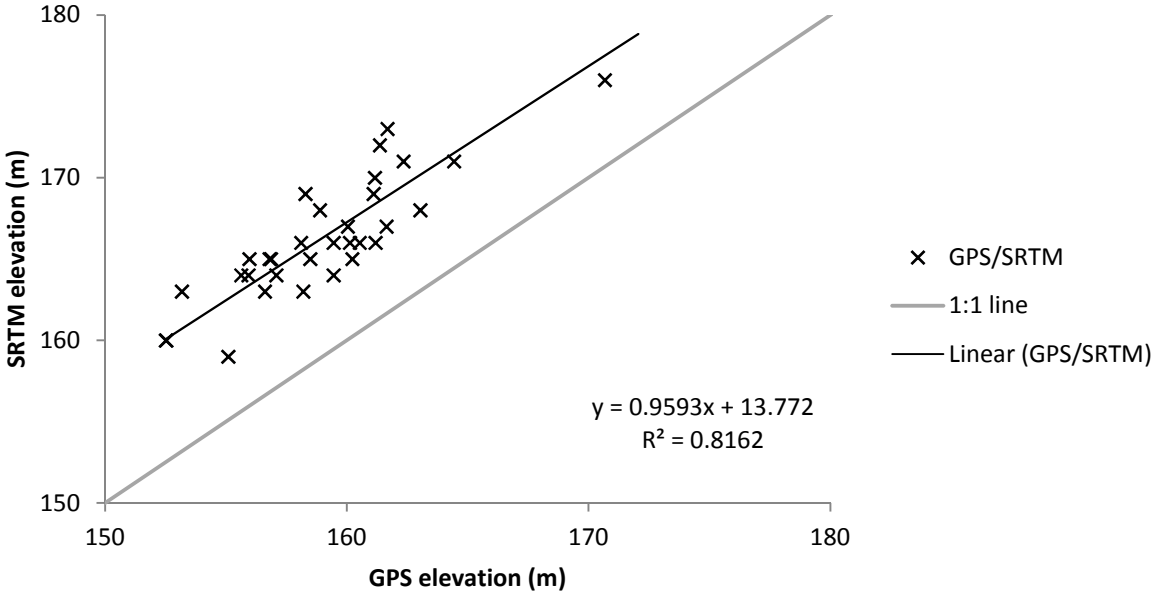

Figure 4.5. Scatter plot illustrating a comparison of SRTM and DGPS elevations for unforested areas of the Beni floodplain.

Absolute accuracy statistics of the SRTM dataset for the Beni floodplain after correction for vertical offset are displayed in table 4.1. In open savanna regions which are characterised by a low density of trees and shrubs vertical accuracy of the SRTM is excellent. RMSE of 1.6 m is indicative of a high level of accuracy, whilst LE90 of 2.7 m far exceeds the pre mission expectations of ± 16m. Indeed, within unforested areas 100% of SRTM elevations were within ± 16 m of ground elevations measured during the DGPS survey.

In areas of broadleaf forest the vertical accuracy of SRTM is much lower, indicated by an RMSE of 12.8 m which is almost an order of magnitude larger than for open savanna areas. LE90 for forested areas falls significantly short of the pre mission accuracy requirements at 21.1 m, although 75% of samples fall within +- 16m of ground elevation. Unsurprisingly the mean error of 11.4 m is

indicative of a substantial positive bias, which is responsible for the poor levels of accuracy observed for forested areas.

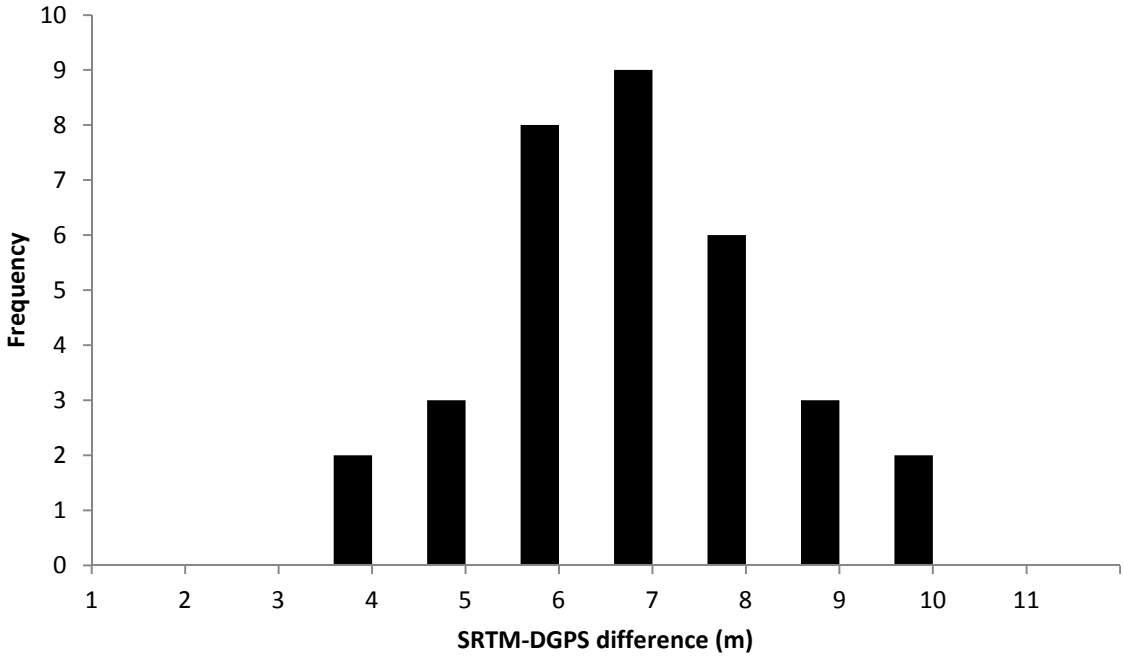

Figure 4.6. Histogram showing the positive vertical offset observed for the SRTM DEM.

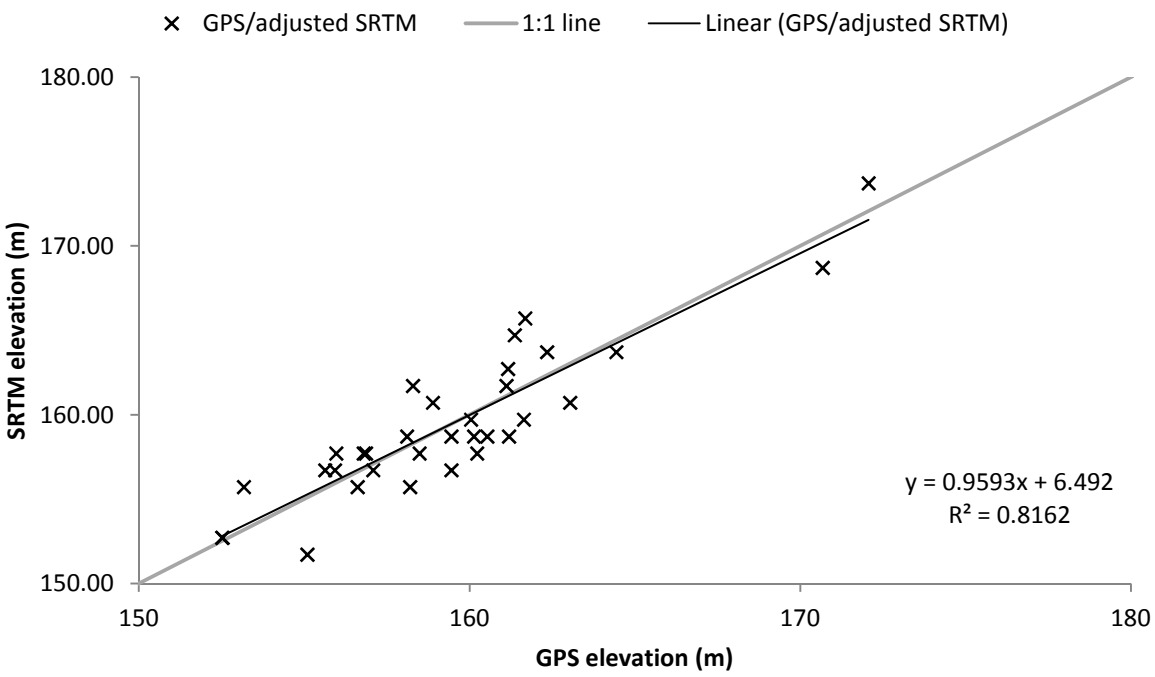

Figure 4.7. Scatter plot illustrating a comparison of DGPS and corrected SRTM elevations for unforested areas of the Beni floodplain.

At 16.2 m LE90, the absolute vertical accuracy for all land covers falls just short of the pre mission accuracy requirements. However this is unsurprising given the significant positive bias observed for forested areas and the proportional overrepresentation of forested areas in the set of GCPs. Overall less than a third of GCPs corresponded to open savanna areas, which actually account for approximately 50 % of the Beni floodplain study area. On the other hand, open areas, were underrepresented in the assessment of the whole floodplain, leading to an underestimation of the accuracy of the SRTM for the floodplain as a whole.

Table 4.1 Absolute vertical accuracy statistics of the SRTM DEM for the Beni floodplain

	Absolute vertical accuracy statistics of the SRTM DEM on the Beni floodplain					
	n	Average (m)	Standard deviation	RMSE (m)	90% confidence level (m)	Samples within +- 16 m
Open savanna	33	0.0	1.7	1.6	2.7	100.0
Broadleaf forest	48	11.4	5.9	12.8	21.1	75.0
All land covers	105	6.6	7.3	9.9	16.2	85.7

4.5.2 SRTM forest interactions

Table 4.2 shows SRTM derived and field measured forest characteristics for the 35 survey sites. Visual analysis of this table reveals that field measured mean canopy height exceeded SRTM canopy height in all instances. SRTM canopy height varied between 5.9 m and 20.6 m, whilst field measured canopy height values were within the range of 12.3 m to 29.6 m. The magnitude of the canopy height residual varied from a minimum of -1.9 m to a maximum of -16 m. The canopy height information contained within table 4.2 is displayed visually in figure 4.8. Points are distributed below the 1:1 line, reflecting the observation that SRTM derived canopy height is consistently lower than field measured canopy height. The relationship between the two canopy height measures appears to be linear, whilst an r^2 value of 0.6415 for a fitted linear model illustrates that the relationship is marked by the presence of a substantial level of noise.

Figures 4.9 and 4.10 show the residual errors produced when the SRTM canopy height predicted by the fitted linear model was subtracted from the

Table 4.2. Canopy height inventory results for individual survey locations.

Plot	Plot DGPS elevation (m)	SRTM elevation (m)	SRTM standard deviation (m)	SRTM canopy height (m)	Mean basal area (m^2)	Plot density (Individuals/ m^2)	Mean canopy height (m)	Standard deviation canopy height (m)	Canopy height residual (m)
1	182.54	200.4	2.0	17.8	0.65	108.2	24.0	8.7	-6.2
2	184.8	202.6	1.0	17.8	0.28	295.4	23.9	4.5	-6.1
3	184.1	196.9	2.2	12.8	0.13	418.9	20.2	3.9	-7.4
4	182.2	192.9	1.8	10.7	0.14	142.9	17.0	6.3	-6.3
5	179.9	199.0	1.6	19.2	0.22	124.0	27.2	5.1	-8.0
6	182.7	201.6	2.1	18.9	0.18	239.1	22.0	7.7	-3.1
7	180.3	194.5	1.3	14.2	0.12	204.7	19.5	5.2	-5.2
8	178.1	193.6	2.9	15.5	0.12	198.5	23.1	5.6	-7.6
9	161.7	170.6	4.0	8.9	0.22	90.2	18.9	5.6	-10.0
10	158.3	166.3	3.0	8.0	0.09	180.3	16.7	3.8	-8.8
11	159.5	169.9	2.3	10.5	0.11	50.5	18.5	3.9	-8.1
12	149.8	169.0	2.5	19.2	0.25	200.2	21.1	6.9	-1.9
13	149.8	169.9	4.3	20.1	0.58	332.8	29.6	4.0	-9.5
14	149.8	167.3	2.8	17.4	0.41	75.5	26.2	7.0	-8.8
15	156.7	167.3	1.4	10.6	0.17	287.5	23.4	5.5	-12.9
16	158.9	164.8	3.6	5.9	0.37	151.4	20.6	6.5	-14.7
17	150.2	158.7	1.6	8.5	0.06	202.0	12.7	2.9	-4.2
18	153.3	164.6	1.3	11.3	0.12	217.6	18.0	4.7	-6.7
19	155.1	162.3	4.2	7.2	0.09	149.7	15.0	5.0	-7.9
20	155.9	162.1	5.0	6.2	0.13	156.8	19.1	3.4	-12.9
21	157.1	167.6	2.2	10.5	0.13	183.4	19.3	4.3	-8.7
22	158.1	171.5	2.8	13.4	0.14	58.9	18.8	5.0	-5.4
23	160.5	168.4	6.0	7.8	0.12	97.4	18.6	6.2	-10.7
24	160.1	160.5	5.5	5.9	0.04	504.2	12.3	2.0	-6.4
25	161.4	168.6	3.1	7.2	0.13	113.7	21.0	5.1	-13.8
26	162.6	169.7	3.4	7.1	0.07	268.5	16.1	5.8	-9.0
27	162.3	172.4	3.3	10.0	0.06	405.7	15.2	3.1	-5.1
28	166.6	179.9	1.4	13.4	0.16	197.5	21.2	6.8	-7.9
29	166.2	182.6	2.2	16.4	0.19	239.1	23.1	7.1	-6.7
30	164.8	176.9	3.7	12.2	0.11	179.5	20.2	3.6	-8.1
31	164.8	177.9	2.1	13.2	0.18	173.2	21.0	5.2	-7.9
32	167.7	180.9	1.7	13.2	0.20	168.7	22.9	6.8	-9.6
33	182.7	199.0	3.6	16.3	0.50	61.9	24.6	9.4	-8.3
34	174.3	181.7	1.3	7.4	0.27	107.5	23.4	5.5	-16.0
35	175.2	195.8	1.7	20.6	0.23	118.5	19.8	5.2	0.7

actual derived SRTM canopy height. In order to establish whether forest physical characteristics were responsible for the noise observed in the relationship between field measured and SRTM derived canopy height, the SRTM canopy height residuals were plotted against numerous variables relating

to forest structure. When plotted against field measured canopy height in figure 4.9 the SRTM canopy height residual points are distributed randomly and show no discernible trend. Indeed no trend was observed when the SRTM canopy height residual was plotted against other forest variables such as plot density. Display of the frequency distribution within a histogram in figure 4.10 illustrates that SRTM canopy height residuals are characterised by a near normal distribution. This suggests that SRTM canopy height residuals may be attributed to random error/noise rather than physical forest properties.

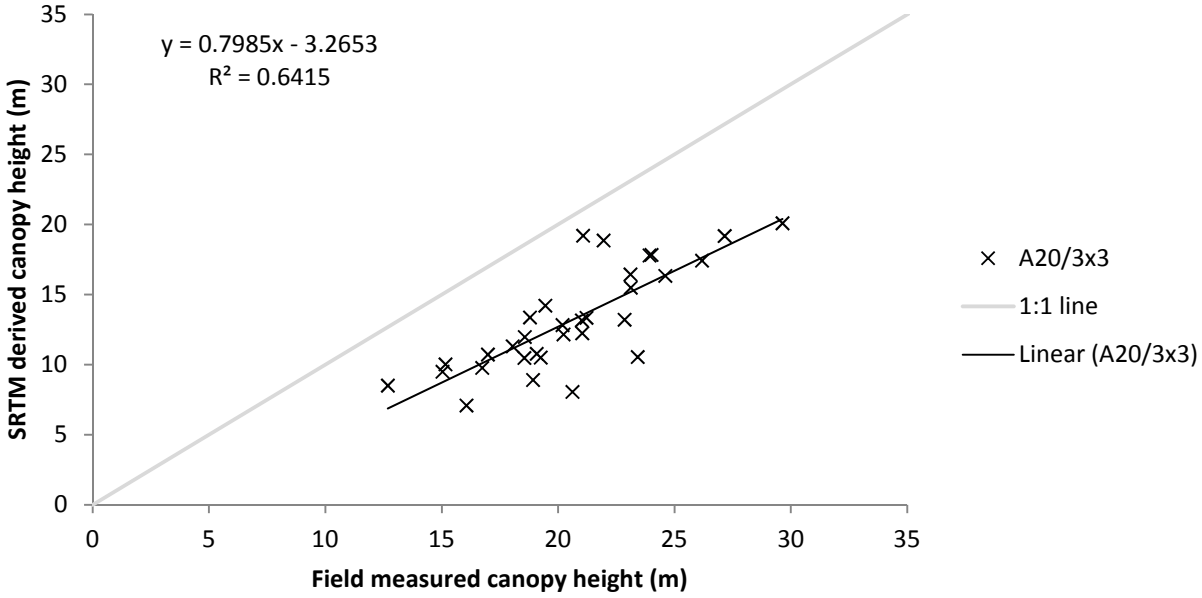

Figure 4.8. Scatter plot comparing field measured canopy height and SRTM derived canopy height for Beni forest plots.

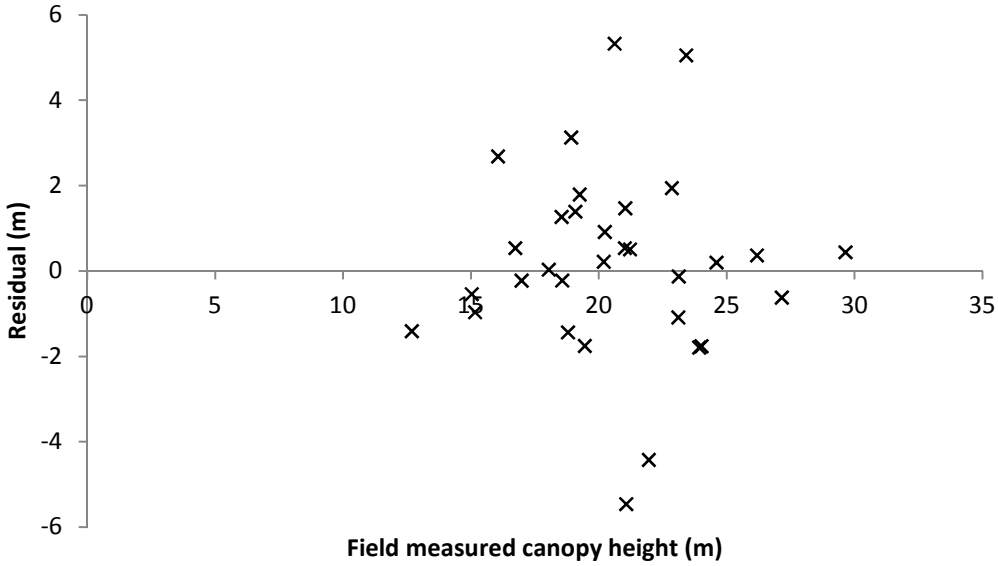

Figure 4.9. Scatter plot showing residuals from the linear regression model shown within figure 4.8.

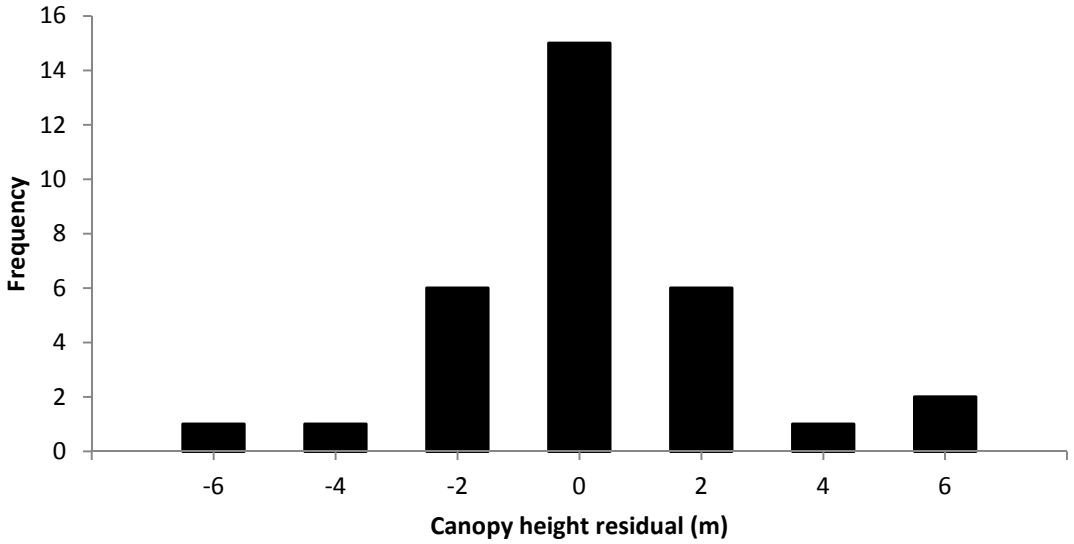

Figure 4.10. Histogram illustrating residuals from the linear regression model shown within figure 4.8.

Table 4.3 details the stand averaged canopy height results, in which the 35 original canopy height plots were grouped into nine stands according to geographical location and forest type, with the aim of reducing the influence of noise in the dataset. Deviation from the linear model is much lower than for the plot by plot analysis, with a maximum deviation of 1.76 m and an average deviation of 0.19 m. The stand averaged results are plotted in figure 4.11, which also shows the recalculated linear model. The relationship between field measured and SRTM derived canopy height remains linear and the coefficient of the linear model at 0.9628 indicates that the two estimates of canopy height are roughly proportional. Further, it is evident that the process of stand averaging significantly reduced the noise in the relationship, indicated by the increase in the value of r^2 to 0.922 (n=9). Based upon the improved stand averaged canopy height results the difference between the mean field measured canopy height of 20.6 m and mean SRTM derived canopy height 13.2 m indicates that the average magnitude of SRTM canopy penetration is 7.4 m.

Hence within Beni floodplain forests the SRTM C-band phase centre is located on average 35% of the distance from the top of the canopy to the ground. However it should be noted that the magnitude of SRTM C-band phase centre canopy penetration shows a degree of variability between different stands. The characteristics of the regression model shown in figure 4.11, which is

characterised by a coefficient of close to 1 and a negative intercept, indicate that the percentage C-band phase centre penetration varies as a function of canopy height. The information contained in table 4.3 indicates that the C-band phase centre is located between 32 % and 44% of the distance from the top of the canopy to the ground, with this percentage decreasing with increasing canopy height.

Table 4.3. Canopy height inventory results for survey locations grouped into stands according to geographic location.

Stand	Constituent plots	SRTM canopy height (m)	SRTM Standard deviation (m)	Mean canopy height (m)	Standard deviation-canopy height (m)	Mean basal area (m^2)	Canopy height residual (m)	Deviation from linear model (m)
1	1, 2, 3, 8	16.3	3.6	24.6	9.4	0.50	-8.3	0.20
2	4, 5, 6, 7	15.7	1.7	21.4	6.1	0.16	-5.6	-1.76
3	9, 10, 11	16.0	2.0	22.8	5.7	0.30	-6.8	-0.87
4	12, 13, 14, 15	9.7	3.1	18.1	4.5	0.14	-8.3	1.64
5	16, 17, 18, 19	16.8	2.8	25.1	5.9	0.35	-8.3	0.10
6	20, 21, 22, 23	9.3	2.7	16.6	4.8	0.16	-7.2	0.85
7	25, 26, 27	11.7	4.0	18.9	4.7	0.13	-7.3	0.38
8	28, 29, 30, 31, 32	9.8	3.2	17.4	4.6	0.09	-7.6	1.06
9	33	13.7	2.2	21.7	5.9	0.17	-8.0	0.56
Mean		13.2	2.7	20.6	5.5	0.20	-7.4	0.19

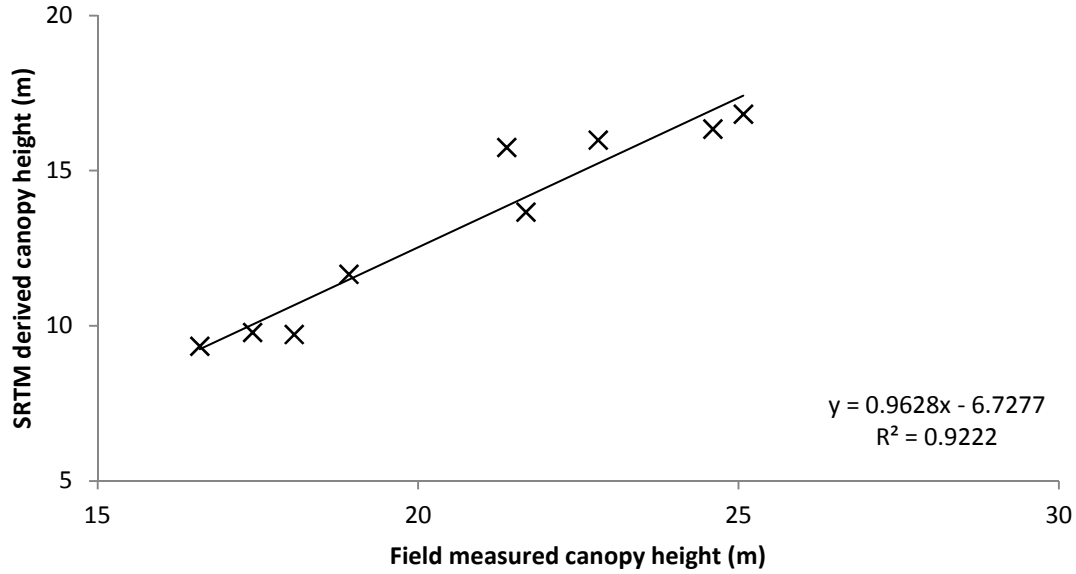

Figure 4.11. Scatter plot illustrating the comparison between field measured canopy height and SRTM derived canopy height when plots are averaged according to geographical location.

4.6 Discussion

The presence of a vertical offset is a common feature of the SRTM dataset. For study areas located in Iowa and North Dakota within the United States, Kellndorfer et al., (2004) found an offset of – 4.0 m and -1.1 m respectively when the SRTM was compared to an NED DEM. For a Norwegian study area Weydahl et al., (2007) reported a vertical offset of 3.3 m. Further, Hofton et al., (2006) compared SRTM elevation to an LVIS laser height dataset, finding that offsets varied from 0 m for regions in Maryland, United States to 4.5 m in Costa Rica. Therefore having been measured at 6.74 m the magnitude of the vertical offset for the Beni study area is higher than has been found for other regions. Nevertheless this falls within the expected range of ± 10 m for the SRTM (Bamler, 1999), whilst the high level of fit observed between the SRTM and GPS elevations and near normal distribution of errors around the mean deviation is indicative of a vertical offset rather than another form of uncertainty. The presence of this offset can be attributed to errors in the attitude and measurement of the length of the interferometric baseline (Kellndorfer et al., 2004). Further, it has been postulated that the firing of Shuttle thrusters at intervals of approximately 100 seconds induced absolute errors in the SRTM which manifest over scales greater than 500 km (Rabus et al., 2003).

If left uncorrected, the presence of such a vertical offset could hold significant implications for the application of SRTM in land surface studies. Perhaps the most significant issue proliferating from the presence of a systematic error relates to the comparability of SRTM with other sources of topographic information and vertically referenced datasets. For example the presence of a vertical offset could directly propagate a lower level of absolute accuracy for the SRTM when assessed with respect to accurate GCPs, thus confounding the true quality of the dataset. Further, in the context of this study an offset of 6.74 m equates to over 30% of the average SRTM derived canopy height of Beni floodplain forests. Intuitively, an error of this magnitude would introduce an unacceptable level of uncertainty into any attempt to retrieve canopy height information from SRTM through comparison with LiDAR waveforms. In addition, vertical offset present within the SRTM may potentially propagate errors indirectly during application of the dataset in land surface process studies. Application of uncorrected SRTM in a flood inundation model would produce

offsets in predictions of water surface elevation, leading to poor model performance when compared to observed water surface elevation data. In this study, successful correction of the vertical offset as illustrated in figures 4.5-4.7 precludes the proliferation of such direct and indirect errors.

The absolute accuracy statistics calculated for the SRTM dataset upon the Beni floodplain area are equivalent or better than for other study areas. Here the accuracy of SRTM for open areas is 2.7 m LE90, which far exceeds the pre mission accuracy requirements of the dataset at 16 m LE90 (Bamler, 1999). Accuracy declines substantially to 21.1 m LE90 for forested areas, which are characterised by a systematic positive bias with respect to ground elevation. For all GCPs accuracy of the SRTM falls just outside the pre mission accuracy requirements, although proportional under representation of open areas means that the actual accuracy of the SRTM is likely to be higher than the value of 16.2 m LE90 shown in table 4.1. For the Vestfold region of Norway Weydahl et al., (2007) found that open areas were characterised by an absolute vertical accuracy of 6.5 m LE90, whilst within forested regions this increased to 14 m LE90. Hence within this region SRTM exhibited a lower level of accuracy in open areas, whilst accuracy in forested regions was higher and exceeded pre mission requirements despite the presence of positive bias. This was most likely attributable to lower and more open canopies which characterise Norwegian forests.

Horizontal error and relative vertical error were not quantified in this study, as GCPs were not of a sufficient density to assess these characteristics. Horizontal error of the SRTM has been assessed in past studies through use of spatial cross correlation, in which the SRTM is shifted in both the x and y directions in order to elucidate its optimum position with respect to a set of GCPs. Generally SRTM has exceeded horizontal accuracy requirements when quantitatively assessed (Rodriguez, 2005), indeed Weydahl et al., (2007) found that horizontal SRTM accuracy was better than 20 m. Here, a qualitative comparison of the SRTM with Landsat TM imagery and GCP location suggested that horizontal errors were less than the width of an SRTM pixel and hence were of a similar order to those observed within past studies.

The low RMSE and LE90 observed for open areas indicate that relative errors were not of a high magnitude for the SRTM within the Beni floodplain study

area. Kellndorfer et al., (2004) found that relative error in the form of Gaussian phase noise constituted a significant source of uncertainty for the 1 arc second SRTM dataset, producing a noise range of up to 13 m and 7 m for study areas in Iowa and North Dakota respectively. The authors found that averaging of elevation within a 7 x 7 pixel window reduced the noise range to less than 4m, whilst averaging over a 25 x 25 pixel window reduced the noise range to less than 1 m. The relatively small influence of phase noise within the Beni study area can be partially attributed to the use of the 3 arc-second dataset, which was produced through averaging of the 1 arc-second dataset within a 3 x 3 pixel window by NASA JPL (USGS, 2005). Further smoothing of the 3 arc-second dataset prior to accuracy assessment using a 3x 3 window can be attributed as the second reason for the insignificance of phase noise within the Beni study area. Although it was not possible to directly assess phase noise within vegetated areas, SRTM is characterised by a higher signal to noise ratio within forested areas in comparison to open areas (Walker et al., 2007). Hence the minimal influence of noise observed within open savannas after implementation of spatial averaging, can be assumed to apply to forested areas.

The results of the SRTM accuracy assessment for the Beni floodplain have both positive and negative implications with regards to the general application of the dataset in land surface studies, and more specifically within the context of this study. After correction of vertical offset, high levels of absolute accuracy observed within areas of open savanna indicate that the smoothed SRTM provides an accurate representation of topography in these areas. The absolute vertical accuracy of the SRTM can be considered excellent given its global continuous coverage. Although alternative sources of topographical data such as LiDAR are able to offer higher levels of vertical accuracy (Bourgine and Baghdadi, 2005), these datasets are often limited in terms of spatial extent or fail to offer the continuous coverage required in order to construct a DEM (Harding and Carabajal, 2005). However, results presented here illustrate that the SRTM fails to provide an accurate representation of ground elevation in forested areas of the Beni floodplain. Indeed the presence of such a systematic positive bias has been observed within other study areas (Berry et al., 2007; Hofton et al., 2007). Hence utilisation of the SRTM in land surface studies which require a bare earth DEM, such as modelling of flood inundation upon the Beni

floodplain, is problematic and further processing is required in order to remove vegetation effects from the SRTM.

The relationship between SRTM derived and field measured canopy height at the plot level exhibited a roughly linear trend characterised by a significant level of noise, with an r^2 value of 0.6415 indicating a reasonable level of fit between the data. Comparatively, when attempting to model the relationship between SRTM C-band phase centre height and observed canopy height at the plot level Kellndorfer et al., (2004) obtained a poor level of fit, indicated by an r^2 value of 0.20. The authors attributed poor model performance to the presence of residual phase noise, which remained in the SRTM as fewer than ten 1 arc-second pixels were averaged for each plot. Kellndorfer et al., (2004) addressed the influence of phase noise through implementation of a novel approach in which plot locations were grouped into bins according to canopy height, facilitating averaging over larger numbers of SRTM pixels. This approach effectively simulated mean observed canopy height and SRTM scattering phase centre height within homogenous stands and resulted in averaging of a minimum of 20 pixels per bin. The linear binning approach successfully ameliorated phase noise; for 20 bins the r^2 value improved to 0.75, whilst for 11 bins r^2 increased to 0.86.

Following the success of this binning strategy, a stand averaging approach was adopted here in order to improve the model for SRTM derived and field measured canopy height for Beni floodplain forests. The approach implemented here varied from that adopted by Kellndorfer et al., (2004), because phase noise did not constitute the primary source of residual errors in the plot level model. At the plot level, average SRTM elevation was extracted from a 3 x 3 pixel window around the location of each survey site and SRTM canopy height was calculated through subtraction of a local measurement of ground elevation acquired using DGPS. Whilst averaging of SRTM elevation within a 3 x 3 window reduced the influence of phase noise, it is hypothesised that this process introduced further uncertainties into the model through adoption of assumptions relating to the spatial heterogeneity of ground elevation and forest structure.

Ground elevation was measured at a single location for each plot and as a result variations in ground elevation over the 3 x 3 pixel window were not

accounted for in calculation of SRTM canopy height. Intuitively forest structure was also assumed to be homogenous over the 0.73 km^2 area. Whilst field observations suggested that floodplain topography was typically flat, variations of several meters could feasibly occur within an area of this size. In addition forest structure exhibited a high level of heterogeneity over relatively small spatial scales upon the Beni floodplain. Therefore a combination of both unquantified topographical variation and forest heterogeneity within the 3 x 3 pixel window were attributable as the sources of residual errors within the plot level model.

Taking into account the aforementioned sources of residual error, plots were grouped into stands according to geographical location and forest type. In order to minimise the uncertainties associated with spatial variability of both ground elevation and forest structure, SRTM canopy height was calculated for each plot using the single SRTM pixel within which the field plot was located. Meanwhile the influence of SRTM phase noise was effectively mitigated through averaging of multiple plots within a stand. This stand averaging procedure proved highly effective in reducing the influence of normally distributed errors observed in the plot level model. Indeed recalculation of the linear model based upon the stand averaged dataset yielded an increase in the quality of the relationship between SRTM derived and field measured canopy height, indicated by an r^2 value of 0.922.

The interaction of the SRTM C-band phase centre with floodplain forest stands located upon the Beni floodplain fall within the broad range which would be expected based upon the results of past studies. On average the SRTM C-band phase centre penetrated 7.4 m into the canopy of Beni floodplain forests, equating to 65 % of the distance from the ground to the top of the canopy. However canopy penetration exhibits a modest degree of variability, indeed the C-band phase centre was located between 56 % and 68% of the distance from the ground to the top of the canopy within the different forest stands. The fitted stand averaged linear model which describes the relationship between SRTM derived and field measured canopy height illustrates that SRTM penetration increases linearly with forest height. This relationship also illustrates that percentage penetration of the C-band phase centre varies with canopy height, decreasing proportionally within taller forests.

Through comparison with GLAS spaceborne LiDAR waveforms, Carabajal and Harding et al., (2006) found that SRTM elevation represented approximately 60 % of the height of forest canopies. This figure was observed to be consistent across five different study sites encompassing different vegetation types including the Amazon Basin, the Tibetan Plateau, east Africa, western Australia and the western United States. Hofton et al., (2006) compared SRTM derived canopy heights to NASA LVIS data for four study sites located within the United States, and a fifth site situated within area of Costa Rica. This study found that SRTM penetrated to approximately 50 % of overall canopy height, with the relationship between LVIS and SRTM derived canopy heights being described adequately by a linear model. The authors found that the linear model for the Costa Rican study area was characterised by a greater coefficient than the models for the United States study areas, illustrating that physical characteristics of forest canopies exert a significant influence upon the magnitude of SRTM penetration into the canopy.

Bourgine and Baghdadi (2005) quantified SRTM canopy penetration for a forested study area within French Guiana through comparison with canopy top and ground elevation data derived through laser surveys. The SRTM C-band phase centre was located on average 8.5 m below the canopy top, constituting approximately 75 % of the distance from the ground to the top of the canopy. Hence the magnitude of SRTM C-band phase centre penetration found in this study falls within the relatively broad range of results found within other studies which have analysed tropical forest stands, both in terms of absolute depth and as a proportion of total canopy height.

Quantification of C-band phase centre interactions with Beni floodplain forests constitutes a precursor to effective utilisation of SRTM within the study area. The linear relationship established between SRTM derived canopy height and field measured canopy height, in addition to the calculation of the average magnitude of SRTM penetration can be utilised in order to facilitate treatment of vegetation effects in the SRTM dataset. Within this study vegetation effects can be considered as a bias to be removed from the SRTM dataset in order to generate a bare earth DEM. Therefore estimates of C-band phase centre penetration can be used to scale independent continuous estimates of forest canopy height, in order to correct the SRTM appropriately. Conversely, where

SRTM vegetation effects are considered a useful signal, knowledge of the magnitude of C-band phase centre penetration facilitates scaling of SRTM derived canopy heights to actual canopy heights, which can subsequently be used to estimate other forest properties such as biomass. The results presented here are particularly significant as this study represents one of the first successful attempts to directly compare forest height derived from the SRTM with field measured canopy height, with the majority of past studies comparing SRTM with LiDAR waveforms (Carabajal and Harding, 2006; Hofton et al., 2006; Bourgine and Baghdadi, 2005).

4.7 Conclusion

The vertical offset of the SRTM dataset for the Beni floodplain was 6.74 m, which is slightly larger than that observed for other study areas (Kellndorfer et al., 2004; Weydahl et al., 2007). After correction of this vertical offset, the absolute vertical accuracy of the SRTM was calculated with respect to a set of 105 highly accurate post processed DGPS survey points. Within open savanna areas which are largely devoid of vegetation, the SRTM exhibits a very high level of accuracy indicated by an RMS error of 1.2 m. In contrast, within forested areas the SRTM is characterised by a significant positive bias and absolute vertical accuracy is lower than 20 m. For all land covers, the SRTM was characterised by 16.2 m linear error at the 90 % confidence interval, falling just outside the stated pre mission accuracy expectations of +- 16 m linear error at 90% confidence (Bamler et al., 1999). In order to put this figure for overall accuracy into context it is important to consider that less than a third of the total GPS points corresponded to open savannas, which actually constitute approximately half of the total area of the floodplain study area. Hence open savannas which are associated with a very high level of accuracy in the SRTM, are proportionally underrepresented in the overall assessment of SRTM accuracy for the floodplain. Overall, the results presented here largely agree with past studies which found that SRTM accuracy was very high within bare ground areas (Rodriguez, 2005; Berry et al., 2007), whilst positive biases associated with vegetation produce much lower levels of accuracy within forested areas (Hofton et al., 2006).

Accuracy assessment confirmed that the SRTM dataset was characterised by a substantial positive bias within forested regions of the Beni floodplain. This

occurs as the SRTM C-band phase centre is scattered by physical elements of vegetation canopies, and thus the elevation reported corresponds to a vertical location between the ground and the top of the canopy (Carabajal and Thompson, 2006). The penetration of the SRTM C-band phase centre into Beni floodplain forest canopies was quantified through comparison of SRTM derived forest height with field measured canopy height data collected at 35 locations within the study area. When analysed at the level of individual sites, the relationship between field measured and SRTM derived canopy height was characterised by a substantial level of noise. However, grouping of canopy height survey locations into stands and averaging according to geographical location and forest characteristics substantially reduced noise in the relationship between SRTM derived and field measured canopy height. Based upon the stand aggregated data, on average the SRTM penetrated 7.4 m into the canopy of Beni floodplain forests, equivalent to approximately 35% of the distance from the top of the canopy to the ground elevation. Whilst penetration magnitude varied between 32 % and 44% for the different stands, an average figure of 35% is considered sufficient to describe SRTM C-band phase centre penetration within Beni floodplain forests. Furthermore, results suggest that the relationship between field measured canopy height and SRTM derived canopy height can be accounted for by a linear model. The magnitude of canopy penetration calculated for Beni floodplain forests is within the range documented for similar types of forest (Bourgine and Baghdadi, 2005; Carabajal and Harding, 2006), whilst Hofton et al., (2006) also found that SRTM C-band phase centre canopy penetration was adequately described by a linear model.

Chapter Five

Beni floodplain bare earth DEM generation

5. Beni floodplain bare earth DEM generation

5.1 Introduction

Elevation and relief are fundamentally important drivers in a wide variety of environmental processes, hence a digital representation of topography is required within a wide breadth of scientific and commercial applications. A grid Digital Elevation Model (DEM) is defined as the digital cartographic representation of the Earth's surface at regularly spaced x and y intervals, using z elevation values referenced to a common vertical datum (USGS, 2005). Unless specifically referred to as a Digital Surface Model (DSM), a DEM must be comprised solely of bare earth elevations and should not contain artefacts related to the presence of surface features such as vegetation (Aguilar et al., 2005). Examples of the use of DEMs can be found within the modelling of environmental phenomena such as floodplain inundation (Bates and de Roo, 2000), landslides (Dietrich et al., 1995) and tectonics (Liu et al., 1998), whilst also being applied within natural resources management, transport planning, and creation of orthoimages (Aguilar et al., 2005).

Despite the clear importance of DEMs and the topographical information which they provide, a significant disparity exists in the availability and quality of such datasets across the globe (Bourgine and Baghdadi, 2005). In 'data rich' regions, such as the UK and North America, rapid advances in LiDAR remote sensing technology have facilitated the production of bare earth DEMs with a high spatial resolution and vertical accuracy (Bates, 2004). In England and Wales, DEMs with a spatial resolution of 2 m or less and a vertical accuracy of 15 cm are available for 68% of the land surface (Environment Agency, 2013). LiDAR surveys of a similar quality are readily available for many regions of the USA, whilst the National Elevation Dataset (NED) offers a seamless bare earth DEM characterised by a spatial resolution of 10 m for the entire area of the conterminous United States (USGS, 2013).

In general, tropical regions can be considered 'data poor' in comparison to the UK and North America, and a clear dearth of high quality topographical information exists within these regions. Acquiring topographical data within tropical regions is often difficult for logistical reasons; persistent cloud cover often precludes the use of optical remote sensing techniques (Hall et al., 2011),

whilst airborne LiDAR surveys are seldom feasible due to financial constraints combined with the challenges associated with large and often remote study areas (Baugh et al., 2013). Therefore Synthetic Aperture Radar (SAR) currently represents the only practical and consistent method by which DEMs can be created within tropical regions (Bourgine and Baghdadi, 2005). Indeed the Shuttle Radar Topography Mission (SRTM), which collected a global topographical dataset which was released at a 90 m spatial resolution using InSAR in February 2000, commonly represents the best source of topographical data within tropical study areas (Farr, 2000).

Although SAR is generally associated with a lower level of vertical accuracy than LiDAR systems, this remote sensing platform is nevertheless able to provide an accurate representation of topography within bare ground areas (Berry et al., 2007). However the accuracy of SAR derived DEMs decreases dramatically within forested regions as radar waves characterised by short wavelengths are unable to fully penetrate vegetation canopies, precluding measurement of the ground surface (Toutin, 2000). Given that many tropical study areas are characterised by extensive forest cover large vertical biases proliferate within SAR derived topographical datasets, which must be classified as DSMs (Breit et al., 2002). SRTM can be considered typical of SAR derived DSMs in terms of accuracy characteristics. Indeed for the Beni study area, results presented in chapter 4 demonstrated that SRTM vertical RMSE for bare ground areas is 1.6 m, whilst this falls substantially to 12.8 m for forested areas. Similar levels of accuracy have been obtained for study areas located across the globe (Hofton et al., 2006; Weydahl et al., 2007).

In regions characterised by extensive forest cover, further processing of SAR DSMs is necessary in order to obtain an accurate representation of the topography of the ground surface (Bourgine et al., 2004). Generation of bare earth DEMs from SAR datasets presents a challenging research problem, as successful correction of vegetation bias requires a continuous representation of canopy height. At present LiDAR surveys constitute the only means by which canopy height can be measured over large areas with continuous spatial coverage (Liu, 2008). LiDAR pulses are characterised by short wavelengths and thus unlike longer wavelength SAR, are able to fully penetrate dense vegetation canopies. In forested areas returned waveforms contain multiple Gaussian

peaks, with the first peak corresponding to the canopy top and the final peak indicating the ground elevation. Intuitively, canopy height can be calculated through subtraction of the first and last returns of the laser waveform (Raber et al., 2002).

Where available, LiDAR surveys have been successfully integrated with SAR datasets in order to quantify biases associated with vegetation and produce bare earth DEMs. For a study area within French Guiana, Bourgine et al., (2004) merged a radargrammetric RADARSAT DSM with highly accurate (vertical error ~2 m) low spatial resolution laser height data. Integration of laser data facilitated generation of a bare earth DEM, which improved the vertical accuracy of the RADARSAT SAR dataset from 25 m to 11 m (Bourgine et al., 2004). In the study area located in French Guiana Bourgine and Baghdadi (2005) merged the SRTM dataset with the same laser survey, producing a bare earth DEM characterised by greater levels of accuracy than those attained with the RADARSAT DEM. Although the aforementioned studies demonstrate the potential for correction of vegetation related biases within topographic datasets, it is important to recognise that highly accurate laser data is not widely available in most tropical regions.

For tropical study areas provision of canopy height information is usually limited to point measurements from field surveys or spaceborne LiDAR platforms such as ICESat GLAS (Abshire et al., 2005). Without the application of some form of extrapolation, point measurements of canopy height do not readily facilitate correction of vegetation effects in SAR derived elevation datasets such as SRTM. Given the level of data provision which characterises many tropical study areas, the simplest approach to generate a bare earth DEM is presented through creation of a zonal average canopy height map which can be subtracted from the SAR DSM (Yamazaki et al., 2012). A zonal map is created through aggregation of point canopy height measurements for different types of forest and extrapolating these average heights in a uniform manner based upon a land cover classification. Wilson et al., (2007) used a zonal averaging approach in order to generate a bare earth DEM for a 30,000 km^2 area of the Central Amazon floodplain, for application within a flood inundation model. Topographic data was sourced from the SRTM DEM and vegetation artefacts were corrected based upon field measurements of canopy height, which were

extrapolated uniformly over the study area using a binary forest mask (Trigg et al., 2009). Although the study did not include a formal accuracy assessment of the bare earth DEM, validation of inundation predictions with respect to water surface elevation measurements derived from satellite altimetry suggested that the corrected floodplain elevation data were characterised by vertical errors of the order at least 4 m (Wilson et al., 2007).

The primary limitation associated with the use of a zonal average canopy height map to correct SAR derived elevation datasets is the assumption of spatially uniform canopy height within distinct forest classes (Baugh et al., 2013). For the SRTM dataset the bias associated with vegetation is dependent upon the height of the canopy, but is also influenced by other physical characteristics such as forest density and degree of canopy closure (Hofton et al., 2006). The zonal average approach to bare earth DEM generation is well suited to study areas which are characterised by homogeneous forest stands. Reliance upon spatially uniform canopy height is more problematic in tropical regions where forest structure is known to be highly heterogeneous, even within stands of the same class (Lu et al., 2003a). Intuitively, errors in bare earth elevation are propagated through under or over prediction of forest height in zonal average maps.

In theory, implementation of an approach to bare earth DEM generation which is able to account for spatial variations in canopy height is more appropriate for areas characterised by highly heterogeneous forest cover. Numerous studies have sought to model spatial variations of canopy height using ancillary variables offering a complete horizontal coverage, in order to extrapolate low density point estimations of canopy height provided by spaceborne LiDAR surveys (Lefsky, 2005). Lefsky et al., (2010) produced a global canopy height map with a spatial resolution of 500 m through integration of GLAS canopy height measurements with MODIS multispectral data. MODIS reflectance images were segmented into patches, and the height of each patch was calculated based upon regression equations developed for each continent. Moderate results were obtained, with patch height predictions being associated with an RMSE of 5.9 m with respect to observed data. Simard et al., (2011) used an alternative approach in order to produce an improved at 1 km resolution canopy height map with wall to wall global coverage. The authors combined GLAS RH100 waveforms and globally available climate data sourced

from the Tropical Rainfall Measuring Mission (TRMM), elevation data from the SRTM and vegetation cover information from the MODIS MOD44B product in a regression tree model. Validation of the canopy height map with respect to in situ measurements at 66 FLUXNET sites yielded an RMSE of 4.4 m.

The global canopy height maps created by Lefsky et al., (2010) and Simard et al., (2011) demonstrate that it is possible to integrate low density point measurements of canopy height with ancillary remote sensing variables in order to predict spatial variations in canopy height over broad scales. However at present this methodology has not been translated to operate at finer scales commensurate with SAR derived topographic datasets such as SRTM. Nevertheless Baugh et al., (2013) utilised the canopy height map of Simard et al., (2011) in order to correct vegetation biases within the SRTM dataset and produce bare earth DEMs for a section of the Central Amazon floodplain in Brazil. As the canopy height map corresponded to the height of the top of the canopy (Simard et al., 2011), penetration of the SRTM C-band phase centre was accounted for by adjusting the canopy heights contained within map by increments of 10%. The bare earth DEMs were subsequently applied in order to provide topographical forcing within a hydrodynamic model, with DEM quality inferred through assessment of model predictions with respect to remote sensing observations of inundation extent, water level and floodplain water storage volume. Results suggested that the best bare earth DEM was produced through substracting 50-60 % of vegetation height from the SRTM. Indeed when applied within the hydrodynamic model predictions of high water inundation extent improved from an RMSE of 0.52 using the SRTM dataset to 0.07 using the corrected DEM, whilst increased performance was observed for the prediction of low water inundation and seasonal water levels.

As a result of the scarcity of LiDAR survey data and difficulties posed by the accurate prediction of canopy height, very few attempts have been made to derive bare earth DEMs from SAR DSMs (Baugh et al., 2013). In the Amazon basin, the resulting dearth of bare earth topographical information has limited the scope of hydrological and hydraulic modelling studies. To date there have been only a handful of attempts to model Amazonian river hydraulics using a two dimensional distributed representation of floodplain topography (Wilson et al., 2007; Baugh et al., 2013). Hence a situation has proliferated in which the

dynamics of floodplain inundation and hydrology of the Amazon basin remain poorly quantified, despite the clear significance of this system in the global hydrological cycle.

Overall, it is clear that the current demand for topographical information cannot be met by LiDAR DEMs in all but the most 'data rich' regions of the globe. In many 'data poor' regions where continuous LiDAR surveys are not feasible, topographical information is provided by alternative remote sensing platforms such as the InSAR derived global scale SRTM dataset (Farr, 2000), which must be corrected in order to generate a true bare earth DEM (Aguilar et al., 2005). In lieu of LiDAR survey data, only a handful of past studies have attempted to produce bare earth DEMs from the SRTM dataset (Wilson et al., 2007; Yamazaki et al., 2012; Baugh et al., 2013), although in these studies DEM accuracy was not directly assessed. Rather DEM quality was inferred based upon the accuracy of predictions of inundation when applied within a hydraulic flood inundation model. It is clear that further work is required in order to investigate the efficacy of methods used to generate bare earth DEMs from SRTM in past studies (Wilson et al., 2007; Baugh et al., 2013), and to explore alternative methods for the derivation of bare earth topographical information for application within hydraulic modelling.

The Beni floodplain study area can be considered typical of the Amazon basin in terms of data provision, indeed the global SRTM dataset constitutes the best available source of topographic data for this region. Given that the Beni floodplain is characterised by extensive forest cover the SRTM does not provide a representation of bare earth topography, which is required in order to facilitate flood inundation modelling later in this study. Therefore this chapter presents one of the first attempts to generate a bare earth DEM for a floodplain in the Amazon basin, using datasets which are typically available for tropical study areas. Here, DEMs will be generated through correction of SRTM based upon the methodologies applied within previous studies (Wilson et al., 2007; Baugh et al., 2013), whilst a new approach is developed which utilises the accuracy of the SRTM elevation within bare earth areas and the sensitivity of SRTM to vertical vegetation structure. Bare earth DEM accuracy will be assessed directly with respect to a set of high quality Ground Control Points (GCPs) collected through a differential GPS survey conducted within the study area.

5.2 Research aims

The overall aim of this chapter is to generate and validate a collection of bare earth DEMs for the Beni floodplain through correction of vegetation biases in the SRTM dataset. This aim will be accomplished through completion of four specific objectives.

1. To use field and remotely sensed datasets in order to derive maps of canopy height for the Beni floodplain study area
2. To generate bare earth DEMs of the Beni floodplain through application of canopy height maps to correct vegetation effects in the SRTM dataset
3. To quantitatively assess the vertical accuracy of the bare earth DEMs through comparison to GCPs obtained through a differential GPS survey
4. To compare and qualitatively assess the characteristics of the different bare earth DEMs in order to elucidate which methodology produces the best representation of floodplain topography

5.3 Data sources

5.3.1 SRTM dataset

For this study the 'version 2' SRTM dataset at 3 arc second (90 m) resolution was obtained through the USGS seamless service (http://seamless.usgs.gov). The version 2 dataset was used here as these data were not subject to void filling algorithms, like SRTM versions 3 and 4 (Reuter et al., 2007). Within these later versions of the SRTM dataset voids were filled by elevation data from auxillary DEMs, which were considered potentially unreliable for the Beni floodplain. The spatial extent of voids was minimal within the SRTM dataset for the study area, thus voids were filled manually here using simple interpolation techniques. The data were acquired as 1^{o} x 1^{o} tiles which were mosaiced using ArcGIS in order to construct a continuous representation of topography for the Beni floodplain study area. The SRTM dataset was subject to minimal processing in order to retain original elevation values, however a relatively small number of voids which were located in areas of water were filled using simple interpolation techniques. In addition, the SRTM dataset was smoothed using a 3 x 3 pixel window in order to reduce the influence of relative errors associated with phase noise (Kellndorfer et al., 2004). Validation of the SRTM in chapter 3 found that in open areas the vertical accuracy is characterised by an RMSE of

1.6 m and 2.7 m linear error at the 90% confidence interval (LE90), far exceeding the pre mission accuracy requirements (Bamler, 1999). In forested areas accuracy declines substantially to LE90 21.1 m due to the presence of a systematic positive bias in the SRTM, which arises as a result of interaction of the SRTM C-band phase centre with physical vegetation elements.

5.3.2 ICESat GLAS vegetation height measurements

The Geoscience Laser Altimeter System (GLAS) instrument was carried aboard the Ice, Cloud and land Elevation (ICESat) satellite which launched on 12th

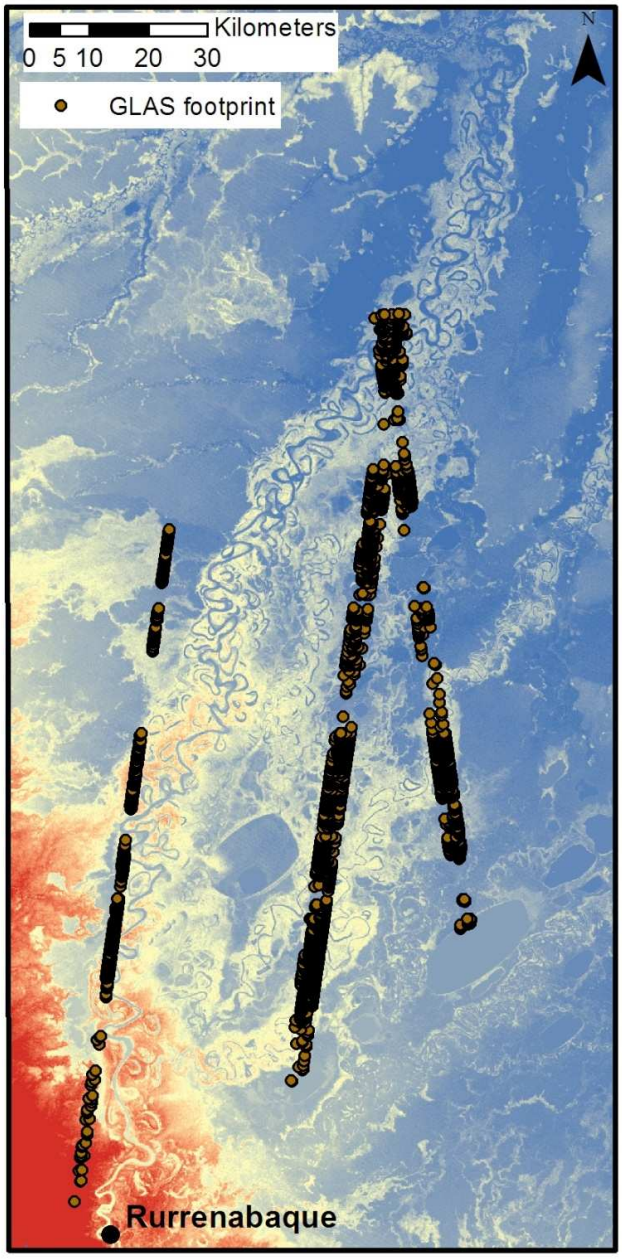

Figure 5.1. Location of GLAS footprints (Saatchi et al., 2011) in the Beni floodplain study area overlain upon the SRTM elevation dataset.

January 2003 (Zwally et al., 2002). GLAS comprised three lasers the first of which (L1) failed on day 38 of the mission, however the remaining lasers (L2 and L3) remained operational until May-June 2006 (Schutz et al., 2005). GLAS lasers operated at a wavelength of 1064 nm and illuminated an ellipsoidal ground footprint possessing a diameter of approximately 65 m. Footprints were located along linear tracks with a spacing of 170 m (Sun et al., 2008). The GLAS sensors were associated with a range precision of less than 2.5 cm, whilst horizontal geolocation error was approximately 5.8 m (Abshire et al., 2005).

Within this study a processed version of the GLAS product was utilised, supplied by NASA Jet Propulsion Laboratory (JPL), in which GLA01 waveforms had been converted to a weighted estimate of forest height. During processing of the dataset by Saatchi et al., (2011), waveforms were filtered in order to retain only those which could be unambiguously identified as forest. The waveforms were analysed and Gaussian peaks identified in order to yield an estimate of Loreys height, a basally weighted measure of forest height, for each GLAS footprint (Magnussen and Boudewyn, 1998). Data were received as tab delimited .txt files containing x,y coordinates and the Loreys height value. The data were subsequently checked for consistency and anomalous canopy height estimates were removed.

5.3.3 Global canopy height map

A number of recent studies have utilised the spaceborne LiDAR waveform dataset collected by GLAS between 2003-2009, in order to construct global maps of forest canopy height (Lefsky et al., 2005; Lefsky et al., 2010; Simard et al., 2011). Global canopy height maps are created through correlation of discrete LiDAR footprints with relevant spatially continuous ancillary datasets- which are then used to predict canopy heights in areas where footprints are not present. Simard et al., (2011) present the most recent and accurate attempt to model global canopy height at a spatial resolution of 1 km, utilising forest type, tree cover, elevation and climatological ancillary variables. Validation of the canopy height map with respect to 66 FLUXNET sites produced an RMSE of 4.4 m (r^2=0.5), superseding the accuracy of Lefsky et al., (2010) which achieved an RMSE of 5.9m (r^2=0.01). The canopy height map was downloaded from NASA JPL at http://lidarradar.jpl.nasa.gov/.

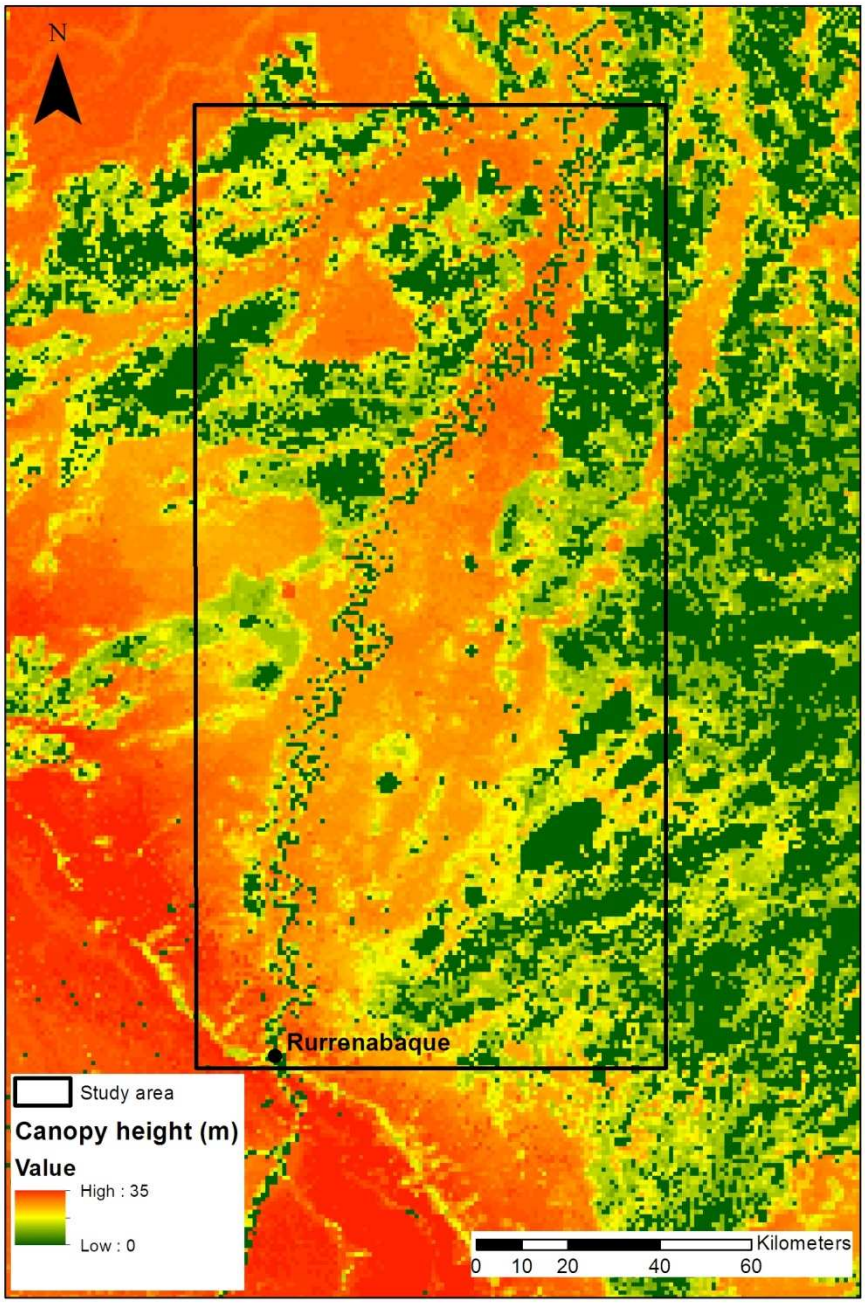

Figure 5.2. Global canopy height map (1 km resolution) subset to the Beni floodplain study area (Simard et al., 2011)

5.3.4 Beni canopy height survey data

Full details of the Beni canopy height survey data and methodology can be found in 4.3.2. Measurements from the 35 survey plots were combined in order to produce an average canopy height for mature forests upon the Beni floodplain. As the canopy height survey data detailed in 4.3.2 were collected from mature forests, these data were supplemented by a further 3 canopy height surveys which were undertaken using an identical methodology in both early and late successional forest stands. In a similar manner to mature forests,

the canopy height measurements from the supplementary survey were combined in order to generate an average canopy height for both the early and late successional forest classes.

5.3.5 Beni floodplain elevation survey

Ground control points were collected across the Beni floodplain study area using a differential GPS. Of the total 105 points, 48 were located in forested areas, 34 represented savanna or pasture land cover, whilst the remaining 23 points were located within other land covers or at the forest savanna transition. Remote sensing observations suggest that land cover of the Beni floodplain comprises approximately 48% forest, 49% savanna or other open areas and 3% water. Therefore forests are over represented in proportional terms, whilst savannas are underrepresented. Further details of the Beni floodplain elevation survey are included in 4.3.3.

5.3.6 Beni floodplain land cover map

The Beni land cover map was derived from Landsat TM imagery in chapter 3 using a combined Linear Spectral Unmixing- Decision Tree classification methodology. The map delineates a total of 7 classes; 3 forest classes (SS1, SS2 and mature) and four non forest classes (pasture, savanna, grasslands and water) at a resolution of 30 m. Validation of the land cover map yielded an overall accuracy in excess of 90 %. Further details on the generation of the floodplain land cover classification can be found in chapter 3.

5.4 Methodology

5.4.1 Preparation of input datasets

In order to facilitate production of bare earth DEMs all requisite datasets were resampled into grids characterised by a common map projection, dimensions and spatial resolution. First the floodplain land cover classification produced in chapter three was resampled to 90 m spatial resolution using ENVI. In order to retain subpixel class information at the new resolution, the original land cover map was separated into a series of seven class images at the original 30 m resolution. These class images were resampled using the pixel aggregate method, creating a new grid for each class at 90 m spatial resolution in which the value of each new 90 m pixel corresponded to the percentage of its area

covered by that particular land cover class within the original 30 m resolution image. These land cover class grids were then subset to the same areal extent as the SRTM dataset and exported to .asc files, the common input format used for input of data into the DEM generation program.

5.4.2 Bare earth DEM generation methodologies

Bare earth DEMs were generated using a program written in C programming language using the Dev C++ integrated development environment and compiler. There was no established methodology relating to correction of vegetation effects in the SRTM in the absence of continuous LiDAR data. Therefore four approaches were devised and implemented here in order to investigate the best method by which to generate bare earth DEMs. The principle difference between the adopted approaches was the specification of canopy height parameters, which propagated variations in the resultant canopy height maps and bare earth DEMs.

Each bare earth DEM generation routine contained four basic functions. In the first function all relevant grids, in the form of .asc files, were loaded into the program and the land cover class grids were used to generate a forest mask, which delineated SRTM pixels requiring correction. All SRTM pixels characterised by greater than 0 % forest cover were included in this mask. In the second function a maximum canopy height map was generated for the study area, based upon parameters which varied between each routine. In the third function the correction for SRTM bias was calculated according to equation 5.1, which generated a 'weighted canopy height' for each forested SRTM pixel.

$$CH_{tot} = (SS1_h \times SS1_p) + (SS2_h \times SS2_p) + (MF_h \times MF_p) \quad (5.1)$$

In this equation CH_{tot} represents the total weighted canopy height for a given forested SRTM pixel. For each forest class SS1, SS2 and Mature Forest (MF) the assigned canopy height $_h$, was multiplied by $_p$, which represented the areal proportion of the pixel covered by a given forest class. Hence this approach assumed that the total canopy height bias contained in the SRTM was a linear combination of its constituent forest classes. Values for $SS1_p$, $SS2_p$ and MF_p were taken from the aggregated class images and thus were invariant between

the different DEM generation routines. Values for $SS1_h$, $SS2_h$ and MF_h were taken from the canopy height maps generated within function two.

The fourth function contained an option whereby the weighted canopy height map could be scaled in order to account for penetration of the SRTM C-band phase centre through multiplication of canopy height by a factor of 0.65. This correction factor was calculated based upon the comparison of field measured and SRTM derived canopy height within chapter 4. This scaling factor was applied according to the specifications illustrated in table 5.1. The final canopy height map was then subtracted from the SRTM in order to produce a bare earth DEM. Intuitively, variations in the characteristics of the bare ground DEMs generated in the different correction routines can be attributed to the definition of maximum canopy height in function two. Further details relating to definition of maximum canopy height parameters in the different routines are elaborated in subsequent sections. In order to thoroughly test the four DEM generation methodologies a total of seven bare earth DEMs were produced, the names and characteristics of these DEMs are displayed in table 5.1.

5.4.2.1 Field derived zonal average canopy height

For the field derived zonal average canopy height routine, spatially uniform maximum canopy height parameters were defined within function two based upon field measurements of Beni floodplain forest stands. A single value for canopy height was assigned to each of the three forest classes; early successional stage, late successional stage and mature forest, based upon averaging of canopy height survey data. These values were subsequently applied in equation 5.1 in order to generate the weighted canopy height map. This canopy height map was subtracted from the SRTM in order to create the bare earth DEM, which was named FAV DEM. Given that canopy height surveys were designed to measure the height of the canopy top FAVP DEM was also generated through application of the correction factor to the canopy height map in function four, in order to account for SRTM penetration. Intuitively as canopy height is assumed to be constant across the floodplain for each forest class, spatial variation in CH_{tot} occurs across the floodplain as a result of variations in the proportion of different forest classes within each pixel.

5.4.2.2 GLAS derived zonal average canopy height

The GLAS zonal average canopy height DEM generation methodology was very similar to the field derived zonal canopy height routine, although canopy height values were obtained from the GLAS dataset. GLAS canopy height measurements were grouped according to forest class using ArcGIS and summary statistics calculated using Microsoft Excel. Four bare earth DEMs were generated using GLAS derived canopy height parameters; GLMED DEM and GLMEDP DEm used the median GLAS canopy height, with the latter being corrected for SRTM penetration. The median GLAS canopy height was selected in order to best represent the average forest height in each class.

5.4.2.3 Spatially variable canopy heights derived using a first order estimated DEM

In the absence of continuous LiDAR surveys, the extrapolation of discrete GLAS canopy height measurements in order to construct a spatially variable map of canopy height for forest stands across the floodplain theoretically presented the best approach to correction of vertical biases present within the SRTM dataset. Through correlation of GLAS canopy height measurements with remote sensing variables sensitive to vertical vegetation structure and offering continuous spatial coverage, it was thought that the basic methodology utilised by Lefsky et al., (2010) and Simard et al., (2011) in order to predict global canopy height could be applied at the local scale of the Beni floodplain. In order to investigate the efficacy of this approach regression models were constructed between GLAS canopy height and a range of remote sensing variables, for example SRTM standard deviation, Landsat TM reflectance and textural measures, TRMM rainfall and other datasets. However no statistically significant relationships were derived, indicating the need for adoption of an alternative approach. Accordingly, the approach to bare earth DEM generation detailed here was devised in order to utilise the high levels of accuracy offered by the SRTM dataset in unforested areas, and its sensitivity to forest structure. This routine was predicated upon the generation of a spatially variable maximum canopy height map through subtraction of a first order estimated bare earth floodplain DEM from the SRTM dataset. The first order estimated bare earth DEM was produced using ArcGIS. Initially the floodplain land cover classification was utilised in order to extract a collection of bare earth elevation

points from the SRTM, which were checked for consistency and supplemented through manual addition of points based upon observations of Landsat TM imagery. Further bare earth elevations acquired through a field survey of bank top elevations were added to the point dataset, substantially increasing the density of bare earth elevation points located in close proximity to the Beni channel. The bare earth DEM was generated through Inverse Distance Weighted interpolation of the bare earth elevation point dataset, providing an approximate representation of floodplain topography in forested areas.

Spatially variable maps of maximum canopy height were produced for each forest class using another C program. In this program the first order interpolated bare earth DEM was subtracted from the SRTM dataset, producing a map of estimated canopy height for all forested pixels across the floodplain. In order to effectively capture and represent broad scale spatial variations of canopy height across the study area, a new aggregated canopy height map was produced for each forest class at a resolution of 1 km. Aggregated maps were produced through averaging of canopy height values for each class within 1 km blocks. In order to exclude partially forested pixels containing unrepresentative forest heights from the analysis, canopy height values were taken exclusively from pixels characterised by 100 % of the relevant forest class.

The main DEM generation program was modified in order to facilitate inclusion of the canopy height maps generated here. Aggregated canopy height maps for each forest class were loaded into the main DEM generation program in function one, eliminating the need for generation of maximum canopy height map in function two. As canopy height was derived from the SRTM dataset, scaling implemented in function four was not required. The DEM generated using this methodology was named INT DEM.

5.4.2.4 Spatially variable vegetation heights based upon global canopy height datasets

In this approach the maximum canopy height map was supplied in the form of a global 1 km resolution canopy height map (Simard et al., 2011). The map was imported into ArcGIS and resampled in order to match the resolution of the SRTM using a nearest neighbour approach. Subsequently the resampled canopy height map was subset to the extent of the Beni floodplain study area

and exported from ArcGIS as a .asc file. Accordingly, the DEM generation program was modified in order to reflect the use of the global canopy height map. Function one was adapted to load the canopy height grid in addition to the land cover grids, whilst function two was removed. In function three class grids were combined in order to provide an aggregate measure of percentage forest cover for each pixel, which was multiplied by the canopy height indicated by the global canopy height map. Two DEMs were produced using this approach; GCH DEM and GCHP DEM, with the latter including the correction for SRTM penetration. This was necessary as the heights included in the map of Simard et al., (2011) represent the height of the canopy top. In this routine, variations in canopy height across the floodplain occurred as a function of maximum canopy height and percentage forest cover, both of which were spatially variable.

Table 5.1. Bare earth DEM information. SV indicates spatially variable canopy height parameter. SRTM penetration correction refers to whether the canopy height values utilised within each approach are corrected in order to account for penetration of the SRTM, demonstrated within chapter 4 to constitute approximately 35 % of total canopy height.

DEM	Approach to SRTM correction	SRTM penetration correction	SS1 height (m)	SS2 height (m)	Mature height (m)
FAV	Field averaged zonal	No	9.75	16.02	20.46
FAVP	Field averaged zonal	Yes	6.34	10.41	13.30
GLMED	GLAS derived zonal	No	8.31	12.37	13.22
GLMEDP	GLAS derived zonal	Yes	5.40	8.04	8.59
GCH	Global canopy height	No	SV	SV	SV
GCHP	Global canopy height	Yes	SV	SV	SV
INT	First order estimated DEM	No	SV	SV	SV

5.4.3 Post processing of DEMs

In order to create ‘finished’ versions of the bare earth DEMs an additional C program was written which implemented a number of post processing procedures. First, DEMs were smoothed through calculation of the focal mean of a 3 x 3 pixel moving window, in order to reduce noise associated with the corrected elevation data. However, the function was modified in order to prevent the smoothing of important floodplain topographical features. Abandoned channels and dry cut offs located within the study area were manually digitised

and converted into a binary mask, which was used to exclude the features from the smoothing process.

Further, the bed elevation of water bodies such as the river channel and cut offs were burned into the DEM. Visual assessment suggested that the elevations of SRTM in areas of water corresponded approximately to the elevation of the water surface during the mission. Therefore in order to provide a first order approximation of the bed elevations of rivers and lakes, 7 m of elevation was removed from the DEMS in regions denoted by a mask which included all pixels characterised by a value exceeding 0.50 in the water class image. Further modifications were required in order to facilitate the application of these bare earth DEMs within the flood inundation model, these are detailed further in chapter 6.

5.4.4 Evaluation of bare earth DEMs

The corrected bare earth DEMs for the Beni floodplain were quantitatively assessed with respect to a set of 105 post processed DGPS points. Standard measures of accuracy were calculated including mean deviation, standard deviation, standard error and RMSE, whilst linear error at 90% confidence level was also computed in order to facilitate assessment of the DEMs with respect to accuracy specifications of the SRTM (Bamler, 1999). Quantitative analysis was supplemented by further qualitative analysis, which was undertaken in order to compare the characteristics of the bare earth DEMs generated through the different routines. In order to facilitate qualitative assessment elevation profiles were extracted from the DEMs and analysed visually in order to determine which routines generated the best representation of floodplain topography.

5.5 Results

5.5.1 Validation of bare earth DEMs with respect to the floodplain elevation survey

Tables 5.2 and 5.3 illustrate the summary accuracy statistics for the bare earth floodplain DEMs, calculated with respect to the DGPS elevations survey for the whole floodplain (n=105) and for forested areas (n=48) respectively. The DEM generation procedures corrected the elevation of the SRTM dataset exclusively within forested areas, therefore the influence of these corrections is most

marked in table 5.2. However table 5.3 was also included in order to illustrate the accuracy of the DEM for the floodplain as a whole. In these tables the mean represents the average deviation between DEM and DGPS elevation, providing an indication of the bias of the bare earth DEM with respect to the ground surface. A positive mean value indicates that the SRTM elevation is positively biased and over predicting elevation, whilst a negative mean indicates that elevation is under predicted. Standard deviation indicates the spread of the deviations, with a lower value indicating a greater consistency in the bare earth DEM. The root mean squared error (RMSE) provides an indicator of absolute accuracy of the DEM with respect to the ground surface, whilst linear error at the 90 % confidence interval (LE90) enables comparison of DEM accuracy with SRTM pre mission specifications (Farr, 2000). Histograms plotted in figures 5.3 to 5.13 visually illustrate the frequency distribution of deviations between the DEMs and DGPS survey elevations.

Table 5.2. Accuracy of bare earth DEMs for forested areas of the Beni floodplain

	FAV	FAVP	GLMED	GLMEDP	GCH	GCHP	INT	SRTM
Mean (m)	-2.0	1.3	0.9	3.1	-3.5	0.3	0.4	6.6
Std deviation (m)	4.7	4.4	4.1	4.8	5.0	3.9	3.5	7.3
Std error (m)	0.4	0.4	0.4	0.4	0.4	0.3	0.3	0.7
RMSE (m)	5.1	4.6	4.1	5.7	6.1	3.9	3.5	9.9
LE90 (m)	8.4	7.6	6.8	9.4	10.0	6.4	5.7	16.2

Table 5.3. Accuracy statistics for Beni floodplain bare earth DEMs including all land covers

	FAV	FAVP	GLMED	GLMEDP	GCH	GCHP	INT	SRTM
Mean (m)	-2.6	2.6	2.0	5.7	-5.4	0.9	0.6	11.7
Std deviation (m)	5.8	5.3	4.9	4.9	5.6	4.8	4.0	6.3
Std error (m)	0.8	0.7	0.7	0.7	0.8	0.7	0.5	0.9
RMSE (m)	6.3	5.9	5.2	7.5	7.7	4.9	4.0	13.3
LE90 (m)	10.4	9.7	8.6	12.4	12.7	8.1	6.5	21.9

For both of the DEMs generated through field averaged zonal methodology, absolute error was roughly halved in comparison to the SRTM. Absolute accuracy improved from 9.9 m for the SRTM to 5.1 m for FAV and 4.6 m for FAVP with respect to the complete floodplain elevation survey. In both table 5.2 and 5.3 FAVP possessed a marginally lower value for standard deviation than

FAV, indicating a greater level of consistency for this DEM. The most significant difference between the two DEMs generated through the field averaged zonal method is in the mean average deviation. For forested areas mean deviation is -2.6 m for FAV and 2.6 m for FAVP. Whilst both DEMs offer a significant improvement in comparison to the SRTM dataset (11.7 m), the results indicate that FAV is negatively biased with respect to true ground elevation, whilst FAVP is positively biased with respect to ground elevation. This difference is reflected in the accuracy statistics for the floodplain as a whole and in the histograms for these DEMS. In figure 5.4 the frequency distribution is negatively skewed, whilst for figure 5.5 the histogram is positively skewed. The histogram for both FAV and FAVP shows a significant improvement in comparison to the SRTM in figure 5.3, with the error distributions being clustered more closely around 0 m.

The four DEMs derived using GLAS derived zonal averages display a range of performance levels. GLMED can be considered the highest quality DEM of this group in terms of quantitative summary statistics in table 5.3. GLMED is associated with lowest value of RMSE at 4.1 m, whilst a mean deviation of 0.9 m is indicative of only a slight positive bias in DEM ground elevation. In comparison GLMEDP offers the lowest level of performance being characterised by an RMSE value of 5.7 m and a mean deviation of 3.1 m, indicative of a substantial positive bias. The performance of these DEMs is reflected in the histograms displayed in figures 5.8 and 5.9. The error distribution for GLMEDP exhibits a large degree of positive skew, in contrast for GLMED the histogram shows an irregular distribution with a large frequency of errors in the range of 0–4 m.

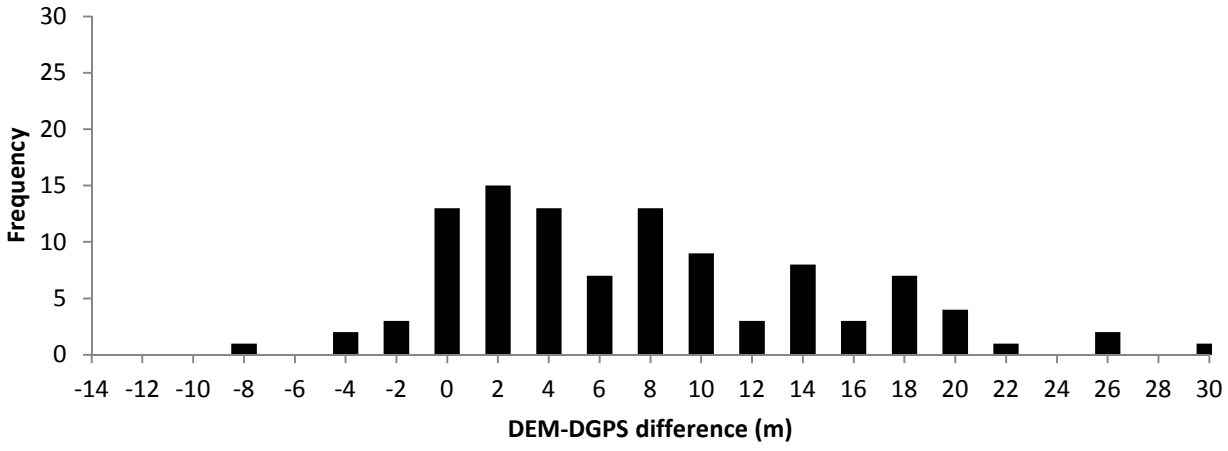

Figure 5.3. Histogram illustrating error distribution of the SRTM with respect to DGPS survey points.

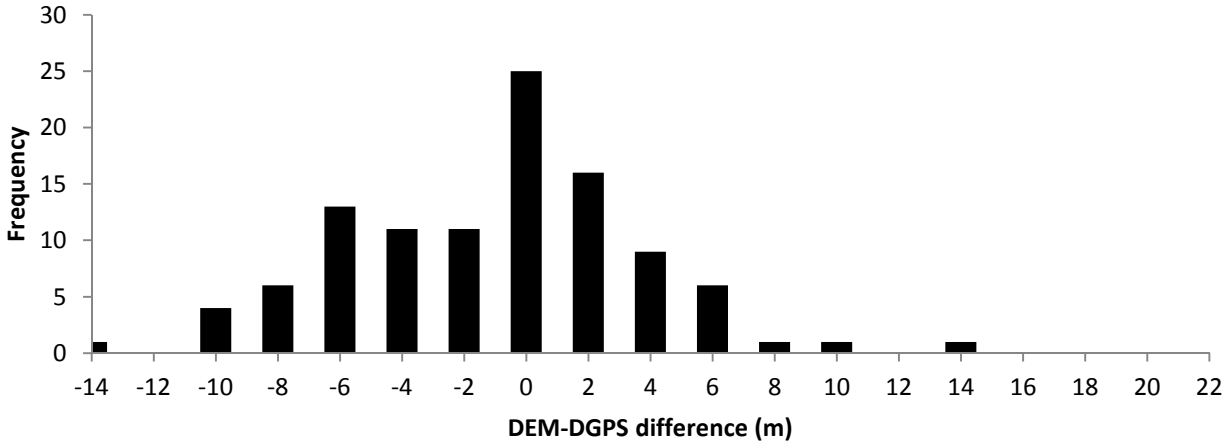

Figure 5.4. Histogram illustrating error distribution of the FAV DEM with respect to DGPS survey points.

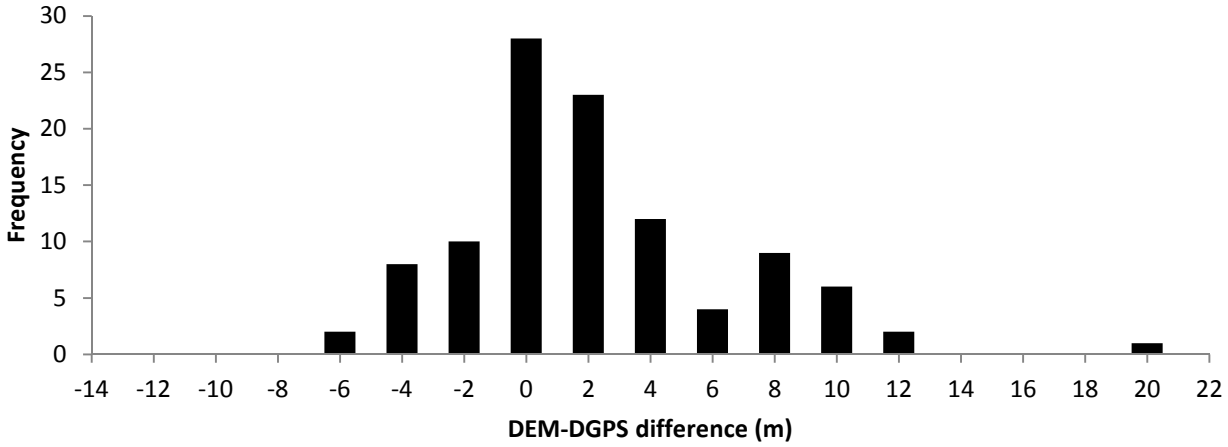

Figure 5.5. Histogram illustrating error distribution of the FAVP DEM with respect to DGPS survey points.

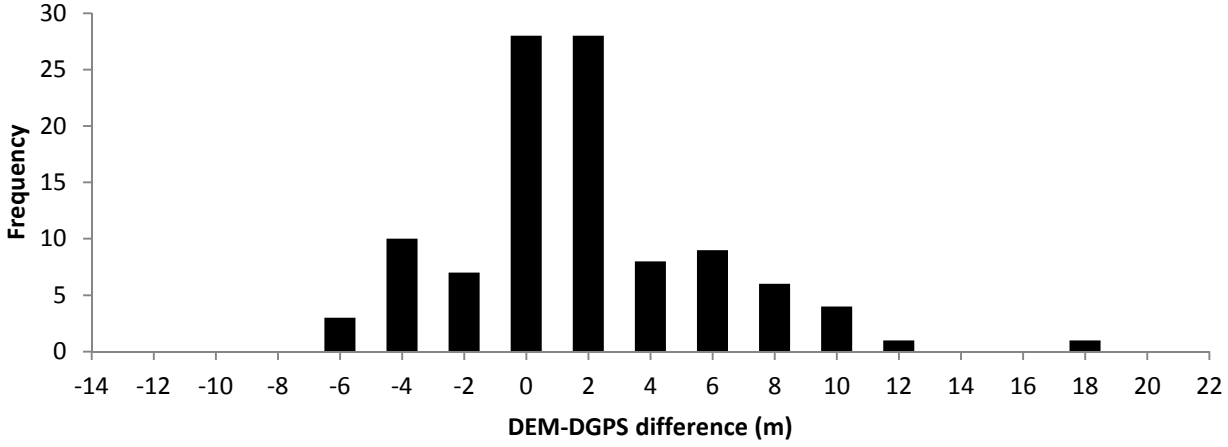

Figure 5.6. Histogram illustrating error distribution of the GLMED DEM with respect to DGPS survey points.

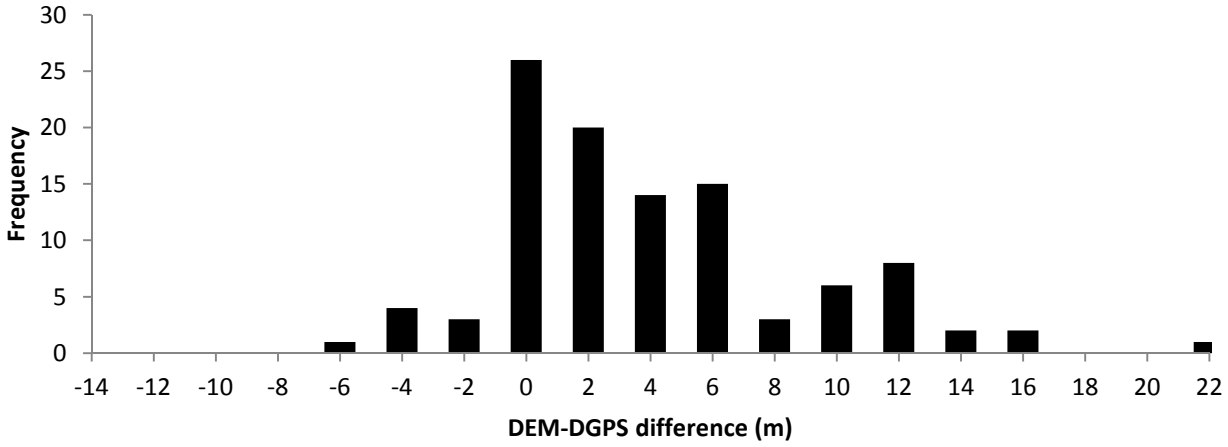

Figure 5.7. Histogram illustrating error distribution of the GLMEDP DEM with respect to DGPS survey points.

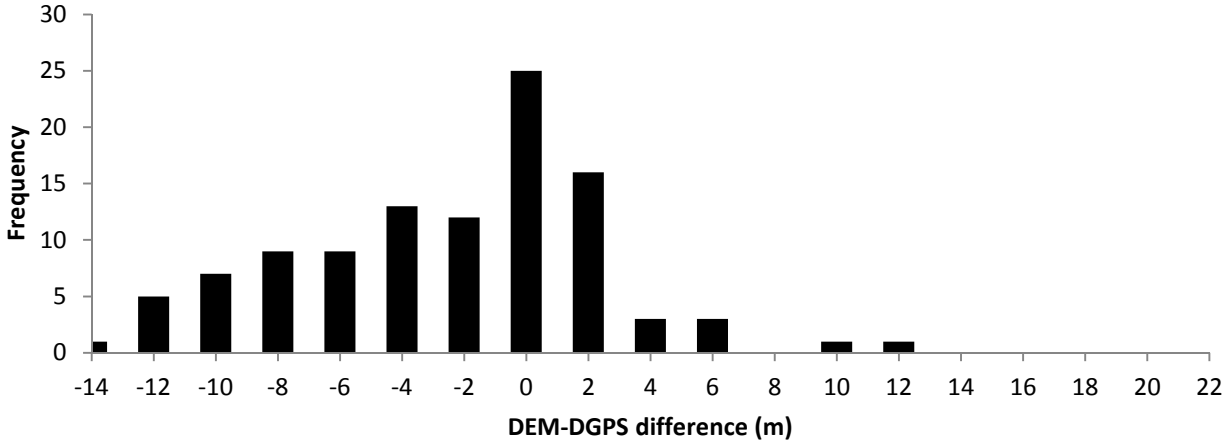

Figure 5.8. Histogram illustrating error distribution of the GCH DEM with respect to DGPS survey points.

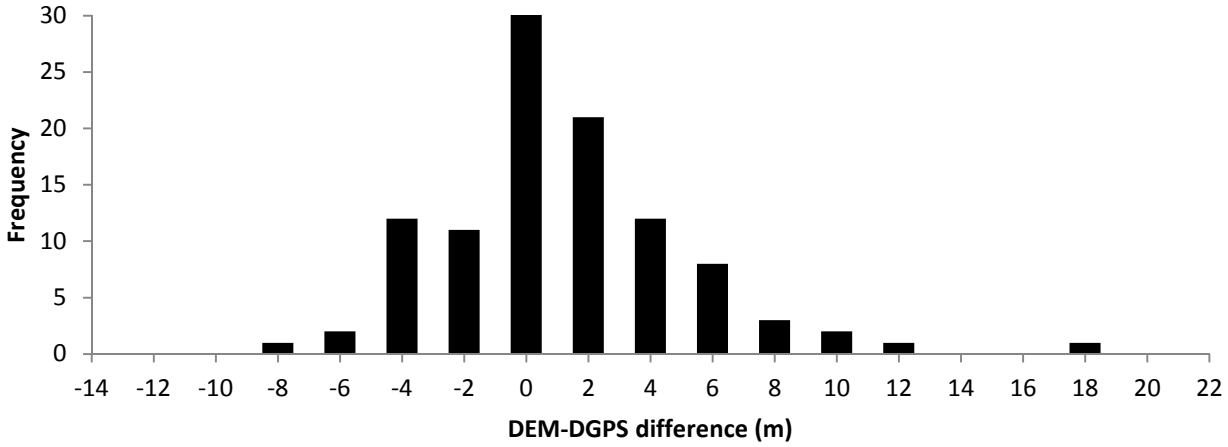

Figure 5.9. Histogram illustrating error distribution of the GCHP DEM with respect to DGPS survey points.

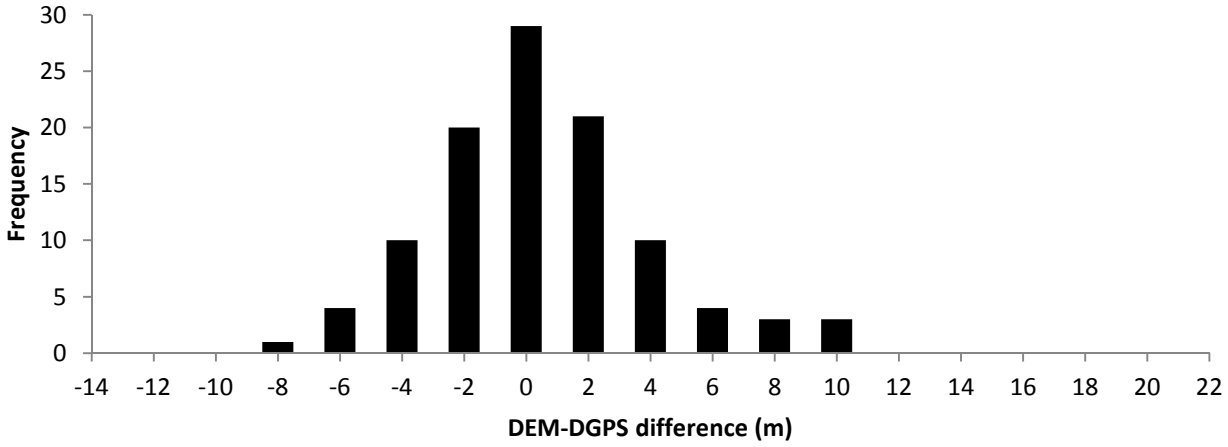

Figure 5.10. Histogram illustrating error distribution of the INT DEM with respect to DGPS survey points

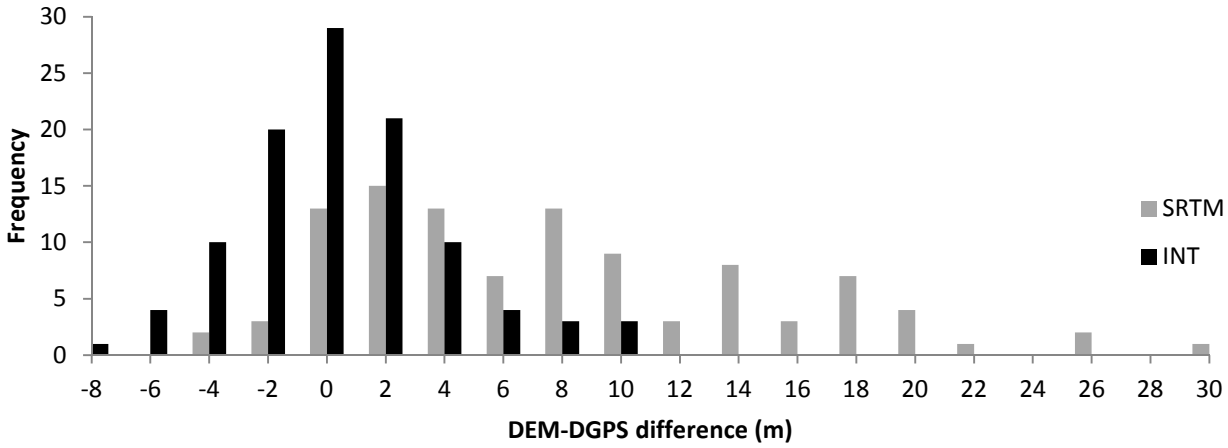

Figure 5.11. Histogram illustrating error distribution of the INT DEM with respect to DGPS survey points. The error distribution of the SRTM dataset is also included here in order to demonstrate the effect of the correction.

Significant differences are observed for the bare earth DEMs generated using the global canopy height map both in terms of summary statistics in tables 5.2 and 5.3 and histograms in figures 5.8 and 5.9. As indicated by RMSE for the floodplain as a whole, absolute accuracy of GCHP (3.9 m) substantially exceeds that of GCH (6.1 m). GCHP also exhibits a substantially lower level of spread in its error distribution, as indicated by the value of standard deviation of 3.9 m compared to 5.0 m for GCH. However perhaps the largest disparity in the performance of the GCH and GCHP is shown by the mean deviation of the DEMs. In forested areas the mean deviation of GCH is -5.4 m, indicating a large negative bias whilst for GCHP a value of 0.9 m indicates a slight positive bias. The difference in error distributions of the two DEMs is emphasised by their respective histograms. Whilst the 0-2 m bin is characterised by the highest frequency for both DEMs, figure 5.10 clearly illustrates the high level of negative

skew which characterises GCH. In contrast figure 5.9 shows that errors for GCHP are quasi normally distributed, whilst displaying a slight positive bias.

Overall, INT DEM, generated using spatially variable canopy height estimated from a first order bare earth DEM offered the highest levels of performance in quantitative validation. INT was characterised by an RMSE of 3.5 m with respect to the complete set of DGPS measurements, a great increase in absolute vertical accuracy in comparison to the SRTM (9.9 m). INT also exhibited the lowest standard deviation of any of the bare earth DEMs at 3.5 m, whilst the mean deviation in forested areas was 0.6 m indicating only a small positive bias. The histogram for INT illustrated in figure 5.10 and 5.11 shows that vertical errors in this DEM with respect to ground elevation are characterised by a normal distribution.

5.5.2 Qualitative comparison of the bare earth DEMs

Figure 5.12 presents an areal map of the standard deviation of the Beni floodplain bare earth DEMs. Standard deviation was computed for each pixel based upon elevation values from each of the seven DEMs generated here. This map was included in order to provide an indication of the spatial agreement between the alternative DEMs. Intuitively, a low value of standard deviation for a given pixel indicates a high level of agreement between elevation values for the different DEMs, whilst higher values of standard deviation indicates a larger range of elevation values and a lower level of agreement between the different DEMs. On a basic level the map illustrates that differences between the DEMs are minimal in unforested savanna and pasture areas. Intuitively deviations of a higher magnitude occur in areas characterised by forest cover where corrections were applied to the SRTM dataset. The majority of the forested area is characterised by a standard deviation of between 3 m and 7 m, indicating that the different approaches to SRTM correction produced significant differences in bare earth topography of the floodplain. Significantly, a spatial pattern emerges where standard deviation remains lower (3-5m) in a 5-10 km wide corridor which encompasses the Beni, whilst an increase in standard deviation (5m-7m) occurs in the extensive area of floodplain forest located to the east of the channel.

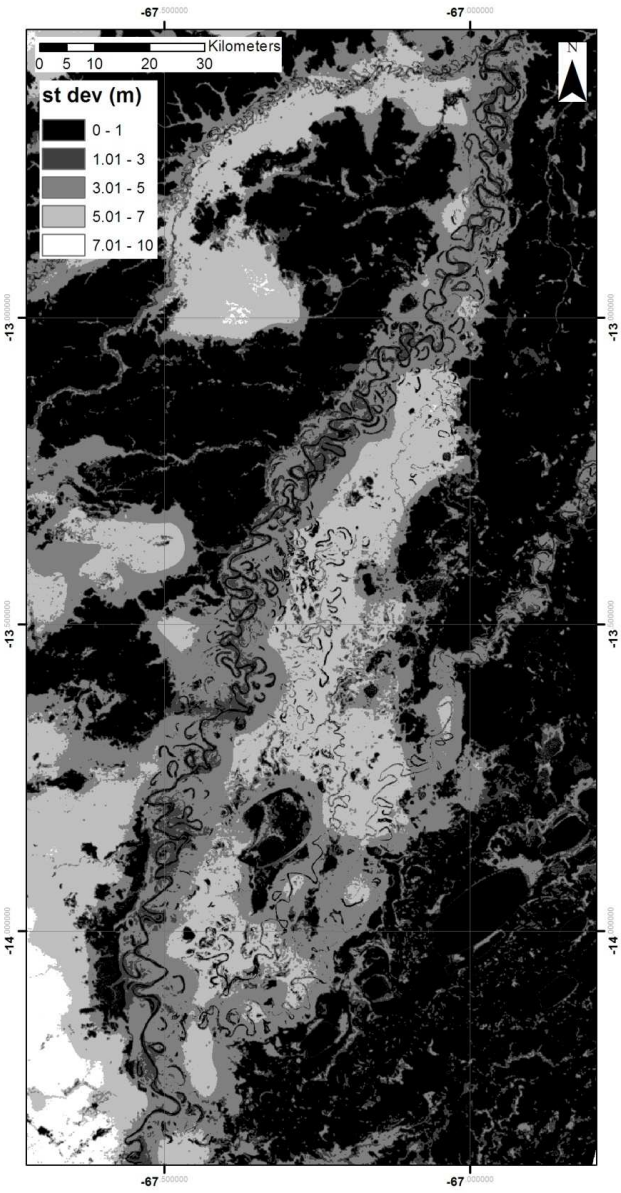

Figure 5.12. Map showing the standard deviation of the seven bare earth DEMs, higher values indicate larger deviations between the DEMs

Figures 5.13–5.19 comprise a final weighted canopy height map, bare earth DEM and elevation deviation image for each SRTM correction routine (table 5.1). A qualitative visual analysis of figure 5.13-5.19 will be undertaken here in order to broadly compare the bare earth DEMs and elucidate their main characteristics. In order to compute elevation deviation images, a composite DEM was produced in which the elevation value for each pixel represented the average elevation for the seven DEMs presented here. The elevation deviation image was subsequently produced for each DEM through subtraction of that DEM from the composite DEM. Hence a negative deviation indicates that the

elevation of a given DEM falls below the average of all DEMs, whilst the reverse is true for positive deviations.

For both of the field averaged zonal canopy height approaches (figure 5.13 and 5.14) canopy height shows a high level of spatial uniformity across the floodplain study area. Spatial variations in canopy height are primarily limited to areas of successional forest located in close proximity to the channel or at the edge of forest stands. Canopy height is consistently higher for the FAV DEM in comparison to the FAVP DEM, due to the linear scaling applied in order to account for SRTM canopy penetration. The FAV DEM is associated with negative deviations of a relatively high magnitude across the floodplain, indicating that bare earth elevations are substantially lower than the average for all DEMs. A visual analysis of the FAV DEM reveals the presence of topographical depressions in areas to the east of the channel and in the distal floodplain. These depressions are perhaps the most striking feature of the FAV DEM and are denoted by the localised areas of dark blue, which indicate that floodplain elevation is up to 10m lower than surrounding lighter blue areas. As a result of lower estimates of canopy height across the floodplain, FAVP DEM is characterised by relatively small positive deviations for the majority of forest stands in the study area. From visual analysis it is clear that topographical depressions, which were a widespread feature within the FAV DEM are much less prevalent in FAVP. Indeed the opposite situation arises in terms of the topographical features displayed within FAVP DEM in comparison to the FAV DEM. Accordingly, the FAVP DEM is characterised by the presence of substantial areas of markedly high elevation. These areas can be identified by white and red colours, particularly in close proximity to the Beni channel and floodplain channels to the east. This contrast in colours indicate that these raised areas are up to 10 m higher than the surrounding floodplain

For the GLAS based zonal approaches (figure 5.15 and 5.16) canopy height maps were characterised by a high level of spatial uniformity and were relatively similar to those observed for the field averaged approaches. The GLMED DEM was associated with a positive deviation of a relatively low magnitude for most of the floodplain forest stands. Like the FAVP DEM, bare earth elevations clear raised areas are evident in close proximity to the Beni channel. The GLMEDP canopy height map was characterised by the lowest estimates of forest height

of any of the approaches employed here, due to the application of the adjustment for SRTM penetration to the canopy height map for the GLMED DEM. This is reflected in the bare earth DEM, which features the presence of raised areas which are higher and occupy a larger area of the floodplain.

Figures 5.17 and 5.18 illustrate the results obtained through correction of the SRTM dataset using a global canopy height map. The canopy height map for the GCH DEM clearly features the largest estimates of forest height of any approach to DEM generation. This is reflected in the strong negative deviation observed for most of the forested area, indicating that bare earth elevations are significantly lower than the average for all DEMs. This is reflected in the bare earth GCH DEM, which is characterised by very low elevations for the entirety of the forested area of the floodplain. Spatial variations in canopy height occur over broad scales in the global canopy height map, hence local variations in forest height are relatively limited. The exception to this is found in close proximity to the main Beni channel, where canopy height is substantially lower than for the large area of floodplain forest to the east of the Beni. As a result, in the GCH DEM bare earth elevation appears substantially higher in the 5-10 km wide corridor adjacent to the Beni. Application of the scaling factor in order to account for SRTM penetration produces significantly lower estimates of forest height across the floodplain in the GCHP canopy height map. This is reflected in the bare earth GCHP DEM, in which negative deviations located within forested areas are much less marked in comparison to the GCH DEM. However raised areas located in close proximity to the channel are increasingly prevalent within GCHP DEM.

Figure 5.19 illustrates the canopy height map, bare earth DEM and deviation image for the SRTM correction routine based upon a first order estimated DEM. The canopy height map exhibits a much higher degree of spatial variability than alternative approaches. Forests which flank the main Beni channel and smaller floodplain channels are generally associated with the highest canopies, whilst lower canopies were generally observed for forests located further from water courses and in the distal floodplain. The deviation image most effectively illustrates the differences between the INT DEM and the other bare earth

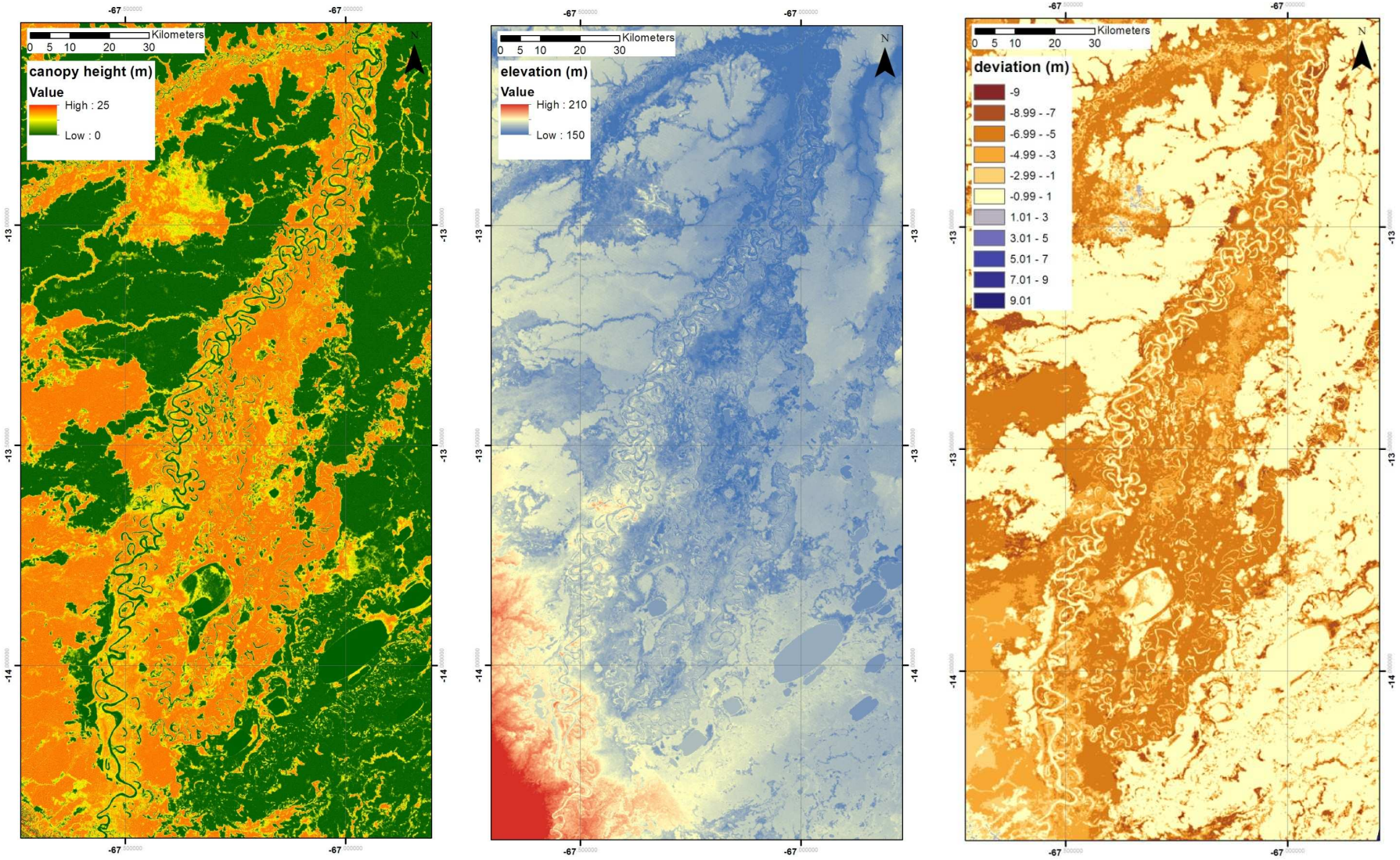

Figure 5.13. Maps showing broad characteristics of FAV DEM. Left- canopy height map. Middle- bare earth DEM. Right- elevation deviation image.

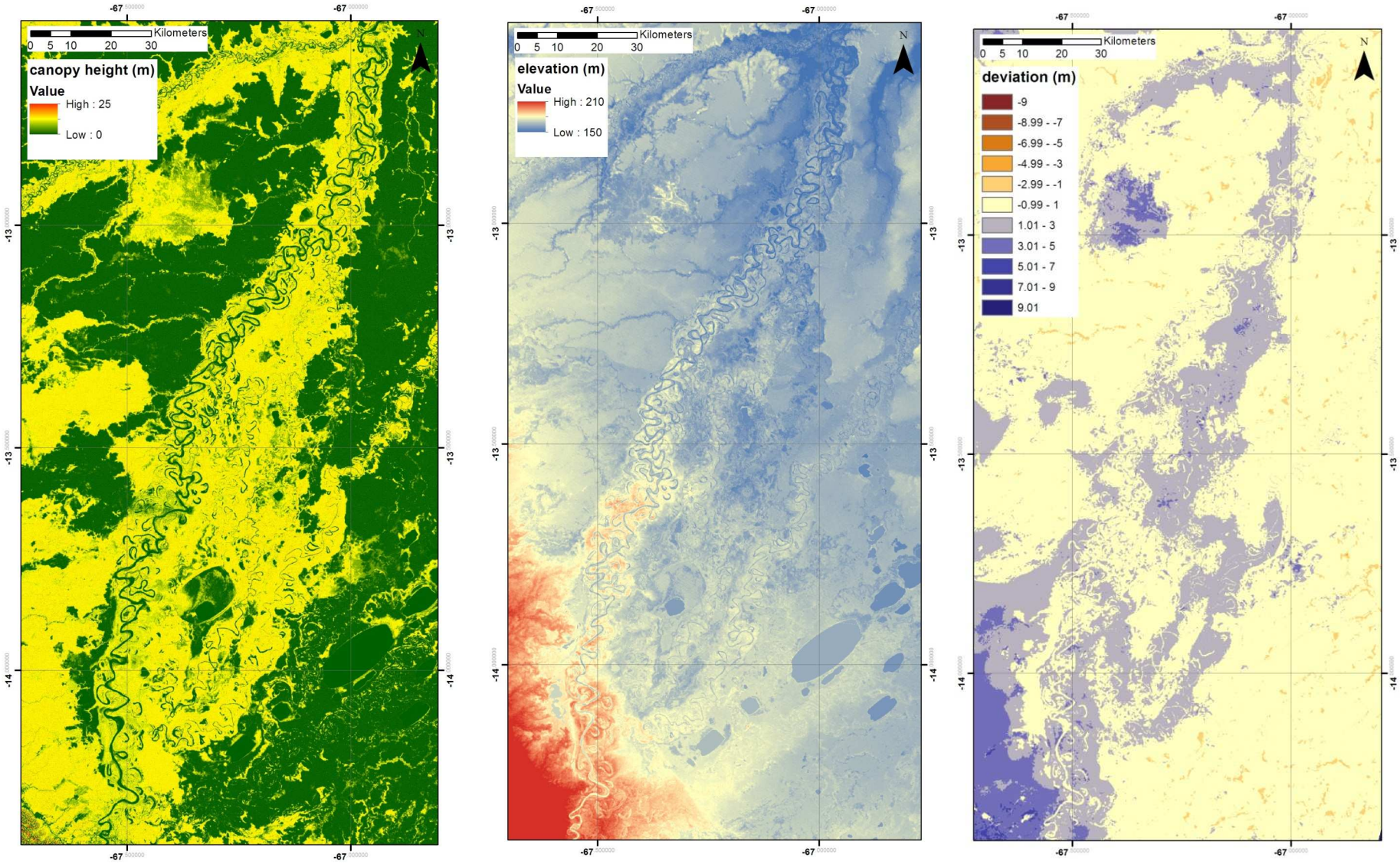

Figure 5.14. Maps showing broad characteristics of FAVP DEM. Left- canopy height map. Middle- bare earth DEM. Right- elevation deviation image.

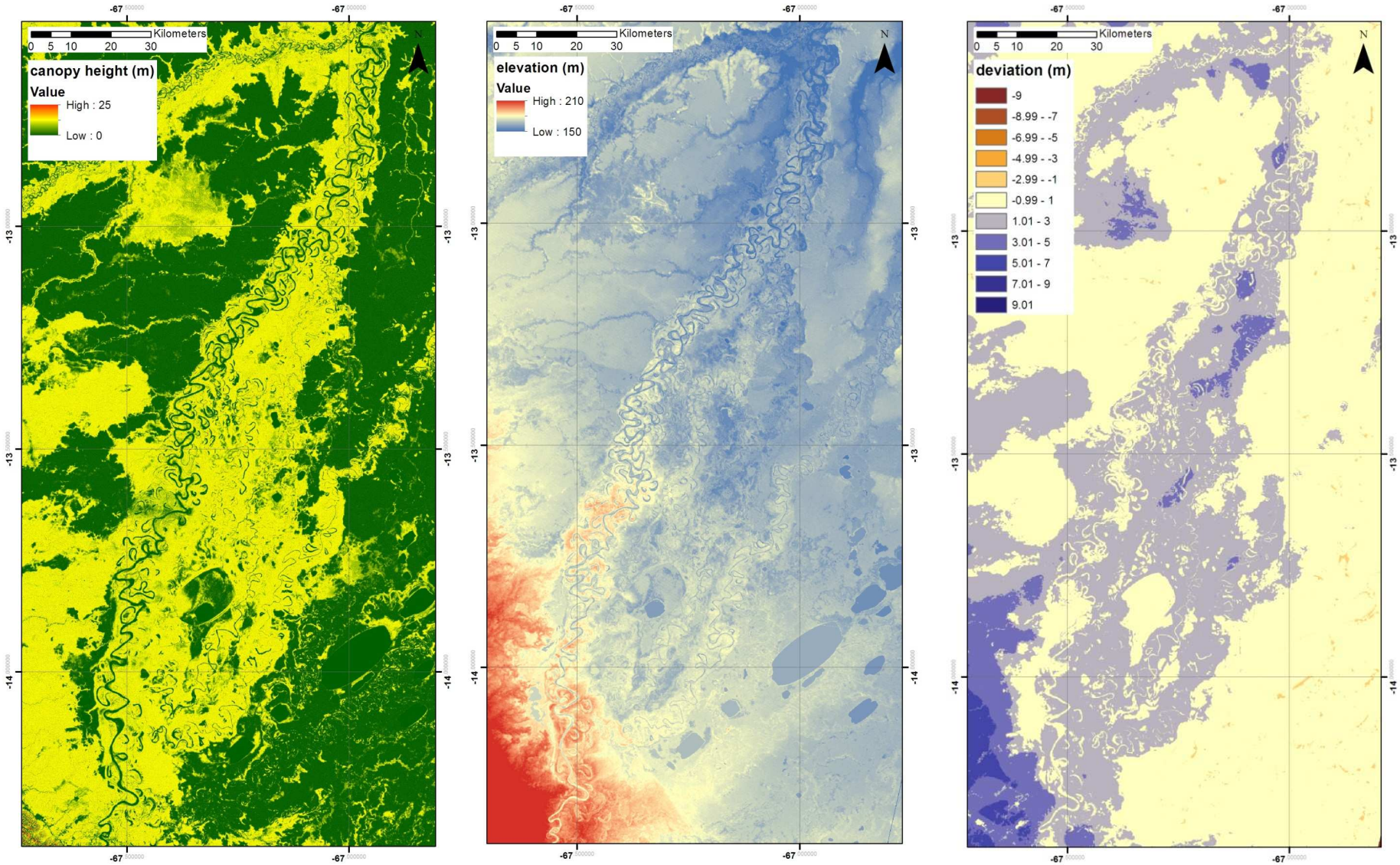

Figure 5.15. Maps showing broad characteristics of GLMED DEM. Left- canopy height map. Middle- bare earth DEM. Right- elevation deviation image.

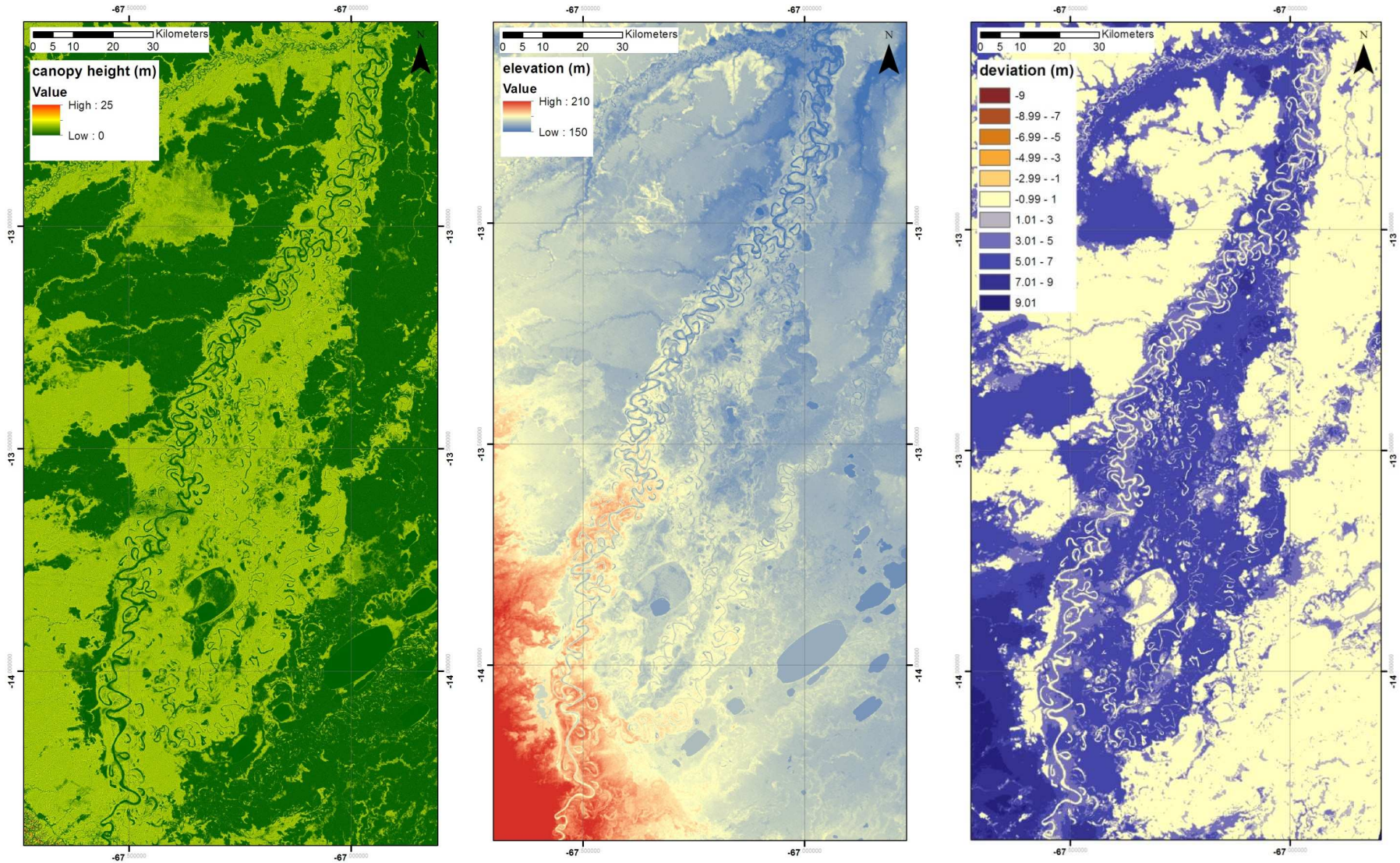

Figure 5.16. Maps showing broad characteristics of GLMEDP DEM. Left- canopy height map. Middle- bare earth DEM. Right- elevation deviation image.

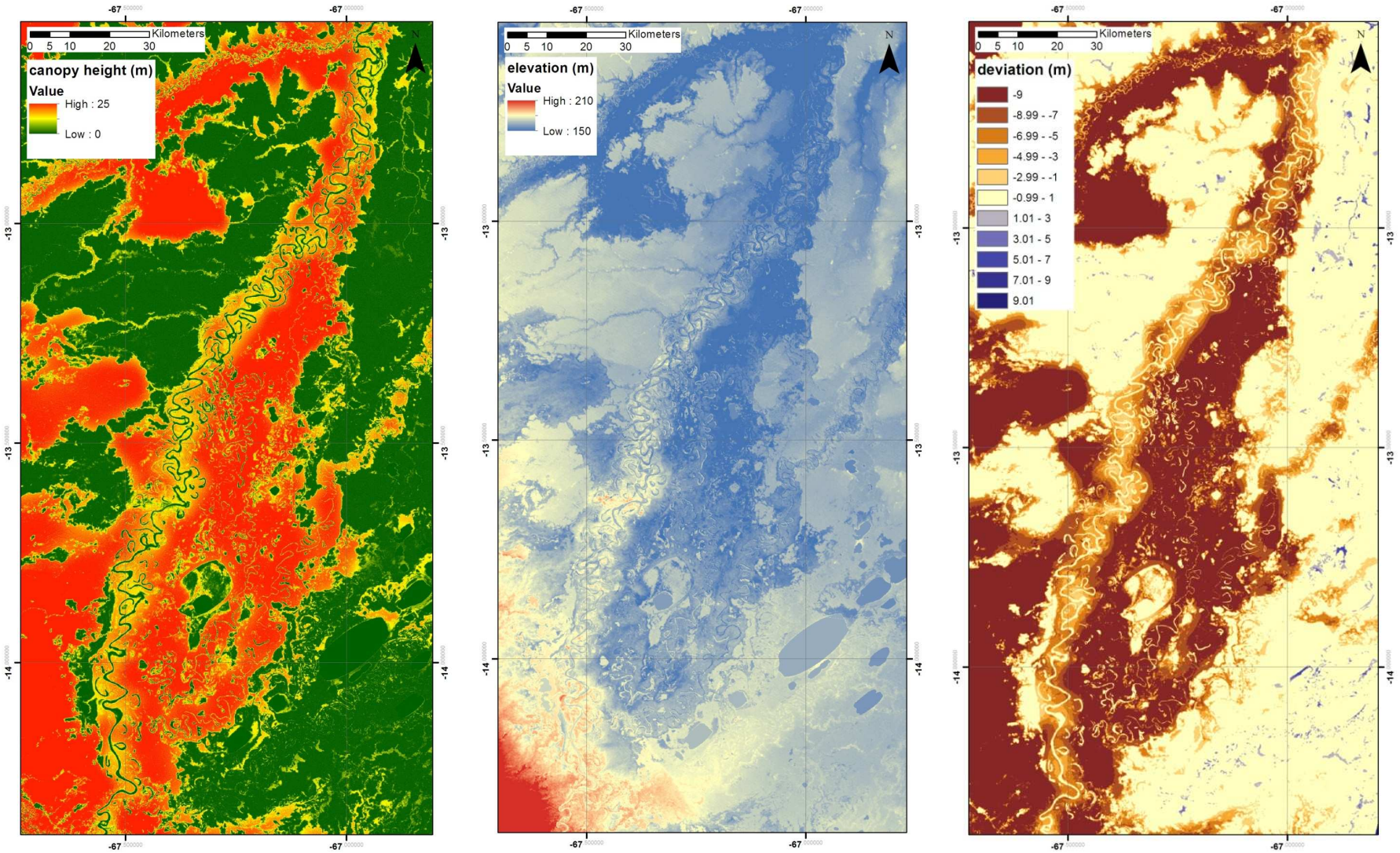

Figure 5.17. Maps showing broad characteristics of GCH DEM. Left-canopy height map. Middle- bare earth DEM. Right- elevation deviation image.

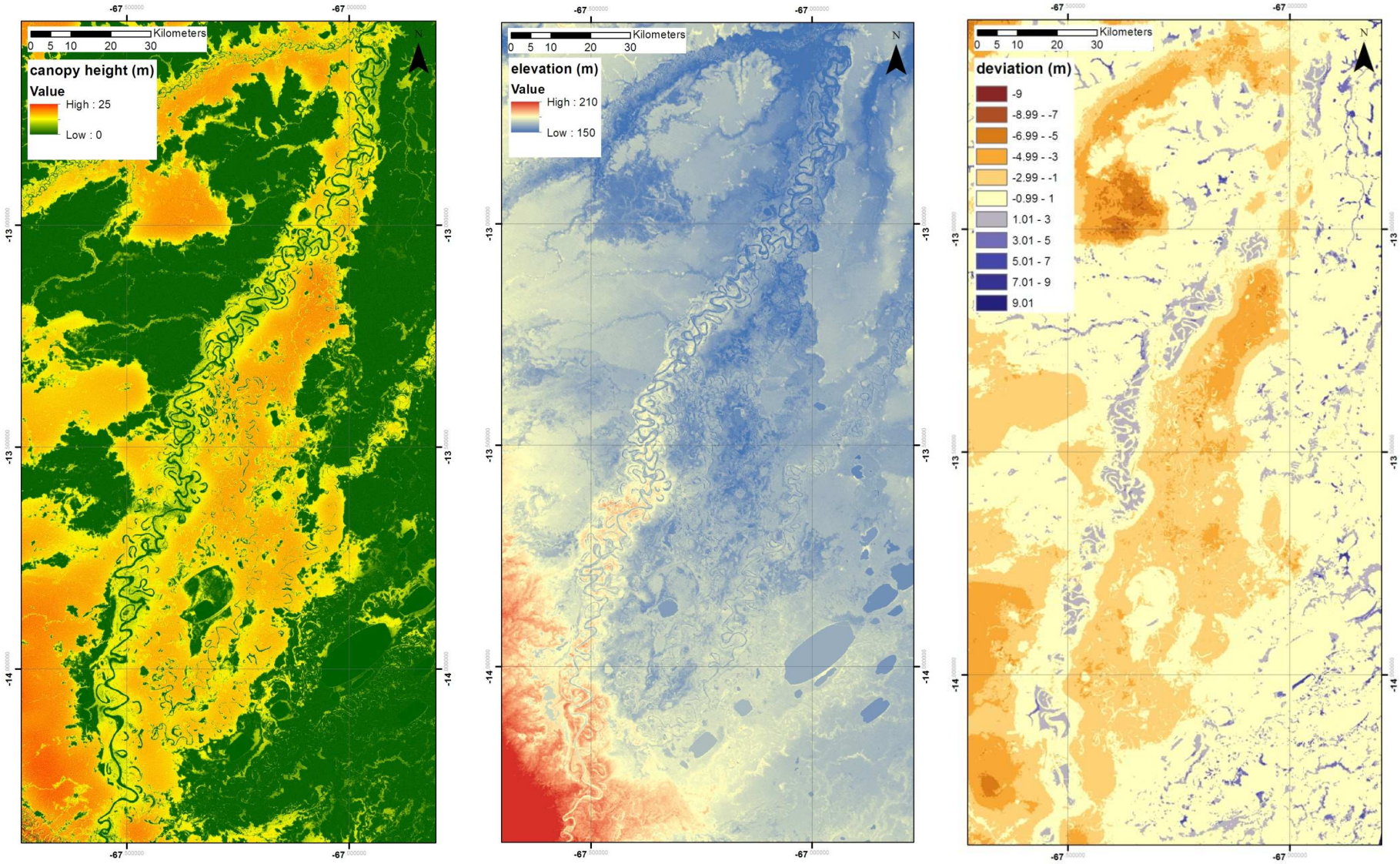

Figure 5.18. Maps showing broad characteristics of GCHP DEM. Left- canopy height map. Middle- bare earth DEM. Right- elevation deviation

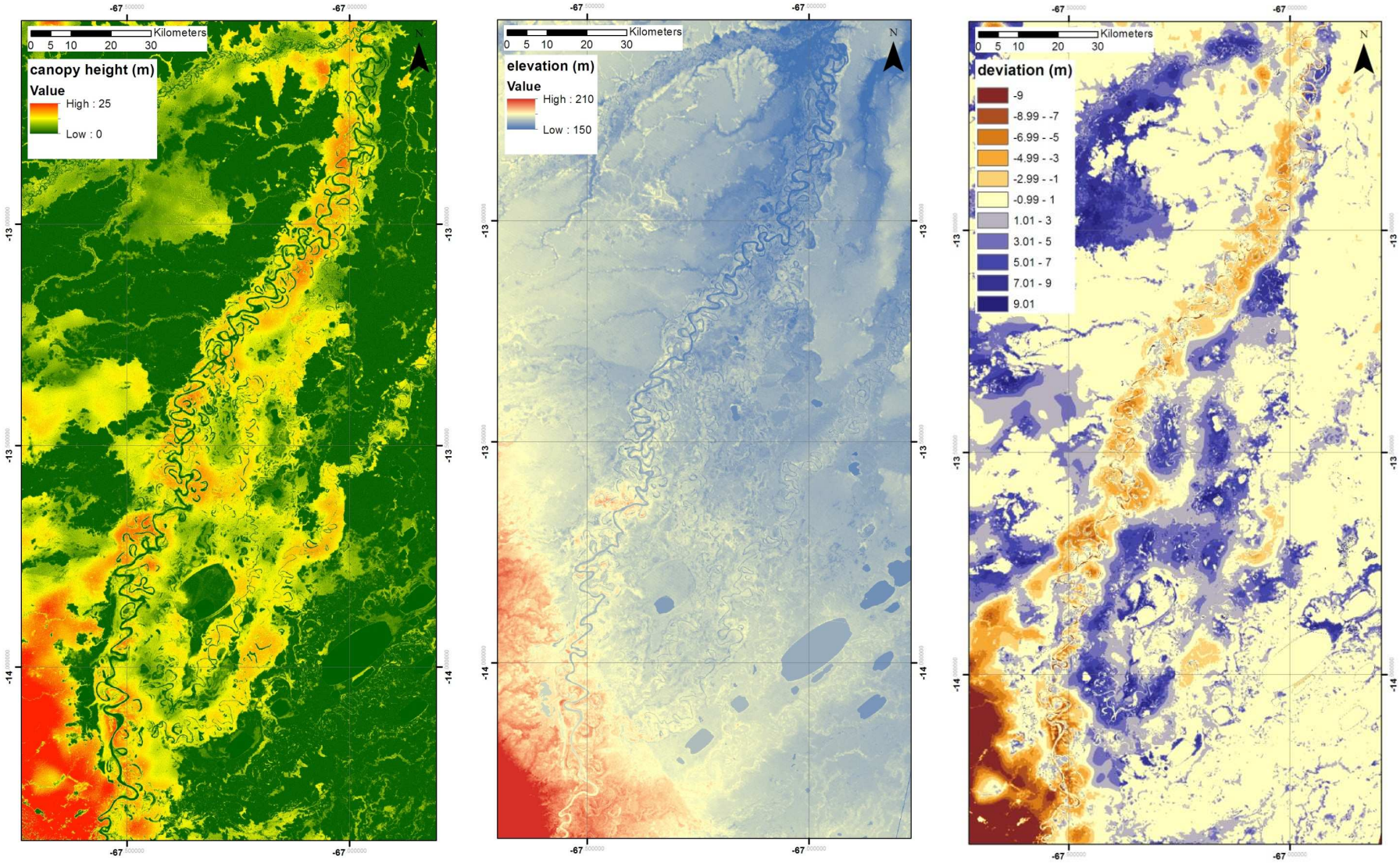

Figure 5.19. Maps showing broad characteristics of INT DEM. Left- canopy height map. Middle- bare earth DEM. Right- elevation deviation image.

DEMs. INT DEM is characterised by lower than average bare ground elevation in close proximity (5-10 km) to the river channel. In contrast, positive deviations are observed for the large area of floodplain forest located on the east side of the channel, as well as for smaller forest stands located in the distal floodplain. Visual analysis reveals that this bare earth DEM is not characterised by the presence of obvious topographical depressions in the large expanse of floodplain forest located to the east of the Beni, which were prominent within the FAV DEM and GCH DEM. Further, raised areas present within close proximity to the main channel and floodplain channels which were prevalent within the FAVP and GLMEDP are not present in the INT DEM.

The broad scale view of the DEMs presented within figures 5.13-5.19 is complemented by a more detailed comparison of the DEMs over smaller scales in figures 5.20-5.40. Accordingly, these figures illustrate topographical profiles extracted from the original SRTM and the corrected DEMs at three locations upon the Beni floodplain. In order to aid this analysis, 'trusted bare earth elevations' are included within the maps of the profiles and the profiles themselves in order to provide an indication of the accuracy of the different DEMs. These trusted elevations were extracted from the SRTM in locations which were characterised by bare earth, determined through visual analysis of Landsat TM imagery, and hence are devoid of biases relating to vegetation. According to the results of chapter 4 bare earth elevations within the SRTM for the Beni floodplain are associated with a high level of accuracy, being characterised by an RMSE of 1.6 m.

The three selected locations were considered to be representative of the floodplain at large, and hence provide an insight into the characteristics of the DEMs produced through different approaches to vegetation correction. Profiles 1 and 2 were extracted from the upstream section of the reach, whilst profile 3 was located further downstream around 100 km north of Rurrenabaque. Figures 5.20 and 5.21illustrate extracted cross sectional profile (profile 1) across the Beni and adjacent floodplain for a meander bend located in the upstream part of the study reach. The topographical profile begins upon the west side of the Beni, from here it stretches east across the downstream section of the point bar and the main channel. From the raised levee deposit on the cut bank side of the meander bend the profile intersects a channel cut off before descending a

relatively shallow slope to an unforested basin at the eastern end of the profile. Dense forest cover characterises the point bar and levee deposit up to a distance of 16 km along the profile. The analysis of the DEMs below will centre around profile 1 (figures 5.20-5.26), although the same basic features of the DEMs are illustrated for profile 2 (figures 5.27-5.33) and profile 3 (figures 5.34-5.40).

Figure 5.22 illustrates the profile extracted from the INT DEM along with the SRTM dataset and trusted bare earth elevations. The representation of the ground surface corresponds closely to the trusted elevations for the length of the profile, strongly suggesting that INT provides an accurate representation of bare earth elevation. Elevation of the bare earth DEM corresponds well to trusted elevations on the point bar, which is characterised by a relatively small level of topographical variability. INT accurately represents the elevation of the levee top on the outside of the meander bend, whilst also capturing the gradient of the slope of the levee to the unforested basin at the end of the profile. Elevation within the INT DEM also appears to correspond well to the trusted bare earth elevation points within figures 5.29 and 5.36 for profile 2 and 3 respectively. The accuracy of these profiles with respect to trusted bare earth elevation suggests that the INT DEM is able to correctly capture floodplain topography both in close proximity to the channel, and also at a greater distance from the channel. These results thus reflect the broader features of the DEM illustrated within figure 5.19, which showed that floodplain topography was relatively consistent, featuring no marked depressions or raised areas. Thus the accuracy of topographical profiles combined with the broader scale consistency of the INT DEM indicate forest height is well represented within the canopy height map utilised within this approach.

The topographical profile for the FAV DEM is illustrated in figure 5.23. The FAV DEM captures bare earth elevation of the point bar and outside of the meander bend successfully, although the degree of topographical variability observed upon the point bar is greater than for the INT DEM. This suggests that canopy height is predicted correctly in close proximity to the river channel. However from 10-15 km along the profile FAV DEM deviates substantially from trusted bare earth elevations, as a result of an apparent over prediction of canopy height, consequently the slope of the levee is not captured successfully. In

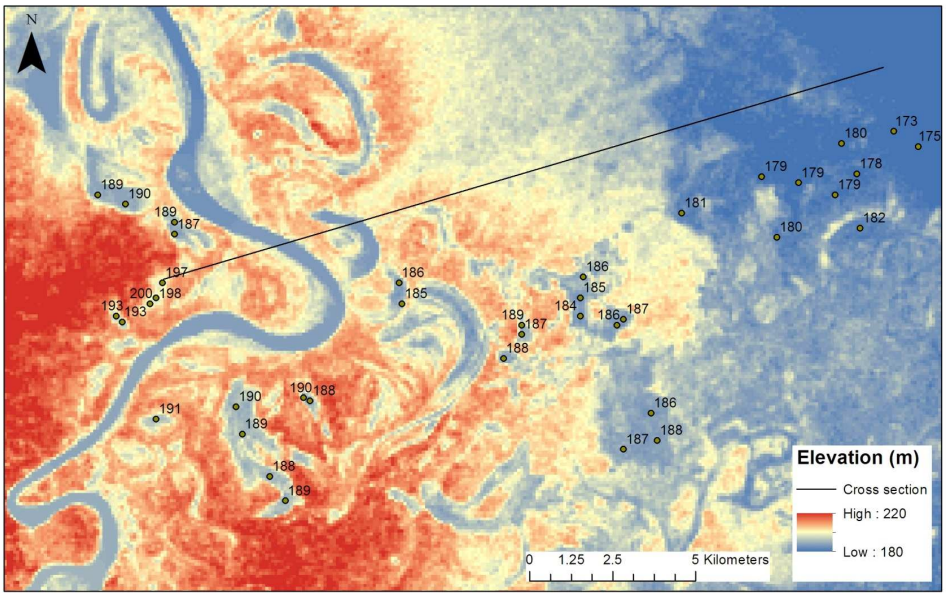

Figure 5.20. SRTM dataset overlain with location of topographical profile 1 and trusted bare earth elevations.

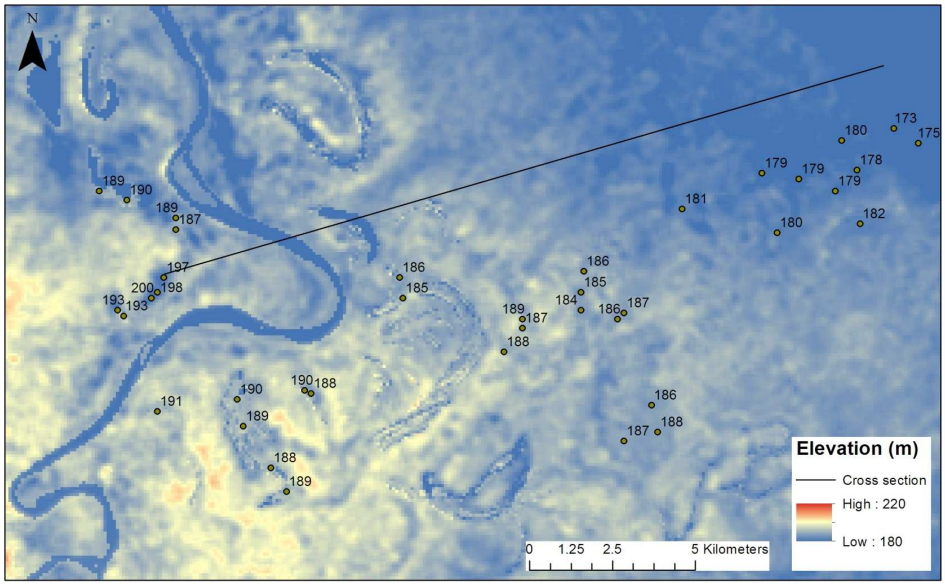

Figure 5.21. INT DEM overlain with location of topographical profile 1 and trusted bare earth elevations.

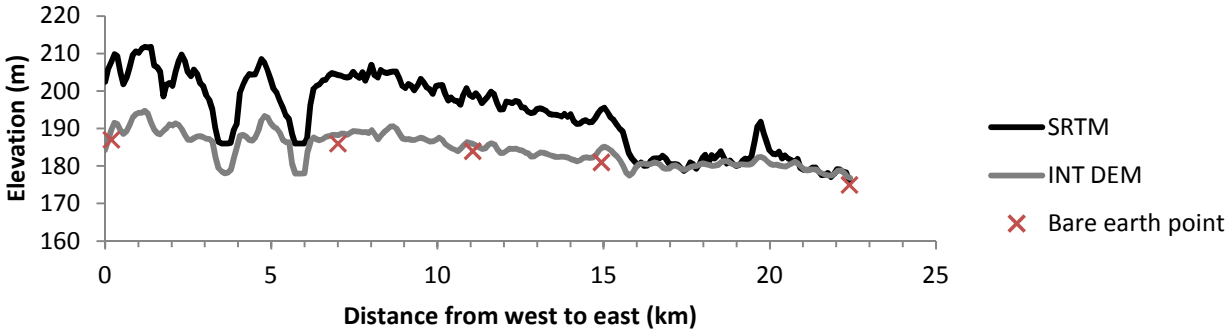

Figure 5.22. Topographical profile 1 showing SRTM and INT DEM along with trusted bare earth elevations.

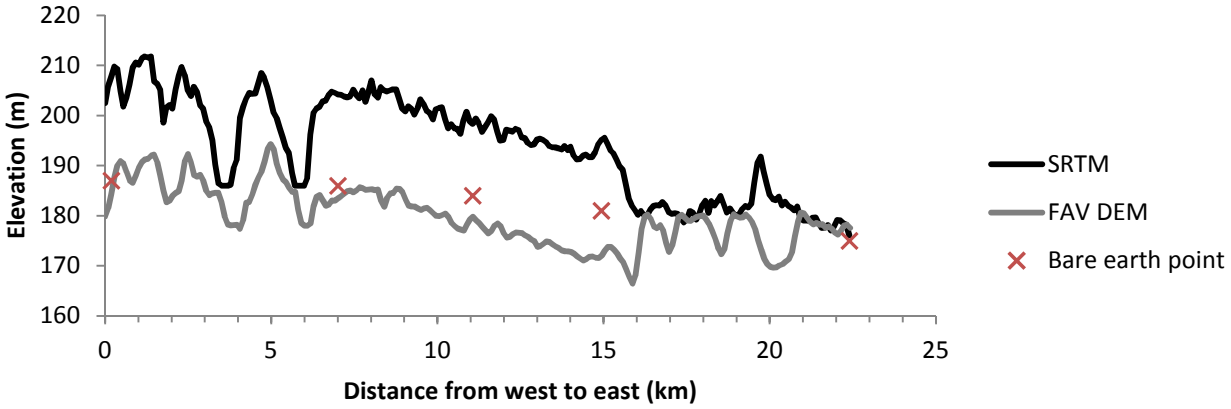

Figure 5.23. Topographical profile 1 showing SRTM and FAV DEM along with trusted bare earth elevations.

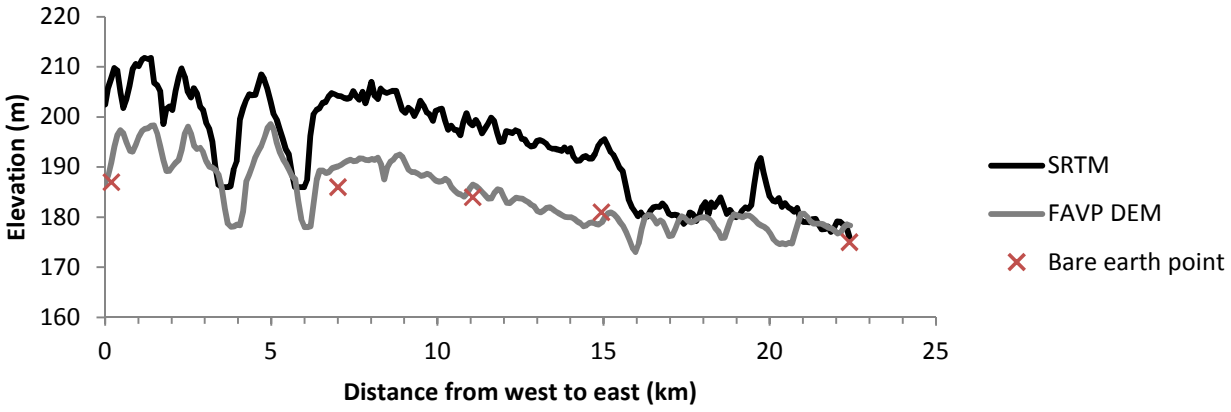

Figure 5.24. Topographical profile 1 showing SRTM and FAVP DEM along with trusted bare earth elevations.

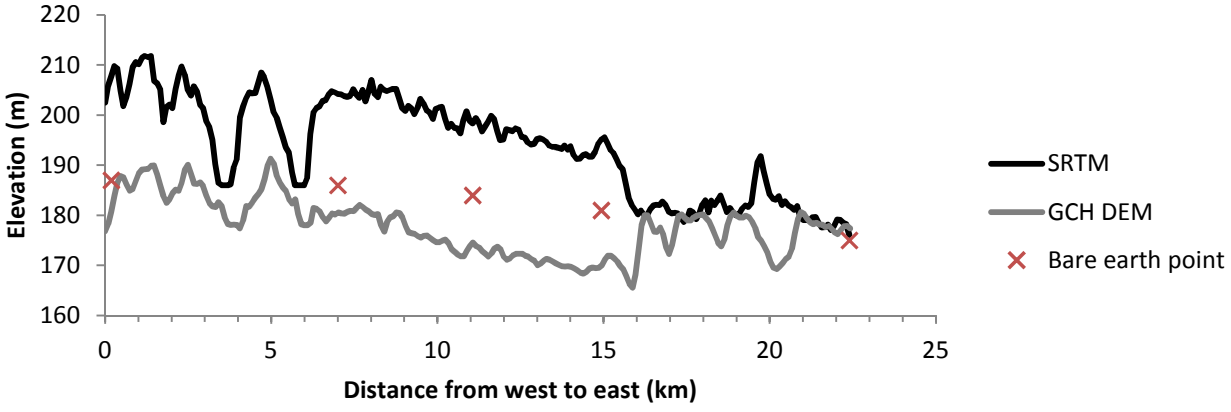

Figure 5.25. Topographical profile 1 showing SRTM and GCH DEM along with trusted bare earth elevations.

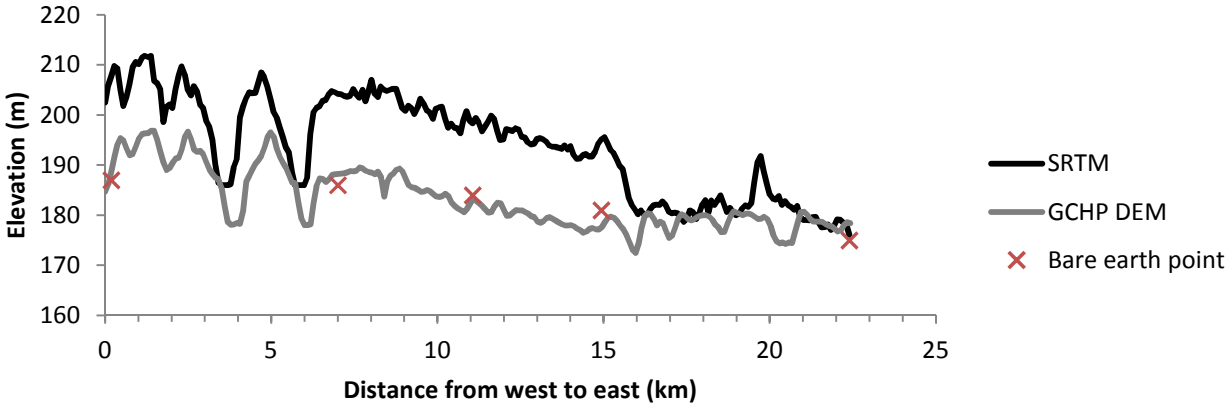

Figure 5.26. Topographical profile 1 showing SRTM and GCHP DEM along with trusted bare earth elevations.

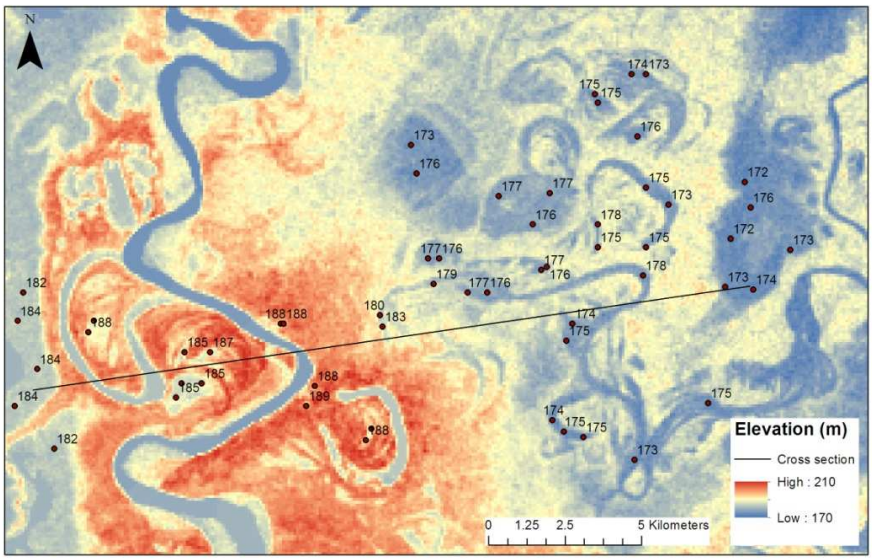

Figure 5.27. SRTM dataset overlain with location of topographical profile 2 and trusted bare earth elevations.

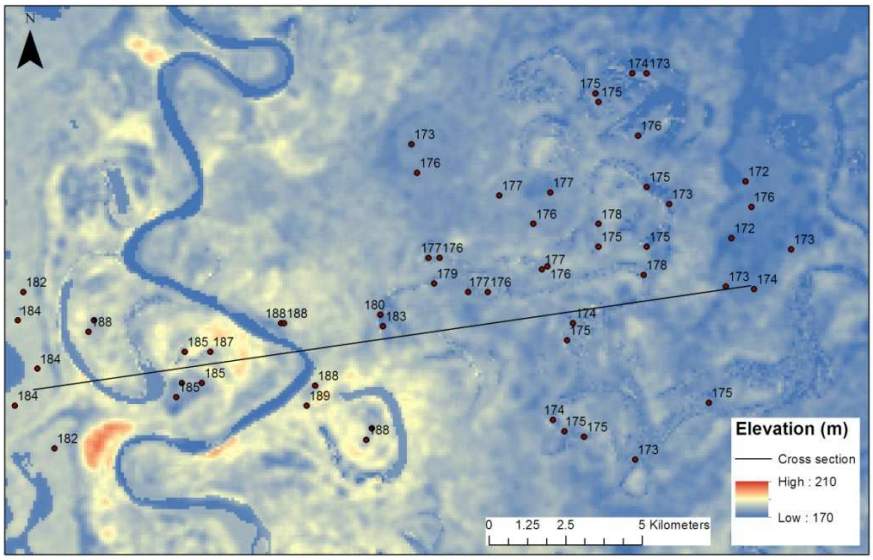

Figure 5.28. INT DEM overlain with location of topographical profile 2 and trusted bare earth elevations.

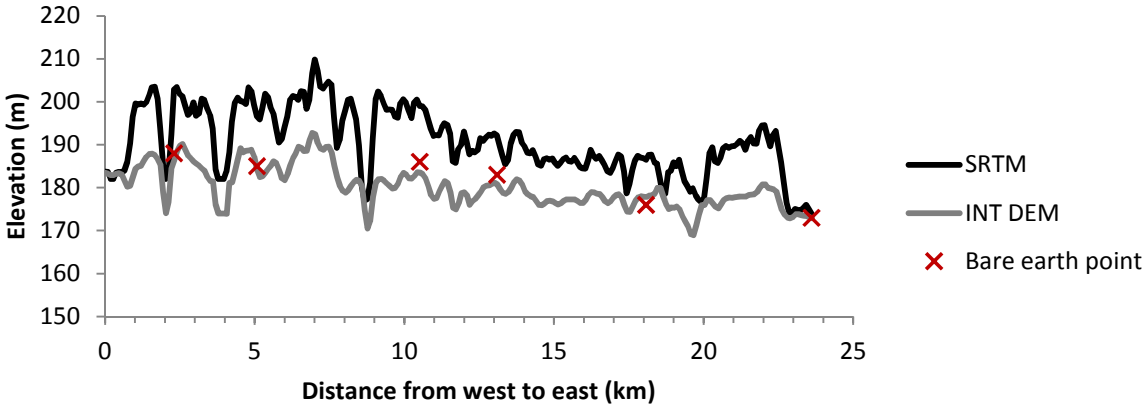

Figure 5.29. Topographical profile 2 showing SRTM and INT DEM along with trusted bare earth elevations.

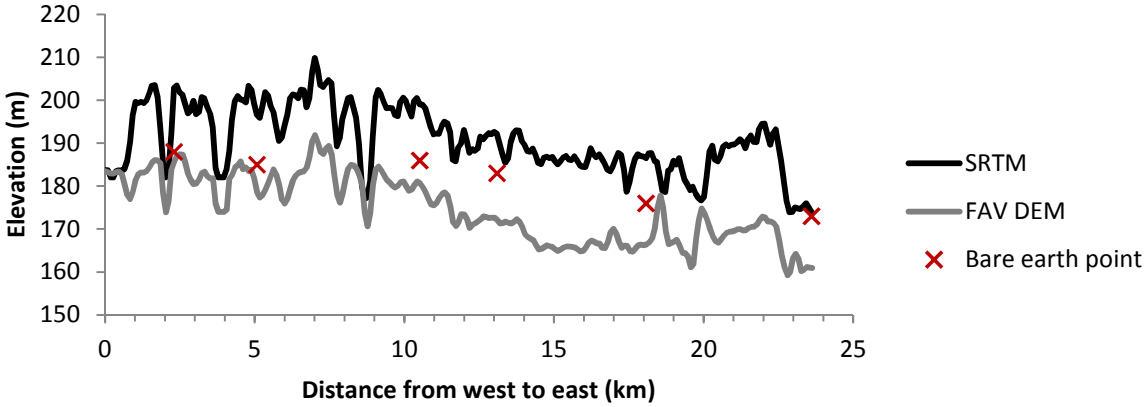

Figure 5.30. Topographical profile 2 showing SRTM and FAV DEM along with trusted bare earth elevations.

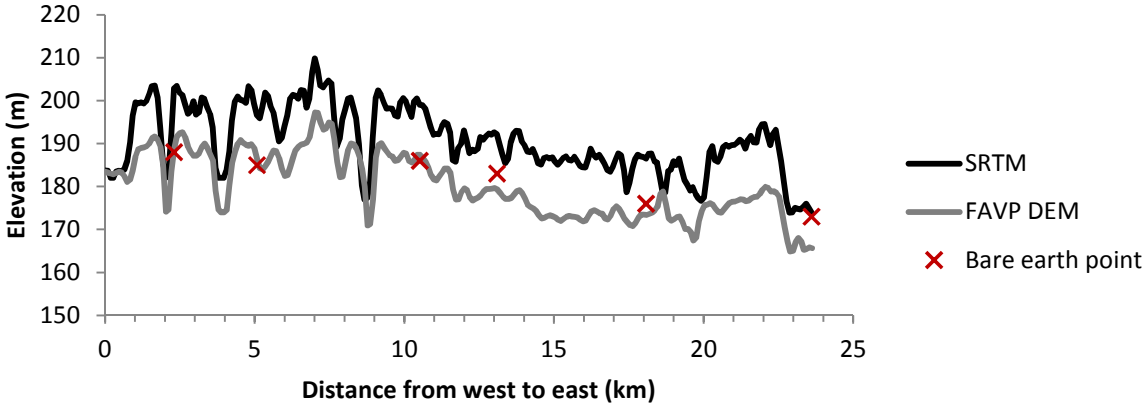

Figure 5.31. Topographical profile 2 showing SRTM and FAVP DEM along with trusted bare earth elevations.

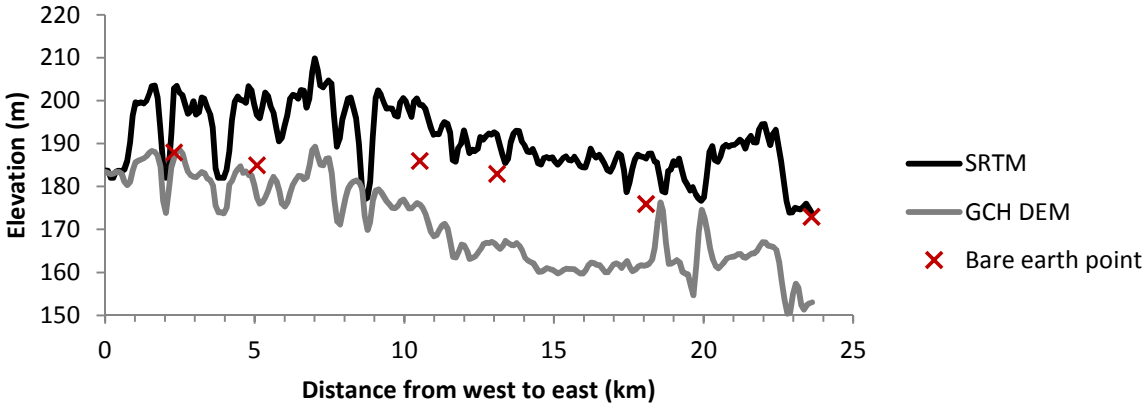

Figure 5.32. Topographical profile 2 showing SRTM and GCH DEM along with trusted bare earth elevations.

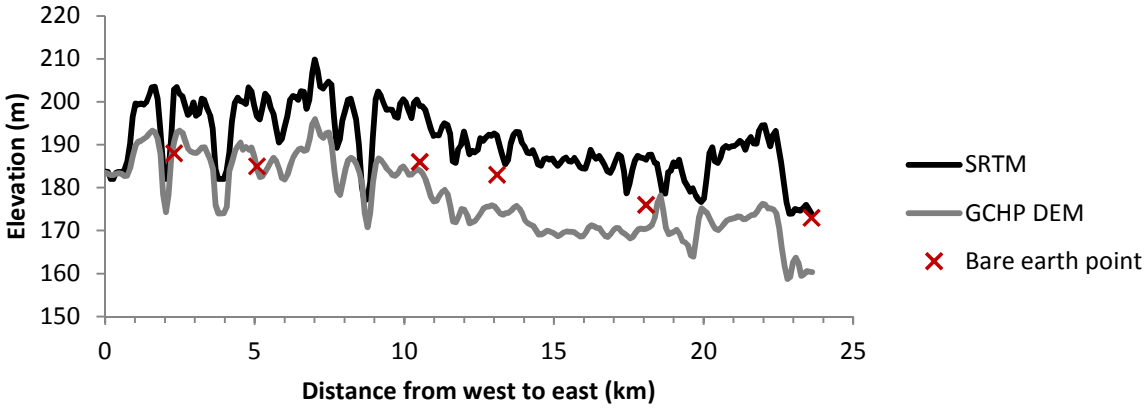

Figure 5.33. Topographical profile 2 showing SRTM and GCHP DEM along with trusted bare earth elevations.

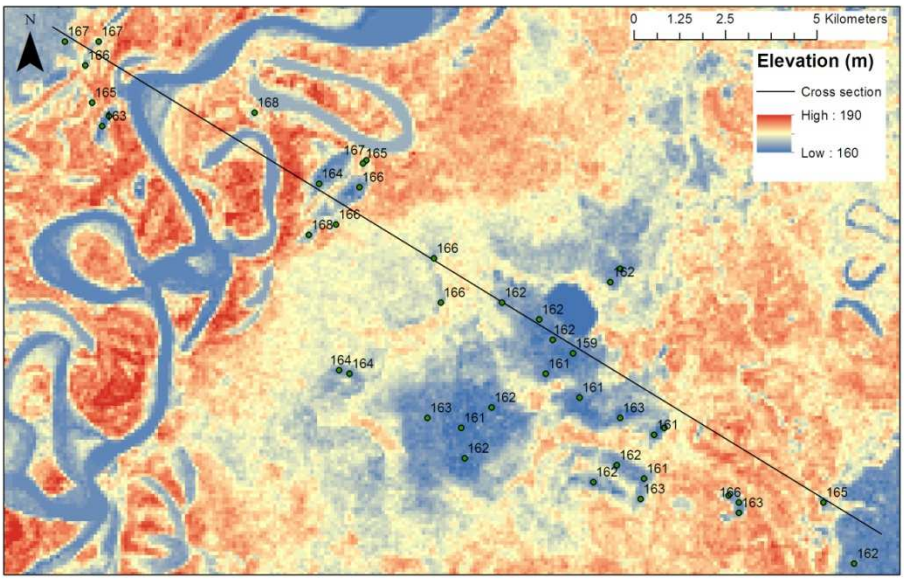

Figure 5.34. SRTM dataset overlain with location of topographical profile 3 and trusted bare earth elevations.

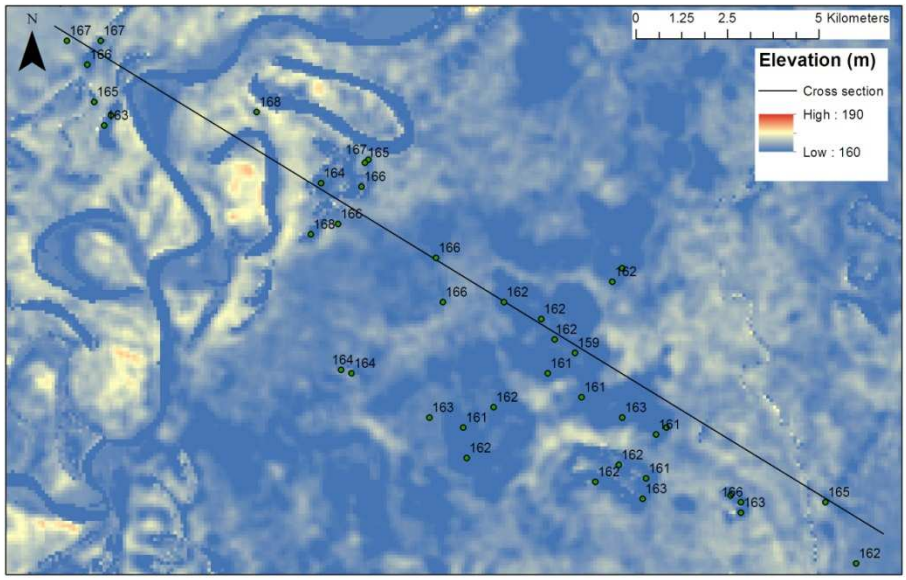

Figure 5.35. INT DEM overlain with location of topographical profile 3 and trusted bare earth elevations.

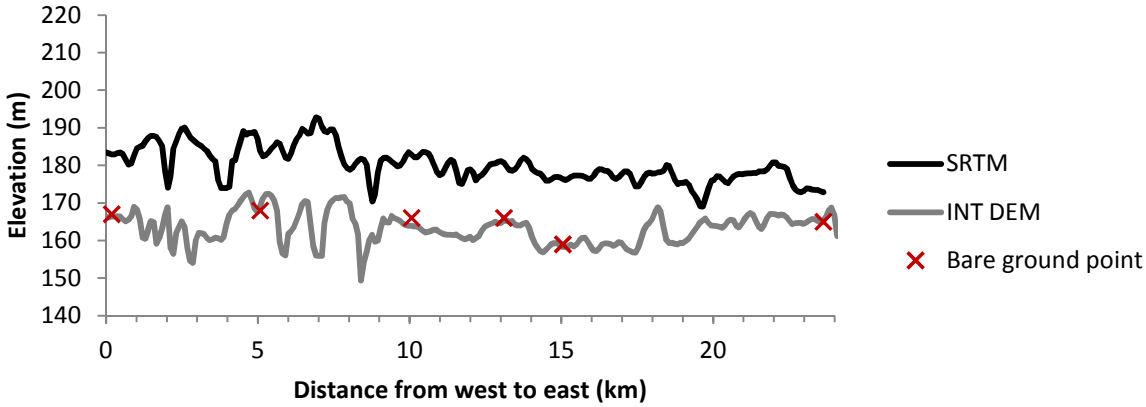

Figure 5.36. Topographical profile 3 showing SRTM and INT DEM along with trusted bare earth elevations.

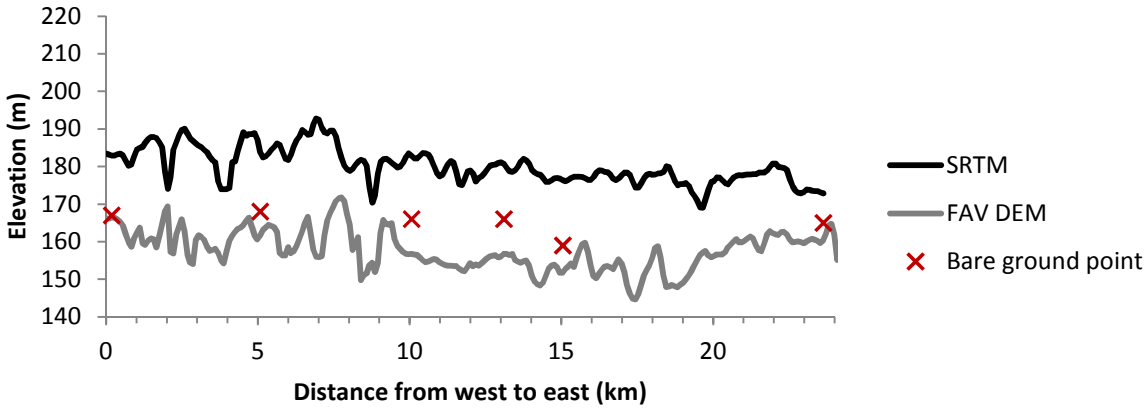

Figure 5.37. Topographical profile 3 showing SRTM and FAV DEM along with trusted bare earth elevations.

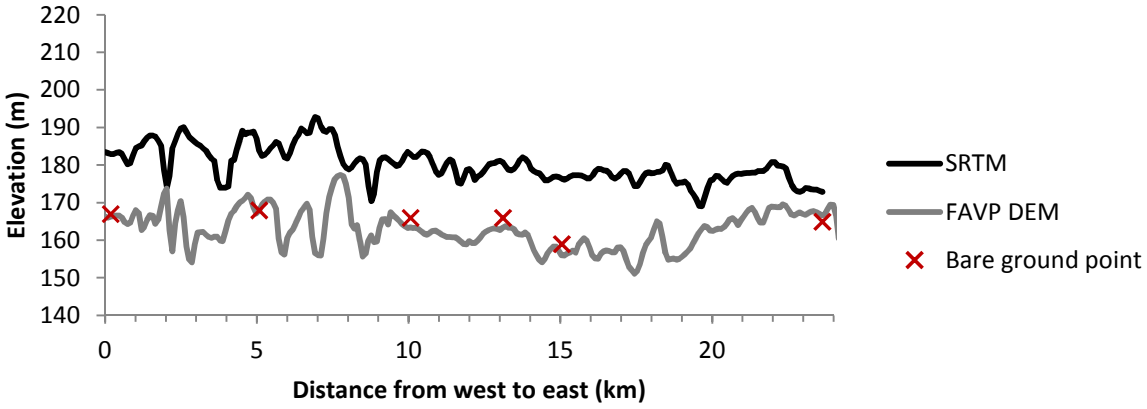

Figure 5.38. Topographical profile 3 showing SRTM and FAVP DEM along with trusted bare earth elevations.

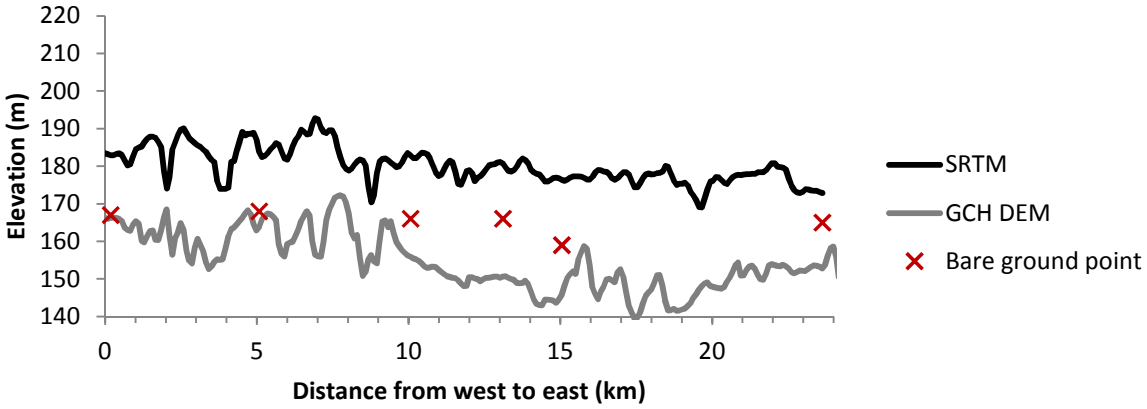

Figure 5.39. Topographical profile 3 showing SRTM and GCH DEM along with trusted bare earth elevations.

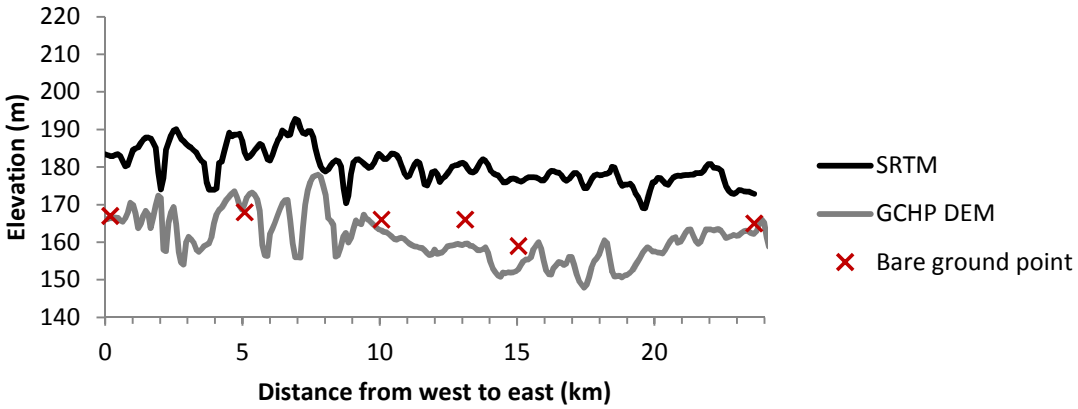

Figure 5.40. Topographical profile 3 showing SRTM and GCHP DEM along with trusted bare earth elevations.

addition, the unforested basin at the eastern end of the profile is characterised by the presence of topographical depressions, which are indicative of erroneous correction of vegetation effects. Under prediction of ground height relative to

bare earth elevation points with increasing distance from the channel is also a feature of profile 2 (figure 5.30) and profile 3 (figure 5.37). Considered in light of the broad DEM behaviour illustrated within 5.13, this suggests canopy height and hence ground elevation appears to be well represented within close proximity to the channel within the FAV DEM. However under prediction of elevation with increasing distance from the channel, coupled with the observation of widespread topographical depressions suggests that the approach used to produce the FAV DEM overestimated forest height outside the channel belt.

Figure 5.24 shows the profile of bare earth elevation associated with the FAVP DEM. In the FAVP DEM the elevation of the point bar deposit and levee on the cut bank side of the Beni deviate positively from the trusted bare earth elevations, indicating an under prediction of canopy height for forests located in close proximity to the river channel. Ground elevation in the FAVP DEM corresponds more closely to trusted elevations with increasing distance from the channel, hence the slope of the levee to the unforested basin is captured effectively. Thus in contrast to the FAV DEM, the approach used to generate FAVP DEM predicts canopy height correctly further from the channel, whilst canopy height is under predicted in close proximity to the channel. For profiles 1 and 2 illustrated within figures 5.31 and 5.38, the FAVP DEM also offers an improved level of performance when predicting bare earth elevation with increasing distance from the channel, in comparison to the FAV DEM. Combined with observations within figure 5.14, these results suggest that the correction of vegetation biases is effective for areas located with greater distance from floodplain channels within FAVP DEM. However, the over prediction of elevation within close proximity to the channel with respect to trusted bare earth points (figure 5.24) combined with the presence of raised areas visible around channels within figure 5.14 suggests that canopy height may be systematically under predicted within these areas.

Figure 5.25 and 5.26 illustrate profiles of floodplain topography for the GCH and GCHP DEMs respectively. Bare earth elevation in the GCH DEM is well captured upon the point bar, whilst elevation falls substantially below trusted bare earth elevations on the outer bank of the meander. This negative deviation with respect to ground elevation increases with distance from the channel,

hence the slope of the levee is not well represented. In a similar manner to the FAV DEM, the topographical basin at the east of the profile is characterised by the presence of erroneous topographical depressions. Overall this indicates that canopy height is over predicted within the approach used to generate the GCH DEM, particularly with increasing distance from the channel. The floodplain profile for the GCHP DEM features a marked over prediction of elevation on the point bar, whilst topography corresponds well to the trusted bare earth points across the levee from the outer bank of the meander to the unforested basin at the east side. Hence the ground elevation profile suggests that canopy height is generally well predicted within the approach utilised in order to produce GCHP DEM, with the exception of the point bar. Similar DEM characteristics are also observed for profiles 2 and 3 within figures 5.32, 5.33, 5.39 and 5.40, with the GCH DEM substantially under predicting elevation in comparison to bare earth points. Considered in the light of the presence of large areas of topographical depressions within forested areas of floodplain within figure 5.17, the profiles presented here suggest that the global canopy height map systematically over predicts canopy height in areas located outside the channel belt, leading to under prediction of floodplain elevation. Correction of the global canopy height map in order to account for SRTM penetration, reduces the under prediction of floodplain elevation with increasing distance from the channel but leads to an over prediction of elevation within the channel belt, indicated by the prevalence of raised topography indicated within figure 5.18 and comparison to trusted bare earth elevations within figures 5.33 and 5.40.

5.6 Discussion

Tropical forest stands in Amazonia are characterised by a high level of spatial heterogeneity in terms of biophysical properties (Lu et al., 2003a). This spatial variability increases within seasonally inundated varzea forests as a result of elevated disturbance linked to processes of flood inundation (Junk et al., 1997). Indeed physical characteristics such as stem density, tree height, species composition, biomass and degree of canopy closure commonly exhibit substantial variations over small spatial scales in inundated forests (Wittmann et al., 2002) Observations undertaken during the field campaign confirmed that Beni floodplain forests are typical of those found for Amazonian varzea, with

physical and structural characteristics varying substantially even within stands of the same forest class.

Accordingly, the heterogeneity of the structural characteristics of Beni floodplain forests is reflected in the vertical bias observed within vegetated areas in the SRTM dataset, which varies substantially across the study area. The magnitude of SRTM vertical bias is primarily dependent upon canopy height (Walker et al., 2007) but is also controlled by variables such as stand density and degree of canopy closure, which influence the nature of interactions between the SRTM C-band phase centre and the forest canopy (Hofton et al., 2006). In addition, given the heterogeneity of Beni floodplain forest structure it is possible that physical forest characteristics may vary independently of one another, producing non linear relationships between canopy height and SRTM vertical bias.

In vegetated areas, quantification of the SRTM vertical bias is required in order to facilitate production of an accurate representation of bare earth elevation (Bourgine and Baghdadi, 2005). In the absence of continuous direct measurements from LiDAR surveys, prediction of forest height across the Beni floodplain presents a challenging research problem. The difficulty of this task is enhanced by the potential for the proliferation of non linear relationships between forest height and the SRTM bias (Hofton et al., 2006). Initially in an attempt to facilitate extrapolation of point canopy height measurements across the floodplain in a spatially variable manner, relationships were sought between point measurements of canopy height and ancillary variables with continuous spatial coverage. This constituted a similar methodology to that employed by Lefsky et al., (2010) and Simard et al., (2011) in order to generate global canopy height maps, although implemented on a local scale. Accordingly univariate and multivariate regression models were constructed using SRTM standard deviation, Landsat TM reflectance, MODIS reflectance, TRMM rainfall and other variables, however statistically significant relationships were not observed. In the absence of sufficiently strong correlations, four alternative approaches to bare earth DEM generation were tested here. The quality of the bare earth DEMs produced using these approaches was largely dependent upon the ability of each approach to accurately represent the spatial variations of SRTM vertical bias across the floodplain.

In the zonal average approach to DEM generation canopy height is assumed to be uniform for each forest class, thus canopy height variations are driven primarily by spatial variations in the distribution of different forest classes across the floodplain. The distribution of forest classes remains constant for each DEM generated through the zonal average approach, hence differences between the DEMs produced using this method can be attributed to the variations in canopy height parameters applied for each forest class. Consequently whilst the FAV, FAVP, GLMED and GLMEDP DEMs are characterised by substantial differences in bare earth elevation and hence vertical accuracy in table 5.2 and 5.3, these DEMs possess many common traits which were evident during the qualitative assessment. The most significant common trait within these DEMs was the inability to correctly predict bare earth elevation both in the proximal and distal floodplain.

Bare earth DEMs generated through both the field and GLAS derived zonal average approaches all exhibit a substantial improvement in vertical accuracy when compared to the SRTM. For the complete DGPS validation set SRTM is characterised by LE90 of 16.2 m and a mean deviation of 6.6 m for the Beni floodplain. For each of the four DEMs generated using zonal average approaches, LE90 was less than 10 m and mean deviation was less than 2 m. Hence these bare earth DEMs substantially exceeded the pre mission SRTM accuracy requirements (Bamler, 1999). FAV DEM was associated with an overall negative bias which can be attributed to the fact that the canopy height map, derived based upon forest inventory results, was not scaled in order to account for SRTM canopy penetration. As a result, the magnitude of SRTM bias was over predicted and bare earth elevation was under estimated for large areas of the floodplain. The scaling factor was applied to the canopy height map for the FAVP DEM, however this yielded only a moderate increase in vertical accuracy in comparison to the FAV DEM within quantitative analysis. Significantly, a mean deviation of 1.3 m indicated the proliferation of positive bias in the FAVP DEM, suggesting that application of the scaling factor led to under prediction of canopy height and over estimation of floodplain elevation. These results suggest that the average canopy height derived from the field survey data under estimated the canopy height for substantial areas of forest located across the floodplain.

The GLMED approach corrected SRTM vegetation effects through application of the median GLAS canopy height, and was associated with the highest absolute accuracy and lowest bias of any DEMs generated through the zonal average approach (table 5.2). After adjustment of canopy height in order to account for SRTM penetration the GLMEDP DEM was characterised by a lower level of absolute accuracy than the GLMED DEM, whilst exhibiting the largest positive bias of any bare earth DEM. These results indicate that the median GLAS derived Loreys height (Saatchi et al., 2010) corresponds well to the average SRTM bias in the Beni floodplain study area, precluding the need for application of the scaling factor in order to account for C-band phase centre penetration.

Despite the clear improvement in quantitative performance exhibited by the zonal average DEMs in comparison to the SRTM, the quality of the representation of bare earth topography is unclear based upon summary statistics alone. Histograms shown in figures 5.3-5.7 illustrate that errors for the DEMs are not normally distributed but rather are skewed or multi modal, indicative of systematic error in the correction of vegetation biases in the SRTM. In addition, qualitative assessment of the DEMs clearly demonstrated the limitations associated with the zonal average approach to SRTM correction. Specifically, the zonal average approach was not able to effectively represent spatial variations in canopy height which characterise floodplain forest stands located within the Beni floodplain study area.

Accordingly, the topographical profiles illustrated in figure 5.23 and 5.24 indicated that the FAV DEM reproduced floodplain topography relatively well in close proximity to the channel, whilst underestimating bare earth elevation in areas located further away from the channel. In contrast for the FAVP DEM bare earth elevation was over estimated in close proximity to the channel, whilst being represented correctly with increasing distance from the channel. The implications of these results are twofold; firstly the results suggest that forest stands located in close proximity to the Beni channel are characterised by higher canopies than surrounding forests. Secondly, the results indicate that the zonal average canopy height maps are not able to account for this spatial variability in canopy height. Analysis of forest inventory data confirmed the existence of this disparity in canopy height, as plots located within the channel

belt (defined here as within 5 km of the main channel) were associated with an average height of 23.1 m whilst forests outside this zone were characterised by an average canopy height of 18.53 m. A t test yielded a t value of 4.34 along with a p value of 0.00007, confirming the difference in height of forests located inside and outside the channel belt. Given that spatially uniform canopy height was assumed for individual forest classes in the zonal average approach, the resulting canopy height maps were unable to account for the increase in canopy height observed for forests located within the channel belt, with associated errors in the bare earth elevations included within the resulting DEMs.

Although incorporation of additional canopy height information into the DEM generation routine could potentially improve the representation of bare earth topography, implementation of this proved to be problematic. Despite the increase in height of forests stands located in close proximity to the river channel, these forests were not characterised by a distinct Landsat TM spectral signature (Lu et al., 2003a). Consequently, it was not possible to separate these forests within the land cover classification. It also proved impossible to manually delineate forests characterised by higher canopies as they could not be reliably defined with an appropriate level of accuracy without further information. In lieu of other options, the only method by which zonal averaged DEMs can be improved is through adjustment of canopy height parameters for each land cover class in order to improve vertical accuracy. However whilst the parameters can be adjusted in order to correctly reproduce bare earth elevation in a given part of the floodplain, the accuracy of the DEM will be compromised in other areas.

Overall, results presented here highlight the limitations associated with application of zonal average canopy height maps in order to correct SRTM vertical biases for the Beni floodplain study area. The inability to account for differences in the canopy height of forest stands located in the proximal and distal floodplain mean that important topographical features within the study area, such as the slope of the floodplain away from the main channel, are not well reproduced within the resulting DEMs. More broadly, the results of this study cast doubts over the validity of the zonal average correction of the SRTM, such as that utilised by Wilson et al., 2007) when applied to study areas characterised by highly heterogeneous tropical forest cover such as the Beni

floodplain. Intuitively this approach is likely to offer a greater level of utility in regions characterised by more homogeneous forest cover, where the assumption of uniform canopy height within forest classes is more appropriate (Weydahl et al., 2007).

As for the DEMs produced using field averaged zonal representations of canopy height, the disparity in performance for GCH and GCHP emphasises the effect of accounting for penetration of the C-band phase centre when correcting for vegetation effects in the SRTM dataset. The approach used to produce the GCH DEM did not account for SRTM penetration into forest canopies and was associated with the poorest level of performance of all DEMs in the quantitative validation. This bare earth DEM was characterised by a high level of negative bias with respect to the DGPS elevation survey, which manifested in the form of widespread erroneous topographic depressions which became evident through analysis of broad DEM characteristics and topographic profiles in the qualitative analysis. This negative bias can be attributed to the fact that the estimates of forest height contained in the global map correspond to the height of the top of the canopy (Simard et al., 2011), far exceeding the elevation of the SRTM C-band phase centre within Beni floodplain forests. Linear scaling of the global canopy height map in order to account for penetration into Beni floodplain forests produced a significant improvement in accuracy of the GCHP DEM. Accordingly, GCHP was associated with the lowest level of bias of any bare earth DEM and exhibited the second best overall performance with respect to summary statistics. Further, the near normal distribution of errors illustrated in figure 5.9 is indicative of a more meaningful correction of vegetation effects than for the DEMs based upon zonal average canopy height. On a basic level this illustrates that the correction of SRTM vertical bias based upon a global canopy height map, adjusted for C-band penetration (Baugh et al., 2013), produces a more accurate DEM than a zonal average canopy height map (Wilson et al., 2007).

However, despite facilitating the production of the second best DEM statistically, the qualitative analysis revealed several limitations posed by the application of a global canopy height map for the correction of SRTM vegetation effects in the Beni floodplain. The first limitation is constituted by the disparity in scale which exists between the global canopy height map and the Beni floodplain study

area. In the canopy height map produced by Simard et al., (2011) forest height varies spatially over very broad scales with respect to the size of the study area. This can be attributed to the fact that the map was produced at a spatial resolution of 1km, through correlation of point estimates of canopy height provided through GLAS with ancillary variables such as rainfall, elevation and tree cover which fluctuate over regional or continental scales.

As has been established previously, Amazonian varzea forests are characterised by high levels of structural heterogeneity over small spatial scales (Lu et al., 2003a). In the case of the Beni floodplain study area a myriad of field and remote sensing observations suggest that this heterogeneity is driven by variables operating over much smaller spatial scales. Hydrological conditions, principally water availability and flood inundation characteristics appear to be preeminent in driving spatial variability of the structural characteristics of Beni floodplain forests (Wittmann et al., 2004). Therefore whilst the canopy height estimates derived from global canopy height map exhibit a greater degree of spatial variation than those observed for the zonal average approaches, the global canopy height map is not able to reproduce finer scale canopy height variability observed for Beni floodplain forests.

The significant decrease in canopy height observed for forests located in close proximity to the Beni channel constitutes the second limitation of the global canopy height approach to bare earth DEM generation. Investigation of the original global canopy height map revealed that canopy height predictions are substantially lower in 1 km^2 pixels containing sections of the river channel. As canopy height in the global map is weighted according to the MODIS MOD44B percentage tree cover product (Simard et al., 2011), 1 km^2 cells containing sections of the river channel are associated with a lower estimate of forest height. This variation in canopy height is counter intuitive based upon aggregated forest height survey results and ultimately manifested in terms of an over prediction of bare earth elevation in close proximity to the river channel, evident in both figures 5.1 and 5.2.

The GCHP DEM represented the second best bare earth DEM generated in this chapter based upon statistical assessment, indicating that the global canopy height map of Simard et al., (2011) captures the average height of Beni

floodplain forest stands very well. However use of the global canopy height map for correction of the SRTM dataset in the Beni floodplain study area was associated with two primary limitations demonstrated within the qualitative analysis. Erroneously low estimates of canopy height observed in close proximity to the Beni channel could be remedied using interpolation techniques, resulting in an improvement in DEM quality in these areas. However, more importantly the global canopy height map is unable to depict the local forest height variations observed within the Beni study area, ultimately resulting in over or under prediction of bare earth elevation for significant portions of the floodplain. This indicates that the approach utilised by Baugh et al., (2013) may propagate substantial errors in bare earth DEMS for Amazonian floodplains characterised by highly heterogeneous varzea forest cover. Indeed the results presented here suggest that global canopy height maps may offer the greatest level of utility in correction the SRTM for larger study areas at coarser resolutions, where local variations in canopy height are less significant.

In quantitative terms the INT DEM was associated with the highest level of performance of all the bare earth DEMs which were produced here. The near normal distribution of errors observed in the histogram for the INT DEM (figure 5.10) was demonstrative of an accurate correction of SRTM vegetation effects. This is an improvement upon other DEM generation approaches which produced multimodal error distributions or which were characterised by high levels of skew, indicating systematic errors in the correction of SRTM. This high level of performance was reflected in the qualitative assessment, indeed the INT DEM represented floodplain topography well with respect to trusted bare earth elevations and was able to reliably reproduce topographical features such as the levee slope away from the channel.

The novel approach to correction of SRTM vegetation effects based upon a first order interpolated DEM produced the most accurate representation of floodplain topography as a result of its ability to represent local scale variations in canopy height which occur within the Beni floodplain study area through utilisation of the sensitivity of the SRTM to vertical vegetation structure (Carabajal and Harding, 2006). Both the canopy height map and deviation map illustrated in figure 5.19 demonstrate a much greater level of spatial variability in canopy height than is observed for the alternative approaches. Through utilisation of a

first order DEM, this approach uses canopy height information contained intrinsically within the SRTM in order to estimate local variations in forest height across the floodplain. Thus this approach circumvents the need to quantify spatial variations in both canopy height and other physical forest characteristics such as stem density and degree of canopy closure, which influence the overall magnitude of SRTM bias (Hofton et al., 2006).

The primary limitation associated with this approach to correction of SRTM vegetation effects is the reliance upon an interpolated bare earth surface, which must be of a high quality in order to facilitate accurate estimations of local vegetation height. The successful interpolation of a bare earth surface is dependent upon the density and accuracy of points in the input dataset (Aguilar et al., 2005), with the quality of the point dataset required is dependent upon the topographical complexity of the study area and accuracy requirements of the interpolated surface. Here bare earth elevation points were initially extracted from the SRTM based upon automated identification of unforested areas using the land cover mask. Incorporation of additional bare earth elevation points manually identified based upon Landsat TM imagery, and measurements from the survey of the Beni bank top substantially increased the density of points located in close proximity to the river channel. Hence in the Beni floodplain study area, the quality of the interpolated surface was sufficient to facilitate the extraction of an accurate canopy height map.

Overall, results obtained here demonstrate that the approach to SRTM correction which utilises a first order interpolated DEM, produces the best DEM for the Beni floodplain study area. The high levels of accuracy, in addition to the ability to reliably represent topographical features, suggests that the INT DEM is ideal for application within floodplain inundation modelling in subsequent chapters. Significantly results indicate that the INT DEM is of an equivalent or higher quality than the DEM utilised by Wilson et al., (2007) for inundation modelling of the Amazon main stem, whilst also performing better than the DEMs generated using through application of a global canopy height map (Baugh et al., 2013). More broadly, the success of this approach to correction of the SRTM suggests that DEMs of a sufficient quality for application within land surface process studies can be generated for other areas of the Amazon basin. Intuitively, utilisation of this methodology would be more problematic in study

sites characterised by a dearth of unforested areas, precluding the extraction of a sufficient density of bare earth elevation points for interpolation, or in study areas characterised by more complex topography which could not be effectively reproduced by interpolation of bare earth points extracted from the SRTM.

5.7 Conclusions

The results of this chapter illustrate that both field and remote sensing derived canopy height information can be effectively utilised in order to correct positive biases which exist in the SRTM dataset, as a result of C-band phase centre interactions with forest canopies. Prior to correction, the SRTM dataset was associated with 16.2 m linear error at the 90% confidence interval, falling just outside SRTM pre mission accuracy requirements of 16 m LE90 (Bamler, 1999). Of the bare earth DEMs generated here the GCH DEM was associated with the lowest level of vertical accuracy, being characterised by an LE90 of 10.0 m. Hence it can be concluded that correction of vegetation effects increased vertical accuracy of the SRTM in all cases. Indeed all bare earth DEMs generated here substantially exceeded the pre mission requirements of SRTM in terms of vertical accuracy (Farr, 2000).

Whilst quantitative validation illustrated that all approaches to correction of vegetation effects improved the vertical accuracy of the SRTM dataset, summary statistics indicated the presence of a significant disparity in the accuracy of the bare earth DEMs. In terms of absolute vertical accuracy, the INT DEM offered the highest level of overall performance, being associated with an RMSE value of 3.5 m. This DEM was also characterised by a low value for mean deviation, indicating a low level of vertical bias. Furthermore, a near normal error distributions illustrated with the error histogram was indicative of a more accurate vegetation correction than observed for the other DEMs. Further qualitative analysis over both broad and local scales illustrated that the INT DEM reproduced floodplain topography in a more realistic manner than the other bare earth DEMs, providing an accurate representation of topographical features upon the floodplain such as the slope of the levee away from the Beni river channel. The high quality of the INT DEM indicates that an approach to DEM generation which is able to account for the substantial levels of spatial variation in canopy height over local scales is advantageous in correction of the SRTM for the Beni floodplain study area.

In contrast, approaches to bare earth DEM generation based upon zonal average canopy height (Wilson et al., 2007) produced DEMs which were characterised by a lower level of absolute vertical accuracy than the INT DEM. Whilst these DEMS nevertheless offered a statistical improvement in comparison to SRTM, when assessed with respect to the floodplain DGPS survey, the error distributions exhibited in histograms were commonly skewed or multi modal indicating a more crude correction of vegetation effects. This was reflected in the results of the qualitative analysis, which revealed that important floodplain topographical characteristics were not well reproduced in these DEMs.

DEM generation based upon correction of SRTM using a global canopy height map (Baugh et al., 2013), offered an improvement in comparison to the zonal average approaches. Indeed GCHP DEM was associated with a higher level of accuracy than the zonal average DEMs in quantitative terms. However qualitative assessment revealed that the DEMs generated based upon global canopy height maps were associated with similar problems to those DEMs derived through the zonal average approaches. Canopy height within the global map varied across broad scales which reflect the remote sensing variables utilised within its production (Simard et al., 2011). Consequently this map was unable to account for local variations in forest height observed across the Beni floodplain, which are dependent upon processes operating at smaller scales, propagating errors within the resulting bare earth topography.

Chapter Six

Beni floodplain inundation modelling

6. Beni floodplain inundation modelling

6.1 Introduction

A review of literature relating to Amazonian floodplain inundation can be found within chapter 1. Indeed section 1.3 provides an overview of the limitations associated with the use of in situ and remote sensing datasets for elucidation of complex inundation dynamics of floodplains in the Amazon basin, and outlines some of the advantages offered by the application of numerical models to this research area. Hence in this introduction, relevant past hydrological and hydraulic modelling studies undertaken within the Amazon basin are reviewed in a greater level of detail, prior to elucidation of the specific aims of this chapter in section 6.2.

The application of hydrological and hydraulic models represents perhaps the most effective way to elucidate a more detailed understanding of the complex spatial and temporal dynamics of inundation upon Amazonian floodplains. A number of past studies have utilised modelling approaches in order to simulate discharge within Amazonian rivers. Richey et al., (1989) provided one of the earliest attempts to model the Amazon river system, investigating the sources and routing of the flood wave along a the main stem Amazon between Sao Paulo de Olivenca and Obidos. The study applied a Muskingum model in order to predict discharge at 20 cross sections, spaced at intervals of 100 km along the 2000 km reach. Floodplain flows were incorporated into the model using a simple 'bathtub' approach, which assumed that the floodplain storage constant, attenuation coefficient and water levels were equivalent to those in the main channel. Based upon model results the authors were able to estimate discharge characteristics for the reach, whilst illustrating that channel-floodplain interactions are significant for the Amazon, indeed results suggested that 30 % of channel flow is derived from water stored upon the floodplain.

Water balance and transport models have also been applied in order to investigate the hydrology of the Amazon basin. Vorosmarty et al., (1989) simulated mean discharge and flood inundation within Amazonia using water balance and transport models with a spatial resolution of 0.5 degrees. Costa and Foley (1997) utilised a coupled land surface and water transport model at a resolution of 0.5 degrees in order to simulate basin wide discharge. Coe et al.,

(2002) applied the terrestrial ecosystem model IBIS in combination with the HYDRA hydrological routing algorithm to simulate discharge and flood inundation within the Amazon basin since 1939. In the model the total volume of water entering the drainage network was calculated by IBIS based upon historical monthly climatic variables. Water input was subsequently routed through terrestrial hydrological systems by HYDRA, which operated on a grid characterised by a spatial resolution of 9 km. Validation with respect to in situ gauge records demonstrated that the model simulated discharge well within the Brazilian Amazon, but significantly underestimated discharge for other areas of Amazonia. Although the coupled water balance/transport models were able to provide insight into the broad hydrological functioning of the Amazon river system, as a result of coarse grid resolution they were unable to effectively reproduce the spatial and temporal complexity of floodplain hydraulics which were shown to be highly significant by Alsdorf et al., (2007).

The scope of early modelling studies was ultimately limited by the poor level of data provision within the Amazon basin. It is widely acknowledged that an accurate representation of bare earth topography is necessary in order to facilitate the accurate simulation of floodplain flows within hydraulic models (Hunter et al., 2007). This is particularly relevant given the complex hydraulic flow dynamics observed upon Amazonian floodplains (Alsdorf et al., 2005). However, accurate bare earth DEMs are not readily available within this region (Yamazaki et al., 2012). DEMs are commonly derived from LiDAR surveys, which are able to measure ground elevation with a high level of accuracy (Nilsson, 1996). In addition, LiDAR pulses are able to penetrate vegetation canopies, thus subtraction of first and last returns of LiDAR waveforms enables elucidation of both canopy height and ground elevation in forested areas (Means et al., 1999). However due to the remote location and large size of Amazonian floodplains, LiDAR derived DEMs are seldom available for application within flood inundation models in this region.

In the absence of LiDAR surveys, the Shuttle Radar Topography Mission constitutes the best source of topographical data for the majority of the Amazon basin. Whilst offering continuous global coverage and a high level of vertical accuracy for the Beni floodplain, demonstrated within chapter 4, the SRTM dataset is characterised by the presence of systematic positive bias within

forested areas (Rabus et al., 2003). Removal of vegetation biases from the SRTM has proven to be highly problematic, and the resulting dearth of bare earth topographical information has limited the application of hydraulic models within the Amazon basin. Nevertheless, in recent years a limited number of studies have attempted to correct vegetation biases within the SRTM, in order to facilitate modelling of inundation upon parts of the Amazon floodplain.

Wilson et al., (2007) presented the first attempt to apply and validate a two dimensional hydraulic model within the Amazon basin. The study applied LISFLOOD-FP, a simple coupled 1D-2D model (Bates and De Roo, 2000), in order to simulate inundation for a 30,000 km^2 area of floodplain within the Brazilian Amazon. Floodplain topography was derived through a spatially uniform correction of vegetation biases in the SRTM, based upon field observations of canopy height in the study area. The model was subsequently validated with respect to water level measurements acquired by TOPEX/POSEIDON satellite altimetry, inundation extent from JERS-1 imagery and water level observations from in situ gauges. Results demonstrated that the model predicted flood inundation with an acceptable level of accuracy during high water, achieving a fit of between 57-73 % with respect to JERS-1 derived flood extent. Accuracy was poorer (23 %) during low water as a result of an inadequate representation of floodplain dewatering. The spatial resolution of the DEM was 270 m, thus small floodplain channels which are known to be important within the process of dewatering were not resolved. In addition, important floodplain hydrologic processes were not included within the model, thus a lack of infiltration also contributed to the incomplete drainage of the floodplain observed within the model simulations.

The study of Baugh et al., (2013) built upon the previous work of Wilson et al., (2007), applying a new inertial formulation of LISFLOOD-FP (Bates et al., 2010) within the same section of the Central Amazon floodplain. Baugh et al., (2013) utilised an improved floodplain bare earth DEM, in which SRTM forest biases were corrected through application of a global canopy height map (Simard et al., 2011). Validation of model simulations was undertaken with respect to flood inundation extent derived from JERS-1 SAR imagery (Hess et al., 2003), TOPEX-POSEIDON water level measurements and data relating to floodplain water storage volumes derived from GRACE (Alsdorf et al., 2010). Results

demonstrated the improvements in model performance accrued through application of the corrected bare earth DEMs in comparison to the uncorrected SRTM dataset. Accuracy of simulated flood extent at high water improved with respect to JERS-1 observations from an RMSE of 0.52 to 0.07, whilst for low water simulation accuracy increased from an RMSE of 0.22 to 0.12. RMSE values were dimensionless, owing to the method of comparison with SAR flood extent. Improvement in simulated floodplain water surface elevation was also observed, indeed RMSE with respect to TOPEX-POSEIDON data increased from 6.61 m in the uncorrected SRTM to 1.84 m in the bare earth DEM (Baugh et al., 2013).

Although the studies of Wilson et al., (2007) and Baugh et al., (2013) have provided a significant contribution to the understanding of Amazonian inundation dynamics, a number of key issues remain unexplored. Firstly, thus far floodplain inundation has only been modelled within the central Amazon floodplain. Given the vast spatial extent of the basin it remains unclear if inundation dynamics of the central Amazon are typical of Amazonian floodplains more broadly. DEMS used within both of the aforementioned studies were characterised by a spatial resolution of 270 m and thus were not able to resolve smaller floodplain water courses which have been shown to be important for facilitating floodplain flows during wetting and dewatering of the floodplain (Alsdorf et al., 2007). It was hypothesised that the inability to resolve these floodplain channels was partially responsible for a lack of floodplain dewatering observed in Wilson et al., (2007) and to a lesser extent Baugh et al., (2013). Further, despite the hypothesised contribution of clear water flooding (driven by local precipitation) to overall inundation (Aalto et al., 2003; Pouilly et al., 2004), both studies do not include any representation of hydrological processes such as precipitation, infiltration, evapotranspiration or groundwater flows. Rather it is simply assumed that rainfall is balanced by evapotranspiration within the model domain. In addition, within chapter 5 of this thesis the methodologies utilised by Wilson et al., (2007) and Baugh et al., (2013) in order to correct vegetation biases within the SRTM were applied for the Beni floodplain. Quantitative and qualitative assessment indicated that these methodologies were not able to adequately account for the local scale variations in canopy height observed within the study area, leading to under and over prediction of bare earth elevation within substantial areas of the floodplain. A novel method of DEM

generation developed within chapter 5 which was able to better account for spatial variations in canopy height produced a more accurate DEM, when subject to quantitative and qualitative assessment.

Overall, whilst in situ and remote sensing observations have provided useful information relating to Amazonian flood dynamics, it is clear that these data sources are associated with significant limitations in terms of spatial and temporal resolution and or coverage (Alsdorf and Lettenmaier, 2003). Meanwhile it is clear that modelling of flood inundation represents the best approach to elucidation of complex spatial and temporal inundation dynamics observed within Amazonian floodplains (Alsdorf et al., 2007). However numerical modelling of river systems within the Amazon basin remains in a stage of relative infancy, primarily due to the paucity of bare earth topographical data for Amazonian floodplains. To date only a handful of attempts have been made to simulate inundation using two dimensional hydraulic codes, which are able to accurately represent the complex flow dynamics observed upon the Amazon floodplain (Wilson et al., 2007; Baugh et al., 2013). Given the vast spatial extent of floodplains within the Amazon basin and the global significance of its river system, it is clear that further studies are required in order to increase understanding of inundation dynamics within Amazonia. Therefore in this chapter the different bare earth DEMs generated within chapter 5 are applied within a coupled 1D-2D hydraulic model code in order to simulate inundation upon the Beni floodplain. The modelling approach includes a basic representation of floodplain hydrology in addition to a representation of the floodplain channel network. Further, this constitutes the first application of a hydraulic flood inundation model for a tributary of the main stem Amazon located in western Amazonia.

6.2 Research aims

The overall aim of this chapter is to simulate flood inundation upon the Beni floodplain using a coupled 1D-2D flood inundation model, and to quantitatively validate the model with respect to observed datasets derived from remote sensing. Specific objectives are

1. To derive areal flood extent from ALOS PALSAR SAR imagery and water surface elevation from TOPEX-POSEIDON satellite laser altimetry data.

2. To undertake an initial analysis of hydraulic model results in order to assess the sensitivity of simulated inundation characteristics to the use of different DEMs and parameter sets.

3. To correct errors identified within the bare earth DEMs during the initial analysis of model results, through conditioning of the DEMs based upon estimation of local water surface elevation across the Beni floodplain.

4. To quantitatively assess model predictions based upon the new DEMs with respect to remotely sensed observations of flood extent and water surface elevation.

6.3 Model description

6.3.1 Channel and floodplain routing

Numerical simulation of floodplain inundation was carried out using a combined 1D and 2D hydraulic model that uses a finite volume approach to solve the shallow water equations. In this model, flow within the main channel and all other significant floodplain channels is modelled using a 1D approach. Floodplain flow, which occupies the majority of the model domain, is modelled using a 2D scheme. This coupled 1D-2D approach is equivalent to that adopted in simpler storage cell codes based on the diffusion wave form of the St Venant equations, such as LISFLOOD (Bates and De Roo, 2000). The model used here is based on the shallow water equations, which can be written in conservative form as:

$$\frac{\partial h}{\partial t} + \frac{\partial q_x}{\partial x} + \frac{\partial q_y}{\partial y} + S = 0 \tag{6.1}$$

$$\frac{\partial q_x}{\partial t} + \frac{\partial \left(q_x^2 / h\right)}{\partial x} + \frac{\partial \left(q_x q_y / h\right)}{\partial y} + \frac{g}{2}\frac{\partial \left(h^2\right)}{\partial x} + gh\frac{\partial z}{\partial x} + \frac{\tau_{bx}}{\rho} = 0 \tag{6.2a}$$

$$\frac{\partial q_y}{\partial t} + \frac{\partial \left(q_y^2 / h\right)}{\partial y} + \frac{\partial \left(q_x q_y / h\right)}{\partial x} + \frac{g}{2}\frac{\partial \left(h^2\right)}{\partial y} + gh\frac{\partial z}{\partial y} + \frac{\tau_{by}}{\rho} = 0 \tag{6.2b}$$

where h is flow depth; t is time; q_x and q_y are unit discharge in the x and y directions; S is a hydrological source term that includes the balance between precipitation, evapotranspiration and infiltration, g is acceleration due to gravity;

ρ is fluid density; z is bed elevation; and τ_{bx} and τ_{by} are bed shear stresses in the x and y directions, which are modelled using a quadratic friction law

$$\frac{\tau_{bx}}{\rho} = \frac{g}{(Ch)^2} q_x \sqrt{q_x^2 + q_y^2} \tag{6.3a}$$

$$\frac{\tau_{by}}{\rho} = \frac{g}{(Ch)^2} q_y \sqrt{q_x^2 + q_y^2} \tag{6.3b}$$

where C is the Chezy friction coefficient.

In the 2D model, x and y directions are aligned with the model grid cell edges (ie perpendicular to one another). In the 1D element of the model that is used to represent channel flow, equations (6.2b) and (6.3b) are neglected, as are all terms in the remaining equations in the y direction. Moreover, the 1D model solves for the unit discharge (q_x) in the downstream direction (ie parallel to the local channel bankline orientation). Coupling of the 1D and 2D model components is achieved by mapping channel depths and unit discharges calculated in the 1D scheme back onto the 2D grid used to represent floodplain flow. This allows mass and momentum fluxes across faces between channel and floodplain cells to be calculated using the 2D scheme, to facilitate the simulation of flow into and out of the channel.

6.3.2 Floodplain hydrology component

The hydrological source term (S) in equation 6.1 represents the net balance between precipitation, evapotranspiration and infiltration. Previous applications of large-scale floodplain inundation models in the Amazon basin have neglected these processes (Wilson et al., 2007; Baugh et al., 2013) and have dealt only with water entering and leaving the channel/floodplain system through the model domain inlet and outlet. Aalto et al. (2003) hypothesise that marked inter-annual differences in floodplain hydraulics are controlled by the degree to which floodplain inundation is driven by local precipitation, hence in this study it was deemed appropriate to include a simple representation of these hydrological processes. To achieve this, each floodplain grid cell is characterised by a sub-surface soil water store of constant maximum depth (D). Time series of precipitation and potential evapotranspiration are used to drive the model (see below for a summary of how these time series were generated). During each

model time step, precipitation is added to the surface water depth (h) in each floodplain cell. Evapotranspiration is removed from the surface water depth or, if the floodplain cell is not inundated (h=0), evapotranspiration is removed from the soil water store (unless the soil water store is empty). Surface water is allowed to infiltrate to the soil water store at a rate (IR) given by:

$$IR = I_{MAX}\left(1 - d / D\right) \tag{6.4}$$

where I_{MAX} is the maximum infiltration rate and d is the depth of water in the soil water store, thus infiltration rates decline as the soil moisture store becomes full. Water drains from the soil moisture store to groundwater at a constant fractional rate (i.e. a constant fraction F of the soil moisture d is lost each day). Although the soil water store is allowed to drain in this way, there is no treatment in the model of groundwater flows or the return of sub-surface water to the surface. These processes are likely important in the context of the long-term hydrological functioning of the Llanos de Moxos wetland complex. However, representation of groundwater flows is beyond the scope of this thesis. Moreover, the data required to define initial conditions are not available for the model domain, hence the soil water store is assumed to be empty at the start of simulations (d=0). While this may be reasonable for the immediate soil surface during the dry season (Haase and Beck, 1989; Hanagarth, 1996) it would not be a suitable approach to initializing a groundwater model unless simulations were carried out with a long “spin-up” phase to allow the model to reach equilibrium.

Drainage of water from the soil water store, combined with the neglect of groundwater flow, results in a small loss of water from the floodplain system in the long-term. In reality, this water may contribute to surface flow (e.g., in floodplain channels) during baseflow conditions. Consequently, dry season channel flows may be slightly under-predicted by the model. However, since the primary goal of this modelling exercise is to simulate floodplain inundation during high flows, under-prediction of dry season flows is not a significant concern. Overall, the treatment of hydrological processes outlined above is less sophisticated than that adopted in several catchment-scale hydrological models that have been implemented in the Amazon (Coe et al., 2008). However, it represents an advance on the treatment of these processes in similar hydraulic

modelling studies (Wilson et al., 2007; Baugh et al., 2013) and provides a first order representation of the floodplain water balance. Moreover, simulation results presented below demonstrate that the model is significantly less sensitivity to hydrological process representation than to the choice of floodplain DEM, representation of surface roughness or channel bed elevation.

6.3.3 Finite volume solution for model equations

Model equations are solved by explicit time integration using a finite volume scheme in which all variables are stored at the cell centers. The solution of fluid mass and momentum equations utilizes a first order Godunov scheme, in which mass and momentum fluxes are computed using the HLL approximate Riemann solver (Harten et al., 1983). The model time step (t) is defined to satisfy the Courant-Friedrichs-Lewy (CFL) stability criterion (effectively, the time step is set to be smaller than the time required for water to cross any individual model grid cell). The numerical schemes adopted here are first order accurate in time and space, which means that mass and momentum fluxes across cell faces are calculated directly using the values of variables in the cells either side of the face, rather than first calculating variable values at the grid cell faces using a higher order interpolation scheme. Higher order (e.g., second order accurate in time and space) Godunov schemes are commonly used to solve the shallow water equations in a range of applications including the simulation of within-channel flows, floodplain inundation and dambreak floods (Fraccarollo and Toro, 1995; Mingham and Causon, 1998; Begnudelli et al., 2010). A higher order version of the 2D scheme used here forms the basis of the morphodynamic model HSTAR (Nicholas et al., 2013) and has previously been validated using acoustic Doppler current profiler data collected in a large sand-bed river (the Rio Paraná, Argentina), as described by Nicholas et al. (2012). A first order accurate numerical scheme is adopted here because this greatly increases model efficiency. This is important in the context of the large spatial scale of the current application. Use of a first order scheme is common in large-scale flood models, such as LISFLOOD (Bates and De Roo, 2000; Bates et al., 2010), and more simplified cellular automaton models that have been used to represent floodplain inundation (Coulthard et al., 2007; Van de Wiel et al., 2007). The current model has several advantages over these alternative approaches. In particular, the form of the shallow water equations used here

includes the spatial acceleration terms that are neglected in these simpler models. Moreover, the Godunov scheme adopted here is unconditionally stable where the CFL condition is met, and is ideally suited to simulation of the inundation of initially dry land, and to the representation of transitions between sub and super-critical flow.

6.3.4 Quadtree grid structure

In order to increase numerical efficiency further, the hydraulic model is implemented using a quadtree grid (figure 6.1, see also Liang et al., 2008), which comprises a set of nested regular grids at a range of spatial resolutions. Cell size increases by a factor of two as one moves from each level in the hierarchy of grids to the next, effectively meaning that each cell is divided into four smaller cells. Model grids used in the current study use a hierarchy with five levels, with minimum and maximum cell sizes of 270 m and 4320 m. The minimum cell size used here matches that used in past large-scale floodplain inundation simulations conducted for tropical rivers in similar environments (Wilson et al., 2007). This cell size was chosen to represent a simple multiple of the SRTM dataset resolution (90 m) and to equate to roughly half the main channel width (c. 450 m).

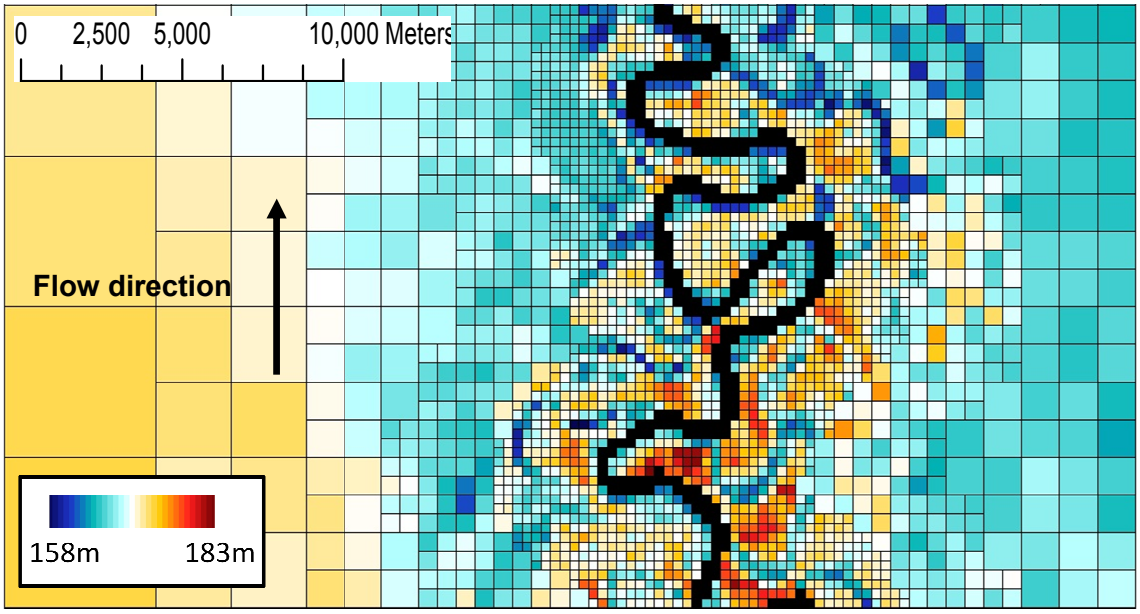

Figure 6.1. Quadtree grid structure used on floodplain, showing portion of model domain including grid cell sizes ranging from 270 m to 4320 m. Grid elevation is derived from the INT DEM and is indicated by the colour scale. Channel cells (those overlain by the 1D channel network) are shaded black and the arrow denotes flow direction.

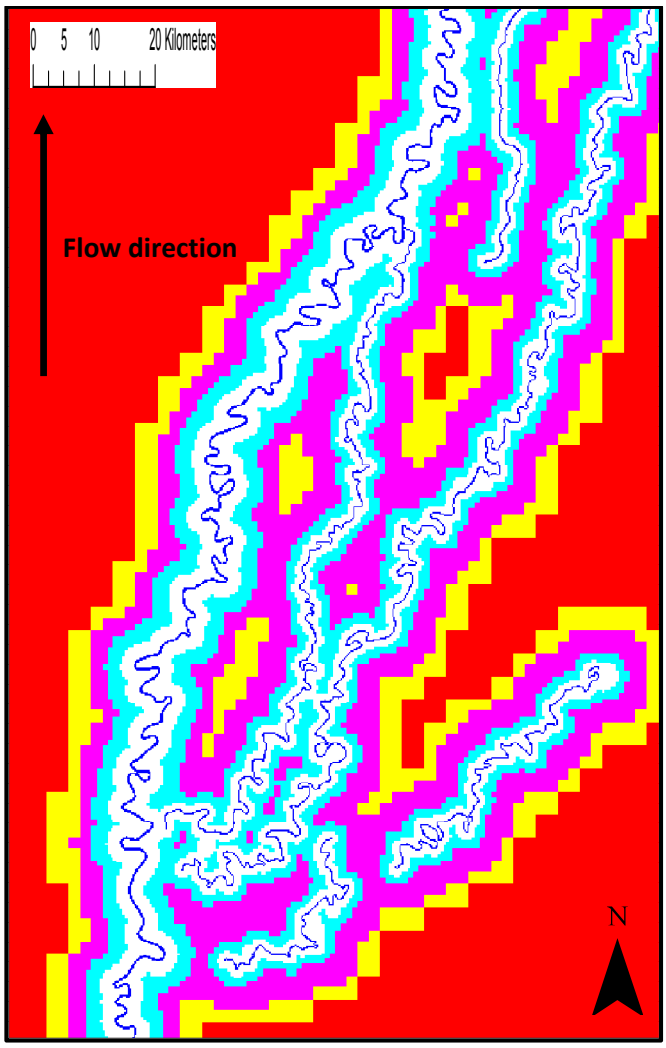

Figure 6.2. Spatial pattern of model grid resolution: White (270 m); pale blue (540 m); magenta (1080 m); yellow (2160 m); red (4320 m). Dark blue lines represent the Rio Beni and floodplain channels.

6.4 Model application

The model code described above was applied to a ~200 km reach of the Beni river and its adjacent floodplain downstream of Rurrenabaque, illustrated in figure 6.3. The model inlet was located at Rurrenabaque where the river emerges from the sub Andes into its foreland basin, whilst the downstream limit of the model domain is located upstream of the confluence of the Rio Beni and the Rio Madidi. Model simulations were undertaken for two separate time periods; 01/09/1997-31/08/2000 and 01/09/2009-31/08/2011 which correspond with the availability of remotely sensed datasets for model validation. Table 6.1 provides further information on the simulation periods, whilst section 6.5 contains further details on the remote sensing datasets used for validation.

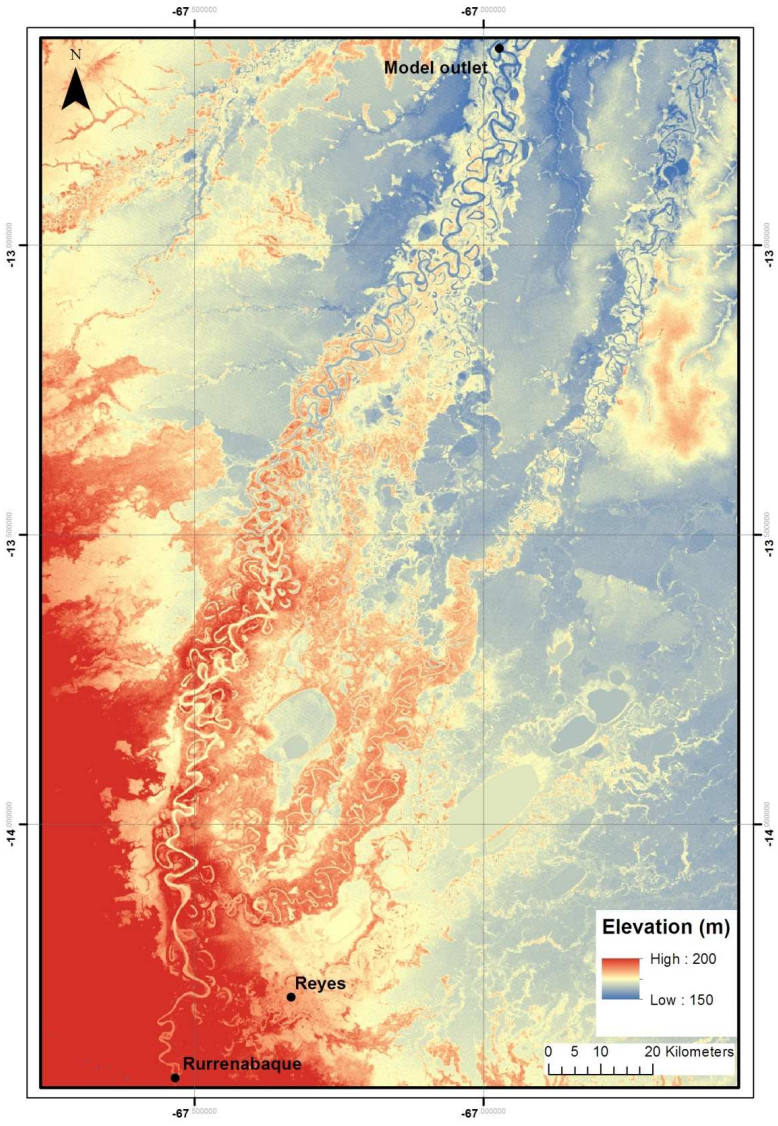

Figure 6.3. Extent of the Rio Beni flood inundation model domain illustrating the location of the inlet at Rurrenabaque and the downstream limit constituted by the confluence with the Rio Madidi. Elevation corresponds to the uncorrected SRTM dataset.

Table 6.1. Details of the two model simulation periods and validation datasets.

Simulation	Start date	End date	Days	Sensor	Variable
a	01/09/1997	31/08/2000	1096	TOPEX-POSEIDON	Water surface elevation
b	01/09/2009	31/08/2011	730	ALOS PALSAR	Inundation extent

6.4.1 Beni floodplain topography and roughness representation

Implementation of the model requires the definition of surface elevation and roughness within each grid cell in the model domain. Three separate model grids were constructed using the bare earth DEMs generated by removing vegetation from the SRTM using the approaches described in chapter 5. The SRTM-derived DEMs used in the modelling were the FAV DEM, GCHP DEM

and the INT DEM, these were selected based upon performance with respect to quantitative and qualitative validation. In order to construct a model grid, the elevation in each model grid cell was set equal to the average elevation for all 90 m cells in the SRTM-derived DEMs contained within the given model cell. Spatial patterns of surface roughness in the model domain were defined using the results of the land cover classification procedure described in chapter 3. Initial simulations were carried out using nine land cover roughness classes. However, due to the difficulty of defining appropriate roughness parameter values, combined with the fact that model sensitivity to roughness was found to be less than sensitivity to the model DEM, this scheme was simplified to include just three classes: channel, forested floodplain and non-forested floodplain.

Table 6.2. Details of the different roughness set ups used in model simulations.

Land cover	Roughness set up (Chezy values $m^{0.5}s^{-1}$)		
	Low	Medium	High
Channel	50	40	30
Forested floodplain	12.5	10	7.5
Non-forested floodplain	25	20	15

Moreover, each model grid cell was simply assigned a roughness class representative of the dominant land cover in that cell (i.e. roughness values were not calculated as the sum of roughness contributed by different land cover types weighted by area). Appropriate roughness values were estimated using values given the literature (Mertes, 1990; Straatsma and Baptist 2008; Trigg et al., 2009;) either for Chezy roughness or for Mannings roughness, with the latter converted to a Chezy value assuming a nominal floodplain flow depth of 1 m. Based upon these estimates, three roughness set ups were established for application within model simulations, detailed in table 6.2.

6.4.2 Representation of the Beni channel and floodplain watercourses

Model implementation also requires the definition of the bed elevation along each of the channels represented using the 1D hydraulic model. This was achieved by defining the long profile of the bank top elevation for each channel, and then deducting from this a constant estimate of the channel depth. A channel depth estimate for the main Rio Beni of c. 11 m was derived using a Chezy resistance law to determine the depth required to convey the estimated

bankfull discharge of 6000-7000 m^3s^{-1} (Gautier et al., 2007; 2010; Environmental Research Observatory (ORE) HyBAm) for the mean channel width (450 m) and slope (0.1 m m^{-1}), based on the intermediate estimate of the main channel Chezy roughness coefficient (40 $m^{0.5}s^{-1}$). This approach implies a constant channel depth throughout the model domain, and hence neglects the possible effects of changes in slope and channel sinuosity. However, a survey conducted as part of project (NE/H009108/1) found no significant downstream change throughout the study reach in bank height relative to the low flow water surface, hence the assumption of constant channel depth at large spatial scales is acceptable here.

The location and width of floodplain channels within the model domain was determined through manual digitisation, based upon Landsat TM multispectral imagery. Each individual floodplain channel was assumed to have a constant width within the model domain, and channel depths were estimated by assuming a constant width:depth ratio equal to that of the main Rio Beni (c. 40). Bank top elevation profiles for each channel were obtained from the SRTM-derived DEMs by extracting elevation from all 90 m floodplain pixels adjacent to the active channels. For the main channel, bank top elevation surveys discussed above provided an additional source of data. However, because these surveys did not extend throughout the whole model domain, because they were collected 11 years after the SRTM dataset, and because no equivalent data were available for other floodplain channels, a consistent approach was adopted for all channels based upon SRTM-derived floodplain elevations. Despite this, it should be noted that bank top elevation data from the field surveys were used to define the elevation of channel-adjacent locations during the construction of the first order bare earth DEM utilized in the generation of the INT DEM.

Long profiles of bank top elevation generated by extracting elevations from the SRTM-derived DEMs were characterised by a high degree of vertical variability, due to noise that is an inherent feature of these DEMs in the presence of vegetation. This leads to unrealistic low and high points in the bank top location, and hence peaks and troughs in the channel bed. To overcome this problem, bank top long profile elevations for use in the model were derived by fitting low order polynomials to the extracted elevation dataset. This approach captures

the main downstream trend in the bank height, but removes the local variability associated with noise in the SRTM data. It should be noted that one implication of extracting elevations from the SRTM-derived DEMs is that channel long profiles differ for each of the three model DEMs. Observations made during the initial phases of model testing suggested that simulated inundation was associated with a high level of sensitivity to the defined channel bed elevation, therefore two additional channel bed elevation configurations were utilised within model simulations. In the first additional configuration channel bed elevation was raised by 1 m, whilst in the second configuration channel bed elevation was raised by 2 m. For ease of explanation, default channel bed elevation is herein referred to as low channel bed, whilst the configurations in which elevation was raised by 1 m and 2 m are referred to medium and high channel bed elevation respectively.

6.4.3 Upstream boundary condition

The upstream boundary condition for the model was constituted by a discharge hydrograph measured at a gauging station located in Rurrenabaque and was supplied by ORE HYBAM. Rurrenabaque thus constituted the inlet of the modelled reach. The hydrograph provided discharge measurements which dated back to 1967 and was characterised by a temporal resolution of 1 day. Checking of the consistency of the hydrograph revealed the presence of gaps in the discharge record, however these gaps were no longer than two days in length and were filled using simple linear interpolation. Discharge hydrographs for the 3 simulated periods are shown in figure 6.4.

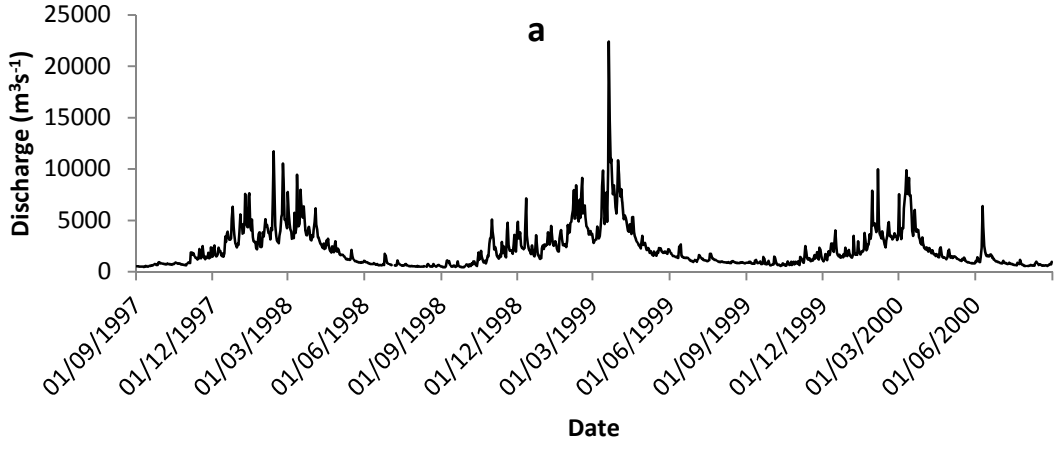

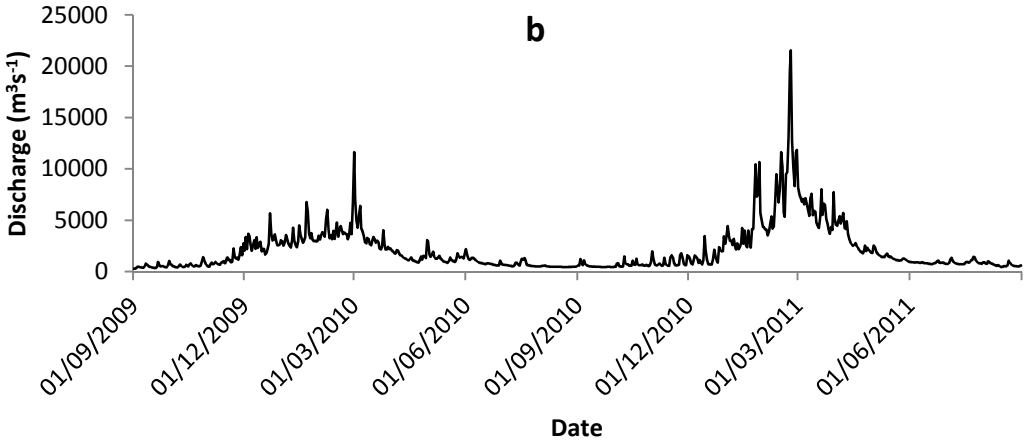

Figure 6.4. Discharge hydrographs from the Rurrenabaque gauge for the simulated periods a (TOPEX-POSEIDON altimetry) and b (ALOS PALSAR inundation extent).

6.4.4 Rainfall input

The final datasets required to implement the numerical model are the hydrological inputs to the model domain, namely precipitation and evapotranspiration. Here a historical time series of daily precipitation was supplied by the Bolivian Meteorological Service for the town of Rurrenabaque, which provided a high quality gauged record dating from 1970 to the present. The distribution of meteorological stations in Bolivia is sparse, hence Rurrenabaque constitutes the only location within the study area where a continuous record of rainfall is available which encompasses each of the periods to be modelled here. Time series of rainfall for the different simulation periods are illustrated in figure 6.5. However, given the large extent of the study area it was deemed that uniform application of this single gauged record across the model domain did not constitute an appropriate representation of spatial variability.

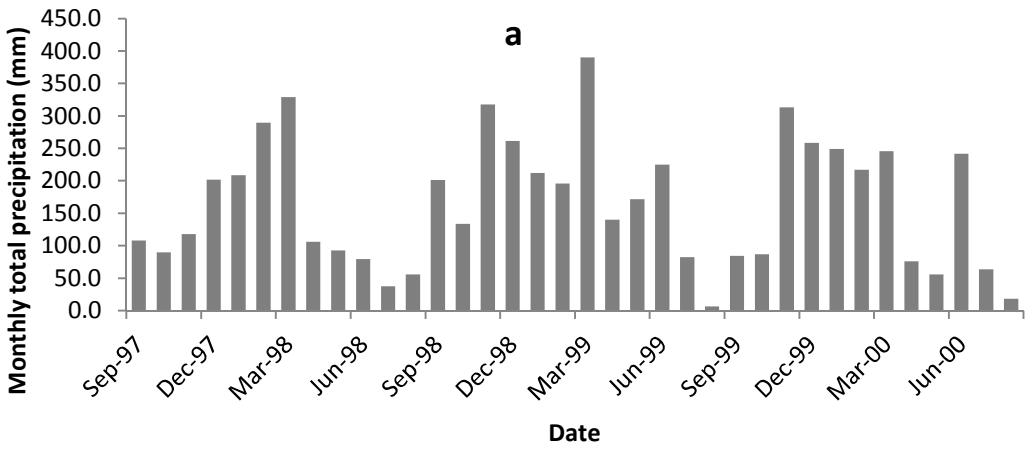

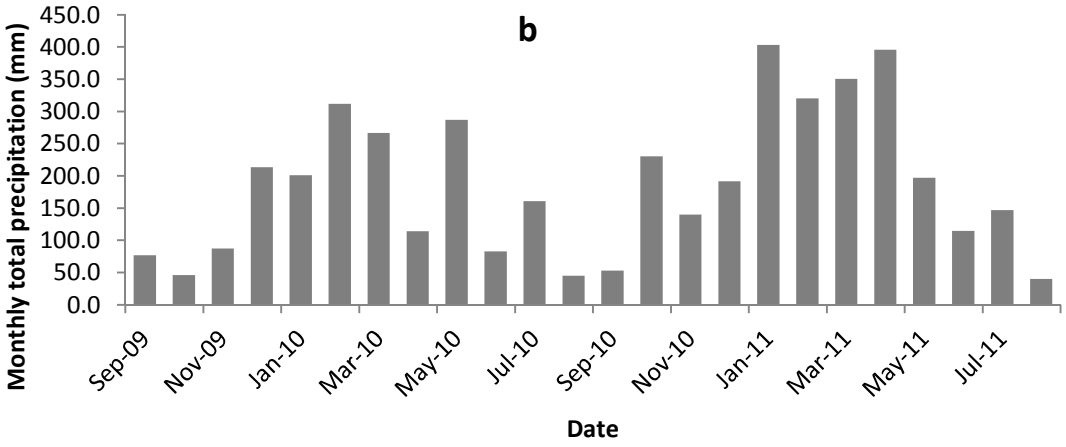

Figure 6.5. Gauged monthly precipitation totals at Rurrenabaque for modelled periods a and b.

The Tropical Rainfall Measuring Mission (TRMM) presented an ideal means to investigate and account for the spatial variability in rainfall across the model domain. TRMM was launched in November 1997 as a partnership between the NASA and the Japanese Space Agency JAXA (Kummerow et al., 2000). The satellite carried a number of instruments in order to facilitate measurement of the atmospheric rainfall column including a 13.8 GHz electronic scanning radar known as the Precipitation Radar along with TRMM Microwave Image (TMI), a passive microwave radiometer in addition to a Visible and Infrared Scanner and Radiometer (Simpson et al., 1996). Thus TRMM constituted the first spaceborne radar instrument capable of measuring precipitation in tropical regions (Adler et al., 2000). TRMM rainfall data has been utilised extensively in tropical climatology studies and validation with respect to ground measurements has demonstrated a high level of agreement (Nicholson et al., 2003; Woolf et al., 2005)

Here the TRMM 3B43 Version 7 data product was obtained from the NASA Goddard Earth Sciences Data and Information Services Center for the period 1998-2012. The 3B43 algorithm produces best estimate precipitation rate (mm/hr) through combination of TRMM and ancillary satellite and ground based datasets. This monthly dataset is available in a gridded format with a spatial resolution of 0.25 degrees. A number of climatologists are currently utilising the strengths of both TRMM rainfall (continuous spatial coverage) and local rain gauge network (highly accurate, extended temporal record) measurements in order to generate spatially distributed historical rainfall datasets within Bolivia (G.Drapeau personal communication), however these datasets were not

available for utilisation here. The implementation of a similar analysis was considered beyond the requirements of this model application, hence a simpler approach was adopted here.

Initially the monthly TRMM rainfall rate grids (mm/hr) were imported into ArcGIS and the monthly rainfall total was calculated for each grid cell (mm). Daily rainfall at the Rurrenabaque gauge was aggregated to produce annual total rainfall for the period from 1998-2012, which was subsequently compared to the monthly precipitation totals extracted from the TRMM grid cell encompassing the Rurrenabaque gauge. This comparison, illustrated in figure 6.6, demonstrated a relatively good level of agreement between remotely sensed and in situ measured rainfall. An additional spatial analysis shown in figure 6.7 indicated that rainfall at Rurrenabaque was well correlated with rainfall across the model domain. The agreement observed in figures 6.6 and 6.7 demonstrated the feasibility of extrapolating gauged measurements of rainfall recorded at Rurrenabaque, in order to account for spatial variability of precipitation across the model domain.

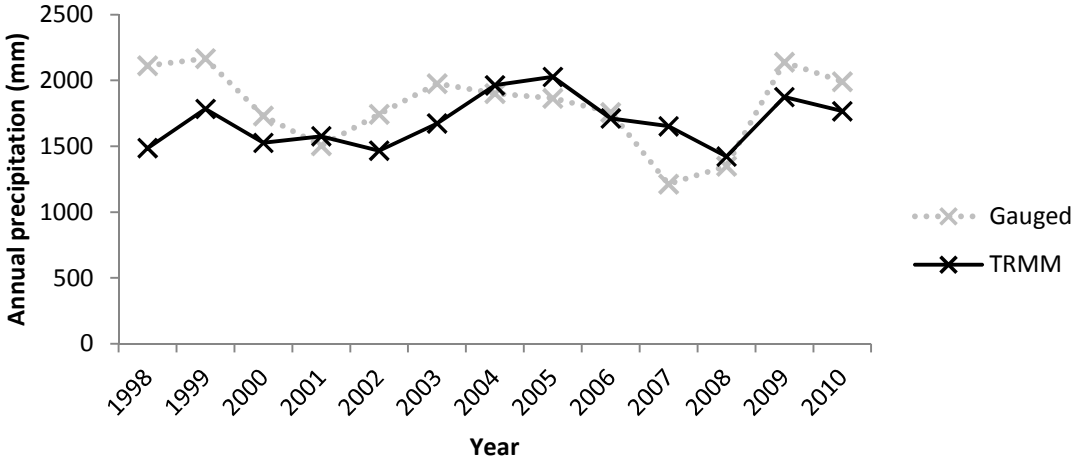

Figure 6.6. Annual total precipitation at Rurrenabaque measured by an in situ rain gauge and derived from the TRMM grid cell encompassing Rurrenabaque.

The application of simple correction factors presented one approach by which to extrapolate the gauged precipitation record across the model domain. In this approach a multiplication factor was established for each TRMM cell based upon the average deviation of rainfall in the cell from gauged rainfall at Rurrenabaque during the period from 1998-2012. This deviation was expressed

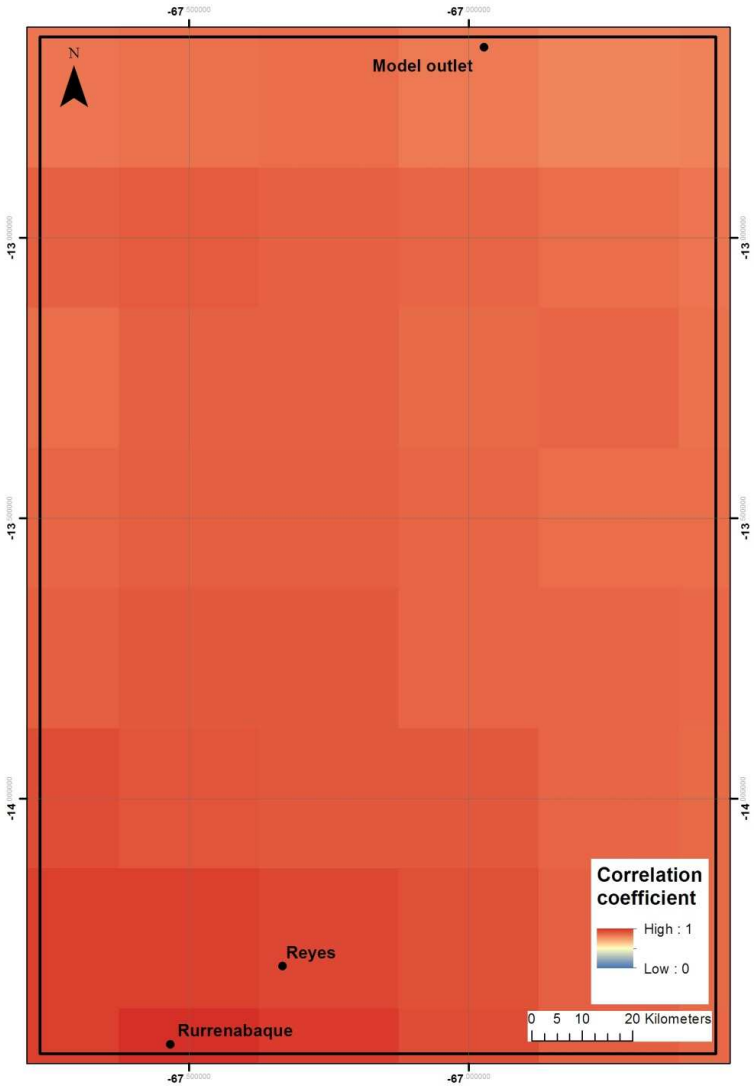

Figure 6.7. Correlation between monthly total rainfall at Rurrenabaque and monthly rainfall totals within TRMM cells located within the model domain for 1998-2010 (n=164).

as a fraction of the rainfall observed at Rurrenabaque, varying spatially across the model domain but remaining constant through time. The second approach was constituted by the application of linear regression models in order to relate monthly precipitation in any given TRMM cell with monthly gauged rainfall at Rurrenabaque over the 1998-2012 period. The two approaches were tested, with both approaches offering a similar level of performance when utilised in order to reproduce a partial gauged record of rainfall at Reyes (figure 6.8-6.10). In the absence of a notable difference in performance, the multiplication factor approach was adopted as it was associated with a higher level of computational efficiency when applied within the model. The final grid of multiplication factors for the Beni floodplain is illustrated in figure 6.11.

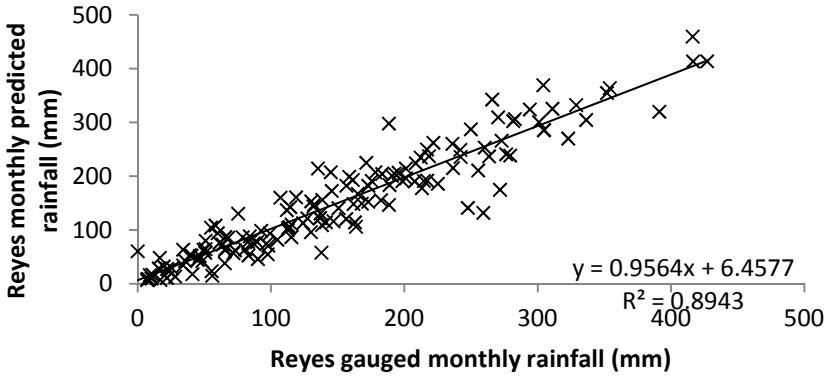

Figure 6.8. Scatter graph showing fit between a gauged monthly rainfall record located at Reyes, and the rainfall predicted for Reyes based upon the application of a multiplication factor to the gauged record of precipitation at Rurrenabaque.

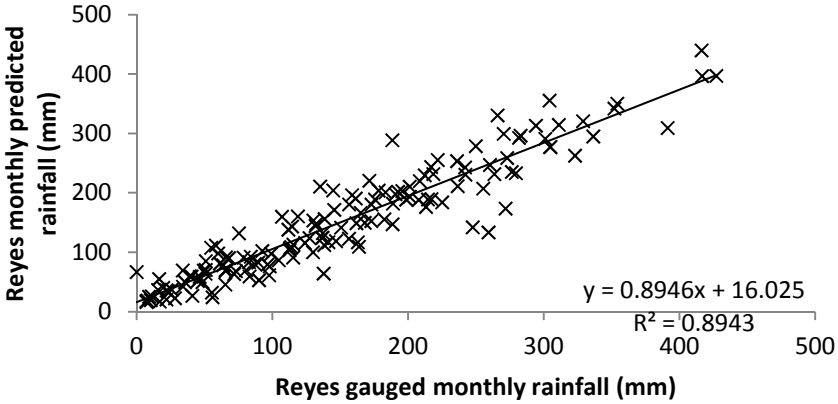

Figure 6.9. Scatter graph showing the level of fit between a gauged monthly rainfall record located at Reyes and the rainfall predicted for Reyes based upon the application of a linear regression model to the gauged record of precipitation at Rurrenabaque.

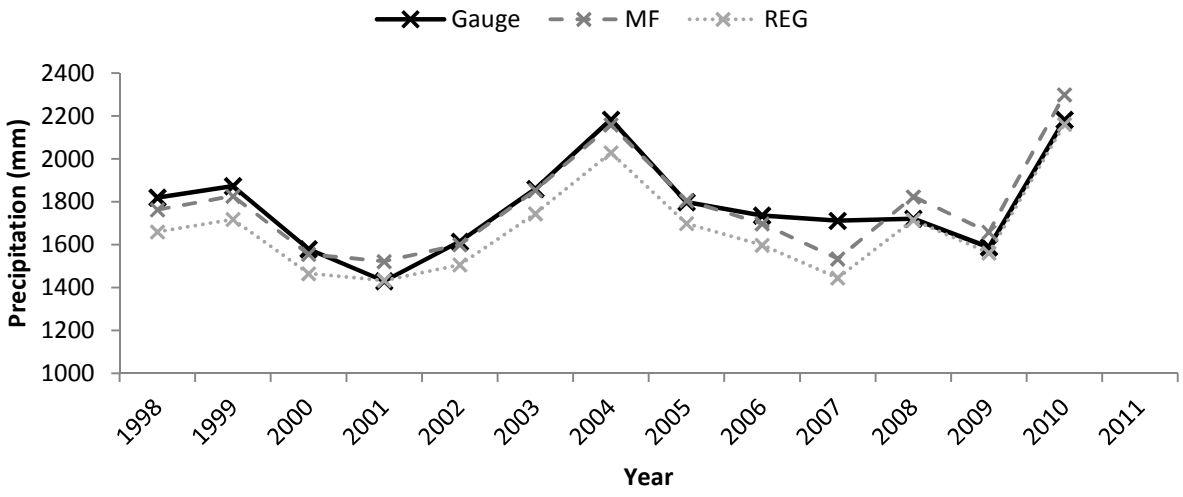

Figure 6.10. Annual total precipitation observed at Reyes from 1998-2010 in addition to predicted annual rainfall based upon extrapolation of the Rurrenabaque gauged record through application of a multiplication factor (MF) and linear regressional model (REG).

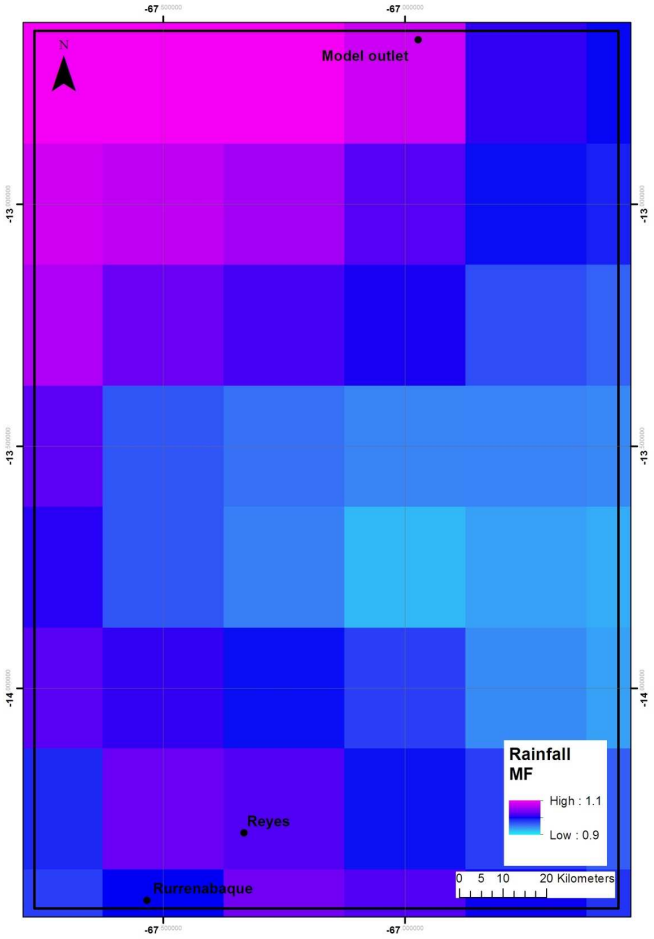

Figure 6.11. Spatial grid of multiplication factors for rainfall within the model domain.

6.4.5 Evapotranspiration

It was also necessary to provide a time series of evapotranspiration as an input into the model. Direct measurement of evapotranspiration is difficult to undertake in the field (Anderson et al., 2011) and no accurate records of evapotranspiration were available for the Rio Beni study area. In lieu of in situ measurements, evapotranspiration data for the study area were provided through the MODIS MOD16 evapotranspiration product. MOD16 represents land surface evapotranspiration comprising all transpiration by vegetation and evaporation from canopy and soil surfaces. ET is calculated from MODIS land cover, Fraction of Photosynthetically Active Radiation (FPAR), Leaf Area Index (LAI) and global surface meteorology data through the updated ET algorithm of Mu et al., (2011), which is based upon the Penman-Monteith equation (Monteith, 1965). A full description of the MOD16 dataset and algorithm can be found in Mu et al., (2011). Here MOD16 monthly actual evapotranspiration data

with a spatial resolution of 1 km were obtained for a 12 year period from January 2000 to December 2011 via ftp from The University of Montana Numerical Terradynamic Simulation group http://www.ntsg.umt.edu/project/mod16 .

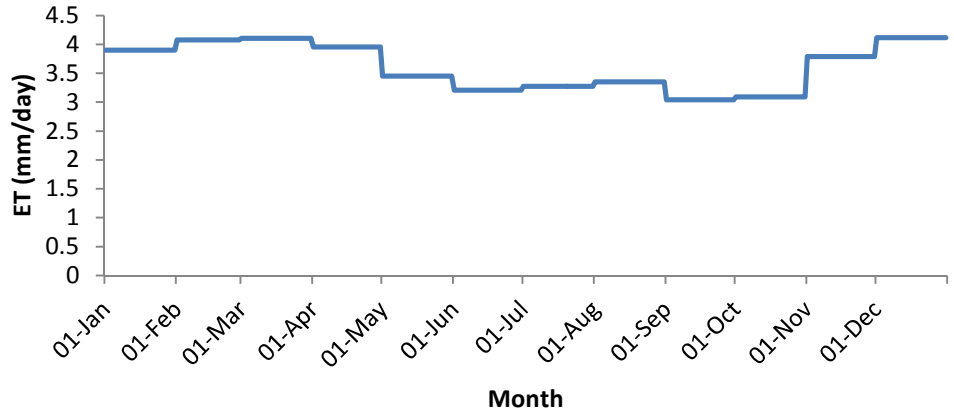

Figure 6.12. Annual cycle of actual evapotranspiration calculated at Rurrenabaque, based upon MOD16 data from 2000-2012.

In order to effectively simulate floodplain hydrology the inundation model required an input time series of evapotranspiration with a length commensurate to rainfall gauge records (1970-2012). This was problematic given that MOD16 ET data was only available from January 2000. Evapotranspiration is a complex process driven by multiple land surface and meteorological variables, hence it was not possible to extend the MOD16 ET time series to 1970 through correlation with rudimentary meteorological variables (ie rainfall and temperature) recorded in Rurrenabaque. Therefore a simple approach was utilised in order to characterise the typical annual cycle of ET within the study area. MOD16 grids of evapotranspiration were loaded into ArcGIS, subset to the extent of the Rio Beni study area and aggregated to a spatial resolution of 0.25 degrees, commensurate with the TRMM precipitation data. For the grid cell encompassing Rurrenabaque the average total ET for each month was calculated over the 12 year period. The average total ET was subsequently divided by the number of days in each month in order to produce a daily estimate of ET. This generated an annual time series of daily ET for Rurrenabaque, illustrated in figure 6.12, which was applied uniformly to each year from 1970-2012. As for precipitation, a complex analysis of spatial variation in evapotranspiration was beyond the scope of this thesis. Hence spatial variation in ET was accounted for in the model domain through

calculation of multipliers for each model cell, using the same methodology, as detailed for precipitation. The spatial distribution of evapotranspiration multipliers across the model domain is illustrated in figure 6.13

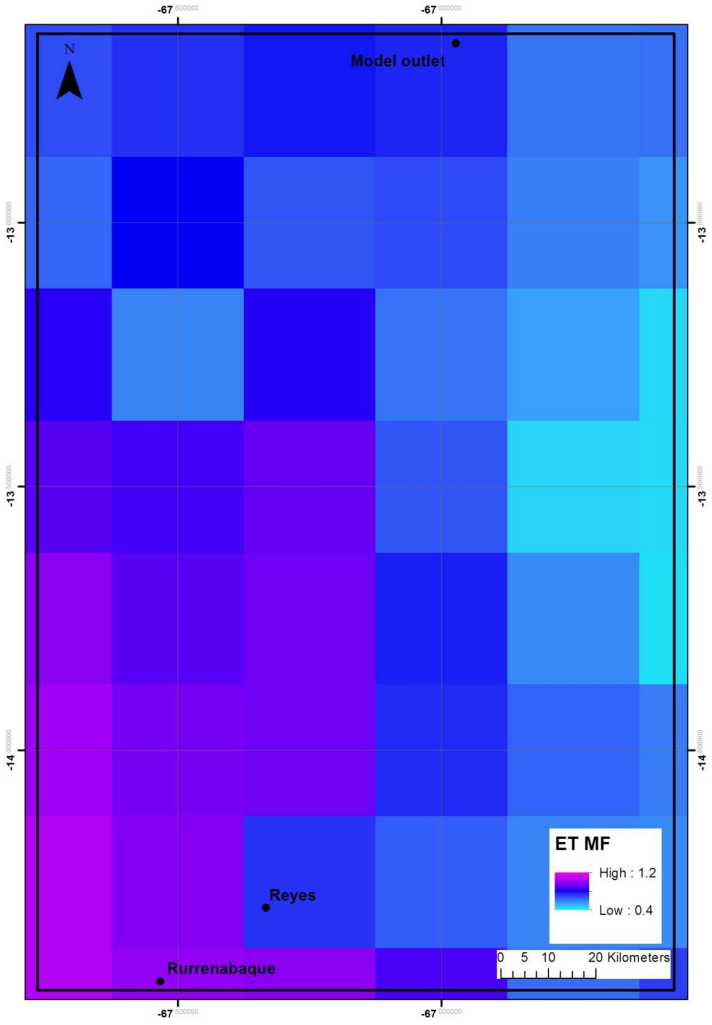

Figure 6.13. Spatial grid of multiplication factors for evapotranspiration within the model domain.

6.5 Datasets for model testing

6.5.1 TOPEX/POSEIDON satellite altimetry data

TOPEX/POSEIDON was a radar altimetric mission which operated from September 1992 to January 2006 (Campos et al., 2001). Satellite altimeters such as T/P are nadir viewing sensors which are able to calculate altimeter range, which corresponds to the distance from the instrument to the Earths surface, through measurement of the time delay from emission of microwave pulses and detection of returned echoes (Birkett et al., 2002). Range measurements can be used to calculate Earth surface topography through accurate location of the satellite within its orbit and the application of

appropriate geophysical correction factors. T/P operated in a repeat orbit with a return frequency of 10 days, during which a total of 254 ascending and descending passes were made. Hence two on board altimetric instruments repeatedly measured mean surface height of the Earth along ground tracks at regular intervals of 580 m every 10 days (Zakharova et al., 2006).

Although originally commissioned by the space agencies of the United States and France (NASA/CNES) in order to measure sea surface elevation, T/P data has proved useful within a number of continental hydrological studies. Radar altimeters are able to measure the elevation of water surfaces through cloud cover and have also demonstrated the ability to measure water level beneath vegetation canopies (Birkett, 1998). Hence T/P is able to measure the water surface elevation of rivers, providing stage data at locations where in situ gauge data is not available, whilst also measuring the height of wetlands and flood waters (Campos et al., 2001). Data from T/P has proved valuable within hydrological studies of the Amazon basin, which despite constituting the largest fluvial system in the world, is marked by a dearth of in situ gauged data. Birkett (1998) utilised T/P data in order to monitor stage at several locations along the Amazon and Solimoes rivers, finding that the altimeter derived water level time series was associated with an RMS of less than 75 cm with respect to gauged data.

The utilisation of T/P data within continental hydrological studies is not without limitations, which can be attributed to the fact that the mission was designed to acquire data for large water bodies such as seas and oceans. Data quality in terrestrial locations is heavily influenced by topographical variation and the presence of different surfaces within the altimeter footprint, whilst the extent of the target water body is also important (Birkett, 1998). Each reported measurement in T/P data corresponds to the average of a maximum of 10 radar echoes. For a larger water bodies the altimeter has a greater chance of achieving a lock increasing the number of echoes averaged for each T/P measurement (Campos et al., 2001). In contrast, for smaller water bodies the averaging of fewer echoes increases the uncertainty of altimeter measurements. Data coverage also presents a significant limitation for the application of T/P in continental hydrological studies. Ground tracks are spaced at a distance of approximately 315 km, whilst the along track ground spacing of

measurements is approximately 580 m. Whilst this enables measurement of water level at multiple locations along large rivers such as the Amazon main stem, smaller rivers may not be observed (Campos et al., 2001).

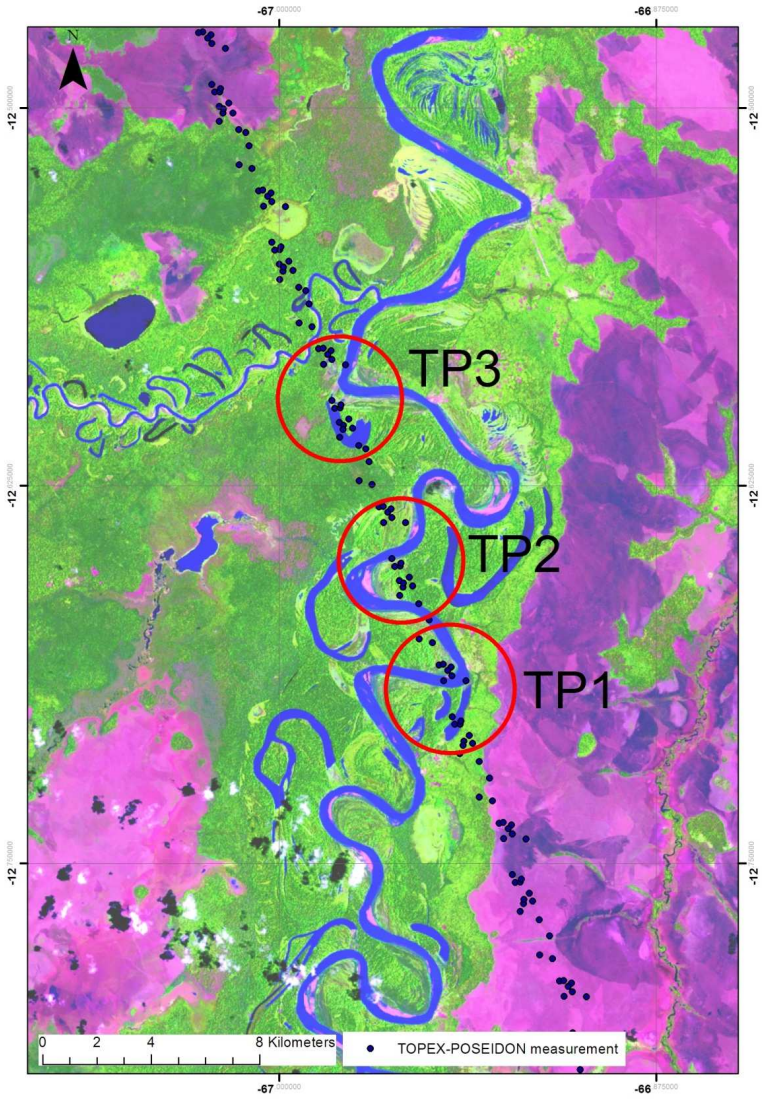

Figure 6.14. TOPEX-POSEIDON footprint locations corresponding to the channel and proximal floodplain area. Time series extracted from these footprints are illustrated in figure 6.17.

For this study TOPEX/POSEIDON data was obtained for pass 201 over a three year period between September 1997 and September 2000. The data was downloaded in the form of Geophysical Data Records (GDRs) via ftp from the NASA PODAAC http://podaac.jpl.nasa.gov/OceanSurfaceTopography/TOPEX-POSEIDON . GDRs contain altimetric data along with a series of geophysical correction factors, which are included in order to facilitate calculation of Earth surface elevation. Whilst range correction models have been optimised over open ocean, the choice of correction factors is less well defined for continental hydrological studies particularly given that certain geophysical variables are not

included over land areas. Following the processing methodology of Campos et al., (2001), here ionospheric, dry tropospheric and solid Earth tide geophysical corrections were applied along with the geoidal correction.

A single TOPEX-POSEIDON ground track (201) intersects the Beni floodplain study area. As is evident within figure 6.16, the location of measurements for each T/P footprint varies with each repeat measurement, therefore water surface elevation time series for individual footprint locations along the ground track were constructed through grouping of the measurements according to latitude and longitude. An initial analysis of the TOPEX POSEIDON dataset revealed that relatively few water surface elevation time series for the study area showed evidence of meaningful seasonal variation which would be expected for the Beni river. Those time series which did demonstrate clear seasonal variation corresponded to the location of the Beni river channel. The provision of a small number of meaningful water level time series for the Beni floodplain study area is not unexpected, indeed Birkett et al., (2002) analysed 230 target T/P footprints within the central Amazonia, finding that only 30-50 % of footprints provided reliable water level time series. This can be attributed to the T/P sensor failing to achieve a 'lock' on small water bodies (Birkett et al., 2002).

Three water level time series were extracted from locations corresponding to the Beni channel and proximal floodplain area for display here (figure 6.16), these time series are illustrated in figure 6.17. TP1 and TP2 both appear to reflect seasonal variability of water level within the Beni channel. The TP3 time series was omitted from the analysis due to a lack of seasonal variation (figure 6.17c). Both TP1 and TP2 appeared to reflect the water level variations which would be expected within the Beni, although based upon visual assessment and analysis of metadata TP1 was judged to be of a higher quality than TP2. As a result TP1 was utilised for model assessment. In order to facilitate comparison water surface elevation time series were extracted from the model cell corresponding to the T/P footprint location. Accuracy of simulated water surface elevation was indicated by calculation of RMSE with respect to the T/P time series.

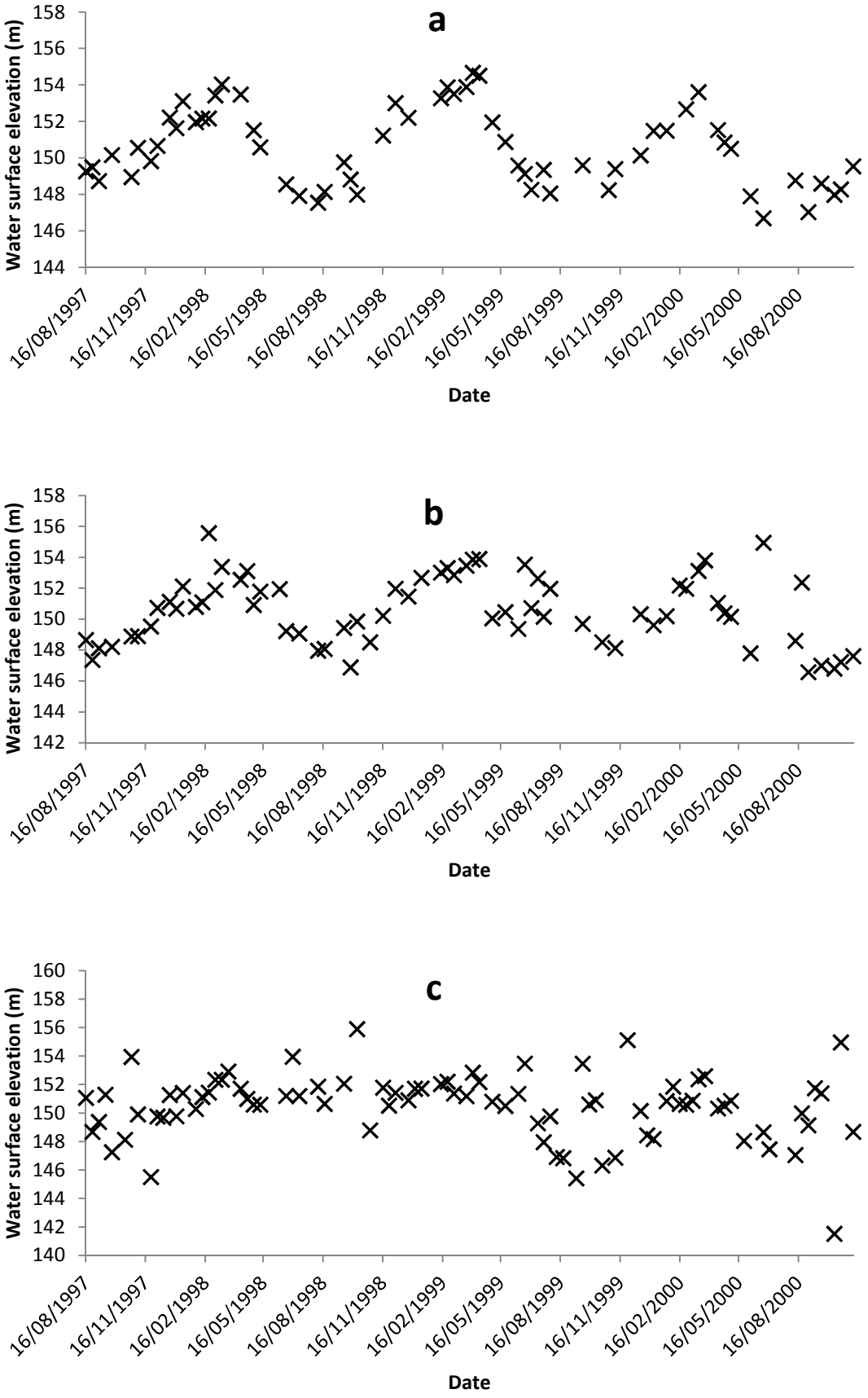

Figure 6.15. Water surface elevation time series extracted at 3 locations for the Beni main channel and proximal floodplain. a) TP1 b) TP2 c) TP3.

6.5.2 ALOS PALSAR Synthetic Aperture Radar imagery

The Phased Array L-band Synthetic Aperture Radar (PALSAR) was launched as one of three sensors aboard the Advanced Land Observing Satellite (ALOS) in January 2006 by the Japan Aerospace Exploration Agency. The PALSAR instrument constitutes the successor to Japanese Earth Resources Satellite (JERS-1), offering enhanced sensor characteristics and a new measurement strategy designed in order to facilitate global scale fine resolution earth surface observations (Rosenqvist et al., 2007). PALSAR operates at L-band (23.6 cm) frequency, is fully polarimetric and is able to operate in five different modes; Fine Beam Single Polarisation, Fine Beam Dual polarisation, Polarimetric, ScanSAR and Direct Transmission. Observations acquired in these different modes vary in terms of swath width, spatial resolution and combination of polarisations (Shimada et al., 2009).

Due to its all weather capability SAR has gained credence as a means to monitor flood inundation (Hess et al., 2003).The use of SAR is advantageous in delineation of flooding due to its ability to detect inundation beneath forest canopies, which it is able to penetrate at specific wavelengths and polarisations (Townsend, 2001). This capability is very important when attempting to delineate inundation dynamics upon forested tropical floodplains which are seasonally flooded (Townsend and Walsh, 1998). In instances where radar pulses are able to penetrate the canopies of flooded forests, microwave energy is reflected specularly by the water surface and vegetation elements such as tree trunks, producing a double bounce effect which yields a high backscattering response (Richards et al., 1987). In contrast, where forests are not inundated microwave energy is scattered in a diffuse manner, producing lower backscattering values (Hess et al., 1995). The increase in backscattering observed during inundation of forests is commonly expressed using wet/dry ratio images, to which thresholds are applied in order to accurately define flood status (Miranda et al., 1997).

Generally SAR sensors operating at longer wavelengths and using horizontal polarisations are most effective for detecting flood inundation beneath forest canopies (Wang et al., 1995). L-band SAR wavelength exceeds the length of vegetation scattering elements, such as leaves, which facilitates a high degree of canopy penetration. In contrast shorter wavelength C-band SAR interacts

with physical vegetation elements more readily and is scattered within the canopy (Pope et al., 1994). Whilst C-band SAR platforms such as RADARSAT have demonstrated some capability in detecting inundation beneath vegetation canopies, their application can be more problematic in dense tropical forests (Townsend, 2001). Consequently L-band JERS-1 imagery has been utilised extensively within the Amazon in order to delineate flood inundation within floodplains characterised by extensive forest cover (Melack and Wang, 1998; Rosenqvist et al., 2002; Hess et al., 2003).

Owing to its more recent launch ALOS PALSAR has thus far been utilised less extensively than JERS-1, however several studies have demonstrated that this dataset can be applied to monitor flood inundation within the Amazon basin. Arnesen et al., (2013) successfully applied ScanSAR images along with ancillary datasets such as Landsat TM/MODIS imagery, elevation data, field photographs and water level records, to derive flood inundation extent for the Curuai Lake floodplain in the lower reaches of the Amazon main stem. The authors used a multi level object based decision tree classification scheme to determine flood inundation status, based upon a rule set developed using a data mining algorithm (Arnesen et al., 2013).

Here L1.5 georeferenced wide swath (360 km) HH polarisation ScanSAR scenes were acquired from the Alaska Satellite Facility (ASF) https://www.asf.alaska.edu/sar-data/palsar/. In total three scenes were obtained, comprising two low water images (03/09/2009, 06/09/2010) and one high water image (06/03/2011). High water inundation extent was derived from the image captured on 06/03/2011, whilst low water inundation extent was extracted from the scene from 06/09/2010. The second low water scene (03/09/2009) was acquired in order to provide an independent image for the calculation of backscattering ratios. Flood inundation extent was derived here from the scenes through application of an approach adapted from that used by Arnesen et al., (2013) for classification of flood extent in the central Amazon floodplain. The method was adapted as dense cloud cover over the study area at the date of wet season image capture prevented the inclusion of ancillary multispectral imagery within the classification procedure. Within the method of Arnesen et al., (2013) multispectral imagery played an important role in separation of the two major non forest classes, open water and soil. The

authors found that backscattering signatures of these classes overlapped, thus making separation based upon PALSAR images alone problematic. This can be attributed to the relatively long wavelength of L-band SAR, which exhibits a low level of sensitivity to relatively smooth target surfaces which favour forward scattering (Hess et al., 2003). Past studies utilising L-band SAR have addressed this problem through application of temporally synchronous multispectral imagery (Silva et al., 2010) or shorter wavelength (C-band) SAR imagery (Evans et al., 2010). Here it proved impossible to find a suitable source of additional imagery, therefore in order to eliminate potential errors in inundated area accrued through confusion between soil and open water, non forested areas were excluded from the analysis. Exclusion of non forested areas prevented penalisation of the model as a result of confusion amongst the soil and open water classes. Consequently, although the non forested area of the floodplain was not formally assessed in this analysis, field and remote sensing observations indicated that the bulk of inundation occurred in the study area occurred within forested areas of the floodplain. The adapted method used to delineate the inundation status of Beni floodplain forests was implemented using a decision tree framework within the ENVI software package, and is elaborated below.

PALSAR images were supplied with pixel values constituted by amplitude, also known as digital numbers, therefore initially amplitude values were converted into normalised backscattering coefficients using the equation 6.4 (Shimada et al., 2009).

$$\sigma^0 = 10 * log_{10}(DN^2) - 83 \quad (6.5)$$

In equation 6.5 DN is radar amplitude, whilst -83 corresponds to the PALSAR calibration coefficient. Subsequently a frost filter with a 5 x 5 pixel window size was applied to the imagery in order to reduce speckle in backscatter (Silva et al., 2010). Beni floodplain forests were delineated through application of a forest mask, derived through aggregation of classes within the land cover classification produced in chapter 3. In addition, the SRTM dataset was included within the classification scheme in order to exclude areas

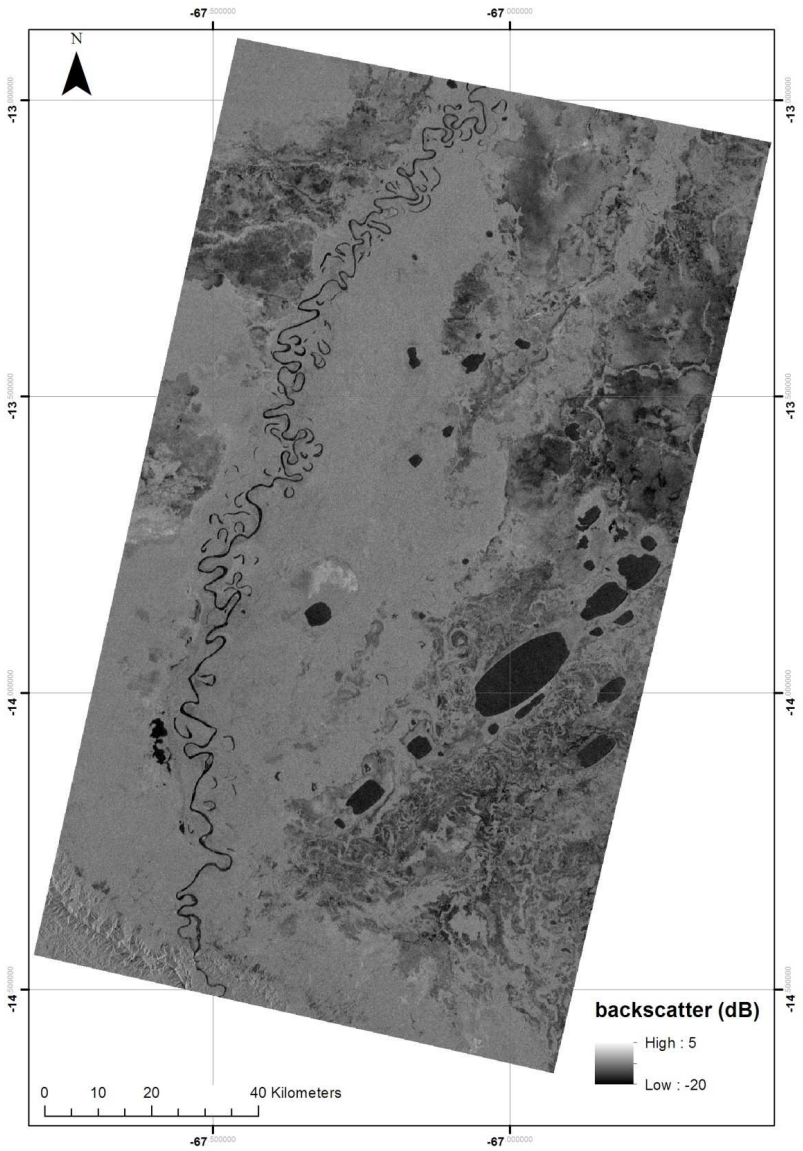

Figure 6.16. ALOS PALSAR scene for the Beni study area at low water 06/09/2010.

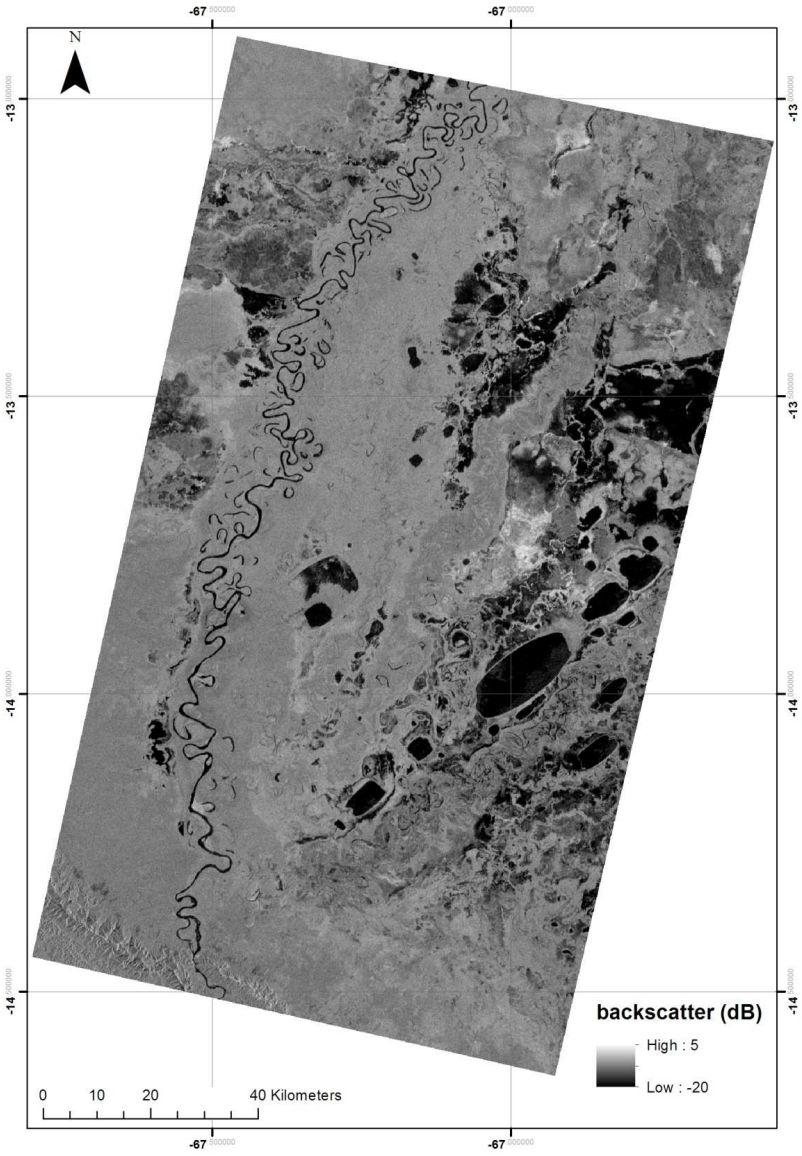

Figure 6.17. ALOS PALSAR scene for the Beni study area at high water 06/03/2011.

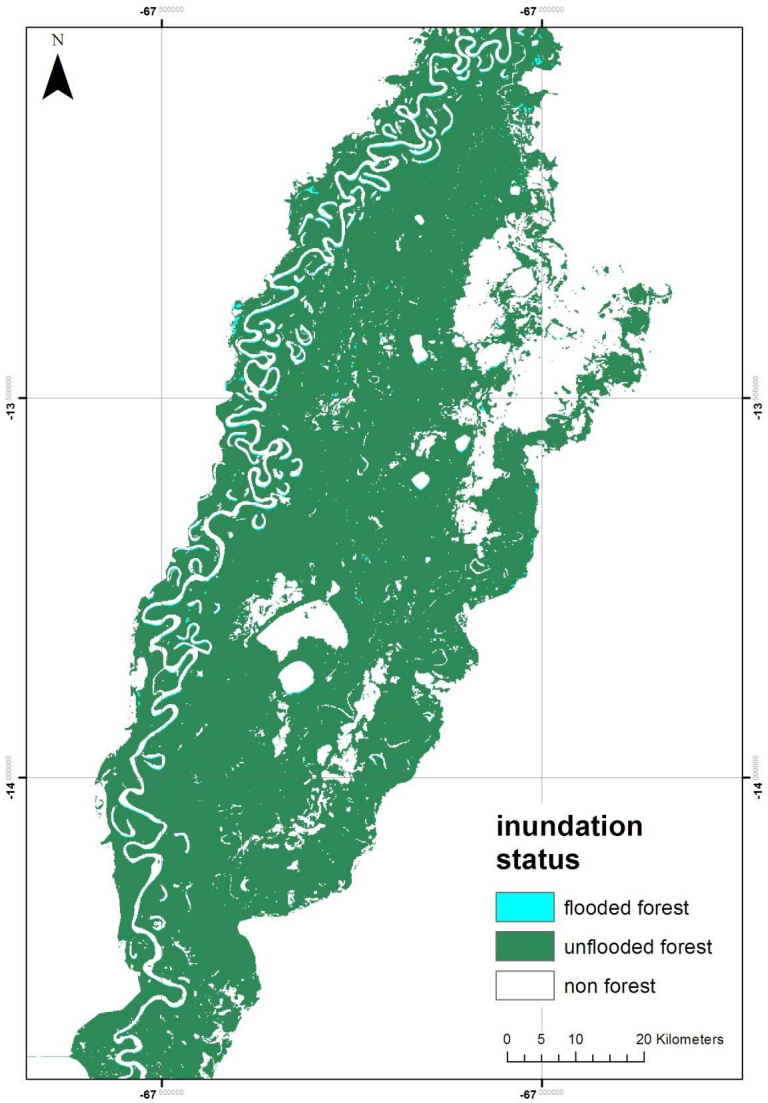

Figure 6.18. Flood inundation extent for the Beni floodplain for low water (06/03/2011) derived from ALOS PALSAR imagery.

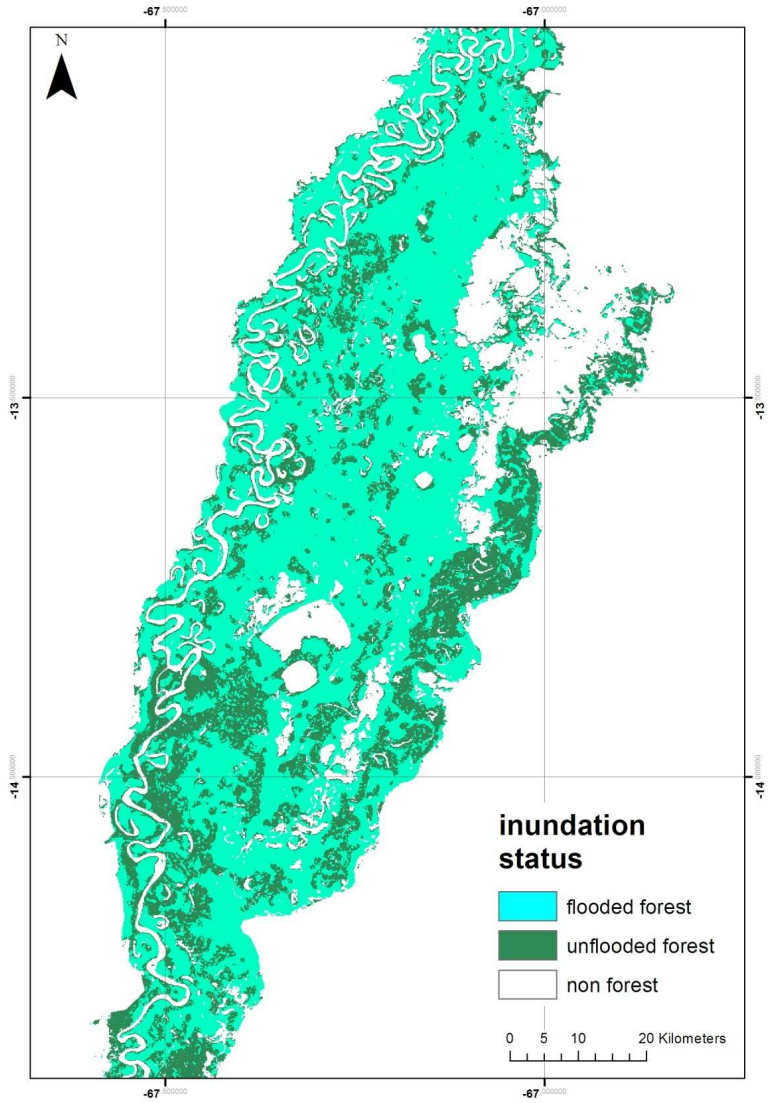

Figure 6.19. Flood inundation extent for the Beni floodplain for high water (06/09/2010) derived from ALOS PALSAR imagery.

characterised by high elevation which did not form part of the floodplain. The flood status of forested pixels was determined through application of a threshold to backscatter ratio images, a technique widely utilised when determining the flood extent of forested areas using SAR imagery (Hess et al., 2003). Both the high (06/03/2011) and low water (06/09/2010) images were divided by an independent low water image (03/09/2009), in order to produce two ratio images. Pixel values within the ratio images therefore reflected any increases in backscattering with respect to the independent low water image that were attributable to flood inundation (Silva et al., 2010). In previous applications of this methodology, inundated area was delineated through the application of a threshold backscatter ratio value, derived based upon independent observations of inundation extent (Arnesen et al., 2013). Here no in situ observations of flood inundation were available for the Beni floodplain, thus it was not possible to define a specific threshold for the study area. Hence the threshold value used to identify flooded areas within the Beni floodplain was taken from Arnesen et al., (2013). This value was deemed appropriate for application here, having been derived from PALSAR ScanSAR imagery for varzea forests of the Curai lake floodplain within the Brazilian Amazon. Within the study of Arnesen et al., (2013) flooded area was predicted with an accuracy of 84-94% when assessed with respect to 500 independent observations of inundation status. The final inundation extent images are illustrated in figures 6.20 and 6.21.

A standard measure of fit *F* is used here in order to compare simulated and observed inundation extent at high water (Bates and De Roo, 2000; Aronica et al., 2002)

$$F = \frac{\mathrm{Num}(\mathrm{S_{mod}} \cap \mathrm{S_{obs}})}{\mathrm{Num}(\mathrm{S_{mod}} \cup \mathrm{S_{obs}})} \tag{6.6}$$

This equation can be written alternatively as:

$$F_{hw} = \frac{\mathrm{FF}}{\mathrm{FF} + \mathrm{FNF} + \mathrm{NFF}} \tag{6.7}$$

Within equation 6.6, $\mathrm{S_{mod}}$ and $\mathrm{S_{obs}}$ are the sets of cells or pixels classified as wet by the model (the threshold depth for a model cell to be classed as inundated was 0.25 m) and satellite observations respectively, whilst Num

indicates the number of members of the set (Bates and De Roo, 2000). In equation 6.7 F_{hw} represents *F* at high water, FF are pixels which are correctly predicted as flooded, FNF are pixels which are wet in the observed dataset but dry in the model and NFF are pixels which are dry in the observed dataset and wet in the model. Therefore *F* represents the area correctly predicted as wet by the model as a fraction of the area observed to be wet. A value of *F*=1 (100%) indicates perfect fit between the modelled and observed inundation, whilst *F*=0 when there is no agreement between modelled and observed inundation. This statistic penalises under and over prediction of flood extent and allows meaningful comparison of the performance of model applications within different reaches (Bates and De Roo, 2000). Importantly this performance measure avoids the biases associated with fit statistics which calculate the number of correctly classified wet/dry pixels as a percentage of total cells within the domain (Horritt and Bates, 2001).

Remotely sensed inundation extent indicated that the forested area of the Beni floodplain considered within this analysis was almost completely dry at the time of low water image capture (06/09/2010). Indeed total inundated area corresponded to an area of less than 50 km^2, a very small area in comparison to the size of the forested area of the floodplain. Hence the application of *F* here in its original form effectively resulted in penalisation of the model for incorrectly predicting inundation of a very small percentage of the floodplain. This statistic was originally formulated in studies of overbank flood events where emphasis was placed upon assessment of inundation extent at high water (Bates and De Roo, 2000; Horritt and Bates, 2001; Lane et al., 2006). *F* was applied in order to assess simulation of low water inundation extent upon the central Amazon floodplain (Wilson et al., 2007), however within the central Amazon floodplain as a relatively larger area of wetland (>2000 km^2) remained inundated through the dry season. Nevertheless low water inundation was poorly predicted in Wilson et al., (2007), with a poor representation of floodplain drainage leading to widespread over prediction of flood extent and an *F* value of 0.21. Preliminary application of *F* for low water inundation upon the Beni floodplain commonly resulted in a value for *F* of lower than 0.01, necessitating the use of an alternative method for model assessment at low water. Hence it was deemed appropriate to modify the fit statistic *F* for application here in order to better reflect the ability of the model to represent dewatering of the floodplain. In order

to do this, pixels which were correctly predicted as not flooded were included in the calculation of F_{lw} demonstrated in equation 6.8.

$$F_{lw} = \frac{\mathrm{FF} + \mathrm{NFNF}}{\mathrm{FF} + \mathrm{FNF} + \mathrm{NFF} + \mathrm{NFNF}} \tag{6.8}$$

In equation 6.8 F_{lw} represents F at low water, FF are pixels which are correctly predicted as flooded, FNF are pixels which are wet in the observed dataset but dry in the model and NFF are pixels which are dry in the observed dataset and wet in the model, NFNF are pixels which are correctly predicted as dry by the model. As a result, in the new form of the *F* statistic correct prediction of all flooded and non flooded areas is associated with an F_{lw} value of 1, whilst the incorrect prediction of all flooded and non flooded areas is associated with an F_{lw} value of 0. Water remaining on the floodplain in the model simulation at the time of low water image capture is indicative of an incorrect representation of dewatering. Flood inundation in these areas is classified as over prediction and the model is penalised accordingly, with F_{lw} decreasing if larger areas of water remain on the floodplain. The main reason for the exclusion of NFNF pixels in the original formulation of F_{lw} was to prevent positive bias in the accuracy statistic through inclusion of large numbers of model cells which were never inundated (Bates and De Roo, 2000). However within the forested area of the Beni floodplain considered in this analysis the number of pixels which were never flooded was relatively small in comparison to flooded areas. It is important to consider that this modified statistic is applied here in order to provide a more meaningful indication of the models ability to represent floodplain dewatering, and resulting values are not directly comparable with results from other modelling studies.

6.6 Preliminary analysis of model simulations

Prior to formal assessment of model results, it was deemed appropriate to undertake a preliminary analysis of simulated inundation characteristics for the Beni floodplain. The first part of this preliminary investigation of model results is constituted by a sensitivity analysis that explores the effect which the use of different DEMs, roughness parameters and channel bed elevations exert upon modelled inundation characteristics. Subsequently, in the second part of this analysis, predicted inundation extent is compared to observed flood extent data derived from PALSAR SAR imagery at high water. This analysis was undertaken in order to provide a quantitative indication of the performance of model simulations undertaken using the bare earth floodplain DEMs derived in chapter 5, and to demonstrate the need for additional refinement of these DEMs. The final part of this analysis is constituted by a brief investigation of model sensitivity to variation of parameters in the hydrological part of the model. As floodplain hydrology was hypothesised to be important in both the wetting and drying of the floodplain, this analysis was conducted with respect to PALSAR derived inundation extent at both high and low water.

6.6.1 Model sensitivity analysis

Inundation characteristics illustrated in figure 6.22b for the INT DEM, differ from those observed for simulations using the FAV DEM (6.22a) and the GCH DEM (6.22c). Perhaps the most marked contrast observed for simulations using the INT DEM is that inundation occurs over a wider area, but is relatively shallow, rarely exceeding a depth of 5m with the exception of floodplain lakes to the east of the domain. This is contrary to the FAV and GCH DEMs, which promote deeper flooding over a smaller overall area. Flooding is more prevalent in proximal areas for INT DEM simulations in comparison to the FAV and GCH DEM model runs, particularly towards the upstream end of the reach, whilst a larger area is flooded in the region of the large floodplain lakes, in comparison to 6.22a and c. Tables 6.3-6.8 provide further quantification of the sensitivity of the model to DEM selection and reflect the observations made in figure 6.22. In general, for a given parameter set inundation extent is highest within simulations forced by INT DEM (table 6.4). In contrast, INT DEM simulations (table 6.7) are characterised by the lowest flood water volume, which is significantly higher for FAV DEM and GCH DEM simulations.

Figure 6.22. Visual illustration of high water (06/03/2011) inundation extent simulated by the model using floodplain elevation for a) FAV DEM b) INT DEM c) GCH DEM. Roughness set up (medium) and channel bed elevation (medium) were constant here.

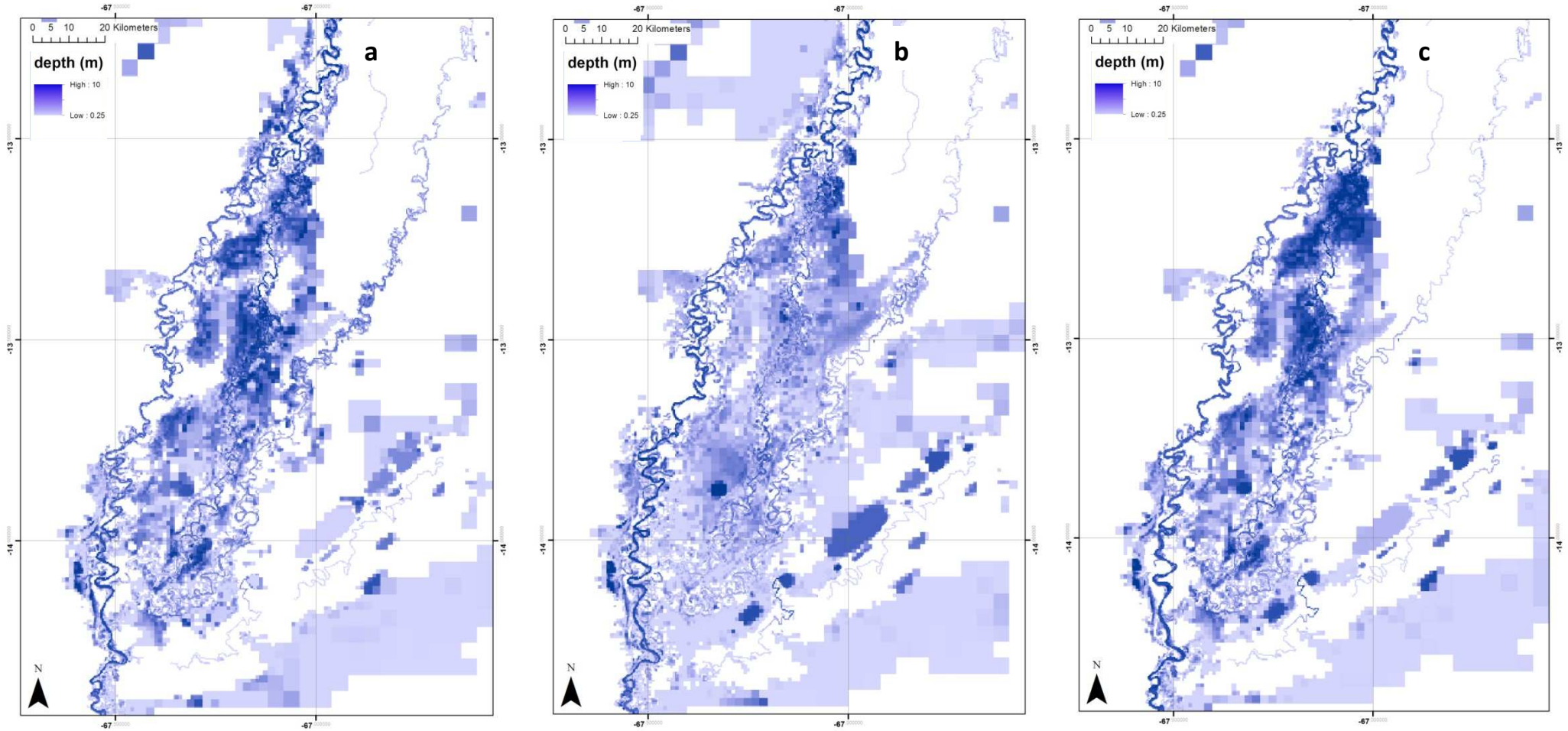

Figure 6.23. Visual illustration of the sensitivity of modelled inundation extent at high water (06/03/2011) to channel bed elevation a) low elevation b) medium elevation c) high elevation. Floodplain DEM (GCH DEM) and roughness configuration (medium) were constant here.

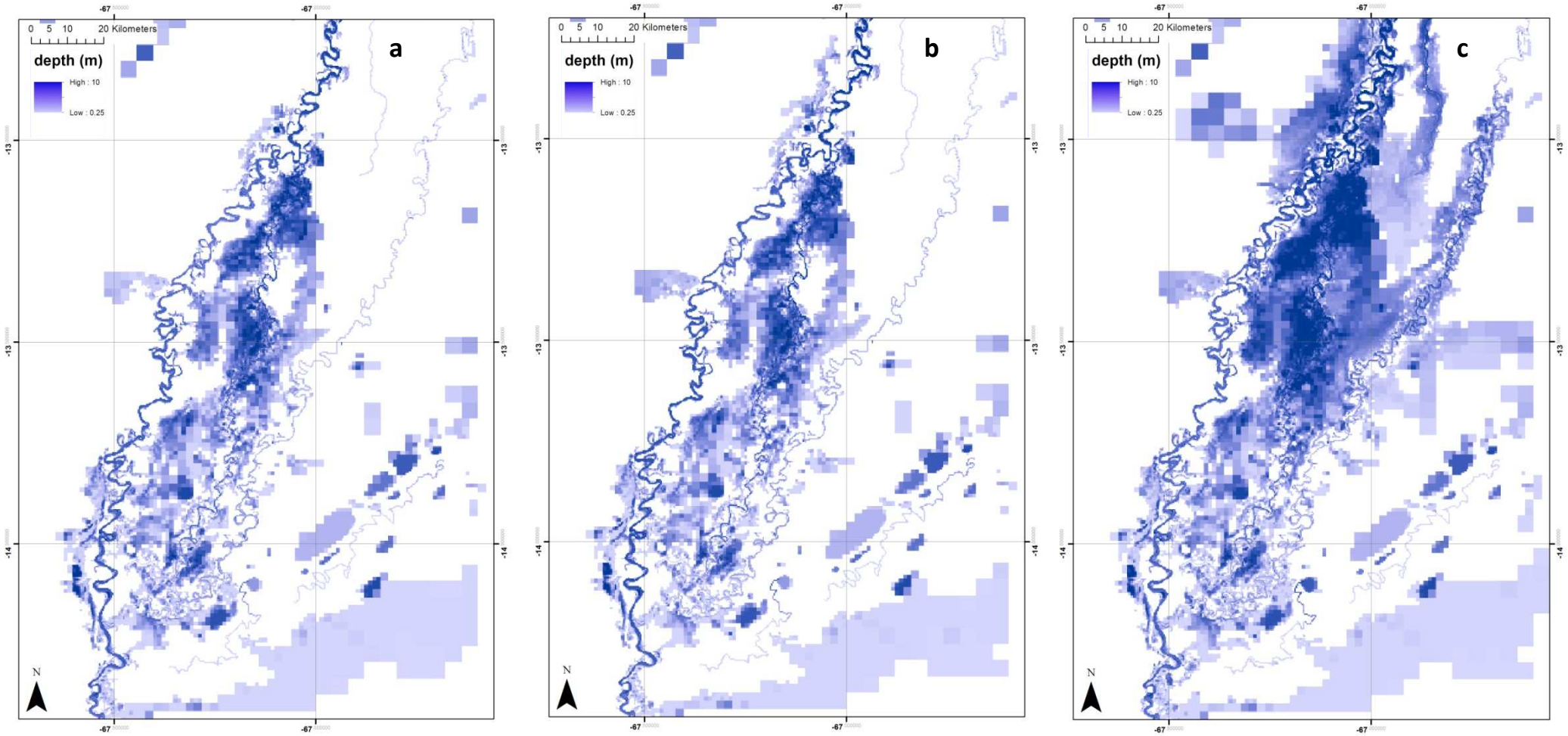

Figure 6.24. Visual illustration of the sensitivity of modelled inundation extent at high water (06/03/2011) to model roughness set up a) low roughness b) medium roughness c) high roughness. Floodplain DEM (INT DEM) and channel bed elevation (medium) were constant here.

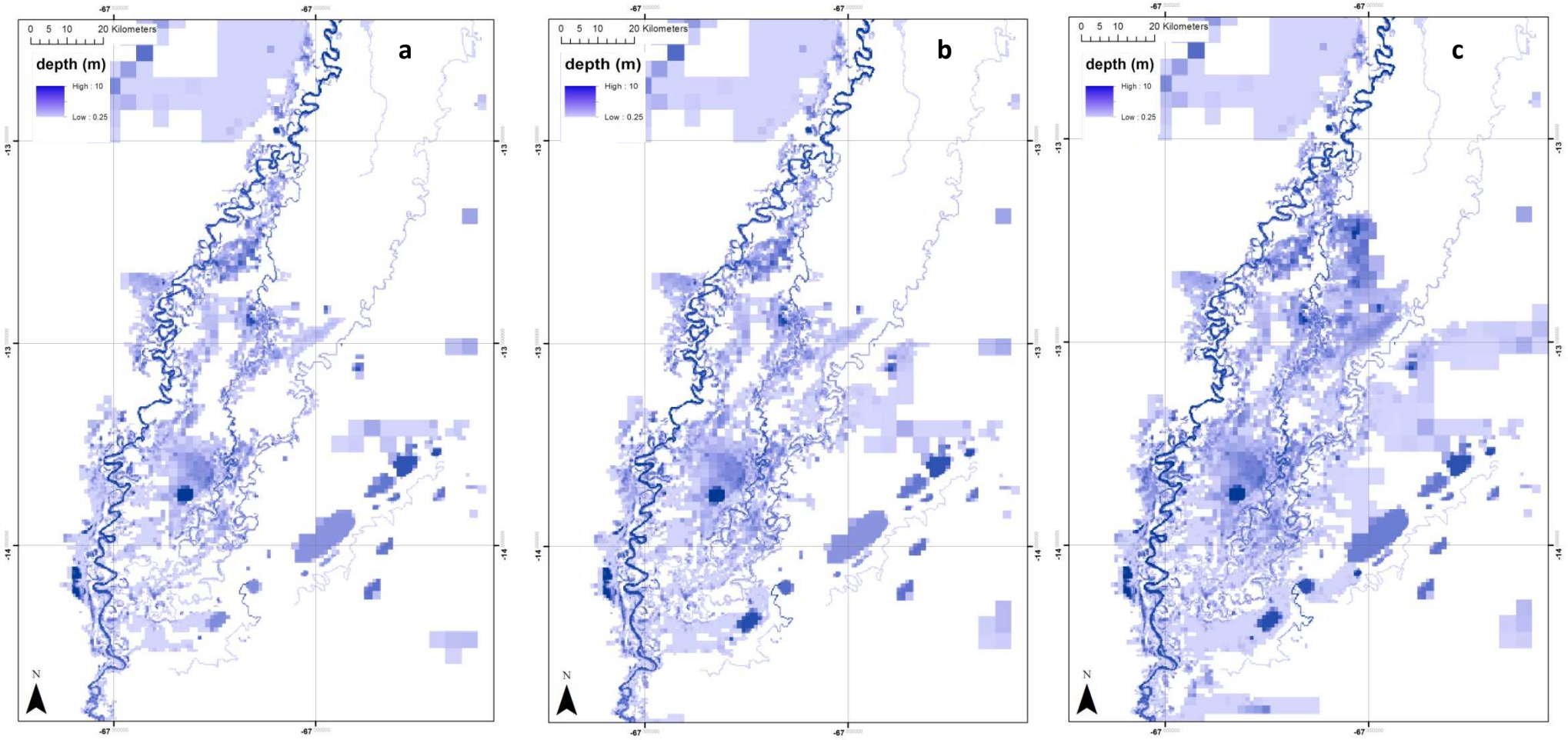

Table 6.3. Modelled inundation extent (km^2) at high water 06/03/2011 for simulations using the FAV DEM and different parameter combinations. M indicates a missing simulation.

Roughness set up	Channel bed elevation		
	Low	Medium	High
Low	4563.3	4768.5	5206.4
Medium	4837.0	5190.8	6386.0
High	6120.4	6512.8	6547.8

Table 6.4. Modelled inundation extent (km^2) at high water 06/03/2011 for simulations using the INT DEM and different parameter combinations.

Roughness set up	Channel bed elevation		
	Low	Medium	High
Low	5184.2	5604.8	6509.6
Medium	5971.9	7047.2	7325.1
High	7792.4	8158.9	9235.5

Table 6.5. Modelled inundation extent (km^2) at high water 06/03/2011 for simulations using the GCH DEM and different parameter combinations. U denotes a missing simulation due to model instabilities.

Roughness set up	Channel bed elevation		
	Low	Medium	High
Low	5173.9	5543.8	6269.0
Medium	6018.0	6029.6	9681.7
High	6587.2	6769.2	U

Analysis of rows of values in tables 6.3-6.5 provides insight into model sensitivity, in terms of inundation extent, with respect to channel bed elevation configuration. Saliently, for simulations undertaken with all DEMs and roughness set ups, inundation extent increases with higher channel bed elevation. This is illustrated visually in figure 6.23, demonstrating that the model exhibits the expected response to increases in bed elevation. Model sensitivity to channel bed elevation in terms of inundation volume, illustrated in tables 6.6-6.8, follows the same pattern as for inundated area. Sensitivity to channel bed elevation varied for the different bare earth DEMs, with simulations undertaken using the GCH DEM characterised by the highest sensitivity (due to the occurrence of extreme values of inundation extent and flood water volume) for

high channel bed elevations), whilst the INT DEM produced more a more consistent and realistic response to variations in this parameter.

Table 6.6. Modelled floodplain water volume (km^3) at high water 06/03/2011 for simulations using the FAV DEM and different parameter combinations.

Roughness set up	Channel bed elevation		
	Low	Medium	High
Low	12.4	12.7	13.3
Medium	13.4	13.9	14.5
High	15.1	15.2	15.1

Table 6.7. Modelled floodplain water volume (km^3) at high water 06/03/2011 for simulations using the INT DEM and different parameter combinations.

Roughness set up	Channel bed elevation		
	Low	Medium	High
Low	8.0	8.4	9.8
Medium	9.2	10.4	11.2
High	11.9	12.9	13.2

Table 6.8. Modelled floodplain water volume (km^3) at high water 06/03/2011 for simulations using the GCH DEM and different parameter combinations. U denotes a missing simulation due to model instabilities.

Roughness set up	Channel bed elevation		
	Low	Medium	High
Low	10.8	11.6	12.5
Medium	12.7	12.6	27.3
High	13.8	15.5	U

Figure 6.24 illustrates model sensitivity to roughness set up for simulations using the INT DEM and a medium channel bed elevation. Simple visual analysis of these maps indicates that inundation extent increases substantially from low roughness in 6.24a to high roughness in 6.24c. The model behaviour illustrated in figure 6.24 is reflected in an increase in flood extent and water volume moving down columns in tables 6.3-6.5 and 6.6-6.8 respectively. Indeed increases in roughness lead to an increase in inundation extent, depth and water volume for all of the bare earth DEMs. As for channel bed elevation, response to changes in roughness varies between the floodplain DEMs. Simulations using the FAV DEM and the INT DEM show a broadly coherent

response to roughness increases, whilst GCH DEM simulations are associated with extreme values of inundation extent and flood water volume at high roughness.

6.6.2 Initial comparison with PALSAR derived high water inundation extent

Figure 6.25 visually illustrates an initial comparison of modelled and observed inundation extent for the Beni floodplain at high water on 06/03/2011, extracted from simulations undertaken using high channel bed elevation and medium roughness set up. Associated statistics are displayed in table 6.9. Visual analysis of figure 6.25 indicates that FF, denoting areas that are both observed and predicted to be flooded, was the most dominant class for simulations using each of the bare earth DEMs (table 6.9). Areas which were correctly predicted as not inundated (NFNF) formed the least frequent class (table 6.9). The two classes which indicate incorrect predictions by the model are FNF (grey) which denoted areas that were observed to be flooded but are predicted as not flooded by the model, and NFF (red) which corresponds to areas that are inundated in model predictions but not inundated within remotely sensed inundation extent. Table 6.9 illustrated the extent of FNF areas exceeded that of NFF areas, indicating that the model under predicted inundation upon the Beni floodplain for the combination of DEMs and parameter sets explored here.

Based upon statistics displayed within table 6.9 and the comparison maps in figure 6.25, model performance appears to be broadly similar for each of the DEMs when combined with high roughness and medium channel bed elevation. Of these simulations highest level of fit was observed for the simulation undertaken using the GCH DEM (0.55), FAV DEM produced the second best fit (0.53) whilst the lowest level of performance was offered by the INT DEM (0.51). Thus the overall range in the fit statistic between the different DEMs was 0.04, a relatively small value. Perhaps the most significant feature of figure 6.25 is the prevalence of substantial areas of FNF pixels located in close proximity to the Beni channel, particularly in the middle and downstream sections of the reach. This is significant, suggesting that systematic under prediction of inundation occurs in the proximal floodplain for simulations using each of the bare earth floodplain DEMs.

Figure 6.25. Initial comparison of modelled and PALSAR derived inundation extent for the Beni floodplain study area at high water (06/03/2011) for a) FAV DEM b) INT DEM c) GCH DEM. All simulations used the same roughness set up (high) and channel bed elevation (low). Inundation status indicates whether a pixel in the model domain is flooded (F) or not flooded (NF) in the inundation extent image and model predictions respectively. For example FNF (grey) indicates that a pixel was observed to be flooded (F) in the remotely sensed inundation extent image, but was predicted as not flooded (NF) in the model simulation.

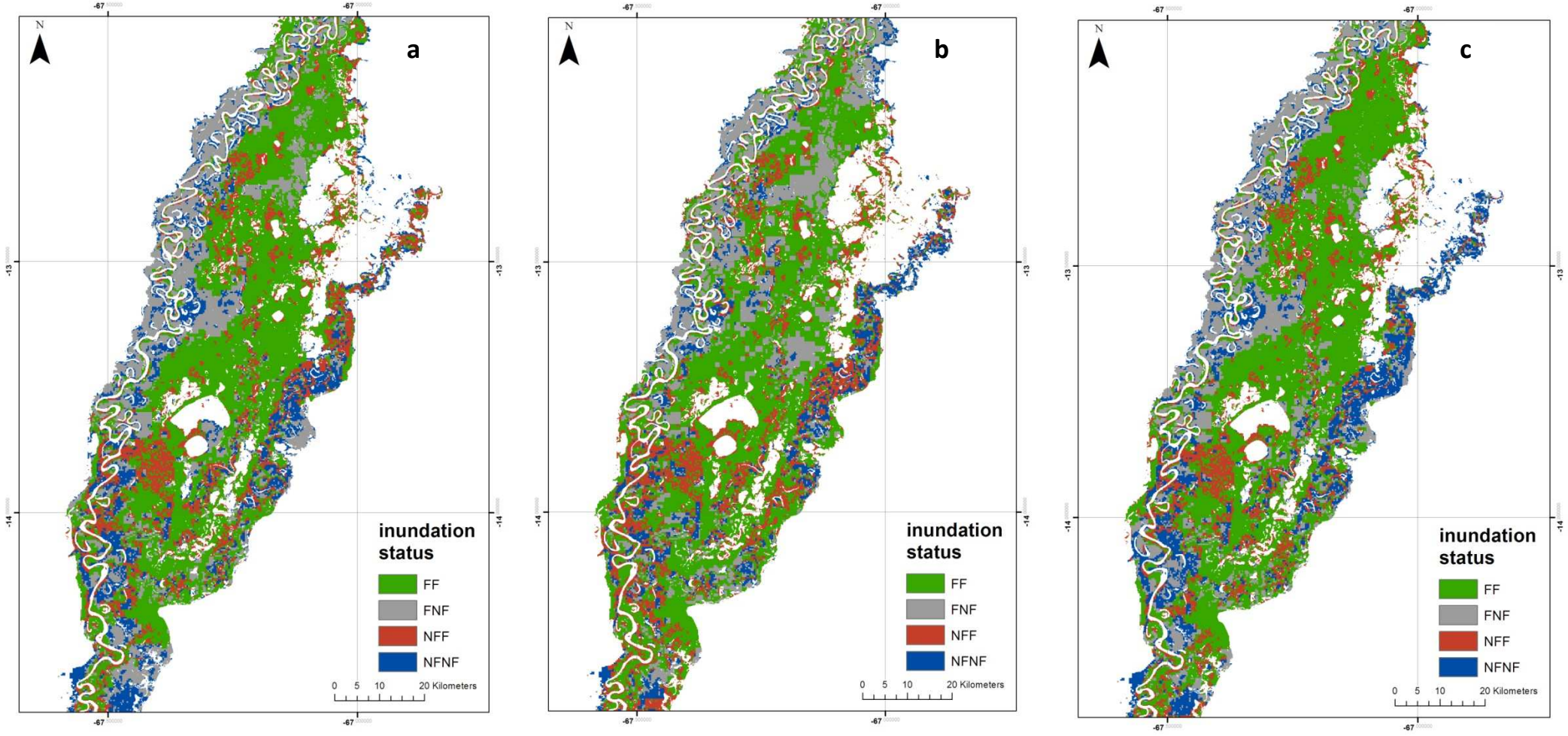

Table 6.9. Comparison between modelled and observed inundation extent at high water (06/03/2011), for simulations using different DEMs with high roughness and medium channel bed elevation parameters. Inundation status indicates whether a pixel in the model domain is flooded (F) or not flooded (NF) in the inundation extent image and model predictions respectively. For example FNF indicates that a pixel was observed to be flooded (F) in the remotely sensed inundation extent image, but was predicted as not flooded (NF) in the model simulation. Values given are areas in km^2, with the exception of Fit (F_{hw}).

Flood status	DEM		
	FAV	INT	GCH
FF	2116.1	2079.3	29158
FNF	1048.2	1084.9	1038.6
NFF	806.7	901.0	728.3
NFNF	604.9	510.6	683.4
Fit (F_{hw})	0.53	0.51	0.55

Table 6.10. Fit (F_{hw}) between modelled and observed inundation extent at high water 06/03/2011 for simulations using the FAV DEM and different parameter combinations.

Roughness set up	Channel bed elevation		
	Low	Medium	High
Low	0.52	0.52	0.52
Medium	0.52	0.52	0.53
High	0.53	0.53	0.54

Table 6.11. Fit (F_{hw}) between modelled and observed inundation extent at high water 06/03/2011 for simulations using the INT DEM and different parameter combinations.

Roughness set up	Channel bed elevation		
	Low	Medium	High
Low	0.37	0.42	0.47
Medium	0.43	0.48	0.50
High	0.50	0.51	0.51

Table 6.12. Fit (F_{hw}) between modelled and observed inundation extent at high water 06/03/2011 for simulations using the GCH DEM and different parameter combinations. U denotes missing simulation due to the occurrence of instabilities.

Roughness set up	Channel bed elevation		
	Low	Medium	High
Low	0.48	0.50	0.52
Medium	0.50	0.51	0.58
High	0.53	0.55	U

Tables 6.10 - 6.12 display the fit statistic (F_{hw}), calculated for observed and modelled inundation extent at high water for different parameter combinations. For simulations undertaken using the FAV DEM (table 6.10), maximum fit was F_{hw}= 0.54, whilst variation in fit across the parameter space was small (0.02). Simulations using the INT DEM were associated with the lowest maximum F_{hw} of 0.51 (table 6.11), but the widest range of fit of any of the DEMs (F_{hw} = 0.37 to 0.51). Maximum F_{hw} for GCH DEM simulations was 0.58 (table 6.12), the highest fit observed for any simulation undertaken in this preliminary analysis. For simulations utilising all DEMs, F_{hw} increased with increases in roughness and channel bed elevation.

6.6.3 Testing of model sensitivity to floodplain hydrology

In the final part of the preliminary model analysis, three different set ups for the hydrological part of the inundation model were tested. These three set ups were named HYD1, HYD2 and HYD3. HYD1 was the default set up for the hydrological part of the model, in which soil water store depth (D) was 17.5 cm, the fractional rate of drainage from the soil water store to ground water (F) was 0.0025 and maximum infiltration rate (I_{max}) was 0.007 mm/day. In HYD2 D was increased to 1 m, F was increased to 0.005, whilst I_{max} remained at 0.007 mm/day. For HYD3 the hydrological source term was excluded from the model equations. All simulations presented here were undertaken with the INT DEM in combination with medium roughness and high channel bed elevation.

Table 6.13. Accuracy statistics for the comparison between model simulations using different hydrological model set ups and PALSAR derived inundation extent at high water.

Measure	Hydrological set up		
	HYD1	HYD2	HYD3
FF (km^2)	1965.7	1899.7	1891.3
FNF (km^2)	1198.5	1264.5	1272.9
NFF (km^2)	831.3	826.5	819.5
NFNF (km^2)	580.4	585.1	592.1
Fit (F_{hw})	0.49	0.48	0.47
Extent (km^2)	7641.1	7325.1	6662.3
Volume (km^3)	11.53	10.90	9.58

Table 6.14. Accuracy statistics for the comparison between model simulations using different hydrological model set ups and PALSAR derived inundation extent at low water.

Measure	Hydrological set up		
	HYD1	HYD2	HYD3
FF (km^2)	26.0	24.6	29.6
FNF (km^2)	22.3	23.8	18.7
NFF (km^2)	1046.0	865.7	1528.5
NFNF (km^2)	3481.6	3661.8	2999.0
Fit (F_{lw})	0.77	0.81	0.66
Extent (km^2)	2937.8	2400.2	2933.2
Volume (km^3)	3.67	3.30	2.43

Based upon table 6.13 and figure 6.26, at high water HYD1 is associated with the highest inundated area, flood water volume and fit of any of the simulations undertaken here, exhibiting marginally higher values than HYD2 for all of these measures. HYD3, in which the hydrological source term was removed from the model, was associated with the lowest fit with respect to observed high water inundation extent. Although the overall difference in F_{hw} between the different simulations was relatively small at 0.02, HYD3 was associated with substantially lower inundated area and flood water volume in comparison to HYD1 and HYD2. On a basic level this demonstrates that rainfall provides a significant contribution to flood water volumes on the floodplain.

Table 6.14 demonstrates that at low water, HYD3 is characterised by a much lower level of fit (F_{lw} =0.66), in comparison to HYD1 (F_{lw} =0.77) and HYD2 (F_{lw} =0.81). This suggests that modelled inundation extent is more sensitive to floodplain hydrology at low water. Given that the floodplain is almost completely dry at the time of low water image capture (figure 6.18), the lower flood extent and flood water volume in HYD 2 translates into an increase in F_{lw}. This is reflected in figure 6.25, in which inundation for HYD2 (figure 6.25b) is limited to localised pools, whilst a marked increase in the area of larger contiguous areas of inundation is evident for HYD3 (figure 6.25c).

Figure 6.26. Inundation extent at high water (06/03/2011) for simulations undertaken using the INT DEM in combination with medium roughness, high channel bed elevation configuration and different hydrological model set ups. a) HYD1 b) HYD2 c)HYD3

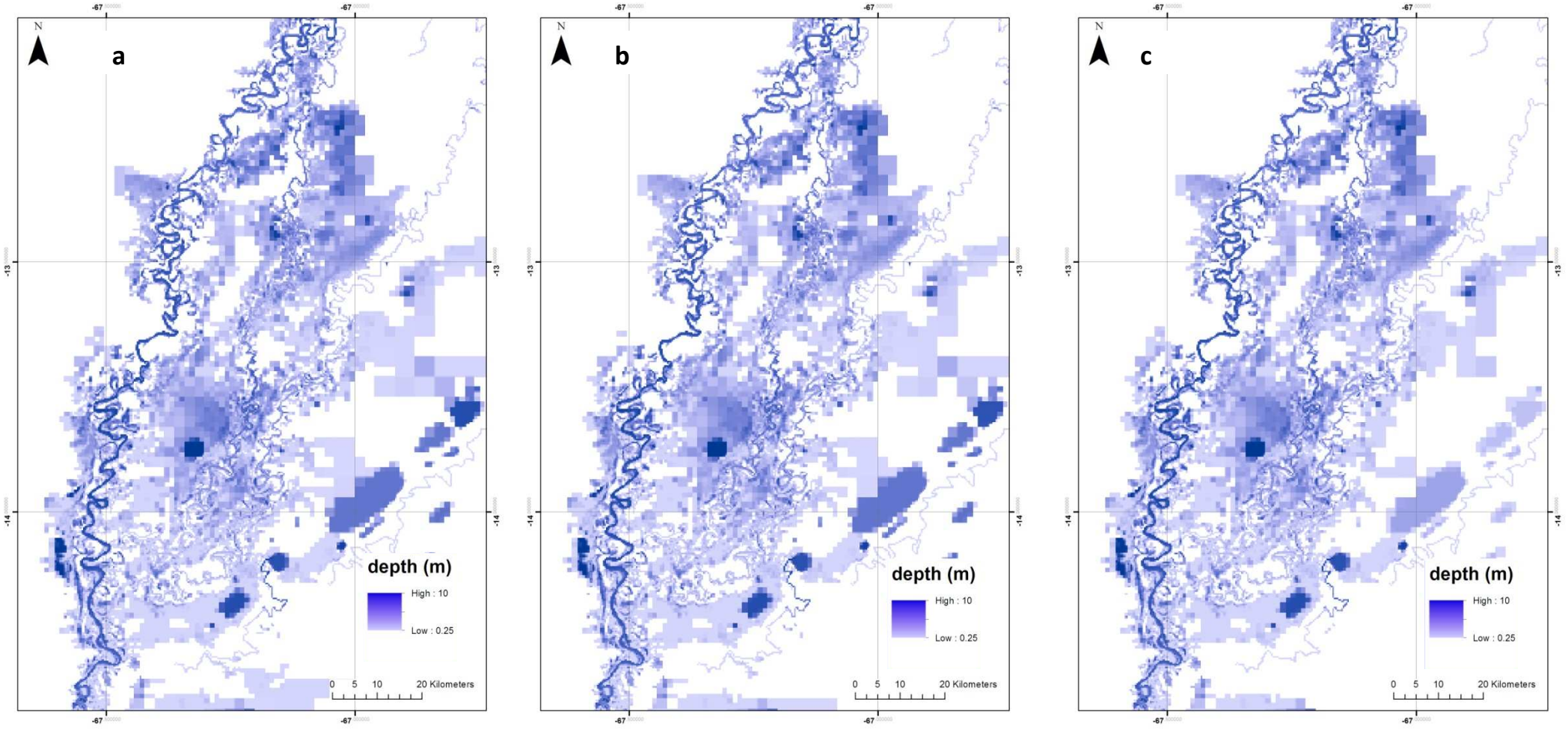

Figure 6.27. Inundation extent at low water (06/09/2010) for simulations undertaken using the INT DEM in combination with medium roughness, high channel bed elevation configuration and different hydrological model set ups. a) HYD1 b) HYD2 c)HYD3

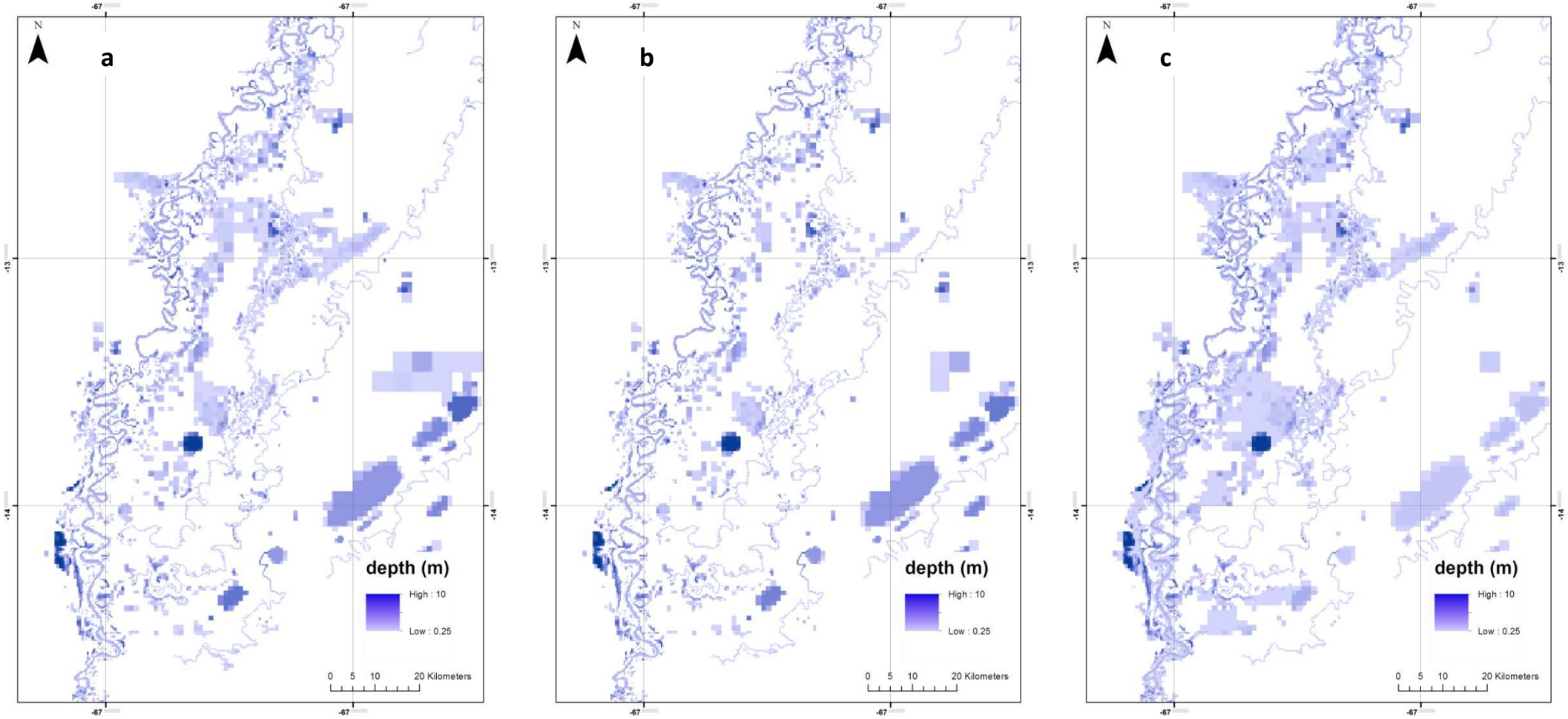

6.7 Refining floodplain bare earth DEMs

In light of the results of initial model simulations, specifically the relatively low values of F_{hw} and the substantial under prediction of inundation observed in close proximity to the river channel, it was deemed necessary to further refine each of the bare earth floodplain DEMs. It is hypothesised that high floodplain elevations in proximal areas, attributable to incomplete removal of vertical biases in the SRTM dataset, precluded the occurrence of inundation within these areas. Hence, an analysis was designed in order to identify areas characterised by erroneously high elevations, and remove these remaining vertical biases. This analysis was undertaken for the FAVP DEM, GCHP DEM and INT DEM using tools within ArcGIS and ENVI software packages.

Areas of the floodplain in which elevation was over predicted due to remaining vertical vegetation bias were identified as those cells within the model domain that were observed to be inundated in the PALSAR derived flood extent image acquired at peak inundation in March 2011, but were not flooded in the model simulation at the corresponding date. In order to ensure consistency between the correction applied to the different DEMs, the simulations used in this process were characterised by medium roughness and medium channel bed elevation parameters. A forest mask, generated based upon the land cover classification in chapter 3, was utilised in order to identify areas characterised by forest cover. A mask was created that delineated the model cells which met these criteria. The next stage of this analysis was constituted by the generation of a map of water surface elevation for the Beni floodplain at high water in March 2011. Water surface elevation was calculated for all flooded cells within the model domain through addition of simulated inundation depth and the height of the floodplain. Subsequently, the floodplain was divided into a grid characterised by a spatial resolution of 5 km. The average water surface elevation was calculated for each cell in the 5 km grid based upon the mean water surface elevation of all flooded model cells within that 5 km cell. Overall this produced a coarse resolution map of water surface elevation across the whole floodplain. The vertical elevation error for each cell included within the mask generated above was quantified through subtraction of the water surface elevation from the bare earth DEM elevation. Histograms of errors calculated for each DEM are illustrated in figures 6.28-6.30.

Having derived a map of vertical error in each of the DEMs through the analysis detailed above it was necessary to define the correction to apply to each of the cells in which elevation was over predicted. The correction applied, ΔZ, was defined according to equation 6.7.

$$\Delta Z = (pE + (1 - p)Emean + H) * C \quad (6.7)$$

In equation 6.7 ΔZ is the elevation (m) removed from each cell. E is the error value for a given cell (the difference between DEM cell elevation and water surface elevation at high flow for cells that should be wet), whilst Emean is the average error value across the floodplain where E > 0. H is a constant nominal flow depth, which is included in the equation to ensure that the adjusted cell elevation is below the water surface elevation so that the cell is likely to be inundated at high flow. C is a constant corresponding to a simple correction factor which can be utilised in order to increase or decrease the magnitude of the correction. A value of C > 1 would lead to a larger amount of elevation being removed from each cells, whilst the reverse is true for C < 1. The constant p is used to adjust the spatial pattern of the Z adjustment across the floodplain. For C = 1 and p=1, the elevation of each cell will be lowered to the height of the water surface. However, this will tend to flatten out the floodplain topography by reducing elevations to the predicted level of the high flow water surface, which is relatively flat owing to its coarse resolution. In this case for a given cell if E < Emean then the cell elevation is lowered by a value greater than E, whilst if E > Emean then the cell elevation is lowered by a value less than E. Here, two new DEMs were produced for each of the original DEMs used within initial model testing in 6.6 utilising the correction procedure detailed above. One new DEM was generated for each or the original DEMs using a value of C = 1 within equation 6.7, these DEMs were named FAV100, GCH100 and INT100. An additional three DEMs were generated through application of equation 6.7 in which C = 1.25, these DEMs were named FAV125, GCH125 and INT125. These additional DEMs were applied in order to provide the topographic forcing within the inundation model for additional simulations, which are utilised for formal validation within section 6.8. The Z adjustments applied in the generation of the new DEMs are illustrated in figure 6.31.

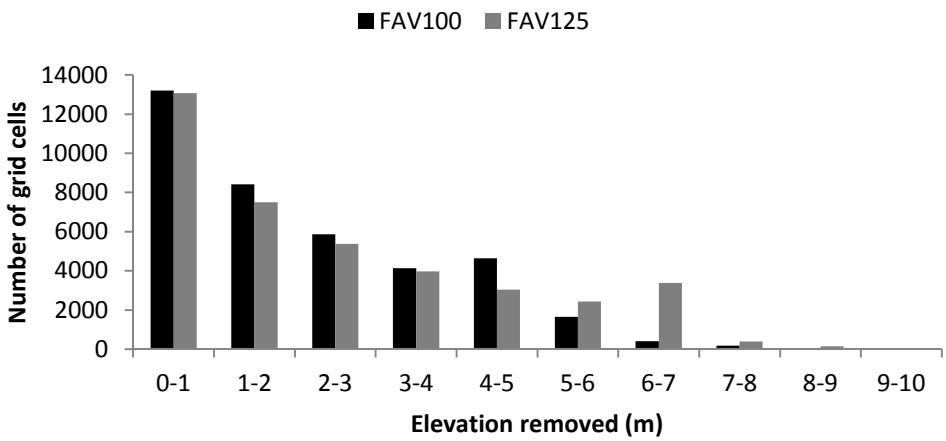

Figure 6.28. Histogram illustrating the elevation removed during the correction of the FAV DEM in order to generate the FAV100 DEM and FAV125 DEM.

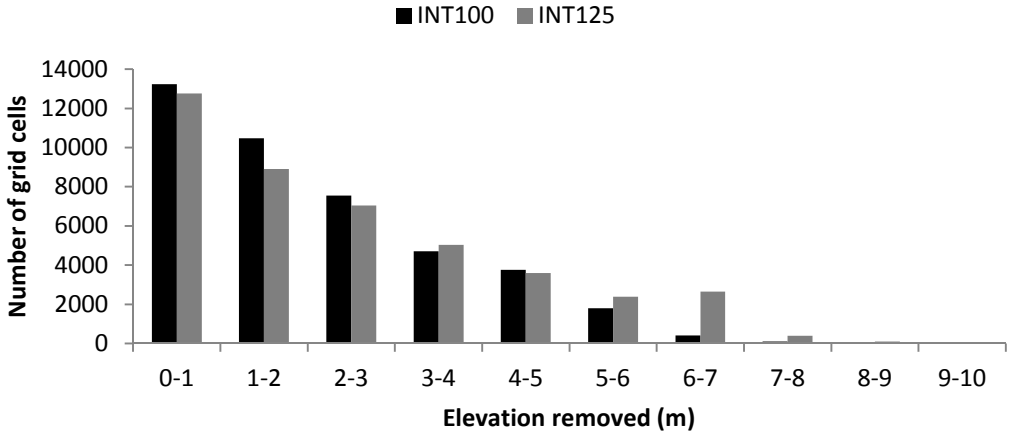

Figure 6.29. Histogram illustrating the elevation removed during the correction of the INT DEM in order to generate the INT100 DEM and INT125 DEM.

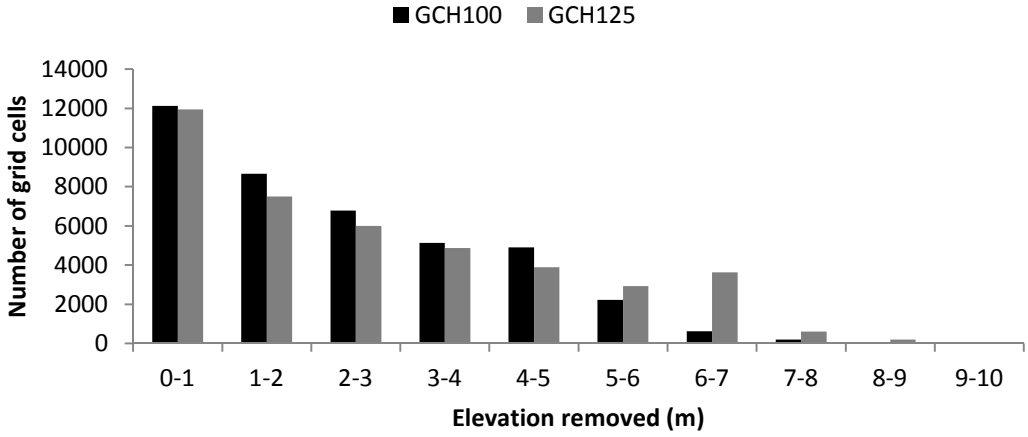

Figure 6.30. Histogram illustrating the elevation removed during the correction of the GCH DEM in order to generate the GCH100 DEM and GCH125 DEM.

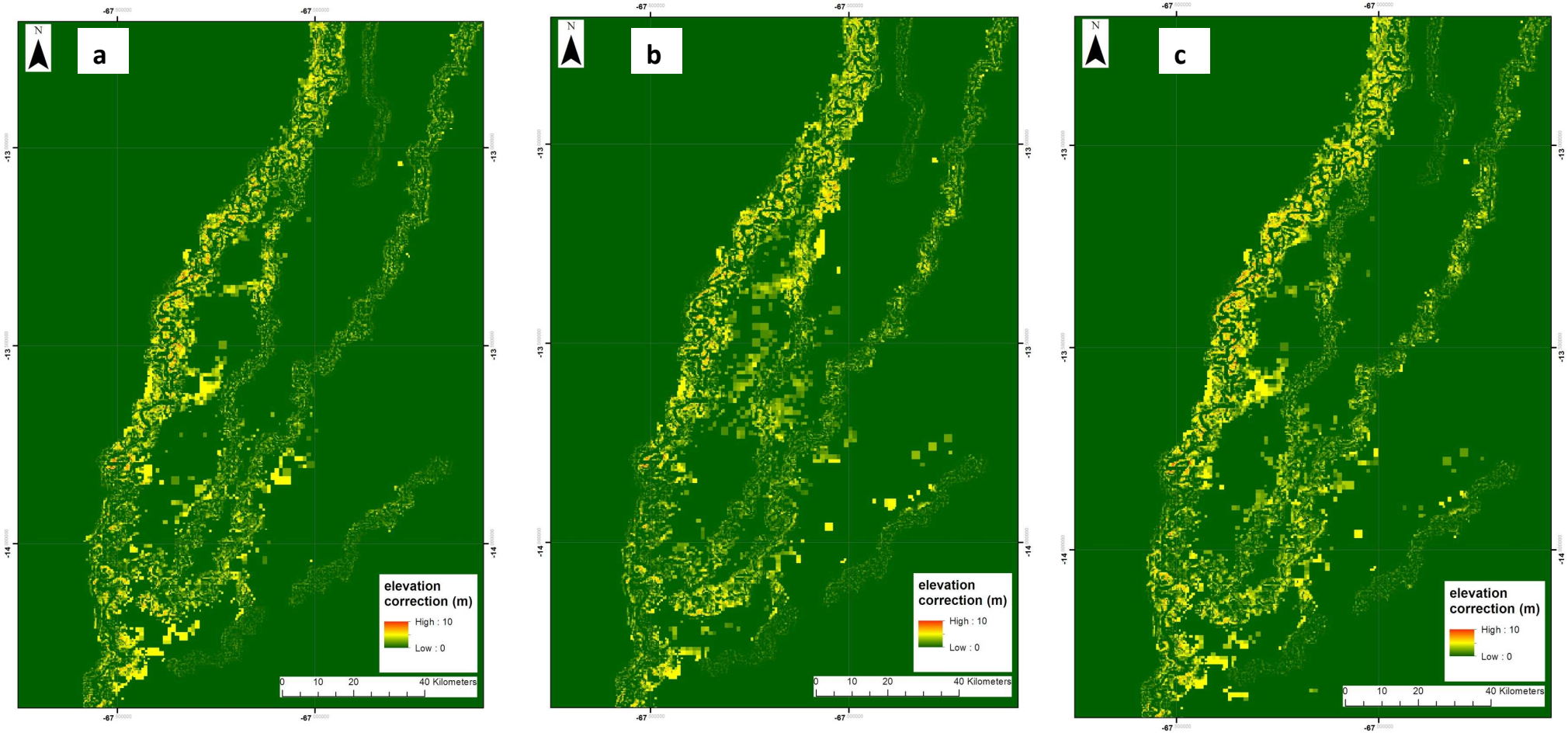

Figure 6.31. Spatial maps illustrating the elevation removed from a) FAV DEM in order to generate FAV100 DEM b) INT DEM in order to generate INT100 DEM c) GCH DEM in order to generate GCH100 DEM.

6.8 Formal model assessment

6.8.1 Assessment of high water inundation extent

Table 6.15-6.17 show summary statistics for model simulations undertaken using the new refined floodplain bare earth DEMs at high water, including fit with respect to ALOS PALSAR derived flood extent within forested areas, inundation extent and water volume within the model domain. On a basic level, for the new refined DEMs, model response to changes in roughness and channel bed elevation were consistent with the sensitivity analysis. It is clear that refining of the DEMs was associated with an increased level of performance within all model simulations, with F_{hw} values exceeding those reported in tables 6.3-6.8 for simulations using the original bare earth DEMs. For the refined FAV DEMs (table 6.15), maximum F_{hw} increased to 0.66, whilst the lowest fit was 0.61, constituting a small overall F_{hw} range of 0.05. Whilst maximum fit increased by 0.11 in comparison to the original simulations, the refined FAV DEM simulations were associated with the lowest levels of accuracy of the new DEMs based upon F_{hw} values. Visual analysis of figure 6.32 illustrates that despite refinement, inundation remains under predicted in the proximal floodplain for simulations undertaken with lower roughness and channel bed elevation parameters, whilst this problem is ameliorated where higher roughness and channel bed elevation parameters are utilised (figure 6.33).

Simulations undertaken using the refined INT DEMs are associated with the highest level of performance of all of the refined DEMs (table 6.16), exhibiting a F_{hw} range of 0.64-0.69. Maximum F_{hw} increased by 0.18 with respect to INT DEM simulations presented in the preliminary analysis, constituting the largest increase in fit achieved through DEM refinement. Figure 6.34 illustrates that the process of DEM refinement typically facilitated an increase in inundation in proximal areas, whilst also propagating larger areas of shallow inundation across the floodplain, accounting for the observed increase in F_{hw} . Overall, refined INT DEM simulations are characterised by shallow inundation (< 5 m depth) over a larger area of the floodplain in comparison with the refined FAV (figure 6.33) and GCH DEMs (figure 6.36), which continue to propagate deeper

flooding over a smaller area of the floodplain. Table 6.17 shows that simulations undertaken using the refined GCH DEMs are associated with fit values ranging

Table 6.15. Summary statistics at high water (06/03/2011) for model simulations with different parameter combinations, using the refined FAV DEMs. Fit (F_{hw}) is fit with respect to flood inundation extent derived from PALSAR SAR imagery.

Measure	Roughness	FAV100			FAV125		
		Channel bed elevation			Channel bed elevation		
		Low	Medium	High	Low	Medium	High
Fit (F_{hw})	Medium	0.61	0.63	0.64	0.64	0.63	0.66
	High	0.63	0.63	0.65	0.65	0.65	0.66
Inundated area (km^2)	Medium	5394.1	5816.0	7343.8	5539.8	5982.2	7461.0
	High	5949.4	6388.2	7509.2	6085.0	6386.3	7418.5
Flood water volume (km^3)	Medium	11.3	12.0	13.0	11.4	12.2	13.2
	High	12.9	13.7	13.9	13.2	13.2	13.6

Table 6.16. Summary statistics at high water (06/03/2011) for model simulations with different parameter combinations, using the refined INT DEMs. Fit (F_{hw}) is fit with respect to flood inundation extent derived from PALSAR SAR imagery.

Measure	Roughness	INT100			INT125		
		Channel bed elevation			Channel bed elevation		
		Low	Medium	High	Low	Medium	High
Fit (F_{hw})	Medium	0.64	0.64	0.68	0.65	0.67	0.69
	High	0.64	0.65	0.69	0.67	0.68	0.69
Inundated area (km^2)	Medium	7718.6	8234.8	10199.4	7841.3	8548.8	9996.8
	High	8529.3	8666.0	13653.8	8599.1	10481.1	13639.0
Flood water volume (km^3)	Medium	9.4	9.9	13.0	9.6	10.3	12.9
	High	11.3	11.3	40.1	11.4	13.3	39.0

Table 6.17. Summary statistics at high water (06/03/2011) for model simulations with different parameter combinations, using the refined GCH DEMs. Fit (F_{hw}) is fit with respect to flood inundation extent derived from PALSAR SAR imagery.

Measure	Roughness	GCH100			GCH125		
		Channel bed elevation			Channel bed elevation		
		Low	Medium	High	Low	Medium	High
Fit (F_{hw})	Medium	0.61	0.63	0.66	0.61	0.62	0.68
	High	0.65	0.67	0.68	0.65	0.67	M
Inundated area (km^2)	Medium	6833.9	6973.6	10193.9	6800.0	6893.7	9591.8
	High	7445.7	11291.7	11775.8	7788.6	10743.9	M
Flood water volume (km^3)	Medium	11.3	12.0	25.8	11.0	11.5	24.2
	High	13.3	33.7	36.8	13.3	30.9	M

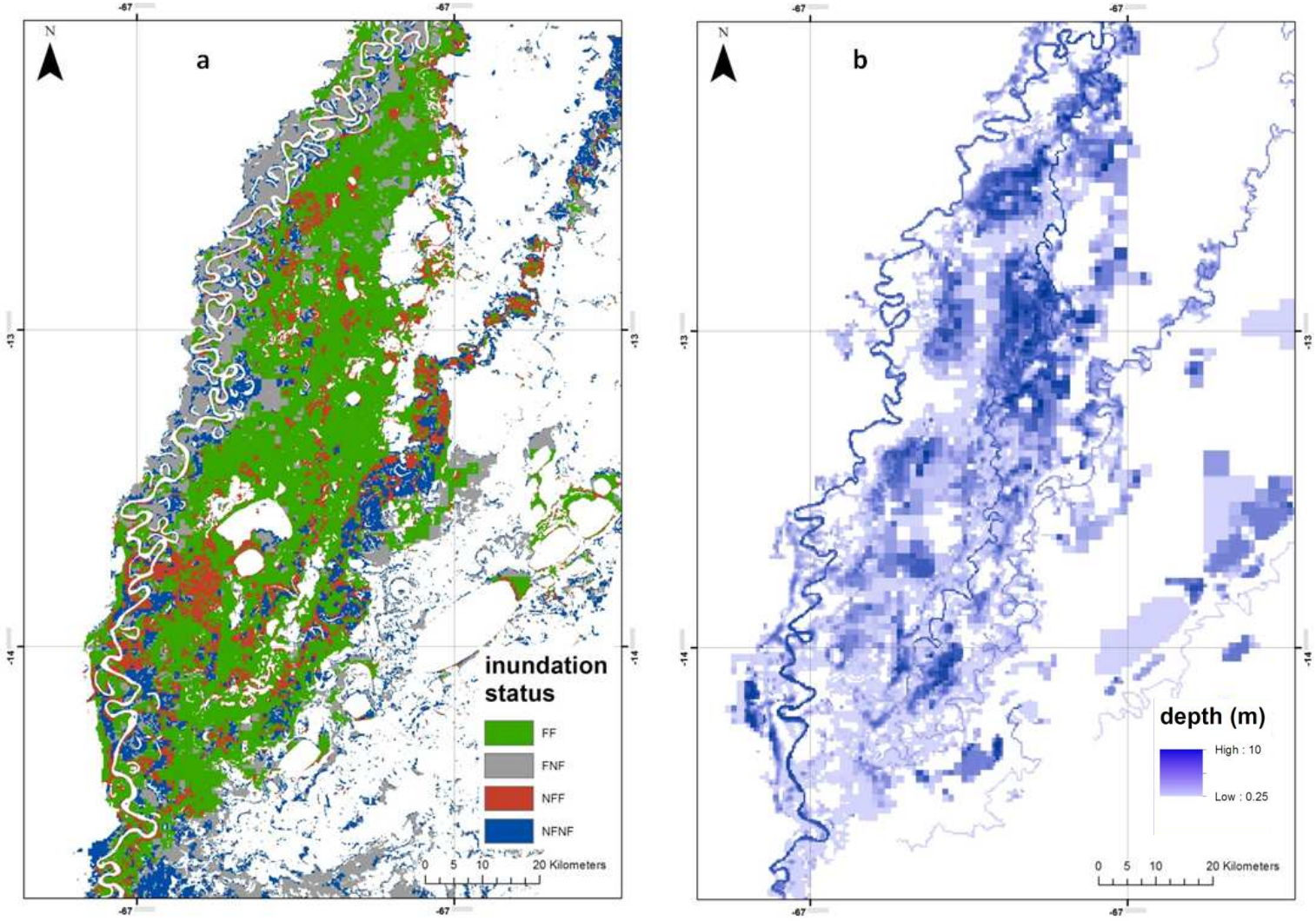

Figure 6.32. Simulated inundation at high water (06/03/2011) using FAV100 DEM, medium roughness and low channel bed elevation a) comparison with PALSAR derived flood inundation extent b) inundation extent and depth (m)

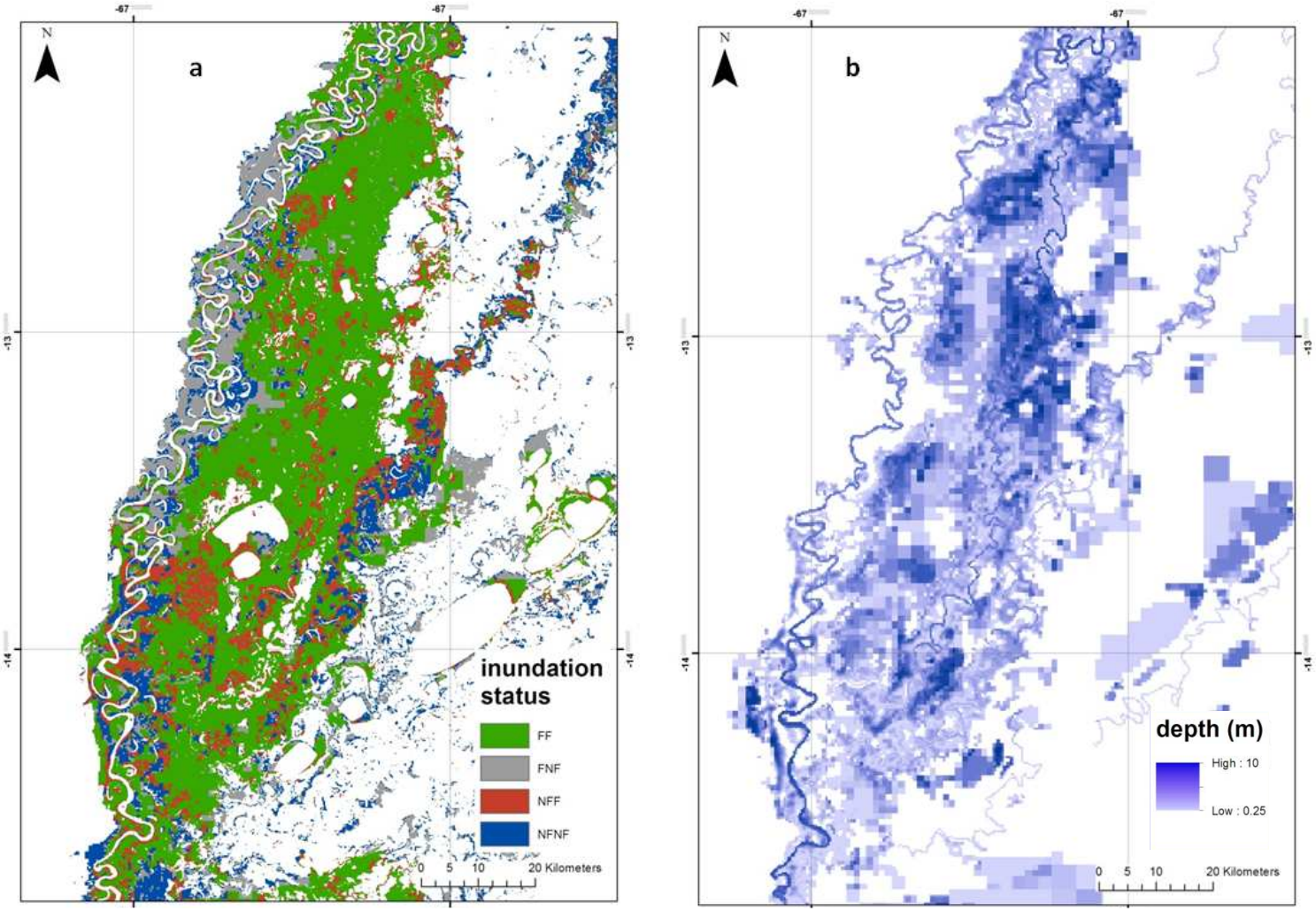

Figure 6.33. Simulated inundation at high water (06/03/2011) using FAV125 DEM, high roughness and high channel bed elevation a) comparison with PALSAR derived flood inundation extent b) inundation extent and depth (m)

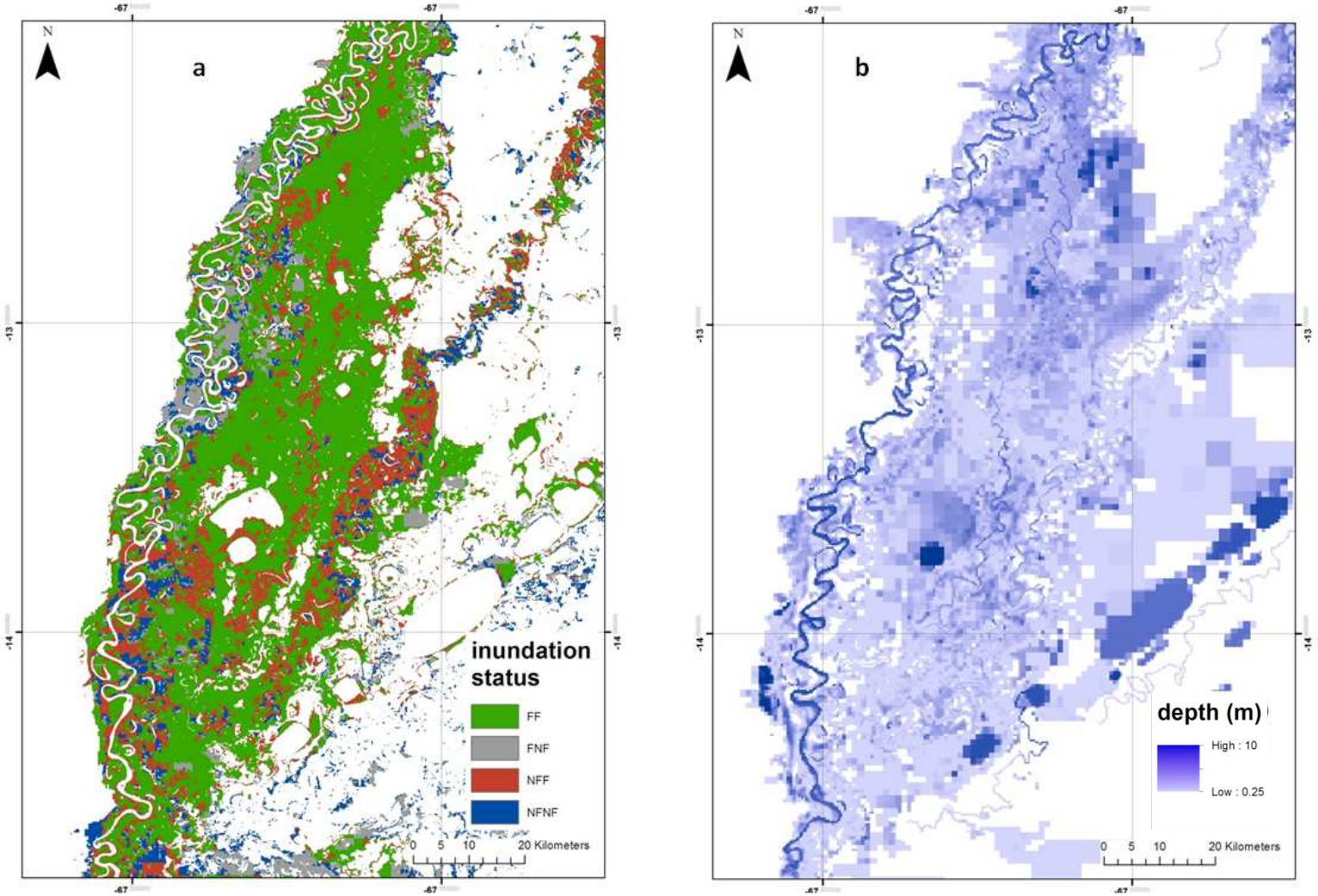

Figure 6.34. Simulated inundation at high water (06/03/2011) using INT100 DEM, medium roughness and high channel bed elevation a) comparison with PALSAR derived flood inundation extent b) inundation extent and depth (m)

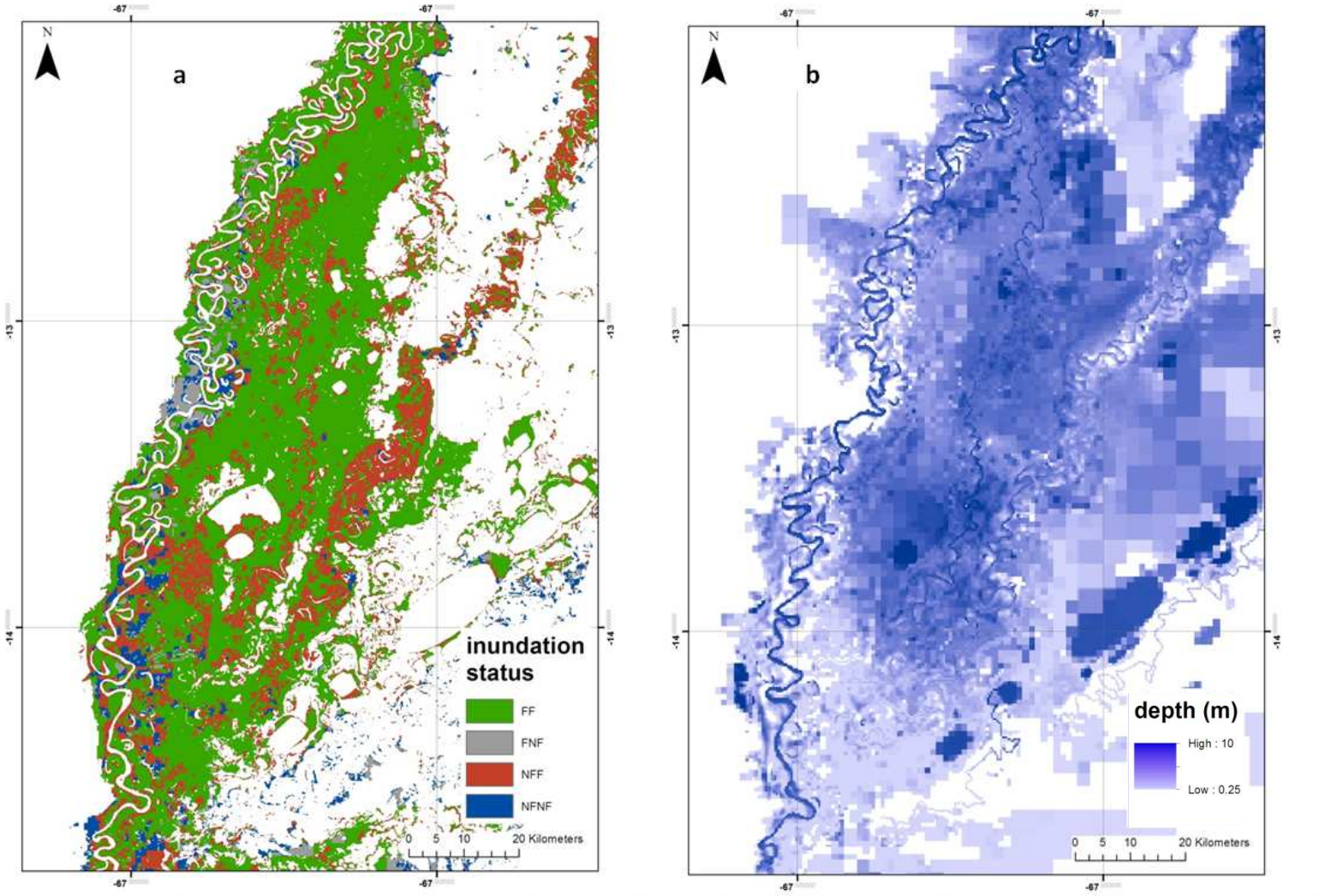

Figure 6.35. Simulated inundation at high water (06/03/2011) using INT100 DEM, high roughness and high channel bed elevation a) comparison with PALSAR derived flood inundation extent b) inundation extent and depth (m)

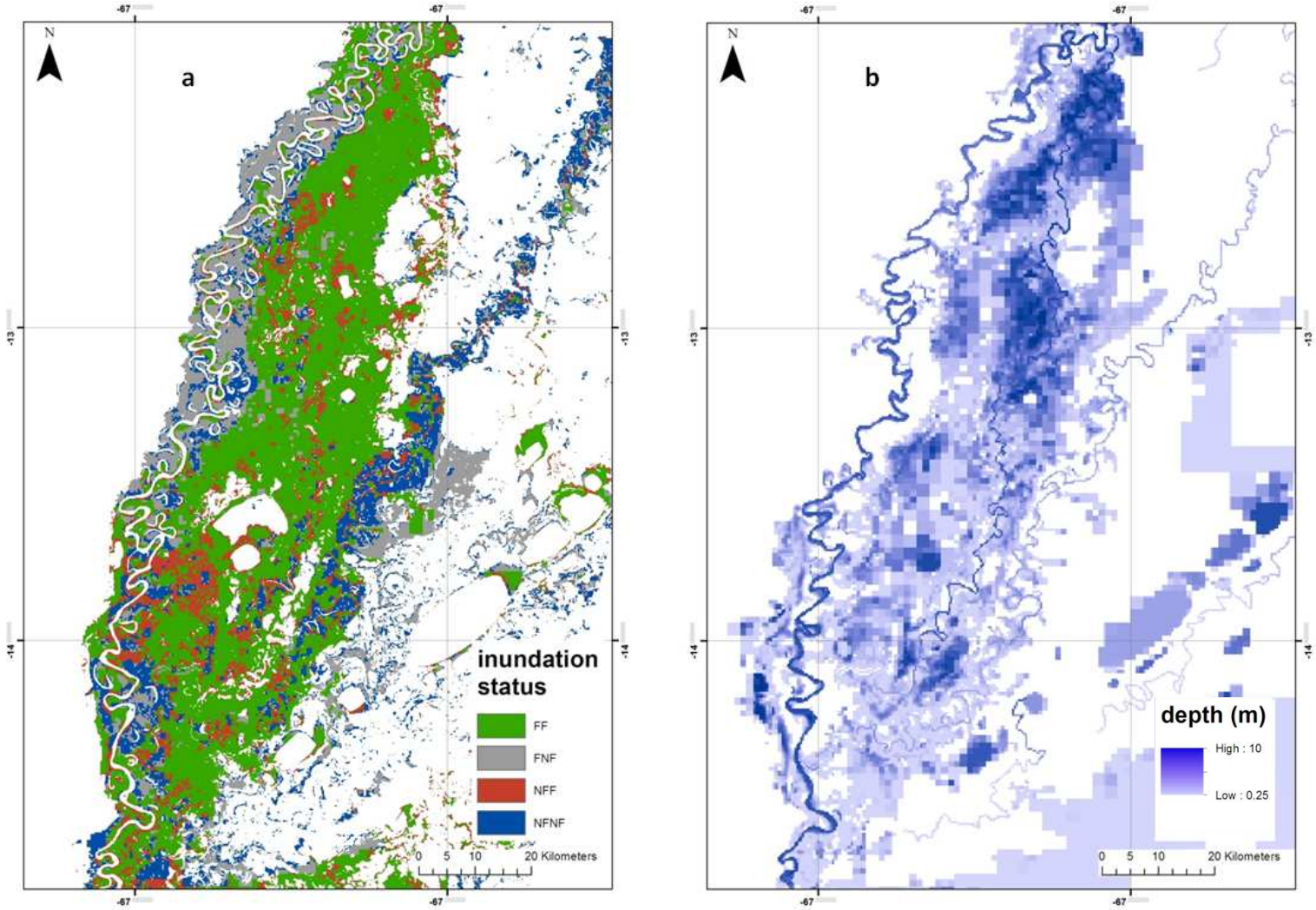

Figure 6.36. Simulated inundation at high water (06/03/2011) using GCH100 DEM, medium roughness and low channel bed elevation a) comparison with PALSAR derived flood inundation extent b) inundation extent and depth (m)

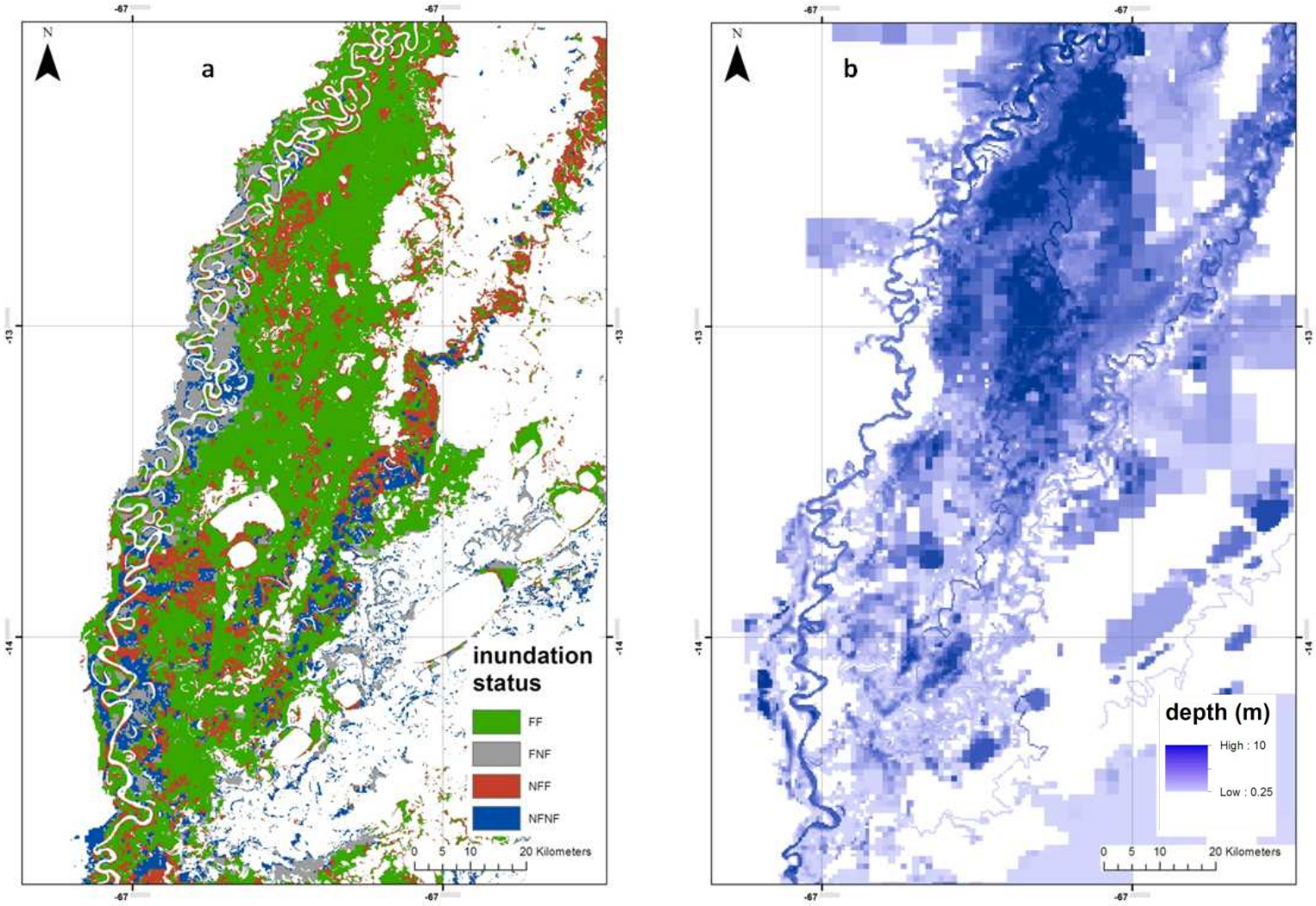

Figure 6.37. Simulated inundation at high water (06/03/2011) using GCH100 DEM, high roughness and high channel bed elevation a) comparison with PALSAR derived flood inundation extent b) inundation extent and depth (m)

from 0.61-0.68, representing an increase in maximum F_{hw} of 0.10. Hence according to values of F_{hw}, the refined GCH DEMs are associated with a lower level of accuracy than the refined INT DEMs, but outperformed refined FAV DEM simulations. Figure 6.36 illustrates that, as for the refined FAV DEMs, inundation remains under predicted in the proximal floodplain for lower roughness and channel bed parameter values, limiting F_{hw} values.

Furthermore, is important to note the occurrence of extreme model behaviour for simulations undertaken using the refined INT and GCH DEMs in combination with roughness and channel bed elevation values from the upper end of the parameter space (tables 6.16 and 6.17). This extreme model behaviour results in very high values for flood volume (>20 km^3) and inundated area, whilst also being associated with high values for $F_{hw.}$ This model behaviour is illustrated visually in figure 6.35 and 6.37, in which it is clear that large areas of the floodplain are inundated to very high depths. This non linear model behaviour is discussed further in section 6.9.

6.8.2 Assessment of low water inundation extent

Tables 6.18-6.20 show results from the comparison of modelled and observed inundation extent, derived from ALOS PALSAR image capture, on 06/09/2010 (low water). Table 6.19 shows that a F_{lw} range of 0.54-0.75 is observed for simulations using the refined FAV DEMs. In all instances, an increase in channel bed elevation results in a decline in F_{lw}, whilst fit is generally lower for simulations using higher roughness set ups. As the floodplain is almost completely dry at low water image capture, increases in F_{lw} generally directly reflect decreases in inundation extent and floodplain water volume. Significantly, substantial variations in fit, inundated area and flood water volume observed across the range of roughness and channel bed elevation parameters, suggests that low water inundation is largely dependent upon the magnitude of flooding at high water within simulations using the refined FAV DEMs. This is reflected in figures 6.38 and 6.39, which visually illustrate large variations in low water flood extent extracted from simulations using different combinations of roughness and channel bed elevation parameters. However, within both figure 6.38 and 6.39, substantial areas of relatively deep flood waters remain upon the floodplain. These flood waters are typically

concentrated within areas which were subject to substantial depths of inundation at high water, and indicate incomplete dewatering of the floodplain.

Table 6.18. Summary statistics at low water (06/09/2010) for model simulations with different parameter combinations, using the refined FAV DEMs. Fit (F_{lw}) is fit with respect to flood inundation extent derived from PALSAR SAR imagery.

Measure	Roughness	FAV100			FAV125		
		Channel bed elevation			Channel bed elevation		
		Low	Medium	High	Low	Medium	High
Fit (F_{lw})	Medium	0.72	0.70	0.57	0.75	0.64	0.58
	High	0.74	0.60	0.54	0.73	0.56	0.51
Inundated area (km^2)	Medium	2829.7	2912.0	3692.3	2659.1	3284.7	3687.1
	High	2740.6	3668.1	4048.9	2790.5	3801.2	4219.2
Flood water volume (km^3)	Medium	3.24	3.53	5.10	3.08	3.93	5.00
	High	3.35	4.84	5.83	3.31	4.84	5.81

Table 6.19. Summary statistics at low water (06/09/2010) for model simulations with different parameter combinations, using the refined INT DEMs. Fit (F_{lw}) is fit with respect to flood inundation extent derived from PALSAR SAR imagery.

Measure	Roughness	INT100			INT125		
		Channel bed elevation			Channel bed elevation		
		Low	Medium	High	Low	Medium	High
Fit (F_{lw})	Medium	0.76	0.69	0.64	0.76	0.72	0.59
	High	0.68	0.65	0.22	0.69	0.62	0.21
Inundated area (km^2)	Medium	3240.6	3717.8	4018.3	3282.9	3486.5	4353.4
	High	3834.2	4069.4	10967.0	3763.5	4207.7	10851.3
Flood water volume (km^3)	Medium	3.04	3.29	3.49	3.01	3.17	3.66
	High	3.45	3.60	34.27	3.39	3.68	33.39

Table 6.20. Summary statistics at low water (06/09/2010) for model simulations with different parameter combinations, using the refined GCH DEMs. Fit (F_{lw}) is fit with respect to flood inundation extent derived from PALSAR SAR imagery.

Measure	Roughness	GCH100			GCH125		
		Channel bed elevation			Channel bed elevation		
		Low	Medium	High	Low	Medium	High
Fit (F_{lw})	Medium	0.73	0.61	0.67	0.69	0.58	0.54
	High	0.71	0.69	0.37	0.59	0.55	U
Inundated area (km^2)	Medium	3226.4	3995.9	3786.4	3421.7	4224.8	4614.0
	High	4088.6	4171.5	10223.9	4285.6	4827.5	U
Flood water volume (km^3)	Medium	3.59	4.21	4.69	3.64	4.36	5.24
	High	3.94	4.30	31.97	4.24	5.06	U

Prior to description of low water results for the refined INT and GCH DEMs, it is significant to note that tables 6.19 and 6.20 highlight the occurrence of extreme

model behaviour, which was described within the previous section for simulations using the refined INT and GCH DEMs. Figures 6.41 and 6.43 demonstrate this behaviour at low water for simulations utilising higher roughness and channel bed elevation parameters, illustrating that large volumes of flood water remain on the floodplain, resulting in low values of F_{lw} (<0.40). Results for these simulations will not be included in the subsequent analysis of low water comparison results for the refined INT and GCH DEMs.

The refined INT DEMs (table 6.19) are characterised by the highest values of F_{lw} for simulations using the refined DEMs, varying between 0.59-0.76 across the range of parameters used here. This is largely a result of the fact that at low water, the refined INT DEMs produce the lowest inundated area and lowest flood water volumes of any simulations undertaken here. Interestingly, for the refined INT DEM simulations, flood water volume which varied between 3.01 km^3 and 3.68 km^3 across the range of roughness and channel bed elevation parameters used here. These flood water volumes were both lower, and were characterised by a much smaller range, than equivalent values observed for the FAV and GCH DEMs, which varied from 3.08-5.83 km^3 and 3.64-5.24 km^3 respectively. Figure 6.40 visually demonstrates typical low water flood extent for simulations using the refined INT DEMs. Whilst a modest area of the floodplain remains inundated in figure 6.40, flood waters are markedly shallower than is observed for the refined FAV and GCH DEMs. This reflects the lower flood water volumes observed for simulations utilising the refined INT DEMs.

F_{lw} ranges from 0.54 to 0.73 for simulations utilising the refined GCH DEMs (table 6.20). This constitutes a lower level of performance than was observed for the refined FAV and INT DEM simulations, and can be attributed to the fact that simulations utilising the GCH were typically characterised by the highest values for inundated area and flood water volume at low water. As for the other DEMs, F_{lw} values tend to decrease with increases in roughness and channel bed elevation. Figure 6.42 illustrates typical low water inundation extent for simulations utilising the GCH DEMs. Low water inundation characteristics propagated by the refined GCH DEMs are similar to those observed for the refined FAV DEMs (figure 6.38). Typically, large volumes of flood water accumulate in areas which are inundated to a significant depth at high water, indicating incomplete drainage of the floodplain.

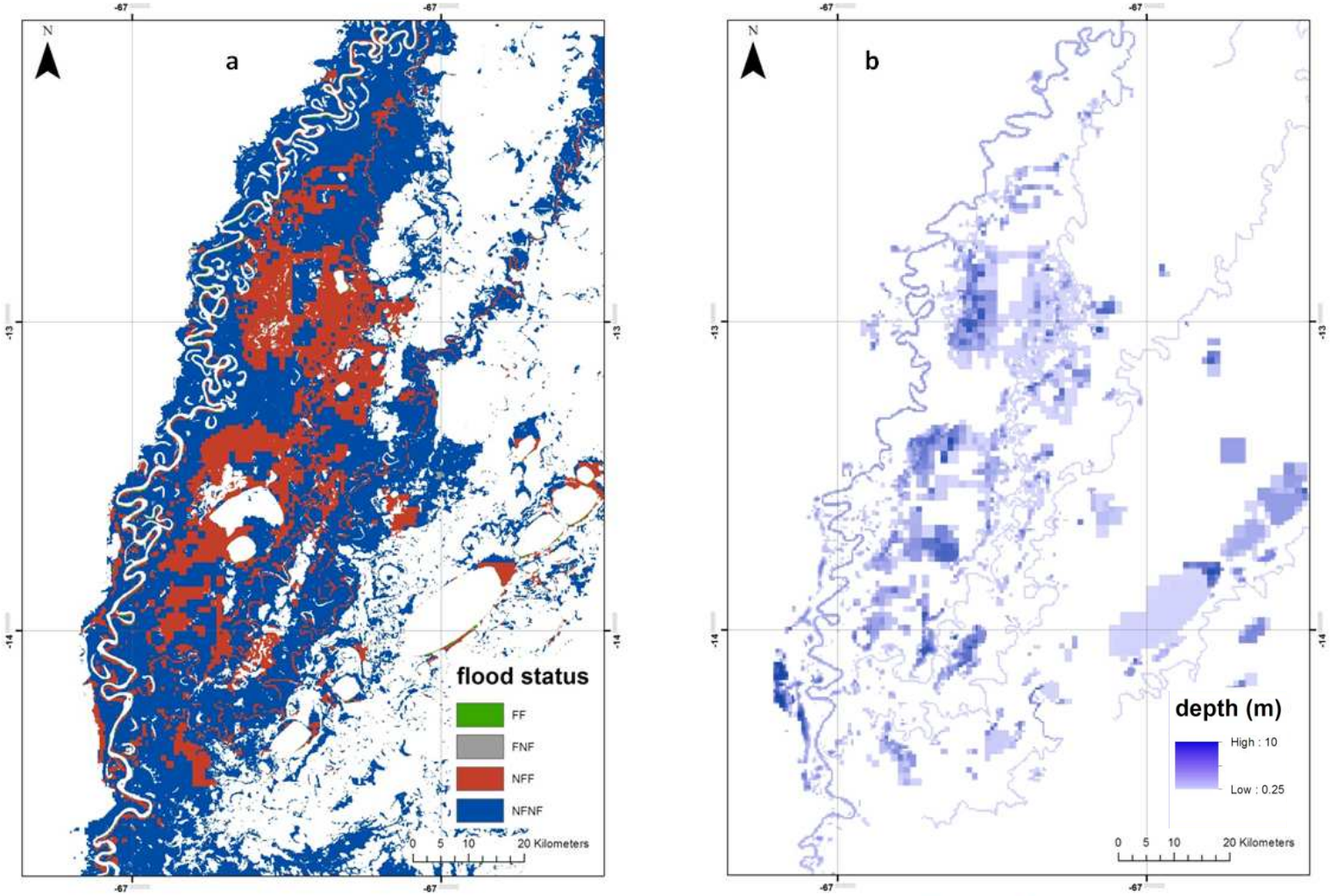

Figure 6.38. Simulated inundation at low water (06/09/2010) using FAV100 DEM, medium roughness and low channel bed elevation a) comparison with PALSAR derived flood inundation extent b) inundation extent and depth (m)

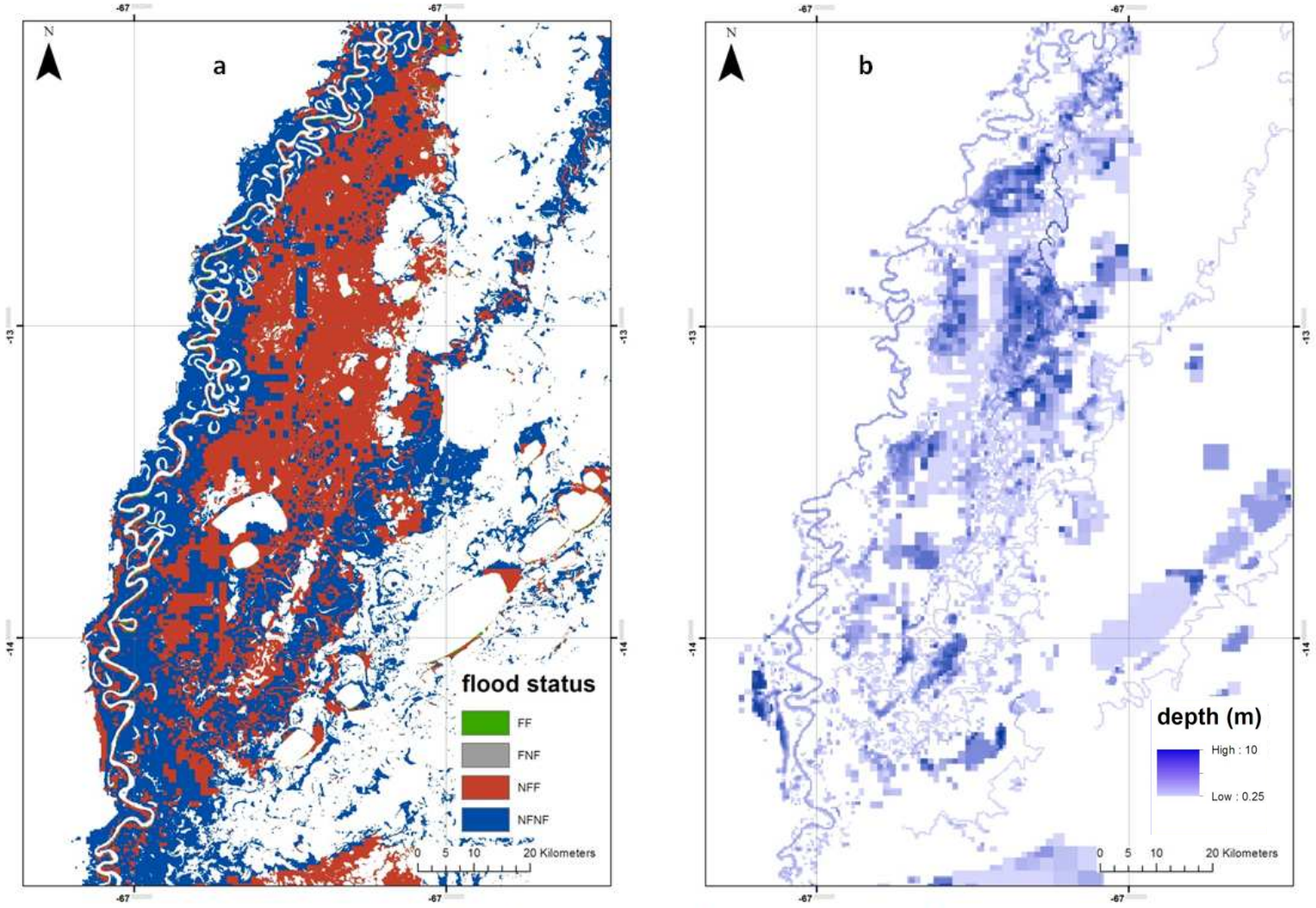

Figure 6.39. Simulated inundation at low water (06/09/2010) using FAV125 DEM, high roughness and high channel bed elevation a) comparison with PALSAR derived flood inundation extent b) inundation extent and depth (m)

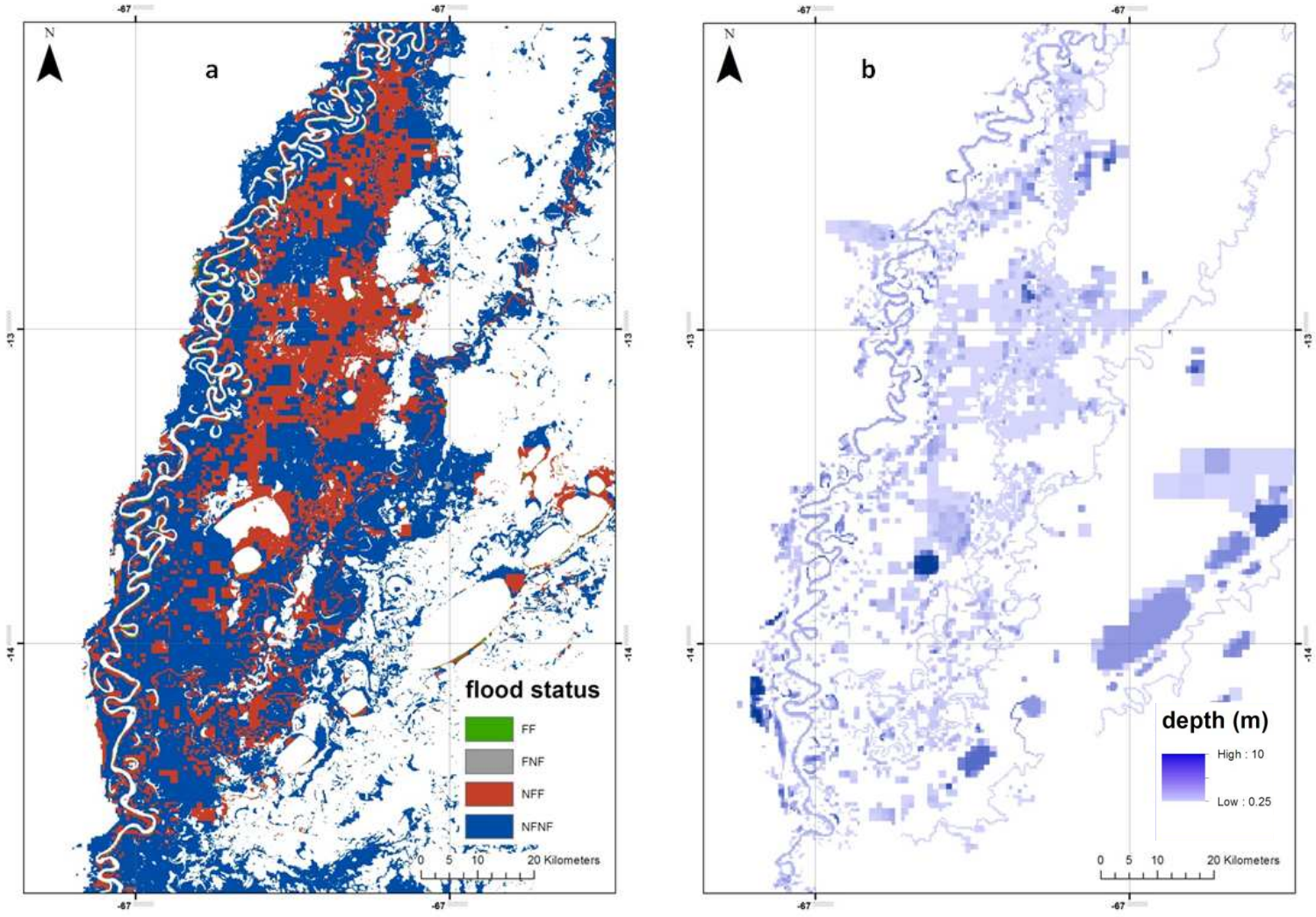

Figure 6.40. Simulated inundation at low water (06/09/2010) using INT100 DEM, medium roughness and high channel bed elevation a) comparison with PALSAR derived flood inundation extent b) inundation extent and depth (m)

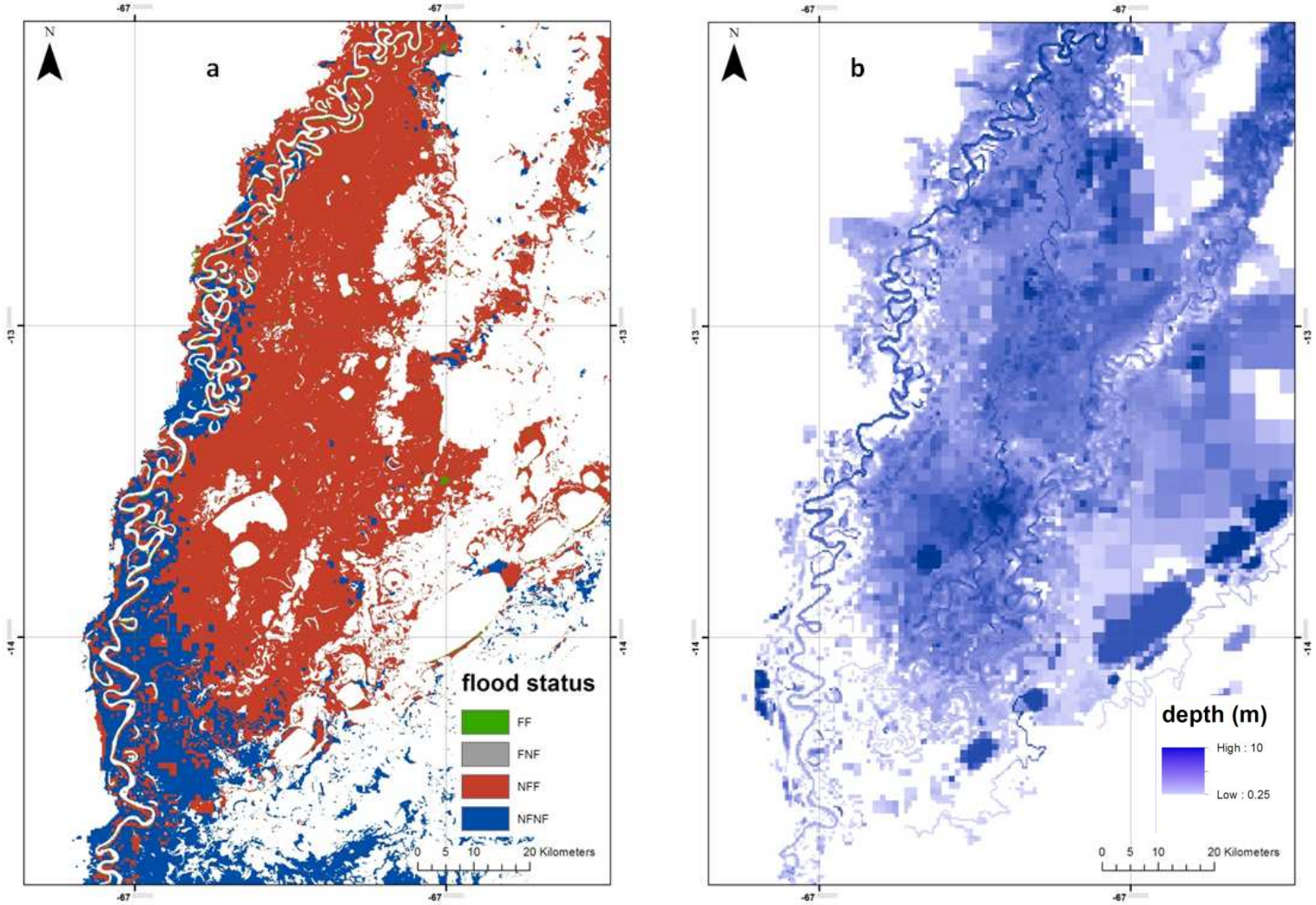

Figure 6.41. Simulated inundation at low water (06/09/2010) using INT100 DEM, high roughness and high channel bed elevation a) comparison with PALSAR derived flood inundation extent b) inundation extent and depth (m)

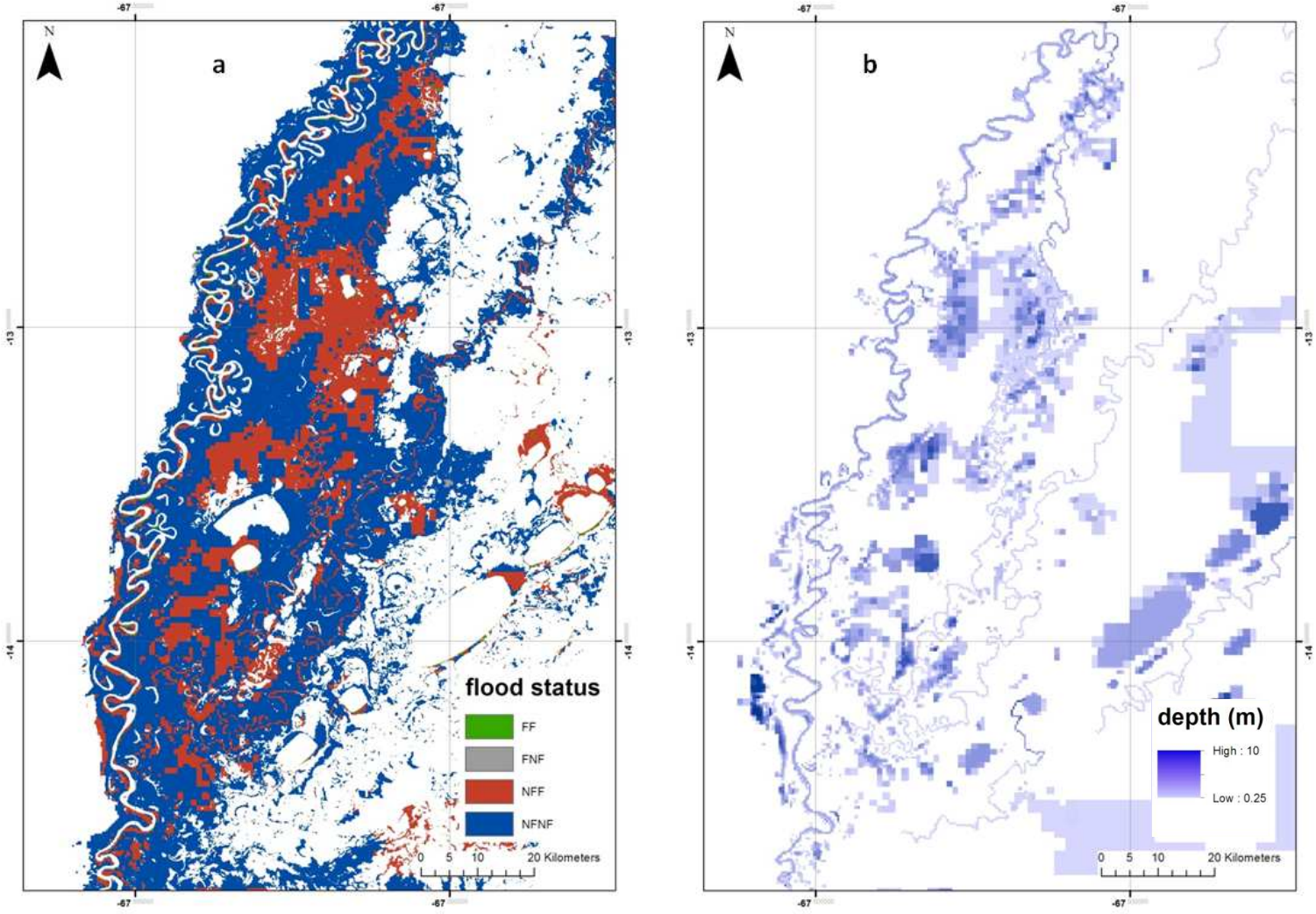

Figure 6.42. Simulated inundation at low water (06/09/2010) using GCH100 DEM, high roughness and low channel bed elevation a) comparison with PALSAR derived flood inundation extent b) inundation extent and depth (m)

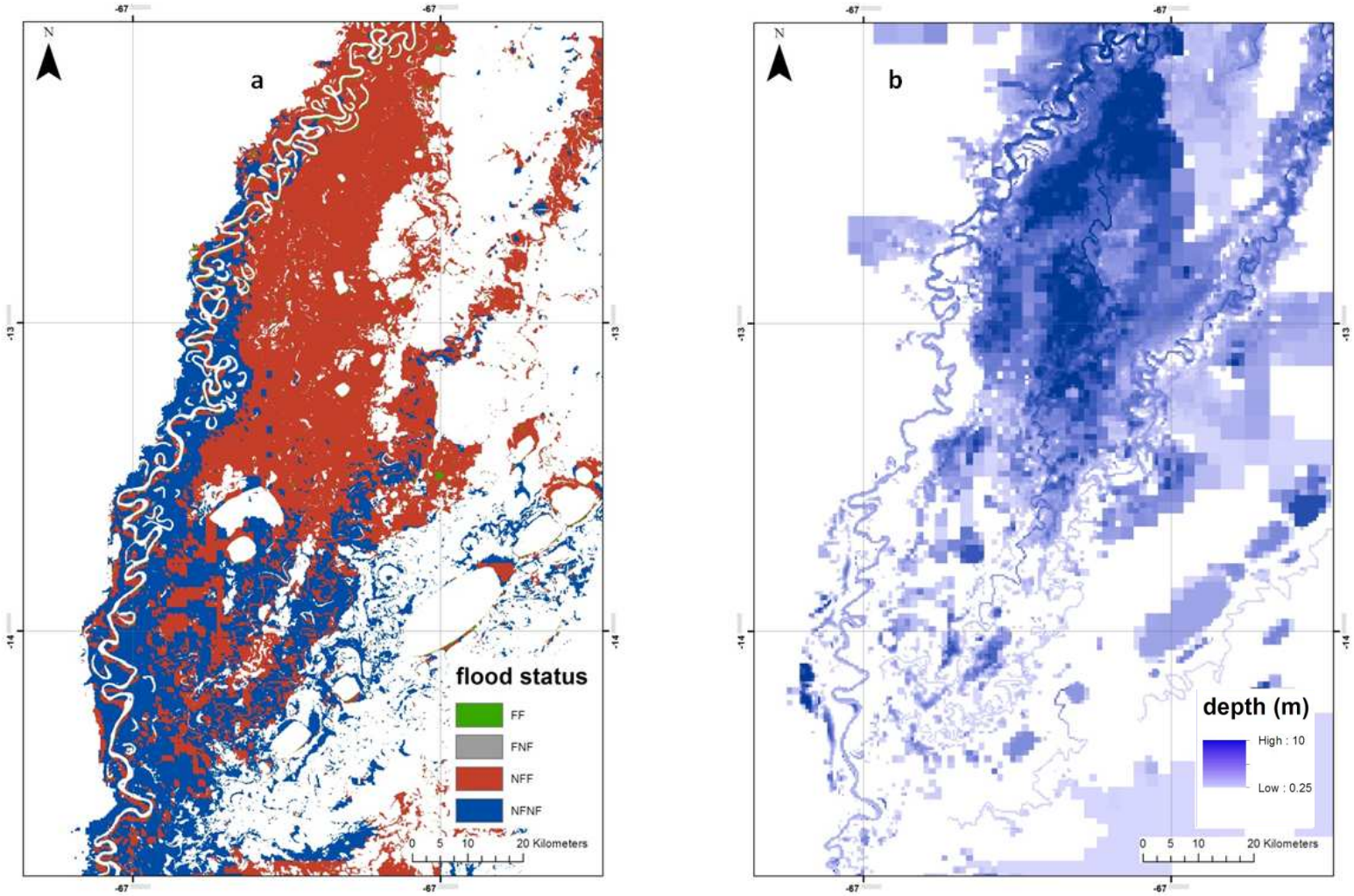

Figure 6.43. Simulated inundation at low water (06/09/2010) using GCH100 DEM, high roughness and high channel bed elevation a) comparison with PALSAR derived flood inundation extent b) inundation extent and depth (m)

6.8.3 Assessment of Beni river water surface elevation with respect to TOPEX-POSEIDON altimetry

Tables 6.22 to 6.27, along with figures 6.44-6.46, present results of the comparison between modelled water surface elevation (WSE) in the Beni river channel and an observed water surface elevation time series acquired by the TOPEX-POSEIDON mission. The comparison is undertaken at the intersection of the TOPEX-POSEIDON (T/P) track with the Beni river, located in the downstream reach of the domain, close to the model outlet. Modelled and observed water surface elevation is compared for a three year period from 01/09/1997 to 31/08/2000, and RMSE is calculated based upon a total of 39 T/P observations. This total set comprises 28 points during high water periods (November-May) and 11 points from low water (June-October).

Tables 6.21 and 6.22 present results from the comparison of modelled and observed water surface elevation for the simulations using the refined FAV DEMs. Overall RMSE values for predicted water surface elevation vary from 3.70-4.57 m for these simulations. For all simulations, water surface elevation is predicted with a higher degree of accuracy at low flow. Based upon RMSE values, simulations undertaken using the refined FAV DEMs are associated with a markedly inferior level of accuracy in terms of WSE in comparison to simulations utilising the alternative refined DEMs. Figure 6.44 provides a visual illustration of T/P WSE and modelled WSE, and can be considered representative of the range of simulations undertaken using the refined FAV DEMs. It is evident that WSE is significantly under predicted within simulations utilising the refined FAV DEMs, which can be attributed as the reason for the low values of RMSE shown in tables 6.22 and 6.23. For both simulations depicted in figure 6.44, WSE is under predicted by 3-5 m during high water. Based upon figure 6.44 it is clear that the model provides a poor representation of the amplitude of the flood wave across the parameter space for FAV DEM simulations. Indeed tables 6.21 and 6.22 indicate that WSE amplitude ranges from a maximum of 6.03 m at the low end of the parameter space to a minimum of 4.93 m at the upper limit of the parameter space. These values are substantially lower than the observed amplitude of 7.97 m for the observed WSE time series obtained from TOPEX-POSEIDON altimetry.

Table 6.21. Assessment of modelled Beni river water surface elevation with respect to TOPEX-POSEIDON altimetry data for simulations using the FAV100 DEM. WSE amplitude corresponds to the modelled amplitude of water surface elevation through the three year study period.

Roughness		Medium			High	
Channel bed elevation	Low	Medium	High	Low	Medium	High
WSE amplitude (m)	6.03	5.21	4.93	5.63	4.84	5.02
Low water RMSE (m)	3.11	2.18	1.71	2.29	1.71	1.53
High water RMSE (m)	5.03	4.77	4.47	4.28	4.25	4.28
Overall RMSE (m)	4.57	4.20	3.89	3.82	3.71	3.72

Table 6.22. Assessment of modelled Beni river water surface elevation with respect to TOPEX-POSEIDON altimetry data for simulations using the FAV125 DEM. WSE amplitude corresponds to the modelled amplitude of water surface elevation through the three year study period.

Roughness		Medium			High	
Channel bed elevation	Low	Medium	High	Low	Medium	High
WSE amplitude (m)	5.96	5.05	4.37	5.44	4.43	4.93
Low water RMSE (m)	3.01	2.18	1.69	2.32	1.70	1.51
High water RMSE (m)	4.87	4.84	4.38	4.70	4.32	4.26
Overall RMSE (m)	4.42	4.26	3.82	4.17	3.77	3.70

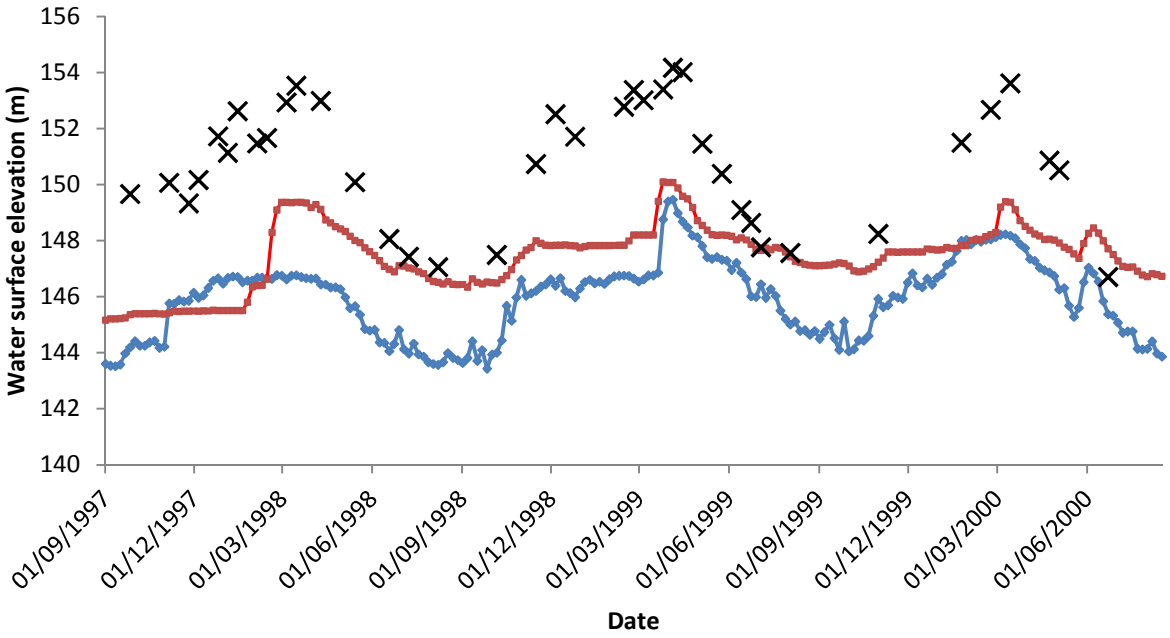

Figure 6.44. Comparison of observed water surface elevation derived from TOPEX-POSEIDON altimetry (black crosses) with modelled time series of water surface elevation. Blue line corresponds to simulation based upon FAV100 DEM with medium roughness and low channel bed elevation. Red line corresponds to the simulation based upon the FAV125 DEM with high roughness and channel bed elevation.

Accuracy of modelled water surface elevation for simulations using the refined INT DEMs are displayed in tables 6.23 and 6.24, exhibiting an overall RMSE

range of 0.92-1.26 m. Based upon these RMSE values, simulations undertaken using the refined INT DEMs are associated with the highest levels of overall accuracy with respect to altimetry data. RMSE values indicate that simulations undertaken using the refined INT DEMs typically predict WSE with a greater level of accuracy at high water. Whilst results do not indicate a clear trend in RMSE values across the parameter space, it is evident that WSE amplitude declines with both increasing roughness and channel bed elevation. Overall, for both INT100 and INT125 the highest levels of overall accuracy in terms of WSE are produced through simulations undertaken using medium roughness and medium channel bed elevation, and high roughness in combination with low channel bed elevation. Simulations using these parameter sets are able to most effectively reconcile WSE accuracy at both high and low water.

Table 6.23. Assessment of modelled Beni river water surface elevation with respect to TOPEX-POSEIDON altimetry data for simulations using the INT100 DEM. WSE amplitude corresponds to the modelled amplitude of water surface elevation through the three year study period. U- unstable simulation.

Roughness		Medium			High	
Channel bed elevation	Low	Medium	High	Low	Medium	High
WSE amplitude (m)	7.11	6.34	5.58	6.91	5.93	U
Low water RMSE (m)	1.31	1.20	1.66	1.25	1.69	U
High water RMSE (m)	1.19	0.80	0.53	0.75	0.76	U
Overall RMSE (m)	1.22	0.93	1.26	0.92	1.10	U

Table 6.24. Assessment of modelled Beni river water surface elevation with respect to TOPEX-POSEIDON altimetry data for simulations using the INT125 DEM. WSE amplitude corresponds to the modelled amplitude of water surface elevation through the three year study period. U- unstable simulation.

Roughness		Medium			High	
Channel bed elevation	Low	Medium	High	Low	Medium	High
WSE amplitude (m)	7.08	6.10	5.37	6.60	5.87	U
Low water RMSE (m)	1.31	1.19	1.74	1.25	1.68	U
High water RMSE (m)	1.22	0.91	0.88	0.83	0.91	U
Overall RMSE (m)	1.24	1.00	1.19	0.96	1.18	U

Figure 6.45 presents a visual comparison of WSE observed by TOPEX-POSEIDON and modelled WSE extracted from simulations for INT125 DEM combined with a medium roughness set up and the full range of channel bed elevation configurations. Based upon visual analysis of 6.45 it is clear that simulations undertaken using the INT DEMs provide a much better representation of water surface elevations for the Beni river, in comparison to

the FAV DEMs. During low water, the observed TOPEX-POSEIDON WSE is typically contained within the range of modelled WSE for the three simulations. At high water, WSE predicted for the different simulations converge and typically correspond well to the T/P altimetry time series. However model simulations typically under predict water surface elevation at the peak of the flood wave by ~1 m.

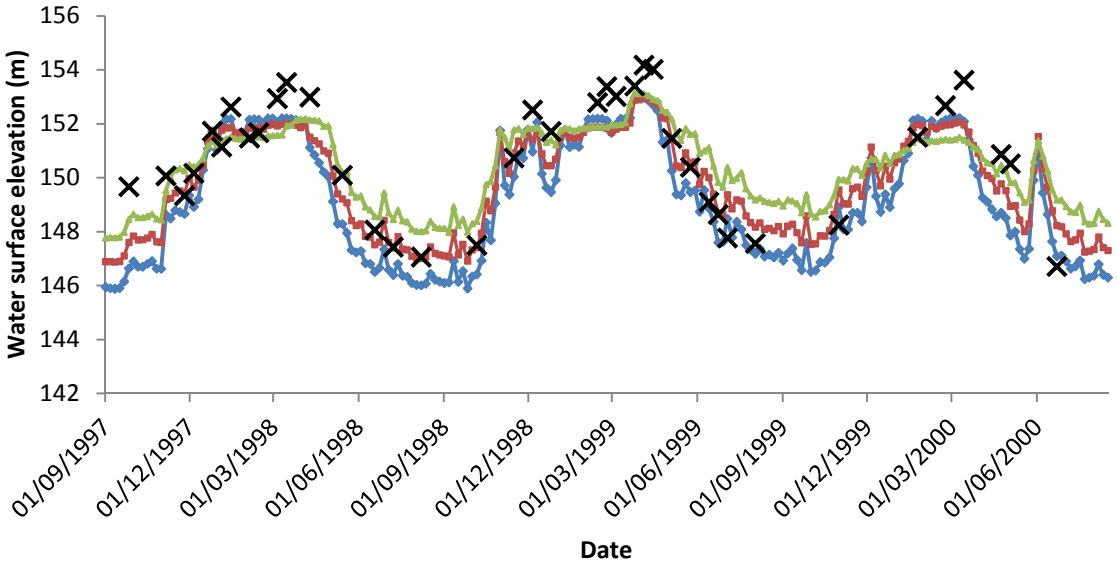

Figure 6.45. Comparison of observed water surface elevation derived from TOPEX-POSEIDON altimetry (black crosses) with modelled time series of water surface elevation. Blue line corresponds to simulation based upon INT125 DEM with medium roughness and low channel bed elevation. Red line corresponds to the simulation based upon the INT125 DEM with medium roughness and medium channel bed elevation. Green line corresponds to the INT125 DEM with medium roughness and high channel bed elevation.

Comparison of observed and modelled water surface elevation for simulations utilising the refined GCH DEMs is displayed in tables 6.25 and 6.26. Overall, RMSE values vary from 1.10 m-1.78 m for simulations utilising these DEMs. Therefore in broad terms, modelled water surface elevation in simulations utilising the refined GCH DEMs is associated with a substantially higher level of accuracy than simulations undertaken using the refined FAV DEMs, but a lower accuracy than for the refined INT DEMs, particularly at low water. As for the INT DEMs, WSE is modelled with a greater degree of accuracy at high water with respect to T/P altimetry. In addition, whilst results do not indicate a clear trend in RMSE values with changes in roughness or channel bed elevation values, it is evident that WSE amplitude declines with both increasing roughness and channel bed elevation.

Table 6.25. Assessment of modelled Beni river water surface elevation with respect to TOPEX-POSEIDON altimetry data for simulations using the GCH100 DEM. WSE amplitude corresponds to the modelled amplitude of water surface elevation through the three year study period. U- unstable simulation.

Roughness		Medium			High	
Channel bed elevation	Low	Medium	High	Low	Medium	High
WSE amplitude (m)	6.47	5.56	4.88	6.46	5.49	U
Low water RMSE (m)	1.47	2.14	2.86	2.12	1.68	U
High water RMSE (m)	0.92	0.69	0.97	0.97	1.68	U
Overall RMSE (m)	1.10	1.28	1.72	1.39	1.18	U

Table 6.26. Assessment of modelled Beni river water surface elevation with respect to TOPEX-POSEIDON altimetry data for simulations using the GCH125 DEM. WSE amplitude corresponds to the modelled amplitude of water surface elevation through the three year study period. U- unstable simulation.

Roughness		Medium			High	
Channel bed elevation	Low	Medium	High	Low	Medium	High
WSE amplitude (m)	6.05	5.26	4.59	6.01	U	U
Low water RMSE (m)	1.48	2.12	2.80	2.14	U	U
High water RMSE (m)	1.15	0.86	1.15	0.78	U	U
Overall RMSE (m)	1.25	1.34	1.78	1.32	U	U

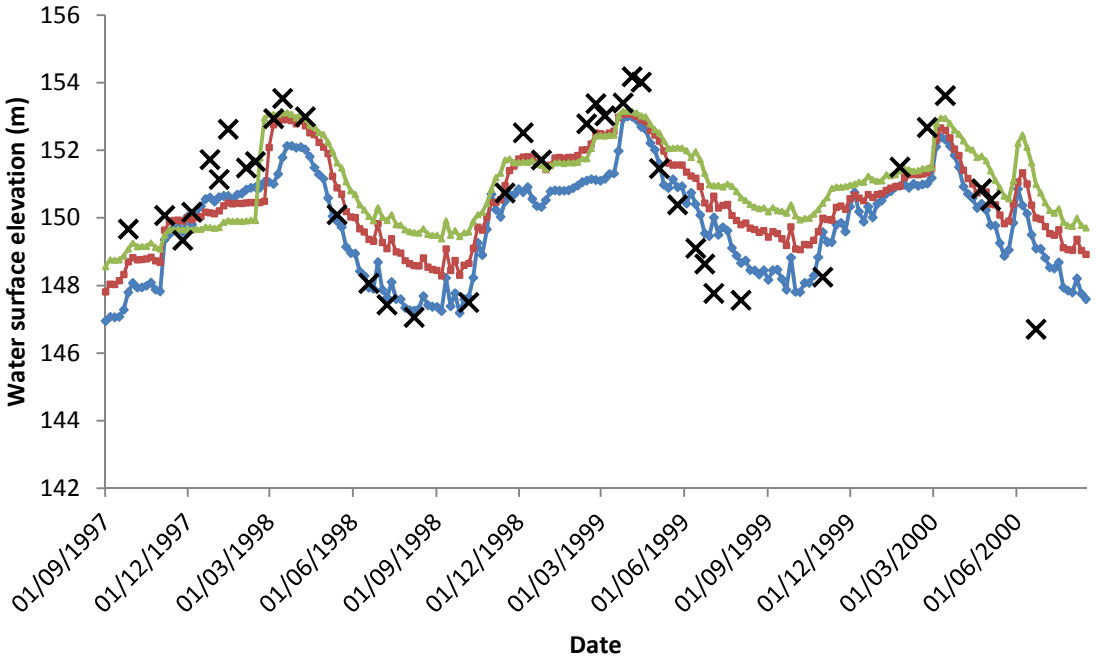

Figure 6.46. Comparison of observed water surface elevation derived from TOPEX-POSEIDON altimetry (black crosses) with modelled time series of water surface elevation. Blue line corresponds to simulation based upon GCH125 DEM with medium roughness and low channel bed elevation. Red line corresponds to the simulation based upon the GCH125 DEM with medium roughness and medium channel bed elevation. Green line corresponds to the GCH125 DEM with medium roughness and high channel bed elevation.

Figure 6.46 facilitates a visual comparison of the TOPEX-POSEIDON WSE observations and modelled WSE time series obtained from simulations utilising the GCH125 DEM combined with medium roughness and the full range of channel bed elevation parameters. Figure 6.46 demonstrates that simulations utilising GCH DEMs are associated with a significantly improved representation of variations in WSE in comparison to the refined FAV DEMs. Low water WSE is predicted most accurately by the simulation characterised by low channel bed configuration (blue line), with low water WSE increasingly over predicted for simulations associated with medium and high channel bed elevations. Modelled WSE converges at high water and peak WSE is underestimated by less than 1m.

6.9 Discussion

In the preliminary results, simulations utilising the INT DEM were associated with the most consistent and physically realistic response to changes in model parameters. Therefore one might expect the INT DEM to offer the highest level of performance in the initial comparison with high water flood extent. However this was not the case, as in fact simulations utilising the INT DEM were typically associated with lower values for F_{hw} than model runs undertaken using the FAV and GCH DEMs. The ranges of F_{hw} observed for simulations undertaken using the FAV DEM, the INT DEM and the GCH DEM were 0.52-0.54, 0.37-0.51 and 0.48-0.58 respectively. This range of F_{hw} was indicative of a poor level of model performance when considered in the context of other hydraulic modelling studies, which are typically able to predict inundation extent with an accuracy of greater than 0.60 (Hunter et al., 2007). Most relevantly, for application of the LISFLOOD-FP model within the central Amazon floodplain, inundation extent was predicted with fit ranging from 0.52-0.72 at high water, with respect to observations based upon JERS-1 SAR imagery (Wilson et al., 2007). Therefore the range of F_{hw} observed here for simulations undertaken using the INT DEM falls below the range of fit reported by Wilson et al., (2007), whilst F_{hw} for simulations using the FAV DEM are located at the lower end of the range of values reported in the aforementioned study. This is particularly interesting, as the methodology used in order to generate the FAV DEM in chapter 5, was the same as that applied by Wilson et al., (2007), for correction of the SRTM in the central Amazon floodplain. This disparity in fit values suggests that additional

factors specific to the Beni floodplain study area preclude prediction of inundation extent with an equivalent level of accuracy as the aforementioned study.

Perhaps the most significant feature of the initial simulations presented in 6.6 is the under prediction of inundation in the proximal floodplain. This is observed in simulations undertaken using all of the bare earth DEMs, but is particularly prevalent for those in which topographical forcing is provided by the FAV DEM and GCH DEM. Intuitively, under prediction of flooding within proximal areas of the floodplain can be attributed to over elevation of these areas within the bare earth DEMs, which prevents cells from becoming inundated during high water. Accordingly, it is clear that the under prediction of inundation in proximal areas of the floodplain directly contributes towards the poor levels of fit observed for preliminary simulations undertaken using all of the bare earth DEMs. However, the presence of raised areas adjacent to the channel has further implications for inundation dynamics here. The low flood water volumes observed in preliminary simulations undertaken using the INT DEM suggest that areas of high elevation adjacent to the channel limit the volume of overbank flow during flood events, leading to under prediction of inundation extent within other areas of the floodplain, as indicated in table 6.9. This is reflected in the low values of F_{hw} which characterise preliminary simulations undertaken using the INT DEM, particularly in combination with low roughness and channel bed elevation configurations. Higher flood water volumes and F_{hw} suggest that this is not such an issue for simulations forced by the FAV DEM and the GCH DEM. However, the spatial patterns of flooding shown within figure 6.22a and 6.22c bring into question the simulation of inundation dynamics based upon these bare earth DEMs. Within these simulations, overbank flow occurs at relatively few locations along the reach, at which large volumes of water flow out of the Beni channel directly into topographical depressions in the floodplain. This process is driven by the high hydraulic gradients which occur as a result of the differences in elevation between the channel and the topographical depressions. Therefore in light of the aforementioned discussion, it was considered necessary to further refine the floodplain DEMs in order to remove the areas of high elevation located in close proximity to the Beni river channel.

For simulations using the FAV DEM and the GCH DEM, poor predictions of inundation extent observed in the preliminary analysis largely represent a manifestation of issues highlighted in the quantitative and qualitative assessment of the DEMs in chapter 5. In quantitative validation the RMSE of the FAV DEM and GCH DEM were calculated at 4.6 m and 3.9 m respectively. The majority of errors removed from these DEMs during the process of DEM refinement in section 6.7, illustrated by the histograms in figures 6.25 and 6.26, are within the range which would be expected based upon these RMSE values. In addition, qualitative assessment of the FAV and GCH DEMs highlighted the fact that the field averaged zonal canopy height map and global canopy height map were unable to reproduce spatial variation in forest height across the floodplain. In particular, that they were unable to reconcile the increase in canopy height observed for forest stands located within the channel belt, with the lower canopy heights in the distal floodplain. Indeed it is this shortcoming that leads to the under prediction of inundation extent in preliminary simulations using these DEMs. Qualitative assessment in chapter 5 suggested that the canopy height map used to generate the INT DEM better accounted for spatial variations in canopy height across the floodplain, including the increase in canopy height observed within forest stands located in the channel belt. However, preliminary results from inundation model simulations clearly suggest that the proximal floodplain is also over elevated within the INT DEM. The implication of model results is that the bare earth elevation points did not provide an accurate representation of ground elevation within some areas of the channel belt, leading to a positively biased first order estimated DEM. As for the FAV DEM and GCH DEMs, the majority of errors removed from the INT DEM during refinement in section 6.7 were within the range which would be expected based upon the RMSE of the DEM (3.5 m). In addition, this suggests that the cross sections extracted from the INT DEM and displayed within 5.22, 5.29 and 5.36 are not typical of topography observed within proximal areas along the entire length of the studied reach of the Beni.

Overall, given the sensitivity of flood inundation dynamics to floodplain topography (Bates, 2011), it is clear that application of bare earth DEMs within a hydraulic model provides a stringent test of their vertical accuracy. Here, preliminary model simulations demonstrate the presence of clear inaccuracies in the bare earth DEMs derived from the SRTM dataset for the Beni floodplain.

Accordingly, results presented in the initial analysis bring into question the wider applicability of the approaches utilised by Wilson et al., (2007) and Baugh et al., (2013) to generate bare earth DEMs for application within flood inundation modelling upon Amazonian floodplains. The higher levels of accuracy achieved by Wilson et al., (2007), in comparison to the results presented here, suggest that a spatially uniform representation of canopy height is more appropriate for the central Amazon floodplain than the Beni study area. This is supported by the high model accuracy reported by Baugh et al., (2013), utilising a bare earth DEM produced through correction of SRTM based upon the global canopy height map produced by Simard et al., (2011) for the same study area. Crucially, neither a spatially uniform canopy height map or the global canopy height map were able to properly account for spatial variations in forest height observed within the Beni study area, directly resulting in the lower levels of predictive accuracy achieved here. This implies that similar problems are likely to arise if these methods are applied in other Amazonian floodplains characterised by highly heterogeneous forest structure, particularly where clear gradients in canopy height exist over relatively small scales. Indeed these results also highlight similar problems arising for the INT DEM, produced through the new novel approach to bare earth DEM generation developed within chapter 5.

Formal model assessment indicated that refining of the floodplain DEMs was effective in improving the simulation of Beni floodplain inundation at high water. For each of the refined bare earth DEMs, the range of F_{hw} improved substantially. Excluding low roughness runs, which were not repeated in the formal assessment, range of fit increased from 0.52-0.54 to 0.64-0.66 for simulations using the refined FAV DEMs, from 0.43-0.51 to 0.64-0.69 for the refined INT DEMs and from 0.50-0.58 to 0.61-0.68 for the refined GCH DEMs. After producing the lowest levels of fit within the preliminary analysis, simulations undertaken using the refined INT DEMs were associated with the highest accuracy in formal assessment, with maximum F_{hw} increasing by 0.18. Whilst flood water volumes did not show a substantial increase between simulations using the original INT DEM and the refined INT DEMs, inundated area typically increased by over 1000 km^2. This indicates that the DEM refinement process successfully removed topographic blockages constituted by areas of raised elevation in close proximity to the Beni channel, not only

allowing inundation of proximal areas, but also improving connectivity to areas of the distal floodplain. A similar effect was observed for the refined FAV DEM and GCH DEMs, indeed there was a marked increase in the instance of shallow flooding across the floodplain in these simulations. However, the associated increase in F_{hw} was smaller than for the refined INT DEM due to the influence of topographic depressions on floodplain flow. Indeed it is hypothesised that flow of water into these depressions limited increases in inundation elsewhere on the floodplain. In context, the high water fit for simulations undertaken with the refined bare earth DEMs fall within the upper range of performance indicated by Wilson et al., (2007). It was difficult to compare model fit with that achieved by Baugh et al., (2013), as a different accuracy measure was used in the aforementioned study. However, based upon the relative accuracy of simulations undertaken using the different DEMs here, it is thought that model predictions presented here are of an equivalent or higher level of accuracy.

Based upon table 6.16 and 6.17 it is clear that there is an increased prevalence of extreme non linear model behaviour for simulations utilising the refined floodplain DEMs. This behaviour was originally observed in the preliminary analysis, for the simulation utilising the GCH DEM in combination with high channel bed elevation, leading to instabilities in one simulation and exceptionally high levels of inundation within another. Within the formal assessment this behaviour is observed for an additional simulation utilising the GCH100 and GCH125 DEMs in combination with medium channel bed elevation and high roughness, in addition to simulations undertaken using the refined INT DEMs in combination with high roughness and high channel bed elevation. High values of F_{hw} produced during assessment with respect to high water inundation extent, suggests that simulations exhibiting this behaviour are associated with a high level of model performance. However, poor values of F_{lw} which result from significant over prediction of low water inundation extent provide quantitative evidence that this model behaviour is erroneous. This is further supported by observational evidence, in that numerous areas of the floodplain visited during the field campaign (for example the tectonically uplifted surfaces to the north east of the domain), for which elevation precluded riverine inundation, became flooded in these simulations. Whilst this behaviour occurs for simulations using both the refined INT DEMs and GCH DEMs, implications are more significant for the latter DEM, as results illustrate that optimum values

of F_{hw} (ie greater than 0.65) can only be achieved through considerable over prediction of inundation extent, volume and depth. In contrast, peak values of F_{hw} are achieved for a range of parameter combinations in simulations using the refined INT DEMs, illustrating that optimum model performance can be achieved without the prediction of an excessive magnitude of flooding. This difference can be attributed to the fact that topographical depressions in the GCH DEMs store large volumes of floodwater, limiting the extent of inundation for typical flood water volumes. Hence these results highlight a negative aspect of the DEM refinement procedure, suggesting that some cells which were already too low in the original bare earth DEM were adjusted to an even lower elevation within the new refined DEMs. In addition, if simulations exhibiting the aforementioned behaviour are excluded from consideration, the refined GCH DEMs produce less accurate predictions of high water inundation extent than the refined FAV DEMs.

The low water PALSAR image was captured on 06/09/2010 and hence it is important to consider that floodplain inundation at this time does not directly reflect dewatering that occurred following the flood event depicted in the high water image (09/03/2011). Hence whilst direct comparison of modelled and observed dewatering was not possible here, the accuracy of inundation extent at low water nevertheless provides an insight into the representation of floodplain drainage within the model. Although complete dewatering is not achieved within any of the simulations undertaken here, it is clear that the representation of floodplain drainage varies substantially between simulations undertaken using the different bare earth DEMs. As for high water, simulations undertaken using the FAV and GCH DEMs are associated with several key common characteristics, the most significant of which is the persistence of relatively large volumes of water within topographic depressions in the floodplain. Based upon visual analysis of spatial patterns of inundation, it appears that water becomes trapped within these depressions as flooding recedes. Due to the significant depths of inundation within the basins, water is not able to drain completely, even considering the representation of infiltration and evapotranspiration provided by the model. In addition, sensitivity of low water flood volume to variations in roughness and channel bed elevation suggests that substantially larger volumes of water remain upon the floodplain

after larger flood events for simulations undertaken using the refined FAV and GCH DEMs.

Values for F_{lw} suggest that the refined INT DEM facilitates an improved representation of floodplain dewatering in comparison to the refined FAV and GCH DEMs. Based upon estimations made at the start of simulations, prior to initial inundation of the floodplain, it is estimated that the volume of permanent water bodies located upon the Beni floodplain is up to 2.5 km^3. Given that flood water volume is typically less than 4 km^3, this indicates that the actual volume of floodwater remaining upon the floodplain is probably less than 2 km^3, a relatively small volume. Furthermore, the fact that low water flood volume is relatively insensitive to variations in roughness and channel bed elevation parameters suggests that the INT DEM facilitates a consistent representation of dewatering, regardless of the preceding flood magnitude. The improved representation of dewatering offered by the INT DEM is attributed to the fact that this DEM provides a more accurate representation of floodplain topography, according to the quantitative and qualitative assessment in chapter 5. The absence of topographic depressions facilitates flow of water down the floodplain, where it leaves the domain either through diffuse overland flow to the east, or through channelised flow within the Beni main stem or one of the floodplain tributaries. A poor representation of floodplain dewatering was highlighted as the major limitation of previous hydraulic modelling studies within the Amazon basin (Wilson et al., 2007; Baugh et al., 2013). However, direct comparison of the representation of dewatering is problematic as a result of the use of the modified low water fit statistic. Wilson et al., (2007) reported the presence of disconnected basins which were unable to drain at low water, demonstrating similar problems to those which were exhibited by the refined FAV and GCH DEMs here. Due to the relatively similar model behaviour observed here for simulations utilising the refined FAV and GCH DEMs, it was assumed that the representation of dewatering in Baugh et al., (2013) was characterised by similar problems to those faced by Wilson et a., (2007). Hence, overall it is thought that the representation of dewatering associated with the INT DEM constitutes an improvement upon previous studies due to a combination of an improved representation of floodplain topography, along with inclusion of additional hydrological processes and floodplain channels.

The final part of formal model assessment was constituted by comparison of modelled and observed water surface elevation, derived through TOPEX-POSEIDON satellite altimetry, for a single location at the downstream end of the studied reach of the Beni river. Broadly speaking, simulations utilising the GCH and INT DEMs were characterised by low values of RMSE, indicating that the passage of the flood wave was well represented within these simulations. For both DEMs, RMSE was lowest at high water, indicating that local floodplain elevation (effectively providing a representation of the height of channel banks) was approximately correct at this location. Overall RMSE was lower for the INT DEM simulations, reflecting the fact that these simulations were able to reproduce low water WSE with a greater level of accuracy, hence better representing the amplitude of the flood wave. It is hypothesised that lower overall RMSE can be attributed to an improved representation of channel long profile and bed elevation for the INT DEM. During model set up, the channel long profile was defined separately for each DEM based upon the slope indicated by the elevation of channel adjacent floodplain cells in that particular DEM. Bed elevation was subsequently adjusted according to floodplain topography in order to prevent the occurrence of unrealistic channel depths. It is thought that the inclusion of channel bank top survey data in the INT DEM generation procedure improved the representation of topography in near channel areas. More accurate representation of the amplitude of the flood wave can also be attributed to the fact that simulations using the INT DEMs were associated with relatively lower volumes of overbank flow, maintaining a greater volume of water in the channel at the downstream end of the reach.

Simulations utilising the refined FAV DEMs show a substantially lower WSE accuracy in comparison to those undertaken using the refined INT and GCH DEMs. Indeed results indicate that water surface elevation is substantially under predicted in all simulations utilising the refined FAV DEMs. This under prediction occurred as a result of very low floodplain elevations which characterised the downstream part of the reach within the FAV DEM. On a basic level, a low floodplain adjacent to the channel facilitates the occurrence of overbank flow at lower elevations, limiting maximum channel water levels. This can be attributed as the reason for the high values of RMSE observed with respect to altimetry data during high water. In addition, as the model uses a 1D flow routing solution for channel flow, this requires definition of a long profile

separate to the DEM during model set up. During this process, channel bed elevation along the reach is adjusted based upon floodplain height in order to ensure that the channel does not become unrealistically shallow (potentially leading to model instabilities discussed previously). Therefore in areas where floodplain elevation is low channel bed elevation is lowered accordingly, thus contributing to poor levels of fit observed during low water for simulations using the FAV DEM.

With the exception of simulations utilising the FAV DEM, results presented here demonstrate that the application of a 1D diffusion wave approach to channel routing, in combination with the assumption of a constant width and depth, provide an appropriate representation of Beni river channel flow. Accordingly, results presented here support the findings of Trigg et al., (2009), who concluded that it was possible to attain a reasonable level of fit between modelled and observed water level for the main stem Amazon through application of a diffusive wave representation of channel flow in combination with assumptions of rectangular geometry and simple slope models. The application of LISFLOOD-FP to the Amazon main stem by Wilson et al., (2007) predicted channel water stage with an RMSE of 3.56 m and 2.09 m for two separate gauges. For the same reach, Baugh et al., (2013) found that RMSE between modelled and observed WSE was typically between 0.8 m and 1.5 m. The increased accuracy observed within the latter study can be attributed to the adoption of a diffusion wave approach to channel routing, which constituted an improvement upon the kinematic solver utilised by Wilson et al., (2007). The typical RMSE values observed here for simulations utilising the INT and GCH DEMs were less than 1.5 m, suggesting that water surface elevation is predicted with an equivalent level of accuracy of past studies within the Amazon basin.

Results presented within the preliminary analysis also explored the sensitivity of predicted flood inundation to changes in hydrological parameters of the numerical model. Broadly speaking the model did not show a substantial level of sensitivity to variations in values for the depth of the soil water store, and fractional loss of water from this store. Accordingly, simulations undertaken using HYD1 and HYD2 were characterised by a similar level of performance at both high and low water. HYD1 promoted greater inundation at high water and

was thus associated with a marginally greater fit value, whilst the HYD2 simulations were associated with a lower level of inundation at low water, indicating more effective representation of dewatering. HYD1 promotes greater inundation as it is associated with a smaller value for the soil water store depth and a lower fractional loss of water from the soil water store to ground water. In contrast, for HYD2 the increased depth of the soil water store, in combination with a higher fractional loss of water to ground water means that this set up promotes greater infiltration, leading to reduced volumes of surface water. Thus the model appears to respond to changes in hydrological parameters in a broadly realistic manner. HYD3, in which the additional hydrological parameters were not included, offered the lowest level of performance of the simulations undertaken with the three different hydrological set ups here, at both high and low water.

Based upon these results, it appears that rainfall provides a small net contribution to inundation at high water, whilst losses of water through hydrological processes (infiltration and evapotranspiration) contribute towards a better fit with observed inundation extent at low water. Although the increase in performance offered by the inclusion of additional hydrological processes in the hydraulic model is relatively small at high water (0.01-0.02), the difference in fit at low water is larger (0.11-0.15), suggesting that the inclusion of additional hydrological processes contributes towards a better representation of floodplain dewatering. Past applications of hydraulic models within the central Amazon (Wilson et al., 2007; Baugh et al., 2013) have not represented rainfall, evapotranspiration or infiltration, instead relying upon the assumption of a net balance between these processes. Results presented here suggest that this assumption, typically applied in traditional hydraulic modelling studies, is not valid for the Beni study area. Although it might be possible to argue that infiltration and evapotranspiration balance out over the course of a year, results presented here suggest that the balance between rainfall inputs into the domain and losses due to ET and infiltration exhibit a level of seasonality which is not accounted for if precipitation, evapotranspiration and infiltration are excluded from the model. Specifically, the studies of both Wilson et al., (2007) and Baugh et al., (2013) reported problems associated with incomplete dewatering of the floodplain after annual flood inundation. Therefore the results presented here suggest that inclusion of a basic representation of hydrological processes offers

the potential to substantially improve the representation of floodplain dewatering.

Both Wilson et al., (2007) and Baugh et al., (2013) hypothesised the importance of floodplain channels in accurate prediction of inundation dynamics within the central Amazon floodplain. Specifically, the authors hypothesised that the inability to resolve floodplain channels which were significantly smaller than model grid resolution (270 m), was a significant factor in the incomplete drainage of the floodplain observed within model simulations. Indeed this is a logical assertion, as floodplain channels have been demonstrated to exert a significant influence upon the wetting and drying of both small and large floodplains (Nicholas and Mitchell, 2003; Alsdorf et al., 2007). Beni floodplain watercourses were represented within the channel network of this hydraulic model, and whilst results presented here do not allow a quantification of the role of this network in conveying water across the floodplain, visual analysis revealed that water levels remain elevated within these channels for significant periods after peak inundation. Hence this implies that these channels provide a contribution to drainage of the floodplain. Nevertheless, it is important to note that significant volumes of water remained on the floodplain in simulations undertaken using the refined FAV DEM and GCH DEM. The primary factor preventing floodplain drainage within these simulations are the topographical depressions present within the floodplain DEMs. As INT DEM provides the best representation of floodplain dewatering here, results suggest that an improved representation of topography is required in order to maintain connection between diffuse flood waters and floodplain channels, in order to maximise floodplain drainage. However, further work is required in order to rigourously quantify the precise volumes of water which are conveyed by the floodplain channel network during wetting and drying of the floodplain.

In light of the previous discussion, it is clear that the accuracy of topographic data presents the most significant limitation of the hydraulic modelling undertaken here. However, the datasets utilised in order to assess model performance constitute another noteworthy limitation of the modelling work undertaken in this chapter. Formal validation of the high and low inundation extent derived from ALOS PALSAR imagery is difficult here in the absence of observed data relating to flood extent, the provision of which is very rare in the

Amazon basin. However, given the high levels of accuracy achieved by Arnesen et al., (2013) using a similar method, it is thought that derived inundation extent is of a similar quality. Birkett et al., (1998) demonstrated that the accuracy of TOPEX-POSEIDON altimetry was better than 0.75 m, with respect to gauge measurements obtained from the main stem Amazon. Here, the T/P water surface elevation measurements were subject to the appropriate corrections and were filtered in order to eliminate unreliable observations according to the methods outlined by Campos et al., (2001). Therefore it is thought that the vertical accuracy of the TOPEX-POSEIDON WSE utilised here is similar to that stated by Birkett et al., (1998), and is sufficient to provide a rigourous test of model performance.

Perhaps a more significant issue is the spatial and temporal coverage of the study area offered by the datasets utilised here, and the associated implications for testing of the dynamic performance of the model. Validation of flood extent at peak inundation is a commonly applied test of hydraulic model performance (Bates and De Roo, 2000, Horritt et al., 2001). In addition, assessment of low water flood extent has gained credence within inundation modelling studies undertaken in Amazonia, providing an indication of how well a model represents floodplain dewatering (Wilson et al., 2007). Inundation extent data are two dimensional in space and thus provide a useful, spatially distributed measure of model performance. However it is important to acknowledge that inundation extent datasets are zero dimensional in time, and hence provide little information on the wetting and drying of the floodplain. This dynamical aspect of floodplain inundation has been demonstrated to be complex and difficult to model (Nicholas and Mitchell, 2003). Hence, although testing undertaken here demonstrates that the model is able to accurately predict high water inundation extent, and provide an improved representation of dewatering in comparison to past studies, the dynamic performance of the model remains less clear. Past studies have utilised floodplain water level time series obtained from T/P in order to facilitate a more dynamic assessment of floodplain inundation (Baugh et al., 2013). However, examination of T/P observations for the Beni floodplain failed to reveal any time series' showing evidence of seasonal water level variations which would be useful in model testing. This was not unsurprising given that the Beni study area was intersected by only one T/P path, and that

Birkett et al., (2002) were only able to extract reliable time series at 30-50 % of target sites within the central Amazon.

Furthermore, the characteristics of the L-band ALOS PALSAR imagery required non forested areas of the floodplain to be excluded from model assessment. Given the spatial distribution of land cover upon the floodplain, the main inundated area of the floodplain located directly to the east of the Beni river was included in the model assessment, in addition to the relatively narrow corridor of forested floodplain to the west of the channel. Based upon interpretation of Landsat TM images and the SRTM dataset in chapter 3, it was hypothesised that the forest-savanna transition to the west of the Beni river was associated with a rapid increase in elevation that precluded widespread inundation. In contrast, to the east of the Beni river model simulations show that large areas of the unforested distal floodplain to the east of the Beni are subject to flood inundation, which could not be quantitatively assessed here. In chapter 4, SRTM exhibited a relatively high degree of accuracy in unforested area (RMSE = 1.2 m), and hence it is thought that the model would provide a more accurate representation of flow dynamics in these areas than in the forested areas which formed part of the quantitative assessment. However, given that the non forested areas of the floodplain are located at a substantial distance from the channel, an accurate simulation of inundation dynamics in the intervening forested areas is likely to be highly significant in determining the accuracy of predictions in these areas. For example, topographical blockages may alter flow paths and preclude flow of flood waters to the distal floodplain, whilst the presence of topographical depressions may reduce the volumes of flow supplied to non forested part of the floodplain, with associated implications for the accuracy of predictions in these areas. Unfortunately, the validation datasets available for the Beni study area do not facilitate assessment of this aspect of model performance.

6.10 Conclusions

Overall, the work presented in this chapter represents the latest of only a handful of studies that have successfully applied a hydraulic inundation model to a floodplain in Amazonia, using a bare earth DEM derived from the global SRTM dataset. Indeed this chapter constitutes the first study which has applied such a model for a tributary outside the central Amazon. The modelling work

undertaken here builds upon the previous studies of Wilson et al., (2007), Trigg et al., (2009) and Baugh et al., (2013).

Preliminary model simulations undertaken using the bare earth DEMs were characterised by relatively poor levels of fit with respect to high water inundation extent, derived from ALOS PALSAR SAR imagery. Maximum values of fit were 0.55, 0.51 and 0.58 for simulations undertaken using the FAV, GCH and INT DEMs respectively. In context, maximum predictive performance of the model was at the lower end of the range of performance (0.52-0.72) observed by Wilson et al., (2007) for the central Amazon. This poor performance was somewhat unexpected given that the FAV DEM was generated utilising an equivalent method to that applied within the aforementioned study, which produced better prediction of inundation extent. Significantly, poor levels of fit were attributed to the over elevation of bare earth DEMs in the proximal floodplain, leading to under prediction of inundation. Over elevation occurred as canopy height maps were unable to account for the increase in forest height observed for varzea forest stands located within the channel belt. Hence, based upon the initial analysis presented here it can be concluded that that methods utilised by Wilson et al., (2007) and Baugh et al., (2013) to correct vegetation effects within SRTM for the central Amazon, may result in poor prediction of inundation dynamics when applied for floodplains within other parts of the Amazon basin. Particularly floodplains that are covered by varzea forest stands featuring high levels of structural heterogeneity (Wittmann et al., 2004).

In order to facilitate more accurate simulation of inundation dynamics on the Beni floodplain, bare earth DEMs were refined through correction of remaining positive elevation biases, based upon a coarse scale map of water surface elevation corresponding to high water. Simulations undertaken using the refined floodplain DEMs demonstrated a substantial increase in accuracy with respect to observed inundation extent during formal validation. Fit at high water increased to a maximum of 0.66, 0.69 and 0.68 for the FAV, INT and GCH DEMs respectively, this increase in fit was driven by greater inundation extent promoted by the new DEMs. Simulations utilising the INT DEM were associated with the highest levels of accuracy, reflecting its superior representation of diffuse shallow floodplain flows. In contrast, the accuracy of simulations undertaken using the FAV and GCH DEMs was limited by the presence of

erroneous topographical depressions in the floodplain, in which large volumes of flood water accumulated to great depths. Nevertheless, model performance at high water was equivalent to that typically achieved within flood inundation modelling studies (Bates and De Roo, 2000;) and was within the upper range of that observed by Wilson et al., (2007) for the central Amazon floodplain.

ALOS PALSAR derived inundation extent indicated that the floodplain was essentially completely dry at low water, with the exception of floodplain lakes to the east of the domain. Simulations undertaken using the INT DEM were associated with the best representation of floodplain dewatering, demonstrating the highest values of F_{lw} of simulations undertaken with any of the refined DEMs. Small flood water volumes and flow depths observed for simulations using the refined INT DEMs at low water indicated almost complete drainage of the floodplain for model runs undertaken with a range of roughness and channel bed elevation parameters. In contrast, for simulations undertaken using the refined FAV DEMs and GCH DEMs, floodplain dewatering was hindered by large volumes of water which became disconnected during flood recession and were unable to drain from topographical depressions. Direct comparison of low water performance with other studies is difficult here, due to the use of a modified accuracy statistic. However, it is thought that the floodplain dewatering simulated here represented an improvement upon representation of this process by Wilson et al., (2007) and Baugh et al., (2013) as a result of an improved floodplain DEM, representation of hydrological processes and inclusion of sub grid scale floodplain channels.

The final part of formal model assessment consisted of a comparison between modelled water surface elevation at a location within the downstream reach of the Beni channel, to a time series of water surface elevation derived from TOPEX-POSEIDON altimetry. Overall, the simulations utilising the refined INT DEM were associated with the lowest RMSE values, typically varying between 0.90 m and 1.30 m. GCH DEM simulations were associated with a higher range of RMSE (0.96 m – 1.72 m), typically over predicting WSE at low flow. RMSE was considerably higher (> 3 m) for simulations utilising the refined FAV DEMs, with this lower level of accuracy attributed to errors in the DEM. Based upon these results, it can be concluded that the 1D diffusion wave representation of channel flow, in combination with the assumption of a constant channel width

and depth provide an appropriate representation of channel flow for the Beni river (Trigg et al., 2009). Furthermore, it can be concluded based upon the results of the formal model assessment that the refined INT DEMs, produced based upon the novel approach devised and implemented in chapter 5, provided the best representation of inundation dynamics. Simulations undertaken using these DEMs outperformed the refined FAV and GCH DEMs, produced using the methodologies of Wilson et al., (2007) and Baugh et al., (2013), according to all quantitative measures.

Based upon the final part of the preliminary analysis it can be concluded that inclusion of a basic representation of floodplain hydrological processes is beneficial for prediction of Beni floodplain inundation. Simulations that included a representation of rainfall, evapotranspiration and infiltration were associated with a higher level of accuracy when assessed with respect to observed inundation extent at both high and low water, in comparison to the simulation undertaken in which the aforementioned processes were not represented in the model. The difference in F_{hw} was small (0.01-0.02) at high water, however the disparity in fit was larger at low water (0.11-0.14), suggesting that the processes of evapotranspiration and infiltration provided a significant contribution to dewatering of the floodplain. More broadly, it can be concluded that assumption of an overall balance between rainfall and evapotranspiration, relied upon within past hydraulic model applications, may not be appropriate for Amazonian floodplains. The role of the sub grid scale channel network in conveying water across the floodplain was not quantified here, thus its contribution to wetting and drying of the mode domain remains uncertain. Visual observations suggested an increase in the depth of these channels following inundation, suggesting that these channels play a role in drainage of the floodplain. However further analysis is required in order to allow more substantitive conclusions to be made.

Chapter Seven

Successional forest development and aboveground wood biomass storage on the Beni floodplain

7. Successional forest development and aboveground wood biomass storage on the Beni floodplain

7.1 Introduction

The characteristics of Amazonian varzea forests, along with their interactions with fluvial processes, and the associated implications for AGWB and carbon storage are detailed extensively in sections 1.5 to 1.9 in chapter 1.Saliently, studies in this area of research undertaken over the past 30 years have enhanced the understanding of the interactions between fluvial processes and varzea forests within the Amazon basin. This research has demonstrated that the processes of lateral channel shifting and flood inundation are responsible for maintaining varzea forest stands in successional stages of development. However, to the present, most of this work has focused primarily upon the influence which fluvial processes exert upon varzea forests in terms of structural characteristics and floristic composition (Kalliola et al., 1992; Wittmann et al., 2004). Only a handful of studies have explored the implications of interactions between fluvial processes and varzea forests in terms of aboveground biomass and carbon storage (Schongart et al., 2008; Peixoto et al., 2009). Further, almost all of the work reviewed in chapter 1 has worked at the scale of individual plots, thus the spatial and temporal scope of these studies is somewhat limited.

Therefore given the significant uncertainties in estimates of aboveground wood biomass within the Amazon basin, detailed in section 1.4, it is clear that further studies are required in order to better quantify AGWB within floodplain forest stands, and to understand how AGWB is influenced by fluvial processes. Here, a space-for-time substitution methodology was utilised in order to characterise the successional development of varzea forest stands located upon the Beni floodplain in terms of both floristic composition and aboveground wood biomass storage and carbon assimilation. Field inventory plot measurements were subsequently integrated with a) a map of floodplain stand age, in order to quantify the influence which processes of channel migration exert upon the balance of aboveground wood biomass and carbon storage within Beni floodplain forests and b) canopy height maps, facilitating estimation of the overall storage and spatial distribution of AGWB within varzea forests located upon the Beni floodplain.

7.2 Research aims

The overall aim of this chapter is to the characterise the successional development of successional forest stands upon the Beni floodplain, with a particular emphasis upon aboveground wood biomass and carbon storage, and to investigate the influence which fluvial processes exert upon Beni varzea. This aim was addressed through completion of three specific objectives.

1. To utilise a space-for-time substitution methodology in order to characterise the successional development of varzea forest stands following new site formation upon the Beni floodplain, with particular emphasis upon storage of aboveground wood biomass.
2. To integrate forest inventory measurements with a map of floodplain stand age in order to quantify the change in aboveground wood biomass and carbon storage for the Beni floodplain forests since 1960.
3. To utilise canopy height maps generated in chapter 5 in order to extrapolate plot scale measurements of aboveground wood biomass across the Beni floodplain study area, and to compare resulting AGWB estimates with published estimates for varzea and Terra Firme stands across the Amazon basin.

7.3 Methodology

7.3.1 Experimental design

No permanent inventory plots exist within the study area, thus the successional development of Beni floodplain forests could not be studied through prospective data collection. In the absence of historical datasets, a space-for-time substitution presented the best opportunity to quantify the successional development of Beni floodplain forests (Pickett, 1991). However, the application of this methodology is predicated upon accurate determination of forest stand age. Fortunately, lateral migration of the Beni river channel produces a mosaic of forest patches upon the adjacent floodplain, which are characterised by different ages and stages of successional development (Worbes et al., 1992). Historical Landsat TM scenes dating from 1975 to 2011 and aerial imagery acquired in 1960 were utilised in order to delineate the ages of these forest stands up to a maximum age of 51 years. The age distribution of identified stands is illustrated in table 7.1.

Table 7.1. Age classes comprising the Beni floodplain stand age map.

Landsat TM Imagery Year	Age class	Maximum vegetation age (years)	Vegetation age class (years)
2009	0	0	0
2004	1	7	2-7
1999	2	12	8-12
1986	3	25	13-25
1975	4	36	26-36
1960	5	51	37-51
n/a	6	Unknown	51 +

In order to accurately locate inventory plots within forests at different stages of successional development, a stand age map was produced for the Beni river floodplain. Landsat TM scenes and aerial images were mosaiced and georeferenced with respect to NASA Geocover images, using ground control points taken from stationary features located within the study area. RMSE of less than a single pixel (30 m) was achieved for each georeferenced Landsat TM image. In order to ensure consistency in delineated stand age, Landsat TM images for each year were selected during the dry season from June to September, during which discharges and rates of channel shifting are low (Gautier et al., 2010). The location of the Beni channel was manually digitised for each Landsat TM scene/aerial image within ArcGIS, producing a set of polygons that represented the location of the channel through the 51 year period. The channel polygons were combined into a single layer and maximum forest age was determined according to when the area most recently formed part of the main river channel, as illustrated in figure 7.1. For example, if a given stand was last part of the river channel in 1986, this stand is assigned a maximum age of 25 years. Overall the map delineated five stand age classes, up to a maximum age of 51 years.

For the field experiment a stratified approach was adopted, in order to accurately and efficiently quantify the successional development of Beni floodplain forests whilst obtaining replicate samples, thus precluding the occurrence of pseudoreplication (Hurlbert, 1984). Accordingly, inventory plots were established at three sites located at different meander bends along the studied reach during two field campaigns which took place in 2011 and 2012. The location of the three field sites is illustrated in figure 7.1, whilst the total

area of forest inventoried at each site is detailed in table 7.2. Site 1 was surveyed in 2011 and constituted the primary site for this study. Here three plots (0.75 ha) were surveyed within each of the five forest age classes, whilst a further three plots were surveyed in older forest stands on the outside of the meander bend. Due to time constraints in the 2012 field campaign forest age classes were sub sampled at sites 2 and 3.

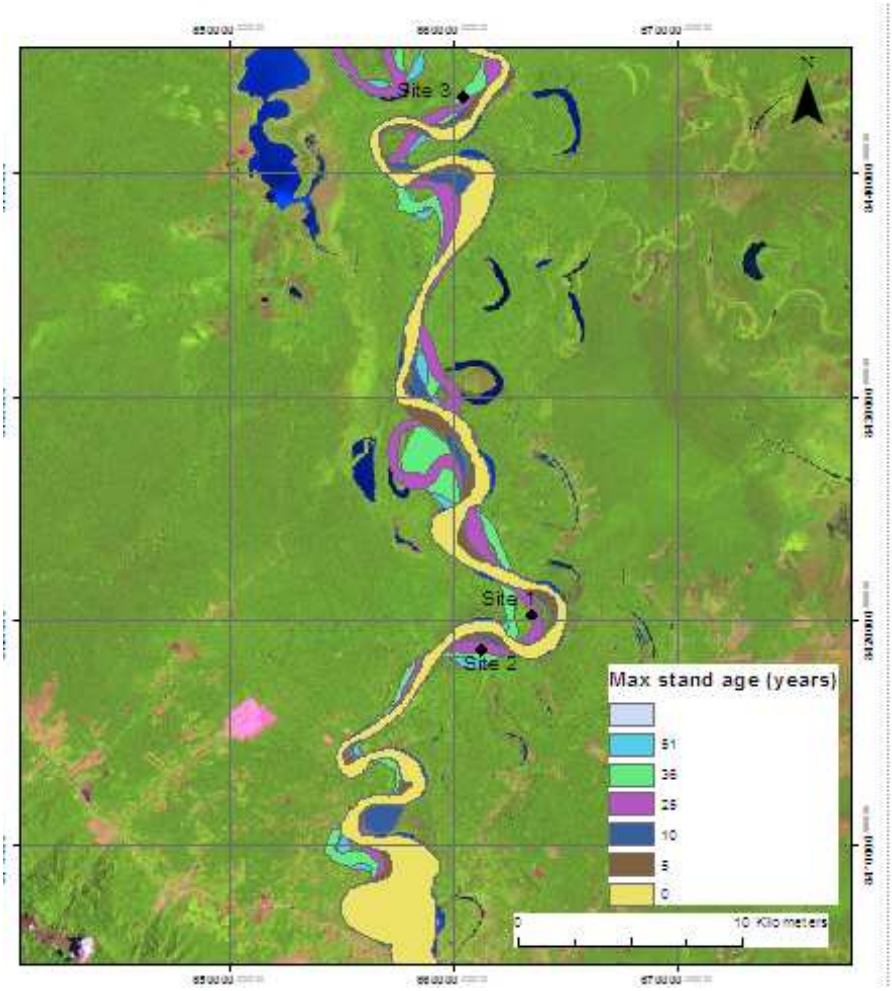

Figure 7.1. Beni floodplain stand age map generated based upon historical Landsat imagery.

Logistical considerations precluded a truly random approach to sampling within age classes, rather the difficulties in accessing dense tropical forest stands demanded the adoption of a more pragmatic approach. At each site a linear transect was constructed, orientated perpendicular to the direction of channel migration and which intersected the different stand age classes. Individual inventory plots were subsequently established parallel to the main transect with a spacing of 50 – 100 m. The experimental design is illustrated visually within figure 7.2. Forest inventories were undertaken in 10 m x 250 m (0.25 ha) plots, as past studies undertaken within tropical forests have illustrated that this

technique provides an improved representation of spatial variability in comparison to a square plot with an identical area. In total, 8.25 hectares of forest was surveyed in the study area.

Table 7.2. Distribution of forest inventoried amongst different floodplain sites and age classes.

Age class	Maximum vegetation age (years)	Inventoried area Site 1 (ha)	Inventoried area Site 2 (ha)	Inventoried area Site 3 (ha)
1	7	0.75	0.25	0.25
2	12	0.75	0	0
3	25	0.75	0.75	0.75
4	36	0.75	0	0.75
5	51	0.75	0.75	0
6	Unknown	0.75	0	0

7.3.2 Forest inventories

In order to quantify forest structure along the successional sequence, 10 m x 250 m (0.25-ha) plots were established within each maximum stand age class. The location and orientation of plots was determined prior to field work according to the vegetation age map, in order to ensure that plots were precisely located within these distinct age classes in the field. Forest plot locations were pre-programmed into a Garmin handheld GPS unit, which was used to navigate to survey locations within the field. After locating the field plot, a compass and 50 m tape were used in order to construct a straight 250 m transect, with poles installed at intervals of 25 m. Further poles were inserted perpendicular to each 25m pole at a distance of 10m from the main transect, producing an inventory plot subdivided into ten 10 m x 25 m subplots.

For the forest inventory, all trees >10 cm diameter at breast height (DBH) were measured within each plot (Chave et al., 2005). In order to reflect the importance of smaller trees within early successional stages trees >5 cm DBH were sampled within subplots 1,6 and 10. Each individual was identified to species in situ and diameter measured at a stem height of 130 cm with a diameter tape. For stems where roots were buttressed or stem irregularities existed, measurement was made directly above these irregularities. Tree height was measured for >50% of individuals using a laser rangefinder.

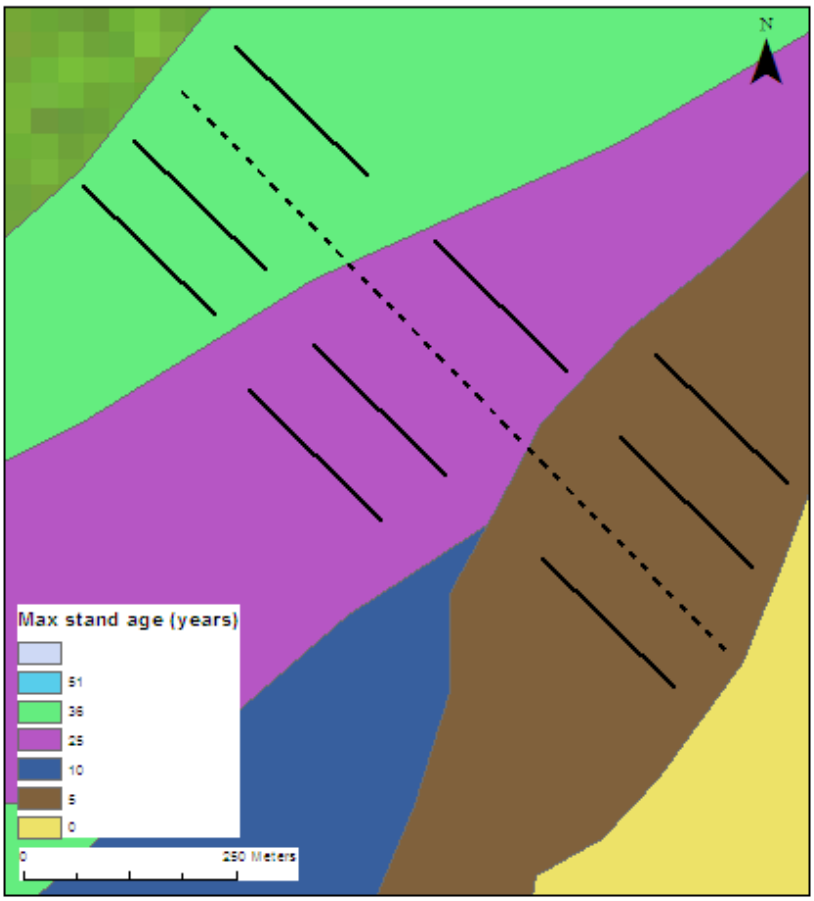

Figure 7.2. A visual representation of the arrangement of forest inventory plots within different stand age classes. Dotted line represents the main access transect, whilst solid lines represent inventory plots spaced ~ 50 m apart.

In addition to floristic inventories, relevant geomorphological site conditions were measured. A vertical benchmark was established within each individual forest plot using a Trimble differential GPS unit, whilst detailed subplot scale topography was acquired through surveys undertaken with an eye level. Sub plot scale relative topography was subsequently integrated with the DGPS benchmark, in order to obtain absolute elevations (vertical accuracy <1m) for each sub-plot. Absolute plot elevation was subsequently converted to a relative elevation through comparison with a water surface elevation survey undertaken using a highly accurate DGPS unit mounted upon a boat used for access to the study sites. This calculation enabled the relative elevation of each plot above water level to be determined, correcting for the downstream slope of the channel and floodplain. Where possible, past levels of flood inundation were elucidated through identification and measurement of the height of water marks on trees (Wittmann et al., 2004). However indicators of past flood levels were not clear for all sites, whilst reliability of flood marks was questionable due to the

rapid vertical growth of stems. Finally, shallow soil samples were obtained from the centre of each forest plot. These shallow soil samples were complemented by the extraction of floodplain sediment cores, up to a depth of 1.5 m at selected locations. Cores and sediment samples were obtained using a specially designed floodplain corer.

7.3.3 Forest inventory data processing and analysis

Floristic inventories were collated and entered into spreadsheets for further analysis. Initially a value for wood density was assigned to each individual using the species name and the global wood density database (Chave et al., 2009). Basic forest structural parameters such as basal area, stem density and diversity were calculated. In order to estimate the height of individuals whose height was not measured directly, diameter-height relationships were established using non linear regression models (Schongart et al., 2008). This analysis was undertaken for each age class in order to account for potential changes in allometry through the successional sequence.

Allometric equations were subsequently applied to forest inventory data in order to produce estimates of aboveground wood biomass (AGWB) and carbon storage. A great number of different allometric regression equations are available for application within tropical forests, with the different equations based upon varying numbers of individual trees harvested from stands in different geographical locations (Brown et al., 1989; Chambers et al., 2001). Due to the difficulty of directly harvesting trees, such regression models are commonly formulated based upon a relatively small number of individuals. Consequently, this can lead to considerable variation in biomass estimates obtained from different allometric regression models (Nelson et al., 1999). Moreover, despite the importance of allometic equations, they are directly tested relatively infrequently (Houghton et al., 2001) and constitute a large source of uncertainty in plot based biomass calculations (Chave et al., 2004). Therefore the application of appropriate allometry is crucial in order to minimise bias and uncertainties associated with plot level estimations of biomass and carbon storage (Ketterings et al., 2001; Chave et al., 2005).

The most diverse tropical forest stands exceed 300 species ha^{-1} (Oliveira and Mori., 1999), effectively precluding the use of species specific regression

models which are commonly applied within less diverse temperate forests (Shepashenko et al., 1998; Brown and Schroeder., 1999). As a consequence of high levels of diversity, mixed species biomass regression models which use wood specific density (p g cm^{-3}) along with either stem diameter (*D* cm) or tree height (*H* m) have gained credence within tropical forest studies (Brown et al., 1989; Chambers et al., 2001; Malhi et al., 2004). Chave et al., (2005) provide a rigorous assessment of an array of existing allometric equations based upon a large dataset of 2410 trees harvested from 27 tropical forest stands. The study concluded that many past studies generated unparsimonious allometric equations, using many fitted parameters which were included in the models in order to minimise residuals and improve performance in goodness of fit measures.

Chave et al., (2005) derived a series of new allometric regression equations for tropical forest types, which were stratified by geographical location, according to annual precipitation and dry season length. The study found that the best performance was achieved by equations that used tree height, diameter and wood specific gravity as a compound predictive variable. Although equations which do not include tree height as a predictive parameter can be used to estimate biomass in most tropical forests, these equations are prone to propagate biomass errors, particularly when applied in forests where diameter height relationships deviate from those in the stands where the equations were derived.

Here, plot level biomass was estimated using two different allometric models taken from Chave et al., (2005), for moist tropical forests characterised by an annual dry season of no greater than four months and annual precipitation between 1500-3500 mm. Equation 7.1 constitutes the primary allometric model and includes height, diameter and wood specific gravity as predictive variables. Equation 7.2 is effectively the same equation as 7.1, but predicts biomass based upon only wood specific gravity and diameter, tree height is parameterised within the equation itself.

$$AGB = \exp(-2.977 + \ln(\rho D^2 H)) \equiv 0.0509 \times \rho D^2 H \quad (7.1)$$

$$AGB = \rho \times \exp\left(-1.499 + 2.148\ln(D) + 0.207(\ln(D))^2 - 0.0281(\ln(D))^3\right) \quad (7.2)$$

Although the wood carbon fraction can exhibit variability between different tree species (Elias and Potvin, 2003), it is commonly assumed that the dry biomass of a tree consists of 50% carbon (Brown and Lugo, 1982). Hence carbon content of inventoried trees was calculated from biomass estimates using a simple correction factor of 0.5 (Roy et al., 2001).

7.3.4 Laboratory analysis of shallow soil samples

A total of 32 soil samples, constituting one taken from the centre of each forest plot, were analysed in the laboratory for total carbon, total nitrogen, total phosphorus and grain size distribution using standard protocols (Appendix A). This lab analysis was undertaken in order to investigate whether soil characteristics were associated with changes in forest structure along the successional sequence. Phosphorus was of particular interest, as Aragao et al., (2009) showed that this nutrient was a limiting factor in the net primary productivity of forest stands across the Amazon basin.

7.3.5 Reach scale carbon balance changes as a result of meander migration

In Amazonia, meandering rivers are responsible for the destruction of substantial areas of mature forests and the creation of new successional forests (figure 7.3). In order to assess the impact which lateral channel migration exerts upon aboveground wood biomass and carbon stocks within Beni floodplain forests, inventory data detailed in 7.3.1-7.3.3 was combined with a floodplain stand age map and canopy height map, generated in chapter 5. The novel method utilised here differs from that used by Peixoto et al., (2009) to investigate the spatial and temporal dynamics of migration of the Solimoes, Japura and Aranapu rivers in the Brazilian Amazon. Peixoto et al., (2009) quantified channel shifting and the creation/loss of floodplain forest stands for a 21 year study period through classification of Landsat TM imagery. Pioneer and late successional forests were separated based upon spectral characteristics, and local estimates of carbon storage for these forest types were applied in order to determine the overall changes in aboveground carbon storage for the studied reach. Here, forest inventory data obtained from three replicate sites along the Beni demonstrated that development of floodplain forest structure was well defined according to forest stand age (figures 7.9-7.11), suggesting that a

map of stand age could be utilised in order to extrapolate plot level biomass/carbon storage measurements over a wider area. Accordingly, a modified stand age map was generated based upon the original map used in order to locate field plots within 7.3.1, precluding the need for automated classification of Landsat TM.

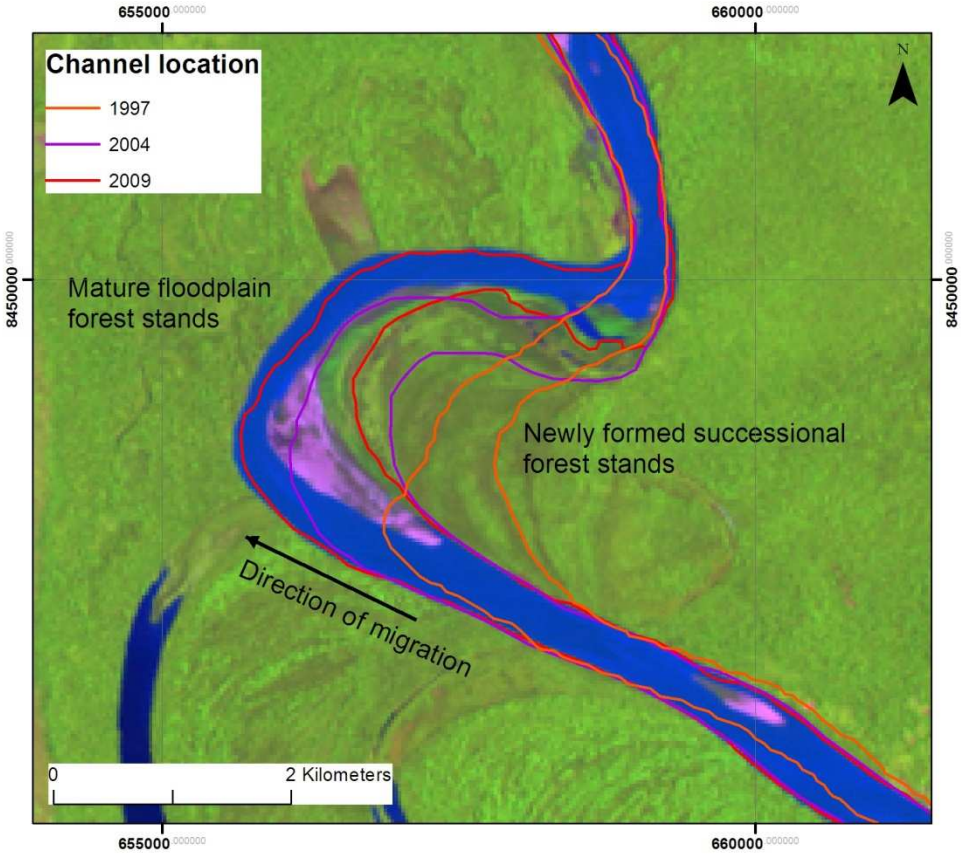

Figure 7.3. Illustration of the process of meander migration and the destruction/creation of forest stands.

As a result of the long intervals between Landsat TM imagery and rapid rates of channel shifting, gaps were present in the original stand age map (figure 7.4). Gaps constituted areas which were not occupied by the channel at any of the historical imagery dates, although it is important to state that this did not mean that they had not been subject to disturbance through channel migration since the start of the study period, which corresponded to the date of the first aerial imagery in 1960. Hence whilst maximum stand age was delimited for areas occupied by the river channel at the dates of historical imagery, the age of relatively large areas of floodplain in close proximity to the channel were not determined. Gaps in the stand age map were not important when locating field plots, however their presence was problematic when attempting to generate a

spatially continuous representation of biomass and carbon storage. Therefore to generate a continuous map of stand age, the channel bank lines that were manually delineated from historical Landsat TM/aerial imagery, were linearly interpolated using ArcGIS in order to predict the position of the river channel for years between imagery dates. The channel position delineated from both historical imagery and through linear interpolation was then utilised to generate the map, with the age of a stand denoted by the most recent date at which it was occupied by the channel. Manual editing was undertaken in order to remove channel cut offs from the stand age map, since these water bodies were not subject to successional vegetation growth since 1960. This map, an example of which is illustrated within figure 7.4, delineates the age of all floodplain forest stands generated through migration of the Beni channel since 1960.

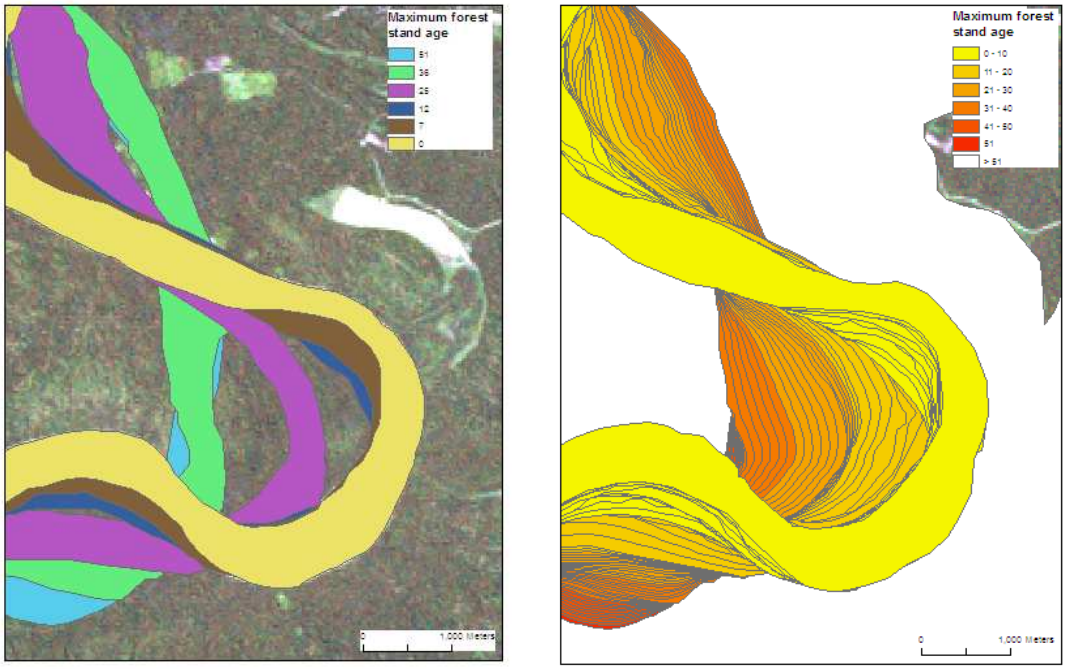

Figure 7.4. Left- original stand age map constructed through manual delineation of the Beni channel in historical Landsat TM imagery. Right- modified stand age map generated through interpolation of historical channel position.

Calculation of the net change in AGWB and carbon storage required quantification of both the biomass gains through growth of new successional forest stands, and the loss of biomass through processes of erosion. Through utilisation of the modified stand age map in combination with inventory data for successional forests, it was possible to estimate the aboveground biomass and carbon stocks for new floodplain forest stands produced through migration of

the Beni channel over the past 50 years. Initially the total area of floodplain constituted by each stand age was calculated in hectares using ArcGIS. These stand age classes were subsequently grouped according to the ages of successional forest surveyed in the field illustrated in table 7.1/7.2, in order to facilitate the direct application of biomass and carbon storage estimates for these ages (table 7.3). Subsequently the area of each age class was multiplied by the corresponding aboveground wood biomass and carbon storage estimate, taking into account uncertainties (Chave et al., 2004), in order to determine total stocks for each age class. Field observations suggested that fresh alluvial sediment deposits were initially colonised by herbaceous vegetation, and growth of woody species begun only after stand elevation had increased by 2-3 meters though continued sediment deposition. This lag in the establishment of woody vegetation, typically two years, was reflected here as floodplain stand ages of one and two years were assumed to contain no AGWB or carbon stocks. Finally, the biomass and carbon storage within each stand age was summed in order to generate a total estimate for newly formed forests along the length of the reach.

Table 7.3. Aboveground wood biomass and carbon storage estimates for successional forest stands of different ages upon the Beni floodplain.

Age class	Maximum vegetation age (years)	Vegetation age class (years)	Aboveground wood biomass and uncertainty (Mg ha^{-1})	Aboveground carbon and uncertainty (Mg ha^{-1})
0	0	0	0	0
1	7	2-7	14.13 ± 3.24	7.07 ± 1.62
2	12	8-12	25.54 ± 5.88	12.77 ± 2.94
3	25	13-25	83.05 ± 19.10	41.53 ± 9.55
4	36	26-36	128.20 ± 29.48	64.10 ±14.74
5	51	37-51	151.32 ±34.80	75.66 ± 17.40

The overall loss of AGWB and carbon attributable to lateral channel shifting was determined through integration of the modified stand age map, forest inventory data and the canopy height map generated in chapter 5. In the first instance, the total area of floodplain lost to erosional processes since 1960 was determined. Since all areas included within the stand age map have been subject to direct disturbance by the river channel during the 51 year study period, the total area of floodplain lost to erosion was calculated through

subtraction of the area occupied by the channel in 1960 from the area of the entire stand age map, including the contemporary channel. Unlike newly formed successional forest stands, AGWB and carbon storage of stands consumed by erosion could not be estimated directly based upon stand age. Therefore the total loss of AGWB and carbon was estimated using a more pragmatic approach, based upon the assumption that the proportional distribution of forest height, aboveground wood biomass and carbon within areas lost to erosion since 1960 were equivalent to the distribution of stands observed within the contemporary floodplain channel belt.

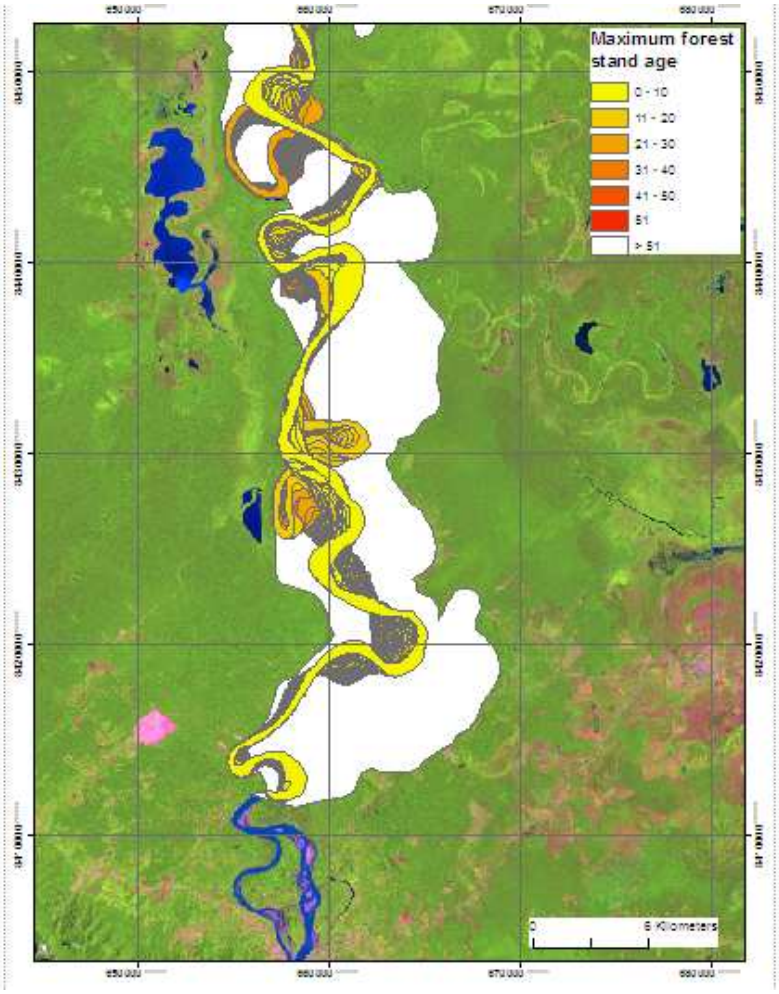

Figure 7.5. Modified stand age map for the upstream part of the study reach, including a mask of the Beni channel belt encompassing forest stands with an age greater than 51 years.

In order to characterise the distribution of biomass within forests located in the contemporary floodplain channel belt, the channel belt was digitised and added to the stand age map (figure 7.5). The channel belt encompassed the area which had not been occupied by the channel during the past 51 years, but showed signs of recent (< 200 years) direct disturbance by the Beni channel

prior the beginning of the record of historical imagery. Hence the newly delineated area encompassed forest stands which were typical of those stands lost through processes of erosion on the outer bank of meander bends (Kalliola et al., 1992). The proportional distribution of the height of forests located within the channel belt was derived from the canopy height map (figure 7.6). The total area of floodplain forest lost to erosion was divided into height classes, reflecting the distribution of canopy height observed within the contemporary channel belt. Through application of the relationship established between forest height and AGWB/carbon storage in 7.3.5 (figure 7.7), the total loss of biomass and carbon as a result of migration of the Beni river since 1960 was estimated. A further discussion of the canopy height-biomass relationship is provided within 7.3.6. The net change in AGWB and carbon stock within Beni floodplain varzea forests, occurring as a result of processes of meander migration since 1960, was calculated through subtraction of the losses related to erosion from the stocks in newly formed successional stands.

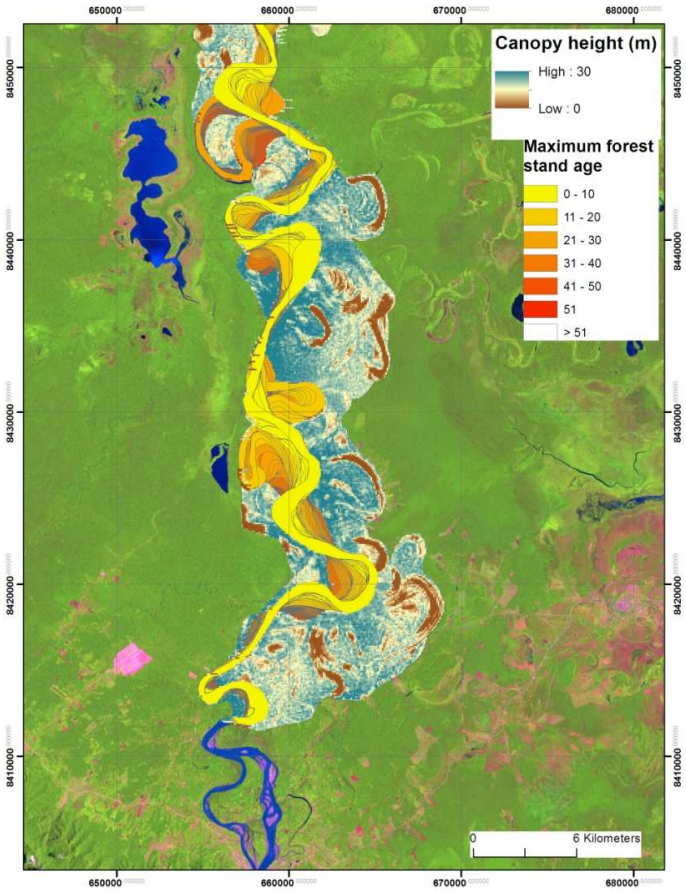

Figure 7.6. Modified stand age map for the upstream part of the study reach, including canopy height for forest stands with age greater than 51 years extracted from INT DEM, generated within chapter 5.

7.3.6 Beni floodplain forest biomass and carbon stocks

Current remote sensing platforms are unable to directly measure forest biomass and carbon storage (Saatchi et al., 2007). Consequently, forest inventories provide the *de facto* method by which to quantify these parameters within Amazonia (Malhi et al., 2006). Whilst inventory plots are able to provide accurate measurements of AGWB and carbon storage at the plot scale (Chave et al., 2005), these measurements are limited in terms of spatial coverage and are unable to characterise AGWB stocks over wider spatial scales (Houghton, 2003). In order to estimate the distribution of aboveground biomass across the Amazon basin, plot level AGWB measurements have been extrapolated through modelling approaches (Potter et al., 2001), interpolation (Malhi et al., 2006) and most recently through correlation with remotely sensed variables which are sensitive to forest structure and are characterised by a continuous spatial coverage (Saatchi et al., 2007). Whilst these studies estimate biomass storage over the entire Amazon basin, a similar methodology can be applied here in order to extrapolate biomass across a smaller study area such as the Beni floodplain, through utilisation of remote sensing variables at a commensurate spatial scale.

Here, estimates of AGWB and carbon stocks were available from a total of 32 forest inventory plots at discrete locations upon the Beni floodplain, detailed in 7.3.1-7.3.3. Canopy height is typically well correlated with biomass (Asner et al., 2012), whilst canopy height maps produced in chapter 5 offer a complete spatial coverage of the study area, presenting an ideal dataset for extrapolation of plot level AGWB measurements. Given that forest characteristics are well defined according to stand age within surveyed plots, the floodplain stand age map can be utilised in order to extrapolate biomass within newly formed successional forest areas. Hence plot level measurements of biomass were integrated with floodplain stand age and canopy height maps in order to generate 250 m spatial resolution AGWB maps for the Beni floodplain study area.

Processes of channel migration and successional vegetation growth in the period between the collection of the SRTM dataset in 2000 and forest inventory data in 2011/2012 precluded the direct integration of the canopy height map (derived from SRTM) and AGWB/carbon stocks derived from forest inventory

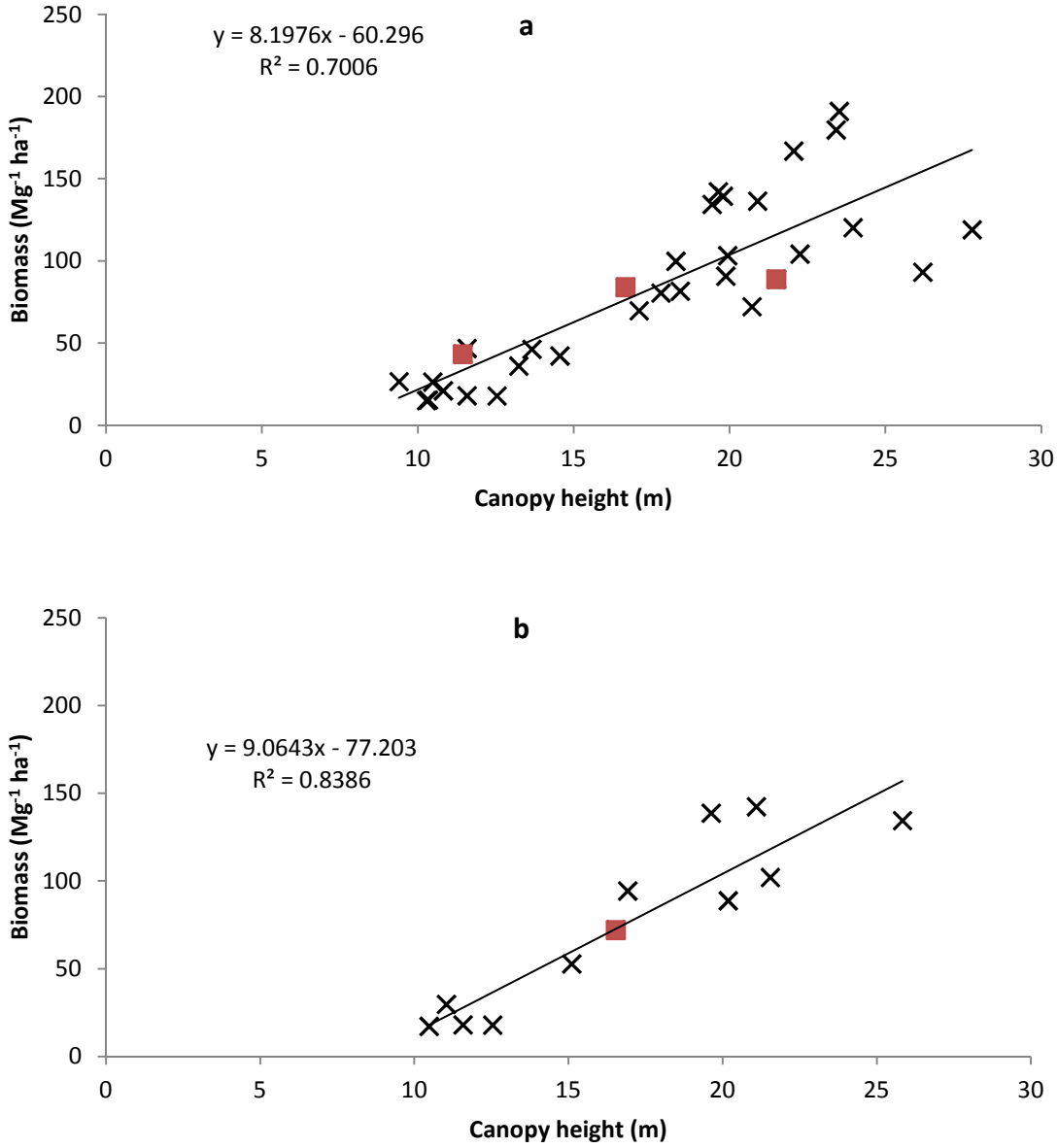

Figure 7.7. Relationship between field measured canopy height and forest biomass for a) individual forest inventory plots b) forest plots aggregated by stand age class and site. Crosses denote successional forests of known stand age and squares represent older forest stands surveyed on the outer bank of a meander bend.

data. However, results generated in chapter 4 demonstrated that field measured canopy height was well correlated with SRTM derived canopy height, calculated through subtraction of GPS ground elevation measurements from SRTM elevation. Therefore, field measured canopy height and AGWB were correlated (figure 7.7), and the latter extrapolated across the study area indirectly using the canopy height maps derived in chapter 5. Two canopy height maps were utilised here; the first was the canopy height map for INT DEM and the second for GCH DEM. For areas of the floodplain characterised by newly formed successional forest stands of known age, biomass was extrapolated through

direct application of inventory estimates according to stand age following the methodology detailed in 7.3.5.

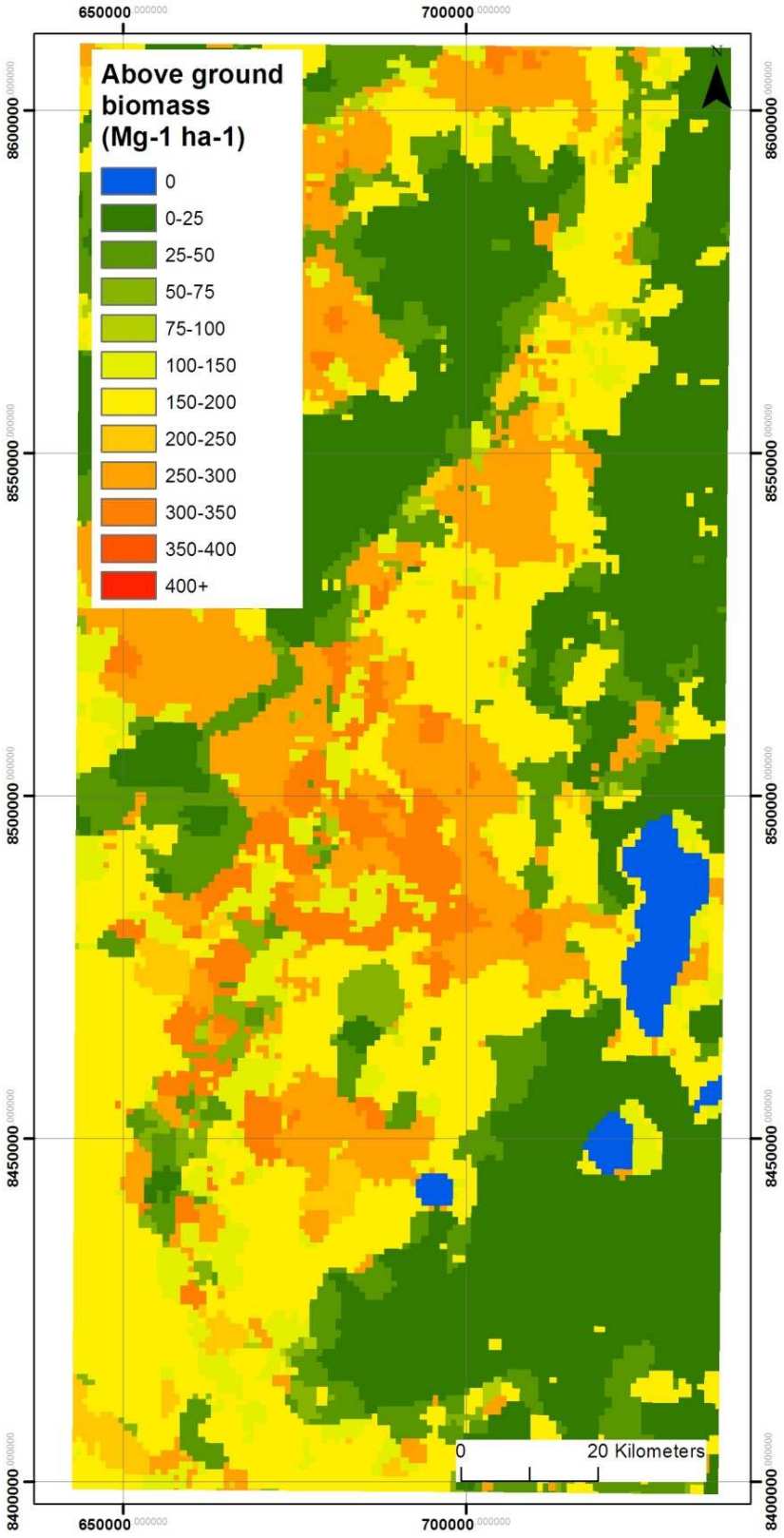

Figure 7.8. Amazonian aboveground biomass map produced by Saatchi et al., (2007), subset to the extent of the Beni study area.

Biomass maps derived here were subsequently compared with a biomass map for the Amazon basin produced by Saatchi et al., (2007), obtained from http://daac.ornl.gov/LBA/guides/LC15_AGLB.html and illustrated in figure 7.8. This comparison was undertaken in order to investigate the differences in spatial distribution of biomass estimated using methodologies applied at different spatial scales. In order to facilitate direct comparison between the datasets, the Amazonian biomass map was first subset to the extent of the Beni study area and resampled to a grid resolution of 250 m. AGWB maps produced here included only aboveground wood biomass contained in varzea forests, whilst the map of Saatchi et al (2007) also included biomass estimates for savanna areas. Hence a forest mask generated as part of the DEM generation procedure in chapter 5 was applied to the resampled Amazonian map in order to eliminate savanna regions and maximise comparability between the datasets. Herein the Beni floodplain aboveground biomass maps will be referred to as follows; Map 1- local AGWB measurements extrapolated based upon INT canopy height map; Map 2- local AGWB measurements extrapolated based upon GCH canopy height map; Map 3- Amazonian biomass map from Saatchi et al., (2007).

7.4 Results

7.4.1 Characterisation of Beni floodplain successional forest development

Figure 7.9 illustrates the diameter distribution of successional forest stands within the Beni varzea. For forest stands within the youngest stand age class (figure 7.9a) >50 % of individuals are characterised by DBH of less than 10 cm and the diameter of > 95 % of individuals is less than 20 cm. Within figure 7.9b forest stand ages of 8-12 years the proportion of individuals with a diameter of 10-20 cm increases dramatically to around 70 %, whilst stems with DBH <10 cm decreased to a proportion of lower than 20 %. Nevertheless, more than 90 % of trees in this age class were characterised by a diameter of less than 20 cm. For the third forest stand age class shown within figure 7.9c (13-25 years) the proportion of individuals with DBH <10 cm and 10-20 cm were roughly equal, accounting for around 30 % of total stems respectively. However a substantial proportion of stems (~40 %) within forest stands aged between 13-25 years are characterised by DBH greater than 20 cm. This trend of increasing stem diameter continues within figure 7.9d (26-36 years). Within these stands the

proportion of stems < 10 cm DBH is minimal and the dominant diameter class remains 10-20 cm. However, greater than 50% of individuals possess diameters greater than 20 cm. The oldest inventoried successional forest stands (figure 7.9e) comprise the lowest overall proportion of individuals with diameter < 20 cm, and therefore intuitively the highest proportion of stems with DBH > 20 cm (~60%). Overall, the diameter distributions illustrated in figure 7.9 indicate a broad trend of increasing stem diameters with advancing age of Beni floodplain successional forest stands.

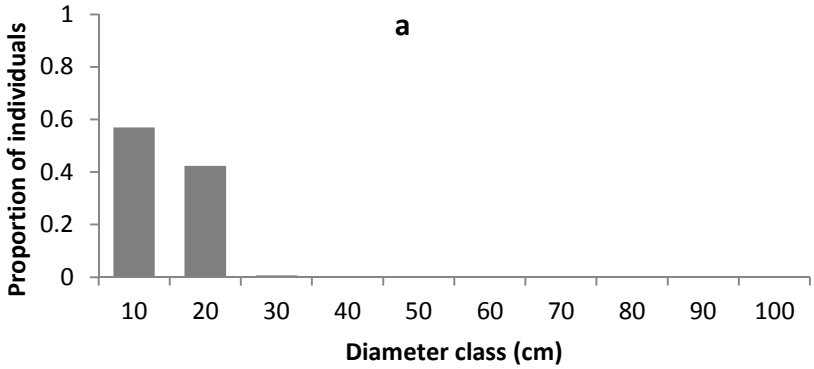

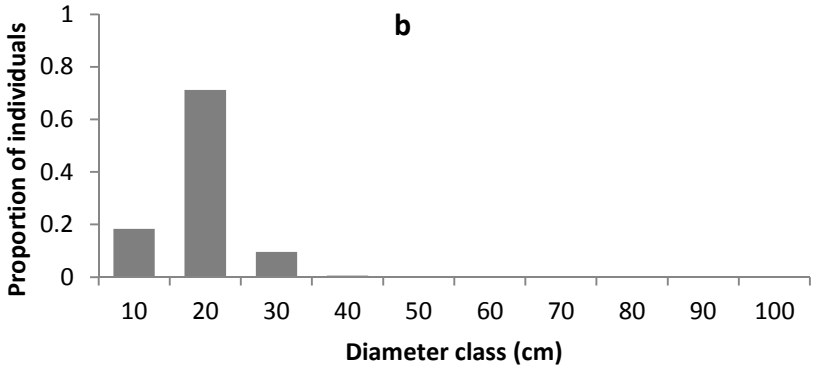

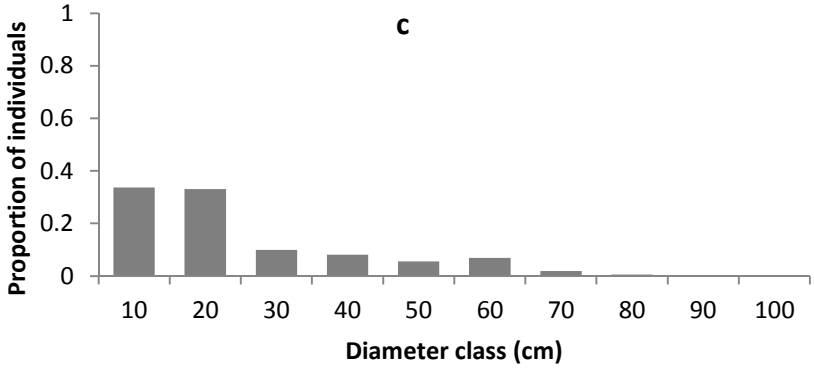

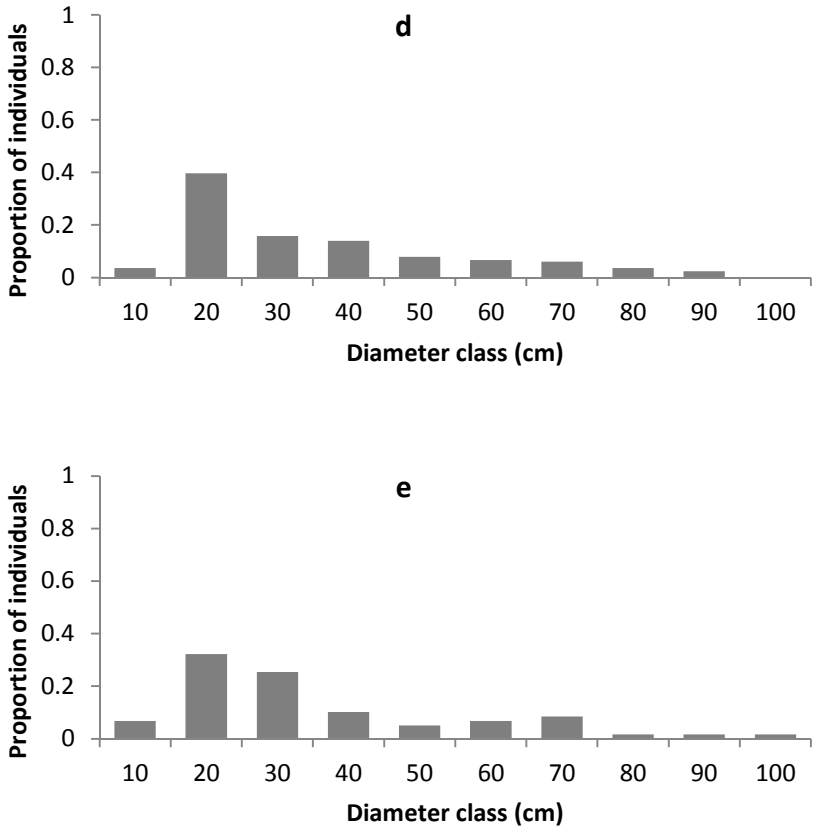

Figure 7.9. Diameter distributions for successional forests characterised by different stand ages a) 2-7 years b) 8-12 years c) 13-25 years d) 26-36 years e) 37-51 years.

Figure 7.10 is constituted by a series of plots which illustrate the changes in key forest structural parameters through successional development of Beni floodplain forest stands. Through plotting of values for individual sites as well as the overall average, the figures provide a visual indication of variability within each forest stand age class. In figure 7.10a, basal area increases with forest stand age, broadly reflecting the increase observed within the diameter distributions. Overall, basal area increases from <5 $m^2 ha^{-1}$ in the youngest forests, to in excess of 20 $m^2 ha^{-1}$ for forests stands between 37-51 years of age. Variability within age classes is lowest for the youngest forests (2-7 years), with the range of basal area relatively consistent for age classes 3,4 and 5 at around 5 $m^2 ha^{-1}$. Stem density, plotted within figure 7.10b, shows a broad decline with increasing forest stand age. For age classes 1 and 2, stem density exceeds 400 individuals per hectare. Stem density decreases dramatically for forests older than 13 years, indeed for the oldest stand age class stem density falls by greater than a factor of two to < 200 individuals per hectare. With the

exception of age class 1, stem density is characterised by a relatively low level of variability amongst the surveyed sites.

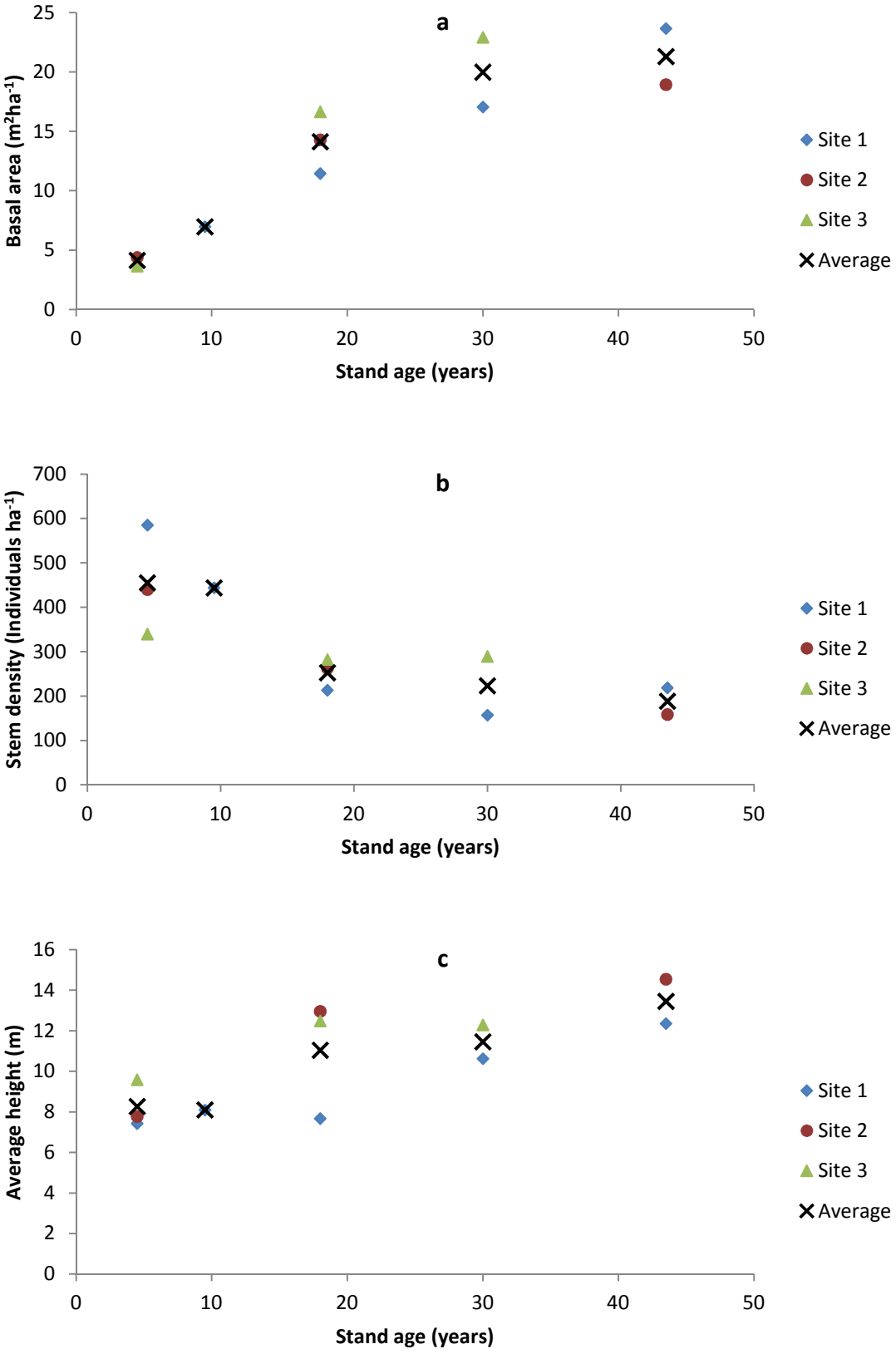

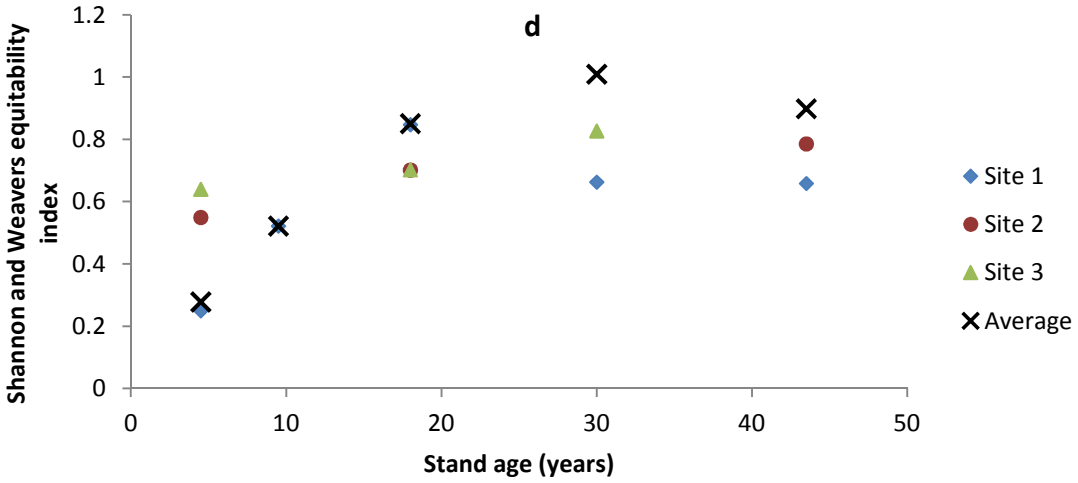

Figure 7.10. Plots illustrating the changes in forest structural parameters with successional forest stand age a) basal area b) stem density c) average tree height d) Shannon and Weaver equitability index (more information on this measure is provided below).

Forest height, depicted in figure 7.10c, also shows a clear increase with advancing succession. Average height increases from ~ 8 m to greater than 13 m within forest stands older than 37 years. Like other forest variables, variability in height is generally low amongst sites, with the exception of the third age class which exhibits a range of ~6 m. The Shannon and Weaver index of equitability (SWE) constitutes a simple measure of species diversity, which accounts for both abundance and evenness of species within a stand. Values range from 0-1, with a value of 0 indicating a monospecific stand, and a value of 1 indicating complete evenness of species within a plot. Significantly, in order to calculate the average SWE for each forest stand age class the inventories for each site were aggregated according to forest stand age. Hence, the average SWE value for each age class shown in 7.10d reflects the SWE for all individuals within a given age across all 3 sites, rather than the average of the SWE calculated for a given age at each site. Figure 7.10d demonstrates a broad increase in SWE with stand age. This trend is indicative of a transition from young monospecific stands to older successional forests that are characterised by a higher level of species diversity.

Figure 7.11 illustrates the AGWB stored in Beni successional floodplain forest stands of different ages. The plotted value represents the average AGWB for each forest age class across different surveyed sites. The two most notable features of figure 7.11 are the clear increase in AGWB through the successional

sequence, and the deviation in AGWB estimates produced by the two allometric equations. Calculations based upon allometric equation 7.1, produce biomass estimates which are substantially lower than those based upon allometric equation 7.2, by a factor of two. AGWB calculated based upon equation 7.1, which includes tree height as an independent parameter, increases from 14.13 ± 3.24 Mg ha^{-1} for forests with an age < 7 years, to 151.32 ± 34.80 Mg ha^{-1} for the oldest age class.

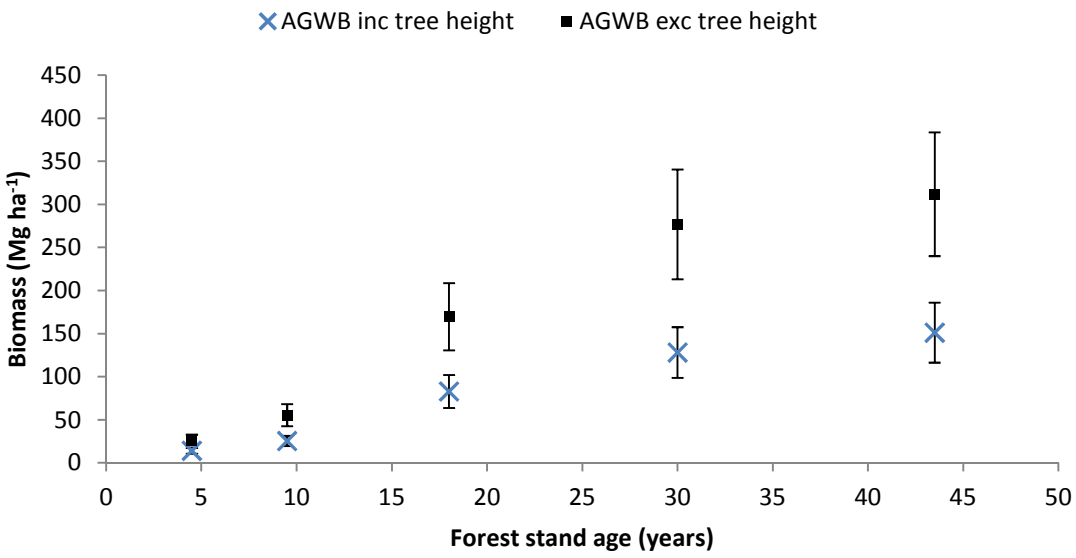

Figure 7.11. Aboveground wood biomass storage for forest stands of different ages, calculated using allometric equations including canopy height (7.1) and excluding canopy height (7.2).

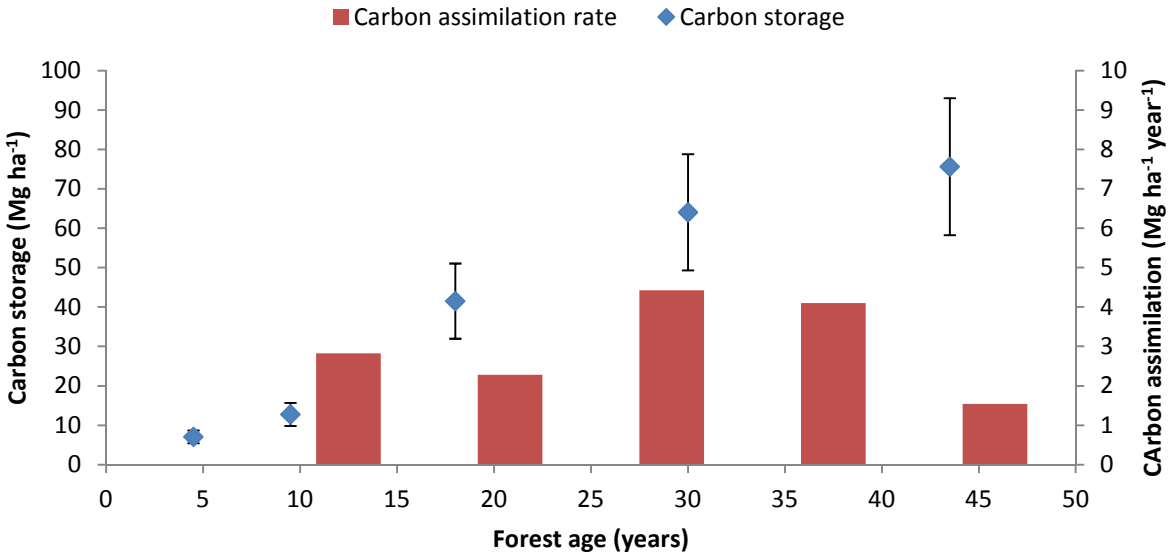

Figure 7.12. Aboveground carbon storage and assimilation rates for successional forests, calculated based upon biomass estimated through equation 7.1.

Figure 7.12 illustrates both aboveground carbon storage in successional forest stands on the Beni floodplain and inferred carbon assimilation rate, calculated based upon space-time substitution. Carbon storage is directly related to biomass storage and hence is characterised by the same upward trend with increasing forest stand age. The youngest successional forests (2-12 years) are associated with moderate rates of carbon assimilation, typically between 2-3 Mg ha^{-1} $year^{-1}$. This increases to a peak rate of 4.42 Mg ha^{-1} $year^{-1}$ for forest age class 3. For forests of age 26-37 years carbon assimilation rate remains above 4 Mg ha^{-1} $year^{-1}$, before decreasing substantially to 1.54 Mg ha^{-1} $year^{-1}$ for the oldest measured successional forests.

Figure 7.13 illustrates the relationships observed between forest structural characteristics and relative stand elevation with respect to Beni river water surface elevation. Given that water marks were not visible within all inventoried forest stands, relative elevation above water level provided the best available proxy for flood inundation magnitude at these locations. For each forest structural variable a relatively clear trend was observed with respect to relative elevation. Basal area, tree height and biomass increased with relative elevation, whilst stem density was inversely related to elevation above water level. Therefore based upon results illustrated in figure 7.13, it is clear that the broad variation in forest structural parameters with respect to relative elevation above the water surface are consistent with the trends observed with respect to forest stand age in figure 7.10.

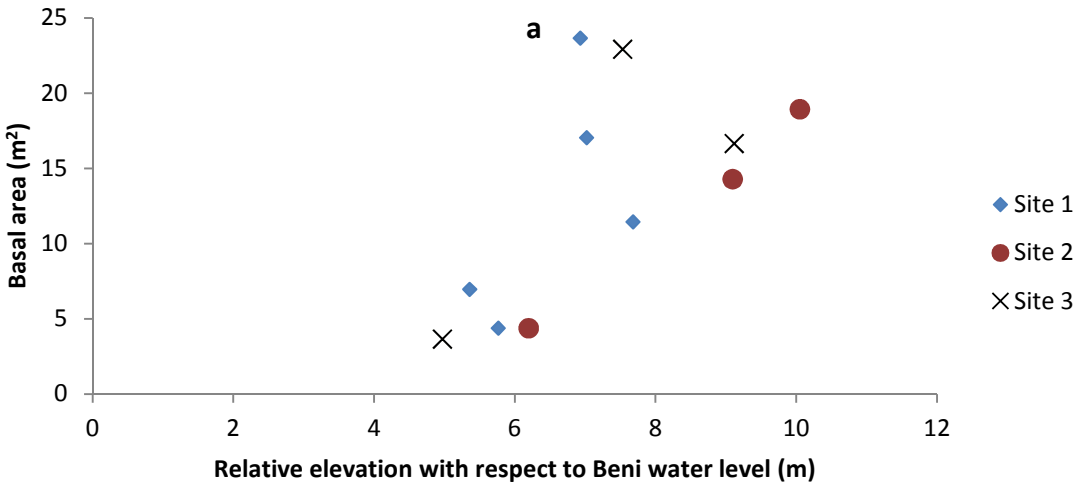

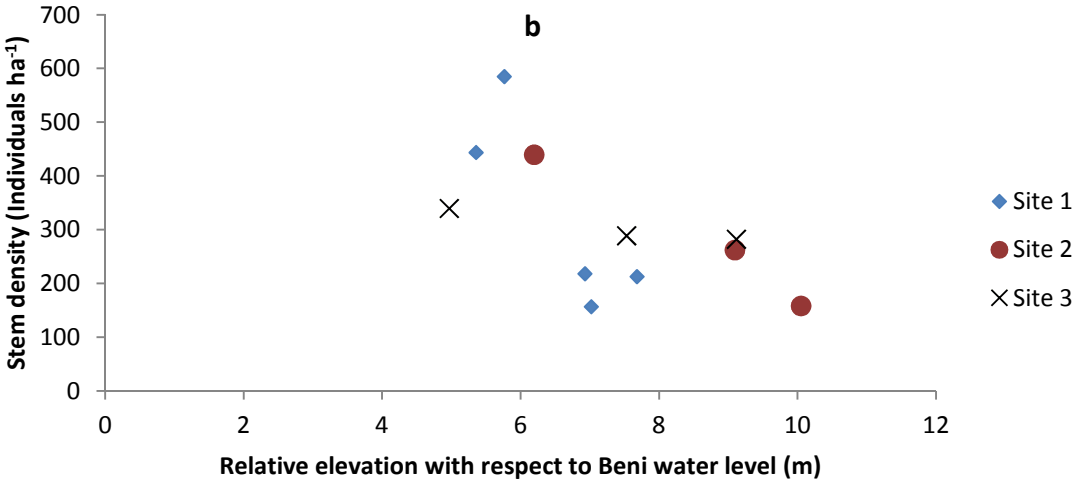
b
Stem density (Individuals ha-1)
700
600
500
400
300
200
100
0
0
2
4
6
8
10
12
Relative elevation with respect to Beni water level (m)
Site 1
Site 2
Site 3

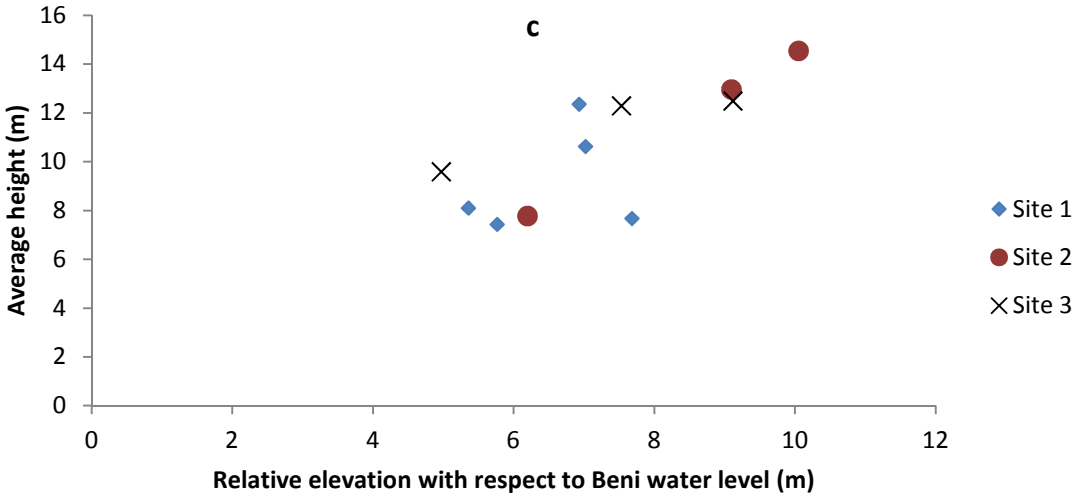
c
Average height (m)
16
14
12
10
8
6
4
2
0
0
2
4
6
8
10
12
Relative elevation with respect to Beni water level (m)
Site 1
Site 2
Site 3

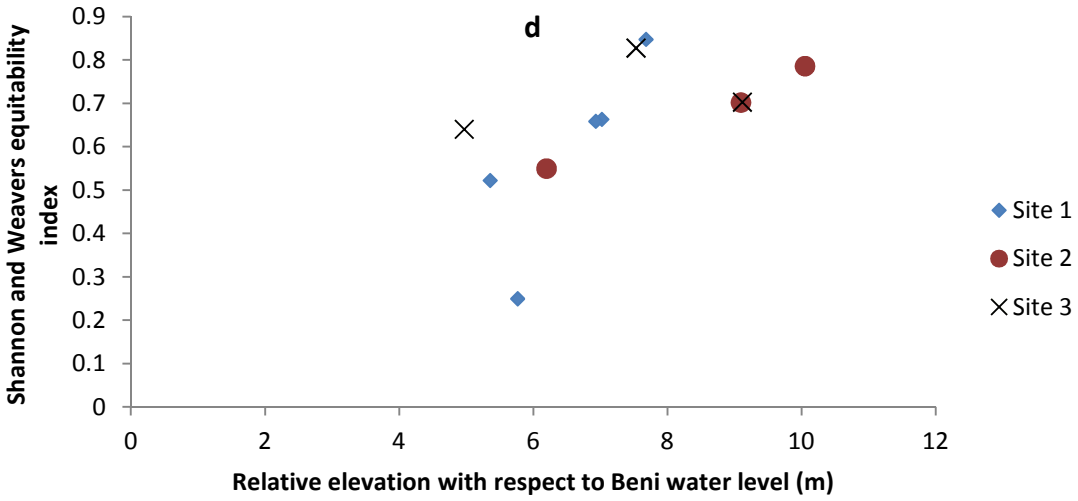
d
Shannon and Weavers equitability index
0.9
0.8
0.7
0.6
0.5
0.4
0.3
0.2
0.1
0
0
2
4
6
8
10
12
Relative elevation with respect to Beni water level (m)
Site 1
Site 2
Site 3

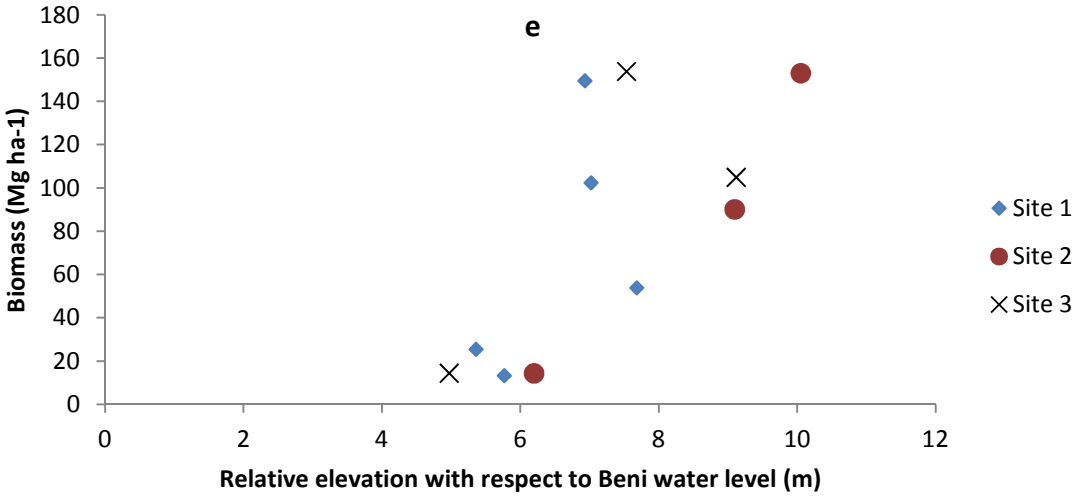

Figure 7.13. Plots illustrating the association between successional forest characteristics and elevation above water level; a) basal area b) stem density c) tree height d) Shannon and Weaver equitability e) aboveground wood biomass.

Figure 7.14 exhibits the grain size and phosphorus content of floodplain sediments for Beni floodplain successional forest stands. These plots, reveal no coherent trends in sediment characteristics when considered with respect to forest stand age or relative elevation above water level. Rather grain size distribution and total phosphorus appear to be predominated by random spatial variability. Analysis of other soil characteristics such as organic and inorganic carbon, nitrogen and soil moisture revealed a similar level of noise and absence of any significant signal. Hence these plots were not included here.

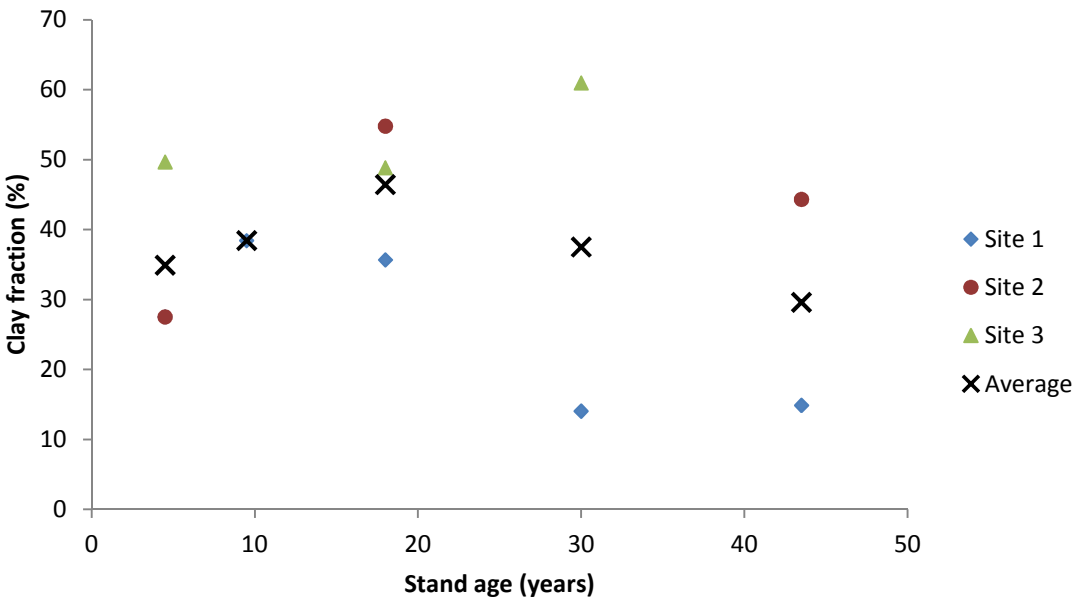

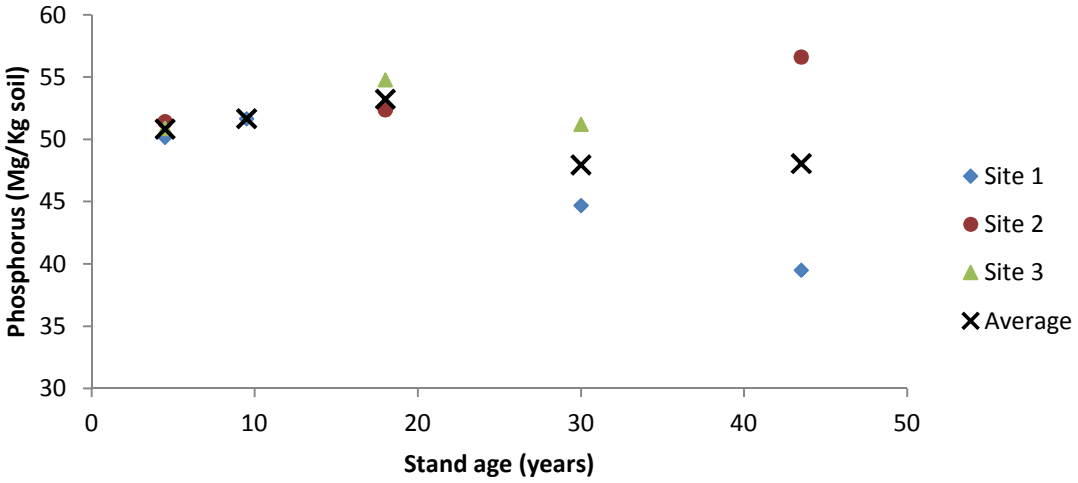

Figure 7.14. Plots showing variation in floodplain sediment characteristics for successional forest stands of different ages a) clay fraction b) phosphorus.

7.4.2 Changes in aboveground wood biomass and carbon storage due to Beni channel migration since 1960

Table 7.4 displays the balance of site loss and creation associated with shifting of the Beni channel during the period 1960-2011. Overall, during the 51 year study period a total of 42,024 hectares of floodplain were lost to erosional processes, constituting 23.28% of the total channel belt area. During the same period, alluvial deposition was responsible for the creation of 38,534 hectares of new floodplain, equating to just over 21% of the channel belt. Therefore averaged over the length of the study period, the loss of floodplain through erosional processes (824 hectares per year) has been roughly balanced by the creation of new sites (755 hectares per year). In the absence of a significant change in channel area between 1960-2011, the difference between loss and creation of sites can be attributed primarily to the occurrence of channel cut offs which constituted a total area of 3649 hectares. Table 7.4 also displays the total area of new stands created during each decade. It is important to consider that these areas reflect only the distribution of new sites delineated by the stand age map in 2011, and hence which were not subject to reworking since their initial deposition. The results illustrate a clear increase in the total area of new sites created in recent decades. Of the total area of new sites delineated in the stand age map, only 3626 hectares (2.01% of channel belt area) were deposited during the nine year period between 1962-1971. In contrast, new sites formed

from 1992-2011 constituted 10,889 hectares of the area depicted in the stand age map, equivalent to 6.03 % of the total channel belt area.

Table 7.4. Summary of the loss of floodplain sites through processes of erosion and creation of new depositional sites associated with meander migration of the Beni since 1960, expressed as absolute area and as a proportion of the overall area of the channel belt.

	Area (km^2)	Area (ha)	Area (% channel belt)
Channel belt area	1805.46	180546	
Total erosion 1960-2011	420.24	42024	23.28
Average annual erosion	8.24	824	0.46
2011 channel area	196.72	19672	10.90
Total new sites 1960-2011	385.24	38524	21.34
Total new sites 2002-2011	108.89	10889	6.03
Total new sites 1992-2001	101.38	10138	5.62
Total new sites 1982-1991	66.52	6652	3.68
Total new sites 1972-1981	56.77	5677	3.14
Total new sites 1962-1971	36.26	3626	2.01
Average annual new site creation	7.55	755	0.42
New lake cut off area 1960-2011	36.49	3649	2.02

Figure 7.15 and table 7.5 display the total area of newly created floodplain comprised by each stand age class, and the contribution of each class to total biomass storage in forest stands created since 1960. In terms of area, forest stands characterised by ages of 13-25 years are associated with the largest extent, making up almost one third of the 38,524 hectares of new sites created since 1960. Distribution of new sites is relatively even for other age classes, with stands of ages 2-7, 8-12, 26-37 and 38-51 years all comprising 13-19 % of the total area of new sites. Stand ages of 0-1 years make up only 6.56% of new floodplain formed since 1960. Intuitively, the distribution of total biomass stored within successional forests formed since 1960 is skewed towards older stands. Due to the lag in colonisation of freshly deposited sediment, stands with age 0-1 year were associated with no biomass storage. Despite constituting just under 30% of the total area of stands formed since 1960, successional forests of 2-12 years contributed less than 7.5% of total biomass storage in newly formed forest stands. The contribution of forest stands of age 13-25 years to total biomass storage was roughly equivalent to their area at 32.59%, whilst older successional forests (26-51 years) constituted over 60% of biomass stored

within newly formed forests, despite comprising < 40% of the total area of new sites formed since 1960.

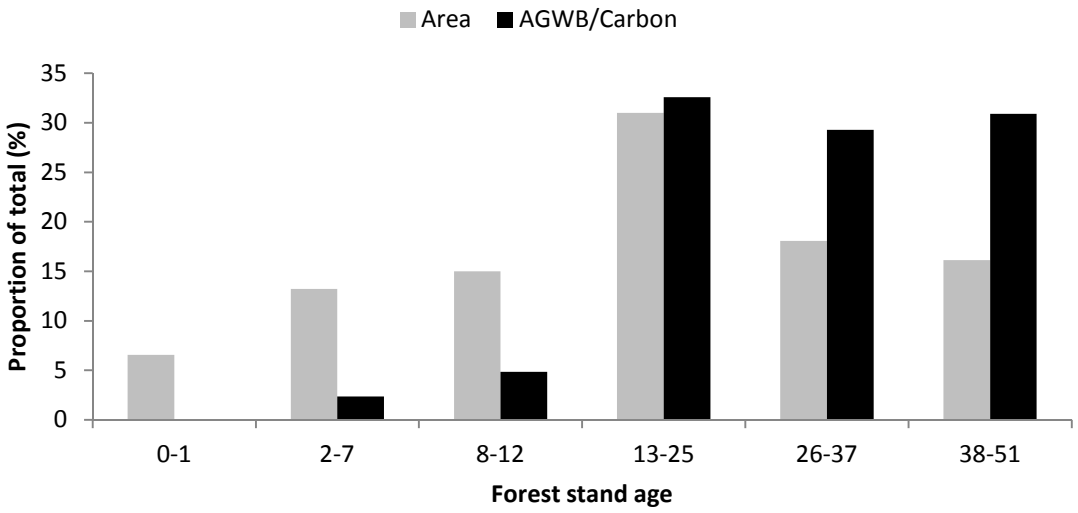

Figure 7.15. Proportional contribution of each stand age class to the total area of new stands created through alluvial deposition and total volume of new biomass stored within successional forests created since 1960.

Table 7.5. Displayed are the absolute (ha) and proportional contribution of each stand age class to the total area of new stands created through alluvial deposition and total volume of new biomass stored within successional forests created since 1960.

Forest stand age (years)	Proportion of total newly created sites (%)	Area of newly formed sites (ha)	Total aboveground wood biomass storage (Mg)	Total aboveground carbon storage (Mg)	Proportion of total aboveground wood biomass/carbon storage (%)	Annual carbon assimilation (Mg year^{-1})
0-1	6.57	2533	0	0.00	0	0
2-7	13.23	5097	71998	35999	2.37	14400
8-12	15.01	5782	147683	73842	4.85	13203
13-25	31.00	11942	991778	495889	32.59	52826
26-37	18.06	6956	891692	445846	29.30	28548
38-51	16.13	6215	940423	470211	30.90	9581
Total	100	38524	3043575	1521787	100	118557

Figure 7.16a illustrates the frequency distribution of canopy height within the Beni channel belt. Canopy height distribution is negatively skewed, with 20-25 m representing the most frequent forest height within this part of the floodplain. A relatively small proportion of pixels are characterised by canopy heights greater than 25 m (~17.5%), whilst canopy heights greater than 30 m are found for only 4% of pixels. Forests characterised by canopy height of less than 20 m

account for 40% of the channel belt area, whilst a significant proportion (10%) is unforested. The frequency distribution of canopy height is subsequently utilised in order to estimate the proportional distribution of AGWB and carbon within this area through application of the regression equation (figure 7.7).

The proportional distribution of AGWB found within the channel belt, illustrated within figure 7.16b, is subsequently applied to the overall area of floodplain lost through erosion through the study period, in order to estimate total AGWB and carbon losses since 1960. Both the proportional distribution of biomass/carbon within the contemporary channel belt and estimated losses since 1960 are included within table 7.6. The distribution of AGWB within the channel belt area, assumed to reflect the biomass lost through erosion since 1960, is characterised by a near normal distribution with respect to canopy height. Forests possessing a canopy height within the range 20-25 m account for the largest proportion of AGWB lost since 1960 (33.63%), whilst 81% of AGWB lost was stored within forests characterised by canopy heights of 15-30 m. Less than 10% of AGWB and carbon lost through erosional processes was stored within forests with height greater than 30 m.

Table 7.6. Summary of the contribution of different canopy height classes to the total channel belt area, and biomass/carbon storage within this area.

Canopy height bin (m)	Number of pixels	Proportion of total channel belt area (%)	Total area (ha)	Aboveground wood biomass storage (Mg)	Aboveground carbon storage (Mg)	Proportion of total aboveground wood biomass/carbon storage (%)
0	11221	9.13	3836	0	0	0
5	5820	4.73	1990	0	0	0
10	7680	6.25	2625	40725	20363	1.06
15	13647	11.10	4665	350440	175220	9.15
20	23536	19.15	8046	842155	421077	22.00
25	39006	31.73	13335	1287446	643723	33.63
30	17047	13.87	5828	961973	480986	25.13
35	4585	3.73	1567	335359	167679	8.76
40	385	0.31	132	10550	5275	0.28
Total	122927	100	42024	3828647	1914323	100

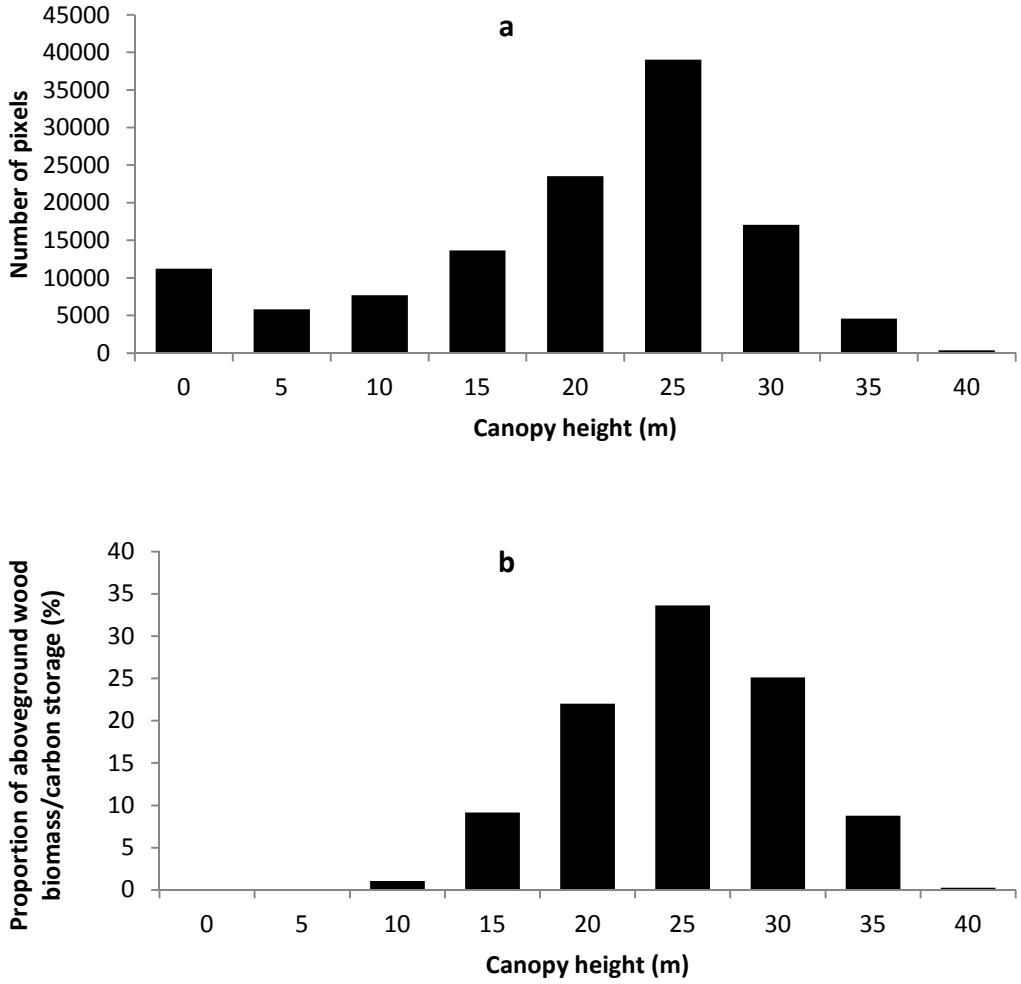

Figure 7.16. a) Histogram displaying the frequency distribution of canopy height for the channel belt area, extracted from the canopy height map b) Histogram illustrating the proportion of total biomass/carbon storage in the channel belt within forests of different heights.

Table 7.7 summarises the overall areas of floodplain created and lost since 1960 in the Beni floodplain study area, along with the associated net changes in aboveground wood biomass and carbon storage. Despite the relative parity in the loss and creation of new sites in terms of area, more significant differences were observed with respect to the balance of AGWB and carbon storage. AGWB and carbon storage within newly created successional forest stands was estimated at 3,043,575 Mg and 1,521,787 Mg respectively, whilst losses due to erosion were estimated at 3,828,647 Mg and 1,914,323 Mg respectively. Therefore during the study period, lateral shifting of the Beni channel resulted in a net loss in AGWB and carbon of approximately 785,072 Mg and 392,536 Mg respectively.

Table 7.7. Overall summary of the creation/ loss of floodplain sites and associated change in biomass/carbon storage since 1960.

	Formed since 1960	Lost since 1960	Balance
Total area (ha)	38523	42024	-3500.53
Total biomass (Mg)	3043575	3828647	-785072
Total carbon (Mg)	1521787	1914323	-392536
Average biomass (Mg^{-1} ha^{-1})	79.00	91.10	-12.10
Average carbon (Mg^{-1} ha^{-1})	39.50	45.55	-6.05

7.4.3 Beni floodplain aboveground wood biomass and carbon storage estimates

Table 7.8 displays the total aboveground wood biomass and carbon stocks estimated for the Beni floodplain study area. It is clear that estimations of AGWB vary substantially between the three maps. Total AGWB storage upon the Beni floodplain is approximately 44.2 million Mg when local plot level AGWB estimates are extrapolated with respect to a local canopy height map (Map 1). Extrapolation of local biomass measurements through a global canopy height map (Map 2) yields a larger estimate of overall AGWB storage of 59.9 million Mg. The highest estimates of AGWB storage for the Beni floodplain (109 Million Mg) are observed within Map 3, derived from the Amazonian biomass map

Table 7.8. Summary of total aboveground wood biomass and carbon storage for the Beni floodplain study area derived through different approaches.

	Local canopy height (Map 1)	Global canopy height (Map 2)	Amazon biomass map (Map 3)
Total biomass storage (Mg)	44209595	59941065	109038517
Total carbon storage (Mg)	22104797	29970532	54519258
Average forest biomass (Mg ha^{-1})	72.69	94.81	179.29
Average carbon storage (Mg ha^{-1})	36.35	47.41	89.64

produced by Saatchi et al., (2007). Thus the biomass estimates for the Beni floodplain derived from the Amazonian biomass map are larger than those estimated based upon extrapolation of plot scale biomass measurements using a local canopy height map by more than a factor of two. The disparity in total aboveground wood biomass stocks for the Beni floodplain is reflected in the

average AGWB calculated for the three maps, shown in table 7.8. For Maps 1 and 2, the average forest biomass is 72.69 and 94.81 Mg ha^{-1} respectively, whilst for Map 3 average forest biomass is much higher at 179 Mg ha^{-1}.

Figure 7.17 and table 7.9 explore the differences between AGWB estimates for Maps 1 and 2, generated through extrapolation of local plot level biomass measurements. For Map 1 (figure 17.7a) the highest proportion of biomass is stored within forests characterised by canopy height of 15-20 m, whilst a roughly equivalent proportion is contained within forests 20-25 m tall. In total, in excess of 65% of AGWB on the floodplain is stored within these canopy height classes. Of the remaining 35% of AGWB, less than 15 % is stored within forests with a canopy height greater than 25 m. In contrast for Map 2 (figure 7.17b) total biomass is distributed less evenly between forests of different heights. The largest volume of biomass (46.95 %) is stored within forests with canopy height 20-25 m, whilst the proportion of AGWB stored within forest characterised by heights > 25 m is larger than for Map 1 (~25%). Intuitively therefore a significantly lower proportion of overall floodplain biomass is stored in forests characterised by lower canopies. The differences observed between the maps in terms of proportional allocation of biomass are reflected in the absolute volumes of biomass, shown in table 7.9. Significantly, within Map 2 the volumes of biomass stored within forests with higher canopies (>20 m) far exceeded those observed for Map 1.

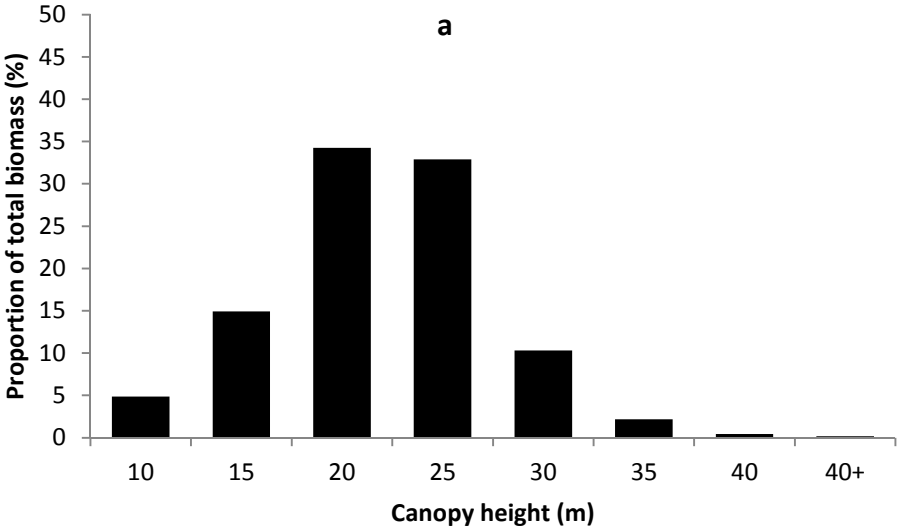

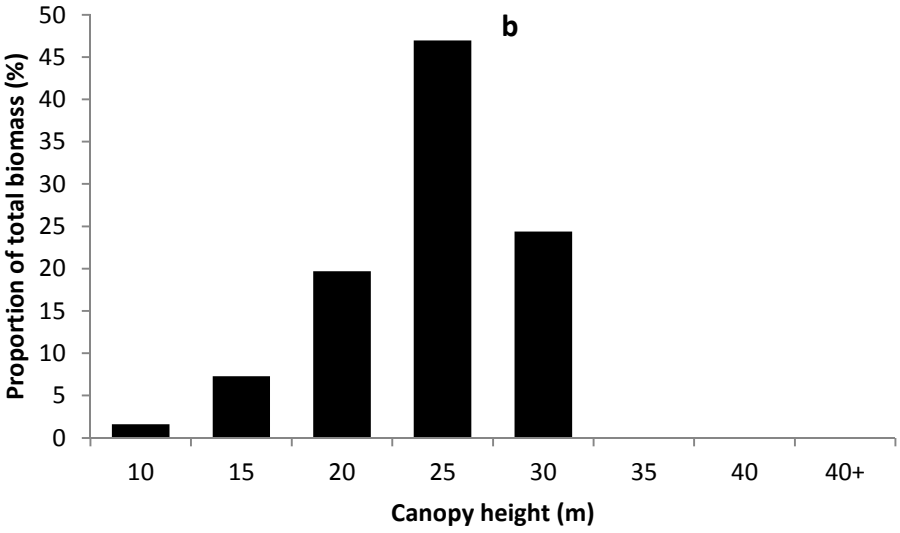

Figure 7.17. Distribution of total floodplain aboveground wood biomass within forests characterised by different canopy height for a) floodplain biomass map generated based upon locally derived canopy height map (Map 1) b) floodplain biomass map generated based upon global canopy height map (Map 2).

Table 7.9. Distribution of total floodplain aboveground wood biomass within forests characterised by different canopy height for floodplain biomass maps generated based upon locally derived canopy height map (Map 1) and a global canopy height map (Map 2).

	Local canopy height (Map 1)		Global canopy height (Map 2)	
Canopy height (m)	Total biomass (Mg)	Proportion total biomass (%)	Total biomass (Mg)	Proportion total biomass (%)
10	2153150	4.87	965624	1.61
15	6596502	14.92	4372667	7.29
20	15135174	34.24	11795403	19.68
25	14532065	32.87	28140588	46.95
30	4562080	10.32	14614462	24.38
35	956297	2.16	52321	0.09
40	190287	0.43	0	0.00
40+	84039	0.19	0	0.00
Total	44209595		59941065	

Figure 7.19 and table 7.10 exhibit the proportional and absolute allocation of total floodplain AGWB within forests characterised by different biomass densities for the three maps. For both figure 7.19a and 7.19b the highest proportion of AGWB is allocated within forests with a biomass density of 100-150 Mg ha^{-1}, although this proportion is substantially higher (59 %) for Map 2 than Map 1 (37%). Both plots are characterised by negatively skewed distributions of biomass, indicating significant storage of AGWB in forests with low biomass densities, particularly within Map 1. Within both Map 1 and Map 2 less than 15% of total floodplain AGWB is stored within forests characterised by

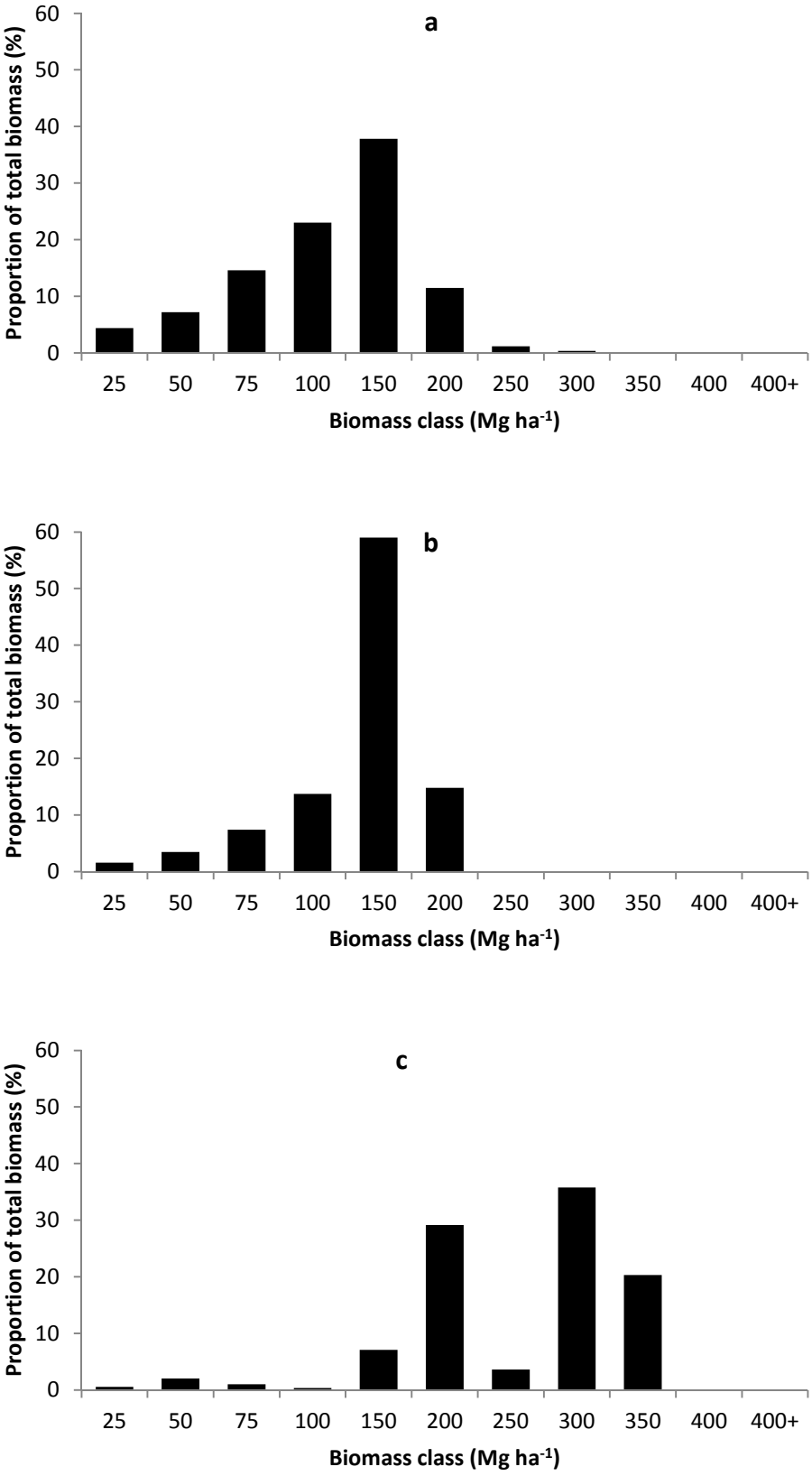

Figure 7.19. Distribution of total floodplain aboveground wood biomass within forests characterised by different biomass density for a) floodplain biomass map generated based upon locally derived canopy height map (Map 1) b) floodplain biomass map generated based upon global canopy height map (Map 2) c) Amazon basin biomass map generated by Saatchi et al., (2007) (Map 3).

biomass density > 150 Mg ha^{-1}. The proportional allocation of biomass demonstrated in 7.19c and table 7.10 (Map 3) is markedly different than that observed for Maps 1 and 2. The distribution of biomass within Map 3 is multi modal, with over 85% of total floodplain AGWB being stored within three classes, 150-200 Mg ha^{-1} (29.15 %), 250-300 Mg ha^{-1} (35.80 %) and 300-350 Mg ha^{-1} (20.33 %). Hence it is evident that a larger proportion of floodplain AGWB is allocated within forests of higher biomass density within Map 3 in comparison to Maps 1 and 2.

Table 7.10. Distribution of total floodplain aboveground wood biomass within forests characterised by different biomass density for floodplain biomass maps generated based upon locally derived canopy height map (Map 1), global canopy height map (Map 2) and derived from the Amazon basin biomass map (Saatchi et al., 2007) (Map 3).

	Local canopy height (Map 1)		Global canopy height (Map 2)		Amazon biomass map (Map 3)	
Biomass class (Mg^{-1} ha^{-1})	Total biomass (Mg)	Proportion total biomass (%)	Total biomass (Mg)	Proportion total biomass (%)	Total biomass (Mg)	Proportion total biomass (%)
25	1948591	4.41	953806	1.59	615026	0.56
50	3177303	7.19	2088029	3.48	2212437	2.03
75	6444174	14.58	4440841	7.41	1130261	1.04
100	10176183	23.02	8229086	13.73	383927	0.35
150	16730946	37.84	35365860	59.00	7742338	7.10
200	5067831	11.46	8863443	14.79	31788626	29.15
250	513291	1.16	0	0.00	3960962	3.63
300	151276	0.34	0	0.00	39037343	35.80
350	0	0.00	0	0.00	22167597	20.33
Total	44209595		59941065		109038517	

Figures 7.20-7.22 provide a visual illustration of the spatial distribution of AGWB upon the Beni floodplain for the three maps presented within this chapter. Intuitively the distribution of biomass across the floodplain in Map 1 and Map 2 reflects that of the respective canopy height maps. In figure 7.20, Map 1 shows a greater level of spatial variability in AGWB, with the highest biomass densities (150-200 Mg ha^{-1}) found within the forests which flank the Beni and smaller floodplain water courses. Biomass storage falls markedly, to lower than 100 Mg ha^{-1} in forests located at a greater distance from river channels. Map 2 (figure 7.21) features a more even distribution of biomass across the study area, with the majority of floodplain forest being characterised by AGWB storage of 100-150 Mg ha^{-1}. The major exceptions are the forests located within close proximity

to the Beni channel, where biomass is generally lower than 100 Mg ha^{-1}. Map 3 (figure 7.22) is characterised by a biomass distribution which differs significantly from Maps 1 and 2. The main expanse of varzea forest located to the east of the Beni channel is characterised by AGWB storage of 150-200 Mg ha^{-1} and 250-300 Mg ha^{-1}. Pockets of forest with lower biomass densities are located amongst the more dominant high biomass stands.

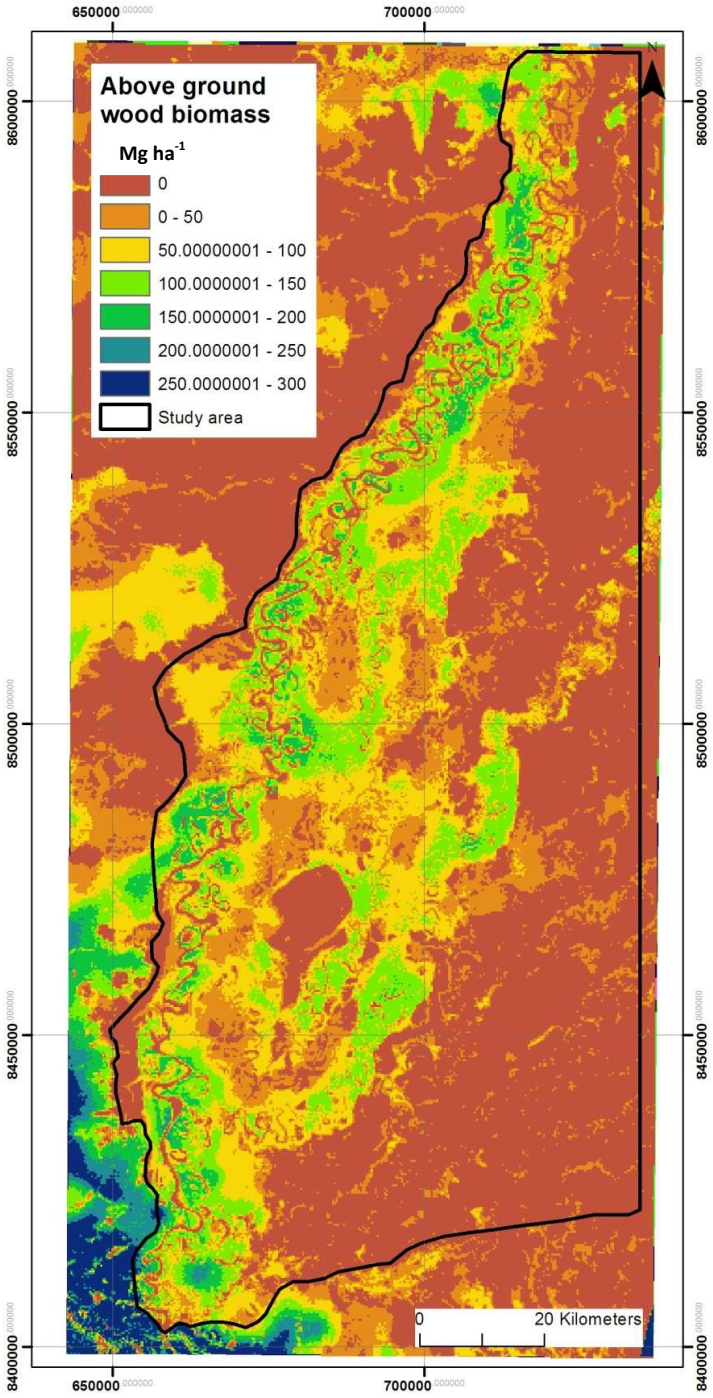

Figure 7.20. Aboveground wood biomass map for the Beni study area based upon local canopy height map (Map 1).

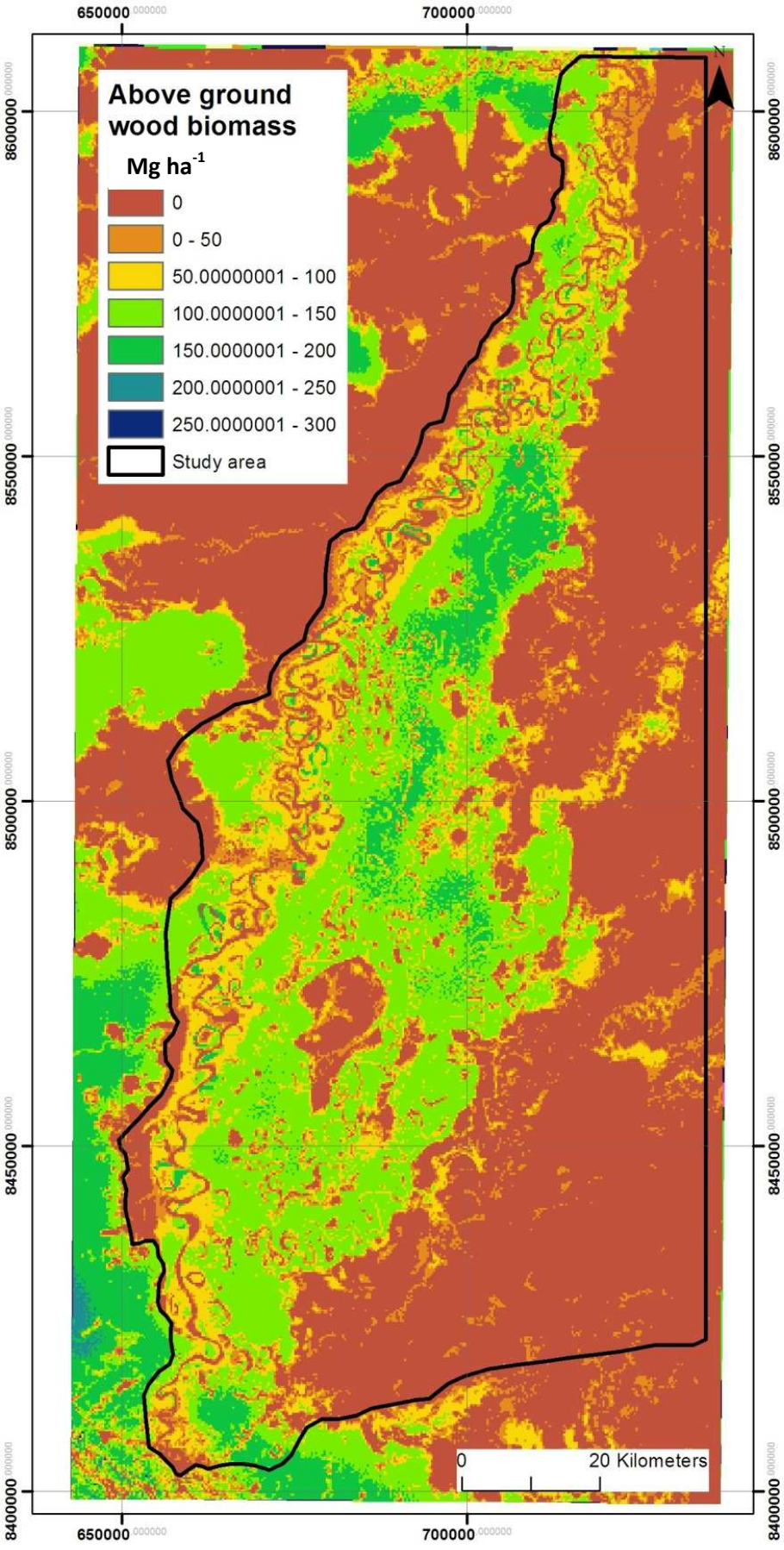

Figure 7.21. Aboveground wood biomass map for the Beni study area based upon global canopy height map (Map 2).

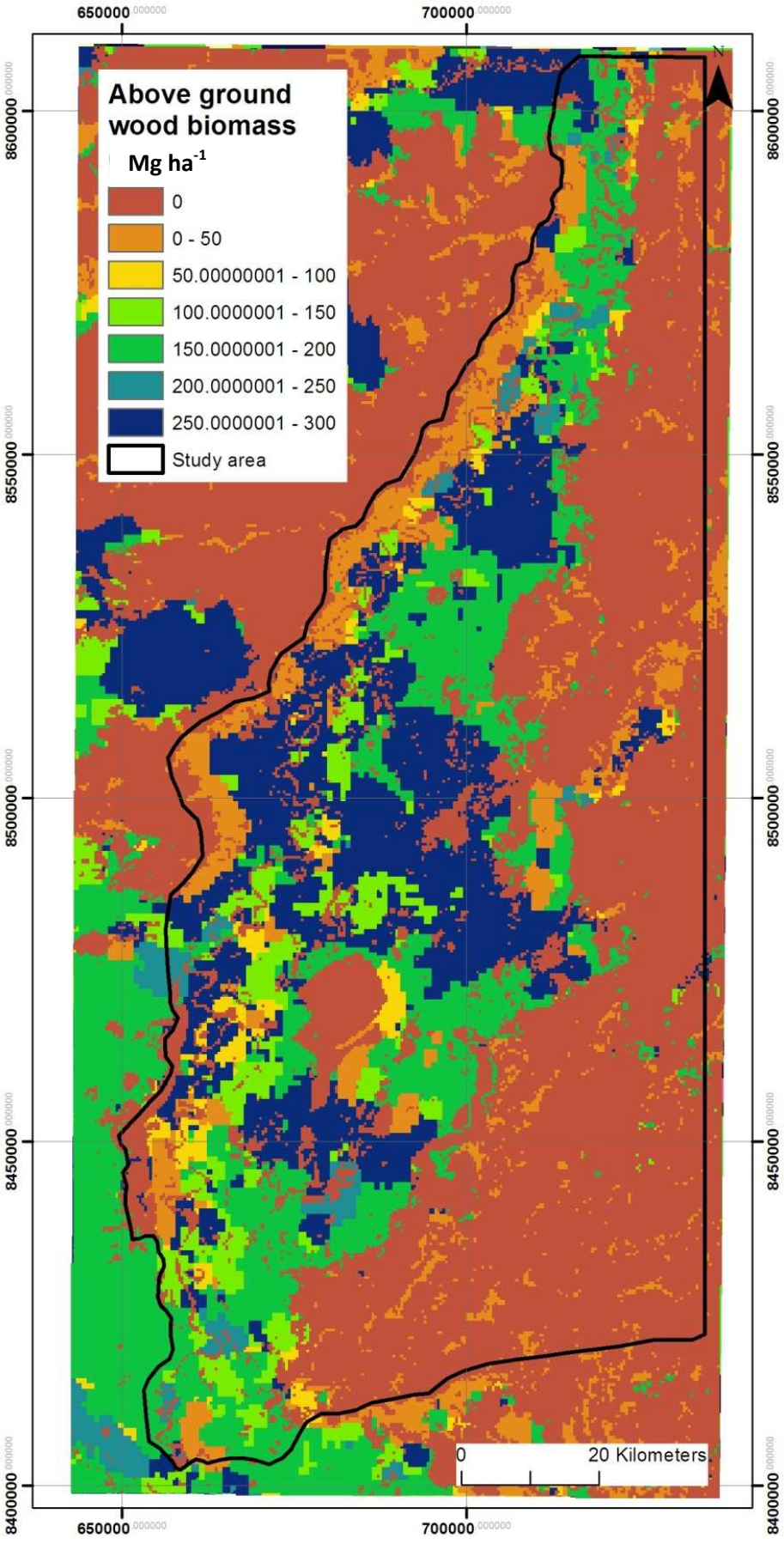

Figure 7.22. Aboveground wood biomass map for the Beni study area derived from the Amazon basin map produced by Saatchi et al., (2007) (Map 3).

7.5 Discussion

7.5.1 Characterisation of Beni successional forest development

The results presented within figure 7.9/7.10 illustrate that successional forest stands located upon the Beni floodplain exhibit a clear zonation according to forest stand age. The youngest forest stands (2-7 years) are monospecific, characterised by light demanding pioneer tree species such as *Tessaria integrifolia* and *Salix humboldtiana*, which form homogenous open canopies. These species are well adapted to the conditions which proliferate during flooding, forming deep primary roots (Wittmann and Parolin, 2005) to aid stability and reducing metabolism during periods of inundation (Piedade et al., 2000). With increasing stand age, stem diameters increase along with other structural variables such as basal area, average height and species diversity. Within forest stands aged 7-25 years there was an increasing abundance of the fast growing *Cecropia spp*, which are found within successional forests across the Amazon basin (Alves et al., 1997). The oldest stands surveyed here (38-51 years) were characterised by species such as *Ficus maxima* and *Inga spp* , which were less well adapted to flood inundation and observed to be common within old growth forest stands within the Beni floodplain. In older stands, canopies are increasingly well stratified and exhibit a higher degree of closure. The stand characteristics documented here are consistent with findings of other studies which have explored successional development of Amazonian varzea forests (Campbell et al., 1992; Worbes et al., 1992; Ayres, 1993)

Results presented in 7.13 also demonstrate a clear relationship between forest structural characteristics and relative elevation above the Beni water level. Basal area, height and SWE are all positively associated with relative elevation, whilst stem density is negatively associated with stand height above water level. Relative elevation was applied here in the absence of consistent water level marks in order to provide a proxy for flood inundation magnitude, based upon the assumption that flood inundation magnitude will be greater for stands with a lower relative elevation (Wittmann et al., 2002). The association between forest structural characteristics and relative stand elevation suggests that the zonation of forest along the successional sequence is to some extent a function of flood inundation characteristics. Thus on a basic level, the dependence of forest characteristics upon flood inundation magnitude reflects the findings of previous

studies which have documented the interactions between flood inundation and varzea forests (Wittmann et al., 2002; Wittmann et al., 2004).

Moreover, the variation of forest structural characteristics illustrated with respect to both floodplain stand age and relative elevation implies a level of covariance between these two variables. For the central Amazon floodplain, Wittmann et al., (2004) found that forest succession and physical site conditions were not independent. Rather the authors found that establishment of successional vegetation modified physical site conditions, providing a greater resistance to flow and encouraging sediment deposition. This initiated a cycle in which enhanced deposition of sediment increased site elevation, leading to establishment of more stable and diverse vegetation, classified as 'allogenic succession' (Burrows 1990). Here the covariance in floodplain stand age and relative elevation implies a similar mode of forest succession within newly formed Beni varzea stands.

Figure 7.23. Beni floodplain successional forest stands, illustrating pioneer herbaceous vegetation at low elevation in the foreground and the growth of woody species upon raised areas behind.

This assessment is also supported by further observational evidence, for instance it was consistently observed that growth of woody vegetation did not occur upon point bar deposits until stand elevation had reached several meters above typical water levels observed for the dry season (figure 7.23). Floodplain sediment cores were taken in order to quantify sedimentation rates within the inventoried forest stands through Pb^{210} chronology. However, sedimentation rates were not consistently obtained across the complete range of stand ages and hence the results were not included here. Deposition rates were typically ~

4-7 cm per year within forest stands inventoried here, with some evidence of a decline for older stands, although this increase was not sufficiently clear to provide quantitative evidence of the role of sedimentation in increasing floodplain elevation. This observational evidence adds credence to the postulation that development of Beni forests occurs through the process of 'allogenic succession' (Tansley, 1929), which has been observed for varzea forests in other regions within the Amazon basin (Wittmann et al., 2004).

Of particular importance within this research is the storage and assimilation of AGWB and carbon within successional varzea forests. Figure 7.11 shows that estimates based upon equation 7.2 are greater than those obtained through application of 7.1 by a factor of two. Given that both allometric equations were derived for moist forests from the same pan tropical tree harvest dataset (Chave et al., 2005), the omission of height as an independent parameter within 7.2 presents an obvious reason for the observed difference in biomass estimates. However as no alternative source of AGWB data is available for the Beni floodplain forests, a quantitative assessment of biomass calculated from the two models is not feasible here. Nevertheless, an examination of the equations and harvest datasets from which they were derived is able to provide an insight into the validity of each set of biomass calculations.

For equation 7.2, tree height is parameterised within the allometric equation itself and thus reflects the heights of trees within the harvested dataset, which were predominantly obtained from old growth Terra Firme forests (Chave et al., 2005). Canopy height within old growth Terra Firme forests commonly exceeds 30 m, much greater heights than most stems surveyed within successional forests upon the Beni floodplain. Indeed typical tree heights for Beni successional varzea stands are illustrated within figure 7.10, and are typically of the order 8-25 m. Therefore, it can be concluded with a high degree of confidence that equation 7.2 significantly over predicts the AGWB of successional varzea forest stands on the Beni floodplain. For a study of the Pantanal wetland forests within the Brazilian Amazon Schongart et al., (2008) observed a similar effect, with the application of allometry excluding tree height as an independent parameter resulting in substantial over prediction of AGWB. Allometric equations which do not use canopy height as an independent parameter are commonly utilised within tropical forest studies as tree height is

difficult to measure and is often omitted from inventory surveys (Chave et al., 2004). The results presented here, along with those of Schongart et al., (2008), strongly suggest that the application of allometry without canopy height as an independent parameter are likely to substantially over predict biomass within varzea forests. Herein, biomass estimates referred to will be those estimated using equation 7.1.As for other forest structural characteristics, AGWB and carbon storage increase with both forest stand age and relative elevation. The increases in AGWB and carbon storage observed here along the successional sequence are driven by the process of allogenic succession (Wittmann et al., 2004). In early successional stages, stands are dominated by fast growing species such as *Tessaria integrifolia* and *Salix humbodtiana*, which are characterised by low AGWB and carbon stocks due to their relatively small diameters and low heights. With continued successional development, increases in stand elevation and declining influence of flood inundation facilitates the establishment of species such as *Ficus spp.*, which are characterised by lower growth rates but higher biomass stocks owing to their larger basal area and higher canopies.

The results presented here represent the first rigorous quantification of the development of AGWB and carbon stocks within successional varzea forests. Hence, although direct comparison with other equivalent estimates is not possible, the AGWB storage of Beni successional forest stands can be contextualised with respect to other forest types. Saatchi et al., (2007) compiled a large database of forest inventory information (>500 plots) collected across the Amazon basin, including 216 terra firme old growth plots, 191 secondary forest plots and 40 floodplain forest plots. Although the plots were characterised by a high level of variation in AGWB, the average AGWB for old growth terra firme forests was 254.8 Mg ha^{-1} and 161.3 Mg ha^{-1} for floodplain forests. Therefore AGWB stocks of successional forest stands of the Beni floodplain are much lower than those of typical terra firme forests. In the youngest successional forests stands, AGWB storage falls significantly below the average for floodplain forests, however within the oldest successional forests measured here (38-51 years) AGWB appears to be roughly equivalent with the average reported for Amazonian floodplain forests (Saatchi et al., 2007). This suggests that the biomass of newly formed successional forests within the Beni floodplain may reach levels approaching that of ‘old growth’ varzea forests within 50 years

of initial site formation. This assertion is supported by the fact that AGWB stocks in older successional forests exceed those measured within older forest stands measured upon the Beni floodplain (figure 7.7). In comparison, after complete clearance of an Amazonian Terra Firme forest stand for agriculture, it is estimated that AGWB approaches values typical of old growth forest after approximately 100 years (Guariguata and Ostertag, 2001). The rapid accumulation of biomass documented here implies that successional varzea forests are associated with a high level of primary productivity.

Carbon assimilation rates illustrated in figure 7.12, increase from an initial 2-3 Mg ha^{-1} $year^{-1}$ within forest stands < 12 years, to greater than 4 Mg ha^{-1} $year^{-1}$ for forests 13-37 years and subsequently falling to less than 2 Mg ha^{-1} $year^{-1}$ for forests older than 38 years. Therefore the 51 year chronosequence captures the increase to peak carbon assimilation rate within successional forests, and the beginning of the subsequent decline to assimilation levels typical of old growth forest stands. It is hypothesised that moderate rates of carbon assimilation within the youngest forest stands (<12 years) are attributable to the presence of light demanding fast growing species, although relatively high magnitudes of inundation impose a limit upon vegetation growth (Wittmann and Parolin, 2005). The highest growth rates are observed within forests between the ages of 12-37 years, where stands are increasingly characterised by the presence of fast growing *Cecropia spp*., whilst the declining influence of flood inundation means that growth rates are less constrained than within younger successional forests. Within the oldest forest stands, the increasing presence of late successional species such as *Ficus maxima* and *Inga spp.*, which are associated with lower growth rates than species found within younger stands, contributes towards the lower rates of carbon assimilation, despite the declining influence of flood inundation. Overall, this provides further evidence that a large proportion of AGWB and carbon stocks contained within mature varzea forest stands are assimilated within the first 50 years of successional forest development.

Peak rates of carbon assimilation calculated for Beni floodplain forest stands (4.42 Mg ha^{-1} $year^{-1}$) were similar to the maximum rate of 4.24 Mg ha^{-1} $year^{-1}$ documented for successional forests of the Pantanal wetland by Schongart et al., (2008), which were subject to disturbance by inundation. It is possible to

view the carbon assimilation rates calculated here in a wider context through comparison to rates of AGWB increase across the Amazon basin for non successional forests, reported by Baker et al., (2004). Average AGWB increases within floodplain forest stands were 2.08 Mg ±0.74 Mg ha^{-1} $year^{-1}$ (equivalent to 1.04 Mg of carbon ha^{-1} $year^{-1}$), whilst the rate was lower for Terra Firme forests at 0.80 ±0.42 Mg ha^{-1} $year^{-1}$(equivalent to 0.40 Mg ha^{-1} $year^{-1}$ carbon). Therefore, peak carbon assimilation rates within Beni successional forest stands are four times greater than the average carbon assimilation within Amazonian varzea forests, and approximately ten times greater than the average for Terra Firme forests (Baker et al., 2004). This suggests that newly formed successional floodplain forests have the potential to sequester a relatively large volume of C in comparison to other types of tropical forest within Amazonia.

Uncertainty is an important component of plot level AGWB and carbon estimations calculated through application of allometric equations to forest inventory data (Ketterings et al., 2001). Uncertainty can arise from four major sources; tree level measurement error; allometric model error; within-plot uncertainty and among plot (landscape scale) uncertainty (Brown, 1997). The relative magnitude of these uncertainties was estimated for tropical forests by Chave et al., (2004). Based upon the calculations of Chave et al., (2004) estimations of AGWB and carbon stocks, averaged here within forest age classes, are reported with an uncertainty of ±23 %. Of the overall 23% uncertainty, 13% is attributed to allometric uncertainty, whilst a further 10% is associated with sampling uncertainty within plots of 0.25 ha. Tree level measurement uncertainty was not included here, as measurement errors were found to average out at stand level (Chave et al., 2004). Landscape scale errors were not included here as AGWB values reported were averaged for multiple plots within each forest stand age class, and thus were assumed to be representative of this class at large.

7.5.2 Changes in aboveground wood biomass and carbon storage due to Beni channel migration since 1960

Results presented in 7.4.2 clearly illustrate that migration of the Beni channel is associated with significant implications in terms of floodplain forest dynamics. Within the study reach 42,024 hectares of forest have been lost through

processes of erosion since 1960, corresponding to 3,828,647 Mg of biomass. Whilst newly formed successional forests occupy a total area of 38,523 hectares and store a total of 3,043,575 Mg of AGWB. Therefore on a basic level it is evident that shifting of the Beni channel has been responsible for the turnover of a substantial area of varzea forest from 1960-2011. In terms of overall balance, the total decrease in AGWB and carbon storage equated to 785,072 Mg and 392,536 ha Mg respectively. In order to put these figures into context, this volume of biomass equates to a loss (for example through deforestation) of approximately 5200 hectares of forest, based upon the average AGWB and carbon stock of Beni floodplain forest stands. Overall varzea biomass storage estimates for the Beni floodplain vary from 44 million Mg to 109 million Mg. Hence when only the overall net loss of AGWB and carbon for the study reach is considered, the effect of channel migration upon forest dynamics appears to be of limited significance, constituting a loss equivalent to less than 2% of the total AGWB storage volume for the whole floodplain over the 51 year study period.

Peixoto et al., (2009) assessed migration of the Japura, Solimoes and Aranapu rivers within the Mamirua Sustainable Development Reserve, and the associated implications of channel shifting for carbon storage within adjacent varzea forests. Although the rivers here are substantially larger than the Beni, with the Solimoes and Japura being associated with average discharges of 71,810 m^3s^{-1} and 17,000 m^3s^{-1} respectively, the channels can be classified as meandering white water rivers and thus provide results comparable with those obtained within this study. Estimates of lateral erosion and accretion, expressed as a percentage of channel area per year in order to adjust for the size of the respective study areas, illustrate that the Beni is more dynamic than the Solimoes, Japura and Aranapu. Average annual erosion and accretion for the Beni over the 51 year study period corresponded to 4.3% and 3.84% of the channel area respectively. For the Solimoes, Japura and Aranapu, annual erosion for the 21 year study period as a proportion of channel area averaged 0.79 % and accretion averaged 0.83%. These findings are broadly consistent with the findings of Gautier et al., (2007), who reported that the Beni was associated with a floodplain recycling rate which was substantially higher than that of the Solimoes reported by Mertes et al., (1996). Gautier et al., (2007) hypothesised that the higher rates of channel migration observed for the Beni

can be attributed to its higher specific stream power (calculated based upon bankfull discharge, longitudinal gradient and channel width) in comparison to the Solimoes. Peixoto et al., (2009) report that erosion and accretion are well balanced for the Solimoes-Japura-Aranapu, this is also the case for the Beni over the 51 year study period, with the observed disparity between erosion and new site creation primarily attributable to the occurrence of cut offs. The occurrence of cut offs constitutes a significant aspect of the geomorphology of the Beni river (Gautier et al., 2007)

Peixoto et al., (2009) estimated changes in AGWB and carbon stocks of varzea forests as a result of channel migration through monitoring changes in the distribution of pioneer and late successional forest stands. Through application of AGWB and carbon storage measurements for these two different types of forest, the authors estimate average annual carbon sequestration of 3185-46,086 Mg year^{-1}, and annual carbon releases of 22,734-64,623 Mg year^{-1} over the 21 year study period. This suggests that annual carbon losses due to erosion are on average 75% higher than carbon accumulation due to new site creation. In comparison, estimates for the Beni indicate that annual carbon losses exceed carbon accumulation by approximately 25%. Therefore the results of Peixoto et al., (2009) suggest that shifting of the Solimoes, Japura and Aranapu within the Mamirua Sustainable Development Reserve are responsible for a significantly greater proportional loss of AGWB and carbon from its adjacent varzea forests each year than the Beni, despite lower rates of channel shifting. The high annual carbon losses calculated by Peixoto et al., (2009) for the Solimoes, Japura and Aranapu rivers therefore appears to be a function of the biomass estimates applied to the lost and newly formed forest stands. Biomass for newly created pioneer forests was 15-217 Mg ha^{-1}, whilst for late successional forests AGWB was estimated between 108-307 Mg ha^{-1} depending upon forest stand age and allometric equation used (Schongart, 2003). Therefore on a basic level the difference between the biomass of the stands lost to erosion and created through deposition is larger than estimates for the Beni. However as these values were applied to the pioneer vegetation and later successional forests in a uniform manner, the overall carbon losses do not take into account variations in AGWB due to stand age. Results presented here show that AGWB and carbon storage exhibit large variations as a function of stand age, thus the failure to account for this variation perhaps contributes to

the large carbon losses calculated by Peixoto et al., (2009). It is thought that the approach utilised here better accounts for the variations in biomass observed within newly created successional stands and forests lost to erosion, and thus presents a more accurate representation of net AGWB change over the study period.

Overall, calculation of the net balance of AGWB and carbon storage as a result of channel migration here can be divided into three primary components; 1- determination of the area of sites lost and new sites created since 1960; 2- estimation of the AGWB and carbon storage of newly created sites; 3- estimation of AGWB and carbon losses through erosion. In order to investigate the efficacy of AGWB and carbon balance estimates presented here and the overall significance of processes of channel shifting for forest dynamics, the three components will be discussed in greater detail below.

Correct determination of the area of sites lost and new sites created is necessary here in order to facilitate accurate calculation of the overall change in AGWB and carbon storage over the study period. As the stand age map is constructed based upon manually digitised channel areas, it is thought that the map intrinsically reflects the spatial variations in rates of lateral channel shifting along the studies reach (Gautier et al., 2007). Lateral migration of the Beni channel is also known to exhibit substantial temporal variations which are related to hydrological characteristics, specifically the number of days of bankfull discharge per year (Gautier et al., 2007). However, the approach utilised here quantifies bulk erosion and deposition between 1960 and 2011, and is unable to resolve finer scale temporal dynamics of channel shifting during the 51 year study period. This is exemplified for the total area of new sites reported within table 7.4, which suggests that the total area of new sites created increases through the course of the study period. The results presented within this table initally appear to be misleading, however it is important to consider that the areas reported reflect the distribution of sites delineated based upon the stand age map, and hence represent the area of stands created within the given decade which remain present in 2011. In light of this, the disparity in the areas of new floodplain created for each decade provide an additional interesting insight, suggesting that a substantial proportion of new sites created during the study period have since been reworked.

The implication of this reworking is that the loss/creation of new sites from year to year may be larger than the average annual rates reported in table 7.4. This is confirmed through comparison with results presented by Gautier et al., (2007) who calculated areas of erosion and deposition on an annual basis from 1996-2001. Results suggested that annual erosion varied from 14.25-24.62 km^2 and deposition varied from 7.4-19.71 km^2, figures substantially higher than those presented here, which were 8.24 km^2 and 7.55 km^2 respectively. Intuitively, this suggests that both AGWB gains and losses associated with channel migration are likely to be higher from year to year in comparison with the annual average rates reported here. This source of uncertainty is difficult to quantify here, although it is hypothesised that additional gains and losses of AGWB and carbon associated with addition erosion and deposition would balance out over the 51 year study period. Therefore whilst the methodology utilised here underestimates average annual erosion/deposition, nevertheless it can be concluded that results presented here provide a sound estimate of the overall balance of AGWB/carbon over the 51 year study period.

Given the extensive collection of inventory data in Beni floodplain successional forest stands along with the stand age map, it is thought that estimates of AGWB and carbon storage for newly created stands are relatively well constrained here. The overall AGWB and carbon assimilation within newly created forest stands is determined by the age distribution of these new forests. Figure 7.15 and tables 7.4-7.5 illustrate that newly formed sites are not equally distributed in terms of age, with a proportionally larger area of these forest stands being characterised by younger ages. The greater proportional contribution of younger forest stands to the overall area of new sites observed here can be attributed to the process of reworking, described above. Specifically, 28 % of forests are between the ages 2-12 years, which are associated with AGWB of less than 30 Mg ha^{-1} and carbon assimilation rates of 2-2.5 Mg $ha^{-1}yr^{-1}$. Approximately 49 % of new forests are characterised by ages 13-37 years, characterised by AGWB storage of 80-130 Mg ha^{-1} and carbon assimilation rates of greater than 4 Mg $ha^{-1}yr^{-1}$. Only 16% of forests are characterised by stand ages of 38-51 years, which store greater than 150 Mg ha^{-1} AGWB and assimilate carbon at a rate of 1.2 Mg $ha^{-1}yr^{-1}$. Based upon the age distribution of newly created sites, it is postulated that continual reworking of newly formed stands through lateral shifting of the Beni maintains substantial

areas of the floodplain within early successional stages, characterised by low AGWB and carbon storage, but high rates of assimilation. This is significant, as in lieu of fluvial disturbance natural forest regeneration within tropical forests usually occurs in the wake of tree falls, which occur over a comparatively limited spatial extent (Chave et al., 1999).

In contrast, estimation of AGWB losses as a result of erosion since 1960 represented perhaps the most uncertain aspect of the calculation of net balance within the study area. Whilst the aerial photographs obtained for 1960 enabled delineation of the river channel for construction of the stand age map, this imagery was not of a sufficient quality to facilitate classification of different forest types, and thus provide an indication of the distribution of biomass within the channel belt at the start of the study period. The two main sources of uncertainty associated with the methodology utilised here are constituted by how well the derived canopy height distribution represents the stands lost to erosion since 1960, and the canopy height-AGWB relationship utilised in order to convert this canopy height distribution into an estimate of biomass. The latter is discussed in more detail in 7.5.3, where it is concluded that the canopy height-AGWB relationship is valid for application within the study area.

Here, the canopy height distribution was derived from the wider channel belt area added to the stand age map, depicted in figure 7.6. As a consequence the distribution of canopy height represents that of ‘old growth’ Beni floodplain forest stands, rather than younger successional forests. The canopy height distribution was taken from older stands, assumed to be typical of the forests located on the outside of meander bends, which are subject to the highest rates of erosion in the study reach (Gautier et al., 2007). However, results here demonstrate that changes in the direction of Beni channel migration results in the reworking of substantial areas of younger successional forest, suggesting that the canopy height distribution extracted from old growth forests might fail to provide an adequate representation of forest stands lost to erosion since 1960. In order to shed light upon this an alternative canopy height distribution, including early successional forests was produced (figure 7.24b). Comparison with the canopy height distribution of old growth forests utilised here, illustrated in figure 7.24a, revealed a relatively small difference in the respective distributions, suggesting that the potential errors accrued here are minimal.

Hence overall the distribution of canopy heights applied here, and the subsequent estimates of lost AGWB and carbon, can be considered an acceptable representation of the forest stands lost since 1960.

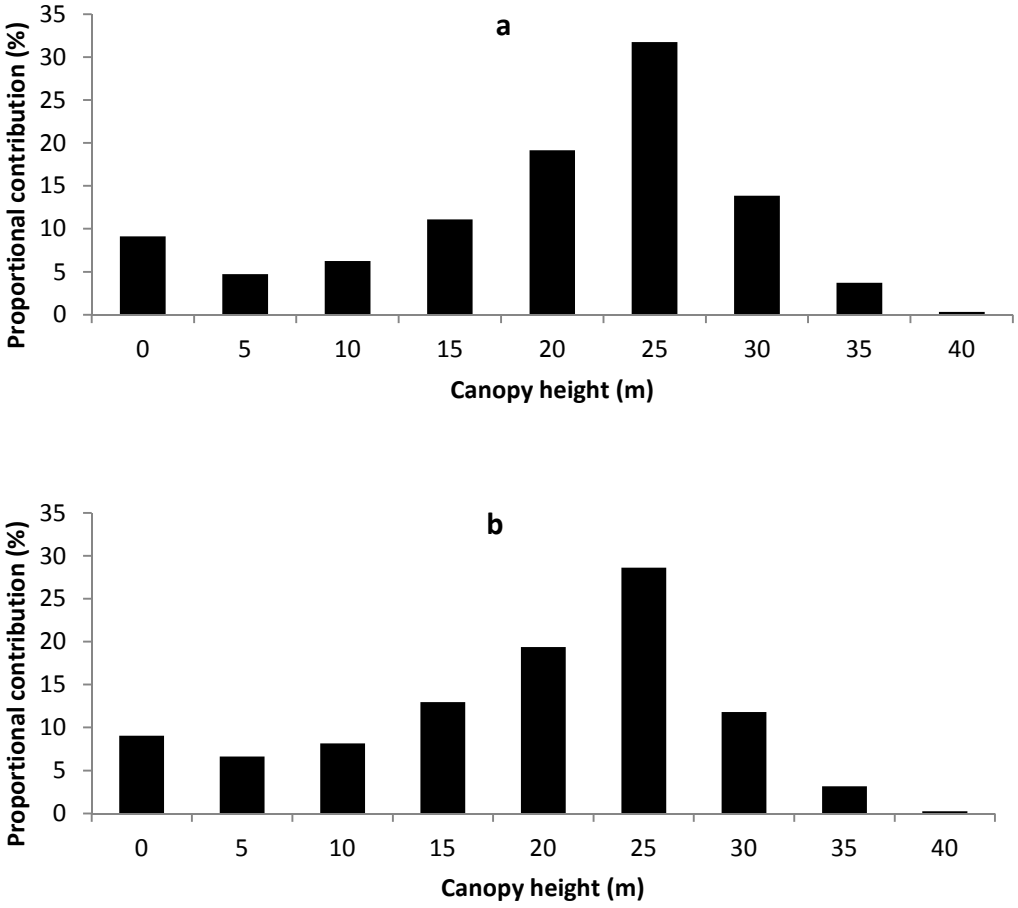

Figure 7.24. Proportional distribution of forests height a) wider channel belt area b) wider channel belt area plus successional forests.

7.5.3 Beni floodplain aboveground wood biomass and carbon storage estimates

Results presented in 7.4.3 show a wide range of estimates for total biomass storage within the Beni floodplain study area. Table 7.8 demonstrates that local estimates of AGWB for the Beni floodplain based upon the global canopy height map (Map 2) exceed those derived based upon the local canopy height map (Map 1) by approximately 35 %. Given that both of these maps were generated based upon the same methodology, the differences between the overall estimates are a function of differences in the respective canopy height maps. The canopy height maps and corresponding bare earth DEMs were discussed at greater length within chapter 5. The differences between these canopy height

maps, elucidated in chapter 5, are reflected in figures 7.17, 7.20 and 7.21, which show that within Map 2 a larger volume of biomass is allocated within forests characterised by higher canopies, in comparison to Map 1.

Extrapolation based upon canopy height represents the best available methodological approach to the generation of a spatially continuous AGWB maps for the Beni floodplain study area. Canopy height is known to be highly correlated with forest biomass (Asner et al., 2010), indeed association of these two variables has been utilised in order to facilitate mapping of AGWB using LiDAR datasets (Drake et al., 2002; Gonzalez et al., 2010; Asner et al., 2012). Regardless of the methodological approach, the proliferation of uncertainty is an important and unavoidable issue when generating AGWB maps through spatial extrapolation of plot scale measurements (Houghton, 2003). Here, a lack of independent spatially distributed biomass data precludes a rigourous validation of the AGWB maps. Nevertheless, potential error sources will be discussed and evaluated in order to assess the relative accuracy of the different AGWB estimates. Uncertainties in AGWB maps presented here can be attributed to two primary error sources; errors in plot level biomass estimates and uncertainties accrued during the process of spatial extrapolation (Malhi et al., 2006). Here, plot level uncertainty is estimated at 23% and is discussed more extensively within 7.5.1, therefore it will not be addressed further here.

The first error source associated with spatial extrapolation is constituted by the AGWB-canopy height relationship established for Beni floodplain forests, illustrated within figure 7.7. The first significant question relates to the applicability of an AGWB-canopy height relationship established for primary successional forests to other stands located across the Beni floodplain. A thorough assessment of the uncertainty associated with the adoption of this approach is precluded here by a lack of further plot level AGWB data. Nevertheless, figure 7.7 demonstrates that AGWB-canopy height measurements obtained from 3 inventory plots established within old floodplain forest stands show a good level of fit with the relationship developed for successional forest stands. An allied issue in the approach utilised here was posed by the application of the AGWB-height relationship beyond the range of forest height and AGWB for which it was established. The relationship was derived based upon plots characterised by canopy heights ranging from 9 m to

28 m (figure 7.7b). Given the canopy height distribution of the Beni floodplain (figure 7.17), some extrapolation of the relationship was unavoidable here. However figure 7.17 and table 7.9 illustrate that the proportion of forests which exceeded the range of heights observed within the inventoried successional forests was relatively small. Indeed for Map 1, approximately 2% of AGWB was allocated within forests characterised by heights of greater than 30 m, whilst this proportion was even lower for Map 2. The uncertainty associated with the AGWB-canopy height relationship was estimated through calculation of the deviation of observed and predicted biomass for the plots illustrated in figure 7.7. This deviation was expressed as a proportion of the observed AGWB and averaged across all plots, producing an error of 12%. The associated value for uncertainty was incorporated into the value for overall uncertainty for Maps 1 and 2.

The second source of error is related to the accuracy of the canopy height maps utilised for extrapolation of AGWB. The local and global canopy height maps applied here were utilised within chapter 5 in order to remove vegetation biases from the SRTM dataset, generating bare earth DEMs. Analysis undertaken in chapter 4 demonstrated that vertical biases in the SRTM dataset were well correlated with field measured canopy height in the Beni floodplain study area. Hence the accuracy of bare earth DEMs, quantitatively assessed with respect to accurate GPS measurements, provide an indication of errors associated with the canopy height maps. Values of RMSE for the local and global canopy height maps were 3.5 m and 3.9 m respectively. The associated AGWB error was subsequently determined through calculation of the variation in biomass errors of the magnitude indicated by canopy height RMSE, across a range of canopy heights. These differences were subsequently averaged in order to produce a single uncertainty value for Map 1 and 2. Based upon this calculation the additional uncertainty of AGWB introduced through error in the canopy height map was estimated at 13 % and 15 % for Map 1 and 2 respectively. Another source of uncertainty was posed by the errors identified in the bare earth DEMs through application in the hydraulic model in chapter 6. The DEMs were refined in order to remove positive biases which remained, primarily in areas close to the Beni river channel. Intuitively, the presence of over elevated areas in the DEM indicates that canopy height was underestimated in these areas. Due to the timeframe of completion of this work, the canopy height maps used here

were those detailed in chapter 5, and did not consider the results of the error analysis in chapter 6. However based upon the results presented in section 6.7, the majority of errors in the DEMs (and hence canopy height maps) were within the range of RMSE (< 3.5 m) used to calculate uncertainty here. Therefore it can reasonably be assumed that the AGWB estimates calculated here represent a slight underestimation of Beni floodplain aboveground wood biomass, although this underestimation would be well within the range of uncertainty calculated here.

In the absence of further spatially distributed plot level biomass estimates, the accurate quantification of other sources of uncertainty, such as errors associated with the representation of the spatial variability of AGWB, could not be quantitatively assessed here. However, the contributions of these error sources were not thought to be significant here. Overall, taking into account potential errors associated with the AGWB-canopy height regression and the canopy height map, in addition to plot level error estimated in 7.4.1, Maps 1 and 2 are characterised by an uncertainty of 48 % and 50 % respectively. Based upon the quality of the canopy height maps utilised here, which were quantitatively validated in chapter 5, it can be concluded that Map 1 offers a better representation of AGWB storage upon the Beni floodplain than Map 2.

In order to contextualise the AGWB estimations for the Beni floodplain it is necessary to compare the results produced here with those obtained for other Amazonian floodplain forests. For Map 1 and 2 the average AGWB of Beni floodplain forests is 72.69 Mg ha^{-1} and 94.81 Mg ha^{-1}. Whilst the provision of AGWB estimates for varzea forests in the literature is poorer than for terra firme forests, it is nevertheless possible to find a number of examples for comparison. Accordingly, Saatchi et al., (2007) found an average AGWB of 161.3 for floodplain forests across Amazonia. For gallery forests in Brazil AGWB was found to range between 127-144 Mg ha-1 (De Paula et al., 1990; Imanaencinas et al., 1995). Baker et al., (2004) reported average AGWB of 164-203 Mg ha-1 for flooded forests within the Noel Kempff national park in Bolivia. Therefore on a basic level the average AGWB values reported for the Beni in table 7.8 can be considered relatively low in comparison to AGWB estimates for other floodplain forest stands.

It is hypothesised that the disparity in average AGWB found for the Beni floodplain and values reported for varzea forest stands in the literature can be attributed to a disparity in the scale of estimates. Values reported from the literature represent the AGWB of inventory plots and are thus discrete in space, and although details of stand characteristics do not accompany the estimates it is likely that inventoried plots were located within old growth floodplain forest stands, or stands characterised by late successional stages. Although AGWB for Beni floodplain forest plots within late successional stages were roughly equivalent to those reported within the literature (> 150 Mg ha^{-1}), the average biomass reported here corresponds to the spatial average for the whole Beni floodplain. Accordingly, the canopy height map derived from SRTM in chapter 5 illustrates that Beni floodplain forest stands are characterised by a substantial level of variation in canopy height. Whilst heights typically reach > 30 m within stands located in close proximity to the Beni channel and floodplain water courses, forest height decreases substantially with greater distance from river channels. Thus a large proportion of Beni floodplain forests are characterised by canopy heights of 10 - 20 m.

Wittmann et al., (2004) demonstrated that the successional stage of varzea forest stands is controlled by flood inundation characteristics, whilst results from this study (figure 7.13) also showed a clear association between relative elevation, a proxy for flood magnitude, and characteristics of successional forest stands, including canopy height. Accordingly this suggests that the canopy height distribution observed across the Beni floodplain reflects the presence of forest stands characterised by a range of successional stages, as a result of flood inundation. Intuitively, these successional forests are characterised by relatively low biomass stocks, thus contributing to the lower overall average AGWB observed for the floodplain study area. This assertion is further supported by visual analysis of the spatial patterns of flood inundation derived from hydraulic modelling undertaken in chapter 6. Results from the flood inundation model demonstrate that raised levees adjacent to river channels are subject to relatively short periods of inundation to a low depth, whilst the longest duration and highest depth of flooding occurs in regions located a greater distance away from river channels. This broadly reflects the distribution of biomass observed upon the Rio Beni floodplain, with the highest biomass density observed within areas subject to the lowest magnitude of flood

inundation. The relationship between flood inundation and the spatial distribution of AGWB is explored further in section 8.1.

Derivation of AGWB estimates for the Beni floodplain study area from an Amazonian biomass map produced by Saatchi et al., (2007) facilitated further contextualisation of the results produced here, whilst also allowing comparison of AGWB estimates derived at different spatial scales. From results illustrated in figure 7.19 and table 7.10 it is clear that the disparity in estimates can be attributed to the fact that much greater volumes of biomass, are allocated within forests characterised by higher AGWB densities (>150 Mg ha^{-1}) in the Amazonian map. Although the AGWB estimates derived from the Amazonian biomass map could not be quantitatively validated, the results presented here, particularly the distribution of canopy height across the floodplain, suggest that Map 3 substantially overestimates biomass storage for the Beni floodplain.

In the specific case of the Amazonian map utilised here (Saatchi et al., 2007), the poor estimates of AGWB for the Beni floodplain study area can be attributed to several sources of error. The first source of error was propagated from the Amazonian land cover map (Saatchi et al., 2005), utilised within the biomass classification methodology in order to separate the basin into major land cover types including inundated and terra firme forests. Within the land cover map inundated forests were distinguished based upon wet and dry season JERS-1 mosaics produced as part of the Global Rainforest Mapping Project (Rosenqvist et al., 2000). Significantly, the high water period for the Beni floodplain from December to April is not synchronous with the wet season JERS-1 mosaics, which were timed to coincide with high water in the central Amazon in May-June. As a result, Beni floodplain forests were delineated as Terra Firme forests rather than varzea within this classification. This error is subsequently reflected in the biomass distribution observed for the Beni floodplain (table 7.10), which contained high biomass densities characteristic of a Terra Firme forest rather than a typical varzea forest. Whilst the incorrect classification of Beni floodplain forests represents the preeminent source of error in the Amazonian biomass map, it is also clear that the spatial distribution of AGWB upon the floodplain, illustrated in figure 7.22, does not reflect local variations of biomass which would be expected within the study area. This demonstrates that the remote sensing variables utilised in the extrapolation of AGWB such as MODIS

NDVI/LAI, Radar backscatter (JERS-1) and coarse scale elevation (SRTM) (Saatchi et al., 2007), do not reflect the environmental gradients which control biomass distribution within the Beni floodplain forests.

It is important to acknowledge that spatial extrapolation of AGWB across large spatial scales constitutes a difficult research problem and the accurate estimation of local biomass variations perhaps constitutes an unreasonable expectation given issues of scale and current data provision within the Amazon. Therefore rather than providing a general critique of the Amazonian biomass map produced by Saatchi et al., (2007), this discussion seeks to highlight the general issues associated with accurate prediction of AGWB within Amazonian floodplain forests. The results presented here strongly imply that current methods utilised in order to extrapolate forest biomass across the Amazon basin are not able to adequately capture the lower biomass densities observed within the Beni floodplain. Specifically, it is postulated here that characteristics of Beni floodplain forests (including AGWB storage) are controlled predominantly by local hydrological factors, namely flood inundation, which maintain large areas of forest within stages of primary and secondary succession (Wittmann et al., 2002; 2004). Thus the coarse scale variables, that are necessarily utilised in order to extrapolate AGWB over the Amazon basin, do not reflect the local scale processes preponderant in controlling the characteristics of floodplain forests. Given current levels of data provision within Amazonia, the broad scale environmental variables utilised by Saatchi et al., (2007) represent the best means to extrapolate AGWB at the basin scale at present. Therefore the deficiencies highlighted for Map 3 are likely to be reflected in other attempts to estimate biomass for the Amazon basin through extrapolation of plot scale AGWB measurements.

7.6 Investigation of the influence of flood inundation upon the distribution of forest biomass on the Beni floodplain

The overall research aim of this thesis, stated at the outset, was to quantify the dynamics of flood inundation and aboveground wood biomass storage upon the Beni floodplain and to explore the interactions between fluvial processes and varzea forest stands within the study area. This aim has been predominantly addressed in chapters 6 and 7. In chapter 6, a 1D-2D hydraulic model code was applied to the Beni floodplain, and quantitative validation with respect to

remotely sensed inundation metrics demonstrated that the model was able to predict flooding with a good degree of accuracy. In chapter 7, the spatial distribution of aboveground biomass upon the Beni floodplain was quantified through extrapolation of plot level AGWB estimates according to a floodplain canopy height map. In addition, the influence which lateral shifting of the Beni channel exerted upon aboveground biomass storage within varzea forest stands since 1960 was also quantified. Whilst a simple visual analysis of modelled inundation characteristics and the spatial distribution of AGWB upon the floodplain appeared to suggest a link between these two quantities, this relationship remains unquantified thus far in this thesis. Therefore in the first part of the overall discussion here, modelled inundation characteristics are intersected with spatial maps of aboveground wood biomass distribution for the Beni floodplain study area.

It is widely acknowledged that both the depth and duration of inundation exert an influence upon the successional stage and structure of varzea forests (Wittmann et al., 2002; Parolin, 2009). Significantly, predictions of flood inundation by the hydraulic model were validated for a single high water and low water image. Therefore whilst this demonstrated the ability of the model to accurately predict high and low water inundation extent, the dynamic performance of the model is less clear. Intuitively, predictions of flood duration are more dependent upon the dynamic performance of the model, and were thus associated with a higher level of uncertainty in comparison to flood depth at high water. Accordingly, depth of inundation at high water was chosen as the variable for comparison with AGWB distribution in this analysis. Further, Wittmann et al., (2002) divided varzea stands into high and low varzea based upon their position along the flood gradient. The flood gradient reflected both duration and magnitude of flooding (Wittmann et al., 2004), implying that the two are strongly linked for Amazonian floodplains. In order to facilitate quantitative assessment of the relationship between inundation and biomass, flood depths at high water (09/03/2011) were extracted from model simulations undertaken using the FAV100, INT100 and GCH100 DEMs in combination with medium roughness and medium channel bed elevation. Biomass map 1, generated in chapter 7, was utilised here as it was thought that this map most accurately reflected spatial distributions of biomass upon the Beni floodplain. Maps were aggregated using ArcGIS and compared at a spatial resolution of 1

km (this resolution was found to produce optimal results during initial investigation of the data).

Figure 8.1 presents a series of scatter plots showing the association between modelled inundation depth at high water, extracted from simulations using the different floodplain DEMs, and aboveground wood biomass upon the Beni floodplain, for each 1 km resolution forested pixel within the model domain. Each plot demonstrates a slight negative trend, indicating a broad decrease in biomass density with increasing inundation depth. However the point distribution suggests that at the scale of the whole floodplain, noise dominates any relationship between inundation depth and AGWB. This is demonstrated by the low r^2 values displayed in the plots.

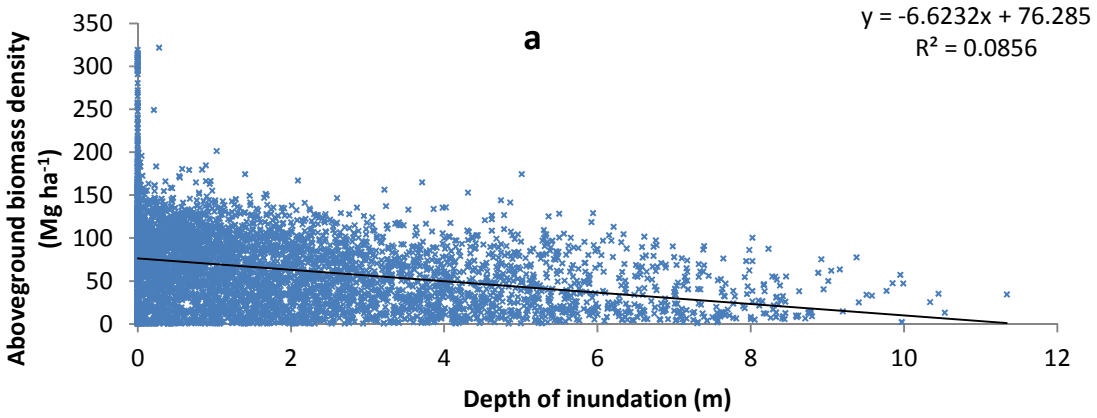

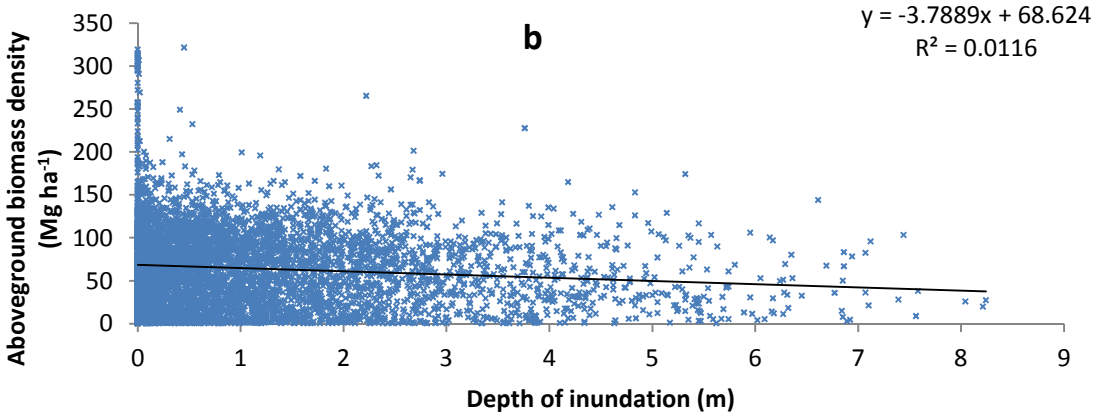

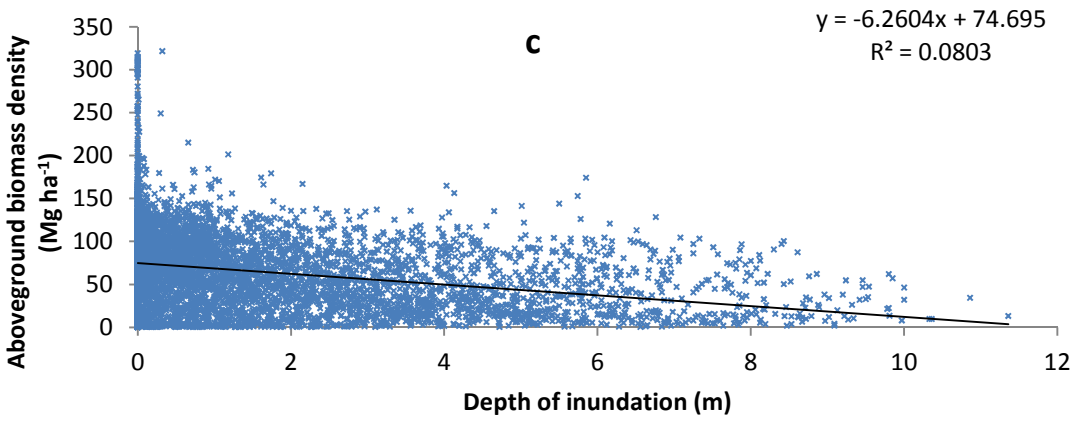

Figure 7.25. Scatter plots showing the relationship between AGWB density within Beni floodplain varzea forest stands (1 km spatial resolution) and depth of inundation at high water for simulations using the a) FAV100 DEM b) INT100 DEM c) GCH DEM (1 km spatial resolution)

Table 7.11 Summary of aboveground wood biomass within high and low varzea forest stands upon the Beni floodplain. Forests are classified according to flood inundation predicted by the hydraulic model. High varzea forests are associated with a modelled inundation depth of > 3 m at high water, low varzea forests are associated with a modelled inundation depth of < 3 m at high water. P-value indicates the statistical significance of mean biomass values for high/low varzea.

	Bare earth DEM used for simulation		
	FAV100	INT100	GCH100
Average aboveground wood biomass for low varzea stands (Mg ha^{-1})	44.13	52.38	43.59
Average aboveground wood biomass for high varzea stands (Mg ha^{-1})	70.12	65.57	69.83
P-value	<0.001	<0.001	<0.001

Given the general negative trend observed within figure 8.1, additional analysis was undertaken. Accordingly, Beni floodplain forests were separated through application of the classification scheme proposed by Wittmann et al., (2002), (in which low varzea forests are characterised by average inundation depth exceeding 3 m, whilst high varzea forests are associated with an annual flood depth of below 3 m) to modelled inundation depths at high water. Mean AGWB density for low and high varzea, classified based upon simulations using each of the floodplain DEMs, are included in table 8.1. Based upon modelled inundation using each bare earth DEM, average AGWB was observed to be higher within high varzea stands. The difference in average AGWB density varied for each simulation, with the GCH and FAV DEMs producing a larger disparity than INT DEM. However, in each instance the P-value was less than

0.001, indicating a significant difference in average biomass between high and low varzea stands upon the Beni floodplain.

With further evidence of some level of association between flood inundation characteristics and AGWB within the study area, the data presented within figure 8.1 were binned according to 1 m intervals of flood inundation depth, and associated results are presented in figure 8.2. Binning of the data resulted in a substantial improvement in the relationship between modelled inundation depth and AGWB density in Beni floodplain forests. For inundation depth extracted from the FAV DEM simulation, a strong negative relationship was observed with AGWB, indicated by an r^2 value exceeding 0.9. Whilst the relationship between AGWB and inundation depth was weaker for the INT DEM and GCH DEM simulations, these plots nevertheless demonstrate a clear decline in biomass with increasing inundation depth.

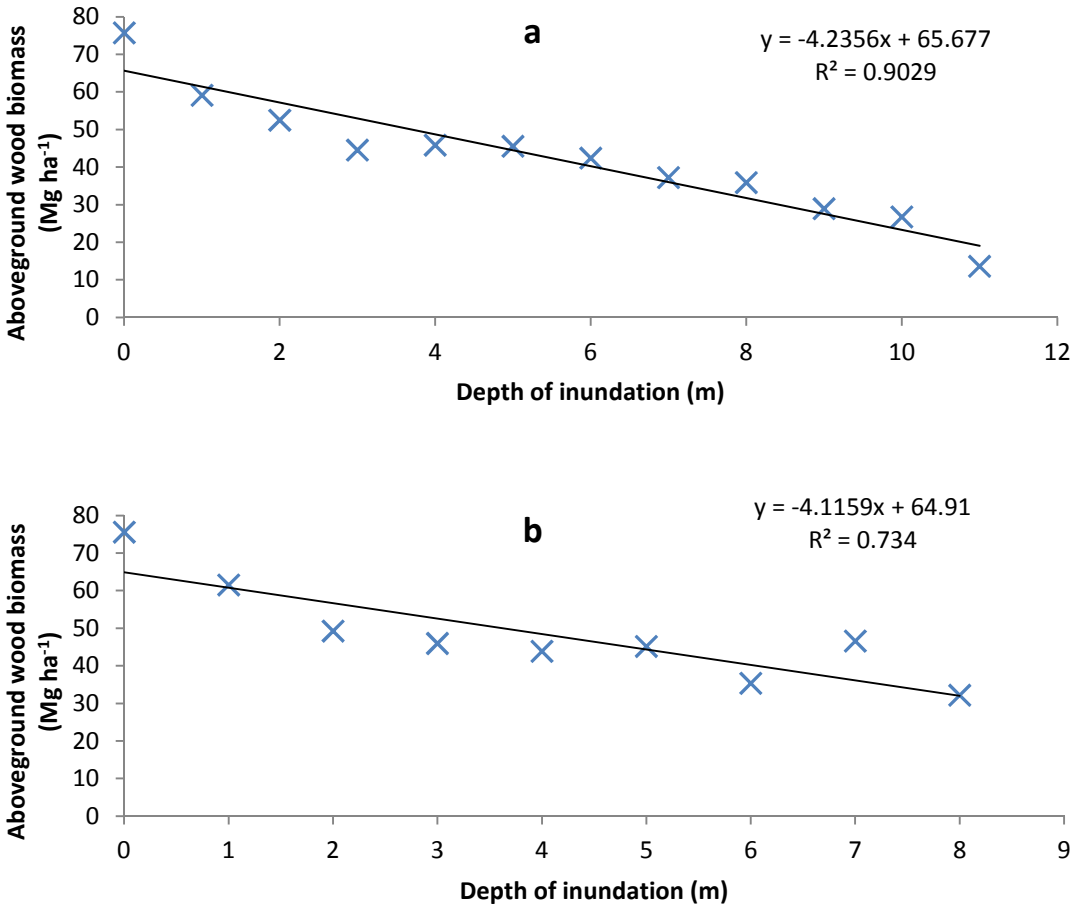

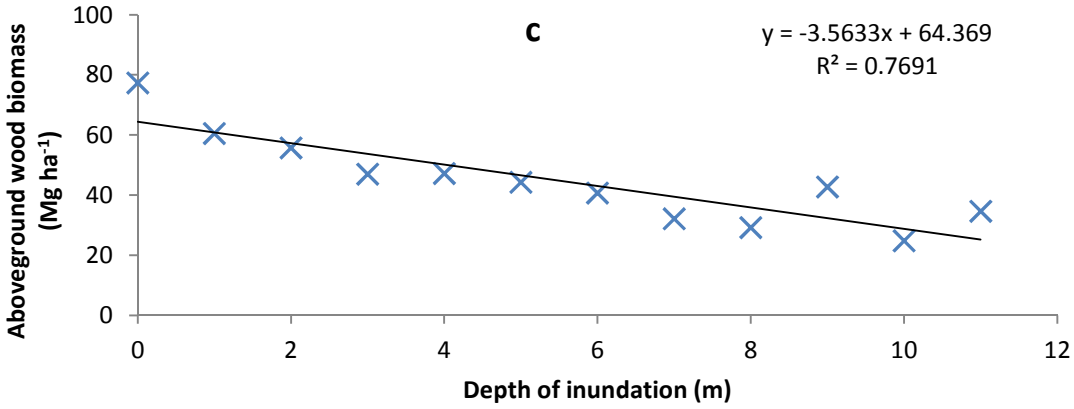

Figure 7.26. Scatter plots showing the relationship between AGWB density within Beni floodplain varzea forest stands (1 km spatial resolution) and depth of inundation at high water for simulations using the a) FAV100 DEM b) INT100 DEM c) GCH DEM (1 km spatial resolution). In these plots data is binned in 1 m inundation depth intervals.

Results presented here demonstrate a clear trend of decreasing aboveground biomass density with increasing inundation depths for varzea forest stands upon the Beni floodplain. It is well known that flood inundation imposes a limit upon the growth of varzea forests (Piedade et al., 2006), controlling successional stage and stand characteristics (Wittmann et al., 2002; 2004). However, the aforementioned studies focussed primarily upon floristic diversity of varzea forests, evaluating the effects of flood inundation at the plot scale through establishing simple relationships between water marks on trees and stage measurements at river gauging stations. Results presented within chapter 7 extended the scope of previous studies in order to consider AGWB in addition to floristic characteristics, demonstrating that biomass increases along the successional forest sequence as relative elevation (a proxy for duration and depth of flood inundation) decreased. The relationship observed here between inundation depth and AGWB is particularly significant, constituting the first investigation of the interaction between fluvial flood inundation and varzea biomass at the scale of a whole floodplain using spatially distributed datasets. Specifically, the results strongly suggest that processes of flood inundation are responsible for maintaining large areas of Beni floodplain varzea forests within early successional stages, characterised by low biomass densities.

The high scatter and low r^2 values, observed in figure 8.1, illustrated that the relationship between flood inundation and AGWB was characterised by a substantial level of noise at the level of individual 1 km resolution pixels. Indeed

a significant relationship was only realised after binning of the data according to flood depth. The noise observed within figure 8.1 was not hugely surprising, particularly given the uncertainties associated with the biomass map and predictions of flood inundation. Uncertainty in the biomass map was estimated at 48 %, and whilst the fit of 0.65-0.70 represents a good level of performance for a hydraulic inundation model, such values nevertheless indicate the occurrence of considerable errors in predicted flood characteristics, particularly given the vertical accuracy of the bare earth DEMs indicated within formal assessment in chapter 5 (>3 m RMSE). It is also probable that a substantial level of noise is propagated through the influence that other environmental variables exert upon biomass density. Specifically, based upon field observations it is hypothesised that water availability, driven by floodplain hydrology, was important for controlling the spatial distribution and characteristics of forest stands upon the Beni floodplain. Numerous other variables have also been shown to exert an important control upon forest characteristics, for example soil types and geology (Malhi et al., 2004). Hence, it is clear that the provision of more accurate predictions of flood inundation and AGWB are required in order to better quantify the relationship established here between flood inundation characteristics and the spatial distribution of AGWB in varzea forests.

A final issue to address is the potential for circularity in the analysis undertaken here. The canopy height map utilised in order to extrapolate plot level estimates of biomass in chapter 7 was derived from the SRTM during generation of the INT DEM in chapter 5. This raises some concerns, particularly given that the INT DEM was utilised in order to provide topographical forcing within one of the hydraulic model simulations from which flood depth information is derived here. However these concerns are allayed through several important considerations. Most significantly, AGWB is compared to flood depths derived from simulations undertaken using the three different floodplain bare earth DEMs. The canopy height maps utilised within the generation of these DEMs were derived from different data sources, hence the representation of ground topography driving patterns of inundation within the model is essentially independent for each DEM for the forested areas considered within this analysis. Furthermore, inundation depth predicted in the simulation undertaken using the INT DEM showed the

weakest relationship with ABWG. Therefore based upon these considerations circularity was not deemed to be a significant problem here.

7.7 Conclusions

Plot scale results demonstrate that Beni floodplain forests show a clear sequence of successional development with increasing stand age. This corresponds well with previous accounts of primary forest succession within other parts of Amazonia (Worbes et al., 1992). The results also demonstrate a strong association between forest structural characteristics and relative stand elevation above water level. Therefore it can be concluded that flood inundation exerts a significant control upon the successional stage of Beni floodplain forests (Wittmann et al., 2002). In addition, the observed covariance between stand age and relative elevation above water level subsequently suggests that the development of young forest stands upon the Beni floodplain occurs through the process of allogenic succession (Wittmann et al., 2004).

Work undertaken for this chapter presented the first attempt to document AGWB storage and carbon assimilation for successional varzea forest stands. Biomass and carbon storage showed a clear development with forest age, indeed AGWB increased tenfold in less than 50 years. As for other forest characteristics, AGWB is positively associated with relative stand elevation (and hence flood inundation). Carbon assimilation rates peaked within successional forests between ages of 13-37 years, and were four times greater than average rates published for varzea stands and ten times greater than for Terra Firme stands (Baker et al., 2004). Curves of AGWB and carbon assimilation for Beni floodplain successional forests suggest that AGWB of successional stands may approach levels similar to old growth floodplain forest stands within 50 years of initial deposition and colonisation. Within tierra forests it has been estimated that this process typically takes 100 years (Guariguata and Ostertag, 2001). Hence it can be concluded that successional varzea forests are associated with lower AGWB storage, but greater carbon assimilation in comparison to old growth varzea and Terra Firme stands.

Results presented within 7.4.2 demonstrate that migration of the Beni channel is associated with an overall net loss of AGWB and storage within floodplain forests. Broadly this finding is in agreement with the study of Peixoto et al.,

(2009) who found that shifting of the Solimoes, Japura and Aranapu channels was responsible for an overall loss of AGWB and carbon within varzea forests of the Mamirua Sustainable Development Reserve within the Brazilian Amazon. Although results presented here suggest that the overall net loss is lower than calculated within the aforementioned study. The net AGWB loss of 785,072 Mg observed over the 51 year study period are modest in the context of the overall floodplain AGWB storage (44-60 million Mg). However processes of channel shifting, particularly erosion of old growth forest and the reworking of large areas of newly formed stands, attain additional significance as they are responsible for maintaining a substantial area of Beni floodplain forests within early successional stages of development. This is important, as young successional forests are associated with low AGWB stocks and high carbon assimilation rates. Hence the results presented here suggest that the turnover of floodplain forest stands as a result of channel shifting may sequester relatively large volumes of carbon within aboveground wood biomass. However, the fate of AGWB and carbon lost through erosion of forest stands within the reach is key to determining whether floodplain forests are ultimately able to act as effective carbon sinks.

Results presented in 7.4.3 demonstrate a large variation in predictions of AGWB storage within varzea forests across the Rio Beni floodplain. The lowest estimate of floodplain AGWB (44 million Mg) was generated through extrapolation of local plot level biomass measurements using a local canopy height map derived from SRTM. The same plot level data extrapolated with respect to a global canopy height map (Simard et al., 2011) produced an estimate of ~59 million Mg. The highest estimates of AGWB stock (109 Million Mg) were extracted from a basin wide map (Saatchi et al., 2007). In lieu of an extensive validation dataset, it was not possible to quantitatively assess the accuracy of the different AGWB storage maps, however it was nevertheless possible to draw broad conclusions regarding the accuracy of these estimates based upon examination of the different methodologies, comparison with limited plot level data, field observations and information drawn from the literature.

It was concluded that the Amazonian biomass map substantially overestimated biomass of the Beni floodplain due to misclassification of forest type. In addition the spatial distribution of biomass derived from the Amazon map did not appear

to reflect local scale variables which are responsible for determining AGWB within the Beni floodplain. It is thought that estimates of AGWB obtained through extrapolation of local estimates of biomass based upon the SRTM derived canopy height map provided a more accurate representation of biomass. Significantly, the distribution of canopy height within the study area suggests that large areas of Beni floodplain forest are maintained in successional stages due to the effects of flood inundation (Wittmann et al., 2002), resulting in average biomass stocks which are lower than those previously reported for floodplain forests in Amazonia (De Paula et al., 1990; Baker et al., 2004; Saatchi et al., 2007).

Overall, based upon the intersection of modelled inundation depth and maps of aboveground wood biomass generated within this thesis, it can be concluded that flood inundation exerts a first order influence upon the biomass density of varzea forests located upon the Beni floodplain. Further, the results presented here serve as an example of the new and unique insight into the interaction between environmental processes which can be achieved through integration of field work, remote sensing techniques and numerical modelling.

Chapter Eight

Discussion

8. Discussion

8.1 The influence of fluvial processes upon aboveground wood biomass stocks within Amazonian varzea forests

Results presented within chapter seven provided new and unique insight into the influence which fluvial processes exert upon floodplain forest ecology, with specific emphasis placed upon aboveground wood biomass storage. Biomass density maps generated for the study area demonstrate that Beni floodplain forests are associated with substantially lower AGWB storage than typical Amazonian terra firme forests, results which support the consensus developed through past studies (Baker et al., 2004). Indeed according to results presented in chapter seven, the average biomass density of Beni floodplain forests is approximately compared to terra firme stands (Phillips et al., 1998). Intuitively, this disparity in biomass stocks can be attributed predominantly to fluvial disturbances, which do not affect terra firme forests.

On a basic level, results presented in 7.4.1 demonstrate that both channel migration and flood inundation modulate varzea forest biomass stocks on the Beni floodplain. Indeed the aboveground wood biomass density of successional forests growing upon fresh alluvial deposits, in place of mature stands lost to fluvial erosion, is shown to reflect their elevation and hence susceptibility to flood inundation. Nevertheless, it is clear that the disturbance regimes imposed by flooding and channel shifting are substantially different. Channel shifting exerts a severe impact upon varzea forest ecology, resulting in the destruction and recreation of entire stands within a single high water event. However, despite the fact that the Beni river is characterised by very high rates of lateral channel shifting, results presented in 7.4.2 illustrate that the areas directly affected are relatively localised when considered in the context of the whole floodplain area. In contrast, whilst the direct disturbance induced by flooding is less severe than for channel migration, inundation impacts a much larger area of the floodplain, as demonstrated in chapter 6.

A synthesis of results obtained within chapters 6 and 7 provides an indication of the relative importance of both flood inundation and channel shifting for floodplain ecology and aboveground wood biomass stocks. Comparison of biomass maps for the Beni floodplain (figures 7.20-7.22) provides a useful indication of the overall impact of fluvial processes upon floodplain forest

AGWB. The disparity in AGWB storage between the Amazonian biomass map (109,038,517 Mg), which fails to account for local fluvial influences, and the locally derived biomass map (44,209,595 Mg) provides an approximation of the net difference in AGWB attributable to fluvial dirsturbances for the Beni floodplain (> 60,000,000 Mg) in comparison to a typical terra firme forest located within this part of the Amazon basin. Over a period of >50 years channel migration was responsible for the erosion of a total of 420 km2 of floodplain, resulting in a net loss of 785,072 Mg of AGWB. As a result, it appears that processes of channel migration account for less than 2% of the total biomass loss associated with fluvial processes. Hydraulic modelling undertaken within Chapter 6 demonstrated that an area of up to 10,000 km^2 of the Beni floodplain may be inundated within large floods. Hence it is hypothesised that flood inundation, which maintains large swathes of the floodplain forest within early successional stages, is a much more significant contributor to the disparity in AGWB between Beni floodplain varzea and terra firme forests.

Due to both logistical and methodological limitations it was not possible to quantitatively assess the impact which sedimentation exerted upon the ecology and aboveground wood biomass stocks of Beni floodplain forests. Nevertheless, previous research and field observations suggest that deposition of sediment overbank is likely to impact upon the ecology and specifically, the aboveground wood biomass, of Amazonian floodplain forests. Results presented in 7.4.1 indirectly demonstrated that overbank sedimentation plays a central role in controlling stand elevation, and subsequently flood inundation characteristics and forest structure. In addition, field observations suggested that deposition of large volumes of sediment upon the Beni floodplain was responsible for the mortality of significant areas of varzea forest. Furthermore, Aragao et al., (2008) demonstrated that phosphorus constitutes a key limiting factor in the growth of Amazonian forests. Hence overbank deposition of mineral rich sediments which characterise white water rivers, is potentially responsible for the supply of nutrients to the varzea forests, leading to enhanced growth rates and AGWB densities.

Further investigation of sedimentation in this thesis was precluded in the first instance by a limitation placed upon the capacity to derive sedimentation rates

observed at the different sites across the Beni floodplain through Pb^{210} geochronology (Aalto et al., 1999). Although optical remote sensing has been utilised in order to measure the concentration of sediment within overbank flood waters, thus providing potential insights into patterns of deposition, both forest and cloud cover obscure flood waters, limiting the applicability of this methodology to the Beni floodplain. Hence further assessment of the influence that overbank sedimentation exerts upon floodplain forest ecology and aboveground wood biomass stocks is recommended, as and when the capacity to accurately delineate spatial patterns of sediment deposition improves. It is important to consider that sedimentation is neither as spatially extensive as flooding (Aalto et al., 2003), nor as physically destructive as channel shifting (Peixoto et al., 2009). Therefore it is hypothesised that the influence which overbank sedimentation exerts upon floodplain forest ecology is likely to be of a lower magnitude than flood inundation and channel shifting.

8.2 Limitations of flood inundation modelling in the Amazon basin

This thesis documents, in its entirety, the process required in order to undertake a hydraulic flood inundation modelling study for a previously unstudied river reach within Amazonia. Application of a coupled 1D-2D hydraulic model code in chapter 6, with topographical forcing provided from a refined bare earth DEM derived from SRTM, predicted inundation upon the Beni floodplain with a good level of accuracy with respect to remotely sensed inundation extent and water surface elevation. Hence the work undertaken here represents the latest in only a handful of hydraulic modelling applications within the Amazon basin which are able to resolve complex floodplain flow dynamics at scales of less than 500 m (Wilson et al., 2007; Trigg et al., 2009; Baugh et al., 2013). Therefore whilst the viability of modelling inundation for Amazon rivers and floodplains has been demonstrated, it is important to consider why hydraulic modelling studies are not more prevalent within this region, particularly given the significance of the Amazon river system within the global hydrological cycle (Richey et al., 1989).

In light of current data provision, the successful implementation of flood inundation modelling for a given study area located in the Amazon basin currently comprises four distinct stages; land cover classification; ground truthing of the SRTM dataset; generation of a floodplain canopy height map and correction of the SRTM dataset; model application and validation with respect to

remote sensing observations. Importantly, the first three stages of this process are associated with the production of a bare earth DEM, which is required in order to provide topographical forcing within hydraulic model application. Other studies undertaken within the central Amazon (Wilson et al., 2007; Baugh et al., 2013) have utilised existing datasets in order to facilitate inundation modelling; for example land cover maps (Hess et al., 2003) and validation datasets (Hess et al., 2003; Alsdorf et al., 2010). However such datasets are not widely available across the Amazon basin and thus the majority of potential new hydraulic model applications would be required to undertake the four aforementioned stages independently. The subsequent discussion details the first three stages of this process, arguing that current provision of bare earth topographic data within Amazonia is prohibitive of more widespread application of hydraulic flood models and is consequently limiting the understanding of complex inundation dynamics of floodplains within this region.

Within this thesis, land cover of the Beni floodplain study area was classified through the application of supervised classification techniques, with the best performance offered by a combined Linear Spectral Unmixing- Decision Tree Classification approach (Lu et al., 2003a). This approach required a considerable level of 'expert' user input, both in terms of interpreting land cover within the study area based upon field observations, iterative selection of sufficiently pure end-members, and implementation of the classification algorithms (Lillesand et al., 2008). Indeed accurate classification of the highly heterogeneous land cover observed within Amazonian floodplains is a problematic task in itself (Lu et al., 2004a), and is predicated upon extensive in situ field observations which are required in order to establish samples for training of the classifier and for validation of the resulting map (Kawakubo et al., 2013). An alternative to the process of manual classification detailed above is presented by the numerous global maps of land cover such as MODIS MCD12Q1 (https://lpdaac.usgs.gov/products/modis_products_table/mcd12q1) and Globcover (http://due.esrin.esa.int/globcover/), which are available for utilisation within the first stage of bare earth DEM generation. Investigation of these global land cover datasets was not reported here, however this was undertaken and revealed that these maps were not of a sufficient quality for use in the correction of the SRTM dataset at the scale of the Beni floodplain study area. Specifically, global land cover maps were unable to effectively and

accurately separate forest and non forest land cover classes, rendering them unsuitable for delineating forested areas requiring correction within the SRTM dataset. Hence within this PhD research project, the problems associated with global land cover maps necessitated the production of a local land cover map for the Beni floodplain. This is likely to be the case for other potential sites for application of hydraulic models across the Amazon basin.

In chapter 4, ground truthing of the SRTM dataset was undertaken with respect to an in situ DGPS survey of floodplain elevation, revealing that the SRTM is characterised by a vertical offset of greater than 6 m for the Beni floodplain. Systematic vertical offsets of up to 5 m are common within the SRTM (Kellndorfer et al., 2004; Weydahl et al., 2007), and must be corrected prior to inundation modelling, in order to ensure comparability of results with other datasets. At present, no highly accurate (ie better than ± 1 m) ground elevation datasets are widely available within Amazonia (Hall et al., 2011), requiring that ground control points, which are necessary in order to facilitate direct quantitative assessment of the accuracy of the SRTM dataset, are collected through in situ surveys. Whilst the spaceborne LiDAR system GLAS (Abshire et al., 2005) offers some potential for measuring ground elevation remotely with a high level of accuracy, these data are available along paths with a relatively wide spacing (figure 5.1), and therefore have a spatial distribution that is not ideal for the purposes of validation of the SRTM. In addition, whilst ground elevation can be retrieved relatively easily from GLAS within open areas from the GLA14 Global Land Surface Altimetry Data product, investigation of this dataset revealed that elevation reported in forested areas did not correspond to the ground surface, but included some measurement of vegetation. Hence, complex processing of GLAS waveforms is required in order to extract bare earth elevation within forested areas of potential floodplain study sites.

The third stage of the process required in order to facilitate inundation modelling within a new Amazonian study area is the generation of a canopy height map, and the subsequent application of this map in order to correct vertical biases within the SRTM dataset. Global maps of canopy height are available (Lefsky et al., 2010; Simard et al., 2011) and can be applied relatively easily in order to correct SRTM vertical bias. Indeed Baugh et al., (2013) proposed the use of the global canopy height map of Simard et al., (2011) in order to facilitate the

systematic correction of the SRTM dataset for floodplains within Amazonia and other tropical regions. Application of this methodology for the Beni floodplain study area within this thesis, demonstrated that the global canopy height map produced a more accurate bare earth DEM than was generated through a spatially uniform canopy height map derived from field measurements (Wilson et al., 2007). However, substantial variations in forest height within the global map typically occurred over scales larger than the Beni floodplain study area. As a result, the global map of Simard et al., (2011) failed to capture small scale variations in canopy height observed upon the Beni floodplain.

Whilst it is possible to adjust the global canopy height map in order to best represent average canopy height upon the floodplain (Baugh et al., 2013), forest height remains over or under predicted within substantial areas of the floodplain. Within the Beni floodplain study area, an increase in the height of forest stands located within the channel belt (not accounted for within the global map) resulted in over elevation of proximal areas of the floodplain DEM, leading to poor predictions of high water inundation by the hydraulic model. In addition, the presence of erroneous topographical depressions in the floodplain as a result of over prediction of canopy height, resulted in incomplete dewatering of the floodplain. A novel method presented here removed vegetation related bias from the SRTM based upon the production of a first order estimated DEM, through interpolation of bare earth points extracted from the SRTM. The application of this approach produced a better bare earth DEM with respect to quantitative and qualitative assessment, this was attributed to the fact that the canopy height map produced through this method reflected local scale variations of forest height within the Beni floodplain. Use of this DEM within the hydraulic model produced the most accurate simulations with respect to remotely inundation extent and water surface elevation. However it is important to note that this method was not easily replicable, requiring incorporation of a multitude of remotely sensed and field datasets and extensive ‘expert’ user input.

This thesis demonstrates the feasibility of accurate modelling of flood inundation for Amazonian floodplains, however the breadth of work required in order to produce a bare earth DEM required to facilitate this modelling also serves to highlight why the number of such studies is disproportionately low when

considered in the context of the global significance of the Amazon fluvial system. In addition, despite the extensive work undertaken here in order to maximise bare earth DEM accuracy, quantitative validation with respect to accurate GCPs demonstrated that each of the floodplain DEMs derived here was associated with a vertical accuracy of worse than 3 m RMSE. This RMSE value was primarily attributable to unavoidable errors propagated during the correction of vegetation biases within the SRTM, and broadly represents the best accuracy which can be achieved in light of current data provision within Amazonian floodplains. Given the first order influence which topography exerts upon flood inundation (Bates and De Roo, 2000) the propagation of errors in model predictions is somewhat inevitable given the quality of current Amazonian floodplain DEMs. The amplitude of the Amazon flood pulse is of the order 9-10 m (Junk et al., 1997) whilst the depth of floodplain flows are commonly much shallower than this (Alsdorf et al., 2005). Therefore an RMSE of greater than 3 m can be considered highly significant in light of the typical flow depths observed upon Amazonian floodplains. In light of the previous discussion it is eminently clear that a dearth of accurate topographical data remains the most significant barrier to more widespread application of inundation modelling within Amazonia.

Bates et al., (2012) stated that the advent of remote sensing, particularly the enhanced availability of LiDAR derived DEMs (Marks and Bates, 2000; French, 2003), provided the stimulus for the rapid development of the science of flood inundation modelling observed within the UK and the Netherlands over the past two decades. Initially, LiDAR was able to provide bare earth terrain data with a spatial resolution of 2-5 m and with a vertical accuracy of the order 10-15 cm RMSE over 20 % of the land surface of the UK (Bates et al., 2004). The scope of LiDAR survey has since expanded, such that around 70 % of the UK has been subject to survey with a maximum resolution and vertical accuracy are of 0.25 m and 5 cm RMSE, respectively (Bates et al., 2012). Prior to the widespread availability of LiDAR derived DEMs, floodplain elevation was derived from cross sectional surveys which were unable to provide a sufficiently accurate representation of topography at a scale commensurate with underlying process variability (Lane et al., 1999). Hence, through providing an accurate representation of floodplain topography at appropriate scales, LiDAR data has facilitated the investigation of important underlying process representation

within flood inundation models and improved understanding of shallow water flooding (Bates et al., 2012). The main finding of this research was the first order influence which topography exerts upon flood inundation (Bates and De Roo, 2000; Nicholas and Mitchell, 2003; Fewtrell et al., 2008). These findings have been reflected within subsequent research, a substantial volume of which has been devoted to developing computationally efficient model codes which are able to incorporate high resolution DEMs (Hunter et al., 2005; Bates et al., 2010; Neal et al., 2010).

At present, flood inundation modelling within Amazonia is characterised by several of the key problems experienced within regions such as the UK prior to the widespread availability of LiDAR survey data. Specifically, DEMs which provide an accurate representation of floodplain topography at the scale of underlying process variability are not widely available. Hence it is clear that an increase in the provision of accurate bare earth topographic data is required in order to stimulate the modelling of flood inundation dynamics within Amazonian floodplains. Airborne or spaceborne LiDAR present the most likely remote sensing platforms to provide these data. The provision of LiDAR is currently limited by the vast extent of the Amazonia and the remote location of many parts of the basin. Indeed at approximately 6.7 million km^2, the Amazon basin is approximately 300 times as large as the UK. Clearly it is not feasible to achieve a full spatial coverage of the Amazon basin with high resolution LiDAR surveys. However the provision of targeted airborne LiDAR surveys for local sites characterised by a high level of significance and which are representative of Amazonian floodplains more widely constitutes a more realistic goal. In addition the increasing capabilities of spaceborne LiDAR survey, demonstrated by sensors such as ICESat GLAS (Abshire et al., 2005), may also offer some potential for the provision of lower resolution LiDAR data over wider spatial extents in the future.

Provision of such LiDAR data would facilitate the direct generation of highly accurate floodplain DEMs, circumventing the need to undertake many of the initial processing steps which are currently required in order to correct the SRTM dataset. In a similar manner to the UK during the past 20 years (Bates et al., 2012), the increased provision of topographic data could help shift the emphasis of research towards the consideration of key research questions

specific to the inundation of Amazonian floodplains; for example the derivation of appropriate friction coefficients for typical floodplain land cover types (Mertes et al., 1996), further research into parameterisation of hydrological processes which attain an additional significance within tropical areas (Aalto et al., 2003; Pouilly et al., 2004), the influence and inclusion of sub grid scale features such as floodplain channels (Wilson et al., 2007), methods to incorporate a representation of channel shifting within longer term simulations of inundation and to explore the potential effects of future Amazon ecosystem change (Poulter et al., 2010) upon flood dynamics.

Increasing availability of LiDAR would also be advantageous for many other related research applications within floodplain forests, including those which have formed part of this thesis. Within chapter 3, Beni floodplain land cover was classified with respect to only multispectral Landsat TM imagery (Lu et al., 2003a). In recent years classification algorithms have developed in order to facilitate inclusion of additional variables to aid in discrimination of land cover types possessing similar spectral signatures. For example Anderson et al., (2010) demonstrated the enhanced ability to distinguish forest types through inclusion of stand elevation from SRTM as an additional data source. In the Beni study area, the slope of the floodplain was associated with a ~ 40 m decrease in elevation along the studied reach, effectively confounding the potential benefits associated with additional information provided by SRTM in the separation of land cover types. However, the addition of accurate stand elevation and forest height from LiDAR survey would undoubtedly enhance the ability to separate the different forest types upon the Beni floodplain.

It is also clear that a greater provision of LiDAR data would contribute to an enhanced ability to estimate above ground wood biomass and carbon storage within the Amazon basin (Asner et al., 2012a). Asner et al., (2012b) demonstrated the potential of LiDAR surveys for providing an efficient means to accurately quantify biomass and carbon stocks within the Colombian Amazon. Indeed the authors developed a ‘universal equation’ to efficiently estimate aboveground biomass and carbon density within a range of forests based upon LiDAR survey measurements and limited in situ forest measurements. This universal equation offered a higher level of accuracy in comparison to traditional methods utilised to quantify spatial distributions of AGWB and carbon (Asner et

al., 2012b). In addition, a systematic analysis of environmental variables provided new insight into ecological controls responsible for variation of AGWB and carbon density, such as elevation, terrain ruggedness and fractional canopy cover. Hence with expanded LiDAR coverage similar analyses could be implemented within other areas of the Amazon, including for varzea forests.

Within chapter 7, extrapolation of plot based biomass measurements with respect to a canopy height map derived from the SRTM dataset demonstrated that above ground wood biomass stocks within the Beni floodplain are substantially lower than would be expected based upon past plot based estimates (Phillips et al., 1998; Baker et al., 2004) and spatial maps for the Amazon basin (Saatchi et al., 2007). Hence the results presented within chapter 7 demonstrate how spatially distributed information relating to vertical forest structure can be utilised in order to elucidate the influence which local scale variables, in this case flood inundation, exert upon distribution of AGWB in the Amazon basin. Within the context of this research project, the availability of LiDAR data would contribute towards a substantial reduction in the levels of uncertainty associated with the aboveground wood biomass storage estimates for the Beni floodplain. More widely, spatially distributed information relating to vertical forest structure from LiDAR data could also facilitate quantification of the influence which other local scale variables exert upon the distribution of biomass across Amazonia (Asner et al., 2009). Such variables could subsequently be incorporated into approaches used in order to extrapolate plot scale measurements to the basin scale (Saatchi et al., 2007), further reducing the uncertainty associated with resulting estimates of Amazonian AGWB stocks.

Therefore overall it can be argued that the application of hydraulic models, and hence a wider process understanding of inundation within Amazonian floodplains, will remain somewhat limited whilst the SRTM represents the best source of data for generation of bare earth DEMs within this region. It is clear that an increased provision of high quality bare earth elevation data is ultimately required in order to facilitate more accurate simulation of the dynamics of flooding within the Amazon basin. The provision of such data, most likely through airborne or spaceborne LiDAR surveys, would also provide substantial benefits to a wide range of research applications for example the classification

of Amazonian land cover (Kawakubo et al., 2013) and derivation of basin scale estimates of biomass (Saatchi et al., 2007).

8.3 Future change in the Amazon basin and potential impacts upon varzea forest dynamics

It has been hypothesised that the Amazon basin will be characterised by rapid rates of ecosystem change over the next century, as a result of a number of inter-related factors (Poulter et al., 2010). One of the pre eminent aspects of this future change are perturbations in water budgets which are predicted to occur within Amazonia as a result of interactions between climatological and land use changes (Coe et al., 2008). Subsequently, it is clear that changes in water budgets are likely to manifest in terms of river discharge regimes, which will subsequently induce significant changes in a range of fluvial processes and annual cycles of inundation (Coe et al., 2009).

Particularly relevant here is the strong connection observed between ENSO and the discharge regime of tropical rivers, including the Amazon (Richey et al., 1989, Ronchail et al., 2005). This is attributable to the fact that rivers are comprehensive integrators of anomalies in rainfall, which occur in response to ENSO, over large spatial scales (Schongart and Junk, 2007). Within Amazonia this manifests in terms of the flood pulse, the timing of which is generally consistent each year, occurring at Manaus within the latter half of June in 55% of years between 1903 and 2004 (Irion et al., 1997). However inter-annual variation in the magnitude of the flood pulse is significant, indeed over the period 1903-2004 the maximum flood level was recorded in 1953 at 29.69 m above sea level (a.s.l), although the lowest water level was 21.76m a.s.l in 1926, a range of almost 8m.

Schongart and Junk (2007) were able to demonstrate the relationship between the magnitude of the annual flood pulse within Amazonian rivers and ENSO phase through retrospective prediction of maximum water levels in Central Amazonia according to anomalies in Southern Oscillation Index (SOI) and sea surface temperatures (SST) within the Pacific Ocean. This study illustrated that flood inundation magnitude increases within cold phase ENSO (La Nina) years, whilst the reverse is true for warm phase ENSO (El Nino) years. This is highly significant when considered in the light of future predictions regarding ENSO fluctuation in response to future global warming. Using a modelling approach,

Timmermann et al., (1999) predict that under scenarios of continuing emissions ENSO is likely to shift such that the mean state resembles current El Nino conditions, whilst being simultaneously characterised by higher inter-annual variability skewed towards cold phase ENSO. Tentatively, based upon the prediction of a shift towards warm phase El Nino conditions within the basin (Timmermann et al., 1999), this suggests that the discharge regime of Amazon rivers is likely to shift towards lower average discharges and a reduced magnitude of the annual flood pulse. Ultimately this is significant as perturbations in discharge are inextricably linked to fluvial processes such as overbank inundation, sedimentation and rates of channel shifting (Leopold and Wolman, 1957).

Within this study the importance of the aforementioned fluvial processes in terms of Amazonian floodplain functioning have been clearly demonstrated. In chapter 7, it was shown that high rates of lateral shifting of the Beni river are responsible for a modest annual net loss of aboveground wood biomass and carbon storage from the floodplain, whilst also being responsible for maintaining relatively large areas of varzea forest within early successional stages. Maintenance of large areas of these successional forests was considered significant, as they are associated with lower AGWB storage, but higher rates of carbon assimilation in comparison to old growth varzea. Similar observations have been made within other areas of the Amazon, indeed a net annual loss of AGWB and carbon was also observed as a result of migration of the Solimoes, Japura and Aranapu rivers in the central Amazon (Peixoto et al., 2009). In addition, the influence of channel shifting upon floodplain forests has been demonstrated for many Amazon rivers (Salo et al., 1986; Kalliola et al., 1992; Lamotte, 1992).

Gautier et al., (2007) demonstrated that rates of channel shifting were dependent upon discharge characteristics of the Beni. Specifically the magnitude of erosion and deposition within the channel, responsible for determining channel migration, was highly correlated with number of days of bankfull discharge per year. Hence a shift towards lower average discharge is likely to result in a decrease in rates of channel shifting, thus reducing the rates at which old growth forest stands are removed and new successional forests are generated. Based upon a synthesis of this information it is hypothesised

that in the first instance a reduction in the rates of lateral channel shifting are likely to lead to a reduction in the annual losses of AGWB and carbon from varzea forests which flank meandering rivers within the Amazon basin. In addition, a reduction in the rate of lateral channel migration will also lead to a decline in the area of primary successional forests, leading to an overall increase in AGWB storage, but decrease in carbon assimilation rates within forests located upon the floodplains of meandering rivers.

Results presented in chapter 7 also demonstrated the influence which flood inundation exerted upon Beni floodplain varzea forest stands. Through analysis of plot data it was shown that flood inundation exerts a first order influence upon forest successional stage (Wittmann et al., 2002) and hence aboveground wood biomass and carbon storage within the Beni floodplain. In addition, a spatial analysis of floodplain AGWB demonstrated that large areas of the Beni floodplain are characterised by successional forest stands, associated with low biomass storage, due to the influence of flood inundation. Through monitoring discharge regimes and measurement of tree rings within the central Amazon floodplain, Schongart et al., (2004) were able to elucidate a relationship between varzea forest growth and ENSO cycles. Results demonstrated that lower discharges associated with El Nino conditions lead to an increase in productivity within floodplain forests due to a lower magnitude of flood inundation and hence a longer growing season. Hence overall this suggests that lower magnitudes of inundation associated with a shift towards El Nino conditions may lead to enhanced AGWB and carbon assimilation and storage within the Beni study area, and in Amazonian varzea forests more generally.

Therefore, further research is required in order to quantify how perturbations in fluvial disturbance regimes relating to future change within the Amazon basin may potentially contribute to changes in above ground biomass and carbon storage and assimilation within Amazonian varzea forests. Knowledge of these interactions is necessary in order to assess how floodplain functioning may respond to future change within the Amazon basin. This is particularly significant given the potential of floodplain forests to absorb carbon released from Terra Firme forests during warm phase ENSO events (Schongart and Junk, 2007). This trend is particularly significant as it is widely acknowledged that non flooded Terra Firme forests are associated with net releases of carbon

during El Nino events, due to droughts and increased risk of fires (Phillips et al., 2009), and thus it has been hypothesised that flooded varzea forests may provide some mitigation of this phenomenon. Although this represents a theoretically sound scenario based upon current information, it is clear that further research is required in order to investigate the efficacy of this hypothesis.

Chapter Nine

Conclusions

9. Conclusions

Whilst being of scientific significance in their own right, chapters 3,4 and 5 of this thesis constituted pre requisite stages to exploration of the overall aim of the PhD research in chapters 6 and 7. Hence the main findings of chapters 3,4 and 5, along with their wider significance are summarised here initially, before drawing final conclusions with respect to the overall aim of this PhD research. Based upon the results presented in chapter 3, it can be concluded that the application of simple per pixel supervised classification approaches to Landsat TM multispectral imagery is sufficient to enable separation of Beni floodplain land cover types with a reasonable degree of accuracy. However as a result of the mixed pixel problem, which is prevalent within the Amazon land cover classification applications, more complex approaches such as a combined linear spectral unmixing- decision tree classification are required to separate different forest types, which are associated with similar spectral signatures. In this regard, results presented within this thesis are in broad agreement with previous work (Shimabukuro et al., 1998; Lu et al., 2004) undertaken within other parts of the Amazon. Broadly speaking, the level of detail and accuracy required within a land cover map depends upon its final end user application. Within Amazonia accurate discrimination of different forest types is commonly required, for example in order to estimate biomass storage in landscapes characterised by mixtures of primary forest and secondary forests of different ages. In such instances, implementation of more complex classification approaches, demanding additional 'expert user' input, is required. Significantly, the results of chapter 3 illustrate that at the scale of typical Amazonian study areas, an accurate classification of land cover can be achieved based upon the application of classification algorithms to Landsat TM scenes, which are both freely available and associated with excellent spatial and temporal coverage.

After correction for systematic vertical offset, the SRTM dataset demonstrated a high level of accuracy within non forested areas of the Beni floodplain (RMSE 1.2 m), whilst absolute accuracy was lower than 20 m within forested areas. Therefore on a basic level, the results presented within chapter 4 reflect the findings of other studies which have validated the SRTM dataset within the Amazon basin (Berry et al., 2007). These initial findings lead to several important conclusions with regards to the SRTM dataset, in particular with

respect to its application within environmental process studies. The vertical offset of the SRTM, found to be 6.74 m for the Beni floodplain, demonstrates the need for validation of this dataset prior to use within applications which rely upon integration of the SRTM with other vertically referenced datasets (Kellndorfer et al., 2004). Furthermore, based upon the results of initial validation it can be concluded that the SRTM does not represent the elevation of the ground surface in vegetated areas (Carabajal and Harding, 2005), requiring that it be classed as a digital surface model (DSM), rather than a digital elevation model (DEM) for areas characterised by tropical forest cover such as the Beni floodplain (Rodriguez, 2005). Hence in a wider context, these conclusions are associated with significant implications for the application of SRTM within studies requiring a bare earth DEM, such as flood inundation modelling (Baugh et al., 2013).

The second part of chapter 4 provided insight into the vertical biases contained within the SRTM dataset, through comparison with field measured canopy height for Beni floodplain forest stands. Saliently, after reduction of noise through spatial averaging (Walker et al., 2007), a linear relationship was observed between SRTM derived canopy height and field measured canopy height. The former was consistently lower than the latter due to penetration of the SRTM C-band phase centre an average distance of 7.4 m into the canopy of Beni floodplain forests. Thus, based upon this finding it can be concluded that the elevation reported within the SRTM corresponds to approximately 35% of the distance from the top of the canopy to the ground, broadly consistent with the findings of other analyses of the SRTM for tropical forests (Hofton et al., 2006). Most importantly, the wider implications of these findings are that a spatially continuous map of canopy height can be adjusted to account for C-band phase centre penetration and applied to the SRTM dataset in order to remove vertical vegetation biases from the DSM, and to generate a bare earth DEM suitable for application within land surface process studies.

Chapter 5 constitutes the first known instance where bare earth DEMs have been derived from SRTM within the Amazon basin, and directly validated with respect to an accurate ground elevation dataset. Three main classes of DEMs were generated, applying approaches to DEM generation utilised within past studies undertaken in the Amazon basin. The first class of DEM was produced

by application of zonal average canopy height maps to the SRTM (Wilson et al., 2007), with forest height derived from field survey and GLAS measurements. In the second method, vertical bias in the SRTM was treated based upon a global canopy height map (Simard et al., 2011) following the approach of (Baugh et al., 2013). The final bare earth DEM was produced using a novel method developed in this PhD research, in which a first order representation of bare earth elevation was produced through interpolation of bare earth elevation points, and was subsequently utilised in order to extract estimations of forest height from the SRTM dataset. The three bare earth DEMs produced were associated with varying levels of accuracy based upon quantitative and qualitative validation, in fact it was found that the novel approach produced the most accurate DEM, whilst the zonal average DEMs were associated with the greatest errors.

However, the overarching conclusion which can be drawn from this chapter is that field and remotely sensed canopy height datasets can be utilised in order to remove vegetation biases from the SRTM DSM, substantially improving accuracy of the dataset such that vertical accuracy far exceeds pre mission accuracy requirements (Bamler, 1999). However, bare earth DEMs derived from the SRTM dataset, using the best available methods (Wilson et al., 2007; Baugh et al., 2013), were nevertheless associated with RMSE values exceeding 3 m, attributable to errors in the estimation of canopy height across the floodplain. Therefore it can be concluded that ~3 m RMSE represents the maximum bare earth DEM accuracy which is realistically achievable based upon current data provision within the Amazon basin. Considering that the amplitude of the Amazon flood wave is ~10 m (Junk, 1997), whilst floodplain flows are typically much shallower than this (Alsdorf et al., 2007), vertical errors exceeding 3 m can be considered significant in terms of the application of SRTM derived bare earth DEMs within flood inundation modelling. Specifically, errors of this magnitude have the potential to propagate erroneous flow dynamics through representation of topographical blockages or depressions upon the floodplain.

A number of important conclusions can be drawn based upon the flood inundation modelling undertaken in chapter 6. As topography exerts a first order influence upon floodplain flow dynamics, application of the bare earth DEMs

within a hydraulic model provided a stringent test of their vertical accuracy. Validation of preliminary model simulations with respect to high water flood extent, derived from ALOS PALSAR, revealed that inundation was systematically under predicted in areas close to the Beni channel. This was caused by over elevation of the bare earth DEMs in this area, which was in turn attributed to the inability of the various canopy height maps utilised in correction of the SRTM to properly account for increases in forest height observed for stands located in close proximity to the Beni channel. In the context of this study, this resulted in poor levels of fit between predicted and observed inundation. However these results allow more broad conclusions to be drawn relating to bare earth DEM quality. Specifically, it can be concluded that approaches to bare earth DEM generation applied within past studies (Wilson et al., 2007; Baugh et al., 2013) are not necessarily able to produce a representation of topography that is sufficiently accurate for application in flood inundation modelling, particularly on floodplains characterised by substantial local variations in canopy height such as the Beni. This is contrary to the assertions of Baugh et al., (2013), who state that an accurate bare earth DEM for use in flood inundation modelling can be derived through correction of the SRTM by application of a global canopy height map.

After refining of the bare earth DEMs in order to remove the remaining forest biases, model performance increased substantially. In the formal assessment, it was found that simulations undertaken using the refined INT DEM (produced based upon the novel method implemented in chapter 5) were characterised by the highest level of accuracy with respect to high water inundation extent, low water inundation extent and water surface elevation within the Beni river channel. It is thought that performance exceeded that of the refined FAV and GCH DEM, as a result of a more accurate representation of floodplain topography, as indicated by DEM assessment in chapter 5. A particular problem identified for the GCH DEM and FAV DEMs, even after refinement, was the presence of relatively large topographical depressions in the floodplain. These depressions limited model performance at high water through the capture of large volumes of overbank flow, limiting inundation within other areas of the floodplain. At low water, large volumes of water remained within these depressions, indicating that they become isolated during recession of flood waters and are unable to drain correctly. Hence the formal model assessment

clearly demonstrates some of the limitations associated with DEMs utilised here, and it can be concluded that DEM generation methodologies applied in past hydraulic modelling studies in the Amazon basin should be applied in combination with thorough quantitative assessment in future studies.

The final conclusion drawn from chapter 6 relates to the inclusion of a representation of hydrological processes within the application of hydraulic inundation models in the Amazon basin. Here, results demonstrated that inclusion of a basic representation of floodplain hydrology resulted in a very small increase (F_{hw}=0.01-0.02) in model performance at high water, whilst the increase in performance was more significant at low water (F_{lw}=0.11-0.15). On a basic level, this demonstrated that rainfall provided a small net contribution at high water, whilst evapotranspiration and infiltration contribute significantly to water losses during floodplain dewatering. Importantly, the seasonal variation in the contribution of hydrological processes demonstrated here suggests that the assumption of a net balance between rainfall and evapotranspiration assumed in past studies (Wilson et al., 2007; Baugh et al., 2013), is not necessarily appropriate for Amazonian floodplains.

Based upon work presented in chapter 7, conclusions can be drawn with regards to the interactions between fluvial processes and functioning of Beni floodplain varzea forests, addressing the overall aim of this thesis. Through results presented for the plot scale analysis, it can be concluded that fluvial processes exert a significant influence upon successional forest development upon the Beni floodplain. Specifically, AGWB demonstrated a clear increase with both stand age and relative elevation above Beni river water level (a proxy for flood inundation characteristics). Hence it can be concluded that flood inundation is responsible for determining the successional stage of varzea forests, whilst based upon the covariance between stand age and relative stand elevation, it can be more tentatively concluded that sedimentation plays a role in forest development through facilitating the process of allogenic succession. These findings largely support conclusions made by Wittmann et al., (2004), but extend the scope of the analysis in order to provide unique insight into the biomass of successional forest stands.

Indeed, the space-time substitution methodology employed within this research facilitates new insight into successional varzea forest growth. Saliently, AGWB

in these stands increased tenfold in less than 50 years, whilst carbon assimilation rates within these forests were four times greater than the average for varzea forests, and ten times greater than the average for Terra Firme forests, based upon previous estimates (Baker et al., 2004). Furthermore, based upon quantitative evidence it can be concluded that biomass of primary successional floodplain forests can reach levels similar to old growth varzea stands within 50 years, roughly half of the time it takes for this process to occur within Terra Firme forests (Guariguata and Ostertag, 2001). Therefore in broad terms, it can be concluded that successional varzea forest stands are highly dynamic within the context of Amazonian forests, being associated with low levels of AGWB storage but very high rates of carbon assimilation. Indeed, perhaps the most significant implication of plot level findings was the potential for fluvial processes to exert a more widespread influence upon varzea forest characteristics, particularly in terms of AGWB, across the Beni floodplain.

Accordingly, based upon further analysis undertaken in chapter 7 it can be concluded that lateral migration of the Beni river channel exerts a substantial control upon AGWB storage and assimilation within floodplain forest stands. It was estimated that channel migration was directly responsible for a net annual AGWB loss for the Beni study area, due to the loss of old growth floodplain forest stands and replacement by early successional stands. A similar result was found by Peixoto et al., (2009) for the Solimoes-Japura rivers, implying that rapid rates of channel migration, which characterise many Amazonian rivers, are responsible for a long term net loss of AGWB and carbon from varzea forests across the basin. However this loss is modest given that it constitutes just 1.5% of total floodplain AGWB over a period of half a century.

Perhaps more important is the fact that continued migration of the Beni river and reworking of the floodplain maintains relatively large areas of forest in early stages of successional development. This is significant as these forests are associated with rates of carbon assimilation which are much higher than other Amazonian forests (Baker et al., 2004). This process attains an increasing significance in the context of the Amazon basin, as natural loss and regeneration of forest in Terra Firme stands typically occurs over comparatively limited areas in response to tree falls (Kalliola et al., 1992). Hence, overall it can be concluded that continuous turnover of floodplain forest stands as a result of

channel migration has the potential to sequester large volumes of carbon within AGWB. However, the efficacy of this assertion is dependent to a large extent upon the fate of carbon lost through processes of fluvial erosion. For instance, if AGWB and carbon lost through lateral channel shifting is transported out of the reach and stored, then channel migration would theoretically lead to a continuous drawdown of atmospheric CO_2 across the Amazon. However, if the lost AGWB is subject to rapid decomposition, the sequestration of carbon within newly formed successional forests would essentially be negated. Hence further research is required in order to quantify the fate of eroded AGWB and carbon, and determine the net contribution of this process across Amazonia.

Based upon spatial extrapolation of plot level biomass estimates according to a canopy height map, it was concluded that AGWB storage for the Beni floodplain study area is substantially lower than would be expected based upon previous estimates for varzea forest stands across the Amazon basin (De Paula et al., 1990: Baker et al., 2004). This disparity was substantial, indeed total floodplain AGWB storage estimates here were less than half of that predicted by a biomass map for the Amazon basin (Saatchi et al., 2007). Intersection of the biomass map with outputs from the hydraulic model demonstrated, for the first time, a significant relationship between inundation characteristics and the spatial distribution of varzea forest biomass at the scale of a whole floodplain. Indeed AGWB was negatively associated with inundation depth, reflecting the conclusions drawn based upon the plot scale analysis. Hence, through integration of results generated within this PhD research, it can be concluded that flood inundation maintains large areas of Beni floodplain forests in stages of successional development, directly contributing to the low biomass stocks which characterise the study area.

Varzea forests comprise an area of up to 500,000 km^2 of the Amazon basin, thus the findings of this study are highly significant, suggesting that the volume of AGWB stored in floodplain forests may be systematically overestimated across Amazonia. In turn, this suggests that varzea forests represent a substantial source of uncertainty in basin scale estimates of biomass (Malhi et al., 2006). The work presented in this thesis has demonstrated that spatial patterns of flood inundation appear to exert a significant influence upon AGWB density within varzea forest stands located upon Amazonian floodplains. Hence,

varzea forests are currently poorly represented in methods which are currently utilised to produce basin wide estimates of AGWB in Amazonia, which extrapolate plot scale biomass measurements with respect to broad scale environmental variables, such as climatic characteristics (Houghton et al., 2001). Accordingly, based upon the results of this study it can be concluded that a basic representation of flood inundation characteristics is required within algorithms used to estimate biomass across Amazonia, in order to provide a more accurate representation of AGWB storage in varzea forests. This would contribute to a reduction in the high levels of uncertainty currently associated with these maps (Saatchi et al., 2007).

Overall, through integration of field data, remote sensing analysis and numerical modelling, this thesis provides a new and unique insight into the dynamics of flood inundation upon Amazonian floodplains, and the interactions between fluvial processes and aboveground wood biomass storage within varzea forests. Accordingly, a wide range of conclusions across a number of fields have been drawn based upon this PhD research. Perhaps the most significant limitation of this research project is constituted by the substantial level of uncertainty associated with bare earth DEMs and subsequent predictions of flood inundation, along with spatial extrapolation of plot level biomass measurements. However, much of the uncertainty propagated here was attributable to the datasets currently available for Amazonia, and was largely unavoidable in the context of this research. Therefore it can be concluded that an improvement in the quality of data provision in the Amazon basin, specifically LiDAR surveys, is required in order to build upon the findings of this thesis.

Appendices

Appendix A. Laboratory protocols

Soil preparation

The soil, on receipt in the laboratory, is usually air-dried. (See below). If the original field volume of the soil is known, then the sample is now weighed, so that any results could be recalculated in terms of field volume.

1) Air Drying of Sample

Samples from the field must first be air-dried. This is usually done by putting the samples onto porous plates and leaving them until they feel dry. This can take considerable time and so alternative methods are;

a) Putting the porous plates into an oven at 40^{0}C
or b) by freeze-drying the samples.

2) 2mm Sieving

When the samples have been air-dried the next stage is to separate out the stone fraction.

The samples are first ground using a mortar and pestle. A rubber pestle is preferable, as this tends not to break the primary particles. The stones can then be sieved out using a 2mm sieve. The grinding and sieving is repeated until only the stones are left (it may even be necessary to brush the fines fraction off the stones).

The weights of both the stone fraction and the fines fraction are then taken and recorded.

3) Stone Analysis

A nest of sieves greater than 2mm is constructed such that the largest sieve is just bigger than the largest stone. The stones are then added to this nest and this is then placed on the sieve shaker.

After shaking the fractions are all weighed and recorded. The best technique is to weigh the fraction in the collecting pan, and then invert each sieve in turn over this pan and gently brush the stones onto it.

Analysis for phosphorus

(Based on Mehta et al 1954 Soil Sci.Soc.Amer.Proc.,18 443-449 and Sommers et al.1972 Soil Sci.Soc.Amer.Proc.,36 51-54)

Reagents

1000 ppm P solution	4.3943 gm KH_2PO_4 to 1 litre with water
5 ppm P solution	5 ml of 1000ppm P to 1 litre with water
1.0 N Hydrochloric acid	86 ml conc. HCl to 1 litre with water
1.0 N Sodium Hydroxide	80 gm NaOH to 2 litres with water
4.0 N Sulphuric acid	56 ml conc. H_2SO_4 to 500 ml with water
Ammonium Molybdate solution	6.4 gm Ammonium molybdate to 200 ml water

Ascorbic acid	20 gm per litre of colourimetric solution
Potassium Antimony Tartrate	1.08 gm APT in 100 ml water
Colorimetric Reagent	500 ml of 4.0 N H_2SO_4 150 ml of Ammonium Molybdate soln 50 ml of APT solution 20 gm ascorbic acid + distilled water to 1 litre

Extraction

N.B. All glassware must be scrupulously clean and acid washed before use.

Approximately 0.5 gm of the soil or sediment is accurately weighed into a 50 ml polypropylene centrifuge tube. (Also prepare a blank by following all the next steps, but without any soil/sediment)

To this is added 40 ml of 1.0N Hydrochloric Acid.

The tube is then stoppered and shaken for 16 hours (i.e. overnight).

After this shaking the tube is centrifuged at 2500 rpm for 15 minutes and the supernatant transferred to a labelled 250 ml conical flask.

40 ml of 1.0 N Sodium Hydroxide is then added to the residue in the tube, which is then stoppered and shaken for 4 hours.

The tubes are then centrifuged again at 2500 rpm for 15 minutes and the supernatant again added to the relevant flask.

A further 40 ml of 1.0 N Sodium Hydroxide is added to the residue, the tube is stoppered and shaken and before being placed in an oven at 90 ^{0}C for 16 hours.

Again the tube is centrifuged at 2500 rpm for 15 minutes and the supernatant added to the relevant flask.

6 ml of conc. Hydrochloric Acid is then added to the flask and the contents transferred to a 200 ml volumetric flask. This is then made up to the 200 ml mark with distilled water and then returned to the conical flask.

Calibration standards

For both the total and inorganic phosphorous a series of standards are prepared to calibrate the UV/VIS spectrophotometer. The series is as follows

0,2,4,6,8,10 ml of 5ppm P

To this is added 5 or 10ml of the blank reagents, depending on how much aliquot is taken for the samples (see below). Then the colorations for both total and inorganic P are obtained as in the following methods for the samples, from the point in the methods when the aliquots have been taken.

A calibration equation can then be obtained using a regression package such as MINITAB, or by using advanced regression in Qpro or Excel if that spreadsheet is used

A) Determination of total phosphorous

The 200ml extract from above is thoroughly mixed and a 5ml or 10ml aliquot is taken and transferred to a 125ml conical flask. (10ml if low values are suspected, otherwise 5ml)

A few anti-bumping granules are added and the solution is then boiled on a hotplate in the fume cupboard until almost dryness.

The flask is then removed from the hotplate and when cool, 1ml of perchloric acid is added.
The flask is then returned to the hotplate where it is heated with care until almost dry. White fumes will then come from the flask and a few drops of water are added. The flask is then repeatedly heated and water added until there are no more perchloric fumes.

The flask is then removed from the hotplate and allowed to cool before the addition of the colorimetric reagent (see below).

B) Determination of inorganic phosphorous

The 200ml extract is thoroughly mixed and then about 40ml is transferred to a 50ml centrifuge tube where it is centrifuged at 2500 rpm for 15 minutes.

Again choose 5 or 10 ml of the supernatant, which is then transferred to a 100 ml beaker

Colouring

The colorimetric solution (see recipe above) is prepared fresh daily.

For the Total Phosphorous determinations, 10ml of the colorimetric solution are pipetted into a 50 ml volumetric flask, which is then made up to the mark with water.

The entire contents of the 50ml flask are then added to the dry residues in the 125ml conical flasks from A above.

For the Inorganic Phosphorous determinations, 10ml of the colorimetric solution are pipetted into the 100ml beakers from B above and the entire contents are then transferred to a 50ml volumetric flask. This is then made up to the mark with distilled water before being returned to the 100ml beaker

Both sets of determinations are then allowed to develop for between 30 and 120 minutes.

The absorption at 890 nm is then measured on the SP6 UV/VIS Spectrophotometer.

Analysis for carbon and nitrogen

Start-up - The NA2500 C/N Analyser

1. Ensure that the oxygen and helium are turned on at the regulators and set to 1.5 bar and 3 bar respectively
2. On the panel press SPC FUN (Special Functions) and then the right arrow - this will show the STD BY flashing.
3. Press ENTER on the panel . The panel should now show ST-BY YES , O2 OFF , He OFF.
4. Press ENTER again so that it now reads ST-BY NO , O2 ON , He ON
5. Press SPC FUN again to return to the temperatures.

The C/N Analyser will now warm up the reaction and reduction furnaces, a process which takes approximately 30 minutes. The lights on the panel graphic showing the furnace heaters will remain steady until the set temperatures are reached, when they will flash on or off.

Do a leak check by blanking the vent, waiting 2 minutes and then winding out the helium thumbscrew. The pressure should not drop. Remove blank and set the helium back to it's setting of 150

Start-up - Computer

1. Check that the computer has the correct dongo on the parallel port, and the correct 9 way connector in the COMS 1 serial port. (The computer is also used for the UV/VIS so check or ask)
2. Switch on the computer
3. Type *Win* to enter the Windows environment
4. Click on the Eager 200 icon in the Eager 200 for Windows group
5. Wait a little , even when the hour glass symbol changes back to the normal arrow. This initialises the Eager card
6. A Grey Window eventually appears showing the serial number of the Eager Card. Click on OK and wait again for 30 seconds or so until the main Eager Window appears.

Cleaning of Tin Boats

If the blank results show contamination then the tin boats are cleaned and dried before being used for analysis.

1. The waterbath is heated to at least 60°C in the fume cupboard.
2. The waterbath is then switched off so as to minimise risk of fire from the chloroform fumes.
3. The boats are put in a beaker, and Chloroform added to just cover the boats. The beaker is then placed in the warm waterbath for about 5 minutes with regular swirling.
4. The Chloroform is then carefully decanted into the Waste Chlorinated Solvent bottle (IMPORTANT that the correct waste bottle is used)
5. Acetone is now added to the boats and again warmed for 5 minutes with occasional swirling
6. The acetone is then carefully decanted into the Waste Acetone Bottle (again important that correct waste bottle is used)
7. The beaker and boats is then placed in an oven at 105° C for ca. 1 hour to dry, before being placed in a dessicator to cool

Weighing of Samples

1. The samples must first be ground to <425µm
2. The balance used is the Sartorius Supermicro in the balance room. This is a very expensive and delicate balance and so initial instruction must be made by a technician. If the pan becomes dirty then consult the technician for cleaning - *it can be very easily broken!*
3. The required sequence is 1 blank, followed by a range of 3 calibration standards, usually EDTA, followed by samples, with the odd check standard
4. The balance is first set up as follows
    a) Turn the RH knob to read W - this may need pulling out before turning if it has been left in it's correct TA position
    b) Turn the LH knobs from the TA position to read 0 000 when level with the steel button. One knob is turned anticlockwise, the other clockwise.
    c) Position the rocker switch at the RH back to on. The display should now go through a self-check and then zero itself.
    d) Ensure that the door to balance room is closed so as to minimise draughts.
    e) Press the MOTOR key on the keypad. This opens the internal door and swings out the weighing pan. Open the RH door on the balance. Press MOTOR again to return to return the weighing pan. Repeat this twice to fully acclimatise the weighing chamber to the room temperature. You are now ready to weigh.
5. Press MOTOR so as to bring the weighing pan out of the weighing chamber.
6. A tin boat is taken using the tweezers provided and carefully placed on the weighing pan.
7. Press MOTOR to return the pan to the weighing chamber and close the external RH balance door
8. Wait for the reading to stabilise and then press ZERO
9. Press MOTOR so as to bring the weighing pan out of the weighing chamber
10. Remove the boat carefully from the weighing pan using the tweezers.
11. Using the micro scoop, add either 20 - 30 mg of sample (about 3 scoops) or up to 15 mg of standard as required.
12. Whilst holding the boat with the tweezers, tap the tweezers so that the sample settles in the bottom of the boat. Put boat in the number 3 hole of the forming block. Using the 'sugar tongs' compress the top of the boat to form 'bomb fins '. (to prevent errors due to slight moisture changes)
13. Return the boat + sample to the weighing pan, close the external door , and press MOTOR to return the pan to the weighing chamber.
14. Wait for the reading to stabilise and note the weight.
15. Press MOTOR to remove pan from weighing chamber, open external door and remove boat using the tweezers.
16. Carefully fold over the 'fins' with tweezers and a micro spatula. Taking care not to puncture the boat, form a cube using the tweezers and micro spatula, ensuring that there are no loose edges that could be caught in the injection mechanism of the C/N analyser.
17. Place the boat in the correct number of the transport block. (With practice the forming and folding can be done whilst the next boat is being zeroed)
18. After all samples have been weighed, the ShutDown of the balance is the reverse procedure - Turn off the rocker switch, put both the LH & RH dials to TA and replace cover.

Eager Programs

Sample Table

This is used to input the details of the samples and also their weights. It can also used to change which sample is the next one to be analysed. There are features such as 'Fill Table' which can be used to expedite entries. The filename is usually unique and a different file is produced for each chromatogram. Note that if the file already exists (directory is C:\EAW\DATA\CHNS) then the new filename will automatically be changed by it's first character being updated e.g. art1.dat will go to brt1.dat

1. The first sample in the table is usually a 'bypass'. This is a sample of anything which is used to condition the system and to ascertain just where the Nitrogen and Carbon peaks are being eluted. (See component table below)
2. The next sample is a blank, followed by three standards, and then the unknowns with the odd check standard.
3. The entry of Blank, Bypass, Standard or Unknown is done through the check box that appears. If Standard is chosen then a choice of standards will appear. These all have the percentages of C and N already calculated. At present we are using EDTA but new standards can be chosen, but these would need the Standard Table edited.
4. Finally the weight of each standard / sample is entered
5. Before quitting Sample Table, the sample to be acquired is set to the first sample , by simply clicking in the top Left Hand cell of the sample table and checking the sample to be acquired box that then appears. - This facility can be used to alter which sample is being acquired
6. The sample table can only be saved by saving the complete method -see below

Component Table

This is used to identify and set the times of the expected component .

1. The bypass sample is run (see *running of samples* below)
2. From the Main Menu, *Component Table* is clicked and the peak times and names can then be entered.
3. The first peak is Nitrogen - usually ca. 75 sec. , with a second Carbon peak at ca. 120 sec.
4. These times can be more precisely using the displayed chromatogram, along with a window setting so that the peak will fall within that window.

If, despite this, some peaks are missed during the actual run, this operation can be still be carried out after the run, and the peaks can then be integrated.

Setting up of Run Times etc.

Care must be taken with adjustments of Run Times as the time set on the instrument must concur with that set in the software.

1. On the Main Menu, click on *Integration Parameters*. This then brings up a box for analysis time , minimum areas etc. , and can be changed by clicking in the relevant box.
2. To change the run time on the instrument itself, press *SetUp* followed by *SetCyc* followed by *Enter*. The run time can then be altered by using the Up/Down arrows.
3. Press *SetUp* (not *Enter*) when correct time has been selected.
4. Always have same time in software and machine.

Calculation Parameters - These are set by the default method, the important parameter here is that the calibration is set to K-factor

Running of the Samples

1. The first, most important step is to check which sample is the sample to be acquired, by looking in *Sample Table*. This can be set as described above by clicking in the Act. Column.
2. *Sample Table* is then closed.
3. From the main menu, the option *View* is clicked, followed by *Sample being acquired*.
4. In the next window, click on *Run* followed by *Start single analysis* when doing the initial bypass, or *Run* followed by *Start analysis* for all the samples.
5. As the samples are being run, the chromatogram is shown. Scaling of this can be altered via *View*.

Calculating and Displaying Results

1. It is well worth looking at the baseline and the start / end of peaks. This is performed by following the methods below for recalculation
2. Once the baselines are satisfactory then from the Main Menu, click on *Recalculation*, followed by *Summarise Results*. The calculation takes a while, but then displays the results, which can then be exported (via *File*) to an Excel .XLS file)
3. If peaks are missing, then parameters can be changed in the Components Table, or Integration Parameters (see above) before recalculating by *Recalculation* - *Recalculation* - *Summarise results*. (See below)

Particle size analysis

Reagents

100vol hydrogen peroxide
0.4% sodium hexametaphosphate — 6.7 gm sodium hexametaphosphate 1.3 gm sodium carbonate to 2 litre with distilled water

Method

This method is a general one where removal of organic material is required prior to particle size analysis by instruments such as the Saturn Digisizer (screening at 1000µm) or Mastersizer (screening at 63µm).

1. The soil is first air-dried and then ground and sieved through a 2 mm sieve, weighing both fractions.

2. 2 - 10 gm (depending on estimated sand content) of the < 2 mm fraction is then accurately weighed into a clean dry beaker. The soil is then dried overnight at 90°C. and then re-weighed to give the oven-dry weight.

3. 10 ml of water is then added to each sample + 5 ml of the hydrogen peroxide. It is often necessary to wait and observe the reaction and to control the effervescence by addition of a few drops of IMS.

4. After 2-3 hours, if the frothing has ceased a further 5 ml of hydrogen peroxide is added and the sample allowed to stand overnight. (More peroxide is added if a higher organic content is suspected)

5. The beakers are now warmed on a hotplate (starting at 80 °C and gradually increasing the temperature to 100 °C) until the reaction is complete and there is a clear supernatant above the sample.

6. The whole of the beaker contents are now carefully transferred to a weighed centrifuge tube, using a policeman on a rod to clean the sides of the beaker. The tubes are centrifuged at 2500 rpm for 1 hour.

7. The centrifuge tube is then dried overnight at 90 °C before being reweighed.

8. Approximately 30 ml of the 0.4% sodium hexametaphosphate solution are added to each tube and initially disaggregated with a spatula.

9. The soil suspension is then screened through a sieve (63µm if using the Mastersizer, 1000µm if using the Saturn digisizer) collecting the screened fraction in a 125 ml bottle. The centrifuge tube is washed with a small amount of the sodium hexametaphosphate and this too is passed through the sieve.

10. The residue (>63 µm or >1000µm) is washed with water, and the centrifuge tube is now completely washed with distilled water, passing the washings through the sieve. The residue on that sieve is now completely washed until no more fines are washed through and all the sodium hexametaphosphate has been washed away. The residue is now washed into a weighed dry 60 ml bottle with distilled water and dried overnight. This is then reweighed (and stored for sand fractionation if >63µm)

11. The screened suspension is then placed in an ultrasonic bath where it is treated for 5 minutes before being run on the MasterSizer (<63µm) or on Digisizer (<1000µm)

12. (If the sand fractionation is done, this uses a series of 100 mm sieves, usually 1000 µm, 500 µm, 250 µm, 125 µm, and 63 µm. Each fraction is accurately weighed on a 4-place analytical balance.)

13. **Calculations - Digisizer:** An excel template can be used to calculate the size distribution (1000µm Digisizer Template.xls found in Arts Directory on the Digisizer computer)

Saturn Digisizer

Modus Operandi

The Saturn digisizer is used for particle sizing up to 1000µm. Each sample has it's own file and the autosampler can be used to batch up to 18 samples at a time (even more can be added whilst the autosampler is in operation). An 'empty' file, containing just parameters, is created for each sample, and then once the sample has been run the data is automatically added and saved. Customer designed reports can then extract results which can then be cut and pasted into other packages. Files (new ones) can be created and samples added to the autosampler schedule even when the machine is running

Connecting

1) Switch on at mains the digisizer5200, Sonics, Mastertech , Aquaprep before switching o the computer
2) Password on the computer is null (just hit return)
3) Double click on Saturn digisizer icon and then wait as the software downloads data from the Digisizer – this takes about 1 minute

Ensure that the deionised water tubs are full (deair if necessary beforehand) and waste tub is empty

Rinsing and Background

1) Click on Unit 1 – Rinse –Digisizer – suggest do 2 rinses
2) Click on unit1 – Background – next – next
3) Background takes about 8 minutes (may be longer if starting from cold). When background is finished, click on next and then look at trace. It should reach zero on the x- axis before the end of the run and also there should be a double drop around about the 6 level

Setting up empty files

1) These must be set up before running the autosampler – however new files can also be set up as the autosampler is processing other samples
2) Click on File – Open – Sample Information (or press F2)
3) The file will just be a *number*.SMP which is automatically incremented. Press OK. Press Save
4) Now click on Replace All – this enables parameters to be set from a previous file to be carried into this file. Pick up a suitable data file from before (usually the last one created) –click on OK – change sample details (and anything else as necessary) and then click on save and then close.

Setting up a schedule for the autosampler

1) Click on Unit1 – MasterTech schedule
2) Click on insert
3) Check (or change) beaker number
4) Click on Browse and pick up the relevant empty sample file
5) Click on OK (Header – Sample Information File)
6) Click on OK (Header – Mastertech Schedule Insert)
7) Samples in the schedule can be edited or deleted by first highlighting them and then pressing the Edit or Delete button
8) Repeat for all the samples in the autosampler and then click on Start
9) Further samples can be added so long as their Sample Information Files have been created

Reports

1) Click on Reports –start report
2) Pick up relevant file
3) Click on OK
4) Choose from lists of 'Reports to generate' by double clicking option
5) Click on OK
6) A good idea is to check 'Goodness of Fit' – the blue trace and the red line should coincide and the fit should be as low a number as possible – preferably less than 5. If curve turns down at top, then repeat but add more sample!
7) Various parts can then be extracted to the clipboard by right clicking by that data

Exporting data to Excel

1. Click on Reports -start report - pick up relevant file –OK - OK
2. Click on Frequency Graph page of the report
3. Right click on graph. If more than 1 graph than the best graph can be chosen by 'hiding' the other graphs. Whilst on right click choose 'Copy as Text'. This puts the results onto the clipboard and they can then be easily pasted into an Excel spreadsheet. The actual graphic can be exported similarly by using 'Copy as metafile'

Stopping an autosampler run

1. When the MasterTech is 'Waiting to redisperse beaker', click on Suspend. (then Yes to confirm)
2. Wait until the Digisizer has completed the sample and is now showing Idle
3. Click on Stop and then Cancel. Click in box to confirm 'Cancel the MasterTech operation'
4. Click on Close – (the Mastertech schedule is now frozen but will be available again even after closing the computer down by clicking on MasterTech schedule)

Finishing Off

1) Click on Unit1 – Rinse – Mastertech then Digisizer.
2) Place an empty beaker on the autosampler and choose that beaker position to rinse to
3) When rinse is completed, add a couple of ml of Sodium Hexametaphosphate to tank. Allow this to circulate a few minutes.
4) Close down software and computer
5) Switch everything off at the mains
6) Empty the waste tub!

Overlay

1) Click on File – Open –Sample Information
2) Pick up first file of sequence
3) Click on Report Options - From the box titled Reports to Generate, highlight the type of graph that is to be overlayed (e.g. cumulative) –click on Edit (just to the right of box)
4) Go to Overlay (right hand side of next window) and choose Samples from the drop down menu - Click on OK (Repeat steps 4 and 5 for any other suitable graphs)
5) You now are returned to Report Options - Click on Overlays (bottom left of screen)
6) Pick up files you wish to overlay by clicking on the Browse button for each overlay
7) Click on OK and then Save and Close. The overlays are now added to that first file.
8) Click on Reports and then Start Report. Pick up the file to which the overlays have just been added. The graphs can be exported by first right clicking in the graph and saving as a metafile – this just puts the graphics on a clipboard. Open another package such as Word and paste the metafile directly in (Ctrl + V)

Bibliography

Bibliography

AALTO, R., MAURICE-BOURGOIN, L., DUNNE, T., MONTGOMERY, D. R., NITTROUER, C. A. & GUYOT, J. L. (2003) Episodic sediment accumulation on Amazonian flood plains influenced by El Nino/Southern Oscillation. *Nature,* 425**,** 493-496.

AALTO, R. & NITTROUER, C. A. (2012) 210Pb geochronology of flood events in large tropical river systems. *Phil. Trans. R. Soc. A* 370**,** 1-35.

ABSHIRE, J. B., SUN, X., RIRIS, H., SIROTA, J. M., MCGARRY, J. F., PALM, S., YI, D. & LIVA, P. (2005) Geoscience Laser Altimeter System (GLAS) on the ICEsat Mission: On-orbit measurement performance. *Geophysical Research Letters,* 32.

ADAMS, J. B., SABOL, D. E., KAPOS, V., FILHO, R. A., ROBERTS, D. A., SMITH, M. O. & GILLESPIE, A. R. (1995) Classification of multispectral images based on fractions of endmembers: application to landcover change in the Brazilian Amazon. *Remote Sensing of Environment,* 52**,** 137-154.

ADLER, R. F., BOLVIN, D. T., CURTIS, S. & NELKIN, E. J. (2000) Tropical rainfall distributions determined using TRMM combined with other satellite and rain gauge information. *Journal of Applied Meteorology,* 39**,** 2007-2023.

AGUIAR, A. P. D., SHIMABUKURO, Y. E. & MASCARENHAS, N. D. A. (1999) Use of synthetic bands derived from mixing models in the multispectral classification of remote sensing images. *International Journal of Remote Sensing,* 20**,** 647-657.

AGUILAR, F. J., AGUERA, F., AGUILAR, M. A. & CARVAJAL, F. (2005) Effects of Terrain Morphology, Sampling Density and Interpolation Methods on Grid DEM Accuracy. *Photogrammetric Engineering and Remote Sensing,* 71**,** 805-816.

ALI, A., QUADIR, D. A. & HUH, O. K. (1989) Study of the river flood hydrology in Bangladesh with AVHRR data. *International Journal of Remote Sensing,* 10**,** 1873-1891.

ALSDORF, D. & LETTENMAIER, D. P. (2003) Tracking fresh water from space. *Science,* 301**,** 1491-1494.

ALSDORF, D. E., BATES, P. D., MELACK, J., WILSON, M. D. & DUNNE, T. (2007) The spatial and temporal complexity of the Amazon flood measured from space. *Geophysical Research Letters,* 34.

ALSDORF, D. E., DUNNE, T., MELACK, J., SMITH, L. & HESS, L. (2005) Diffusion modelling of recessional flow on central Amazonian floodplains. *Geophysical Research Letters,* 32.

ALVES, D. S., SOARES, J. V., AMARAL, S., MELLO, E. M. K., ALMEIDA, S. A. S., DA SILVA, O. F. & SILVEIRA, A. M. (1997) Biomass of primary and secondary vegetation in Rondonia, Western Brazilian Amazon. *Global Change Biology,* 3**,** 451-461.

ANDERSON, M. C., HAIN, C., WARDLOW, B., PIMSTEIN, A., MECIKALSKI, J. R. & KUSTAS, W. P. (2011) Evaluation of drough indices based on thermal remote sensing of evapotranspiration over the continental United States. *Journal of Climate,* 24**,** 2025-2044.

ARAGAO, L. E. O. C., MALHI, Y., METCALFE, D. B., SILVA-ESPEJO, J. E., JIMENEZ, E., NAVARETTE, D., ALMEIDA, S., COSTA, A. C. L., SALINAS, N., PHILLIPS, O. L., ANDERSON, L. O., ALVAREZ, E., BAKER, T. R., GONCALVEZ, P. H., HUAMAN-OVALLE, J., MAMANI-SOLORZANO, M., MEIR, P., MONTEAGUDO, A., PATINO, S., PENUELA, M. C., PRIETO, A., QUESADA, C. A., ROZAS-DAVILA, A., RUDAS, A., SILVA, J. A. & VASQUEZ, R. M. (2009) Above- and below-ground net primary productivity across ten Amazonian forests on contrasting soils. *Biogeosciences,* 6**,** 2759-2778.

ARNESEN, A. S., SILVA, T. S. F., HESS, L., NOVO, E. M. L. M., RUDORFF, C. M., CHAPMAN, B. D. & MCDONALD, K. C. (2013) Monitoring flood extent in the lower Amazon River floodplain using ALOS/PALSAR ScanSAR images. *Remote Sensing of Environment,* 130**,** 51-61.

ARONICA, G., HANKIN, B. & BEVEN, K. (1998) Uncertainty and equifinality in calibrating distributed roughness coefficients in a flood propagation model with limited data. *Advances in Water Resources,* 22**,** 349-365.

ARONICA, G. T. & LANZA, L. G. (2005) Drainage efficiency in urban areas: a case study. *Hydrological Processes,* 19**,** 1105-1119.

AYRES, J. M. (1993) As matas de varzea do Mamiraua. . *Estudos de Mamiraua,* 1**,** 1-123.

BAKER, T. R., PHILLIPS, O. L., MALHI, Y., ALMEIDA, S., ARROYO, L., DI FIORE, A., ERWIN, T., KILLEEN, T., LAURANCE, S. G., LAURANCE, W. F., LEWIS, S., LLOYD, J., MONTEAGUDO, A., NEILL, D., PATINO, S., PITMAN, N., SILVA, J. A. & R.V, M. (2004) Variation in wood density determines spatial patterns in Amazonian forest biomass. *Global Change Biology,* 10**,** 504-562.

BALSLEV, H., LUTTEYN, J., YLLGAARD, B. & HOLM-NIELSEN, L. B. (1987) Composition and structure of adjacent unflooded and floodplain forest in Amazonian Ecuador. *Opera Botanica,* 92**,** 37-57.

BAMLER, R. (Ed.) (1999) *The SRTM mission: A worldwide 30m resolution DEM from SAR interferometry in 11 days.,* Heidelberg, Wichmann Verlag.

BARTHOLOME, E. & BELWARD, A. S. (2005) GLC2000: a new approach to global land cover mapping from Earth observation data. *International Journal of Remote Sensing,* 26.

BATES, P. D. (2000) Development and testing of a sub grid-scale model for moving-boundary hydrodynamic problems in shallow water. *Hydrological Processes,* 14**,** 1073-1088.

BATES, P. D. (2004) Remote sensing and flood inundation modelling. *Hydrological Processes,* 18**,** 2593-2957.

BATES, P. D. & DE ROO, A. J. P. (2000) A simple raster-based model for flood inundation simulation. *Journal of Hydrology,* 236**,** 54-77.

BATES, P. D., HORRITT, M. S. & FEWTRELL, T. J. (2010) A simple inertial formulation of the shallow water equations for efficient two-dimensional flood inundation modelling. *Journal of Hydrology,* 387**,** 33-45.

BATES, P. D., WILSON, M. D., HORRITT, M. S., MASON, D. C., HOLDEN, N. & CURRIE, A. (2006) Reach scale floodplain inundation dynamics observed using airborne synthetic aperature radar imagery: Data analysis and modelling. *Journal of Hydrology,* 328**,** 306-318.

BATISTELLA, M. (2001) Landscape Change and Land-Use/Land-Cover Dynamics in Rondonia, Brazilian Amazon. PhD Dissertation, Indiana University, Bloomington, Indiana**,** 399.

BATISTELLA, M., NOBRE, A. P., BUSTAMENTE, M. & LUIZAO, F. J. (2009) Results from LBA and a vision for future Amazonian research. *Amazonia and Global Change***,** 555-563.

BAUGH, C. A., BATES, P. D., SCHUMANN, G. & TRIGG, M. A. (2013a) SRTM vegetation removal and hydrodynamic modeling accuracy. *Water Resources Research,* 49**,** 5276-5289.

BAUGH, C. A., BATES, P. D., SCHUMANN, G. & TRIGG, M. A. (2013b) SRTM vegetation removal and hydrodynamic modeling accuracy. *Water Resources Research,* 49**,** 5276-5289.

BEGNUDELLI, L. A., VALIANI, B. F. & SANDERS, S. (2010) A balanced treatment of secondary currents, turbulence and dispersion in a deth-integrated hydrodynamic and bed deformation model for channel bends. *Advances in Water Resources,* 33**,** 17-33.

BELWARD, A. S., ESTES, J. E. & KILNE, K. D. (1999) The IGBP-DIS global 1 km land cover data set DISCover: a project overview. *Photogrammetric Engineering and Remote Sensing,* 65**,** 1013-1020.

BENDIX, J. & HUPP, C. R. (2000) Hydrological and geomorphological impacts on riparian plant communities. *Hydrological Processes,* 14**,** 2977-2990.

BENZ, U., HOFMANN, P., WILLHAUCK, G., LINGENFELDER, I. & HEYNEN, M. (2004) Multi-resolution, object oriented fuzzy analysis of remote sensing data for GIS-ready information. *ISPRS Journal of Photogrammetry and Remote Sensing,* 58**,** 239-258.

BERGMANN, H. & RICHTIG, G. (1990) Decision support for Improving Storm Drainage Management in Suburban Catchments. *Proceedings of the Fifth International Conference on Urban Storm Drainage***,** 1429-1434.

BERRY, P. A. M., GARLICK, J. D. & SMITH, R. G. (2007) Near-global validation of the SRTM DEM using satellite radar altimetry. *Remote Sensing of Environment,* 106**,** 17-27.

BHANG, K. J., SCHWARTZ, F. W. & BRAUN, A. (2007) Verification of the vertical error in C-Band SRTM DEM using ICESat and Landsat-7, Otter Tail County, MN. *Geoscience and Remote Sensing,* 45**,** 36-44.

BIRDSEY, R. A. & LEWIS, G. M. (2003) Carbon in U.S forests and wood products, 1987-1997, State-by-state estimates, Gen. Tech. Rep.

BIRKETT, C. (1998) Contribution of the TOPEX NASA radar altimeter to the global monitoring of large rivers and wetlands. *Journal of Geophysical Research: Atmospheres,* 34**,** 1223-1239.

BIRKETT, C. M., MERTES, L., DUNNE, T., COSTA, M. H. & JASINSKI, M. J. (2002) Surface water dynamics in the Amazon Basin: Application of satellite radar altimetry. *Journal of Geophysical Research,* 107.

BLASHKE, T. (2010) Object based image analysis for remote sensing. *ISPRS Journal of Photogrammetry and Remote Sensing,* 65**,** 2-16.

BLUMBERG, D. G. (2006) Analysis of large aeolian (wind-blown) bedforms using the Shuttle Radar Topography Mission (SRTM) digital elevation data. *Remote Sensing of Environment,* 100**,** 179-189.

BLYTH, K. & BIGGIN, D. S. (1993) Monitoring floodwater inundation with ERS-1 SAR. *Earth Observation Quarterly,* 42**,** 6-8.

BOARDMAN, J. W. (1989) Inversion of imaging spectrometry data using singular value decomposition. *Proceedings of 12th Canadian Symposium on Remote Sensing, IGARSS '89, SPIE,* 4**,** 2069-2072.

BOTKIN, D. B., JANAK, J. F. & WALLIS, J. R. (1972) Some ecological consequences of a computer model of forest growth. *Journal of Ecology,* 60**,** 849-872.

BOURGINE, B. & BAGHDADI, N. (2005) Assessment of C-band SRTM DEM in a dense equatorial forest zone. *Comptes Rendus Geoscience,* 337**,** 1225-1234.

BOURGINE, B., BAGHDADI, N., HOSFORD, S. & DANIELS, P. (2004) Generation of a ground-level DEM in a dense equatorial forest zone by merging airborne laser data and a top-of-canopy DEM. *Canadian Journal of Remote Sensing,* 30**,** 913-926.

BOURREL, L., MOREAU, S. & PHILLIPS, L. (1999) Dinamica de las inundaciiones en la cuenca amazonica de Bolivia. *Revista Boliviana de Ecologia y Conservacion Ambiental,* 6**,** 5-17.

BREIT, H., KNOPFLE, W., ADAM, N. & EINEDER, M. (2002) SRTM X-SAR DEM of Europe- Results and algorithmic improvements. *Geoscience and Remote Sensing Symposium, 2002,* 1**,** 155-157.

BRENNER, A. C., ZWALLY, H. J., BENTLEY, C. R., CSATHO, B. M., HARDING, D. J., HOFTON, M. A., MINSTER, J. B., ROBERTS, L., SABA, J. L. & THOMAS, R. H. (2003) Derivation of Range and Range distributions From Laser Pulse Waveform Analysis for Surface Elevations, Roughness, Slope and Vegetation Heights, Geoscience

Laser Altimeter System Algorithm Theoretical Basis Document Version 4.1, URL: http://www.csr.utexas.edu/glas/atbd.html.

BRONDIZIO, E., MORAN, E., MAUSEL, P. & WU, Y. (1996) Land cover in the Amazon estuary: Linking of TM with botanical and historical data. *Photogrammetric Engineering and Remote Sensing,* 69**,** 921-930.

BROWN, C. G. (2003) Tree height estimation using Shuttle Radar Topography Mission and ancillary data. PhD Thesis, Department of Electrical Engineering and Computer Science, The University of Michigan, Ann Arbor, MI.

BROWN, C. G. & SARABANDI, K. (2003) Estimation of red pine tree height using Shuttle Radar Topography Mission and ancillary data. *IEEE Geoscience and Remote Sensing Symposium,* 4**,** 2850-2852.

BROWN, C. G., SARABANDI, K. & PIERCE, L. E. (2005) Validation of the Shuttle Radar Topography Mission height data. *IEEE Transactions of on Geoscience and Remote Sensing,* 43**,** 1707-1715.

BROWN, S. (1997) Estimating biomass and biomass change of tropical forests. Rome: FAO.

BROWN, S. & LUGO, A. E. (1992) Aboveground biomass estimates for tropical moist forests of the Brazilian Amazon. *Interciencia,* 17**,** 8-18.

BUDRESKI, K. A., WYNNE, R. H., BROWDER, J. O. & CAMPBELL, J. B. (2007) Comparison of a segment and pixel-based non-parametric land cover classification in the Brazilian Amazon using multitemporal Landsat TM/ETM+ imagery. *Photogrammetric Engineering and Remote Sensing,* 73**,** 813-827.

BULLOCK, J. (1996) Plants. IN SUTHERLAND, W. J. (Ed.) *Ecological Census Techniques: A Handbook.* Cambridge, Cambridge University Press.

CALMANT, S. & SEYLER, F. (2006) Continental surface waters from satellite altimetry. *Comptes Rendus Geoscience,* 338**,** 1113-1122.

CAMPBELL, D. G., STONE, J. L. & ROSAS, A. (1992) A comparison of the phytosociology and dynamics of three floodplain (varzea) forests of known ages, Rio Jurua, western Brazilian Amazon. *Biological Journal of Linnean Society,* 108**,** 213-237.

CAMPOS, I. D., MERCIER, F., MAHEU, C., COCHONNEAU, G., KOSUTH, P., BLITZKOW, D. & CAZENAVE, A. (2001) Temporal variations of river basin waters from TOPEX/POSEIDON satellite altimetry. *Comptes*

Rendus De L Academie Des Sciences Serie Ii Fascicule a-Sciences De La Terre Et Des Planetes, 333**,** 633-643.

CARAJABAL, C. & HARDING, D. (2005) ICESat validation of SRTM C-band digital elevation models. *Geophysical Research Letters,* 32.

CARAJABAL, C. & HARDING, D. (2006) SRTM C-Band and ICESat Laser Altimetry Elevation Comparisons as a Function of Tree Cover and Relief. *Photogrammetric Engineering and Remote Sensing,* 72**,** 287-298.

CHAMBERS, J. Q., DOS SANTOS, J., RIBEIRO, R. J. & HIGUCHI, N. (2001) Tree damage, allometric relationships and above-ground net primary production in central Amazon forest. *Forest Ecology and Management,* 152**,** 73-84.

CHAPIN, F. S., ZAVALETA, E. S., EVINER, V. T. & NAYLOR, R. L. (2000) Consequences of changing biodiversity. *Nature,* 405**,** 234-242.

CHAVE, J. (1999) Study of structural, successional and spatial patterns in tropical rain forests using TROLL, a spatially explicit forest model. *Ecological Modelling,* 124**,** 233-254.

CHAVE, J., ANDALO, C., BROWN, S., CAIRNS, M. A., CHAMBERS, J. Q., EAMUS, D., FOLSTER, H., FROMARD, F., HIGUCHI, N., KIRA, T., LESCURE, J., P, NELSON, B. W., OGAWA, H., PUIG, H., RIERA, B. & YAMAKURA, T. (2005) Tree allometry and improved estimation of carbon stocks and balance in tropical forests. *Oecologia,* 145**,** 87-99.

CHAVE, J., CONDIT, R., AGUILAR, S., HERNANDEZ, A., LAO, S. & PEREZ, R. (2004) Error propagation and scaling for tropical forest biomass estimates. *Phil. Trans. R. Soc. B,* 359**,** 409-420.

CHAVE, J., COOMES, D. A., JANSEN, S., LEWIS, S. L., SWENSON, N. G. & ZANNE, A. E. (2009) Towards a worldwide wood economics spectrum. *Ecology Letters,* 12**,** 351-366.

CHAVEZ, P. S. (1996) Image-based atmospheric corrections-revisited and improved. *Photogrammetric Engineering and Remote Sensing,* 62**,** 1025-1036.

CHIDLEY, T. R. E. & DRAYTON, R. S. (1986) The use of SPOT-simulated imagery in hydological mapping. *International Journal of Remote Sensing,* 7**,** 791-799.

CHOUDHURY, B. J. (1989) Monitoring global land surface using NIMBUS-7 37 GHz data: theory and examples. *International Journal of Remote Sensing,* 10**,** 1579-1605.

CHOUDHURY, B. J. (1991) Passive microwave remote sensing remote sensing contribution to hydrological variables. *Surveys in Geophyics,* 12**,** 63-84.

CLARK, D. A., BROWN, S., KICKLIGHTER, D. W., CHAMBERS, J. Q., THOMLINSON, J. R. & NI, J. (2001b) Measuring net primary production in forests: Concepts and field methods. *Ecology applications,* 11**,** 356-370.

CLARK, D. A., BROWN, S., KICKLIGHTER, D. W., CHAMBERS, J. Q., THOMLINSON, J. R., NI, J. & HOLLAND, E. A. (2001a) Net primary production in tropical forests: An evaluation and synthesis of existing field data. *Ecology applications,* 11**,** 371-384.

COBBY, D. M., MASON, D. C. & DAVENPORT, I. J. (2001) Image processing of airborne scanning altimetry for improved river flood modelling. *ISPRS Journal of Photogrammetry and Remote Sensing,* 56**,** 121-138.

COE, M. T., COSTA, M. H., BOTTA, A. & BIRKETT, C. (2002) Long-term simulations of discharge and floods in the Amazon Basin. *Journal of Geophysical Research,* 107**,** 1-17.

COE, M. T., COSTA, M. H. & HOWARD, E. A. (2008) Simulating the surface waters of the Amazon River Basin: impacts of new river geomorphic and flow parameterisations. *Hydrological Processes,* 22**,** 2542-2553.

COE, M. T., COSTA, M. H. & SOARES-FILHO, B. S. (2009) The influence of historical and potential future deforestation on the stream flow of the Amazon River- Land surface processes and atmospheric feedbacks. *Journal of Hydrology,* 369**,** 165-174.

COSTA, M. H. & FOLEY, J. A. (1997) Water balance of the Amazon Basin: Dependence on vegetation cover and canopy conductance. *Journal of Geophysical Research: Atmospheres (1984-2012),* 102**,** 23973-23989.

COSTA, M. P. F. (2004) Use of SAR satellites for mapping zonation of vegetation communities in the Amazon floodplain. *International Journal of Remote Sensing,* 25**,** 1817-1835.

COULTHARD, T. J., HICKS, D. M. & VAN DE WIEL, M. J. (2007) Cellular modelling of river catchments and reaches: Advantages, limitations and prospects. *Geomorphology,* 90**,** 192-207.

CRAWFORD, R. M. M. (1992) Oxygen availability as an ecological limit to plant distribution. *Advances in Ecological Research,* 23**,** 93-185.

CURKENDALL, D., FIELDING, E., CHENG, T. & POHL, J. (2003) A computational grid based system for continental drainage network extraction using SRTM digital elevation models. *IEEE ICPP Workshops***,** 181-190.

DE OLIVEIRA, P. E. (1992) A Palynological record of Late Quaternary vegetation and climatic change in Southeastern Brazil. *PhD Thesis,* Ohio State University University.

DE OLIVEIRA, P. E. (2000) Palaeoecology and climate of the Amazon basin during the last glacial cycle. *Journal of Quaternary Science,* 15**,** 347-356.

DEFRIES, R. S. & TOWNSHEND, J. R. G. (1994) Global land cover: comparison of ground-based data sets to classifications with AVHRR data, In: G.M Foody and P.J Curran (Eds.). *Environmental remote sensing from regional to global scales,* Chichester: Wiley**,** 84-110.

DEL GROSSO, S., PARTON, W., STOHLGREN, T., ZHENG, D., BACHELET, D., PRINCE, S., HIBBARD, K. & OLSON, R. (2008) Global potential net primary production predicted from vegetation class, precipitation and temperature. *Ecology applications,* 89**,** 2117-2126.

DENEVAN (1980) La geografia cultural aborigen de los Llanos de Mojos. *Libreria Editorial Juventud: La Paz, Bolivia*.

DEUTSCH, M., RUGGLES, F. H., GUSS, P. & YOST, E. (1973) Mapping of the 1973 Mississippi river floods from the Earth Resources Technology Satellite. *Proceedings, International Symposium on Remote Sensing and Water Resources Management,,* American Water Resources Association, Proceedings No. 17**,** 39-55.

DIETRICH, W. E., REISS, R., HSU, M. L. & MONTGOMERY, D. R. (1995) A process-based model for colluvial soil depth and shallow landsliding using digital elevation data. *Hydrological Processes,* 9**,** 383-400.

DJORDJEVIC, S., PRODANOVIC, D. & MAKSIMIOVIC, C. (1999) An approach to simulation of dual drainage. *Water Science and Technology,* 39**,** 95-103.

DONG, Y., MILNE, A. K. & FORSTER, B. C. (2000) A Review of SAR Speckle Filters: Texture Restoration and Preservation. *Geoscience and Remote*

Sensing Symposium, 2000. Proceedings. IGARSS 2000. IEEE 2000 International, 2**,** 633-635.

DOUGLAS, I. (1999) Hydrological investigations of forest disturbance and land cover impacts in South-East Asia: a review. *Phil. Trans. R. Soc. B,* 354**,** 1725-1738.

DRAPEAU, G. (2013) Email regarding the integration of TRMM and rain gauge data in Bolivia. IN BUCKLEY, S. (Ed.). Exeter.

DUMONT, J. F. (1996) Neotectonics of the Subandes-Brazilian craton boundary using geomorphological data: the Maranon and Beni basins. *Tectonophysics,* 257**,** 137-151.

DUMONT, J. F. & HANAGARTH, W. (1993) River shifting and tectonics in the Beni Basin. *Third International Conference of Geomorphology, Hamilton, Canada.*

DUNNE, T., MERTES, L., MEADE, R. H., RICHEY, J. E. & FORSBERG, B. R. (1998) Exchanges of sediment between floodplain and channel of the Amazon river in Brazil. *GSA Bulletin,* 110**,** 450-347.

ENVIRONMENT AGENCY (2013) Geomatics LIDAR. IN AGENCY, E. (Ed.) *LIDAR.*

ESA/ESRIN (1995) *First ERS thematic Working Group Meeting on Flood Monitoring.* Frascati, Italy.

EVANS, T. L., COSTA, M. P. F., TELMER, K. H. & SILVA, T. S. F. (2010) Using ALOS/PALSAR and RADARSAT-2 to map land cover and seasonal inundation in the Brazilian Pantanal. *IEEE Journal of Selected Topics in Applied Earth Observations and Remote Sensing,* 3**,** 560-575.

FARR, T. & KOBRICK, M. (2000) Shuttle Radar Topography Mission produces a wealth of data. *AGU EOS,* 81**,** 583-585.

FEARNSIDE, P. M. (1992) Forest biomass in Brazilian Amazonia: comments on the estimate by Brown and Lugo. *Interciencia,* 17**,** 19-27.

FIELD, C. B., BEHRENFELD, M. J., RANDERSON, J. T. & FALKOWSKI, P. (1998) Primary Production of the Biosphere: Integrating Terrestrial and Oceanic Components. *Science,* 10**,** 237-240.

FISHER, P. (1997) The pixel: a snare and a delusion. *International Journal of Remote Sensing,* 18.

FOOD AND AGRICULTURE ORGANISATION (1993) Forest Resources Assessment 1990- Tropical Countries. *FAO Forestry Paper,* 112.

FOODY, G. M. (2000) Mapping land cover from remotely sensed data with a softened feedforward neural network classifcation. *Journal of Intelligent and Robotic Systems,* 29**,** 433-449.

FOODY, G. M. (2002) Status of land cover classification accuracy assessment. *Remote Sensing of Environment,* 80**,** 185-201.

FOSTER, R. B. (Ed.) (1980) *Heterogeneity and disturbance in tropical vegetation,* Sunderland, Sinauer Associates.

FOSTER, R. B., ARCE, B. J. & WACHTER, T. S. (Eds.) (1986) *Dispersal and the sequential plant communities in Amazonian Peru floodplain,* Dordrecht, Dr W Junk.

FRACCAROLLO, L. & TORO, E. F. (1995) Experiemental and numerical assessment of the shallow water model for two-dimensional dam-break type problems. *Journal of Hydraulic Research,* 33**,** 843-864.

FRANCESCHETTI, G., IODICE, A., MADDALUNO, S. & RICCIO, D. (2000) Effect of antenna mast motion on X-SAR/SRTM performance. *IEEE Transactions of on Geoscience and Remote Sensing,* 38**,** 2361-2372.

FRAPPART, F., SEYLER, F., MARTINEZ, J. M., LEON, J. & CAZENAVE, A. (2005) Floodplain water storage in the Negro River basin estimated from microwave remote sensing of inundation area and water levels. *Remote Sensing of Environment,* 99.

FRICKER, H. A., BORSA, A., MINSTER, J. B., CARAJABAL, C., QUINN, K. & BILLS, B. (2005) Assessment of ICESat performance at the salar de Uyuni, Bolivia. *Geophysical Research Letters,* 32.

FRIEDL, M. A., MCIVER, D. K., HODGES, J., ZHANG, X. Y., MUCHONEY, D., STRAHLER, A. H. & WOODCOCK, C. E. (2002) Global land cover mapping from MODIS: algorithms and early results. *Remote Sensing of Environment,* 83**,** 287-302.

FU, C., HAN, D., KIM, S. T. & GLOERSEN, P. (1988) Users guide for the Numbus 7 Scanning Multichannel Microwave Radiometer (SMMR). *Reference Publication 1210, US National Aeronautics and Space Administration: Washington DC*.

GARCIA-HARO, F. J., GILABERT, M. A. & MELIA, J. (1996) Linear spectral mixture modeling to estimate vegetation amount from optical data. *International Journal of Remote Sensing,* 17**,** 3373-3400.

GAUTIER, E., BRUNSTEIN, D., VAUCHEL, P., JOUANNEAU, J. M., ROULET, M., GARCIA, C., GUYOT, J. L. & CASTRO, M. (2010) Channel and floodplain sediment dynamics in a reach of the tropical meandering Rio Beni. *Earth Surface Processes and Landforms,* 35**,** 1838-1853.

GAUTIER, E., BRUNSTEIN, D., VAUCHEL, P., ROULET, M., FUERTES, O., GUYOT, J. L., DAROZZES, J. & BOURREL, L. (2007) Temporal relations between meander deformation, water discharge and sediment fluxes in the floodplain of the Rio Beni (Bolivian Amazonia). *Earth Surface Processes and Landforms,* 32**,** 230-248.

GLOERSEN, P., CAMPBELL, W. J., CAVALIERI, D. J., COMISO, J. C., PARKINSON, C. L. & ZWALLY, H. J. (1992) Arctic and Antarctic Sea Ice, 1978-1987: Satellite Passive-Microwave Observations and Analysis. *NASA SP-511, National Aeronautics and Space Administration; Washington DC*.

GOMES PEREIRA, L. M. & WICHERSON, R. J. (1999) Suitability of laser data for deriving geographical information. A case study in the context of management of fluvial zones. *ISPRS Journal of Photogrammetry and Remote Sensing,* 54**,** 105-114.

GRACE, J. (2004) Understanding and managing the global carbon cycle. *Journal of Ecology,* 92**,** 189-202.

GRAF, W. L. (1994) Plutonium in the Rio Grande: Environmental change and contamination in the nuclear age. *New York, Oxford University Press***,** 329.

GRATZER, G., CANHAM, C., DIECKMANN, U., FISCHER, A., IWASA, Y., LAW, R., LEXER, M., SANDMANN, H., SPIES, T. A. & SPLECHTNA, B. E. (2004) Spatio-temporal development of forests- current trends in field methods and models. *OIKOS,* 107**,** 3-15.

GUIMBERTEAU, M., DRAPEAU, G., RONCHAIL, J., SULTAN, B., POLCHER, J., MARTINEZ, J. M., PRIGENT, C., GUYOT, J. L., COCHONNEAU, G., ESPINOZA, J. C., FILIZOLA, N., FRAIZY, P., LAVADO, W., DE OLIVEIRA, E., POMBOSA, R., NORIEGA, L. & VAUCHEL, P. (2012) Discharge simulation in the sub-basins of the Amazon using ORCHIDEE forced by new datasets. *Hydrology and Earth System Sciences,* 16**,** 911-935.

GUYOT, J. L. (1993) Hydrogeochimie des Fleuves de l'Amazonie Bolivienne. *ORSTOM,* (Coll. Etudes et Theses).

GUYOT, J. L., JOUANNEAU, J. M. & WASSON, J. G. (1999) Characterisation of river bed and suspended sediments in the Rio Madeira drainage basin (Bolivian Amazonia). *Journal of South American Earth Science,* 12**,** 401-410.

HAASE, R. & BECK, S. (1989) Structure and Composition of Savanna Vegetation in Northern Bolivia: A preliminary report. *Brittonia***,** 80-100.

HALL, A. C., SCHUMANN, G., BAMBER, J. L. & BATES, P. D. (2011) Tracking water level changes of the Amazon Basin with space-borne remote sensing and integration with large scale hydrodynamic modelling: A review. *Physics and Chemistry of the Earth***,** 223-231.

HALL, J. W., TARANTOLA, S., BATES, P. D. & HORRITT, M. S. (2005) Distributed Sensitivity Analysis of Flood Inundation Model Calibration. *American Society of Civil Engineers, Journal of Hydraulic Engineering,* 131**,** 117-126.

HALL, M., NATIONAL, H., FRANK, E., HOLMES, G., PFAHRINGER, B. & REUTEMANN, P. (2009) The WEKA data mining software: An update. *SIGKDD Explorations,* 11**,** 10-18.

HALLBERG, G. R., HOYER, B. E. & RANGO, A. (1973) Application of ERTS-1 imagery to flood inundation mapping. *NASA Special Pub. No. 327, Symposium on significant results obtained from the Earth Resources Satellite-1, Vol. 1, Technical presentations, Section A***,** 745-753.

HAMILTON, S. E., SIPPEL, S. J. & MELACK, J. (2002) Comparison of inundation patterns among major South American floodplains. *Journal of Geophysical Research,* 107.

HAMILTON, S. E., SIPPEL, S. J. & MELACK, J. (2004) Seasonal inundation patterns in two large savanna floodplains of South America: the Llanos de Moxos (Bolivia) and the Llanos del Orinoco (Venezuela and Colombia). *Hydrological Processes,* 18**,** 2103-2116.

HAMILTON, S. K. (1999) Potential effects of a major navigation project (the Paraguay-Parana Hidrovia) on inundation in the Pantanal floodplains. *Regulated Rivers: Research and Management,* 15**,** 289-299.

HAMILTON, S. K., SIPPEL, S. J., CALHEIROS, D. F. & MELACK, J. (1997) An anoxic event and other biogeochemical effects of the Pantanal wetland on the Paraguay river. *Limnology and Oceanography,* 42**,** 257-272.

HAMILTON, S. K., SIPPEL, S. J. & MELACK, J. (1996) Inundation patterns in the Pantanal wetland of South America determined from passive microwave remote sensing. *Archiv fur Hydrobiologie,* 137**,** 1-23.

HANAGARTH, W. (1993) Acerca de la geoecología de las sábanas del Beni en el noreste de Bolivia. *Instituto de Ecologia, Universidad Mayor de San Andres: La Paz, Bolivia*.

HANAGARTH, W. (1996) Biogeographie der Beni_Savannen (Bolivien). *Geographische Rundschau,* 48**,** 662-669.

HANAGARTH, W. & SARMIENTO, J. (1990) Reporte preliminar sobre la geoecologia de la sabana de Espiritu y sus alredores (Llanos de Moxos, departamento del Beni, Bolivia). *Ecologia en Bolivia,* 16**,** 47-75.

HANSEN, M. C., DEFRIES, R. S., TOWNSHEND, J. R. G. & SOHLBERG, R. (2000) Global land cover classification at 1 km spatial resolution using a classification tree approach. *International Journal of Remote Sensing,* 21**,** 1331-1364.

HAPKE, B. (1981) Bidirectional reflectance spectroscopy, 1, theory. *Journal of Geophysical Research,* 86**,** 3039-3054.

HARTEN, A., LAX, P. D. & VAN LEER, B. (1983) On upstream differencing and Godunox-type schemes for hyperbolic conservation laws. *SIAM Reviews,* 25**,** 35-61.

HENSLEY, S., ROSEN, P. & GURROLA, E. (2000) Topographic map generation for the Shuttle Radar Topography Mission C-band SCANSAR interferometry. *Proceeding of SPIE,* 4152**,** 179-189.

HESS, L., MELACK, J., NOVO, E. M. L. M. & BARBOSA, C. C. F. (2003) Dual-season mapping of wetland inundation and vegetation for the central Amazon basin. *Remote Sensing of Environment,* 87**,** 404-428.

HESS, L., MELACK, J. & WANG, Y. (1995) Delineation of inundated area and vegetation along the Amazon floodplain with the SIR-C synthetic-aperture radar. *IEEE Transactions of on Geoscience and Remote Sensing,* 33**,** 896-904.

HESS, L. L., MELACK, J. M. & SIMONETT, D. S. (1990) Radar detection of flooding beneath the forest canopy- a review. *International Journal of Remote Sensing,* 11**,** 1313-1325.

HOFTON, M. A., BLAIR, J. B., MINSTER, J. B., WILLIAMS, N. P., BUFTON, J. L. & RABINE, D. (2000) An airborne scanning laser altimetry survey of Long Valley, California. *International Journal of Remote Sensing,* 21**,** 2413-2437.

HOFTON, M. A., DUBAYAH, R., BLAIR, J. B. & RABINE, D. (2006) Validation of SRTM Elevations Over Vegetated and Non-vegetated Terrain Using Medium Footprint Lidar. *Photogrammetric Engineering and Remote Sensing,* 72**,** 279-285.

HOUGHTON, R. A., LAWRENCE, K. T., HACKLER, J. L. & BROWN, S. (2001) The spatial distribution of forest biomass in the Brazilian Amazon: a comparison of estimates. *Global Change Biology,* 7**,** 731-746.

HSU, M. H., CHEN, S. H. & CHNAG, T. J. (2000) Inundation simulation for urban drainage basin with storm sewer system. *Journal of Hydrology,* 234**,** 21-37.

HUGGEL, C., SCHNEIDER, D., MIRANDA, J., DELGADO GRANADOS, H. & KAAB, A. (2008) Evaluation of ASTER and SRTM DEM data for lahar modelling: A case study on lahars from Popocatepetl Volcano, Mexico. *Journal of Volcanology and Geothermal Research,* 170**,** 99-110.

HUNTER, N. M., BATES, P. D., HORRITT, M. S. & WILSON, M. D. (2006) Improved simulation of flood flows using storage cell models. *Water Management,* 159**,** 9-18.

HUNTER, N. M., BATES, P. D., HORRITT, M. S. & WILSON, M. D. (2007) Simple spatially-distributed models for predicting flood inundation: a review. *Geomorphology,* 90**,** 208-225.

HUPP, C. R. (2000) Hydrology, geomorphology and vegetation of Coastal Plain Rivers in south-eastern USA. *Hydrological Processes,* 14**,** 2991-3010.

HURLBERT, S. (1984) Pseudoreplication and the design of ecological field experiments. *Ecological Monographs,* 54**,** 187-211.

INPE (2002) Monitoring of the Brazilian Amazon Forest by Satellite 2000-2001. Insituto Nacional de Pesquisas Espaciais**,** 21.

INTERGOVERNMENTAL PANEL ON CLIMATE CHANGE (1995) *Climate Change 1995: The Science of Climate Change*, Cambridge University Press.

IRION, G., JUNK, W. J. & MELLO, J. A. S. N. (1997) The large Central Amazonian river floodplain near Manaus: geological, climatological, hydrological and geomorphoological aspects. IN JUNK, W. J. (Ed.) *The Central Amazon Floodplains. Ecology of a pulsing system.* Berlin, Springer.

ISHIKAWA, A. & SAKAKIBARA, T. (1984) A Proposal of a New Simulation Model 'grid method' for Urban Storm Runoff Analysis and Design of Stormwater Systems. *Proceedings of the 3rd International Conference of Urban Storm Drainage* 1**,** 245-253.

JOHNSON, W. C. (2000) Tree recruitment and survival in rivers: Influences of hydrological processes. *Hydrological Processes,* 14**,** 3051-3074.

JOHNSSON, M. J. & MEADE, R. H. (1990) Chemical weathering of fluvial sediments during alluvial storage: The Macuapanim Island point bar, Solimoes River, Brazil. *Journal of Sedimentary Petrology,* 60**,** 827-842.

JONES, H. & R.A, V. (2010) *Remote Sensing of Vegetation: Principles, Techniques and Applications,* Oxford, Oxford University Press.

JUNK, W. J. (Ed.) (1983) *Ecology of swamps on the middle Amazon,* Amsterdam, Elsevier.

JUNK, W. J. (Ed.) (1989) *Flood tolerance and tree distribution in central Amazonian floodplains,* London, Academic Press.

JUNK, W. J. (Ed.) (1997) *General aspects of floodplain ecology with special reference to Amazonian floodplains,* Berlin, Springer.

JUNK, W. J., BAYLEY, P. B. & SPARKS, R. E. (1989) The flood pulse concept in river-flood systems. *Proceedings of the International Large River Symposium, Ottawa, Canadian Special Publications of Fisheries and Aquatic Sciences,* 106**,** 110-127.

JUNK, W. J., OHLY, J. J., PIEDADE, M. T. F. & SOARES, M. G. (2000) *The Central Amazon Floodplain: Actual Use and Options for a Sustainable Management,* Leiden, Netherlands, Backhuys Publishers.

KALLIOLA, R. J., SALO, J. S., PUHAKKA, M. & RAJASILTA, M. (1991) New Site Formation and Colonising Vegetation in Primary Succession on the Western Amazon Floodplains. *Journal of Ecology,* 79**,** 877-901.

KALLIOLA, R. J., SALO, J. S., PUHAKKA, M., RAJASILTA, M., HAME, T., NELLER, R. J. & RASANEN, M. E. (1992) Upper Amazon Channel Migration. *Naturwissenschaften,* 79**,** 75-79.

KASISCHKE, E. S. & BOURGEAU-CHAVEZ, L. L. (1997) Monitoring South Florida wetlands using ERS-1 SAR imagery. *Photogrammetric Engineering and Remote Sensing,* 63**,** 281-291.

KAWAKUBO, F. S., MORATO, R. B. & LUCHIARI, A. (2013) Use of fraction imagery, segmentation and masking techniques to classify land-use and land-cover types in the Brazilian Amazon. *International Journal of Remote Sensing,* 34**,** 5452-5467.

KAWAKUBO, F. S., MORATO, R. B., MIDAGLIA, C., GOMIDE, M. L. C. & LUCHIARI (2009) Land use and vegetation cover mapping of an indigenous land area in the state of Mato Grosso (Brazil) based on spectral linear mixing model, segmentation and regional classification. *Geocarto International,* 24**,** 165-175.

KEELING, C. D. & WHORF, T. P. (Eds.) (1999) *Atmospheric CO_2 records from sites in the SIO air sampling network,* Carbon Dioxide Information Analysis Center, Oak Ridge National Laboratory.

KELLER, M., PALACE, M. & HURTT, G. (2001) Biomass estimation in the Tapajos National Forest, Brazil: examination of sampling and allometric uncertainties. *Forest Ecology and Management,* 154**,** 371-382.

KELLNDORFER, J. M., WALKER, W. S., PIERCE, L. E., DOBSON, C., FITES, J. A. & HUNSAKER, C. (2004) Vegetation height estimation from Shuttle Topography Mission and National Elevation Datasets. *Remote Sensing of Environment,* 93**,** 339-358.

KESEL, R. H., YODIS, E. G. & MCCRAW, J. (1992) An approximation of the sediment budget of lower Mississippi river prior to major human modification. *Earth Surface Processes and Landforms,* 17**,** 711-722.

KNOX, J. C. (1987) Historical valley floor sedimentation in the upper Mississippi Valley. *Association of American Geographers Annals,* 77**,** 224-244.

KOBAYASHI, Y., SARABANDI, K. & DOBSON, M. C. (2000) An evaluation of the JPL TOPSAR for extracting tree heights. *IEEE Transactions on Geoscience and Remote Sensing***,** 2446-2454.

KOCAK, G., BUYUKSALIH, G. & JACOBSEN, K. (2004) Analysis of digital elevation models determined by high resolution space images.

International Archives of Photogrammetry and Remote Sensing, 35**,** 636-641.

KOCH, A. & HEIPKE, C. (2001) Quality assessment of digital surface models derived from the Shuttle Radar Topography Mission. *IEEE Geoscience and Remote Sensing Symposium,* 6**,** 2863-2865.

KOHAVI, R. & QUINLAN, R. (2002) Decision tree discovery. IN KLOSGEN, W. & J.M, Z. (Eds.) *Handbook of data mining and knowledge discovery.* Oxford, Oxford University.

KOHLER, P., HUTH, A. & DITZER, T. (1999) Concepts for the aggregation of tropical tree species into functional types and the application on Sabahs dipterocarp lowland rainforests. *Journal of Tropical Ecology*.

KOLSTROM, M. (1998) Ecological simulation model for studying diversity of stand structure in boreal forests. *Ecological Modelling,* 111**,** 17-36.

KUMMEROW, C., SIMPSON, J., THIELE, O., BARNES, W. & CHANG, A. T. C. (2000) The Status of the Tropical Rainfall Measuring Mission (TRMM) after two years in orbit. *Journal of Applied Meteorology,* 39**,** 1965-1982.

LAMOTTE, S. (1990) Fluvial dynamics and succession in the lower Ucayali River basin, Peruvian Amazonia. *Forest Ecology and Management,* 33**,** 141-156.

LEE, J. S., JURKEVICH, L., DEWAELE, P., WAMBACQ, P. & OOSTERLINCK, A. (1994) Speckle filtering of synthetic aperture radar images: A review. *Remote Sensing Reviews,* 8**,** 313-340.

LEEMANS, R. (1992) Simulation and future projection of succession in a Swedish broad-leaved forest. *Forest Ecology and Management,* 48**,** 305-319.

LEFSKY, M. A., HARDING, D., KELLER, M., COHEN, W. B., CARAJABAL, C. & ESPIRITO-SANTO, F. D. B. (2005) Estimates of forest canopy height and aboveground biomass using ICESat. *Geophysical Research Letters,* 32.

LEON, J. G., CALMANT, S., SEYLER, F., BONNET, M. P., CAUHOPE, M., FRAPPART, F., FILIZOLA, N. & FRAIZY, P. (2006) Rating curves and estimation of average water depth at the upper Negro River based on satellite altimeter data and modeled discharges. *Journal of Hydrology,* 3-4**,** 481-496.

LEOPOLD, L. B. & WOLMAN, M. G. (1957) River channel patterns- braided, meandering and straight. *US Geological Survey Professional Paper,* 282-B.

LEWIN, J., DAVIES, B. E. & WOLFENDEN, P. J. (1977) Interactions between channel change and historic mining sediments. IN GREGORY, K. J. (Ed.) *River channel changes.* Chichester, John Wiley.

LEWIS, W. M., HAMILTON, S. K., LASI, M. A., RODRIGUEZ, M. & SAUNDERS, J. F. (2000) Ecological determinism on the Orinoco floodplain. *Bioscience,* 50**,** 681-692.

LIANG, Q., DU, G., HALL, J. W. & BORTHWICK, A. G. L. (2008) Flood inundation modelling with an adaptive quadtree grid shallow water equation solver. *Journal of Hydraulic Engineering,* 134**,** 1603-1610.

LILLESAND, T. M., KIEFER, R. W. & CHIPMAN, J. W. (2008) *Remote Sensing and Image Interpretation: Sixth Edition,* Hoboken, John Wiley and Sons.

LIU, J. G. & ASHTON, P. S. (1998) FORMOSAIC: an individual-based spatially explicit mode for simulating forest dynamics in landscape mosaics. *Ecological Modelling,* 106**,** 177-200.

LIU, X. (2008) Airborne LiDAR for DEM generation: some critical issues. *Progress in Physical Geography,* 32**,** 31-49.

LOUBENS, G., LAUZANNE, L. & LE GUENNEC, B. (1992) Les milieux aquatiques de la region de Trinidad (Beni, Amazonie, bolivienne). *Revue d'Hydrobiologie Tropicale,* 3**,** 21.

LOVELAND, T. R., REED, B. C., BROWN, J. F., OHLEN, D. O., ZHU, J. & YANG, L. (2000) Development of a global land cover characteristics database and IGBP DISCover from 1-km AVHRR data. *International Journal of Remote Sensing,* 21**,** 1303-1330.

LOVELAND, T. R., ZHU, J., OHLEN, D. O., BROWN, J. F., REED, B. C. & YANG, L. (1999) An analysis of the IGBP global land-cover characterisation process. *Photogrammetric Engineering and Remote Sensing,* 65**,** 1021-1032.

LU, D., BATISTELLA, M. & MORAN, E. (2003a) Integration of vegetation inventory data and Thematic Mapper image for Amazonian successional and mature forest classification. *Proceedings of the ASPRS 2003 Annual Conference,* Anchorage, Alaska.

LU, D., BATISTELLA, M. & MORAN, E. (2007) Land-cover classification in the Brazilian Amazon with the integration of Landsat ETM+ and Radarsat data. *International Journal of Remote Sensing,* 28**,** 5447-5459.

LU, D., BATISTELLA, M., MORAN, E. & MAUSEL, P. (2004a) Application of spectral mixture analysis to Amazonian land-use and land-cover classification. *International Journal of Remote Sensing,* 25**,** 5345-5358.

LU, D., MAUSEL, P., BATISTELLA, M. & MORAN, E. (2004b) Comparison of land-cover classification methods in the Brazilian Amazon basin. . *Photogrammetric Engineering and Remote Sensing,* 70**,** 723-731.

LU, D., MAUSEL, P., BRONDIZIO, E. & MORAN, E. (2002) Assessment of atmospheric correction methods for Landsat TM data applicable to Amazon basin LBA research. *International Journal of Remote Sensing,* 23**,** 2651-2671.

LU, D., MORAN, E. & BATISTELLA, M. (2003b) Linear mixture model applied to Amazonian vegetation classification. *Remote Sensing of Environment,* 87**,** 456-469.

LUCAS, R. M., HONZAK, M., FOODY, G. M., CURRAN, P. & CORVES, C. (1993) Characterising tropical secondary forests using multitemporal Landsat sensor imagery. *International Journal of Remote Sensing,* 14**,** 3061-3067.

LUYSSAERT, S., INGLIMA, I., JUNG, M., RICHARDSON, A. D. & REICHSTEIN, M. (2007) CO_2 balance of boreal, temperate and tropical forests derived from a global database. *Global Change Biology,* 13**,** 2509-2537.

MAGNUSSEN, S. & BOUDEWYN, P. (1998) Derivation of stand heights from airborne laser scanner data with canopy-based quantile estimators. *Canadian Journal of Forest Research,* 28**,** 1016-1031.

MAGNUSSEN, S., EGGERMONT, P. & LARICCIA, V. N. (1999) Recovering tree heights from airborne laser scanner data. *Forest Science,* 45**,** 407-422.

MALHI, Y., ARAGAO, L. E. O. C., METCALFE, D. B., PAIVA, R., QUESADA, C. A., ALMEIDA, S., ANDERSON, L. O., BRANDO, P., CHAMBERS, J. Q., COSTA, A. C. L., HUTYRA, L., OLIVIERA, P., PATINO, S., E.H, P., ROBERTSON, A. L. & TEIXEIRA, L. M. (2009) Comprehensive

assessment of carbon productivity, allocation and storage in three Amazonian forests. *Global Change Biology,* 15**,** 1255-1274.

MALHI, Y., BAKER, T. R., WRIGHT, T., ALMEIDA, S., ARROYO, S., FREDERIKSEN, T., GRACE, J., HIGUCHI, N., KILLEEN, T., LAURANCE, W. F., LEANO, C., LEWIS, S., MEIR, P., MONTEAGUDO, A., NEILL, D., NUNES VARGAS, P., PANFIL, S. N., PATINO, S., PITTMAN, N., QUESADA, C. A., RUDAS, A., SALOMAO, R., SALESKA, S., SILVA, N., SILVIEIRA, M., SOMBROEK, W. G., VALENCIA, R., VASQUEZ-MARTINEZ, R., VIEIRA, I. C. G. & VINCENTI, B. (2004) The above-ground coarse wood productivity of 104 neotropical forest plots. *Global Change Biology,* 10**,** 1-29.

MALHI, Y. & GRACE, J. (2000) Tropical forests and atmospheric carbon dioxide. *Trends in Ecology and Evolution,* 15**,** 332-344.

MALHI, Y., WOOD, D. & BAKER, T. R. (2006) The regional variation of aboveground live biomass in old-growth Amazonian forests. *Global Change Biology,* 12**,** 1107-1138.

MARRON, D. C. (1992) Floodplain storage of mine tailings in the Belle Fourche river system: A sediment budget approach. *Earth Surface Processes and Landforms,* 7**,** 675-685.

MARTINELLI, L. A., VICTORIA, R. L., DE CAMARGO, P. B., CASSIA PICCOLO, M., MERTES, L., RICHEY, J. E., DEVOL, A. H. & FORSBERG, B. R. (2003) Inland variability of carbon-nitrogen concentrations and delta^{13}C in Amazon floodplain (varzea) vegetation and sediment. *Hydrological Processes,* 17**,** 1419-1430.

MARTINEZ, J. M. & LE TOAN, T. (2007a) Mapping of flood dynamics and spatial distribution of vegetation in the Amazon floodplain using multitemporal SAR data. *Remote Sensing of Environment,* 108**,** 209-223.

MARTINEZ, J. M. & LE TOAN, T. (2007b) Mapping of flood inundation dynamics and spatial distribution of vegetation in the Amazon floodplain using multitemporal SAR data. *Remote Sensing of Environment,* 108**,** 209-223.

MAURICE-BOURGOIN, L., RONCHAIL, J., VAUCHEL, P., AALTO, R., GUYOT, J. L. & GALLAIRE, R. (2003) ENSO climate connection to flooding of the Beni River, a large Andean tributary of the Amazon. *Geographical Research Abstracts,* 5**,** 9895.

MAUSEL, P., WU, P., LI, Y., MORAN, E. & BRONDIZIO, E. (1993) Spectral identification of succession stages following deforestation in Amazonia. *Geocarto International,* 8**,** 11-20.

MAYLE, F., LANGSTROTH, R., FISHER, R. A. & MEIR, P. (2007) Long-term forest-savannah dynamics in the Bolivian Amazon: implications for conservation. *Phil. Trans. R. Soc. B,* 362**,** 291-307.

MCCLEARY, A. L., CREWS-MEYER, K. A. & YOUNG, K. R. (2008) Refining forest classifications in the western Amazon using an intra-annual multitemporal approach. *International Journal of Remote Sensing,* 29**,** 991-1006.

MCKENNEY, R., JACOBSEN, R. B. & WERTHEIMER, R. C. (1995) Woody vegetation and channel morphogenesis in low gradient, gravel bed streams in the Ozark Plateaus, Missouri and Arkansas. *Geomorphology,* 13**,** 175-198.

MEADE, R. H. (1985) Suspended sediment in the Amazon River and its tributaries in Brazil during 1982-1984. *U.S Geological Survey Open-File Report,* 85**,** 39.

MEANS, J. E., ACKER, S. A., HARDING, D., BLAIR, J. B., LEFSKY, M. A., COHEN, W. B., HAMON, M. E. & MCKEE, W. A. (1999) Use of Large-Footprint Scanning Airborne Lidar to Estimate Forest Stand Characteristics in the Western Cascades of Oregon. *Remote Sensing of Environment,* 67**,** 298-308.

MELACK, J. & FORSBERG, B. R. (2001) Biogeochemistry of Amazon floodplain lakes and associated wetlands. IN MCCLAIN, M. E., VICTORIA, R. L. & RICHEY, J. E. (Eds.) *The Biogeochemistry of the Amazon Basin and its Role in a Changing World.* New York, Oxford University Press.

MELACK, J., HESS, L., GASTIL, M., FORSBERG, B. R., HAMILTON, S. K., LIMA, I. B. T. & NOVO, E. M. L. M. (2004) Regionalisation of methane emissions in the Amazon Basin with microwave remote sensing. *Global Change Biology,* 10**,** 530-544.

MELACK, J. & WANG, Y. (1998) Delineation of flooded area and flooded vegetation in Balbina Reservior (Amazonas, Brazil) with synthetic aperture radar. *Verhandlungen des Internationalen Vereinigung Limnologischen,* 26**,** 2374-2377.

MERTES, L. (1990) Hydrology, hydraulics, sediment transport and geomorphology of the Central Amazon floodplain [PhD. thesis]. *Seattle, University of Washington*, 225.

MERTES, L. (2002) Remote sensing of riverine landscapes. *Freshwater Biology,* 47, 799-816.

MERTES, L., DUNNE, T. & MARTINELLI, L. A. (1996) Channel-floodplain geomorphology along the Solimoes-Amazon River, Brazil. *GSA Bulletin,* 180, 1089-1107.

METCALFE, D. B., MEIR, P., ARAGAO, L. E. O. C., GALBRAITH, D., FISHER, R. A. & CHAVES, M. (2010) Shifts in plant respiration and carbon use efficiency at a large scale drought experiment in the eastern Amazon. *New Phytologist,* 187, 608-621.

MIGHAM, C. G. & CAUSON, D. M. (1998) High resolution finite-volume method for shallow water flows. *Journal of Hydraulic Engineering,* 124, 605-614.

MILNE, A. K., HORNE, G. & FINLAYSON, C. M. (1998) Monitoring wetland inundation patterns using RADARSAT multitemporal data. *RADARSAT ADRO Final Symposium, October, Montreal, Quebec*, 13-15.

MIRANDA, F. P., FONSECA, L. E. N., BEISL, C. H., ROSENQVIST, A. & FIGUEIREDO, M. D. M. A. M. (1997) Seasonal mapping of flood extent in the vicinity of the Balbina Dam (Central Amazonia) using RADARSAT-1 and JERS-1 SAR data. IN AHERN, F. J. (Ed.) *RADARSAT for Amazonia: Results of ProRADAR investigations.* Ottawa, Canada Centre for Remote Sensing.

MONTEITH, J. L. (1965) Evaporation and environment. *Symposium of the society of experimental biology,* 19, 205-224.

MOREAU, S. & BOURREL, L. (1997) Hydrogeodynamics of the wetlands of the Bolivian Amazon. IN AHERN, F. J. (Ed.) *RADARSAT for Amazonia: Results of ProRADAR Investigations.* Ottawa, Canada Centre for Remote Sensing.

MU, Q., MAOSHENG, M. & RUNNING, S. (2011) Improvements to a MODIS global terrestrial evapotranspiration algorithm. *Remote Sensing of Environment,* 115, 1781-1800.

MUSTARD, J. F. & SUNSHINE, J. M. (1999) Spectral analysis for Earth Science: Investigations using remote sensing data. IN RENCZ, A. N.

(Ed.) *Remote Sensing for the Earth Sciences: Manual of Remote Sensing, vol 3.* New York, Wiley.

NEAL, J. C., FEWTRELL, T. J. & TRIGG, M. A. (2009) Parallelisation of storage cell flood models using OpenMP. *Environmental Modelling and Software,* 24**,** 872-877.

NEWTON, A. (2007) *Forest Ecology and Conservation: A Handbook of Techniques,* Oxford, Oxford University Press

NICHOLAS, A. P., ASHWORTH, P. J., SAMBROOK SMITH, G. H. & SANDBACH, S. D. (2013) Numerical simulation of bad and island morphodynamics in anabranching mega-rivers. *Journal of Geophysical Research,* 118**,** 1-26.

NICHOLAS, A. P. & MITCHELL, C. A. (2003) Numerical simulation of overbank processes in topographically complex floodplain environments. *Hydrological Processes,* 17**,** 727-746.

NICHOLAS, A. P., SANDBACH, S. D., ASHWORTH, P. J., AMSLER, M. L., BEST, J. L., HARDY, R. J., LANE, S. N., ORFEO, O., PARSONS, D. H., REESINK, A. J. H., SAMBROOK SMITH, G. H. & SZUPIANY, R. N. (2012) Modelling hydrodynamics in the Rio Parana, Argentina: an evaluation and inter-comparison of reduced complexity and physics based models applied to a large sand-bed river. *Geomorphology,* 169-170**,** 192-211.

NICHOLSON, S. E., SOME, B., MCCOLLUM, E., NELKIN, E., KLOTTER, D., BERTE, Y., DIALLO, B. M., GAYE, I., KPABEBA, G., NDIAYE, O., NOUKPOZOUNKOU, J. N., TANU, M. M., THIAM, A., TOURE, A. A. & TRAORE, A. K. (2003) Validation of TRMM and Other Rainfall Estimates with a High-Density Gauge Dataset for West Africa. Part II: Validation of TRMM Rainfall Products. *Journal of Applied Meteorology,* 42**,** 1355-1369.

NILSSON, M. (1996) Estimation of tree heights and stand volume using an airborne lidar system. *Remote Sensing of Environment,* 56**,** 1-7.

ORMSBY, J. P., BLANCHARD, B. J. & BLANCHARD, A. J. (1985) Detection of lowland flooding using active microwave systems. *Photogrammetric Engineering and Remote Sensing,* 51**,** 317-328.

PAROLIN, P. (2001) Morphological and physiological adjustments to waterlogging and drought in seedlings of Amazonian floodplain trees. *Oecologia,* 128**,** 326-335.

PAROLIN, P. (2009) Submerged in darkness: adaptations to prolonged submergence by woody species of Amazonian floodplains. *Annals of Botany,* 103**,** 359-376.

PAROLIN, P. & JUNK, W. J. (2002) The effect of submergence on seed germination in trees of Amazonian floodplains. *Boletim do Museu Paraense Emilio Goeldi Serie Botanica,* 18**,** 321-329.

PEIXOTO, J. M. A., NELSON, B. W. & WITTMANN, F. (2009) Spatial and temporal dynamics of river channel migration and vegetation in central Amazonian white-water floodplains by remote sensing techniques. *Remote Sensing of Environment,* 113**,** 2258-2266.

PENNER, J. E., CHARLSON, R. J. & SCHWARTZ, S. E. (1994) Quantifying and minimising uncertainty of cliamte forcing by anthropogenic aerosols. *Bulletins of the American Meteorological Society,* 75**,** 375-400.

PERUCCA, E., CAMPOREALE, C. & RIDOLFI, L. (2006) Influence of river meandering dynamics on riparian vegetation pattern formation. *Journal of Geophysical Research,* 111.

PHILLIPS, O. L., MALHI, Y., HIGUCHI, N., LAURANCE, W. F., NUNEZ, P. V., VASQUEZ, R. M., LAURANCE, S. G., FERRIERA, L. V., STERN, M., BROWN, S. & GRACE, J. (1998) Changes in the Carbon Balance of Tropical Forests: Evidence from Long-Term Plots. *Science,* 282.

PICKETT, S. T. A. (1991) Long-term studies: past experiences and recommendations for the future. IN RISSER, P. G. (Ed.) *Long-term ecological research. An international perspective.*, John Wiley and Sons.

PIEDADE, M., JUNK, W. J. & PAROLIN, P. (2006) Phenology, fruit production and seed dispersal of Astrocaryum jauari (Arecacease) in Amazonian black-water floodplains. *Revista de Biologia Tropical,* 54.

PIEGAY, H., BORNETTE, G., CITTERIO, A., HEROUIN, E., MOULIN, B. & STATIOTIS, C. (2000) Channel instability as a control on silting dynamics and vegetation patterns within perifluvial aquatic zones. *Hydrological Processes,* 14**,** 3011-3029.

PLAFKER, G. (1964) Oriented lakes and lineaments of northeastern Bolivia. *Bulletins of the Geological Society of America,* 75**,** 503-522.

POPE, K. O., REY-BENAYAS, J. M. & PARIS, J. F. (1994) Radar remote sensing of forest and wetland ecosystems in the Central Amazon tropics. *Remote Sensing of Environment,* 48**,** 205-219.

PORTE, A. & BARTELINK, H. H. (2002) Modelling mixed forest growth: a review of models for forest management. *Ecological Modelling,* 150**,** 141-188.

POTTER, C. S., BROOKS-GENOVESE, V., KLOOSTER, S. A., BOBO, M. & TORREGROSA, A. (2001) Biomass burning losses of carbon estimated from ecosystem modelling and satellite data analysis for the Brazilian Amazon region. *Atmospheric Environment,* 35**,** 1773-1781.

POUILLY, M., BECK, S., MORAES, M. & IBANEZ, C. (2004) Diversidad Biologica en la Llanura de Inundacion del Rio Mamore- Importancia Ecologica de la Dinamica Fluvial. *Centro de Ecologia,* Santa Cruz, Bolivia.

POULTER, B., ARAGAO, L. E. O. C., HEYDER, U., GUMPENBURGER, M., HEINKE, J., LANGERWISCHE, F., RAMMIG, A., THONICKE, K. & CRAMER, W. (2010) Net biome production of the Amazon Basin in the 21st century. *Global Change Biology,* 16**,** 2062-2075.

PRANCE, G. T. (1979) Notes on the vegetation of Amazonia III. The terminology of Amazonian forest types subject to inundation. *Brittonia,* 31**,** 26-38.

PRETZSCH, H. (1992) *Konzeption und Konstruktion von Wuchmodellen fuer Rein- und Mischbestaende,* Forstl Forschungsber, Ludwig Maximilians Universitaet Munchen.

PUHAKKA, M. & KALLIOLA, R. J. (1995) Floodplain vegetation mosaics in western Amazonia. *Biogeographica,* 71**,** 1-14.

PUISSANT, A., HIRSCH, J. & WEBER, C. (2005) The utility of texture analysis to improve per-pixel classification for high to very high spatial resolution imagery. *International Journal of Remote Sensing,* 26**,** 733-745.

QUESADA, C. A., LLOYD, J., SCWARZ, M., BAKER, T. R., PHILLIPS, O. L., PATINO, S., CZIMCZIK, C., HODNET, M. G., HERRARA, R., ARNETH, A., LLOYD, G., MALHI, Y., DEZZEO, N., LUIZAO, F. J., SANTOS, A. J. B., SCHMERLER, J., ARROYO, L., SILVIEIRA, M., PRIANTE FILHO, N., JIMENEZ, E., PAIVA, R., VIEIRA, I. C. G., NEILL, D., SILVA, J. A., PENUELA, M. C., MONTEAGUDO, A., VASQUEZ, R. M., PRIETO, A.,

RUDAS, A., ALMEIDA, S., HIGUCHI, N., LEZAMA, A. T., LOPEZ-GONZALEZ, G., PEACOCK, J., FYLLAS, N. M., ALVAREZ DAVILA, E., ERWIN, T., DE FIORE, A., CHAO, K. J., HONORIO, E., KILLEEN, T., PENA CRUZ, A., PITMAN, N., NUNES VARGAS, P., SALOMAO, R., TERBORGH, J. & RAMREZ, H. (2009a) Regional and large scale patterns in Amazon forest structure and function are mediated by variations in soil physical and chemical properties. *Biogeosciences Discussion,* 6**,** 3993-4057.

RABER, G. T., JENSEN, J. R., SCHILL, S. R. & SCHUCKMAN, K. (2002) Creation of Digital Terrain Models Using an Adaptive LiDAR Vegetation Point Removal Process. *Photogrammetric Engineering and Remote Sensing,* 68**,** 1307-1315.

RABUS, B., EINEDER, M., ROTH, A. & BAMLER, R. (2003) The Shuttle Radar Topography Mission- A new class of digital elevation models acquired by spaceborne radar. *Photogrammetric Engineering and Remote Sensing,* 57**,** 241-262.

RASANEN, M. E., SALO, J. S. & KALLIOLA, R. J. (1987) Long-term fluvial perturbance in the Western Amazon basin: Regulation by sub-Andean tectonics. *Science,* 238**,** 1398-1401.

REUTER, H. I. & NELSON, A. (2007) An evaluation of void filling interpolation methods for SRTM data. *International Journal of Geographical Information Science,* 21**,** 938-1008.

REUTER, H. I., NELSON, A. & JARVIS, A. (2007) An evaluation of void-filling interpolation methods for SRTM data. *International Journal of Geographical Information Science,* 21**,** 101-116.

RIBEIRO, J., HOPKINS, M., VICENTINI, A., SOTHERS, C. & COSTA, M. H. (1999) Flora de Reserva Ducke, Guia de identificacao das plantas vasculares de uma floreste de terra firme na Amazonia central. *INPA-DFID, Manaus*.

RICHARDS, J. A. & JIA, X. (1999) Remote Sensing Digital Image Analysis: An Introduction. Springer-Verlag, Berlin, Germany**,** 363.

RICHARDS, K., BRASINGTON, J. & HUGHES, F. (2002) Geomorphic dynamics of floodplains: Implications and a potential modelling strategy. *Freshwater Biology,* 47**,** 559-579.

RICHEY, J. E., MELACK, J., AUFDENKAMPE, A. K., BALLESTER, V. M. & HESS, L. (2002) Outgassing from Amazonian rivers and wetlands as a large tropical source of atmospheric CO_2. *Nature,* 416**,** 617-620.

RICHEY, J. E., NOBRE, C. & DESER, C. (1989) Amazon River Discharge and Climate Variability: 1903 to 1985. *Science,* 246**,** 101-103.

RIERA, B., PELISSIER, R. & HOULLIER, F. (1998) Caracterisation d'une mosaique forestiere et de sa dynamique en foret tropical humide sempervirente. *Biotropica,* 30**,** 251-260.

RIGNOT, E. J. M., SALAS, W. & SKOLE, D. L. (1997) Mapping deforestation and secondary growth in Rondonia, Brazil, using imaging radar and Thematic Mapper data. *Remote Sensing of Environment,* 59**,** 167-179.

RIGNOT, E. J. M. & VAN ZYL, J. (1993) Change detection techniques for ERS-1 SAR data. *IEEE Transactions of on Geoscience and Remote Sensing,* 31**,** 896-906.

ROBERTS, D. A., BATISTA, G. T., PEREIRA, J. L. G., WALLER, E. K. & NELSON, B. W. (1998a) Change identification using multitemporal spectral mixture analysis:applications in eastern Amazonia. IN LUNETTA, R. S. & ELVIDGE, C. D. (Eds.) *Remote Sensing Change Detection : Environmental Monitoring Methods and Applications.* Chelsea, Ann Arbor Press.

ROBERTS, D. A., GARDNER, M., CHURCH, R., USTIN, S. L., SCHEER, G. & GREEN, R. O. (1998b) Mapping chaparral in the Santa Monica mountains using multiple endmember spectral mixing models. *Remote Sensing of Environment,* 65**,** 267-279.

RODRIGUEZ-ITURBE, I., PORPORATO, A., RIDOLFI, L., ISHAM, V. & COX, D. (1999) Water balance at a point: The role of climate, soil and vegetation. *Proceedings of the Royal Society London, Ser A,* 455**,** 3789-3809.

RODRIGUEZ, E., MORRIS, C. S. & BELZ, J. E. (2006) A global assessment of the SRTM performance. *Photogrammetric Engineering and Remote Sensing,* 72**,** 249-260.

RODRIGUEZ, E., MORRIS, C. S., BELZ, J. E., CHAPIN, E. C., MARTIN, J. M., DAFFER, W. & HENSLEY, S. (2005) An Assessment of the SRTM Topographic Products. *Nasa Jet Propulsion Laboratory*.

RONCHAIL, J., BOURREL, L., COCHONNEAU, G., VAUCHEL, P., PHILLIPS, L., CASTRO, A. & DE OLIVEIRA, R. (2005) Inundations in the Mamore Basin (south-western Amazon-Bolivia) and sea-surface temperature in Pacific and Atlantic oceans. *Journal of Hydrology,* 302**,** 223-238.

RONCHAIL, J., COCHONNEAU, G., MOLINIER, M., GUYOT, J. L., GUIMARAES, V. & DE OLIVEIRA, E. (2002) Interannual rainfall variability of the Amazon Basin and sea-surface temperatures in the Pacific and Atlantic Oceans. *International Journal of Climatology,* 22**,** 1663-1686.

ROSEN, P., HENSLEY, S., GURROLA, E., CHAN, S. & MARTIN, J. (2001) SRTM C-band topographic data: Quality assessments and calibration activities. *IEEE Geoscience and Remote Sensing Symposium,* 2**,** 739-741.

ROSENQVIST, A., FORSBERG, B., PIMENTEL, T., RAUSTE, Y. A. & RICHEY, J. E. (2002) The use of spaceborne radar data to model inundation patterns and trace gas emissions in the central Amazon floodplain.

ROSENQVIST, A., SHIMADA, M., ITO, N. & WATANABE, M. (2007) ALOS PALSAR: A pathfinder mission for global-scale monitoring of the environment. *IEEE Transactions of on Geoscience and Remote Sensing,* 45**,** 3307-3316.

SAATCHI, S. S., HARRIS, N., BROWN, S., LEFSKY, M. A., MITCHARD, E., SALAS, W., ZUTA, B., BUERMANN, W., LEWIS, S. L., HAGEN, S., PETROVA, S., WHITE, L., SILMAN, M. & MOREL, A. (2011) Benchmark map of forest carbon stocks in tropical regions across three continents. *Proceedings of the National Academy of Sciences,* 108**,** 9899-9904.

SAATCHI, S. S., HOUGHTON, R. A., DOS SANTOS ALVALA, R. C., SOARES, J. V. & YU, Y. (2007) Distribution of aboveground live biomass in the Amazon basin. *Global Change Biology,* 13**,** 816-837.

SAATCHI, S. S., NELSON, B. W., PODEST, E. & HOLT, J. (2000) Mapping land cover types in the Amazon Basin using 1 km JERS-1 mosaic. *International Journal of Remote Sensing,* 21**,** 1201-1234.

SAKAMOTO, T., NGUYEN, N. V., KOTERA, A., OHNO, H., ISHITSUKA, N. & YOKOZAWA, M. (2007) Detecting temporal changes in the extent of annual flooding within the Cambodia and Vietnamese Mekong Delta from

MODIS time-series imagery. *Remote Sensing of Environment,* 109**,** 295-313.

SALO, J. S. & KALLIOLA, R. J. (Eds.) (1991) *River dynamics and natural forest regeneration in the Peruvian Amazon,* Frome, Unesco Man and the Biosphere Series 6.

SALO, J. S., KALLIOLA, R. J., HAKKINEN, I., MAKINEN, Y., NIEMELA, P., PUHAKKA, M. & COLEY, P. D. (1986) River dynamics and the diversity of Amazon lowland forest. *Nature,* 322**,** 254-258.

SALTELLI, A. (2000) What is sensitivity analysis? IN SALTELLI, A., CHAN, K. & SCOTT, E. M. (Eds.) *Sensitivity Analysis.* Chichester, Wiley.

SALTELLI, A., RATTO, M., ANDRES, T., CAMPAGOLONGO, J., CARIBONI, J., GATELLI, M., SASSANA, M. & TARANTOLA, S. (2008) *Global Sensitivity Analysis; The Primer,* Chichester, Wiley.

SANYAL, J. & LU, X. (2004) Application of Remote Sensing in Flood Management with Special Reference to Monsoon Asia: A Review. *Natural Hazards,* 33**,** 283-301.

SARABANDI, K. & LIN, Y. C. (2000) Simulation of interferometric SAR response for characterising the scattering phase centre statistics of forest canopies. *IEEE Geoscience and Remote Sensing Symposium***,** 115-125.

SCARANO, F. R., CATTANIO, J. H. & CRAWFORD, R. M. M. (1994) Root carbohydrate storage in young saplings of an Amazonian tidal varzea forest before the onset of the wet season. *Acta Botanica Brasilica,* 8**,** 129-139.

SCHIMEL, D. S., HOUSE, J. I., HIBBARD, K., BOUSQUET, P., CIAIS, P., PEYLIN, P., BRASWELL, B. H., APPS, M. J., BAKER, D., BONDEAU, A., CANADELL, J., CHURKINA, G., CRAMER, W., DENNING, A. S., FIELD, C. B., FRIEDLINGSTEIN, P., GOODALE, C., HEIMANN, M., HOUGHTON, R. A., MELILLO, J. M., MOORE, B., MUDIYARSO, D., NOBLE, I., PACALA, S. W., PRENTICE, I. C., RAUPACH, M. R., RAYNER, P. J., SCHOLES, R. J., STEFFEN, W. L. & WIRTH, C. (2001) Recent patterns and mechanisms of carbon exchange by terrestrial ecosystems. *Nature,* 414**,** 169-172.

SCHLUTER, U. & CRAWFORD, R. M. M. (2001) Long-term anoxia tolerance in leaves of Acorus calamus L. and Iris pseudacorus. *Journal of Experimental Botany,* 52**,** 2213-2225.

SCHONGART, J. (2003) Dendrochronologische Untersuchungen in Uberchwemmungs-waldern der arzea Zentralamazoniens. IN BOHNEL, H., TIESSEN, H. & WEIDELT, H. J. (Eds.) *Gottinger Beitrage zur Land- und Forstwirtschaft in den Tropen und Subtropen.* Gottingen, Germany.

SCHONGART, J., ARIERA, J., FELFILI FORTES, C., CEZARINE DE ARRUDA, E. & NUNES DA CUNHA, C. (2008) Carbon dynamics in aboveground wood biomass of wetland forests in the northern Pantanal, Brazil. *Biogeosciences Discussions,* 5**,** 2103-2130.

SCHONGART, J. & JUNK, W. J. (2007) Forecasting the flood-pulse in Central Amazonia by ENSO-indices. *Journal of Hydrology,* 335**,** 124-132.

SCHONGART, J., JUNK, W. J., PIEDADE, M., AYRES, J. M., HUTTERMANN, A. & WORBES, M. (2004) Tele-connection between tree growth in the Amazonian floodplains and the El Nino-Southern Oscillation effect. *Global Change Biology,* 10**,** 581-597.

SCHUELER, T. R. & HOLLAND, H. K. (2000) Practice of watershed protection. Wetter is not always better: flood tolerance of woody species. *Technical Note #52 from Watershed Protection Techniques 1: 208-210 Article 35. Centre for Watershed Protection, Ellicott City, MD*.

SCHUTZ, B., ZWALLY, H. J., SHUMAN, C. A., HANCOCK, D. & DIMARZIO, J. P. (2005) Overview of the ICESat mission. *Geophysical Research Letters,* 32.

SELLERS, P. J., DICKINSON, R. E., RANDALL, D. A. & BETTS, A. K. (1997) Modeling the exchanges of energy, water and carbon between continents and the atmosphere. *Science,* 275**,** 502-509.

SHAO, G. F., SCHALL, P. & WEISHAMPEL, J. F. (1994) Dynamic simulations of mixed broadleaved- Pinus koraiensis forests in the Changbaishan biosphere reserve of China. *Forest Ecology and Management,* 70**,** 169-181.

SHIMABUKURO, Y. E., BATISTA, G. T., MELIO, E. M. K., MOREIRA, J. C. & DUARTE, V. (1998) Using shade fraction image segementation to evaluate deforestation in Landsat Thematic Mapper images of the Amazon region. *International Journal of Remote Sensing,* 19.

SHIMADA, M., ISOGUCHI, O., TADANO, T. & ISONO, K. (2009) PALSAR radiometric and geometric calibration. *IEEE Transactions of on Geoscience and Remote Sensing,* 47**,** 3915-3932.

SILVA, T. S. F., COSTA, M. P. F. & MELACK, J. (2010) Spatial and temporal variability of macrophyte cover and productivity in the eastern Amazon floodplain: A remote sensing approach. *Remote Sensing of Environment,* 114**,** 1998-2010.

SIMPSON, J., KUMMEROW, C., TAO, W. K. & ADLER, R. F. (1996) On the tropical rainfall measuring mission (TRMM). *Meteorology and Atmospheric physics,* 60**,** 19-36.

SINGER, R. B. & MCCORD, T. B. (1979) Mars: large scale mixing of bright and dark surface materials and implications for analysis of spectral reflectance. *Proceedings of the 10th Lunar and Planetary Science Conference, Houston, USA***,** 1835-1848.

SIPPEL, S. J., HAMILTON, S. K. & MELACK, J. (1992) Inundation area and morphometry of lakes on the Amazon River floodplain, Brazil. *Archives of Hydrobiology,* 123**,** 385-400.

SIPPEL, S. J., HAMILTON, S. K., MELACK, J. & NOVO, E. M. L. M. (1998) Passive microwave observations of inundation area and the area/stage relation in the Amazon River floodplain. *International Journal of Remote Sensing,* 19**,** 3055-3074.

SIPPEL, S. J., HAMILTON, S. K., MELACK, J. M. & CHOUDHURY, B. J. (1994) Determination of inundation area in the Amazon River floodplain using the SMMR 37 GHz polarisation difference. *Remote Sensing of Environment,* 48**,** 70-76.

SKOLE, D. L., CHOMENTOWSKI, W. H., SALAS, W. A. & NOBRE, A. D. (1994) Physical and human dimensions of deforestation in Amazonia. *Bioscience***,** 314-322.

SMALL, C. (2001) Estimation of urban vegetation abundance by spectral mixture analysis. *International Journal of Remote Sensing,* 22**,** 1305-1334.

SMALL, C. (2004) The Landsat ETM+ spectral mixing space. *Remote Sensing of Environment,* 93**,** 1-17.

SMITH, B. & SANDWELL, D. (2003) Accuracy and resolution of Shuttle Radar Topography Mission data. *Geophysical Research Letters***,** 1467-1470.

SMITH, L. (1997) Satellite remote rensing of river inundation area, stage and discharge: a review. *Hydrological Processes,* 11**,** 1427-1439.

SMITH, M. B. (2006) Comment on 'Analysis and modeling of flooding in urban drainage systems'. *Journal of Hydrology,* 317**,** 355-363.

SMITH, M. O., JOHNSTON, P. E. & ADAMS, J. B. (1985) Quantitative determination of mineral types and abundances from reflectance spectra using principle components analysis. *Journal of Geophysical Research,* 90**,** 797-804.

STRAATSMA, M. W. & BAPTIST, M. J. (2008) Floodplain roughness parameterisation using airborne laser scanning and spectral remote sensing. *Remote Sensing of Environment,* 112**,** 1062-1080.

SUN, D., YU, Y. & GOLDBERG, M. D. (2011) Deriving Water Fraction and Flood Maps From MODIS Images Using a Decision Tree Approach. *IEEE Journal of Selected Topics in Applied Earth Observations and Remote Sensing,* 4**,** 1939-1404.

SUN, G., RANSON, K. J., KHARUK, V. I. & KOVACS, K. (2003) Validation of surface height from Shuttle Radar Topography Mission using shuttle laser altimeter. *Remote Sensing of Environment,* 88**,** 401-411.

SUN, G., RANSON, K. J., KIMES, D. S., BLAIR, J. B. & KOVACS, K. (2008) Forest vertical structure from GLAS: An evaluation using LVIS and SRTM data. *Remote Sensing of Environment,* 112**,** 107-117.

TIAN, H., MELILLO, J. M. & KICKLIGHTER, D. W. (1998) Effect of interannual climate variability on carbon storage in Amazonian ecosystems. *Nature,* 398**,** 664-667.

TIMMERMANN, A., OBERHUBER, J., BACHER, A., ESCH, M., LATIF, M. & ROECKNER, E. (1999) Increased El Nino frequency in a climate model forced by future greenhouse warming. *Nature,* 398**,** 694-697.

TOUTIN, T. (2000) Evaluation of radargrammetric DEM from RADARSAT images in high relief areas. *Geoscience and Remote Sensing,* 38**,** 782-789.

TOWNSEND, P. A. (2001) Mapping Seasonal Flooding in Forested Wetlands Using Multi-Temporal Radarsat SAR. *Photogrammetric Engineering and Remote Sensing,* 67**,** 857-864.

TOWNSEND, P. A. & WALSH, S. J. (1998) Modeling floodplain inundation using an integrated GIS with radar and optical remote sensing. *Geomorphology,* 21**,** 295-312.

TOWNSHEND, J. R. G. (1992) Land cover. *International Journal of Remote Sensing,* 13**,** 1319-1328.

TREUHAFT, R. N. & SIQUEIRA, P. R. (2000) Verical structure of vegetated land surfaces from interferometric and polarimetric radar. *Radio Science,* 35.

TRIGG, M. A., WILSON, M. D., BATES, P. D., HORRITT, M., ALSDORF, D., FORSBERG, B. & VEGA, M. C. (2009) Amazon flood wave hydraulics. *Journal of Hydrology,* 374**,** 92-105.

TRUEHAFT, R. N., LAW, B. E. & ASNER, G. P. (2004) Forest attributes from radar interferometric structure and its fusion with optical remote sensing. *Bioscience,* 54**,** 561-571.

UHL, C., NEPSTAD, D., BUSCHBACHER, R. & CLARK, K. (1990) Studies of ecosystem response to antural and anthropogenic disturbances provide guidelines for designing sustainable land use systems in Amazonia. *Alternatives to deforestation: steps towards sustainable use of the Amazon rainforest***,** 24-42.

ULABY, F. T., MOORE, R. K. & FUNG, A. K. (1981) Microwave Remote Sensing: Active and Passive. *Volume 1: Microwave Remote Sensing Fundamentals and Radiometry, Addison-Wesley, Reading MA*.

USGS (2003) Shuttle Radar Topography Mission documentation: SRTM Topo. http://edcftp.cr.usgs.gov/pub/data/srtm/Documentation/SRTM_TOPO.txt.

USGS (2005) Shuttle Radar Topography Mission (SRTM)- 'Finished' products. IN SURVEY, U. S. G. (Ed.).

USGS (2013) National Elevation Dataset: About. IN USGS (Ed.) *National Elevation Dataset.*

USTIN, S. L., HART, Q. J., DUAN, L. & SCHEER, G. (1996) Vegetation mapping on hardwood rangelands in California. *International Journal of Remote Sensing,* 17**,** 3015-3036.

VAN DE WIEL, M. J., COULTHARD, T. J., MACKLIN, M. G. & LEWIN, J. (2007) Embedding reach-scale fluvial dynamics within the CAESAR cellular automaton landscape evolution model. *Geomorphology,* 90**,** 283-301.

VAN DER MEER, F. & DE JONG, S. M. (2000a) Improving the results of spectral unmixing of Landsat Thematic Mapper imagery by enhancing the orthoganality of end members. *International Journal of Remote Sensing,* 21**,** 2781-2797.

VAN DER MEER, F. & DE JONG, S. M. (2000b) Improving the results of spectral unmixing of Landsat Thematic Mapper imagery by enhancing the orthogonality of end-members. *International Journal of Remote Sensing,* 21**,** 2781-2797.

VANNOTE, R. L., MINSHALL, G. W., CUMMINS, K. W., SEDELL, J. R. & CUSHING, C. E. (1980) The River Continuum Concept. *Canadian Journal of Fisheries and Aquatic Science,* 37**,** 130-137.

VELOSO, H. P., RANGEL FILHO, A. L. R. & LIMA, J. C. A. (1991) Classificao da Vegetao Brasiliera, adaptada a um Sistema Universal. IBGE, Rio de Janeiro.

VILA DA SILVA, J. S. & KUX, H. J. H. (1992) Thematic mapper and GIS data integration to evaluate the flooding dynamics within the Pantanal, Mato Grosso do Sul State, Brazil. *Proceedings, 1992 Int. Geosci. Remote Sens. Symp. (IGARSS '92)* 1478-1480.

VITOUSEK, P. (1994) Beyond global warming: ecology and global change. *Ecology,* 75**,** 1861-1876.

VOESENEK, L. A. C. J., RIJNDERS, J. H. G. M., PEETERS, A. J. M. & VAN DE STEEG, H. M. V. (2004) Plant hormones regulate fast shoot elongation under water: from genes to communities. *Ecology applications,* 85**,** 16-27.

VOROSMARTY, C. J., MOORE, I., GRACE, A. L., GILDEA, M. P., MELILO, J. M., PETERSON, B. J. & RASTETTER, E. D. (1989) Continental-scale models of water balance and fluvial transport: an application to South America. *Global Biogeochemical Cycles,* 3**,** 241-265.

WAINWRIGHT, J. & MULLIGAN, M. (2004) *Environmental modelling: finding simplicity in complexity,* Chichester, John Wiley and Sons.

WALKER, W. S., KELLNDORFER, J. M. & PIERCE, L. E. (2007) Quality assessment of SRTM C- and X-band interferometric data: Implications for retrieval of vegetation canopy height. *Remote Sensing of Environment,* 106**,** 428-448.

WANG, Y., HESS, L., FILOSO, S. & MELACK, J. (1995) Understanding the Radar Backscattering from Flooded and Nonflooded Amazonian Forests: Results from Canopy Backscatter Modelling. *Remote Sensing of Environment,* 54**,** 324-332.

WEYDAHL, D. J., SAGSTUEN, J., DICK, O. B. & RONNING, H. (2007) SRTM DEM accuracy assessment over vegetated areas in Norway. *International Journal of Remote Sensing,* 28**,** 3513-3527.

WILSON, M. D., BATES, P. D., ALSDORF, D., FORSBERG, B., HORRITT, M., MELACK, J., FRAPPART, F. & FAMIGLIETTI, J. (2007) Modelling large-scale inundation of Amazonian seasonally flooded wetlands. *Geographical Research Letters,* 34.

WITTMANN, F., ANHUF, D. & JUNK, W. J. (2002) Tree species distribution and community structure of Central Amazonian varzea forests by remote sensing techniques. *Journal of Tropical Ecology,* 18**,** 851-860.

WITTMANN, F., JUNK, W. J. & PIEDADE, M. (2004) The varzea forests in Amazonia: flooding and the highly dynamic geomorphology interact with natural forest succession. *Forest Ecology and Management,* 196**,** 199-212.

WITTMANN, F., SCHONGART, J. & MONTERO, J. C. (2006a) Tree species composition and diversity gradients in white-water forests across the Amazon Basin. *Journal of Biogeography,* 33**,** 1334-1347.

WITTMANN, F., SCHONGART, J., PAROLIN, P., WORBES, M., PIEDADE, M. & JUNK, W. J. (2006b) Wood specific gravity of trees in Amazonian white-water forests in relation to flooding. *IAWA Journal,* 27**,** 255-268.

WOLFF, D. B., MARKS, D. A., AMITAL, E., SILBERSTEIN, D. S., FISHER, B. L., TOKAY, A., WANG, J. & PIPPITT, J. L. (2004) Ground Validation for the Tropical Rainfall Measuring Mission (TRMM). *Journal of Atmospheric and Oceanic Technology,* 22**,** 366.

WORBES, M. (1985) Structural and other adaptations to long-term flooding by trees in Central Amazonia. *Amazoniana,* 9**,** 459-484.

WORBES, M. (1995) How to measure growth dynamics in tropical trees- a review. *IAWA Journal,* 16**,** 337-351.

WORBES, M., KLINGE, H. & REVILLA, J. D. (1992a) On the dynamics, floristic subdivision and geographical distribution of varzea forests in Central Amazonia. *Journal of Vegetation Science,* 3**,** 553-564.

WORBES, M., KLINGE, H., REVILLA, J. D. & MARTIUS, C. (1992b) On the dynamics, floristic subdivision and geographical distribution of varzea forests in central Amazonia. *Journal of Vegetation Science,* 2**,** 553-564.

YAMAZAKI, D., BAUGH, C. A., BATES, P. D., KANAE, S., ALSDORF, D. & OKI, T. (2012) Adjustment of spaceborne DEM for use in floodplain hydrodynamic modeling. *Journal of Hydrology,* 436-437**,** 81-91.

YAO, J. (1970) Influence of growth rate on specific gravity and other selected properties of Loblolly Pine. *Wood Science and Technology,* 4**,** 163-175.

YU, D. & LANE, S. N. (2006) Urban fluvial flood modelling using a twodimensional diffusion-wave treatment, part 1: mesh resolution effects. *Hydrological Processes,* 20**,** 1541-1565.

ZAKHAROVA, E. A., KOURAEV, A. V., CAZENAVE, A. & SEYLER, F. (2006) Amazon River discharge estimated from TOPEX/Poseidon altimetry. *Comptes Rendus Geoscience,* 338**,** 188-196.

ZANOBETTI, D., LONGERE, H., PRIESSMAN, A. & CUNGE, J. A. (1970) Mekong delta mathematical model program construction. *American Society of Civil Engineers,* 96**,** 181-199.

ZEBKER, H. A., FARR, T. G., SALAZAR, R. P. & DIXON, T. H. (1994) Mapping the worlds topography using radar interferometry: The TOPSAT mission. *Proceedings of the IEEE,* 82**,** 1774-1786.

ZWALLY, H. J., SCHUTZ, B., ABDALATI, W., ABSHIRE, J. B., BENTLEY, C. R., BRENNER, A. C., BUFTON, J. L., DEZIO, J., HANCOCK, D., HARDING, D., HERRING, T., MINSTER, B., QUINN, K., PALM, S., SPINHIRNE, J. & THOMAS, R. H. (2002) ICESats laser measurements of polar ice, atmosphere, ocean and land. *Journal of Geodynamics,* 34**,** 405-445.